Transactions of the ASME®

Transactions of the ASME, Journal of Turbomachinery (ISSN 0889-504X) is published quarterly (Jan., Apr., July, Oct.) for $125.00 per year by The American Society of Mechanical Engineers, 345 East 47th Street, New York, NY 10017. Second class postage paid at New York, NY and additional mailing offices. POSTMASTER: Send address change to Transactions of the ASME, Journal of Turbomachinery, c/o THE AMERICAN SOCIETY OF MECHANICAL ENGINEERS, 22 Law Drive, Box 2300, Fairfield, NJ 07007-2300.

CHANGES OF ADDRESS must be received at Society headquarters seven weeks before they are to be effective. Please send old label and new address.

PRICES: To members, $36.00, annually; to nonmembers, $125.00.
Add $15.00 for postage to countries outside the United States and Canada.

INDEXED by Applied Mechanics Reviews and Engineering Information, Inc.
Canadian Goods & Services Tax Registration #126148048

Journal of Turbomachinery

Published Quarterly by The American Society of Mechanical Engineers

VOLUME 113 • NUMBER 3 • JULY 1991

TECHNICAL PAPERS

(Contents Continued on p. 338)

(Contents Continued)

Heat Transfer in Rotating Serpentine Passages With Smooth Walls

J. H. Wagner

B. V. Johnson
United Technologies Research Center,
East Hartford, CT 06108

F. C. Kopper
Pratt and Whitney,
Commercial Engine Business,
East Hartford, CT 06108

Experiments were conducted to determine the effects of buoyancy and Coriolis forces on heat transfer in turbine blade internal coolant passages. The experiments were conducted with a large-scale, multipass, smooth-wall heat transfer model with both radially inward and outward flow. An analysis of the governing flow equations showed that four parameters influence the heat transfer in rotating passages: coolant-to-wall temperature ratio, Rossby number, Reynolds number, and radius-to-passage hydraulic diameter ratio. These four parameters were varied over ranges that are typical of advanced gas turbine engine operating conditions. It was found that both Coriolis and buoyancy effects must be considered in turbine blade cooling designs and that the effect of rotation on the heat transfer coefficients was markedly different depending on the flow direction. Local heat transfer coefficients were found to decrease by as much as 60 percent and increase by 250 percent from no-rotation levels. Comparisons with a pioneering stationary vertical tube buoyancy experiment showed reasonably good agreement. Correlation of the data is achieved employing dimensionless parameters derived from the governing flow equations.

Introduction

In advanced gas turbine engines, increased temperatures, stage pressure ratios, and rotor speeds are used to increase thrust/weight ratios and reduce the specific fuel consumption. Hence, the turbine blades are subjected to increased external gas path heat loads in addition to increased levels of stress. Efficient internal convection cooling is essential to achieving good fuel consumption and acceptable blade life. Knowledge of the local heat transfer in the cooling passages is extremely important in the prediction of blade metal temperatures, i.e., blade life. Rotation of turbine blade cooling passages gives rise to Coriolis and buoyancy forces that can significantly alter the local heat transfer in the internal coolant passages from the development of cross stream (Coriolis), as well as radial (buoyant) secondary flows. Buoyancy forces in gas turbine blades are substantial because of the high rotational speeds and coolant temperature gradients. Earlier investigations (e.g., Eckert et al., 1953) with single pass co- and counterflowing stationary coolant passages indicated that there can also be substantial differences in the heat transfer when the buoyancy forces are aligned with or counter to the forced convection direction. A better understanding of Coriolis and buoyancy effects and the capability to predict the heat transfer response to these effects will allow the turbine blade designer to achieve cooling configurations that utilize less flow and that reduce thermal stresses in the airfoil.

The complex coupling of the Coriolis and buoyancy forces has prompted many investigators to study the flow field generated in unheated, rotating circular and rectangular passages without the added complexity of buoyancy (Hart, 1971; Wagner and Velkoff, 1972; Moore, 1967; Johnston et al., 1972; Rothe and Johnston, 1979). These investigators have documented strong secondary flows and have identified aspects of flow stability that produce streamwise-oriented, vortexlike structures in the flow of rotating radial passages.

The effects of buoyancy on heat transfer without the complicating effects of Coriolis-generated secondary flow have been studied in vertical stationary ducts. Effects of buoyancy on heat transfer were reported by Eckert et al. (1953), Metais and Eckert (1964), and Brundrett and Burroughs (1967). Flow criteria for forced-, mixed-, and free-convection heat transfer were developed for parallel flow and counterflow configurations by Eckert et al. (1953) and Metais and Eckert (1964). Based on these experimental results, buoyancy forces would be expected to cause significant changes in the heat transfer in turbine blade coolant passages and be strongly dependent on flow direction (radially inward versus radially outward).

The combined effects of Coriolis and buoyancy forces on heat transfer have been studied by a number of investigators. Heat transfer in rotating, smooth-wall models has been investigated by Guidez (1989), Clifford (1985), Iskakov and Trushin (1983), Morris (1981), Morris and Ayhan (1979), Lokai and Gunchenko (1979), Johnson (1978), and Mori et al. (1971). Large increases and decreases in local heat transfer were found to occur by some investigators under certain conditions of rotation while others showed lesser effects. Analysis of these results does not show consistent trends. The inconsistency of

Contributed by the International Gas Turbine Institute and presented at the 35th International Gas Turbine and Aeroengine Congress and Exposition, Brussels, Belgium, June 11–14, 1990. Manuscript received by the International Gas Turbine Institute January 17, 1990. Paper No. 90-GT-331.

the previous results is attributed to differences in the measurement techniques, models, and test conditions.

A comprehensive experimental program was formulated to identify and separate effects of Coriolis and buoyancy for the range dimensionless flow parameters encountered in axial flow, aircraft gas turbines. The overall objective of this experimental program was to acquire and correlate benchmark-quality heat transfer data for a multipass, coolant passage under conditions similar to those experienced in the blades of advanced aircraft gas turbines. Heat transfer results were obtained under varying conditions of flow rate, rotation, model radius, and wall-to-coolant temperature difference. The experiments were conducted by varying each parameter while holding the remaining parameters constant. The data was analyzed to separate the effects of Reynolds number, Coriolis forces, buoyancy, streamwise location, flow direction, and geometric location in the coolant passage (i.e., leading or trailing surfaces).

The results presented in this paper are from the first phase of a three-phase program directed at studying the effects of rotation on a multipass model with smooth and rough wall configurations. The first phase utilized the smooth wall configuration. Subsequent phases to be reported in the future include surface roughness elements oriented at 90 and 45 deg to the flow direction. Local heat transfer results were obtained along the smooth-wall coolant passage and around its periphery for radial outflow and inflow conditions. This paper presents heat transfer results obtained in the first, second, and third radial passages of a multipass, smooth-wall, square passage model. The results for outward flow in the first passage were previously presented by Wagner et al. (1991). The flow direction in the first and third passage was radially outward. The flow direction of the connecting second passage was radially inward. The effect of flow direction on heat transfer in rotating coolant passages is the main focus of this paper. The results will show that significant differences occur in the heat transfer depending on flow direction and surface location. A paper with a more comprehensive discussion of the heat transfer in the turn regions is forthcoming and will be published after additional analysis.

The facility, data acquisition, and data reduction techniques employed in this experiment were discussed in the Wagner et al. (1991) paper and will not be repeated. However, the description of the model will be repeated for the convenience of the reader.

Description of Experimental Equipment: Heat Transfer Model

The heat transfer model was designed to simulate the internal multipassage geometry of a cooled turbine blade (Fig. 1*a*). The model consists of three straight sections and three turn sections, which were instrumented, followed by one uninstrumented straight section, as shown in Fig. 1(*b*). Data presented herein were obtained in the first, second, and third passages with radially outward, inward, and outward flow, respectively. The model passages are square with a sidewall dimension of 0.5 in. (12.7 mm). The heated length of the first passage is 14 hydraulic diameters and is comprised of 16 heated copper elements at four streamwise locations. Four elements form the walls of the square coolant passage at each streamwise location.

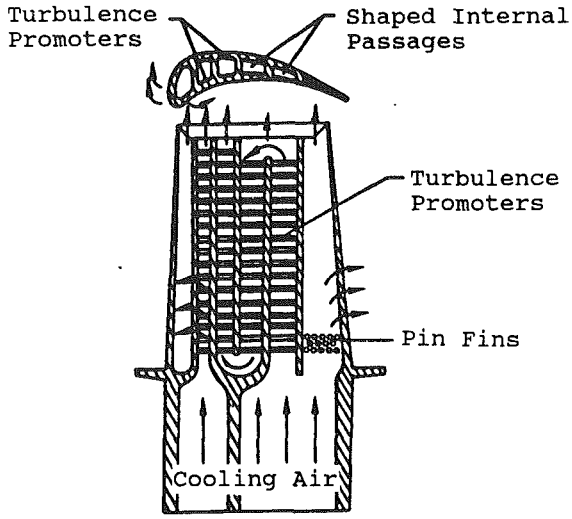

Fig. 1(*a*) Typical turbine blade internal convection cooling configuration (from Han et al., 1984)

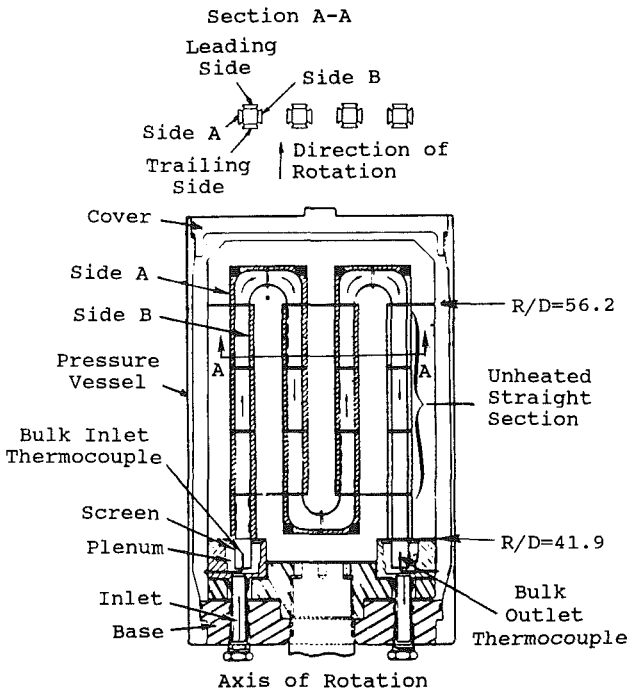

Fig. 1(*b*) Cross-sectional views of coolant passage heat transfer model assembly

Nomenclature

A = area of passage cross section
D = hydraulic diameter
Gr = rotational Grashof number
h = heat transfer coefficient
k = thermal conductivity
m = mass flow rate
Nu = Nusselt number $= h^*D/k$
Pr = Prandtl number
R = radius
Re = Reynolds number $= m^*D/\mu/A$
Ro = rotation number $= \Omega^*D/V$
T = temperature
V = mean coolant velocity
x = streamwise distance
$\Delta\rho/\rho$ = density ratio $(\rho_b - \rho_w)/\rho_b$
μ = absolute viscosity
ρ = coolant density
Ω = rotational speed

Subscripts

b = bulk property
f = film property
in = inlet to model
w = heated surface location
x = based on streamwise location
∞ = fully developed, smooth tube

Superscripts

$\bar{}$ = average

The two cross-sectional views shown in the figure show the orientation of the leading, trailing, and sidewall surfaces. Each copper element is heated on the side opposite the test surface with a thin film, 0.003 in. (0.1 mm), resistance heater. Each element is 0.150 in. (3.8 mm) thick and is thermally isolated from surrounding elements by 0.060 in. (1.5 mm) thick fiberglass insulators. The insulating material separating the copper elements at each streamwise location resulted in a 0.04 in. (1.0 mm) chamfer in the corners, which yielded a hydraulic diameter in the straight sections of 0.518 in. (13.2 mm). The power to each element was adjusted to obtain an isothermal wall boundary condition. In practice, temperature gradients less than 2°F (1°C) were achieved. The heat flux between elements with a 2°F (1°C) temperature difference was estimated to be less than 2 percent of a typical stationary heat flux.

Testing was conducted with air at nondimensional flow conditions typical of advanced gas turbine designs. The required dimensionless rotation numbers were obtained with rotation rates of 1100 rpm or less by operating the model at a pressure of approximately 10 atm. The model inlet air temperature was typically 80°F (27°C) and the copper elements were held at 120°F, 160°F, 200°F, and 240°F (49°C, 71°C, 93°C, and 116°C) for coolant-to-wall temperature differences of 40°F, 80°F, 120°F, and 160°F (22°C, 44°C, 67°C and 89°C). Temperatures of the copper elements were measured with two chromel-alumel thermocouples inserted in drilled holes of each element. Heat transfer coefficients were determined by performing an energy balance on each copper element to obtain the convected heat flux and the local coolant temperature. See Wagner et al. (1991) for additional information about the data reduction procedure.

Nusselt numbers and Reynolds numbers were calculated for each element. The fluid properties in the Nusselt and Reynolds numbers were evaluated at the film temperature, i.e., $T_f = (T_w - T_b)/2$. All the heat transfer results presented herein have been normalized with a smooth tube correlation for fully developed, turbulent flow. The constant heat flux Colburn equation, adjusted for constant wall temperature, was used to obtain the Nusselt number for fully developed, turbulent flow in a smooth tube (Kays and Perkins, 1973). The resulting equation for the constant wall temperature condition with a Prandtl number equal to 0.72 is as follows:

$$\mathrm{Nu}_\infty = 0.0176\ \mathrm{Re}^{0.8}$$

An uncertainty analysis of the data reduction equations showed that approximately 3/4 of the estimated uncertainty in calculating heat transfer coefficient was due to the measurement of temperature in the model. The uncertainty of the heat transfer coefficient is influenced mainly by the wall-to-coolant temperature difference and the net heat flux from each element. Uncertainty in the heat transfer coefficient increases when either the temperature difference or the net heat flux decreases. For increasing x/D, the uncertainty increases because the wall-to-coolant temperature difference decreases. For low heat fluxes (i.e., low Reynolds numbers and on leading surfaces with rotation) the uncertainty in the heat transfer increased. Estimates of the error in calculating heat transfer coefficient typically varied from approximately ±6 percent at the inlet to ±20 percent at the exit of the heat transfer model for the baseline test conditions. The uncertainty in the lowest heat transfer coefficient on the leading side of the third passage with rotation is estimated to be 30 percent.

Results

Forward. Heat transfer in stationary experiments with smooth passages is primarily a function of the Reynolds number (a flow parameter) and the streamwise distance from the inlet, x/D (a geometric parameter). However, when rotation is applied, the heat transfer is also strongly influenced by the coupled effects of Coriolis and buoyancy and becomes asymmetric around the passage. An unpublished analysis of the equations of motion by Suo (1980), similar to that of Guidez (1989), showed that the basic dimensionless fluid dynamic parameters governing the flow in a radial coolant passage were the Reynolds number, the rotation number, $\Omega D/V$, the fluid density ratio, $\Delta\rho/\rho$, and the geometric parameter, R/D. Note that the rotation parameter is the reciprocal of the Rossby number, $V/\Omega D$, and governs the formation of cross-stream secondary flow. The rotation number, $\Omega D/V$, the fluid density ratio, $\Delta\rho/\rho$, and the geometric parameter, R/D, appear in the governing equation as a buoyancy parameter. This buoyancy parameter, $(\Delta\rho/\rho)\ (R/D)(\Omega D/V)^2$, is the equivalent of $\mathrm{Gr}/\mathrm{Re}^2$ for stationary heat transfer. Thus, with rotation, the heat transfer is primarily a function of two geometric parameters (x/D and surface orientation relative to the direction of rotation) and three flow parameters (Reynolds number, rotation number, and the buoyancy parameter).

Due to the vector nature of the equations of motion, it can be expected that flow direction can also have a significant effect on the coolant flow. In the parallel flow case the flow is radially inward, coincident with buoyancy-driven flow for heated walls. For the counterflow case the flow is radially outward, opposite to the direction of the buoyancy-driven flow. Flow direction (i.e., radially inward or outward) and a fixed radially outward directed force field, created by the rotating reference frame, establish the potential for parallel and counterflow situations as observed by Eckert et al. (1953) in their vertical tube experiment.

The format of this paper is to show the effects of each of the primary variables (x/D, rotation number, density ratio) on the heat transfer about a baseline flow condition to develop an understanding of the cause/effect relationships. The entire body of experimental results is then examined to determine the effect of the buoyancy parameter on the heat transfer for certain locations in the coolant passage.

Baseline Experiments. Two baseline experiments, one stationary and one rotating, were conducted to obtain data for comparison with all other data generated in this program. The stationary and rotating baseline experiments had dimensionless flow conditions that consisted of a Reynolds number of 25,000 and an inlet density ratio, $(\Delta\rho/\rho)_i = (T_w - T_b)/T_w$, of 0.13. The rotating baseline experiment had a rotation number, $\Omega D/V$, of 0.24 and a radius ratio at the average model radius, R/D, of 49. These values were selected because they are in the central region of the operating range of current large aircraft gas turbine engines.

Stationary. Streamwise variations of Nusselt number for the stationary baseline test are shown in Fig. 2. The Nusselt number for fully developed, turbulent flow in a smooth tube with constant wall temperature is shown for comparison. In general, the heat transfer decreases in all three instrumented passages by about 25 percent from the first to the last heat transfer element of each straight section.

From Fig. 2 it can also be seen that the heat transfer in the turn sections increases by a factor of approximately two compared to the fully developed, smooth passage heat transfer value. The heat transfer on the sidewall elements is complex and is indicative of heat transfer caused by a highly three-dimensional flowfield.

The streamwise distributions of the average heat transfer ratio for the stationary baseline experiment are shown in Fig. 3 for the first two heated straight sections. The wall-to-wall variation of the heat transfer results from the four surfaces around the circumference of each coolant passage are also shown. Results from other investigators (Boelter et al., 1948; Aladyev, 1954; Yang and Liao, 1973) are shown for comparison.

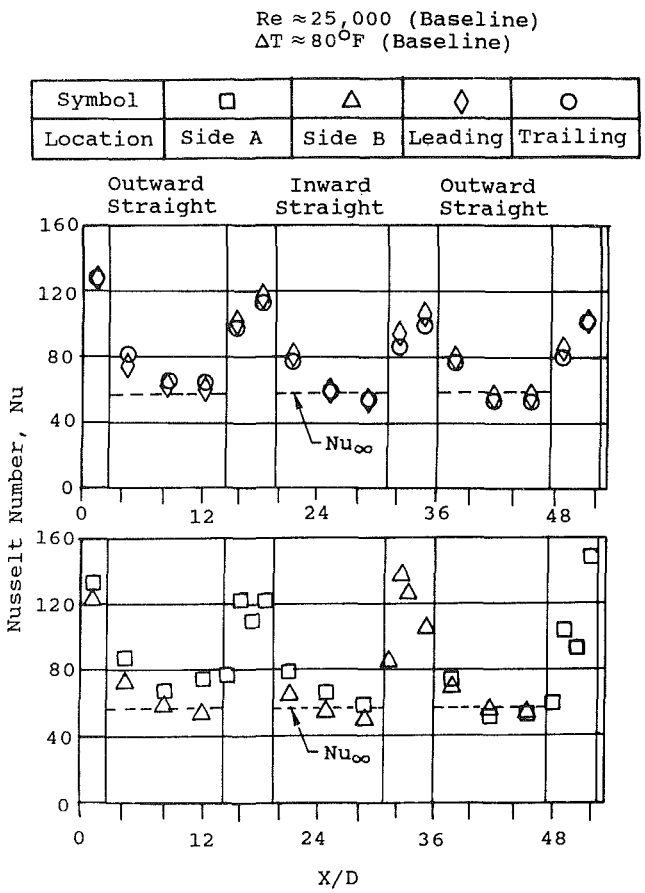

Fig. 2 Heat transfer results for stationary flow condition

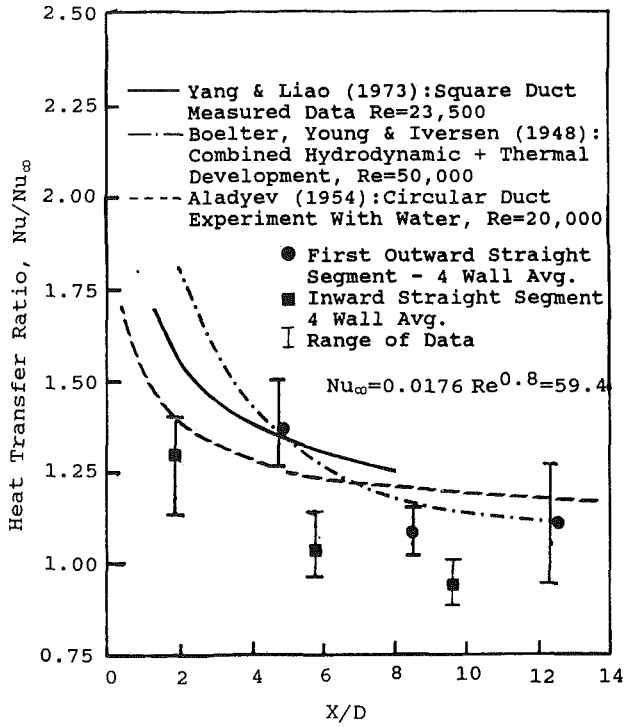

Fig. 3 Comparison of heat transfer results in straight passages for the stationary flow condition with previous entrance region heat transfer results

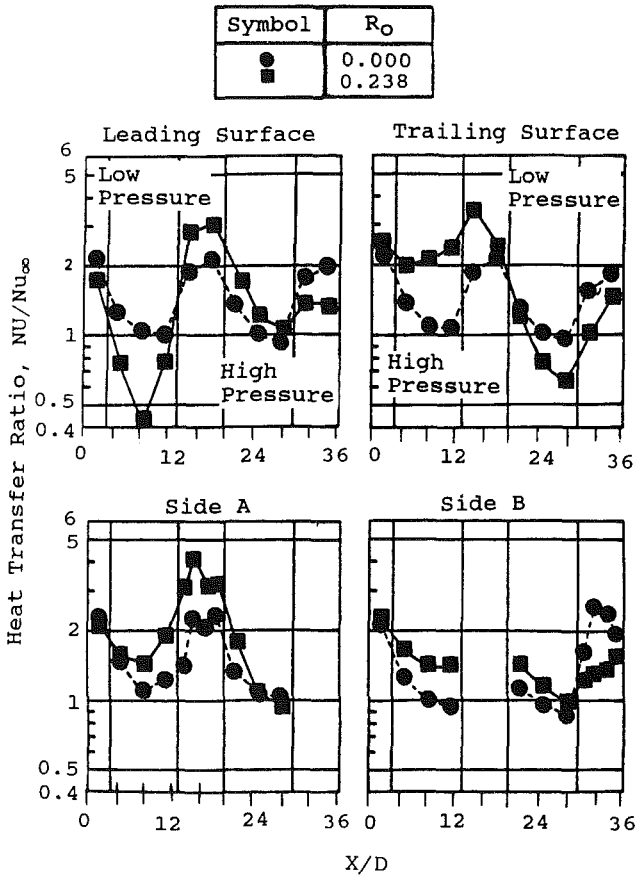

Fig. 4 Variation of heat transfer ratio with streamwise location for "rotating" baseline flow condition; Re = 25,000, Ro = 0.24, $(\Delta\rho/\rho)_i = 0.13$

The streamwise variations in average heat transfer ratio for each passage are indicative of developing flow in the entrance region of a passage. Heat transfer ratio decreases with increasing streamwise location, x/D, to about 1.0 near the exit of each passage. A heat transfer ratio of 1.0 is that expected for fully developed, turbulent flow with a constant wall temperature. Although the mean inlet velocity profiles for the first passage were conditioned to be hydrodynamically "fully developed," it would be expected that the streamwise variation in heat transfer would be similar to that in a duct with an unheated starting length. This is evident in the data. The heat transfer distributions in the second and third passages also indicate that a development process occurs that is attributed to secondary flow effects of the turn. The wall-to-wall variations in heat transfer ratio for each streamwise location are less than 15 percent, indicating good passage symmetry.

Rotating. The streamwise distributions of heat transfer ratio for the rotating baseline condition for the first two coolant passages are shown in Fig. 4. The streamwise distributions of heat transfer ratio from the stationary baseline test are also shown. With rotation, heat transfer increases and decreases by factors of more than two from the trailing and leading surfaces, respectively, compared to the heat transfer from the stationary baseline test. The heat transfer from the sidewall surfaces increases by 20 to 50 percent. Note that the local heat transfer ratio on the leading side of the first coolant passage decreases rapidly with increasing streamwise distance to about 40 percent of the stationary value at $x/D = 8.5$ and then increases at the larger x/D location. The heat transfer ratio on the trailing side of this passage increases with increasing streamwise distance to almost 2.5 times that of a fully developed, smooth tube. This results in a 5:1 ratio of the heat transfer coefficients between the trailing and leading surfaces.

The effect of rotation on the heat transfer in the second, inward-flowing passage is significantly different compared to that in the first, outward flowing passage. The heat transfer increases only about 10 to 20 percent on the leading surfaces

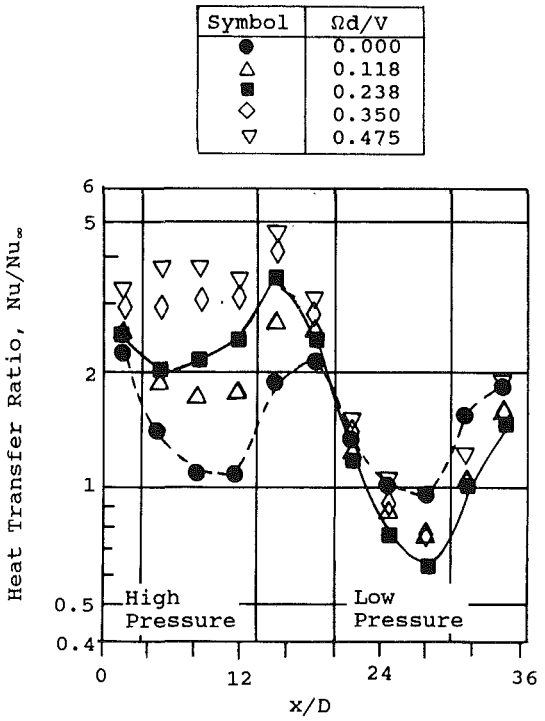

Fig. 5(*a*) Effect of rotation number on heat transfer ratio for trailing surfaces; Re = 25,000, $(\Delta\rho/\rho)_i = 0.13$, $R/D = 49$

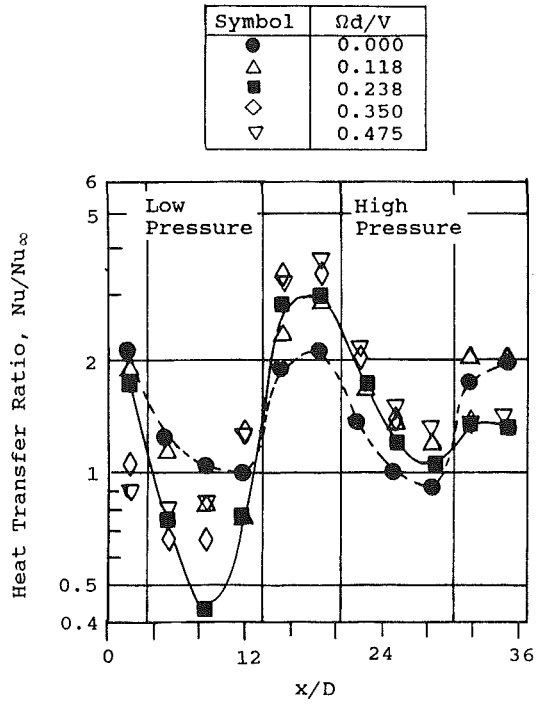

Fig. 5(*b*) Effect of rotation number on heat transfer ratio for leading surfaces; Re = 25,000, $(\Delta\rho/\rho)_i = 0.13$, $R/D = 49$

compared to the stationary results. The heat transfer on the trailing surfaces decreases by 5 to 30 percent compared to the stationary values. These modest changes in heat transfer on the leading and trailing surfaces in the second passage result in a substantially reduced leading-to-trailing surface heat transfer variation.

The effect of rotation on the heat transfer from the sidewall surfaces in the straight passages resulted in heat transfer increases ranging from 0 to 50 percent.

A comprehensive discussion of the effects of rotation on heat transfer in the first passage was presented by Wagner et al. (1991). In summary, the difference in heat transfer between the rotating and nonrotating flow conditions is primarily attributed to the secondary flows associated with the Coriolis force and the buoyancy. The decrease in heat transfer near the inlet of the passage on the leading surfaces of the first passage was attributed to the stabilizing of the near-wall flow. The subsequent increase in heat transfer near the end of the first passage was postulated to occur when the passage secondary flows become more developed and interact with the buoyant, stabilized near-wall flow on the leading side of the passage.

The change in heat transfer due to rotation is somewhat different for the second, inward-flowing passage, compared to the change observed in the first passage. For the inward-flowing passage the heat transfer is expected to increase on the leading surfaces and decrease on the trailing surfaces, opposite to the effect noted in the first passage. Eckert et al. (1953) showed that average heat transfer was reduced in a stationary, parallel flow configuration, where the mean convective flow direction and the buoyancy-induced flow direction are the same (i.e., as in the second, inward-flowing passage). The effects of rotation are in general agreement with the aforementioned discussions, except that heat transfer did not decrease nearly as much on the trailing surfaces of the second passage compared to the leading surfaces of the first passage. Additionally, the large increases in heat transfer expected on leading surfaces of the second passage did not occur as they did on the trailing surfaces of the first passage.

The difference in the heat transfer on the high pressure sides of the coolant passage (i.e., trailing surfaces in the first, outward, flowing passage and leading surfaces in the second, inward-flowing passage) is believed to be a result of the combined effects of the formation of boundary layer vortices (Johnston et al., 1972; Eckert et al., 1953) and to counteracting buoyancy effects caused when the buoyancy force direction is aligned with the flow direction. When a counterflow situation exists (i.e., buoyancy opposite to that of flow direction), the combined effects of buoyant and Coriolis-driven secondary flows causes an increase in heat transfer. When a parallel situation exists (i.e., aligned buoyancy and flow direction) the combined effects are less because of a counteraction of the two flow mechanisms. Further discussion of these effects will be presented in subsequent sections.

The baseline results with rotation showed significant changes in the heat transfer in the first passage on the leading, trailing, and turn surfaces but relatively smaller changes on the sidewall surfaces. Therefore, the following discussion will focus on the heat transfer results from only the leading and trailing surfaces in the straight sections of the coolant passage with both inward and outward flow and will focus on the differences between inward versus outward flow. Discussion of effects of rotation on the heat transfer in the turn regions of the coolant passage are deferred to a subsequent paper.

Varying Rotating Number. The rotation number, $\Omega D/V$, was varied from 0 to 0.48 for this series of flow conditions. The Reynolds number, inlet density ratio, and radius ratio were held constant at the nominal values of 25,000, 0.13, and 49, respectively.

High Pressure Surfaces. Increasing the rotation rate causes significant increases in heat transfer on the trailing surfaces (Fig. 5*a*) of the first passage but lesser increases on the leading surfaces in the second passage (Fig. 5*b*). Heat transfer in the first passage increased by more than a factor of 3.5 for the largest value of rotation parameter (0.48) compared to stationary heat transfer values. Compared to the stationary results, heat transfer on the leading, high-pressure side of the second passage experienced modest increases of approximately 50 percent. The effects on heat transfer due to Coriolis-generated secondary flows might be expected to be approximately

the same for the first and second passages. The difference in heat transfer between the outward and inward-flowing passages is therefore attributed to the different effects of buoyancy in the counterflowing first passage (radially outward flow) and the coflowing second passage (radially inward flow).

The lesser increase in the heat transfer ratio on the high-pressure side of the second passage is attributed to a reduction in the generation of near-wall turbulence. In the first passage the near-wall buoyancy-driven flow was inward toward the axis of rotation and the coolant flow was outward. This counterflow situation generated additional near-wall turbulence due to the strong shear gradient. This destabilizing of the shear flow combined with the cross-stream secondary flows generated by Coriolis forces causes large increases in heat transfer in the first passage. However, when the flow and the buoyancy-driven near-wall flows are coincident, as in the second passage, the generation of near-wall turbulence may be diminished because of the relatively weaker near-wall shear layer. Therefore, the combined effects of the buoyant and the cross-stream secondary flows in the second passage on the heat transfer was less. The magnitude of the buoyancy effect on the heat transfer is unclear in that the buoyancy effect on the heat transfer in the second passage may be zero (which implies a modest Coriolis-dominated heat transfer increase) or negative (which implies a larger Coriolis-dominated heat transfer increase, which is offset by a reduction due to buoyancy). Ongoing numerical simulations of these test points will help in the understanding of this complex flow field.

Low-Pressure Surfaces. In contrast to the continual increase in heat transfer with increasing rotation number on the trailing side, the heat transfer ratio decreases with increasing rotation number on the leading side of the passage near the inlet. For all the remaining locations on the leading side of the passage, the heat transfer ratio decreases and then increases again with increasing rotation number. Heat transfer from the trailing, low-pressure surfaces of the second passage also had large decreases in heat transfer. Heat transfer in the second passage decreased to almost 60 percent of the stationary heat transfer level compared to 40 percent in the first passage. In the second passage, the heat transfer decreased and then subsequently increased again as the rotation rate was increased.

The decreases in the heat transfer ratio are attributed, for the most part, to the cross-stream flow patterns as well as the stabilization of the near-wall flow on the leading side of the passage (Johnston et al., 1972). The cross-stream flows cause heated, near-wall fluid from the trailing and sidewall surfaces to accumulate near the leading side of the coolant passage, resulting in reduced heat transfer. In addition, the rotation stabilizes the shear layers along this wall and further reduces the turbulent transport of heat. The increase in the heat transfer ratio in the latter half of the coolant passage for the larger rotation numbers is attributed to the large-scale development of the Coriolis generated secondary flow cells. Similar effects of rotation are noted for the low-pressure surfaces in both the first and second passages, irrespective of flow direction. These results suggest that the heat transfer on low-pressure surfaces is dominated by Coriolis-generated cross-stream flows, which cause a stabilization of the near-wall flows, and that the heat transfer on the high-pressure surfaces is affected by a combination of Coriolis and buoyant effects. Therefore, it can be expected that the correlations of local heat transfer data may be substantially different depending on local flow conditions (i.e., due to differing near-wall shear gradients).

Varying Density Ratio. The inlet density ratio, $(\Delta\rho/\rho)_1$, was varied from 0.07 to 0.22 for this series of flow conditions. The Reynolds number, rotation number, and radius ratio were held constant at the baseline values of 25,000 0.24, and 49, respectively. Heat transfer was obtained at a fixed rotation number and, therefore, conclusions can be obtained regarding the effects of buoyancy for flow conditions near the rotating baseline flow conditions.

Increasing the inlet density ratio (i.e., the wall-to-coolant temperature difference) from 0.07 to 0.22 causes the heat transfer ratio in the first passage to increase on all trailing surfaces by as much as 50 percent (Fig. 6*a*) and on the leading surfaces by as much as 100 percent (Fig. 6*b*). The exception to the general increase in heat transfer with increasing density ratio occurred near the inlet of the first passage on the leading side, where the heat transfer ratio is observed to decrease slightly.

Heat transfer in the second, inward-flowing passage increases with increases in the temperature difference (Fig. 6). In general, the increases in heat transfer in the second passage were approximately half of those in the first passage (on the order of 10 to 50 percent compared to maximum relative increase of 100 percent in the first passage). The differences in heat transfer behavior due to changes in the density ratio between the first and second passages are attributed to the differing mechanisms of Coriolis and buoyancy interaction. If the effect of Coriolis-generated secondary flow on heat transfer is similar (regardless of flow direction) and the effect of density

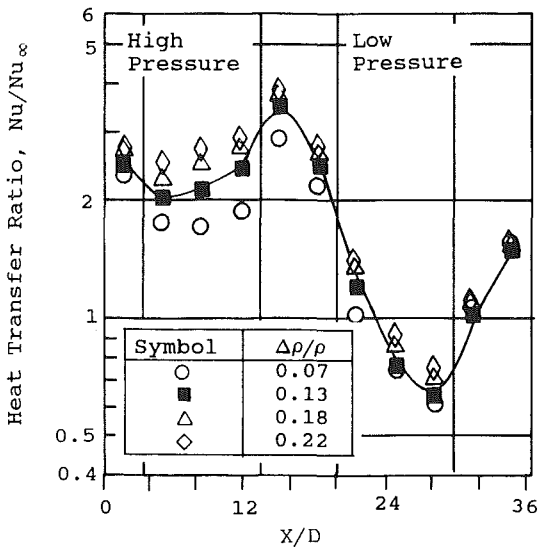

Fig. 6(*a*) Effect of wall-to-coolant density difference on heat transfer ratio for trailing surfaces; Re = 25,000, Ro = 0.24, *R/D* = 49

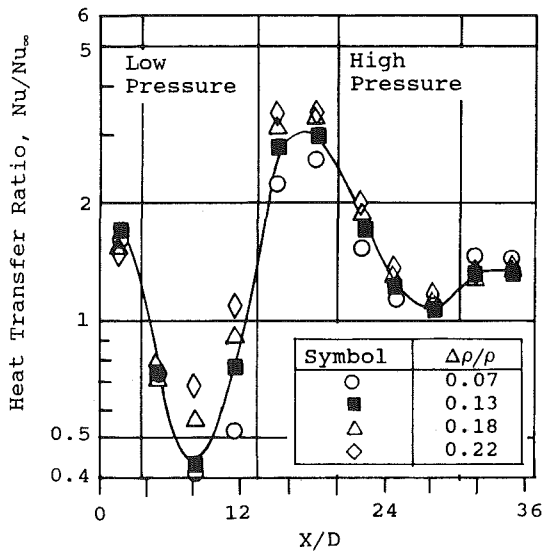

Fig. 6(*b*) Effect of wall-to-coolant density difference on heat transfer ratio for leading surfaces; Re = 25,000, Ro = 0.24, *R/D* = 49

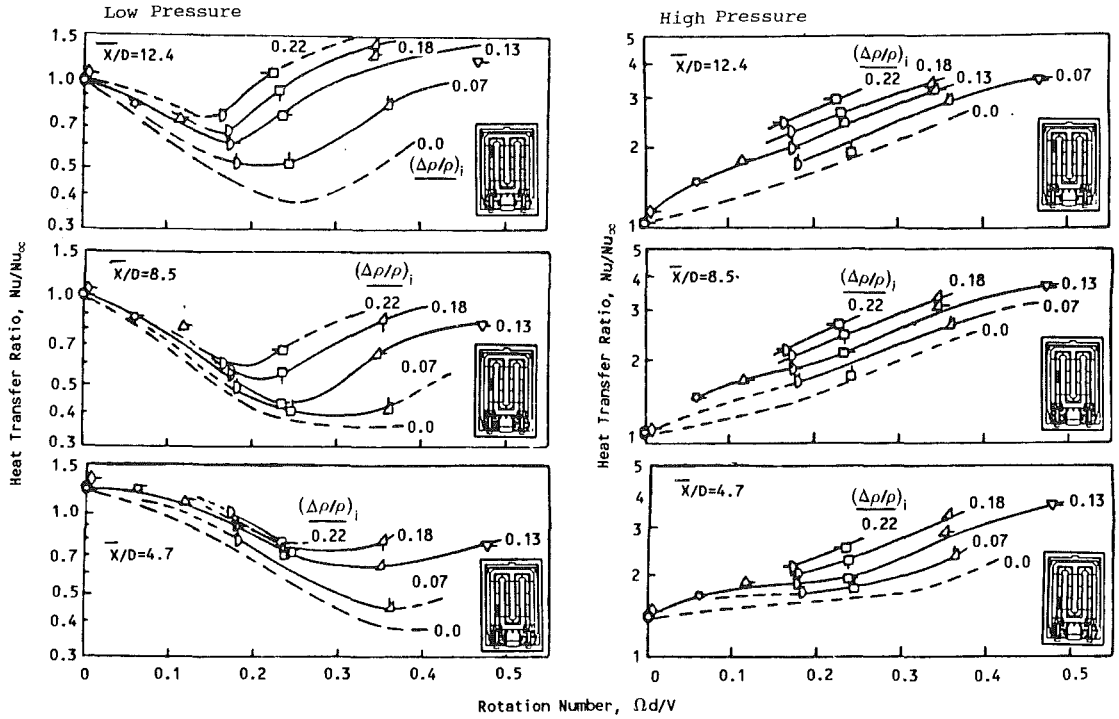

Fig. 7(*a*) Effect of rotation number and density ratio on heat transfer ratios in the first passage; Re = 25,000, *R/D* = 49

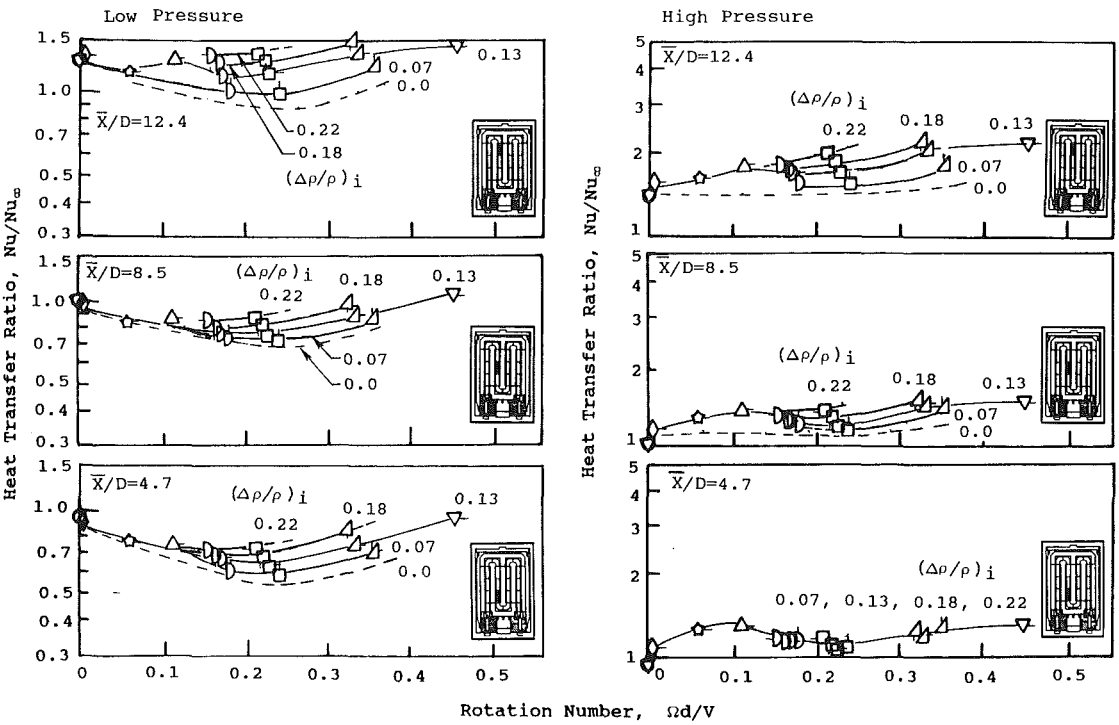

Fig. 7(*b*) Effect of rotation number and density ratio on heat transfer ratios in the second passage; Re = 25,000, *R/D* = 49

ratio for fixed rotation number generally causes heat transfer to increase, then the interaction of the two effects is significant and also counteracting. The counteraction of the two effects was deduced because of the relatively small increases in heat transfer on the high-pressure side of the second passage.

Varying Rotation Number and Density Ratio. Additional data from parametric variations of density ratio and rotation parameter were necessary to isolate the effects of rotation and buoyancy. The inlet density ratio was varied from 0.07 to 0.22 for selected rotation numbers. Heat transfer results from these experiments were plotted versus inlet density ratio with rotation number as a secondary variable. The distributions of heat transfer ratio with density ratio (not shown) were extrapolated for each value of the rotation number to obtain a value of the heat transfer ratio for a density ratio of 0.0 (i.e., limit as ΔT approaches 0.0). The heat transfer results obtained from the experiments plus the extrapolated values for a density ratio of 0.0 (dashed lines) are presented in Fig. 7 as the variation of heat transfer ratio with the rotation number with the density

ratio as the secondary variable for three streamwise locations for the first and the second passage. Heat transfer results in the first passage were thoroughly discussed by Wagner et al. (1991). Therefore, the following discussion will concentrate on the differences in the heat transfer from the first and second passages.

High-Pressure Surfaces. Heat transfer results from the high-pressure side of the first and second passages are shown in Fig. 7 for ranges of rotation number and density ratio. Note that there is no effect of density ratio on the heat transfer ratio for a rotation number of 0 when film properties are used for the dimensionless heat transfer and flow parameters. Increasing the rotation number causes local increases in the heat transfer in the first passages by as much as 3.5 compared to the heat transfer for a rotation number of 0. Whereas the heat transfer ratios for the high-pressure surfaces increase sharply with increases in either the density ratio or the rotation number, with one exception, heat transfer in the second passage is relatively unaffected by variations of either parameter. The exception is near the inlet of the second passage, just downstream of the first turn. At this location the heat transfer increases slightly with increases in the rotation parameter and the density ratio. However, for larger x/D in the second passage, the effect on the heat transfer for variations in rotation or density ratio diminishes.

Low Pressure Surfaces. The heat transfer from the low-pressure surfaces from the first and second passages (Fig. 7) is more complex than that from the high-pressure surfaces. Heat transfer in the first passage decreases with increasing rotation number for low values of rotation number (i.e., $\Omega D/V<0.2$ at the downstream location) and then subsequently increases again with increases in rotation for larger values of rotation number. Additionally, as with the high-pressure surfaces in the first passage, heat transfer increases with increases in the density ratio. A similar characteristic in the heat transfer distributions is observed in the second passage for radial inflow as well. However, with one exception, the large effects of density ratio observed on the low-pressure surfaces of the first passage are diminished in the second passage. The exception is that heat transfer is slightly increased with increasing density ratio near the inlet of the second passage.

The more complicated heat transfer distributions on the low-pressure surfaces of the coolant passages are attributed to (1) the combination of buoyancy forces and the stabilization of the near-wall flow for low values of the rotation number and (2) the developing, Coriolis-driven secondary flow cells for the larger values of the rotation number. It is postulated that the relatively large effects from variations in density ratio near the inlet of the second passage and the small effects near the end of the second passage are due to the development of the near-wall thermal layers. Near the inlet of the second passage, the thermal layers are postulated to be thin because of the strong secondary flows in the first turn region. With increasing x/D, the turn-dominated secondary flows diminish and the counteracting effect of buoyancy and the Coriolis-generated secondary flow increases.

Correlating Parameters

The analysis of the equations of motion for flow in rotating radial passages by Suo (1980), discussed above, showed that (1) the cross-stream flows will be proportional to the rotation number, $\Omega D/V$, and (2) the buoyant flows will be proportional to the buoyancy parameter, $(\Delta\rho/\rho)\ (R/D)(\Omega D/V)^2$.

The combined effect of the cross-stream flows and the buoyant flows is not easily ascertained from the equations of motion. The preceding discussions indicate that the combined effects are quite complex and are a strong function of flow direction. Therefore, the flow direction is also considered in the following paragraphs.

The buoyancy parameter defined above is equivalent to the ratio of the Grashof number (with a rotational gravitation term, $R\Omega^2$) to the square of the Reynolds number and has previously been used to characterize the relative importance of free and forced-convection in the analysis of stationary mixed-convection heat transfer. Guidez (1989) used a similar analysis to establish appropriate flow parameters for the presentation of his results. These parameters, $\Omega D/V$ and $(\Delta\rho/\rho)$ $(R/D(\Omega D/V)^2$, will also be used in the present discussion of

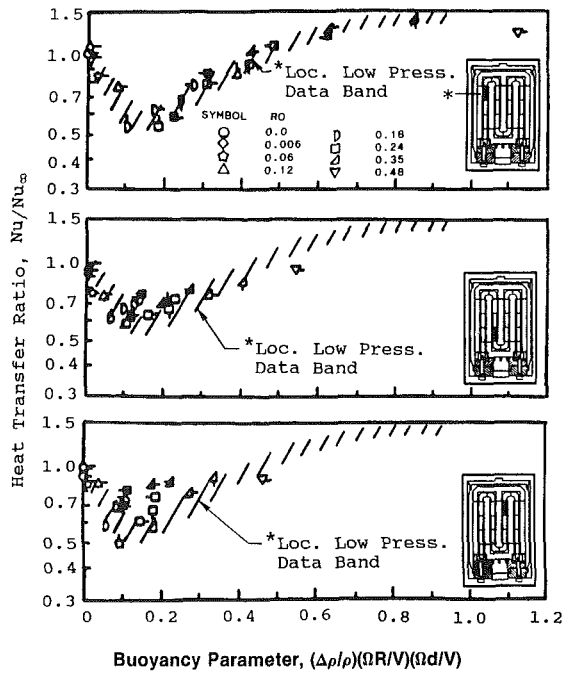

Fig. 8(a) Comparison of heat transfer ratios from the low-pressure surfaces of the first, second, and third passages

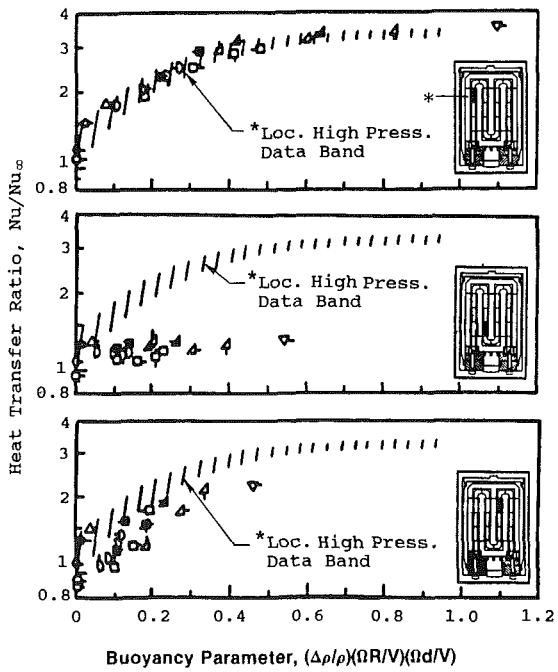

Fig. 8(b) Comparison of heat transfer ratios from the high-pressure surfaces of the first, second, and third passages

the effects of Coriolis and buoyancy forces on the heat transfer for inward and outward flow directions.

The data were analyzed to determine the effects of flow direction (radially inward or radially outward) on the heat transfer characteristics and to determine the differences between the first passage with outward flow downstream of an inlet, the second passage with inward flow downstream of a 180 deg turn and the third passage with outward flow downstream of a 180 deg turn. The variations of heat transfer ratio with buoyancy parameter for the heated surface at the most downstream location from the inlet or a turn for each of the three passages are shown in Fig. 8. This is the streamwise location for each passage where heat transfer for stationary test conditions asymptotically approached the value of heat transfer for turbulent, fully developed flow.

The data presented in Fig. 7 showed that the effects of Coriolis and buoyancy forces are coupled in the first two passages through the entire operating range investigated. The results from Fig. 7 plus additional results from the third passage are combined with those for $R/D=33$ and are presented in Fig. 8 as the variation of the heat transfer ratio with the buoyancy parameter based on the local density ratio and radius, R. Thus, the range of the buoyancy parameter decreases with increasing values of x/D (i.e., decreasing temperature difference with increasing x). The range of heat transfer ratio for the last location in the first passage is shown as a shaded band with the results from the second and third passages for comparison.

Heat transfer distributions from the low-pressure surfaces of each of the three passages exhibit a similar relationship with the buoyancy parameter. Heat transfer decreases with increasing values of buoyancy between 0.0 and 0.15. Heat transfer subsequently increases again with increasing values of buoyancy. Heat transfer on the low-pressure surfaces of rotating coolant passages is governed by complex relationships of streamwise location, rotation number and buoyancy parameter. However, the heat transfer results are reasonably well correlated in the first two passages by the buoyancy parameter for values of buoyancy parameter greater than 0.2.

The heat transfer results from the high-pressure surfaces in the first passage are correlated well by the buoyancy parameter. The second passage with radially inward flow had different heat transfer characteristics than the first and third passages with radially outward flow. Whereas the heat transfer ratios for the high-pressure surfaces of the first and third passages increased with the buoyancy parameter, the heat transfer in the second passage was lower and relatively independent of buoyancy parameter for values of buoyancy greater than 0.05. These results for coflowing and counterflowing buoyancy effects on the high-pressure surfaces are generally consistent with the stationary combined free- and forced-convection experiments of Eckert et al. (1953). They measured decreased levels of heat transfer for the coflowing condition (i.e., similar to that of radially inward flow in rotating systems). A more comprehensive comparison with Eckert's results is presented in the next section.

Comparison With Previous Stationary Experimental Results

Thus far this study has shown that rotational forces strongly influence turbulent heat transfer in rotating smooth passages for conditions found in gas turbine blades. However, variations in heat transfer caused by rotation have been shown to be less for radially inward flowing passages than for radially outward flowing passages. These effects of flow direction in the present rotating heat transfer experiments are compatible with stationary heat transfer experiments conducted by Eckert et al. (1953). Three experiments were conducted in a large vertical circular tube (stationary) where they examined mixed-, free, and forced-convection heat transfer. These results are plotted as Nu_x versus Gr_x in Figs. 9 and 10. A free-convection limit consisting of a curve fit through the results of Eckert's free-convection experiment is shown in each figure. Circumferentially averaged results from the present rotating heat transfer experiment are shown as the symbols in Figs. 9 and 10. Heat transfer data shown with the same symbol are for the same rotation number at three wall-to-coolant temperature differences.

The heat transfer results from the radially outward flowing passage from the present work are compared to results from the 1953 counterflow experiments in Fig. 9. For the stationary counterflow experiments the wall thermal boundary layer, under gravity-induced buoyancy forces, moves in a direction opposite to the mainstream flow. This is analogous, in a buoyant sense, to the rotating conditions with the radially outward flowing passage where the buoyancy force is induced by rotation and toward the axis of rotation. The averaged heat transfer data measured in the present experiments agree remarkably well with Eckert's. The increasing slope through the data indicated the flow is in the mixed flow regime and buoyancy influences the circumferentially averaged heat transfer. For large values of Gr_x, heat transfer rates approach the free convection limit as established by Eckert. The data also indicate a higher free convection limit at the lower values of Gr_x. Eckert also noticed this trend when he compared the extreme forced-

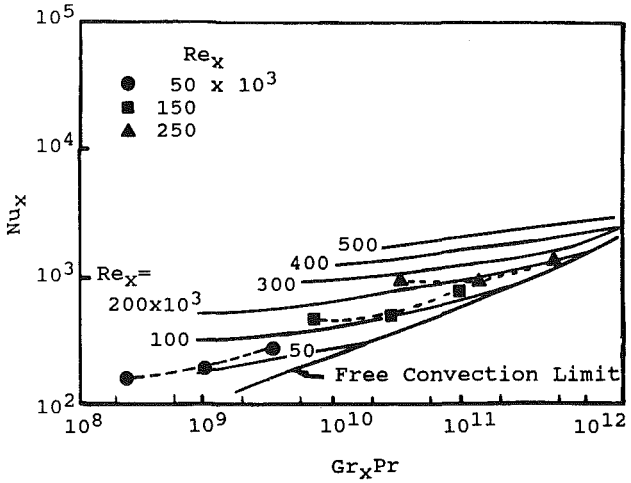

Fig. 9 Comparison of circumferentially averaged heat transfer results for the first passage with stationary, counterflow heat transfer results (Eckert et al., 1953)

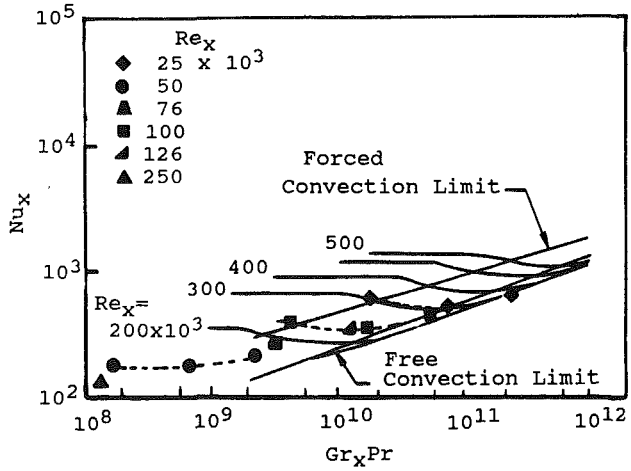

Fig. 10 Comparison of circumferentially averaged heat transfer results for the second passage with stationary, parallel heat transfer results (Eckert et al., 1953)

convection data at high Grashof numbers with the free convection data. For low values of Gr_x, forced convection dominates the heat transfer. As can be seen in the figure, the forced convection limit was not reached with the present set of experiments.

Shown in Fig. 10 are the present heat transfer results from the radially inward flowing passage with the curve-fit results from Eckert. For this flow condition the buoyancy force and flow direction are coincident. Again, the present, average heat transfer results agree very well with those of Eckert. These results show that when the buoyancy acts in the same direction as the turbulent mainstream, heat transfer is inhibited in the mixed-convection regime. Both Eckert's results from stationary experiments and the present results from experiments with rotation show a local decrease in heat transfer for values of Gr_xPr in this mixed-convection region. This local decrease is particularly important when these heat transfer results are compared with those from the counterflow experiments. When Nusselt numbers for similar flow conditions for the radially outward and inward flowing cases are compared, the counterflow (radially outflow) heat transfer is almost 70 percent greater than the corresponding parallel flow heat transfer (e.g., $Nu_x = 875$ compared to 520). Eckert noted that the counterflow situation could result in heat transfer levels as much as twice those in the parallel flow case. This is especially significant when these results are circumferential averages of heat transfer around the perimeter of the coolant passage. As shown in previous discussion, local heat transfer rates can be significantly higher and lower than the circumferential averages.

Concluding Comments

This paper has presented an extensive body of experimental data from heat transfer experiments in a rotating square passage with smooth walls. The analysis of these experimental results to determine the separate effects of forced convection, Coriolis, buoyancy, and flow direction on the heat transfer has resulted in the following observations and conclusions:

1 Density ratio and rotation number were found to cause large changes in heat transfer for radially outward flow and relatively small changes for radially inward flow.

2 The heat transfer ratio was found to be primarily a function of a buoyancy parameter on the low-pressure surfaces of the coolant passages, regardless of flow direction.

3 The heat transfer ratio on the high-pressure surfaces was significantly affected by flow direction. The heat transfer was found to be a strong function of a buoyancy parameter for the high-pressure surfaces for radially outward flow, whereas the heat transfer was relatively unaffected by a buoyancy parameter for the radially inward flowing high-pressure surface.

4 Increasing the density ratio generally caused an increase in heat transfer. However, the increase in heat transfer for the inward-flowing passage was considerably less than that for outward-flow.

5 Circumferentially averaged heat transfer results compared favorably with a previous stationary parallel and counterflow mixed-convection heat transfer experiment by Eckert et al. (1953). Heat transfer from the radially outward flowing passages compared with Eckert's counterflow case while the radially inward flowing results compared with Eckert's parallel flow case.

Acknowledgments

The work published in this paper was supported by the NASA/Lewis Research Center under the HOST Program, Contract No. NAS3-23691 to the Pratt and Whitney Commercial Engine Business/Engineering Division, and by the United Technology Corporation's independent research program. The heat transfer models used in this program were furnished by the Pratt and Whitney Commercial Products Division. The experimental portion of the program was conducted at the United Technologies Research Center. The authors gratefully acknowledge the assistance of Mr. A. W. Higgins (P&W) and Ms. S. Orr (UTRC) in the performance of this program. The authors are appreciative of the support and guidance by the contract monitor team at NASA/Lewis Research Center, especially Dr. Frederick C. Yeh, and by their colleagues at P&W and UTRC.

References

Aladyev, I. T., 1954, "Experimental Determination of Local and Mean Coefficients of Heat Transfer for Turbulent Flow in Pipes," NACA TN 1356 (translation from Russian).

Boelter, L. M. K., Young, G., and Iverson, H. W., 1948, NACA TN 1451, Washington, DC.

Brundrett, E., and Burroughs, P. R., 1967, "The Temperature Inner-Law and Heat Transfer for Turbulent Air Flow in a Vertical Square Duct," *Int. J. Heat Mass Transfer*, Vol. 10, pp. 1133–1142.

Clifford, R. J., 1985, "Rotating Heat Transfer Investigations on a Multipass Cooling Geometry," AGARD Conference Proceedings No. 390: Heat Transfer and Cooling in Gas Turbines, May 6–10.

Eckert, E. R. G., Diaguila, A. J., and Curren, A. N., 1953, "Experiments on Mixed-, Free- and Forced-Convective Heat Transfer Connected With Turbulent Flow Through a Short Tube," NACA Technical Note 2974.

Guidez, J. 1989, "Study of the Convective Heat Transfer in a Rotating Coolant Channel," ASME JOURNAL OF TURBOMACHINERY, Vol. 111, pp. 43–50.

Han, J. C., Park, J. S., and Lei, C. K., 1984, "Heat Transfer and Pressure Drop in Blade Cooling Channels With Turbulence Promoters," NASA Contractor Report 3837.

Hart, J. E., 1971, "Instability and Secondary Motion in a Rotating Channel Flow," *J. Fluid Mech.*, Vol. 45, Part 2, pp. 341–351.

Iskakov, K. M., and Trushin, V. A., 1983, "Influence of Rotation on Heat Transfer in a Turbine-Blade Radial Slot Channel," *Izvestiya VUZ. Aviatsionnaya Tekhnika*, Vol. 26, No. 1, pp. 97–99.

Johnson, B. V., 1978, "Heat Transfer Experiments in Rotating Radial Passages With Supercritical Water," ASME *Heat Transfer* (bound proceedings from 1978 ASME Winter Annual Meeting).

Johnston, J. P., Halleen, R. M., and Lezius, D. K., 1972, "Effects of Spanwise Rotation on the Structure of Two-Dimensional Fully Developed Turbulent Channel Flow," *J. Fluid Mech.*, Vol. 56, Part 3, pp. 533–557.

Kays, W. M., and Perkins, H. C., 1973, "Forced Convection, Internal Flow in Ducts," in: *Handbook of Heat Transfer*, W. M. Rohsenow and J. P. Hartnett, eds., McGraw-Hill, pp. 7–28 and 7–33.

Lokai, V. I., and Gunchenko, E. I., 1979, "Heat Transfer Over the Initial Section of Turbine Blade Cooling Channels Under Conditions of Rotation," *Therm. Enging.*, Vol. 26, pp. 92–95.

Metais, B., and Eckert, E. R. G, 1964, "Forced, Mixed, and Free Convection Regimes," ASME *Journal of Heat Transfer*, Vol. 86, pp. 295–296.

Moore, J., 1967, "Effects of Coriolis on Turbulent Flow in Rotating Rectangular Channels," M.I.T. Gas Turbine Laboratory Report No. 89.

Mori, Y., Fukada, T., and Nakayama, W., 1971, "Convective Heat Transfer in a Rotating Radial Circular Pipe (2nd Report)," *Int. J. Heat Mass Transfer*, Vol. 14, pp. 1807–1824.

Morris, W. D., and Ayhan, T., 1979, "Observations on the Influence of Rotation on Heat Transfer in the Coolant Channels of Gas Turbine Rotor Blades," *Proc. Inst. Mech. Engrs.*, Vol. 193, pp. 303–311.

Morris, W., 1981, *Heat Transfer and Fluid Flow in Rotating Coolant Channels*, Research Studies Press.

Rothe, P. H., and Johnston, J. P., 1979, "Free Shear Layer Behavior in Rotating Systems," ASME *Journal of Fluids Engineering*, Vol. 101, pp. 117–120.

Suo, M., 1980, Unpublished Notes, United Technologies Research Center.

Wagner, J. H., Johnson, B. V., and Hajek, T. J., 1991, "Heat Transfer in Rotating Passages With Smooth Walls and Radial Outward Flow," ASME JOURNAL OF TURBOMACHINERY, Vol. 113, pp. 42–51.

Wagner, R. E., and Velkoff, H. R., 1972, "Measurements of Secondary Flows in a Rotating Duct," ASME *Journal of Engineering for Power*, Vol. 94, pp. 261–270.

Yang, J. W., and Liao, N., 1973, "An Experimental Study of Turbulent Heat Transfer in Converging Rectangular Ducts," ASME *Journal of Heat Transfer*, Vol. 95, pp. 453–457.

Parametric and Numerical Study of Fully Developed Flow and Heat Transfer in Rotating Rectangular Ducts

H. Iacovides

B. E. Launder

Mechanical Engineering Department,
University of Manchester Institute of Science and Technology,
Manchester M60 1QD, United Kingdom

This work is concerned with fully developed constant-density turbulent flow through rectangular straight ducts rotating in an orthogonal mode. Ducts of both square and 2:1 aspect ratio cross sections have been examined. For the square duct, predictions have been performed for Reynolds numbers of 33,500 and 97,000 and for the 2:1 aspect ratio duct the computations were carried out for a Reynolds number of 33,500. Values of the inverse Rossby number ($Ro = \Omega D/W_b$) ranged from 0.005 to 0.2. Except in the immediate vicinity of the wall, the standard high-Reynolds-number version of the k–ϵ model is used to account for the effect of turbulence. Across the near-wall sublayer the damping of turbulence is modeled through a low-Reynolds-number one-equation model. Low rotational speeds cause the formation of a pair of symmetric streamwise vortices. At higher rotational speeds, flow instabilities on the pressure side lead to transition to a more complex four-vortex structure. The transition point depends on both the cross-sectional geometry and the flow Reynolds number. Moreover, over a range of Rossby number, either two- or four-vortex solutions are possible depending upon initial conditions. The rotation leads to significant differences between the values of friction factor and Nusselt number on the suction and pressure surfaces of the duct. The degree of heat transfer augmentation on the pressure side is found to depend on the Reynolds number as well as on Rossby number. In contrast, heat transfer attenuation on the suction side is only Rossby-number dependent.

1 Introduction

The effects of rotation on the hydrodynamic and thermal characteristics of internal flows have considerable practical implications for the design of turbine blade cooling passages. Cooling passages have irregular cross sections and rotate in an orthogonal mode of rotation where the axis of rotation is normal to the predominant flow direction. Under such circumstances the interaction between the cross-stream components of the Coriolis force and the slow-moving near-wall fluid generates a secondary flow recirculation pattern. The near-wall fluid is driven from the pressure side toward the suction side of the passage and the faster-moving core fluid moves toward the pressure side. This onset of secondary flow leads to an increase in the average levels of friction factor and wall heat transfer rates around the perimeter but also to substantial circumferential variations. In the case of incompressible rotating flows, the two dimensionless parameters that determine the character of the flow are the Reynolds number and the inverse Rossby number, $Ro = \Omega D/W_b$.

Most of the earlier experimental work on rotating duct flows concentrated on flow visualization tests (Hart, 1971) and on static pressure and mean velocity measurements (Wagner and Velkoff, 1972; Hill and Moon, 1962; Moore, 1967). More recently Morris and Harasgama (1985) provided fully developed heat transfer data for a rotating square duct. Their data appear to show relatively small perimetral variations in local Nusselt number. Guidez (1989), on the other hand, and also Wagner et al. (1991) in their studies of developing flows through rotating rectangular ducts, measured substantial local wall heat flux variations. Numerical studies of fully developed flow carried out by the present authors concerning both circular (Iacovides and Launder, 1987a) and square (Iacovides and Launder, 1987b) cross-sectioned ducts have also resulted in the prediction of similarly strong local wall heat flux and shear stress variations. Another interesting aspect of the square-duct computations was the transition at high Rossby numbers from a symmetric double-vortex structure to a symmetric four-vortex structure. This phenomenon has also been observed in corresponding laminar-flow studies by Speziale (1982) and Kheshgi and Scriven (1985). A limited flow-visualization investigation carried out by Hart (1971), in which the motion of a set of dylines along a line normal to the duct symmetry plane

Contributed by the International Gas Turbine Institute and presented at the 35th International Gas Turbine and Aeroengine Congress and Exposition, Brussels, Belgium, June 11–14, 1990. Manuscript received by the International Gas Turbine Institute January 13, 1990. Paper No. 90-GT-24.

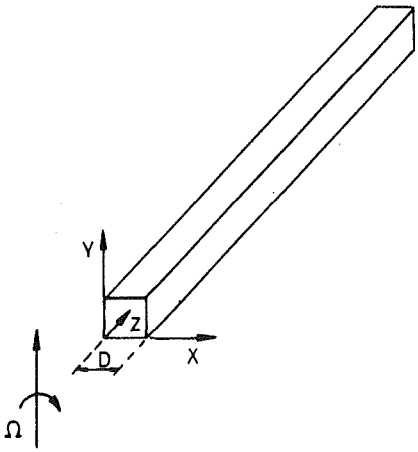

Fig. 1 Coordinate system

was observed, provides evidence that tends to confirm the existence of these flow instabilities in turbulent flow.

In this work we report the results of a numerical parametric study of fully developed constant-density flow through rotating rectangular ducts. Ducts of square cross section and of 2:1 aspect ratio have been considered. The value of the inverse Rossby number is progressively raised from 0 to 0.2. For the square duct, two sets of predictions have been obtained: one for a Reynolds-number value of 32,500 and one for 97,500. For the 2:1 aspect ratio duct the computations were confined to a Reynolds-number value of 32,500. The objective is to assess the effects of Reynolds and Rossby number on the flow. Consideration is given both to the detailed flow structure and to parameters of engineering interest, such as local and average Nusselt numbers and friction factors.

2 Turbulence Modeling Aspects

The authors' earlier work on rotating duct flows has shown that, in fully developed constant-density cases, the use of an algebraic second-moment closure (ASM) resulted in predictions similar to those obtained with a k–ϵ effective-viscosity model (Iacovides and Launder, 1987a, 1987b). For this reason, only k–ϵ predictions have been carried out in this study. In the near-wall regions, the authors' past experience in three-dimensional turbulent internal flows indicates that the use of the wall-function approximation is inappropriate (Choi et al., 1989). This has also been one of the conclusions of Lin et al.'s (1985) computational investigation of developing flow in rotating ducts. In our previous computations of rotating flows the use of Van Driest's mixing-length model across the wall sublayer, matched to a transport-based turbulence model outside the wall region, has been felt to be reasonably satisfactory. Nevertheless, because of the strong near-wall secondary flows created in these flows and having regard for the sensitivity of the local friction factors and wall heat transfer rates on the model of turbulence in the near-wall sublayer, it was decided that Wolfshtein's (1969) low-Reynolds-number one-equation model would be a more appropriate near-wall model choice. At this level transport effects on the turbulent kinetic energy are accounted for.

3 Equations of Motion

The equations of fluid motion are formulated for the rotating Cartesian coordinate system shown in Fig. 1. The z direction is the streamwise flow direction, and the axis of rotation is in the y direction. The fully developed flow equations are as follows:

Mean Momentum Transport

$$\frac{\partial}{\partial x}(UU)+\frac{\partial}{\partial y}(VU)=-\frac{1}{\rho}\frac{\partial P}{\partial x}-\Omega^2 H_x+2\Omega W+\frac{\partial}{\partial x}\left(\nu_{\text{eff}}\frac{\partial U}{\partial x}\right)+\frac{\partial}{\partial y}\left(\nu_{\text{eff}}\frac{\partial U}{\partial y}\right)$$

$$\frac{\partial}{\partial x}(UV)+\frac{\partial}{\partial y}(VV)=-\frac{1}{\rho}\frac{\partial P}{\partial y}+\frac{\partial}{\partial x}\left(\nu_{\text{eff}}\frac{\partial V}{\partial x}\right)+\frac{\partial}{\partial y}\left(\nu_{\text{eff}}\frac{\partial V}{\partial y}\right)$$

$$\frac{\partial}{\partial x}(UW)+\frac{\partial}{\partial y}(VW)=-\frac{1}{\rho}\frac{\partial P}{\partial z}-\Omega^2 H_z-2\Omega U+\frac{\partial}{\partial x}\left(\nu_{\text{eff}}\frac{\partial W}{\partial x}\right)+\frac{\partial}{\partial y}\left(\nu_{\text{eff}}\frac{\partial W}{\partial y}\right)$$

$\nu_{\text{eff}}=\nu+\nu_t$ and H_x and H_z are the distances from the center of rotation in the x and z direction, respectively.

Continuity

$$\frac{\partial U}{\partial x}+\frac{\partial V}{\partial y}=0$$

Nomenclature

C_f = friction factor
$C_{\epsilon 1}$, $C_{\epsilon 2}$, C_μ = turbulence modeling constants
D = hydraulic diameter
H = distance from the center of rotation
k = turbulent kinetic energy
l = turbulent length scale
Nu = Nusselt number
P = pressure
P_k = turbulent kinetic energy generation rate
Pr = molecular Prandtl number
Re = Reynolds number
Ro = inverse Rossby number
U = mean velocity in x direction
U_τ = wall shear velocity
V = mean velocity in y direction
W = mean velocity in z direction
W_b = bulk velocity
x = cross-stream flow direction normal to the axis of rotation
Y = distance from the wall to the point in question
y = cross-stream flow direction parallel to the axis of rotation
y^+ = nondimensional wall distance
z = streamwise flow direction
ϵ = turbulent kinetic energy dissipation rate
Θ = temperature
ν = kinematic viscosity
ν_t = turbulent kinematic viscosity
ρ = density
σ = turbulent Prandtl number
Ω = angular velocity of coordinate rotation

Subscripts

0 = nonrotating reference state
P = pressure wall
S = suction wall
T = top wall

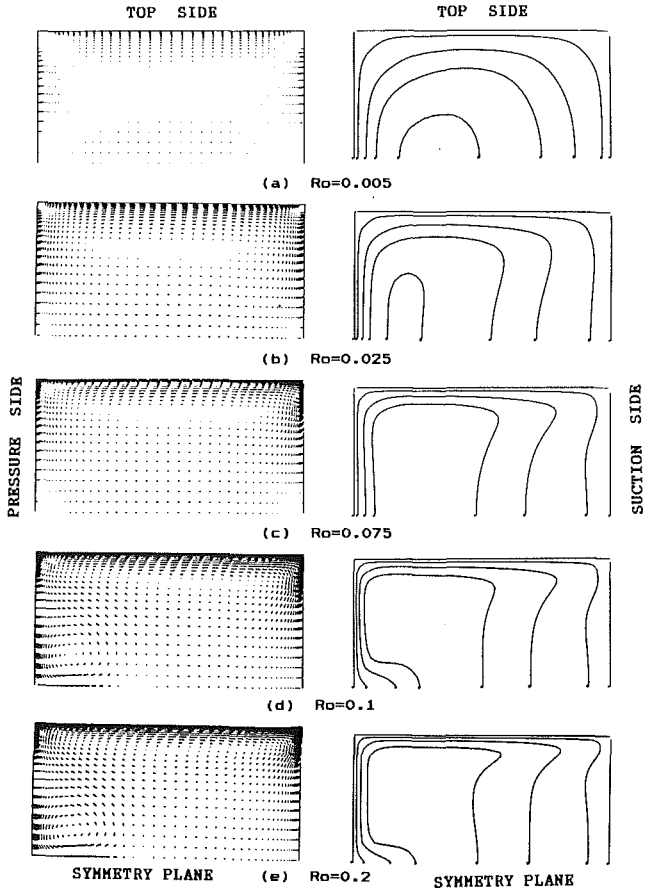

Fig. 2 Secondary velocity vectors and axial velocity contours for the square rotating duct at Re = 32,500

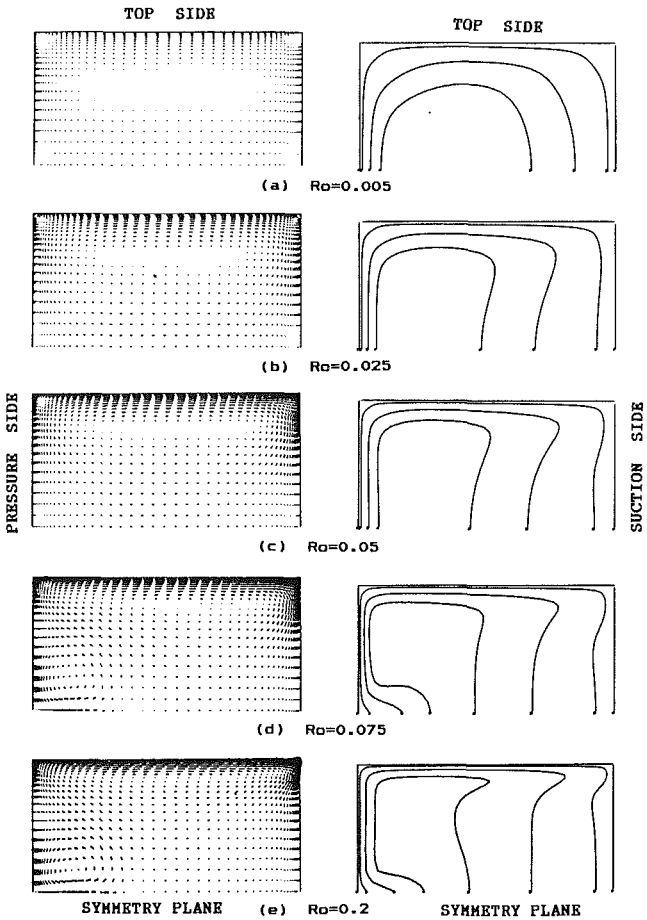

Fig. 3 Secondary velocity vectors and axial velocity contours for the square rotating duct at Re = 97,500

Enthalpy Equation

$$\frac{\partial}{\partial x}(U\Theta)+\frac{\partial}{\partial y}(V\Theta)=\frac{\partial}{\partial x}\left\{\left(\frac{\nu}{\mathrm{Pr}}+\frac{\nu_t}{\sigma_\Theta}\right)\frac{\partial\Theta}{\partial x}\right\}+\frac{\partial}{\partial y}\left\{\left(\frac{\nu}{\mathrm{Pr}}+\frac{\nu_t}{\sigma\Theta}\right)\frac{\partial\Theta}{\partial y}\right\}$$

Turbulence Modeling Equations. The turbulent viscosity ν_t is obtained by the following two expressions:

- in the high-Reynolds-number k–ϵ region

$$\nu_t = C_\mu k^2/\epsilon;$$

- in the low-Reynolds-number one-equation region

$$\nu_t = C_\mu l_\mu k^{1/2}$$

where $l_\mu = 2.4Y\{1-\exp-(0.016y^*)\}$

$$y^* = \sqrt{k^{1/2}}Y/\nu,$$

Y being the distance from the wall to the point in question.

Turbulent Kinetic Energy (k) Transport Equation

$$\frac{\partial}{\partial x}(Uk)+\frac{\partial}{\partial y}(Vk)=\frac{\partial}{\partial x}\left\{\left(\nu+\frac{\nu_t}{\sigma_k}\right)+\frac{\partial}{\partial y}\left\{\left(\nu+\frac{\nu_t}{\sigma_k}\right)\frac{\partial k}{\partial y}\right\}+P_k-\epsilon\right.$$

where $P_k=\left\{\left(\frac{\partial U}{\partial y}+\frac{\partial V}{\partial x}\right)^2+\left(\frac{\partial W}{\partial y}\right)^2+\left(\frac{\partial U}{\partial x}\right)^2+\left(\frac{\partial V}{\partial y}\right)^2\right\}\nu_t.$

Where the k–ϵ model is used, ϵ is obtained from a separate transport equation:

$$\frac{\partial}{\partial x}(U\epsilon)+\frac{\partial}{\partial y}(V\epsilon)=\frac{\partial}{\partial x}\left\{\left(\nu+\frac{\nu_t}{\sigma_\epsilon}\right)\frac{\partial\epsilon}{\partial x}\right\}+\frac{\partial}{\partial y}\left\{\left(\nu+\frac{\nu_t}{\sigma_\epsilon}\right)\frac{\partial\epsilon}{\partial y}\right\}+C_{\epsilon1}\frac{\epsilon}{k}P_k-C_{\epsilon2}\frac{\epsilon^2}{k}$$

In the one-equation region

$$\epsilon = k^{3/2}/l_\epsilon$$

where $l_\epsilon = 2.4Y[1-\exp-(0.236y^*)]$.

We note that, in the one-equation model, certain constants have been redefined to make it internally consistent with the k–ϵ model.

4 Numerical Aspects

A finite-difference control-volume numerical solver described in earlier publications (Iacovides and Launder, 1987b) has been used in this investigation. It is based on the well-known TEACH methodology. The staggered-grid approach is employed and conservation of mass and momentum is ensured through the integration of the transport equations over each control volume. Cross-stream numerical diffusion is minimized through the use of the quadratic upstream interpolation scheme (QUICK) for the discretization of the mean-flow convection terms.

Due to the flow symmetry, only half the duct cross section needs to be considered with symmetry boundary conditions at $y=0$. The use of a low-Reynolds-number model in the near-wall region enables the application of no-slip wall-boundary conditions. For the enthalpy equation, constant-wall-temper-

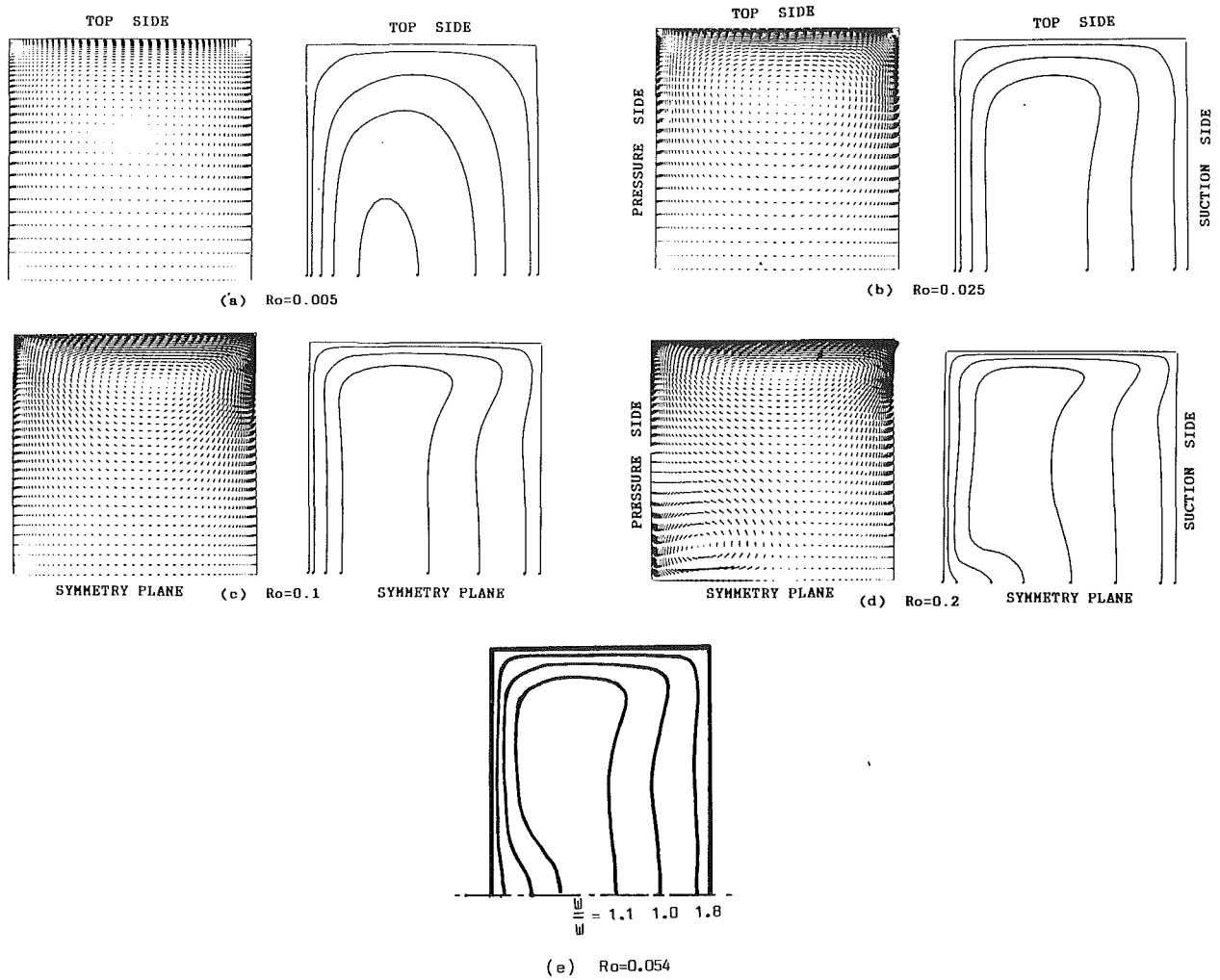

Fig. 4 Secondary velocity vectors and axial velocity contours for 2:1 aspect ratio duct at Re = 32,500

ature boundary conditions are imposed. The streamwise pressure gradient $\partial P/\partial z$ is assumed to be uniform across the duct and its level is determined from the overall continuity principle.

For the square geometry, a nonuniform mesh of 67 by 35 nodes (in the x and y directions) has been employed. The authors' earlier study of rotating duct flows has demonstrated that such a nonuniform mesh can produce flow predictions identical to those of significantly finer meshes provided the degree of nonuniformity is kept low. For the 2:1 aspect ratio duct computations, ten extra nodes were added in the y direction, resulting in a 67 by 45 mesh. In both geometries the ten nodes closest to the wall were located within the low-Reynolds-number one-equation region. The value of y^+ ($\equiv yU_\tau/\nu$) at the wall-adjacent nodes was always, less than 3. This ensures that these nodes are within the viscosity-dominated subregion where turbulent stresses are negligibly small. At the interface between the two- and the one-equation model regions, the y^+ values ranged between 80 and 120.

5 Presentation and Discussion of Results

Except where otherwise noted, all the computations presented here were obtained by starting with the stationary case and then gradually increasing the rotational speed. For the square duct, the flow evolution for Re = 32,500 is shown in Fig. 2 through a set of secondary velocity vector plots and streamwise velocity contour plots for values of the inverse Rossby number ranging from 0.005 to 0.2. As already explained, orthogonal-mode rotation leads to the formation of a pair of symmetric streamwise vortices, the strength of which increases with the inverse Rossby number. As the contour plots indicate, fluid with high streamwise momentum is convected by the secondary velocity toward the pressure side of the duct. This displacement of the fast-moving fluid becomes stronger at higher values of inverse Rossby number. As Ro is progressively increased, the core-region secondary flow toward the pressure surface and up toward the top wall means that the fluid with highest streamwise velocity is displaced off the symmetry plane. This in turn reduces the secondary flow on the symmetry plane because the Coriolis force ΩW is reduced. Indeed, by Ro = 0.1 the secondary flow on the axis has reversed direction with an extra counterrotating vortex being formed. This we hereafter refer to as the four-vortex structure since there are two pairs of vortices on either side of the symmetry plane. Further increase of Ro to 0.2 (a level somewhat above most internal cooling applications) brings little further change to the flow pattern.

Figure 3 shows the corresponding flow behavior at Re = 97,500. The rotating-flow evolution is similar to the one observed at Re = 32,500. One significant difference is that, at the higher value of Reynolds number, transition to a four-vortex structure occurs earlier, for an inverse Rossby number between 0.05 and 0.075. This is because, at the higher Reynolds number, the viscous forces are less significant relative to the inertial forces and, for a given Rossby number, the viscous terms are also less significant relative to the Coriolis terms.

The predictions for the 2:1 aspect ratio duct are displayed in Fig. 4. The mean flow field appears to be similar to that

observed in rotating square-duct flows. Because of the difference in cross-sectional geometry, the bulk of the secondary motion occurs farther away from the symmetry line. Another significant difference from the square-duct predictions is that, for a given Reynolds number, transition to a four-vortex mean-flow structure now occurs at a higher Rossby number (between 0.1 and 0.2 for Re = 32,500). This is due to the fact, that as the aspect ratio is increased, for a given rotational speed, the Coriolis forces are less significant (in the limit of an infinite aspect ratio there are no mean secondary motions).

Very recently our colleague Mr. T. Bo has been making further computations with the code for this 2:1 aspect ratio. He has examined *inter alia* the effect of successively *reducing* the inverse Rossby number starting from the above result for Ro = 0.2. From this exploration a substantial hysteresis in the transition between the two- and four-vortex state has become apparent. As the level of Ro is progressively reduced, the extra pair of secondary vortices gradually diminish in strength; the streamwise velocity contours for the lowest value of Ro for which the four-vortex mode was obtained (0.0535) are shown in Fig. 4(*e*). A more complete account of this bimodal behavior will be provided in a forthcoming publication.

The predicted distribution of local friction factor at Re = 32,500 (for both geometries) is shown in Fig. 5.[1] Initially the levels of friction factor on the top and pressure surfaces increase with rotation, while the suction side levels are reduced. Maximum and minimum values are located at the pressure and suction side symmetry points, respectively. For inverse Rossby numbers higher than 0.05 the pressure- and suction-side C_f levels appear to remain constant, while those on the top side continue to rise. The local maximum that appears on the suction side in the vicinity of the corner is clearly due to secondary-flow impingement. When the four-vortex flow structure is established, however, there is a substantial abrupt increase in the levels of C_f on the pressure side. The extra pair of vortices also cause a sharp fall in the local value of C_f in the vicinity of the symmetry line. At the highest inverse Rossby numbers considered (0.2) there is an almost 2:1 ratio in pressure-to-suction side levels of friction factor for the square duct. The corresponding ratio for the rectangular duct is approximately 1.5:1. Another interesting point is that, for Ro greater than 0.05, the maximum value of the local skin friction occurs on the top surface. This is more evident in the case of the 2:1 aspect ratio duct. A similar trend has also been observed by the authors in their numerical investigation of flows through rotating circular pipes. At a Reynolds number of 97,500 the computations for a square duct show a similar overall behavior to those presented above and are therefore not included here.

The corresponding local Nusselt number plots are shown in

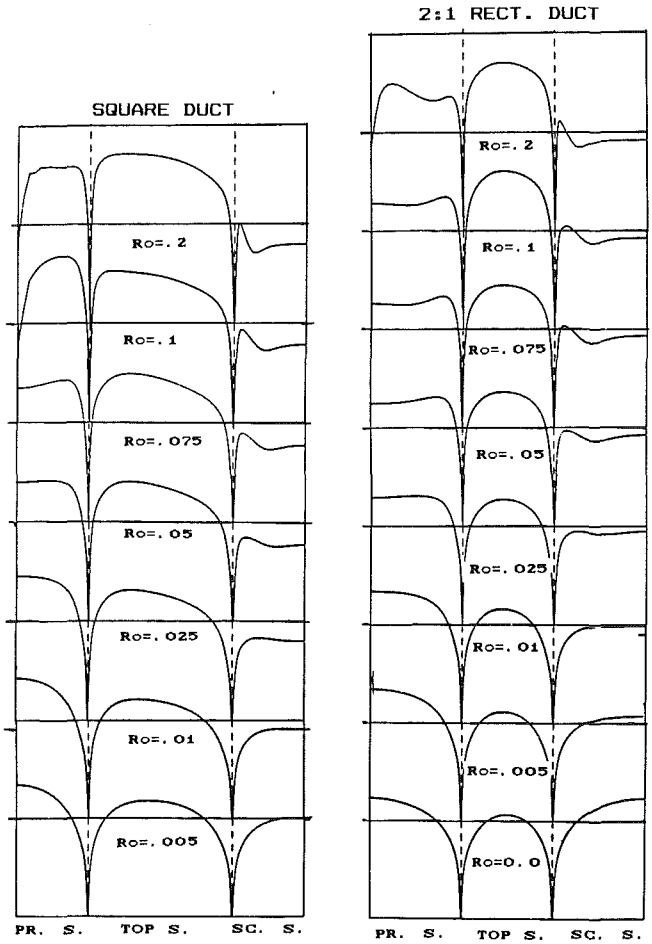

Fig. 5 Predicted distribution of the local normalized friction factor (C_f/C_{f_0}) for Re = 32,500

[1]All results shown arise from successively increasing Ro.

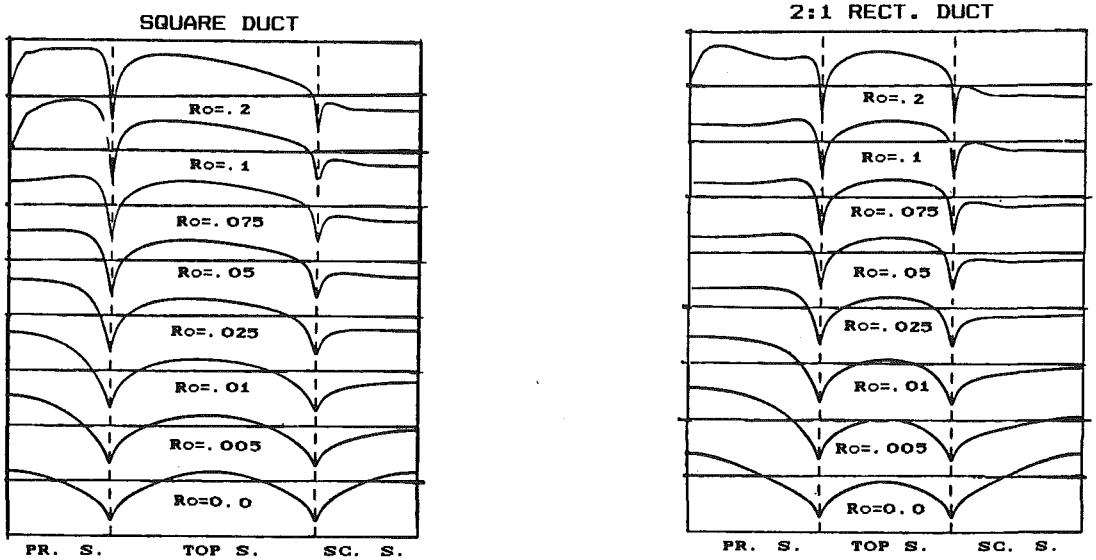

Fig. 6 Predicted distribution of the local normalized Nusselt number (Nu/Nu_o) for Re = 32,500

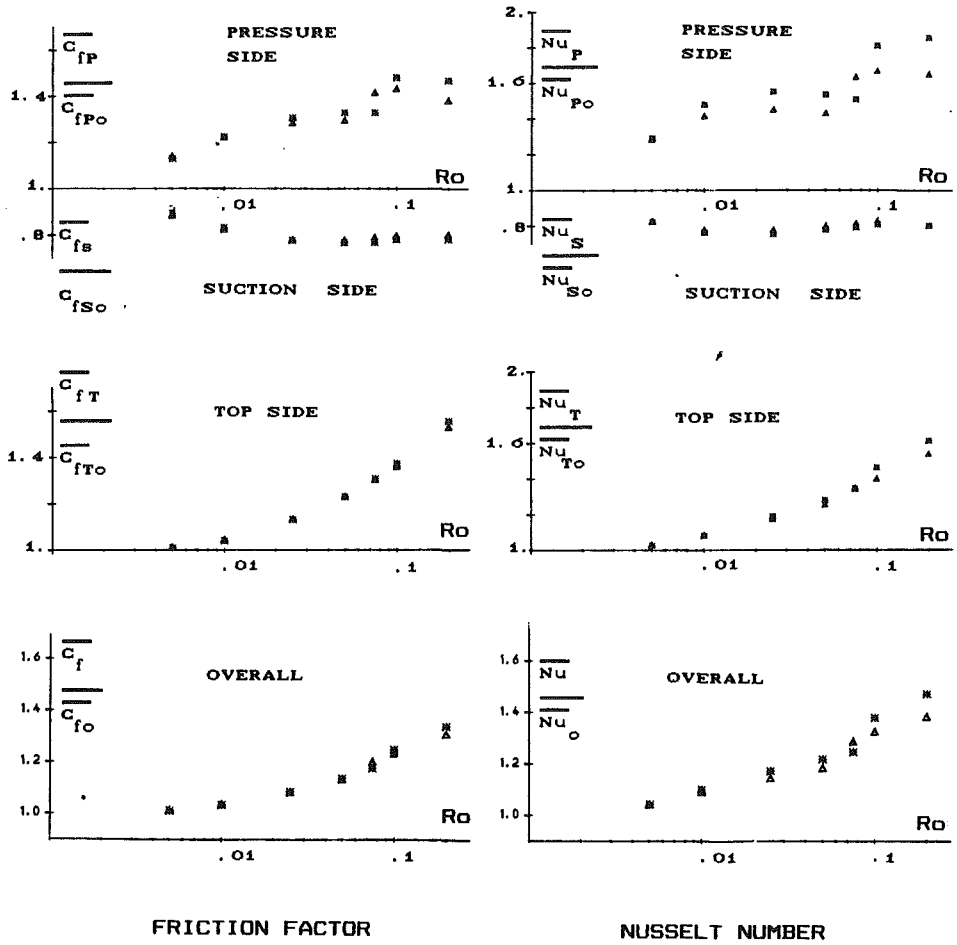

Fig. 7 Rossby-number dependence of individual side and total average friction factor and Nusselt number for square duct; * predictions for Re = 32,500; △ predictions for RE = 97,500

Fig. 6. The overall distribution is broadly similar to that of the local friction factor for both geometries. However, one significant difference from the friction-factor behavior is that the maximum local Nusselt number value is located at the pressure side for all the rotational speeds examined.

Figure 7 shows the Rossby-number dependence of the average friction factor and Nusselt numbers. Individual side averages as well as the overall average have been plotted. All values are normalized with the fully developed stationary duct flow values for the same Reynolds number. The pressure- and suction-surface plots indicate that, even at low values of Ro, there is a strong augmentation of the heat flux rate on the pressure surface and an equally strong suppression on the suction side. As already pointed out, the sudden jump in the average pressure side values of $\overline{Nu}$ and $\overline{C_f}$ is due to the onset of the four-vortex structure. This sudden rise is followed by either a leveling off or even a slight reduction as the inverse Rossby number is further increased. The average values on the suction side drop to about 80 percent of the stationary-duct values when the inverse Rossby number reaches a value of 0.025. Beyond this point there is no further reduction at higher rotational speeds. The suction side values show no Reynolds-number dependence. On the pressure side, however, the computations at the lower Reynolds number produce values of $\overline{Nu}$ and $\overline{C_f}$ that display a greater Rossby-number sensitivity. These findings are in qualitative agreement with Guidez's measurements. At the higher Reynolds number the pressure-to-suction side ratio for $\overline{C_f}$ is almost 2:1 and for $\overline{Nu}$ 2.5:1 at Ro = 0.2. The top-surface and overall average values of $\overline{C_f}$ and Nu display a more gradual and monotonic rise with Rossby number. A weak Reynolds-number dependence is also evident, particularly in the variation of the heat transfer coefficient. At Ro = 0.2 the computations indicate a 40 percent rise in $\overline{C_f}$ over the stationary duct value and nearly a 50 percent rise in $\overline{Nu}$.

The corresponding parametric behavior of $\overline{Nu}$ and $\overline{C_f}$ for the duct with 2:1 aspect ratio is shown in Fig. 8. Both the friction and heat transfer coefficients show a similar Rossby-number dependence to that observed in the square duct. In agreement with the earlier observations, it can be seen that the rotational effects are not as strong in the rectangular rotating duct as in the square duct. The highest ratio between pressure and suction side values is now under 1.5:1 for $\overline{C_f}$ and under 2:1 for $\overline{Nu}$. At Ro = 0.2 the overall friction factor is enhanced by about 30 percent compared with its stationary value and $\overline{Nu}$ by about 40 percent.

The computed side-averaged values of heat flux are also compared with Guidez's measurements for rotating flow after 7.6 diameters of development (i.e., non-fully developed flow). Rotational buoyancy effects that were ignored in the current computations were also present in the experimental data.[2] In view of this, it may be said that the current predictions are in reasonable qualitative agreement with the measurements. At the higher inverse Rossby numbers the predicted levels of heat transfer enhancement (or suppression) are similar to the measured ones. The greater discrepancies that appear at the lower rotational speeds can be attributed to the developing nature

[2]When the fluid moves away from the center of rotation, the rotational buoyancy force is likely to thicken the boundary layer along the top wall. This in turn would enhance the secondary flow and lead to a stronger perimetral variation in Nusselt number.

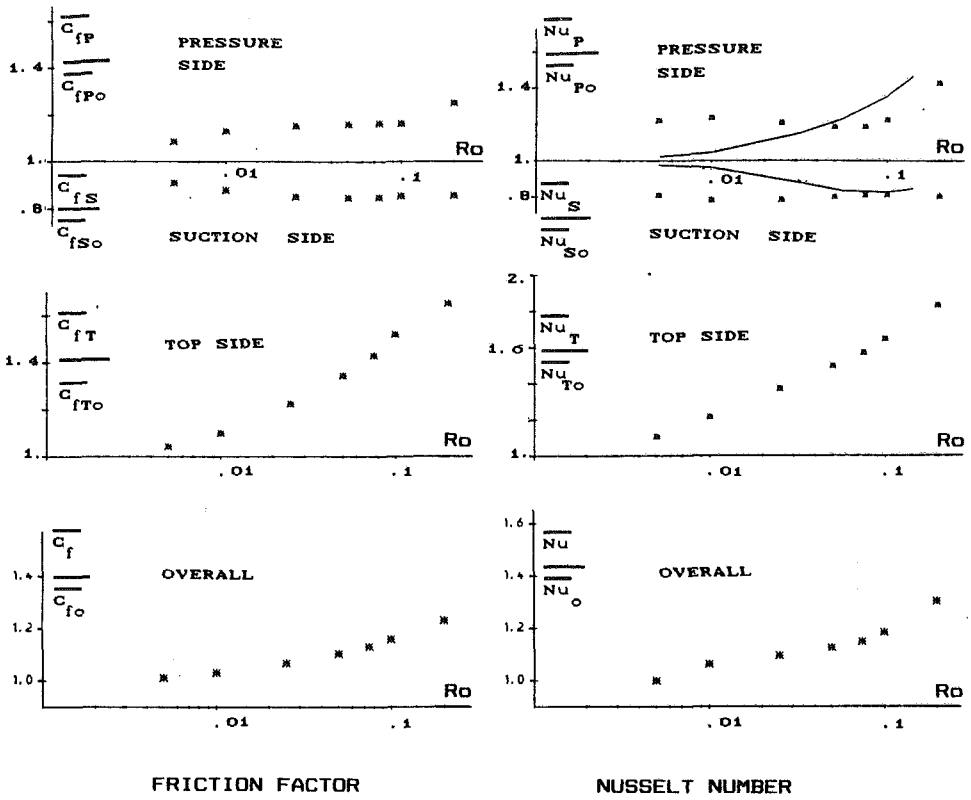

Fig. 8 Rossby-number dependence of individual side and total average friction factor and Nusselt number for the 2:1 aspect ratio duct: * predictions for fully developed flow at Re = 32,500; — experimental data for developing flow at $x/D = 7.4$ (Guidez)

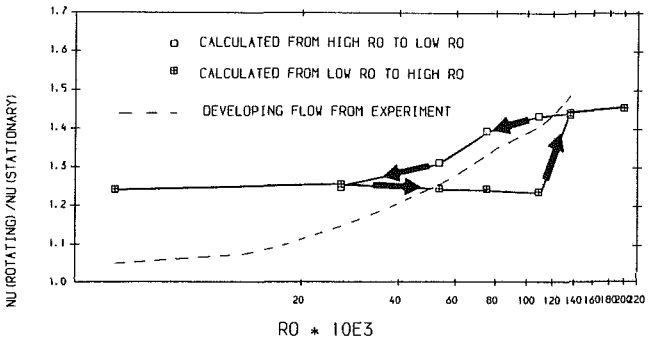

Fig. 9 Normalized Nusselt number on pressure surface of 2:1 duct showing hysteresis between two- and four-vortex modes

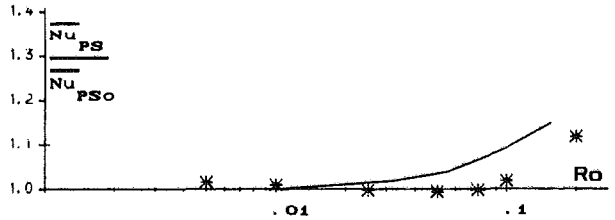

Fig. 10 Comparison for combined pressure and suction side averaged Nusselt number

of the measured flow. In Fig. 9 we see, in the latest UMIST calculations, the effect of the hysteresis mentioned earlier on the mean Nusselt number on the pressure surface (Bo, personal communication). The upper loop relates to the four-vortex mode, while the lower loop corresponds to a two-vortex pattern. A difference of up to 20 percent in the levels of Nusselt number for the two patterns of behavior is observed. Interestingly, the upper and lower branches span Guidez's data. Within the computational accuracy of the results, the average heat transfer levels on the other walls are not affected by whether a two- or four-vortex pattern is prevalent.

Finally, Fig. 10 compares variations in the computed and measured levels of Nusselt number averaged over both the pressure and suction surfaces as Ro is increased. Again, agreement is close enough to inspire further confidence in the validity of the current predictions.

6 Conclusions

In this work an extensive numerical study of the effects of Coriolis forces on fully developed rotating duct flows has been presented. The k–ϵ/one-equation computations show that as the rotation rate is increased, because of flow instabilities on the pressure side, the secondary flow undergoes a transition from the well-known double-vortex structure to a four-vortex regime. Transition occurs earlier at higher Reynolds numbers where viscous effects are less significant. It also occurs earlier in the square than the rectangular duct due to the weaker net Coriolis forces in the latter case. Over a finite range of rotation numbers, including levels of Ro of turbomachine interest, either a two- or four-vortex solution may be achieved depending on the initial conditions.

The Coriolis-induced secondary flow causes considerable augmentation of the heat transfer coefficient on the pressure and top surfaces (up to 90 percent over the stationary value) and suppresses the suction side coefficients to around 80 percent of the stationary value. The variation of the average heat transfer appears to be independent of Reynolds number on the suction side; indeed, the levels become almost independent

of Ro at high rotation number. The pressure- and top-side heat transfer rates continue to rise at higher rotational speeds and are also Reynolds-number dependent. Although the cooling passages in turbine blades may not be long enough for fully developed flow to be established, the present results (normalized with respect to nonrotating flow) provide a guide (and possibly an upper limit) to the effects to be found in developing flow. Indeed, the predicted trends and Nusselt-number levels are in good qualitative agreement with existing measurements of developing flow in rotating ducts.

Further work is now in progress aimed at including rotational buoyancy effects and at extending the computations to the case of developing flow. These results will be reported in a forthcoming paper.

Acknowledgments

The research has been supported by Rolls-Royce plc under Research Brochure B1D2-125D. Our thanks are due to Mr. T. Bo for making available an extract from his recent computations. The camera-ready mats were produced with appreciated care by Mrs. L. J. Ball.

Authors' names are listed alphabetically.

References

Choi, Y. D., Iacovides, H., and Launder, B. E., 1989, "Numerical Computation of Turbulent Flow in a Square-Sectioned 180-deg Bend," ASME *Journal of Fluids Engineering*, Vol. 111, pp. 59–68.

Guidez, J., 1989, "Study of the Convective Heat Transfer in a Rotating Coolant Channel," ASME JOURNAL OF TURBOMACHINERY, Vol. 111, pp. 43–50.

Hart, J. E., 1971, "Instability and Secondary Motion in a Rotating Channel Flow," *J. Fluid Mech.*, Vol. 45, pp. 341–351.

Hill, P. G., and Moon, I. M., 1962, "Effect of Coriolis on the Turbulent Boundary Layer in Rotating Fluid Machines," Massachusetts Institute of Technology Gas Turbine Lab. Rep. No. 69.

Iacovides, H., and Launder, B. E., 1987a, "The Numerical Simulation of Flow and Heat Transfer in Tubes in Orthogonal-Mode Rotation," *Proc. 6th Symp. on Turbulent Shear Flows*, Toulouse, France.

Iacovides, H., and Launder, B. E., 1987b, "Turbulent Momentum and Heat Transport in Square-Sectioned Duct Rotating in Orthogonal Mode," *Num. Heat Transfer*, Vol. 12, pp. 475–491.

Kheshgi, H. S., and Scriven, L. E., 1985, "Viscous Flow Through a Rotating Square Channel," *Phys. Fluids.*, Vol. 28, pp. 2968–2979.

Lin, S. J., Briley, W. R., and McDonald, H., 1985, "Numerical Study of Three-Dimensional Viscous Flows With Systems Rotation," AIAA Paper No. 85-1691.

Moore, J., 1967, "Effects of Coriolis on Turbulent Flow in Rotating Rectangular Channels," Massachusetts Institute of Technology Gas Turbine Lab. Rep. No. 89.

Morris, W. D., and Harasgama, S. P., 1985, "Local and Mean Heat Transfer on the Leading and Trailing Surfaces of a Square-Sectioned Duct Rotating in the Orthogonal Mode," *Proc. AGARD Conf. No. 390*, France.

Speziale, C. G., 1982, "Numerical Study of Viscous Flow in Rotating Rectangular Ducts," *J. Fluid Mech.*, Vol. 122, pp. 251–271.

Wagner, J. H., Johnson, B. V., and Hajek, T. J., 1991, "Heat Transfer in Rotating Passages With Smooth Walls and Radial Outward Flow," ASME JOURNAL OF TURBOMACHINERY, Vol. 113, pp. 42–51.

Wagner, R. E., and Velkoff, H. R., 1972, "Measurements of Secondary Flows in a Rotating Duct," ASME *Journal of Engineering for Power*, Vol. 94, pp. 261–270.

Wolfshtein, M., 1969, "The Velocity and Temperature Distribution in One-Dimensional Flow With Turbulence Augmentation and Pressure Gradient," *Int. J. Heat Mass Transfer*, Vol. 12, p. 301.

Heat Transfer Measurements in Rectangular Channels With Orthogonal Mode Rotation

W. D. Morris
Professor,
Mechanical Engineering,
University College of Swansea,
Singleton Park,
Swansea, SA2 8PP, United Kingdom

G. Ghavami-Nasr
Research Officer,
British Steel, plc.,
Welsh Research Laboratories,
Port Talbot SA13 2NG, United Kingdom

The influence of rotation on local heat transfer in a rectangular-sectioned duct has been experimentally studied for the case where the duct rotates about an axis orthogonal to its own central axis. The coolant used was air with the flow direction in the radially outward direction. This rotating flow geometry is encountered in the internal cooling of gas turbine rotor blades. Local Nusselt number variations along the duct have been determined over the trailing and leading surfaces. In general terms Coriolis-induced secondary flows are shown to enhance local heat transfer over the trailing surface compared to a stationary duct forced convection situation. The converse is true on the leading surface where significant impediment to local heat transfer can occur. Centripetal buoyancy is shown to influence the heat transfer response with heat transfer being improved on both leading and trailing surfaces as the wall-to-coolant temperature difference is increased with other controlling parameters held constant. Correlating equations are proposed and the results compared with those of other workers in the field.

Introduction

It is common practice to include active cooling in the design of modern high-performance gas turbine rotor blades using air bled from suitable stages in the compressor section. The air is fed to the root section of the blade and subsequently flows through a series of internal passages in either a predominantly radially outward or inward direction depending on the complexity of the heat transfer duty required.

Because the coolant is moving in the radial direction while simultaneously rotating with the blade, it is subjected to the combined effect of a Coriolis and centripetal acceleration field. These inertial effects have been shown significantly to alter the flow and cooling characteristics of the system in relation to the nonrotating case, which corresponds to simple forced convection. The present paper reports the results of an experimental investigation of the influence of these rotationally induced inertial effects on forced convection in a rectangular-sectioned duct, the geometric description of which is illustrated in Fig. 1.

In broad terms the Coriolis forces tend to create a secondary flow in planes perpendicular to the main flow direction, which encourages the migration of core region flow toward the trailing surface of the cooling channel with a return flow to preserve continuity along the wall regions as shown in Fig. 1. This secondary flow promotes better heat transfer in the vicinity of the trailing surface in comparison to that on the leading surface. The Rossby number, Ro, is a convenient parameter for quantifying the influence of Coriolis acceleration in a rotating flow. It is defined as the ratio of the mean throughflow velocity of the fluid along the duct to a peripheral velocity formed by the product of the angular velocity and a convenient length scale representation of the flow geometry. For consistency with the customary definition of a duct Reynolds number, the hydraulic diameter of the duct is appropriate in the present case for the definition of a Rossby number. The Rossby number may be thought of as a measure of the relative strength of inertial-to-Coriolis forces acting on the fluid.

The centripetal forces are hydrostatic in the absence of fluid density gradients. However, with heated flow the density is functionally related to temperature via an appropriate equation of state. Under these circumstances the centripetal forces produce a buoyant interaction, which also modifies the flow and heat transfer characteristics of the cooling system in comparison to the stationary case.

Free convection due to the earth's gravitational field is nondimensionally characterized using the well-known Rayleigh number, Ra. In the present case a similar parameter may be used to characterize the effect of rotationally induced buoyancy with the "g" term in the customary Rayleigh number replaced by a convenient measure of the centripetal acceleration experienced by the fluid.

It may be expected that the heat transfer coefficient at some axial location downstream of the entry plane will be functionally related to other operating parameters via a nondimensional equation having the form

$$\mathrm{Nu} = \Phi[\mathrm{Re}, \mathrm{Pr}, \mathrm{Ro}, \mathrm{Ra}, z/d] \quad (1)$$

where Φ is an unknown function and

Contributed by the International Gas Turbine Institute and presented at the 35th International Gas Turbine and Aeroengine Congress and Exposition, Brussels, Belgium, June 11–14, 1990. Manuscript received by the International Gas Turbine Institute February 12, 1990. Paper No. 90-GT-138.

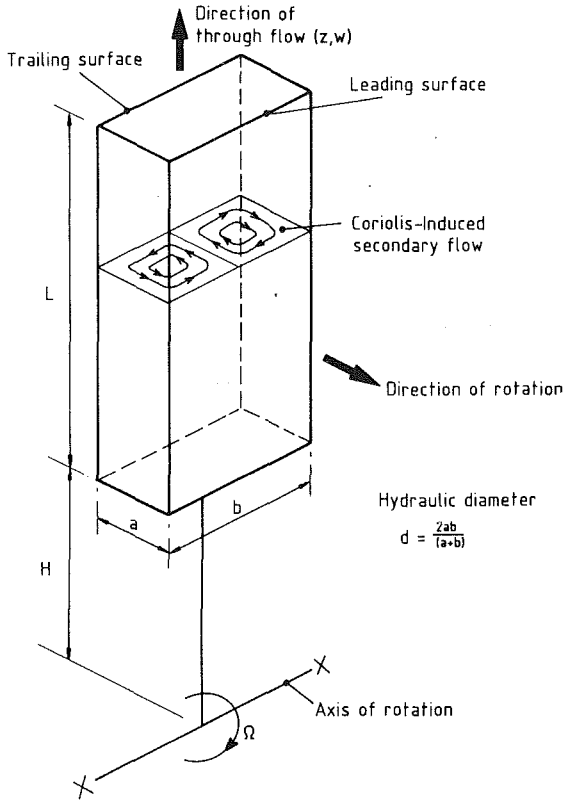

Fig. 1 Rotating flow geometry

$$\mathrm{Nu}=\frac{hd}{k} \quad \text{(Nusselt number)} \tag{2}$$

$$\mathrm{Re}=\frac{wd\rho}{\mu} \quad \text{(Reynolds number)} \tag{3}$$

$$\mathrm{Pr}=\frac{\mu C_p}{k} \quad \text{(Prandtl number)} \tag{4}$$

$$\mathrm{Ro}=\frac{w}{\Omega d} \quad \text{(Rossby number)} \tag{5}$$

$$\mathrm{Ra}=\frac{\beta(H+z)\Omega^2\rho^2 C_p d^3(T_w-T_f)}{\mu k} \quad \text{(Rayleigh number)} \tag{6}$$

Note that all symbols are defined in the nomenclature.

The Rayleigh number may be rewritten in terms of the Rossby, Reynolds, and Prandtl numbers to give

$$\mathrm{Ra}=\left[\frac{\mathrm{Re}}{\mathrm{Ro}}\right]^2 \mathrm{Pr}\left[\epsilon+\frac{z}{d}\right]\beta(T_w-T_f) \tag{7}$$

where

$$\epsilon=H/d \quad \text{(eccentricity ratio)} \tag{8}$$

which permits equation (1) to be alternatively expressed as

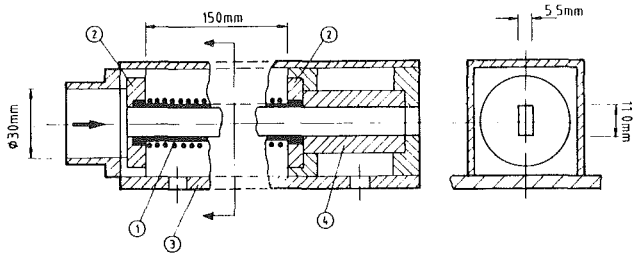

Fig. 2 Test section construction

$$\mathrm{Nu}=\Phi[\mathrm{Re},\mathrm{Pr},\ \mathrm{Ro},\ \epsilon,\ \beta(T_w-T_f),\ z/d] \tag{9}$$

if preferred.

Equation (1) or the equivalent version given by equation (9) must be consistent with an appropriate forced convection correlation when the duct is stationary.

Because of the three dimensionality of the total flow system, equation (1) will also be influenced by the circumferential location at a given axial location. In the present paper the effect of the rotational nondimensional groups has been experimentally studied on the centerlines of the leading and trailing surfaces.

Clearly rotor blade designers must take into account these rotationally induced effects if reliable performance predictions are to be made of cooling capability and blade life. A number of investigations into the effect of rotation on flow and forced convection in ducts rotating in this so-called orthogonal mode have been reported over the last few years [1–20]. The current investigation was undertaken to create a data base of fundamental results for the validation of CFD codes and to develop empirical correlations for quantifying the likely effect of rotation on heat transfer in a design role.

Apparatus

Figure 2 shows the constructional details of the rectangular test section used for the investigation. The actively heated section (1) was cast in Nimonic alloy (thermal conductivity = 11.6 W/mK), using the investment or lost wax method, to give an internal cross section of 11.0 by 5.5 mm and subsequently machined to give a uniform thickness of 1.0 mm. A 6.0-mm-long enlarged section at the inlet and exit ends of the heated channel permitted attachment to thermally insulated support bushes (2), which themselves were screwed to a duralumin base plate (3). The length of the actively heated test section, between the insulating bushes, was 150 mm. A thermally insulated extension piece (4) was attached to the exit end of the test section to permit the insertion of a mixing gauze to facilitate measurement of the exit coolant bulk temperature.

The test section was electrically heated using Nichrome resistance wire of 0.5 mm diameter spirally wound over the exterior surface. To prevent the heater coils centrifuging when in operation, notches were cut on the external corners to act as locators.

Temperature was measured on the leading and trailing sur-

Nomenclature

A = const
B = const
C = const
D = const
a = duct cross-sectional dimension
b = duct cross-sectional dimension
C_p = specific heat
d = hydraulic diameter
h = heat transfer coefficient
k = thermal conductivity
w = mean axial velocity
z = local axial position
H = eccentricity
Nu = Nusselt number
Pr = Prandtl number
Ra = Rayleigh number
Re = Reynolds number
Ro = Rossby number
T_f = fluid bulk temperature
T_w = wall temperature
β = expansion coefficient
ϵ = eccentricity ratio
μ = viscosity
ρ = density
Φ = function
Ω = angular velocity

Table 1 Range of nondimensional variables

Reynolds number range	10,000 - 25,000
Rossby number range	50 maximum
Rayleigh number range	$4 \times 10^5 - 3 \times 10^6$

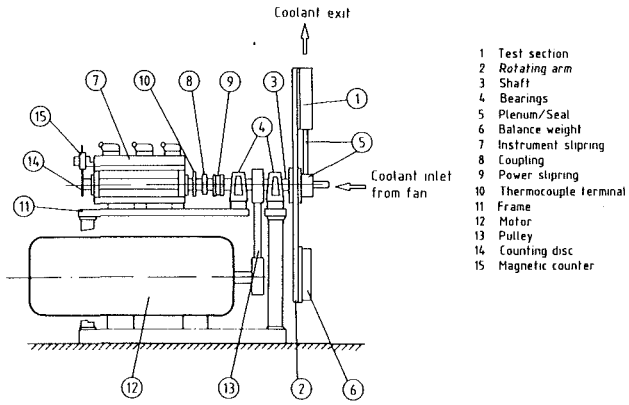

Fig. 3 Test facility

faces of the test section using chromel/alumel thermocouples. Eleven thermocouples were used on each of these surfaces and axially located to divide the heated section into ten equidivisions (i.e., 15 mm axial separation). Each thermocouple was actually located so that its sensing junction was midway through the wall thickness. Mutual electrical insulation between the test section wall, thermocouples, and heating wire was achieved using layers of Kapton insulating tape.

The temperature of the coolant air was also measured using chromel/alumel thermocouples. For the air inlet temperature a single thermocouple located in the immediate entry plenum supplying air to the test section was used. Two similar thermocouples located downstream of the mixing gauze located in the exit adiabatic extension piece (4) were used to monitor the exit coolant bulk temperature.

After assembly and mounting onto the duralumin base plate the test section was externally insulated using bulk fiber insulation tape and Systoflex glass fiber and finally encased in a duralumin sheet cover, thus forming a compact subassembly.

The test section was mounted on a rotating arm so that the midspan eccentricity of the actively heated channel was 250 mm. The rotating arm formed part of a general rotating facility involving a controlled drive system, power and instrumentation slip-ring assemblies, air delivery system including rotary seals, and settling plenum, as indicated in Fig. 3. Further constructional details have been published previously [9, 13].

All thermocouple signals were monitored with a Solatron System 35 data acquisition system. Air flow rate was measured using an Anubar differential pressure meter. Rotor speed was measured with a magnetic encoder and digital timer counter and heater power with a conventional wattmeter. A pressure regulator facilitated control of the flow to enable Reynolds numbers to be held within ±1 percent of nominal values for a run series.

Experimental Details

The strategic aim of the investigation was to measure experimentally the local heat transfer on the leading and trailing surfaces of this rotating rectangular channel and to assess the effect of rotation on an otherwise ducted flow forced convection problem. Heat transfer was quantified using the customary Nusselt number as indicated above. In order to determine the

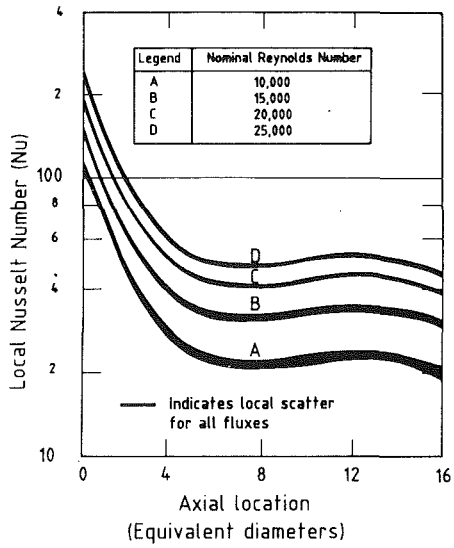

Fig. 4 Local heat transfer variation at zero rotational speed (leading and trailing surfaces)

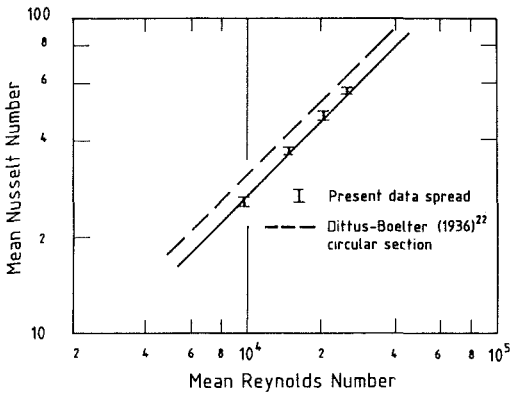

Fig. 5 Variation of mean Nusselt number with mean Reynolds number, at zero rotational speed (evaluated over 16 effective diameters)

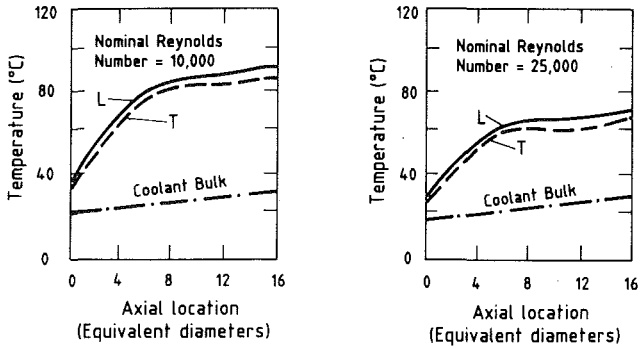

Fig. 6 Typical variation of temperature over the leading and trailing surfaces with rotation present (angular velocity = 1800 rpm)

local Nusselt number, it is necessary to know the axial variation of heat flux from the channel wall and the locally prevailing difference between the wall temperature and the bulk temperature of the coolant. The method of heating employed tends to produce a reasonable approximation to uniform generation along the duct axis, that is, the radial direction when rotating. However, because of axial conduction along the walls of the channel and inevitable external loss to atmosphere through the insulation surrounding the test section, a proportion of the

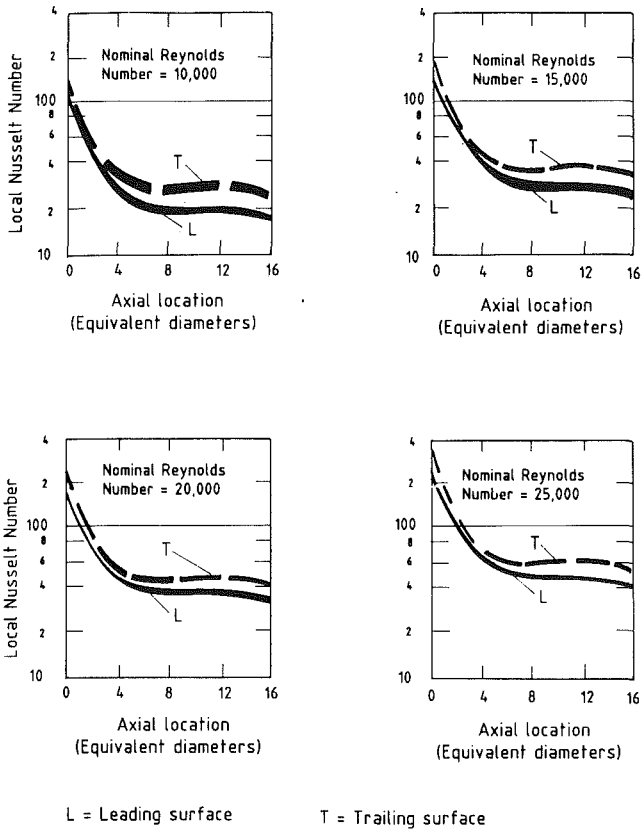

Fig. 7 Comparison of local Nusselt numbers over leading and trailing surfaces (angular velocity = 1800 rpm)

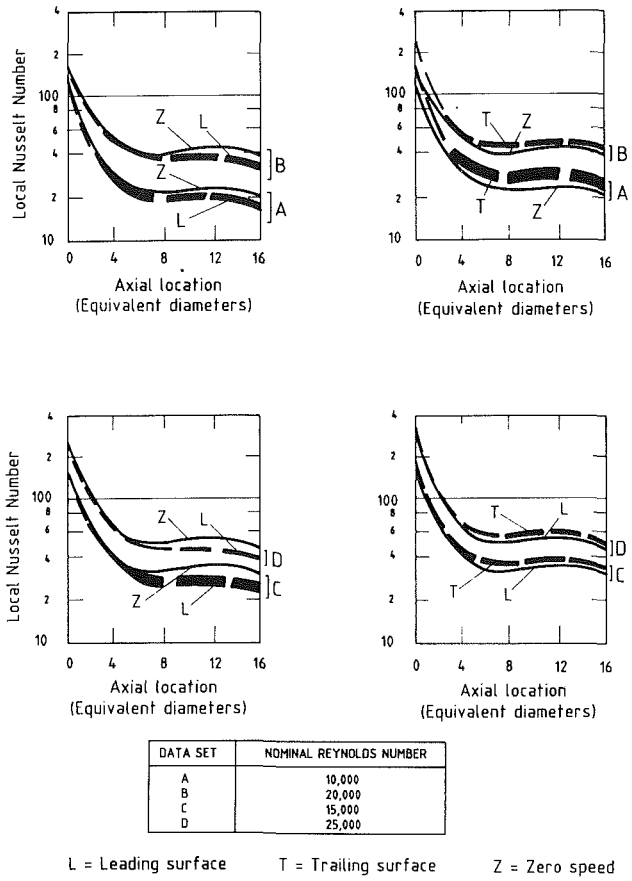

Fig. 8 Comparison of local Nusselt numbers over leading and trailing surfaces with corresponding zero speed controls (angular velocity = 1800 rpm)

generated energy does not get transferred to the coolant. To account for this a series of heat loss calibrations was undertaken with the internal convective space of the test section packed with soft insulation. These calibrations were conducted at all rotational speeds used for the main test program and produced a series of external loss coefficients, which could be applied on a local basis along the test section. Additionally, using the measured axial distribution of duct wall temperature, an allowance for axial conduction could be made numerically from curve-fitted polynomials of the wall temperature distribution. The final outcome of this energy accountancy procedure was an axial distribution of heat flux at the leading and trailing surfaces of the test section. Estimates of heat losses suggest the calculated heat fluxes were subject to a ± 10 percent error.

Having determined the flux distribution, the bulk temperature of the coolant was calculated by straightforward integration along the actively heated part of the test assembly. Comparison of the finally calculated air bulk temperature with that actually measured in the adiabatic exit mixing chamber gave an indication of the overall energy accountancy. In general unaccounted or stray energy losses were less than 10 percent of the total energy supplied to the heater section.

A data processing program was prepared to calculate the wall heat flux distribution and the bulk temperature of the coolant using the strategy outlined above. Subsequently local values of all appropriate nondimensional groups, as indicated by equation (1), were calculated and filed on disk for printout or graph plotting as necessary.

Table 1 gives the range of operating conditions covered by the tests.

Results and Discussion

Commissioning and validation experiments, undertaken at zero rotational speed, confirmed that the processed data gave good agreement with accepted forced convection recommendations. There was no systematic variation in the spanwise wall temperature between the leading and trailing surfaces. Figure 4 shows the variation of local Nusselt number measured along the stationary test section for the entire range of Reynolds numbers tested. The thickness of each Reynolds number band spans data scatter resulting from five sets of heater power settings used. In this figure, as with other plots of local Nusselt number to follow, the final 20 percent of the test section has been ignored due to end loss uncertainties.

Figure 5 shows the variation of mean Nusselt number, integrated over the initial 16 effective diameters of the test section, for these zero speed validation tests, with mean Reynolds number. The data are approximately 15 percent below the Dittus–Boelter [20] line for forced convection assuming an effective diameter analogy. These zero speed data were subsequently used as a benchmark with which to evaluate the effect of rotation.

When the experiments were repeated with rotation the leading surface of the duct was systematically found to operate at a higher temperature than the trailing surface, as indicated by the raw data samples presented in Fig. 6. This, of course, is consistent with the presence of a Coriolis-driven cross-stream secondary flow causing relatively cool fluid from the central duct region to spiral onto the trailing surface, thus stimulating enhanced cooling.

Figure 7 shows the typical variation of local Nusselt number on the leading and trailing surfaces obtained with rotation. Clearly the heat transfer on the trailing surface can be significantly enhanced relative to the leading surface; this is consistent with a number of previously published works with other duct cross sections. In this figure it is interesting to draw attention to the data band widths associated with each Reyn-

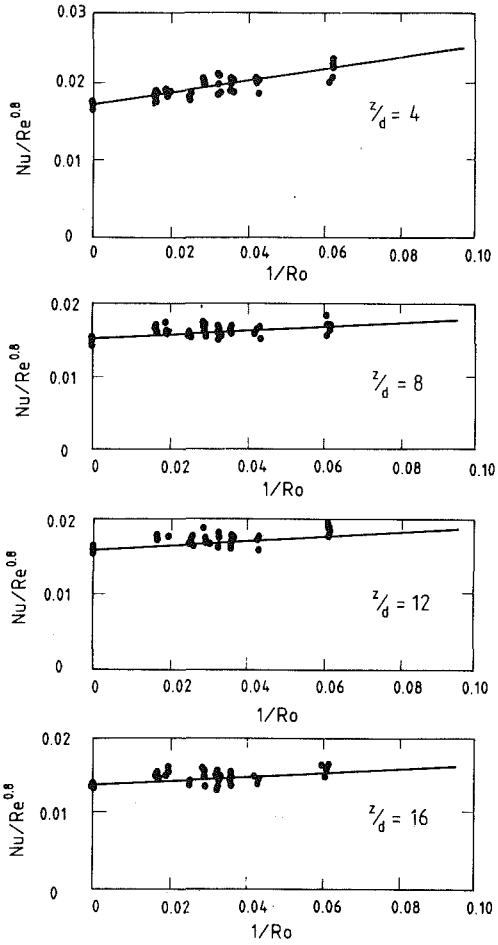

Fig. 9 Effect of rotation on local heat transfer on trailing surface

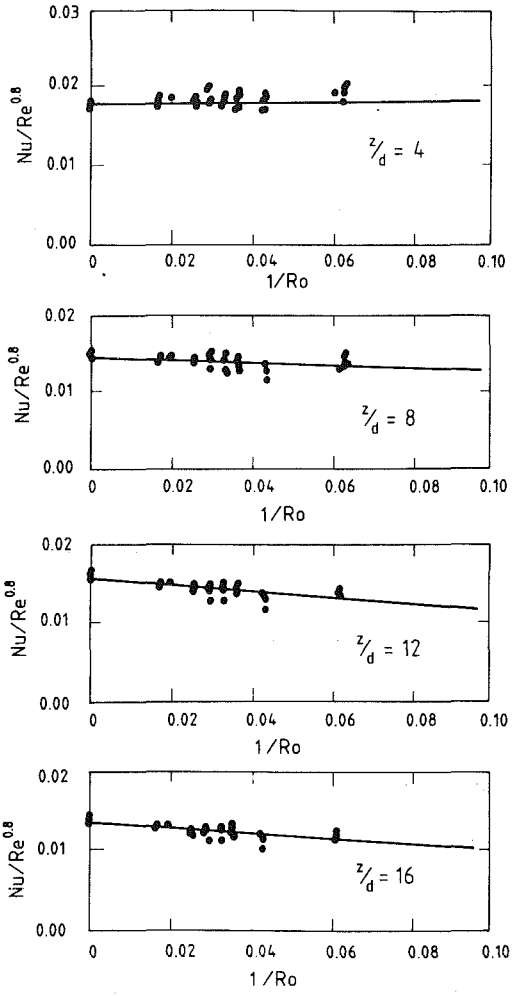

Fig. 10 Effect of rotation on local heat transfer on the leading surface

Table 2 Trailing edge correlating constants

z/d	A	B
4	0.0176	3.989
8	0.0151	1.682
12	0.0163	1.632
16	0.0140	1.750

olds number curve. At the lower Reynolds number values there is a tendency for the bandwidth to be wider. When it is remembered that each Reynolds number sequence involves about five individual tests undertaken with closely controlled but nominally fixed values of the Reynolds and Rossby number, but with varying heater power settings, it is apparent that centrifugal buoyancy is affecting the lower Reynolds number data. This point will be returned to later in the paper.

Although the relatively better heat transfer on the trailing surface would appear to be beneficial from the viewpoint of blade cooling system design, it is important to assess the effect of rotation on both surfaces in relation to what might be expected with purely forced convection. This is illustrated in Fig. 8 where the data for the leading and trailing surfaces are individually compared with the corresponding zero speed data. Note that this was directly possible by virtue of the experimental control of the overall test program to ensure that there was no more than ± 1 percent variation in the Reynolds number at test section inlet for every Reynolds number batch of tests.

Figure 8 shows that the trailing surface heat transfer was better than that suggested by pure forced convection. However, the heat transfer over the leading surface is impaired compared with the stationary case. This is confirmation of an important observation found with other cross-sectional duct shapes, in that blade designs using stationary-generated heat transfer correlations can result in a failure to predict the occurrence of local hot spots over the leading surface of the coolant passage.

Although some evidence of a buoyant action is evident, its effect is not very significant over the speed range covered in this study. By ignoring buoyancy as a first approximation and assuming that conventional forced convection could be taken into account via a term involving the Reynolds number raised to the power 0.8, it was possible to examine the influence of the Coriolis forces in isolation.

At various values of downstream location, Fig. 9 shows the variation of local Nusselt number with the reciprocal of the Rossby number for the trailing surface. The ordinate of this figure is the quotient of the Nusselt number and the 0.8th power of the Reynolds number, which has the effect of attempting to isolate the normal forced convection effect. Within the confines of experimental scatter this plot was able to demonstrate a consistent trend at a variety of downstream spanwise locations with all Reynolds/Rossby number combinations straddling the correlating line indicated in the figure. The increased heat transfer compared to a zero speed operation is clearly demonstrated. Each correlating line shown had the mathematical structure

$$\mathrm{Nu} = A(1 + B/\mathrm{Ro})\mathrm{Re}^{0.8} \tag{10}$$

where the constants A and B were dependent on the axial

Table 3 Leading edge correlating constants

z/d	A	B
4	0.0176	0
8	0.0151	-1.236
12	0.0156	-2.417
16	0.0140	-2.280

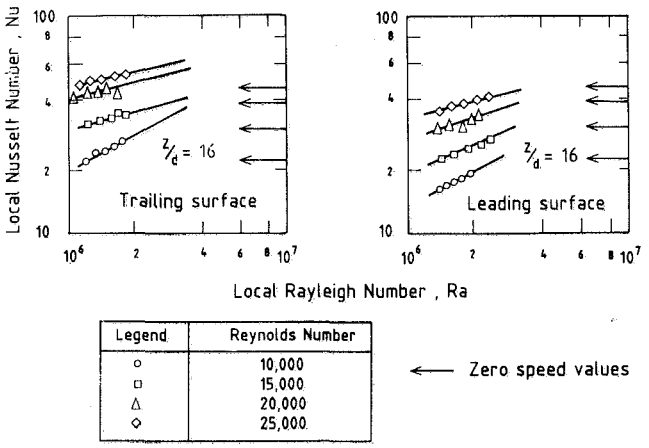

Fig. 11 Typical influence of centripetal buoyancy on local heat transfer (rotational speed = 1800 rpm)

location. Table 2 shows the values proposed for these constants.

Figure 10 illustrates a similar plot for the leading surface. With the exception of the data shown at $z/d=4$ (near the entry plane) there is a systematic reduction in local heat transfer as the rotational speed increases. Similar correlating equations to those used for the trailing edge gave values of the correlating constants A and B as indicated in Table 3 for the leading surface.

When tests were conducted at fixed Reynolds number and rotational speed, but with varying levels of wall-to-fluid bulk temperature difference, evidence of a buoyant interaction was noted. It was found that an increase in local Nusselt number with increases in the Rayleigh number occurred on both leading and trailing surfaces at all axial locations. Figure 11 illustrates the trends found at the highest rotational speed used for an axial location $z/d=16$.

It was not found possible, because of data limitations, to incorporate this buoyancy effect into the correlating equations. However, it is interesting qualitatively to illustrate the importance of buoyancy by noting the tendency for the slopes of the individual lines shown in Fig. 11 to approach zero as the Reynolds number is increased. If each individual line is assumed to be expressed as

$$\mathrm{Nu}=C\,\mathrm{Ra}^{D} \tag{11}$$

where C and D are constants, then curve fitting the data permits D to be evaluated. It was found that for a given axial location the slope of equation (11) could be uniquely related to the Rossby number at all Reynolds numbers used in the program. Figure 12 shows the outcome of this study for the trailing edge. As the Rossby number is increased the slope systematically approaches an asymptote of zero corresponding to a horizontal line. Further data obtained with higher values of Rayleigh number of $\beta(T_w-T_f)$ are needed to quantify the effect of rotational buoyancy, but it must now be recognized that the results of a number of studies have demonstrated a tendency

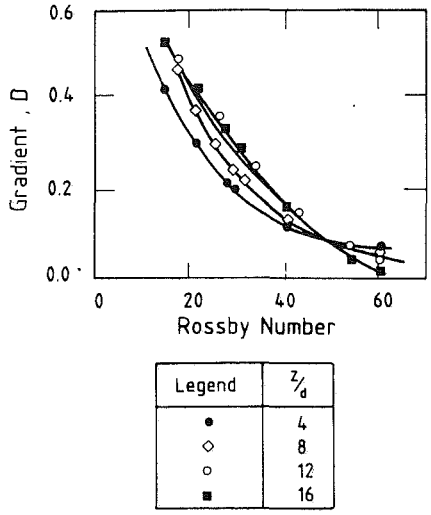

Fig. 12 Effect of Rossby number on the sensitivity to buoyancy

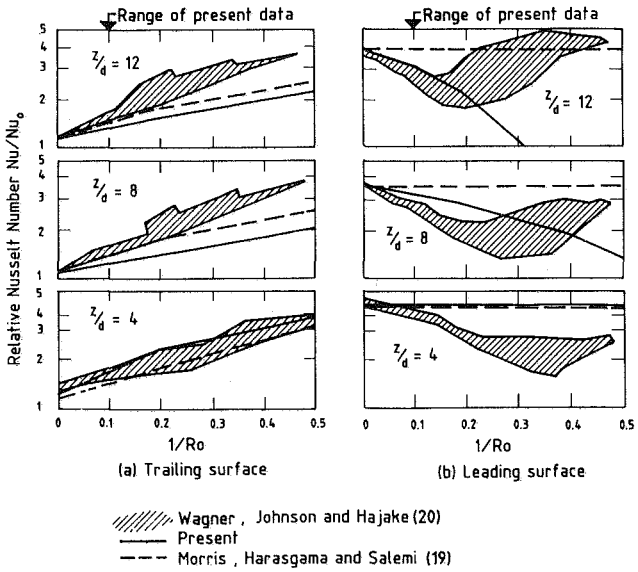

Fig. 13 Comparison of extrapolated present results with those of other workers

for heat transfer to increase with Rayleigh number when the flow is from root to tip.

The correlations proposed for the trailing and leading surfaces are compared with the results of Wagner et al. [20] in Figs. 13(a) and 13(b), respectively. The Wagner data were actually obtained with a square-sectioned duct with lower Rossby numbers than the work reported here. The individual data lines of Wagner et al. clearly demonstrated a similar buoyancy effect to that described above. The hatched zones in Figs. 13(a) and 13(b) cover all the data shown by Wagner et al. Superimposed on these figures are the correlations proposed here for three values of axial location. Additionally the correlations proposed by Morris and Harasgama [13] for a square-sectioned duct are illustrated. Although exact agreement is not evident, there are similar trends over the range of variables covered by the present study.

Closure

The investigation reported here for a rectangular-sectioned duct confirms that orthogonal mode rotation produces an enhancement of local and mean heat transfer on the trailing surface of the duct and that this effect results from a Coriolis-

induced cross-stream secondary flow. On the leading surface of the duct local and mean heat transfer can be significantly impaired in relation to the corresponding nonrotating flow situation. This, in the practical situation of rotor blade cooling, can give rise to local overheating.

Although not fully understood as yet, it is apparent that rotational buoyancy is affecting both leading and trailing surfaces with a tendency for the local and mean heat transfer to increase with increases in the wall to fluid temperature difference.

The data collected will be useful for the validation of numerical codes being developed to assess the influence of rotation of ducted flow forced convection problems.

Acknowledgments

The authors wish to thank The Ministry of Defence, Rolls Royce, Plc. and the Science and Engineering Research Council for financial support and encouragement to undertake this program of work.

References

1 Barua, S. N., "Secondary Flow in a Rotating Straight Pipe," *Proc. Roy. Soc., A*, Vol. 227, 1955, p. 133.

2 Benton, J. S., and Boyer, D., "Flow Through a Rapidly Rotating Conduit of Arbitrary Cross-Section," *J. Fluid Mech.*, Vol. 26, Part I, 1969.

3 Mori, Y., and Nakayama, W., "Convective Heat Transfer in Rotating Radial Circular Pipes (1st Report—Laminar Region)," *Int. J. Heat Mass Transfer*, Vol. 11, 1968, p. 1027.

4 Ito, H., and Nanbu, K., "Flow in Rotating Straight Pipes of Circular Cross-Section," ASME *J. Basic Engineering*, Vol. 93, 1971, p. 383.

5 Lokai, V. I., and Limanski, A. S., "Influence of Rotation on Heat and Mass Transfer in Radial Cooling Channels of Turbine Blades," *Izvestiya VUZ, Aviatsionnya Tekhnika*, Vol. 18, No. 3, 1975, p. 69.

6 Metzger, D. E., and Stan, R. L., "Entry Region Heat Transfer in Rotating Radial Tubes," presented at the AIAA 15th Aerospace Sciences Meeting, Los Angeles, 1977; Paper No. 77-189.

7 Skiadaresis, D., and Spalding, D. B., "Heat Transfer in a Pipe Rotating About a Perpendicular Axis," ASME Paper No. 77-WA/HT-39, 1977.

8 Zysina-Molozken, L. M., Dergach, A. A., and Kogan, G. A., "Experimental Investigation of Heat Transfer in a Radially Rotating Pipe," *HGEEE High Temp.*, Vol. 14, 1977, p. 988.

9 Morris, W. D., and Ayhan, T., "Observations on the Influence of Rotation on Heat Transfer in the Coolant Channels of Gas Turbine Rotor Blades," *Proc. IMechE*, Vol. 193, No. 21, 1979, p. 303.

10 Morris, W. D., and Ayhan, T., "Experimental Study of Turbulent Heat Transfer in a Tube Which Rotates About an Orthogonal Axis," *Proc. XIV ICHMT Symposium on Heat and Mass Transfer in Rotating Machinery*, Dubrovnik, Yugoslavia, Aug. 30-Sept. 3, 1982.

11 Morris, W. D., *Heat Transfer in Rotating Coolant Channels*, Research Studies Press, Wiley, New York, 1981.

12 Clifford, R. J., Morris, W. D., and Harasgama, S. P., "An Experimental Study of Local and Mean Heat Transfer in a Triangular-Sectioned Duct Rotating in the Orthogonal Mode," ASME *Journal of Engineering for Gas Turbines and Power*, Vol. 106, 1984, pp. 661-667.

13 Morris, W. D., and Harasgama, S. P., "Local and Mean Heat Transfer on the Leading and Trailing Surfaces of a Square Sectioned Duct Rotating in the Orthogonal Mode," presented at Heat Transfer and Cooling in Gas Turbines, AGARD-CP-390, Bergen, Norway, May 6-10, 1985.

14 Clifford, R. J., "Rotating Heat Transfer Investigations on a Multi-pass Cooling Geometry," presented at Heat Transfer and Cooling in Gas Turbines, AGARD-CP-390, Bergen, Norway, May 6-10, 1985.

15 Iskakov, K. M., and Trushin, V. A., "The Effect of Rotation on Heat Transfer in the Radial Cooling Channels of Turbine Blades," *Teploenergetika*, Vol. 32, 1985, pp. 52-55.

16 Wagner, J. H., Kim, J. C., and Johnson, B. V., "Rotating Heat Transfer Experiments With Turbine Airfoil Internal Passages," ASME Paper No. 86-GT-133, 1986.

17 Johnston, J. P., Halleen, R. M., and Lezius, D. K., "Effects of Spanwise Rotation on the Structure of Two-Dimensional Fully Developed Turbulent Channel Flow," *J. Fluid Mechanics*, Vol. 56, 1972, pp. 537-557.

18 Dittus, F. W., and Boelter, L. M. K., *Univ. Calif. Publs., Engng.*, Vol. 2, 1930, p. 443.

19 Morris, W. D., Harasgama, S. P., and Salemi, R., "Measurements of Turbulent Heat Transfer on the Leading and Trailing Surfaces of a Square Duct Rotating About an Orthogonal Axis," ASME Paper No. 88-GT-XX.

20 Wagner, J. H., Johnson, B. V., and Hajek, T. J., "Heat Transfer in Rotating Passages With Smooth Walls and Radial Outward Flow," ASME Paper No. 89-GT-XX.

An Experimental Investigation of Heat Transfer in an Orthogonally Rotating Channel Roughened With 45 deg Criss-Cross Ribs on Two Opposite Walls

M. E. Taslim

L. A. Bondi

Mechanical Engineering Department,
Northeastern University,
Boston, MA 02115

D. M. Kercher

General Electric Company,
Aircraft Engines,
Lynn, MA 01910

Turbine blade cooling is imperative in advanced aircraft engines. The extremely hot gases that operate within the turbine section require turbine blades to be cooled by a complex cooling circuit. This cooling arrangement increases engine efficiency and ensures blade materials a longer creep life. One principle aspect of the circuit involves serpentine internal cooling passes throughout the core of the blade. Roughening the inside surfaces of these cooling passages with turbulence promoters provides enhanced heat transfer rates from the surface. The purpose of this investigation was to study the effect of rotation, aspect ratio, and turbulator roughness on heat transfer in these rib-roughened passages. The investigation was performed in an orthogonally rotating setup to simulate the actual rotation of the cooling passages. Single-pass channels, roughened on two opposite walls, with turbulators positioned at 45 deg angle to the flow, in a criss-cross arrangement, were studied throughout this experiment. The ribs were arranged such that their pitch-to-height ratio remained at a constant value of 10. An aspect ratio of unity was investigated under three different rib blockage ratios (turbulator height/channel hydraulic diameter) of 0.1333, 0.25, and 0.3333. A channel with an aspect ratio of 2 was also investigated for a blockage ratio of 0.25. Air was flown radially outward over a Reynolds number range of 15,000 to 50,000. The rotation number was varied from 0 to 0.3. Stationary and rotating cases of identical geometries were compared. Results indicated that rotational effects are more pronounced in turbulated passages of high aspect and low blockage ratios for which a steady increase in heat transfer coefficient is observed on the trailing side as rotation number increases while the heat transfer coefficient on the leading side shows a steady decrease with rotation number. However, the all-smooth-wall classical pattern of heat transfer coefficient variation on the leading and trailing sides is not followed for smaller aspect ratios and high blockage ratios when the relative artificial roughness is high.

Introduction

Modern turbine blades are designed with internal cooling passages arranged in a serpentine pattern. These passages are often roughened with rib shape turbulence promoters called turbulators. The turbulators, which are usually repeated along one wall or two opposite walls within the cooling path, significantly affect the flow pattern and heat transfer.

The ability to predict analytically the effects of rib roughness on the flow field and heat transfer, especially in a rotating frame, is limited. Therefore, many experimental investigations have been conducted in order to determine those configurations that produce the optimum results in terms of both heat transfer and pressure drop. The pertinent geometric parameters involved in these experimental investigations are passage aspect ratio, AR; turbulator angle of attack, α; pitch-to-height ratio, S/e; blockage ratio, e/D_h, and the manner by which turbulators are positioned with respect to each other. Interested readers are referred to the work done by Burggraf (1970), Han (1984), Han et al. (1978, 1985), Metzger et al. (1983), Metzger (1989), Sparrow and Tao (1982), Taslim and Spring (1987, 1988) and Webb et al. (1971). However, in a great majority of these investigations, the test section is stationary; thus the rotational effects that play an important role in establishing the flow field and heat transfer behavior in the passage are not taken into consideration.

Contributed by the International Gas Turbine Institute and presented at the 35th International Gas Turbine and Aeroengine Congress and Exposition, Brussels, Belgium, June 11–14, 1990. Manuscript received by the International Gas Turbine Institute January 17, 1990. Paper No. 90-GT-332.

In the presence of rotation, the Coriolis and centripetal accelerations generate secondary flows that, especially in a rib-roughened passage of high blockage ratio, can change the flow structure and heat transfer behavior significantly. The orthogonal mode of rotation, in which the passage's longitudinal axis is perpendicular to the axis of rotation, describes the configuration of an internal cooling passage of a turbine blade. In such a mode, the secondary flows induced by Coriolis accelerations and centripetal buoyancy have a significant effect on the flow field and heat transfer. In addition to those pertinent geometric parameters for the stationary case mentioned above, the following parameters play an important role in the study of an orthogonally rotating test section: rotational Reynolds number, $J_{Dh} = \Omega D_h^2/\nu$, Rotational Rayleigh number, Ra $= (r/D_h)J_{Dh}\text{RoRePr}\beta\Delta T$, Rotation number, Ro $= \Omega D_h/U_m$, Grashof number, Gr = Ra/Pr, and centripetal Buoyancy Parameter, Gr/Re^2. The studies described below present the investigations conducted in this area.

Mori et al. (1971) investigated a straight circular pipe, both theoretically and experimentally, under the influence of orthogonal rotation using the naphthalene sublimation technique. The investigations were performed in both laminar and turbulent regimes. First, by assuming a boundary layer along the wall, an analytical study was performed for a turbulent flow in the hydrodynamically and thermally fully developed region (theoretical analysis of a fully developed laminar flow was previously completed in their first report, 1968). Second, using air as the working fluid, experimental data were taken in a straight circular tube of 9-mm diameter for a range of Reynolds number from 1000 to about 10,800, rotational speed of 0 to 1000 rpm, and T_{wall} of 25°C to 45°C. It was concluded that Nusselt numbers did not increase for the turbulent case as much as they did for the laminar case when rotation was introduced. Experimental and analytical results were in agreement for the Nusselt number for both laminar and turbulent cases.

Johnston et al. (1972) studied the effects of spanwise rotation in a rectangular duct for a fully developed flow. Water was used as the working fluid and dye was injected for flow visualizations. The Reynolds number ranged from 2500 to 36,000 and the rotation number from 0.01 to 0.25. Their conclusion was that turbulence increased on the trailing side and decreased on the leading side. The changes in flow structure were attributed to the Coriolis forces due to radial motion and spanwise rotation. Zysina-Molozhen et al. (1977) investigated a radially outward turbulent flow. Their results showed that flow took on a laminarlike pattern under the presence of rotation. No significant rotational effects were noticed for Reynolds numbers greater than 2.5×10^4. Morris and Ayhan (1979) tested two passages with diameters of 4.85 mm and 10 mm. Air was flown radially outward at Reynolds numbers of 5000, 10,000, and 15,000, and rotational speeds of 0, 1000, and 2000 rpm. Results showed that for fixed Reynolds and Rayleigh numbers, heat transfer increased with Rossby number. With a 15 percent mean scatter band, all rotating data could be correlated by

$$\text{Nu}_m = 0.022\text{Re}^{0.8}\left[\frac{\text{Ra}}{\text{Re}^2}\right]^{-0.186}\text{Ross}^{0.33}$$

Morris and Ayhan (1981) studied turbulent local and mean heat transfer in a tube of circular cross section in an orthogonal mode of rotation. They examined radially outward and inward flows. Results showed that, for a radially inward flow, mean heat transfer coefficient increased with the rotational Rayleigh number and decreased with Rossby number for a fixed rotational buoyancy. Under the condition of radially outward flow, the Coriolis acceleration improved heat transfer but centripetal buoyancy adversely affected it. Wagner et al. (1986) investigated heat transfer phenomena in rotating, two-pass serpentine, turbulated passages. Two models were tested: a two-leg model with a smooth 180 deg bend; and an engine-scale model of a typical multipass cooled turbine airfoil. The two-leg model had an aspect ratio of 0.25 and Reynolds number was varied from 15,000 to 30,000 for rotational speeds of up to 700 rpm. The engine-scale model was tested over a range of rotation number from 0 to 0.09. It was concluded that average heat transfer coefficients on the leading and trailing surfaces can change significantly depending upon flow direction and Rossby number.

Harasgama and Morris (1988) investigated three test sections. The first was a triangular duct with data taken on the leading side only and flow traveling radially inward. The second was a square duct with a radially inward flow while the third was a circular tube with radially outward flow. For the last two cases, data were taken on both trailing and leading surfaces. Reynolds number ranged from 7000 to 25,000 and rotation number varied from 0 to about 0.1. It was concluded that radially inward flows produced a higher mean Nusselt

Nomenclature

a = test section width (see Fig. 2)
A_h = total area of each heater
AR = aspect ratio of passage = a/b
b = test section height
C_p = specific heat at constant pressure
D_h = hydraulic diameter of passage
e = turbulator (rib) height
Gr = Grashof number = Ra/Pr $= (r/D_h)J_{Dh}\text{RoRe}\beta\Delta T$
h_t = heat transfer coefficient on turbulated wall
J_{Dh} = rotational Reynolds number based on hydraulic diameter $= \Omega D_h^2/\nu$
Nu_o = Nusselt number in a smooth channel, stationary case, from Dittus-Boelter = $0.023\text{Re}^{0.8}\text{Pr}^{0.4}$
Nu_s = Nusselt number on the turbulated wall for stationary case
Nu_r = Nusselt number on the turbulent wall for rotating case
P = perimeter
Pr = Prandtl number
$\dot{q}''$ = heat flux generated by electric heater
$\dot{q}_b''$ = heat flux lost through back of test section
$\dot{q}_r''$ = heat flux lost by radiation
r = radial distance from the point under investigation to the axis of rotation
Ra = rotational Rayleigh number $= r\Omega^2(T_s - T_m)\beta D_h^3\text{Pr}/\nu^2 = (r/D_h)J_{Dh}\text{RoRePr}\beta\Delta T$
Re = Reynolds number based on test section hydraulic diameter
Ro = Rotation number = $\Omega D_h/U_m = J_{Dh}/\text{Re}$
Ross = Rossby number = 1/Ro
S = turbulator (rib) pitch
St = Stanton number = $h/\rho U_m C_p$
ΔT = $T_s - T_m$
T_f = film temperature $(T_m + T_s)/2$
T_m = air mixed mean temperature
T_s = surface temperature
U_m = mean velocity of air
X = distance from the turbulated section entrance to the point under investigation
α = angle of attack
β = coefficient of thermal expansion
μ = dynamic viscosity of air
ν = kinematic viscosity of air
ρ = density
Ω = angular velocity

number due to rotation compared with the stationary case. Increased centripetal buoyancy futher increased heat transfer on the leading side and reduced it on the trailing side. When the rotational Reynolds number increased, the heat transfer coefficient decreased on the leading side. Radially outward flows produced a reduction in average Nusselt number on the leading side in comparison to the stationary case.

Morris et al. (1988) measured heat transfer coefficients on the leading and trailing surfaces of a square rotating duct. With flow traveling radially outward, the rotation number ranged from 0 to 0.08 and Reynolds number from 7200 to 44,000. Results indicated that the Coriolis-induced secondary flows increased local heat transfer coefficients on the trailing surface when compared to the stationary case and had little effect on the leading surface. Wagner et al. (1991) investigated a four-pass serpentine smooth duct of square cross section. Rotation number was varied from 0 to 0.48 and Reynolds number was held at a constant value of 25,000. Buoyancy effects, by varying the inlet density, were studied on the heat transfer coefficient of flow traveling outward on the first leg of the test section. Results concluded that heat transfer enhancement varied significantly on both the leading and trailing surfaces from the inlet to a location of $X/D_h \leq 12$. Enhancement in heat transfer varied on the different surfaces due to changes in density. As density and the buoyancy parameter, Gr/Re^2, were increased, heat transfer was always enhanced.

Taslim et al. (1991) measured heat transfer coefficients in a spanwise rotating passage with two opposite rib-roughened walls, where $S/e = 10$, $AR = 1$, and the rib angle of attack $\alpha = 90$ deg. Three blockage rations were tested (0.133, 0.25, and 0.333). Reynolds number ranged from 15,000 to 50,000 while the rotational Reynolds number varied between 300 and 1400 and the rotational number varied from 0 to 0.08. On the trailing surface, the smallest rib blockage measured an enhancement (relative to nonrotating) up to 46 percent whereas the highest blockage experienced insignificant enhancement of only 6 percent. The same trend was observed on the leading side. After an initial high enhancement at low rotation number, there was a continued decrease in the heat transfer coefficient with increasing rotation number on both leading and trailing surfaces for the two lowest blockages. This trend is opposite to the observed trend for trailing smooth surfaces. The initial high enhancement on the leading surface at low rotation number is a noted difference from smooth leading surfaces.

Taslim et al. (1989) continued the investigation of rotational effects on heat transfer in spanwise rotating channels. The test sections were turbulated on two opposite walls with square turbulators at an angle of attack of 45 deg in a criss-cross arrangement. Two aspect ratios were investigated, 2 and 0.5. All test sections had a constant pitch-to-height ratio of 10 with varying blockage ratios. Reynolds number ranged from 11,000 to 55,000 and rotation number from 0 to 0.3. Results showed that rotational effects were more pronounced in channels with low blockage and high aspect ratios. As rotation number increased, the heat transfer coefficient increased on the trailing surface and decreased on the leading surface.

The goal of this investigation was to determine the influence of rotation, rib roughness, and aspect ratio on heat transfer, in a typical internally cooled gas turbine blade. The working fluid chosen was air, running through a single-pass cooling passage, which was subjected to a constant heat flux boundary condition. Only two opposite walls of the passage were rib roughened. Constant heat flux was applied to one of the two turbulated walls. This arrangement is closer to the actual turbine blade since in multiple cooling passage blades there exists a large temperature gradient between the adjacent walls. It is, however, planned to run tests with four heated walls under otherwise identical conditions and compare the results. The air flow was radially outward in the test sections, which were rotated in a manner similar to actual turbine blades.

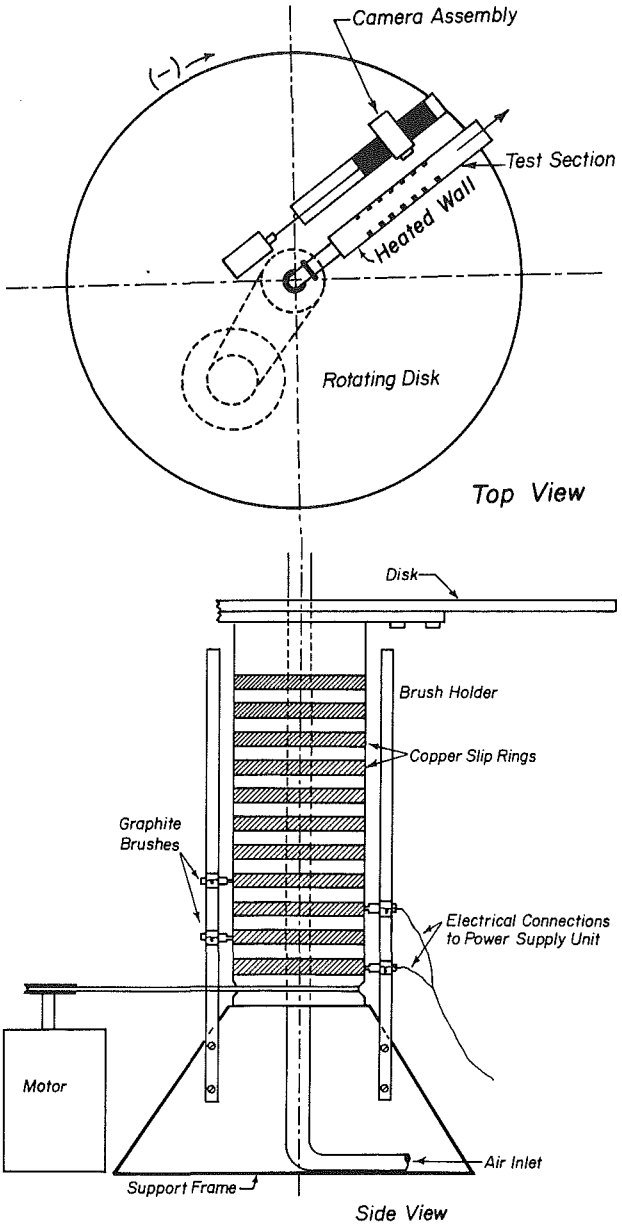

Fig. 1 Experimental apparatus

Experimental Apparatus and Procedure

Channels, roughened with turbulators positioned at an angle of 45 deg with flow direction and a constant pitch-to-height ratio S/e of 10 were investigated for two aspect ratios. The turbulators were located on opposite walls in a criss-cross configuration. The measurement surface was constructed of 1.02-cm-thick white pinewood on which four custom-made etched foil heaters were affixed. A liquid crystal sheet was placed over these heaters to display isotherms. Photographs of these isotherms were taken for heat transfer coefficient measurement purposes. Liquid crystals display areas of constant temperature compared to thermocouples that only measure temperature at discrete points. This feature provided a more detailed and accurate temperature distribution measurement. The test sections were constructed of 1.27-cm-thick plexiglass on three walls. The fourth wall was the wooden measurement section shown in Fig. 2. All test sections were 1.17 m in length. Three test sections at an aspect ratio of unity were constructed with a cross section of 3.81 cm × 3.81 cm. All turbulators had a square cross-sectional area and were constructed of plexiglass.

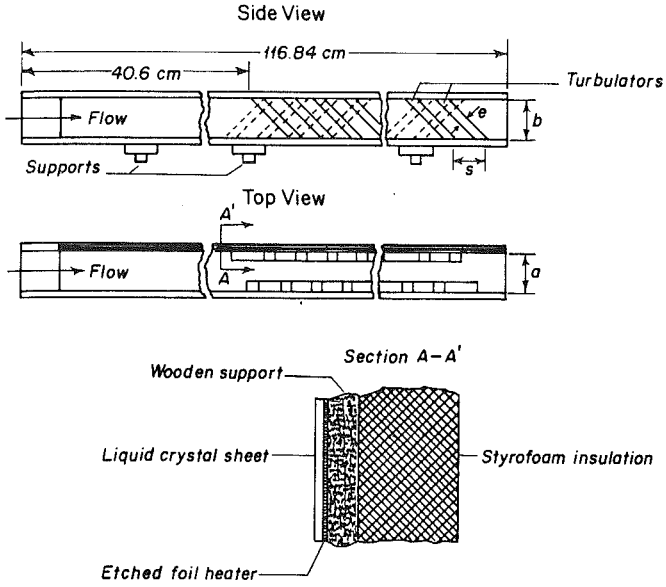

Fig. 2 A typical test section

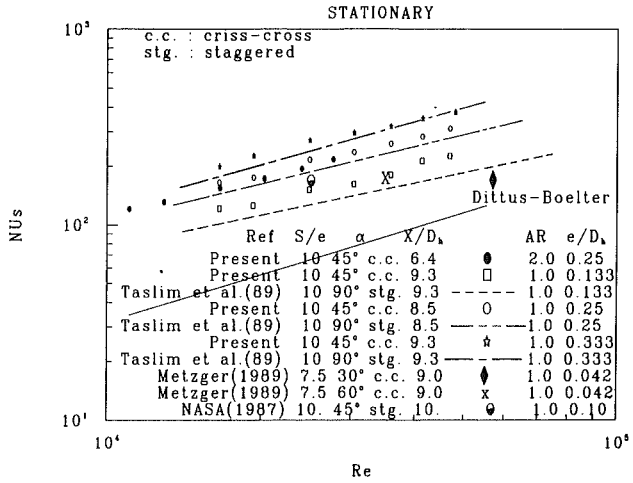

Fig. 3 Variation of Nu with Re for stationary cases

These three test sections had turbulator heights, e, of 0.508 cm, 0.953 cm, and 1.27 cm corresponding to three different blockage ratios, e/D_h, of 0.133, 0.250, and 0.333, respectively. The fourth test section had an aspect ratio of 2, with a cross section of 3.81 cm × 7.62 cm, and a turbulator height of 1.27 cm, corresponding to a 0.25 blockage ratio. 5.08 cm of styrofoam insulation covered the test section on all four sides to minimize heat losses to the environment except for a small window at the camera location. The rotating test apparatus consisted of a horizontally positioned 2.438-m-dia circular disk driven by a 5-hp reversible motor. Test sections were mounted radially on the disk. Air was directed into a plenum from the center of the disk through a rotary joint and into the test section. The electric power was supplied to the test section through a slip-ring assembly. Color photographs of the isotherms were obtained from a camera mounted on a track positioned parallel to the test section. An X/D_h well beyond the turbulated section entrance (for $AR = 2$: $X/D_h = 6.4$ and for $AR = 1$: $X/D_h = 9$) was chosen for the camera position. The heaters were powered using a custom-designed control panel and each heater was independently controlled with a variable transformer.

Experimental data were taken on the turbulated walls of the four test sections in both rotating and stationary modes. Rotational speeds of 50, 100, 150, and 200 rpm were set in the counterclockwise (positive rotation) and clockwise (negative rotation) directions shown in Fig. 1. The two rotational directions allowed data to be taken on both the trailing and leading surfaces of the test section. Reynolds numbers ranged from 15,000 to 50,000.

Prior to any testing, the liquid crystal sheet was calibrated. The calibration procedure is explained in detail by Bondi (1989). A shade of green corresponding to a temperature of 37°C, which was most distinct, was chosen as the reference color.

For a given mass flow rate and angular velocity, after the system reached thermal equilibrium, i.e., the isochromes on the liquid crystal sheet remained stagnant, a photograph was taken of the entire area between two adjacent ribs. The heater power supply was then increased, forcing isotherms to move so that another segment of the region of interest could be recorded on film. The above procedure was repeated until the reference isotherm had covered the entire area between two turbulators. An average of 15 photographs were required to cover the entire area of interest with the reference temperature. This concludes a set of data for a single Reynolds number. Then the flow rate was increased and the above process was repeated for all remaining Reynolds numbers and angular velocities. Data were archived and organized using an interactive computer program on a VAX 8650 main frame. The heat transfer coefficient corresponding to each picture was then calculated from

$$h = \frac{\dot{q}'' - \dot{q}_b'' - \dot{q}_r''}{T_s - T_m}$$

where T_s is the surface temperature and T_m is the air mixed mean temperature calculated from the energy balance between the test section entrance and the camera location. $\dot{q}_b''$ is the total heat loss through the back of the test section and $\dot{q}_r''$ is the radiational loss from the heated wall to the other three unheated walls of the test duct. Air properties were evaluated at the film temperature, T_f.

The second step in the process of data reduction was digitizing the reference color from the photographs taken to use in the calculation of the area-weighted average heat transfer coefficient. A dedicated software package with an active tablet and a magnetic field mouse was utilized for digitization. The area-weighted average heat transfer coefficient was then calculated from

$$h_t = \sum_{1}^{np} \left(\frac{h_1 a_1 + h_2 a_2 + \cdots + h_{np} a_{np}}{a_1 + a_2 \cdots + a_{np}} \right)$$

where np is the total number of pictures taken for a given Reynolds number, a_1 through a_{np} are the areas covered with the reference color, and h_1 through h_{np} are the measured heat transfer coefficients corresponding to those areas.

Results and Discussion

The buoyancy parameter, $\mathrm{Gr/Re}^2 = (r/D_h)R_0^2\beta\Delta T$, ranged from 1.3×10^{-5} to 0.072. The effect of centripetal buoyancy on Nusselt number was not investigated since the liquid crystal reference temperature selected required relatively small temperature differences between the wall and fluid of approximately 14°C. Results for the leading and trailing sides of the test sections are plotted together (in order to compare them conveniently) and are identified by the sign of rotation and rotational Reynolds numbers. To an observer looking at the disk from the top (see Fig. 1), negative rotation values represent clockwise rotation with the heated wall on the leading side of the test section. Similarly, positive values denote counterclockwise rotation with the trailing side under investigation. Heat transfer coefficients are measured only on the turbulated wall between ribs. Rib fin-type effects were not investigated. Ex-

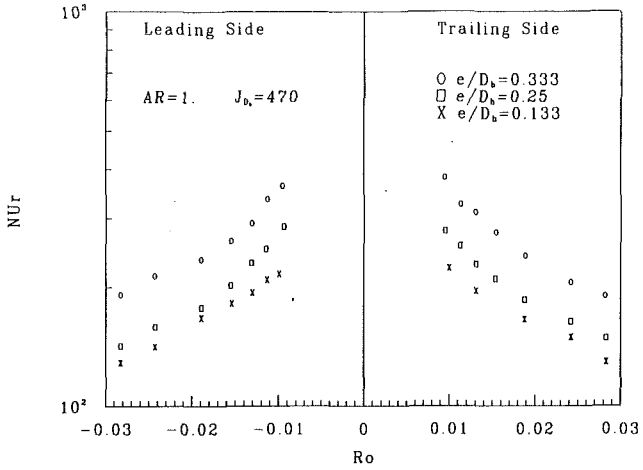

Fig. 4 Nu, versus Ro for $AR = 1$ at $J_{D_h} = 470$

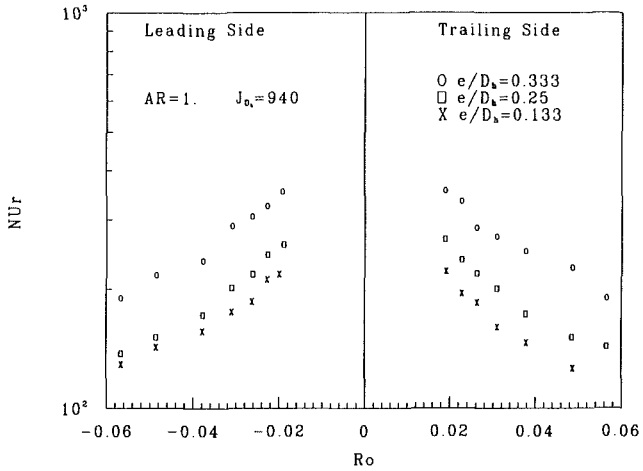

Fig. 5 Nu, versus Ro for $AR = 1$ at $J_{D_h} = 940$

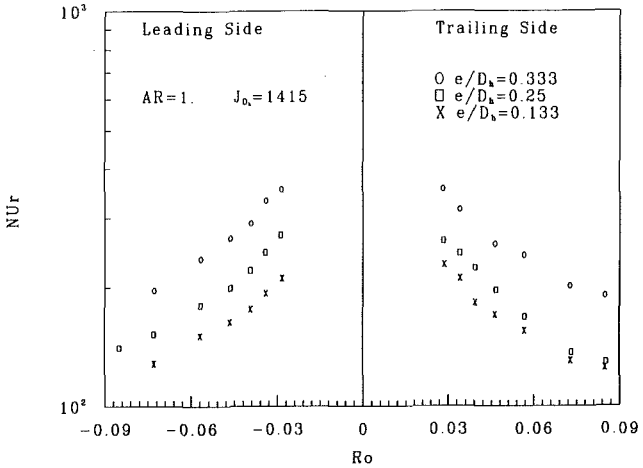

Fig. 6 Nu, versus Ro for $AR = 1$ at $J_{D_h} = 1415$

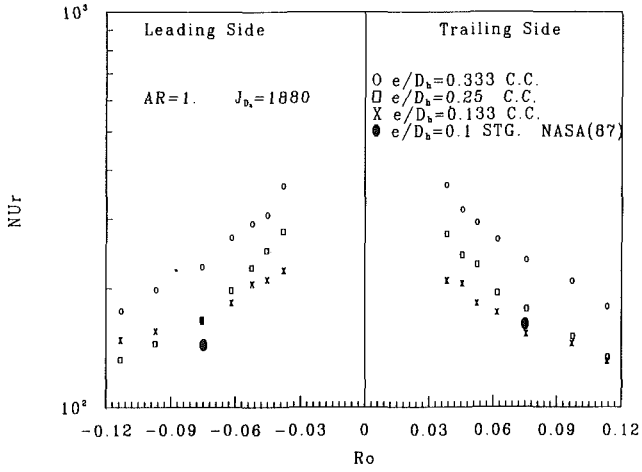

Fig. 7 Nu, versus Ro for $AR = 1$ at $J_{D_h} = 1880$

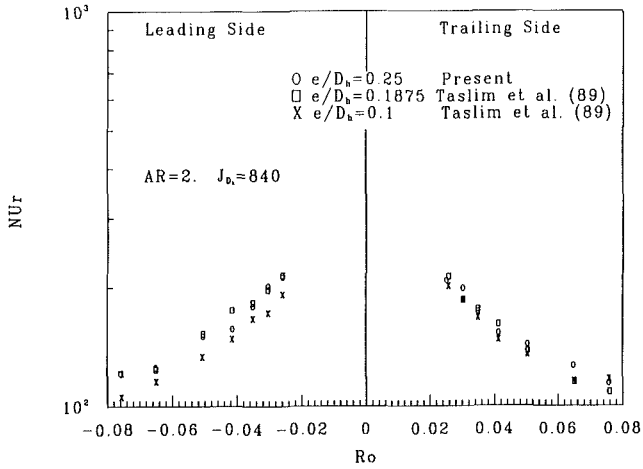

Fig. 8 Nu, versus Ro for $AR = 2$ at $J_{D_h} = 840$

perimental results presented here are all for one region between a pair of turbulators, well beyond the test section entrance. Uncertainty in the heat transfer coefficient measurements, following the method of Kline and McClintock (1953), is estimated to be about 6 percent. Details of the uncertainty analysis are presented by Bondi (1989).

Figure 3 demonstrates the variation of Nusselt number with Re for the stationary test sections. Nusselt number shows a substantial increase with increasing rib blockage ratio. This increase is due to separation, reattachment, and recirculation of the flow as it passes over the turbulated surface. Significant mixing rates between the high-temperature air near the heated wall and the low-temperature air away from it results in this strong behavior. These results will be further used to compare the rotating versus stationary cases for identical test conditions. Two data points from Metzger (1989) are plotted for angles of attack of 30 and 60 deg in the criss-cross arrangement. The 60 deg case at the same X/D_h, although having a geometry of a lower pitch-to-height ratio and blockage ratio, compares favorably with the present data. The much lower Nusselt number for the 30 deg criss-cross case contributed to its much lower blockage ratio, criss-cross arrangement, and angle of attack. The NASA (Hajek et al., 1987) 45 deg data, although staggered with slightly lower blockage ratio, agree well with the present stationary data in Fig. 3 and rotational data in Fig. 7. The Dittus-Boelter correlation is also plotted to show the effects of rib roughness on heat transfer enhancement. A comparison between the present data for an aspect ratio of unity and the data published previously for an aspect ratio of 2, both for a blockage ratio $e/D_h = 0.25$, indicates a slight increase in heat transfer coefficient for a decrease in passage aspect ratio. Figure 3 also shows the present 45 deg criss-cross data compared with 90 deg staggered data reported by Taslim et al. (1991) at the same blockage aspect ratios. The 45 deg criss-cross configuration indicates superior heat transfer characteristics at all wall roughnesses as also reported by Metzger (1989).

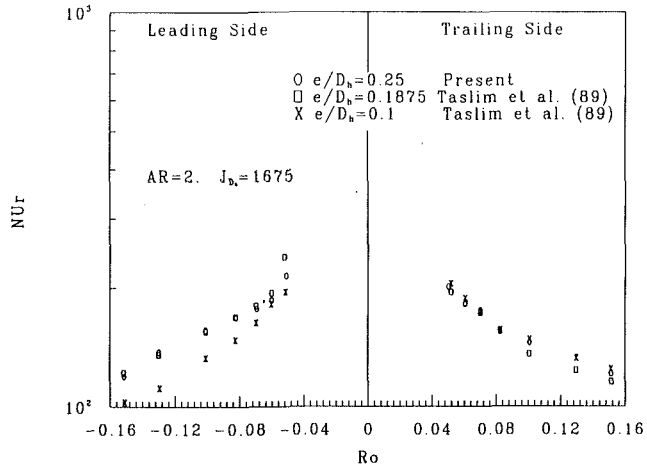

Fig. 9 Nu_r versus Ro for $AR = 2$ at $J_{D_h} = 1675$

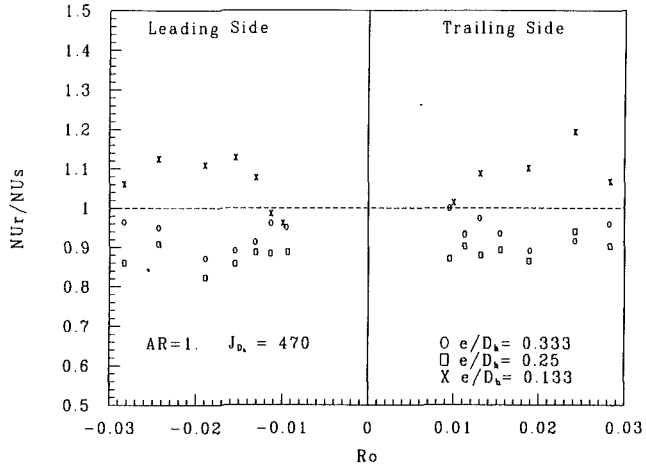

Fig. 12 Nu_r/Nu_s versus Ro for $AR = 1$ at $J_{D_h} = 470$

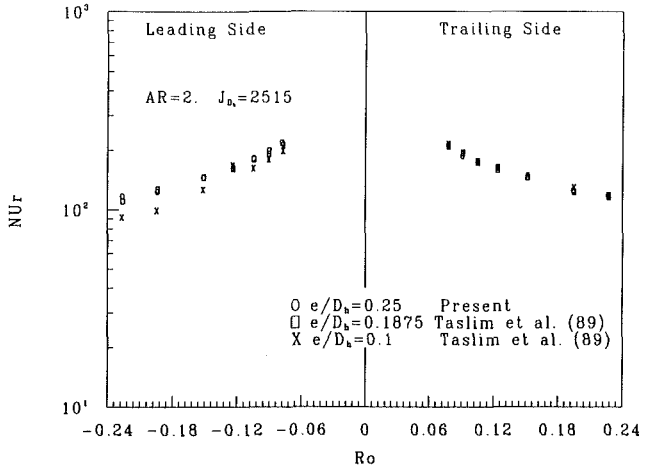

Fig. 10 Nu_r versus Ro for $AR = 2$ at $J_{D_h} = 2515$

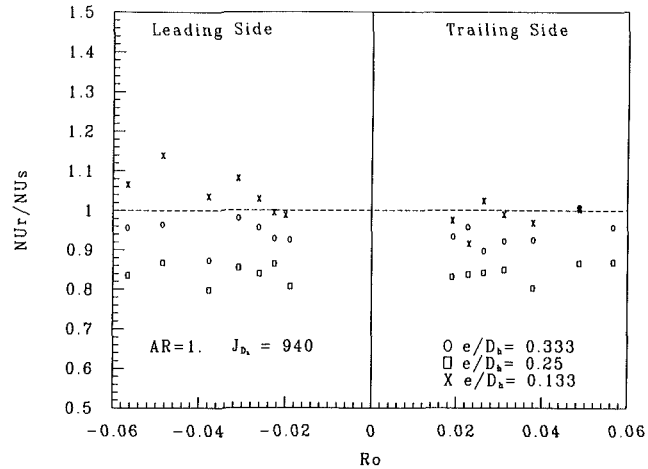

Fig. 13 Nu_r/Nu_s versus Ro for $AR = 1$ at $J_{D_h} = 940$

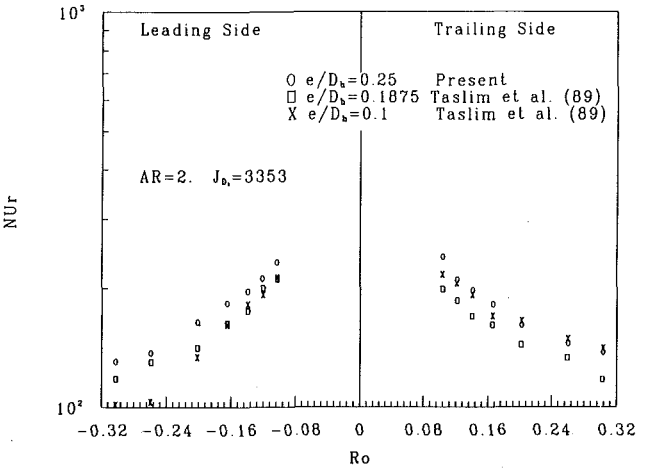

Fig. 11 Nu_r versus Ro for $AR = 2$ at $J_{D_h} = 3353$

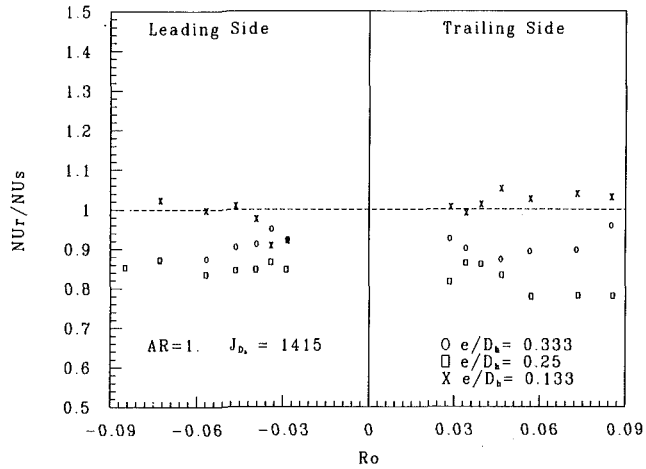

Fig. 14 Nu_r/Nu_s versus Ro for $AR = 1$ at $J_{D_h} = 1415$

The variation of Nusselt number versus rotation number is shown in Figs. 4–11. Results are also shown from Taslim et al. (1989) for $AR = 2$, with $e/D_h = 0.1$ and 0.1875. Each figure is for a specific rotational Reynolds number, J_{D_h}, as a result of a constant angular velocity, Ω. As discussed previously, positive rotation numbers refer to the trailing surface measurements and negative numbers refer to measurements and negative numbers refer to measurements on the leading surface. In all cases tested, for a fixed J_{D_h}, Nusselt number decreases as rotation number increases. This behavior coincides with that of the stationary pattern since as a result of constant angular velocity, higher Rotation numbers correspond to lower air mean velocity, U_m, which results in a lower Nusselt number. On both the leading and trailing surfaces, Nusselt numbers increase with increasing blockage ratios, for all three geometries tested for the aspect ratio of 1. An aspect ratio of 2,

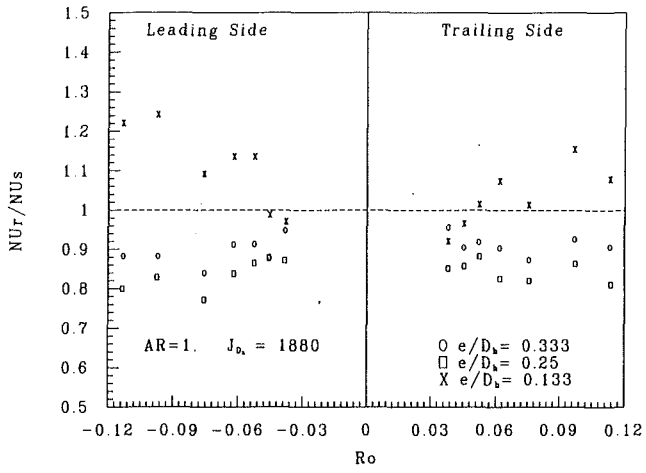

Fig. 15 Nu_r/Nu_s versus Ro for $AR = 1$ at $J_{D_h} = 1880$

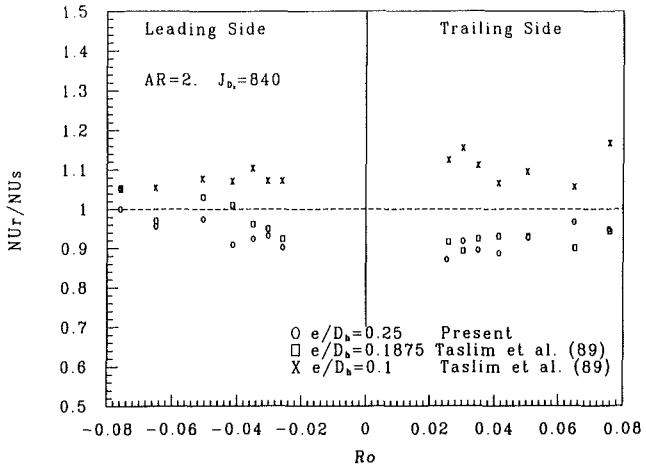

Fig. 16 Nu_r/Nu_s versus Ro for $AR = 2$ at $J_{D_h} = 840$

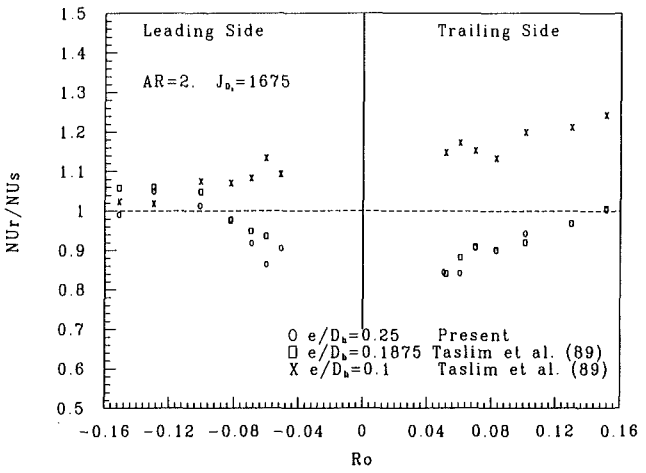

Fig. 17 Nu_r/Nu_s versus Ro for $AR = 2$ at $J_{D_h} = 1675$

however, shows less sensitivity to the blockage ratio in general. Higher blockage ratios exhibit higher Nu on the leading side but as J_{D_h} increases, Nusselt number shows less sensitivity to the blockage ratio. On the trailing side, however, at high rotational Reynolds numbers, the smaller blockage ratio produces a higher Nu. It seems that, at high rotational Reynolds numbers, the Coriolis forces suppress the mixing effects of high blockage ratios.

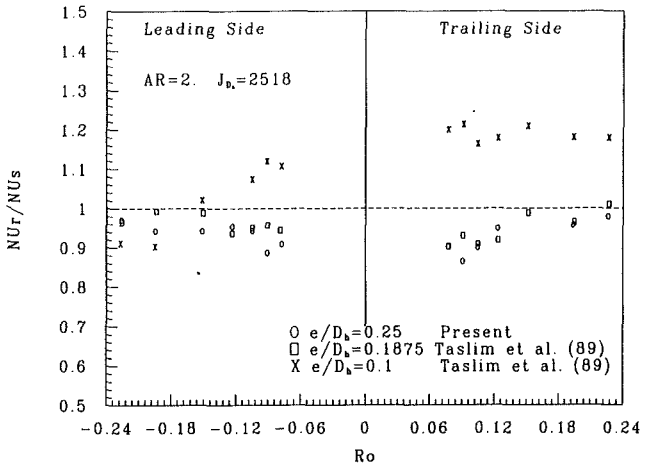

Fig. 18 Nu_r/Nu_s versus Ro for $AR = 2$ at $J_{D_h} = 2518$

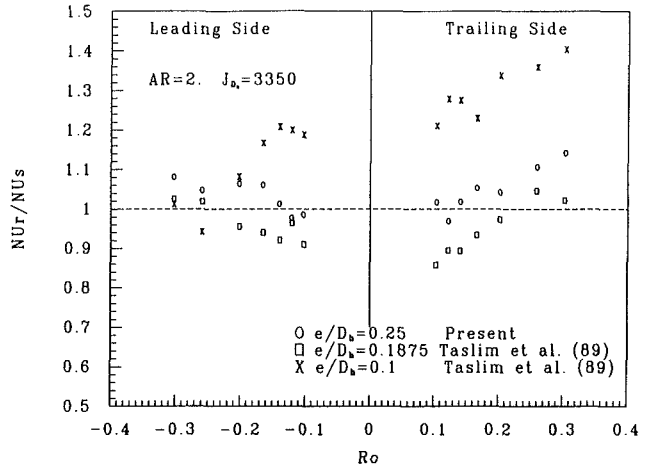

Fig. 19 Nu_r/Nu_s versus Ro for $AR = 2$ at $J_{D_h} = 3350$

The rotational effects on heat transfer are presented by plots of the ratio of Nusselt numbers for the rotating case to that of stationary case, Nu_r/Nu_s versus rotation number for all J_{D_h} values. It is apparent that Nu_r/Nu_s values greater than unity imply heat transfer enhancement as rotation occurs. On Figs. 12–19,it is evident that rotation has a significant effect on the Nusselt number ratio. For the case of a rotating all-smooth-wall test section, it is shown (see Morris, 1981) that the heat transfer coefficient on the trailing side increases with rotation compared to that of the stationary case while a decrease in heat transfer coefficient is observed on the leading side. Such behavior is due to the fact that, in a spanwise rotating channel, Coriolis forces cause a tendency for the flow to separate from the leading side and push against the trailing side. However, for a rib-roughened passage, this behavior is only noticed for low blockage and high aspect ratios ($AR = 2$ and $e/D_h = 0.1$, Taslim et al, 1989) as shown in Figs. 16–19. An aspect ratio of 2 with higher blockage ratios (0.1875 and 0.25) and all three blockage ratios associated with aspect ratio of unity do not follow this pattern. For these cases, first, variation of Nusselt number with rotation number is not as pronounced and, second, the Nusselt number ratios remain below unity for most rotation numbers tested. This behavior may be due to the limited relative space between turbulated walls, especially for $AR = 1$, inadequate for the flow to separate from the leading side and push against the trailing side. A maximum increase of about 40 percent in heat transfer coefficient due to rotation for the aspect ratio of 2 is observed on the trailing

surface for the blockage ratio of 0.1 (Fig. 19). The maximum decrease is about 15 percent for the blockage ratio of 0.25 on the trailing surface. For the aspect ratio of unity a maximum enhancement of about 25 percent due to rotation is observed for the small turbulators, $e/D_h = 0.1333$, on the leading surface of the test section. A maximum decrease of about 23 percent on the leading surface resulted from the medium-sized turbulators, $e/D_h = 0.25$.

Conclusion

Based on the results presented here, it can be concluded that rotational effects are more pronounced in turbulent passages of higher aspect and lower blockage ratios for which a steady increase in heat transfer coefficient is observed on the trailing side as rotation number increases while the heat transfer coefficient on the leading side shows a steady decrease with rotation number. The all-smooth-wall classical pattern of heat transfer coefficient variation on the leading and trailing sides is not entirely followed for smaller aspect ratios and higher blockage ratios, i.e., as the rotation number increases, on the trailing side a rotational enhancement is associated with low blockage ratios while on the leading side any general decrease is associated with high blockage ratios.

Acknowledgments

Financial support of the General Electric Company, Aircraft Engines, Lynn, MA is hereby gratefully acknowledged. The authors would also like to thank Mr. R. E. Gladden for his valuable suggestions during the course of this investigation.

References

Bondi, L. A., 1989, "An Experimental Study of Heat Transfer in a Spanwise Rotating Channel Turbulated With 45 Degree Angle of Attack Criss-Cross Ribs," M.S. Thesis, Mechanical Engineering Department, Northeastern University, Boston, MA.

Burggraf, F., 1970, "Experimental Heat Transfer and Pressure Drop With Two Dimensional Turbulence Promoters Applied to Two Opposite Walls of a Square Tube," *Augmentation of Convective Heat and Mass Transfer*, A. E. Bergles and R. L. Webb, eds., ASME, New York, pp. 70–79.

Hajek, T. J., Wagner, J. H., and Johnson, B. V., 1987, "Coolant Passage Heat Transfer With Rotation," *Turbine Engine Hot Section Technology*, NASA Conference Publication No. 2493.

Han, J. C., Glicksman, L. R., and Rohsenow, W. M., 1978, "An Investigation of Heat Transfer and Friction for Rib-Roughened Surfaces," *Int. J. Heat Mass Transfer*, Vol. 21, pp. 1143–1156.

Han, J. C., 1984, "Heat Transfer and Friction in Channels With Two Opposite Rib-Roughened Walls," ASME *Journal of Heat Transfer*, Vol. 106, No. 4, pp. 774–781.

Han, J. C., Park, J. S., and Lei, C. K., 1985, "Heat Transfer Enhancement in Channels With Turbulence Promoters," ASME *Journal of Engineering for Gas Turbines and Power*, Vol. 107, pp. 628–635.

Harasgama, S. P., and Morris, W. D., 1988, "The Influence of Rotation on the Heat Transfer Characteristics of Circular, Triangular, and Square-Sectioned Coolant Passages of Gas Turbine Rotor Blades," ASME JOURNAL OF TURBOMACHINERY, Vol. 110, pp. 44–50.

Johnston, J. P., Halleen, R. M., and Lezius, D. K., 1972, "Effects of Spanwise Rotation on the Structure of Two-Dimensional Fully Developed Turbulent Channel Flow," *J. Fluid Mech.*, Vol. 56, Part 3, pp. 533–557.

Kline, S. J., and McClintock, F. A., 1953, "Describing Uncertainties in Single-Sample Experiments," *Mechanical Engineering*, Vol. 75, pp. 3–8.

Metzger, D. E., Fan, C. S., and Pennington, J. W., 1983, "Heat Transfer and Flow Friction Characteristics of Very Rough Transverse Ribbed Surfaces With and Without Pin Fins," *Proc. ASME-JSME Thermal Engineering Joint Conference*, Vol. 1, pp. 429–436.

Metzger, D. E., 1989, "Effects of Rib Angle and Orientation on Local Heat Transfer in Square Channels With Angled Roughness Ribs," presented at the Compact Heat Exchanger Symposium, Stanford University, CA.

Mori, Y., Fukada, T., and Nakayama, 1971, "Convective Heat Transfer in a Rotating Radial Circular Pipe (2nd Report)," *Int. J. Heat Mass Transfer*, Vol. 14, pp. 1807–1824.

Morris, W. D., and Ayhan, T., 1979, "Observations on the Influence of Rotation on Heat Transfer in the Coolant Channels of Gas Turbine Rotor Blades," *Proc. Inst. Mech. Eng.*, Vol. 193, No. 21, p. 303.

Morris, W. D., 1981, "Heat Transfer and Fluid Flow in Rotating Coolant Channels," Research Studies Press, United Kingdom.

Morris, W. D., and Ayhan, T., 1981, "Heat Transfer in a Rotating Tube With Radially Inward Flow," University of Hull, Department of Engineering Design and Manufacture, Report No. EDM/4/81.

Morris, W. D., et al., 1988, "Measurements of Turbulent Heat Transfer on the Leading and Trailing Surfaces of a Square Duct Rotating About an Orthogonal Axis," ASME Paper No. 88-GT-114.

Sparrow, E. M., and Tao, W. O., 1982, "Enhanced Heat Transfer in a Flat Rectangular Duct With Streamwise-Periodic Disturbances at One Principal Wall," ASME *Journal of Heat Transfer*, Vol. 105, pp. 851–861.

Taslim, M. E., and Spring, S. D., 1987, "Friction Factors and Heat Transfer Coefficients in Turbulated Cooling Passages of Different Aspect Ratios, Part I: Experimental Results," presented at the 23rd AIAA/ASME/SAE/ASEE Joint Propulsion Conference, San Diego, CA, Paper No. AIAA-87-2009.

Taslim, M. E., and Spring, S. D., 1988a, "An Experimental Investigation of Heat Transfer Coefficients and Friction Factors in Passages of Different Aspect Ratios Roughened With 45° Turbulators," presented at the ASME National Heat Conference, Houston, TX, ASME HTD-Vol. 96, Vol, 1.

Taslim, M. E., and Spring, S. D., 1988b, "Experimental Heat Transfer and Friction Factors in Turbulated Cooling Passages of Different Aspect Ratios, Where Turbulators are Staggered," presented at the 24th AIAA/ASME/SAE/ASEE Joint Propulsion Conference, Boston, MA, Paper No. AIAA-88-3014.

Taslim, M. E., Chrysafis, C., and Kercher, D. M., 1989, "An Experimental Study of Heat Transfer in a Spanwise Rotating Channel Turbulated With 45 Degree Criss-Cross Ribs," presented at the ASME Winter Annual Meeting, San Francisco, CA.

Taslim, M. E., Rahman, A., and Spring, S. D., 1991, "An Experimental Investigation of Heat Transfer Coefficients in a Spanwise Rotating Channel With Two Opposite Rib-Roughened Walls," ASME JOURNAL OF TURBOMACHINERY, Vol. 113, pp. 75–82.

Wagner, J. H., Kim, J. C., and Johnson, B. V., 1986, "Rotating Heat Transfer Experiments With Turbine Airfoil Internal Flow Passages," ASME Paper No. 86-GT-133.

Wagner, J. H, Johnson, B. V., and Hajek, T. J., 1991, "Heat Transfer in Rotating Passages With Smooth Walls and Radial Outward Flow," ASME JOURNAL OF TURBOMACHINERY, Vol. 113, pp. 42–51.

Webb, R. L., et al., 1971, "Heat Transfer and Friction in Tubes With Repeated-Rib-Roughness," *Int. J. Heat Mass Transfer*, Vol. 14, pp. 587–660.

Zysina-Molozhen, L. M., et al., 1977, "Experimental Investigation of Heat Transfer in a Radially Rotating Pipe," *HGEEE High Temp.*, Vol. 14, p. 988.

J. O. Medwell

W. D. Morris
Department of Mechanical Engineering.

J. Y. Xia

C. Taylor
Department of Civil Engineering.

University College, Swansea,
Swansea SA2 8PP United Kingdom

An Investigation of Convective Heat Transfer in a Rotating Coolant Channel

A numerical method is presented for the determination of heat transfer rates in a cylindrical cooling duct within turbine blades that rotate about an axis orthogonal to its own axis of symmetry. The equations of motion and energy are solved in conjunction with the k–ϵ model of turbulence using the finite element method. The predicted results are compared with experimental data and it is clearly demonstrated that conduction in the solid boundary must be taken into account if satisfactory agreement is to be achieved. Excluding these effects can lead to an overestimation of the maximum wall temperature by approximately 50 percent.

Introduction

The high cost of development for testing the performance of gas turbine components and systems has made the quest for "design right first time" methodologies particularly attractive. The aero gas turbine rotor blade is a notable example and Fig. 1 illustrates how the relative cost of development to design has been reduced over the years. This reduction may be attributed in part to the application of computerized methods of design assessment together with well-compiled data bases reflecting acquired technical and scientific know-how.

In order to assess the operational life of a proposed rotor blade at the design stage, the stresses must be determined. Prior to making the stress prediction, it is necessary to determine the temperature distribution throughout the blade material. To accomplish this step, a prediction method for solving the heat conduction equation in three dimensions is required together with a specification of the thermal boundary conditions to be imposed on the external surface of the blade and on the surfaces of any internal coolant holes incorporated into the blade.

The present paper discusses fundamental research aimed at the accurate specification of the thermal boundary conditions on these internally cooled surfaces of the blade and has the strategic aim of integrating into an overall "design right first time" philosophy for the blade, validated computer codes, which treat the manner in which the convection process inside a cooling passage is affected by the fact that the blade is rotating.

Typical blade cooling passages involve spanwise holes located within the blade, as illustrated in Fig. 2. In practice these holes may be either circular or noncircular in cross section, may incorporate fins and ribs to enhance local heat transfer, and may be interconnected in a multipass manner. Because of the spanwise orientation, most individual passages may be considered to be straight with the mainline direction of coolant flow aligned so as to be orthogonal to the axis about which the blade rotates.

To demonstrate the theoretical methods being developed and the supportive role of fundamental experimentation with which to attempt validation and improvement of those theoretical methods, the case of a coolant hole having circular cross section will be treated in this paper, so that the basic flow geometry is as shown in Fig. 3.

When studying convection problems it is customary to isolate the fluid flow from any solid surface that bounds the flow via prescribed boundary conditions. This means in practice that relatively simple thermal boundary conditions corresponding to constant surface temperature or constant heat flux are often used. During the course of this investigation it was recognized that conduction in the wall material from which a rotor blade is manufactured plays an important role in the establishment of the prevailing thermal boundary conditions at the interface between the coolant and the internal surface bounding the coolant. For this reason and also to permit a better theoretical

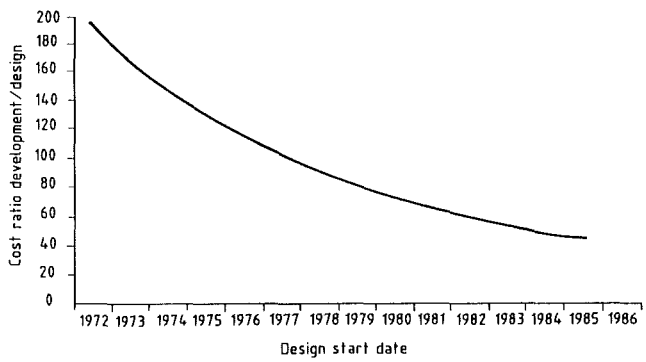

Fig. 1 Relative cost of development to design

Contributed by the International Gas Turbine Institute and presented at the 35th International Gas Turbine and Aeroengine Congress and Exposition, Brussels, Belgium, June 11–14, 1990. Manuscript received by the International Gas Turbine Institute January 17, 1990. Paper No. 90-GT-329.

model of the experimental apparatus to be constructed, the combined or conjugate problem linking the fluid and the containing metal duct was treated as a total system.

Theoretical Considerations

The Navier–Stokes equations, expressing the momentum conservation principle, are customarily referred to an inertial reference frame in accordance with the requirements of Newtonian mechanics. If the motion of the coolant in the present case is referred to the rotating channel itself, then the inertia terms of the Navier–Stokes equations must be modified to include Coriolis and centripetal effects as described by Morris and Ayham [1]. Under these circumstances the Navier–Stokes equations for constant property turbulent flow may be expressed as

$$\rho u_j \frac{\partial u_i}{\partial x_j} = -\frac{\partial p}{\partial x_i} + \frac{\partial}{\partial x_j}\left[(\mu+\mu_t)\right]\left[\frac{\partial u_i}{\partial x_j}+\frac{\partial u_j}{\partial x_i}\right] + 2\rho(\bar{\Omega}\times\bar{u})\cdot\bar{I}_i + \rho\Omega_j^2 x_i \sin(\Omega_j, x_i) \quad (1)$$

where $\bar{\Omega}$ is a rotating vector, $\bar{u}$ is the fluid velocity vector, and $\bar{I}$ is the unit vector; the other symbols have the meanings shown in the nomenclature.

It should be noted that the centripetal terms in equation (1) are conservative and may be absorbed into the pressure gradient term if the fluid is assumed to have invariant properties. However, if the density of the fluid is temperature dependent then a buoyant-type interaction is possible coupling the velocity and temperature fields. This point will be discussed in more detail later in the paper.

The temperature field must satisfy the energy conservation principle, which may be expressed, for nondissipative flow, as

$$\rho u_j \frac{\partial T}{\partial x_j} = \frac{\partial}{\partial x_j}\left\{\left[\frac{\mu}{\sigma}+\frac{\mu_t}{\alpha_t}\right]\frac{\partial T}{\partial x_j}\right\} \quad (2)$$

The flow field must also satisfy the continuity principle, which, in the present context, may be written as

$$\frac{\partial u_i}{\partial x_i} = 0 \quad (3)$$

Equations (1)–(3) cannot be solved unless a turbulence model is postulated with which to evaluate the turbulent contribution to the effective viscosity. For this work a k–ϵ two-equation turbulence model has been adopted so that

$$\mu_t = C_\mu \rho\, k^{1/2} l \quad (4)$$

where

$$l = k^{3/2}/\epsilon \quad (5)$$

The turbulent parameters k and ϵ are linked to the two transport equations

$$\rho u_j \frac{\partial k}{\partial x_j} = \frac{\partial}{\partial x_j}\left[\left[\mu+\frac{\mu_t}{\sigma_k}\right]\frac{\partial k}{\partial x_j}\right] + (\mu+\mu_t)\frac{\partial u_i}{\partial x_j}\left[\frac{\partial u_i}{\partial x_j}+\frac{\partial u_j}{\partial x_i}\right] - \frac{C_D\sigma k^{3/2}}{l} \quad (6)$$

$$\rho u_j \frac{\partial \epsilon}{\partial x_j} = \frac{\partial}{\partial x_j}\left[\left[\mu+\frac{\mu_t}{\sigma_\epsilon}\right]\frac{\partial \epsilon}{\partial x_j}\right] + C_1\rho\, k\frac{\partial u_i}{\partial x_j}\left[\frac{\partial u_i}{\partial x_j}+\frac{\partial u_j}{\partial x_i}\right] - \frac{C_2\rho\epsilon^2}{k} \quad (7)$$

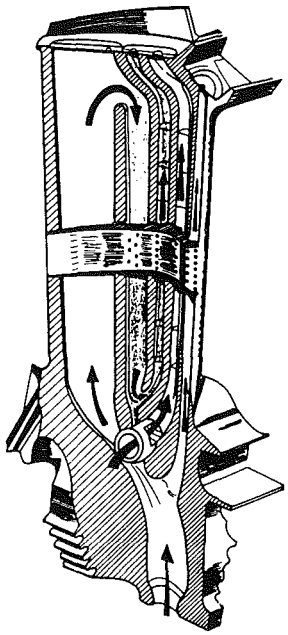

Fig. 2 Cross section of gas turbine rotor blade

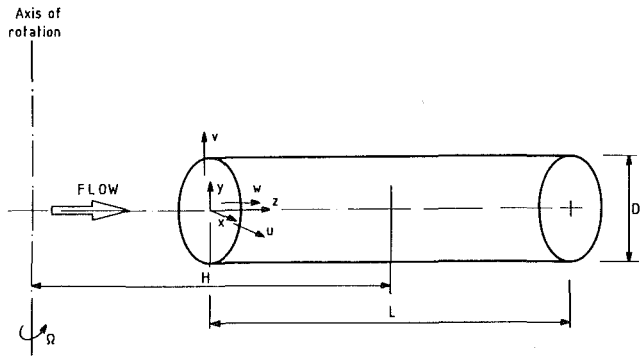

Fig. 3 Rotating geometry and coordinate system

Nomenclature

C_μ = defined in equation (4)
C_D, σ_k = defined in equation (6)
C_1, C_2, σ_ϵ = defined in equation (7)
D = diameter of rotating tube
H = eccentricity of midplane of rotating tube
k = kinetic energy of turbulence
K = coefficient of thermal conductivity
L = length of rotating tube
l = length scale of turbulence
Nu = Nusselt number
p = time-averaged pressure
Re = Reynolds number
Ra = rotational Rayleigh number
Ro = Rossby number
T = temperature
$u_{i,j}$ = time-averaged velocity
$x_{i,j}$ = coordinate direction
y^+ = dimensionless distance to nearest wall
F.E.M. = finite element method
ϵ = dissipation rate of turbulent kinetic energy
μ = dynamic viscosity
μ_t = turbulent viscosity
ρ = density
σ = Prandtl number
σ_t = turbulent Prandtl number
τ_i = fluid traction as defined by equation (8)
Ω_i = rotational velocity
(Ω_j, x_i) = angle between Ω_j vector and x_i direction

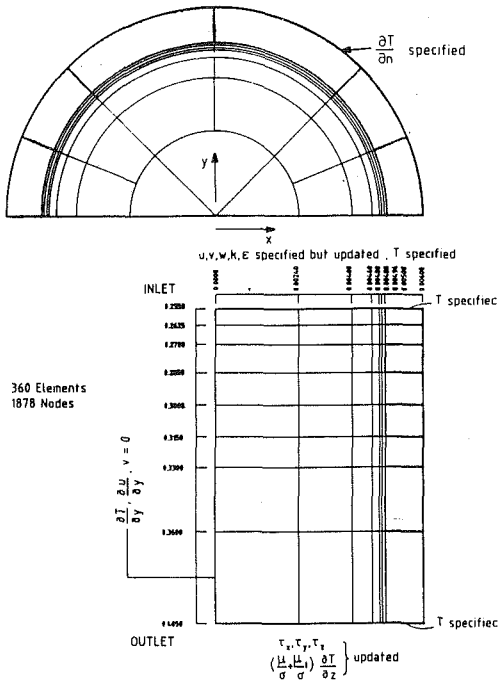

Fig. 4 Fluid-solid mesh in x-y and y-z planes and boundary conditions

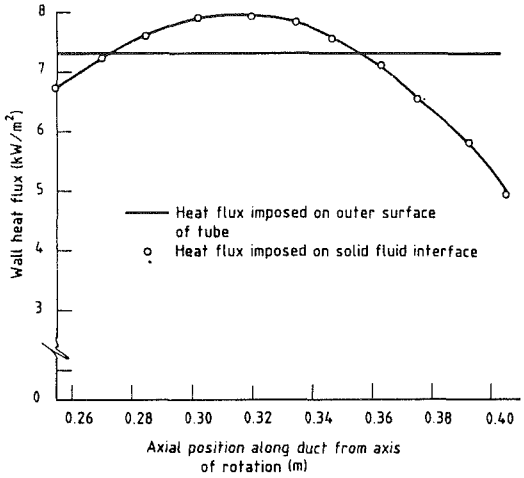

Fig. 5 Typical variation of heat flux along duct wall (Re = 15,000, Ro = 0.0406, Ra = 1586×10^6)

Boundary Conditions

Uncoupled System. The boundary conditions (see Fig. 4) to be applied to the fluid domain that has a heat flux imposed on the solid wall have already been discussed in detail in [2]. For convenience they will be briefly described here. First, when dealing with confined turbulent flow, a standard procedure of terminating the fluid domain some distance from the solid boundary is adopted. The transfer of shear and heat from the physical boundary, through the near-wall zone to the main body of the fluid, is usually achieved using wall functions of the logarithmic type. In addition to these velocity distributions, turbulence quantities were specified on the upstream element boundaries and traction conditions on the downstream boundaries. The tractions, which are shear stresses, are defined as updated on the appropriate boundaries and are given by

$$\tau_i = -pl_i + (\mu_t + \mu)\frac{\partial u_i}{\partial x_i} l_j \tag{8}$$

where l_i and l_j are the direction cosines of the unit outward normal to the boundary in the direction denoted by the suffix.

For heat transfer, the fluid inlet temperature is specified, which is compatible with the experimentally measured temperature gradient imposed at the fluid–solid interface (see Fig. 5). Additionally, appropriate symmetry conditions were invoked on the central longitudinal diametric plane of the geometry under consideration.

Coupled System. In this section the effect of conduction is modeled in the wall of the metal pipe through which the coolant fluid is flowing. The reason for this is that in the experimental apparatus, which will be described later, heat is applied to the outside of a relatively thick-walled tube using an electrical resistance heater, thus producing a constant flux. It should also be re-emphasized that in practice the cross-sectional areas of the coolant channels can constitute only a small proportion of that of the blade and conduction effects are expected to be significant. Therefore they must be included if a numerical approach is to be compared with experimental results and used with any coefficients at the design stage.

The complete fluid system requires exactly the same conditions cited previously. However, an additional equation must now be included into the solution procedure to reflect the transport of heat in the solid wall by conduction, i.e.,

$$\frac{\partial}{\partial x_i}\left[K\frac{\partial T}{\partial x_i}\right] = 0 \tag{9}$$

This must be accompanied by the appropriate boundary conditions, which are specified flux along the outside of the tube and specified temperatures on the annular surface of the tube at inlet and exit, as shown in Fig. 4.

Values of constants used are referred to [6]:

$\sigma = 0.7, \quad \sigma_k = 0.645, \quad C_D = 0.4184, \quad C_1 = 1.45,$

$C_2 = 0.18, \quad C_\mu = 0.22, \quad \sigma_\epsilon = 1.3$

$\sigma_t = 0.7$	$y^+ \le 5$
$\sigma_t = 1.4 - 0.7\ (13 - y^+)/8$	$5 < y^+ \le 13$
$\sigma_t = 1.4$	$13 < y^+ \le 17$
$\sigma_t = 0.95 + 0.45\ (25 - y^+)/8$	$17 < y^+ \le 25$
$\sigma_t = 0.95$	$y^+ > 25$

Method of Solution

A conventional primitive variable Galerkin based finite element formulation is used to discretize the coupled set of equations governing the fluid motion.

Quadrilateral isoparametric elements with reduced order for pressure are used, and the resulting nonlinear, nonsymmetric matrix equation can be written in the form

$$H\beta = f \tag{10}$$

Typical formulations leading to the evaluation of the nonlinear coefficients in the left-hand-side matrix are now contained in standard texts. All variables, including temperature, can be incorporated into the vector β. However, the temperature equation was solved separately since, for the problems analyzed, the buoyancy effects were very small and were, in fact, neglected during most calculations.

A relaxation factor of 0.8 was used on each variable while a convergence criterion of 1 percent on each variable was considered to be adequate.

One variation on the above scheme was the incorporation of a matrix symmetrizing technique, which considerably reduced computer core requirements. This innovation is particularly useful when undertaking analyses, where the global unsymmetric matrices are quite large.

The solution procedure for the coupled solid/fluid problem is as follows:

1 The flow properties were evaluated for the new set of elements. After the flow parameters were obtained in the main

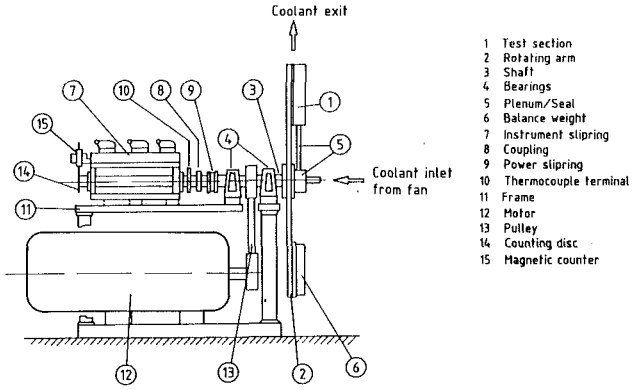

Fig. 6 Test facility

Table 1 Constructional details of test section

Heated length (mm)	150
Bore diameter (mm)	10
Mid-span eccentricity (mm)	330
Calming length prior to commencement of heating (mm)	255
Wall thickness (mm)	1.12

flow domain, a new set of elements (a very fine mesh for the near-wall region) were added into the computational model, as shown in Fig. 4 for heat transfer from the solid wall into the coolant. Since heat transfer depends on the fluid flow, the nodal values of velocity for the new mesh must be evaluated. This can be accomplished in two ways. The first uses the wall functions and the other interpolates using shape functions. In the present work, since the finite element is a 20-noded quadrilateral, a quadric shape function fit would be the most convenient.

2 The boundary conditions were specified as shown in Fig. 4 and an initial temperature value assigned everywhere except in the solid wall.

3 $\left[\frac{\mu}{\sigma}+\frac{\mu_t}{\sigma_t}\right]\frac{\partial T}{\partial y}$ values were evaluated as an outlet boundary condition and the governing equation solved for temperature.

4 Steps (2) and (3) were repeated and the updated values imposed as boundary conditions on the flow part of the upstream boundary until the required convergence criteria were satisfied.

Experimental Apparatus

Although numerous geometric configurations have been studied experimentally by this research group, including coolant channels having circular, square, rectangular, and triangular cross sections, data obtained from studies using a circular-sectioned tube have been used for these initial studies.

A schematic line diagram of the apparatus, which was designed to model a single-pass cooling channel with radially outward flow, is shown in Fig. 6. In essence the rig comprised a rotating arm to which could be attached test section subassemblies representing experimental models of the flow geometry being studied. Constructional details of the test section used are typified in Fig. 6. For the present comparisons the test section geometric features were as shown in Table 1.

The rotor arm, with its attached test section, was mounted on a shaft and supported by means of two self-aligning bearings. The rotor assembly was driven with a 20 kW controlled motor, giving a maximum speed capability of nominally 2000 rev/min and the rotor speed measured with a shaft-mounted magnetic encoder and electronic timer.

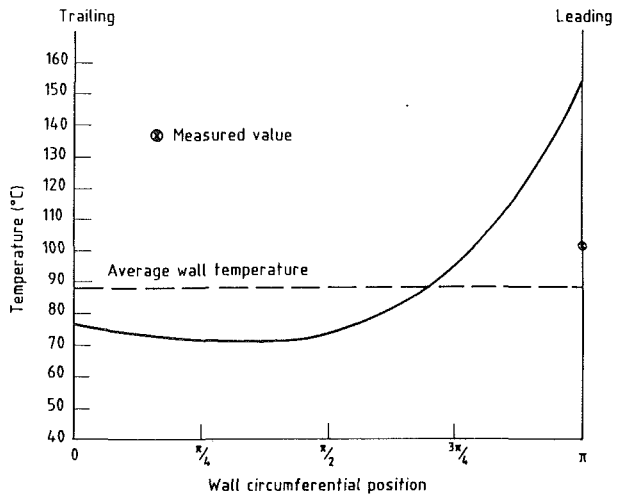

Fig. 7 Circumferential wall temperature variation without wall conduction at 10.5 diameters from inlet (Re = 5500, Ro = 0.115, Ra = 1.53 × 10⁶)

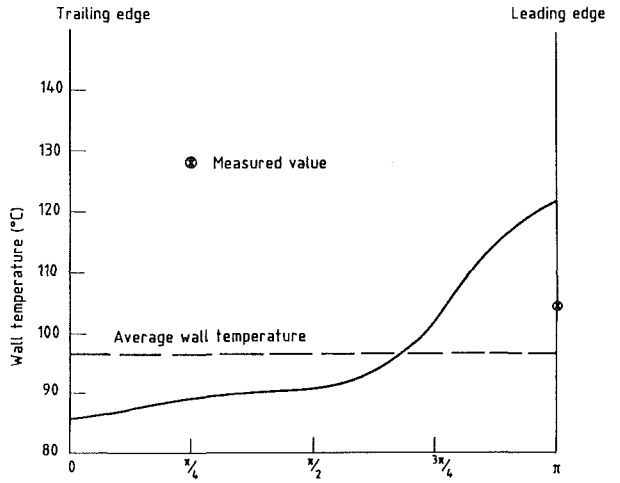

Fig. 8 Circumferential wall temperature variation without wall conduction at 10.5 diameters from inlet (Re = 15,000, Ro = 0.0406, Ra = 1.586 × 10⁶)

Air was used as the test fluid and could be blown through the test section via a rotating seal centrally located on the main rotor arm. The air flow was monitored with either an Annubar system, a rotameter, or a Hastings flow meter to enable cross checking.

The test tube was made from stainless steel and electrically heated with spirally wound resistance wire. Power for the heater was taken from a variable transformer through a shaft-mounted power slip ring and measured with a conventional wattmeter.

The temperature on the leading edge of the test section was measured at ten equiaxial locations along the section by means of copper/constantan thermocouples. Additionally, the inlet and exit temperature of the air flowing through the test section was measured using similar thermocouples. Thermocouple signals were taken from the rotor via silver/silver graphite instrumentation slip rings mounted at one end of the rotor shaft. These signals were logged with Mycalex 5000 data logging system and a DEC 11/34 digital computer.

The entire test section assembly was surrounded with Kawool thermal insulation to minimize external heat losses and cocooned into a self-contained subassembly, which could be easily fitted to and removed from the main rotor system.

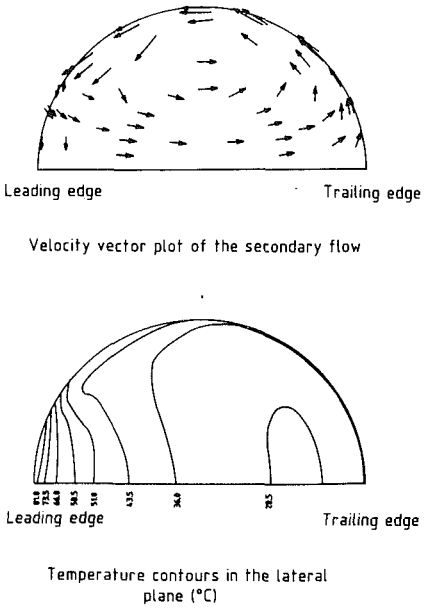

Fig. 9 Flow and heat transfer conditions in cross section at 10.5 diameters from inlet (Re = 5500, Ro = 0.115, Ra = 1.53×10^6)

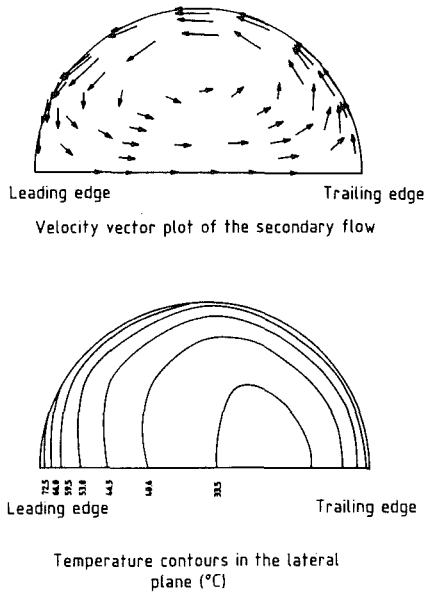

Fig. 10 Flow and heat transfer conditions in cross section at 10.5 diameters from inlet (Re = 15,000, Ro = 0.0406, Ra = 1.586×10^6)

Even with external lagging, some unknown proportion of the heat generated in the test section heater is unavoidably lost to the atmosphere. Thus not all the energy dissipated in the heater is transferred to the coolant. To account for this, a series of loss calibrations were conducted at each of the rotational speeds planned for so-called production experiments. In this way it was possible to determine the axial variation of heat flux along the test section and the corresponding variation of the bulk temperature of the coolant. Typically, the experiments were controlled so that no more than 10 percent of the total energy dissipated was unaccountable.

Results

A comprehensive comparison of the predicted isothermal flow data and experimental data has already been carried out [2]. In this, predicted variations of circumferential pressure,

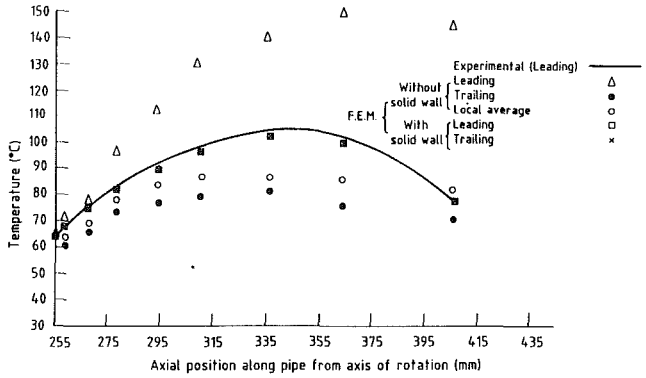

Fig. 11 Comparison of predicted axial wall temperature distributions with experimental values (Re = 5500, Ro = 0.115, Ra = 1.53×10^6)

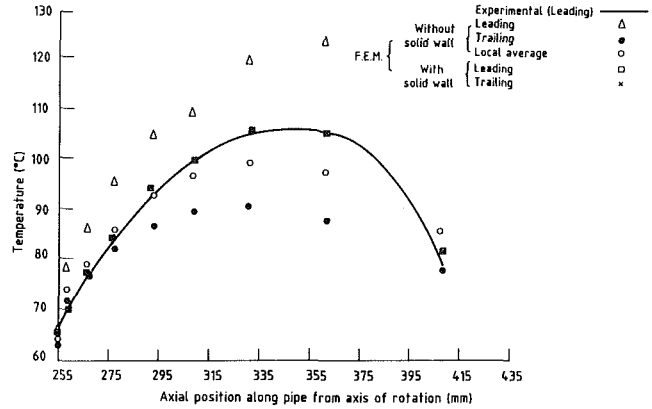

Fig. 12 Comparison of predicted axial wall temperature distributions with experimental values (Re = 15,000, Ro = 0.0406, Ra = 1.586×10^6)

in the form of dimensionless coefficients and friction factor–Reynolds number relationships were tested with the empirical data of [3, 4, 5] and good agreement obtained. Reference [2] also contained a comparison of measured and predicted average Nusselt–Reynolds number values for an imposed heat flux variation on this solid wall–fluid interface; see Fig. 5. These correlations were produced by first calculating circumferential and axial distributions of temperature at the solid wall. For the case considered, i.e., solid boundary conduction excluded, it can be seen that the numerical method predicts large variations in temperature, the lowest temperature being on the trailing edge of the tube (Figs. 7 and 8). This is a consequence of the "washing" effect of the secondary flow, which transports fluid from the trailing edge along the wall of the pipe toward the leading edge. The relative strengths of the secondary flows and their consequent effect on the fluid temperature distributions are illustrated in Figs. 9 and 10 for two Reynolds numbers at the same speed of rotation. These diagrams demonstrate the importance of the Coriolis acceleration, which is characterized by the so-called Rossby number.

At the higher Rossby number, Fig. 7 indicates that the numerical method predicts a maximum temperature approximately 50 percent greater than the experimental value measured at the same position.

The introduction of conduction in the solid boundary into the analyses has the immediate effect of averaging the circumferential wall temperatures. Indeed, the difference between leading and trailing edge temperature at the higher Rossby number was calculated to be 0.1°C. The importance of the wall conduction is clearly portrayed in Figs. 11 and 12 where the variation of temperature is plotted against axial position in the pipe. Excellent agreement is obtained between the predicted values, which include wall conduction, and the exper-

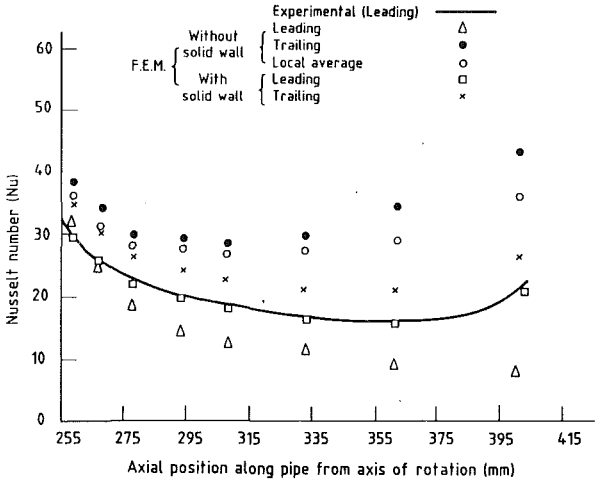

Fig. 13 Comparison of predicted axial variation of heat transfer with experimental values (Re = 5500, Ro = 0.115, Ra = 1.53×10^6)

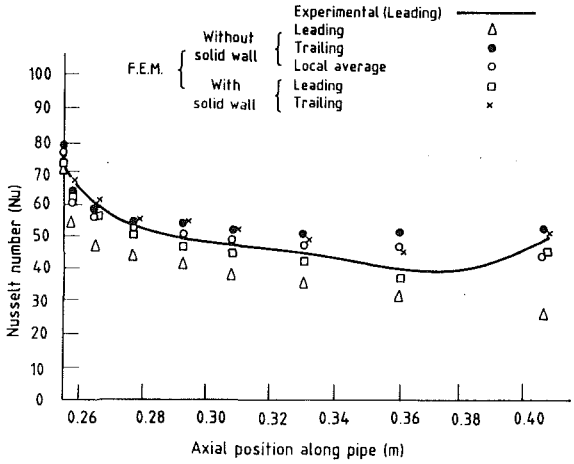

Fig. 14 Comparison of predicted axial variation of heat transfer with experimental values (Re = 15,000, Ro = 0.0406, Ra = 1.586×10^6)

imental data at both values of Reynolds and Rossby numbers. However, the numerical values excluding conduction, which have been averaged circumferentially, underpredict measured values by a maximum of 20 percent at the higher Rossby number.

Figures 13 and 14 depict the axial variations of local Nusselt number using the same format as the previous diagrams. Here, both sets of predicted results straddle the measured curve, the better agreement being again achieved by including wall conduction. In this case, no attempt has been made to average the theoretical results in order to illustrate the difference in wall temperature gradients, and therefore heat fluxes, that occur at the leading and trailing edges.

Finally, the overall heat transfer characteristics are illustrated in Fig. 15 where the mean value of Nusselt number Nu_m has been plotted against the dimensionless grouping of $[Ra/Re^2]^{-0.186} Ro^{0.33} Re^{0.8}$ as suggested by Morris and Ayham [1]. Again, the improvement between experimental and predicted

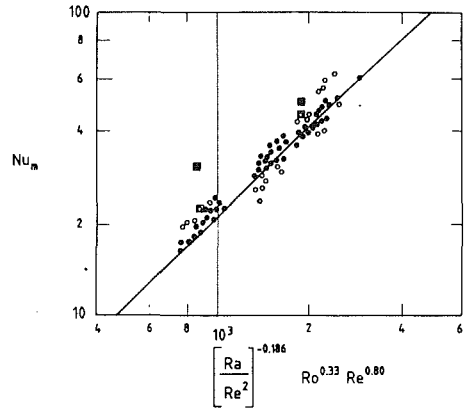

Fig. 15 Comparison of predicted mean heat transfer rates with measured values

values achieved by introducing wall conduction is particularly marked at the higher Rossby number.

Conclusions

It is apparent from the results presented here that the finite element method is a viable technique for determining the heat transfer characteristics in the cooling ducts of gas turbine blades. In particular, it has demonstrated that any predictive method must include the conduction in the solid boundary in order to produce realistic wall temperatures and local and overall heat transfer coefficients. This is of prime importance at Rossby numbers similar to those encountered at engine operating conditions (e.g., Ro = 0.115).

Finally, it should be emphasized that the current finite element method does not, in the course of the solution, employ upwinding techniques. Thus the introduction of spurious damping is avoided, which, although having a relatively minor effect on axial velocity distributions, can significantly change the secondary flow patterns. It has already been shown elsewhere that this has an important influence on the heat transfer phenomena.

Acknowledgments

The authors acknowledge with thanks the financial support of Rolls-Royce plc, Bristol, U.K., for this investigation.

References

1 Morris, W. D., and Ayham, T., "Observations on the Influence of Rotation on Heat Transfer in the Coolant Channels of Gas Turbine Blades," *Proc. IMechE*, Vol. 193, No. 21, 1979, pp. 303–311.

2 Taylor, C., Rance, J., and Medwell, J. O., "A Method for the Prediction of Coriolis Induced Secondary Flows and Their Influence on Heat Transfer in Rotating Ducts," *Eng. Comput.*, Vol. 2, No. 1, 1985, pp. 1–12.

3 Mori, Y., Fukada, T., and Nakayama, W., "Convective Heat Transfer in a Rotating Radial Circular Pipe," *Int. J. Heat Mass Transfer*, Vol. 14, 1971, pp. 1807–1824.

4 Ito, H., and Nanbu, K., "Flow in Rotating Straight Pipes of Circular Cross Section," ASME *Journal of Basic Engineering*, Vol. 93, 1971, pp. 383–394.

5 Trefethan, L., "Flow in Rotating Radial Ducts," GEC Report No. 559L350-A, 1957, pp. 1–27.

6 Xia, J. Y., "Finite Element Method and 3-D Turbulent Flow and Heat Transfer," Ph.D. thesis, Dept. of Civil Engineering, University College of Swansea, United Kingdom, 1989.

Turbulent Heat Transfer and Friction in a Square Channel With Discrete Rib Turbulators

S. C. Lau

R. D. McMillin

J. C. Han

Department of Mechanical Engineering,
Texas A&M University,
College Station, TX 77843

Experiments study the turbulent heat transfer and friction for fully developed flow of air in a square channel with discrete rib turbulators. The discrete ribs are staggered on two opposite walls of the channel in alternate rows of three and two ribs. Nine rib configurations are examined: transverse ribs with an angle of attack (α) of 90 deg, discrete ribs with α = 90 deg, parallel arrays of discrete ribs with α = 45 deg and −45 deg on alternate rows, and parallel and crossed arrays of discrete ribs with α = 60, 45, and 30 deg. The rib height-to-hydraulic diameter ratio and the rib pitch-to-height ratio are 0.0625 and 10, respectively. The Reynolds number ranges from 10,000 to 80,000. Results show that the average Stanton number in the 90 deg discrete rib case is about 10 to 15 percent higher than that in the 90 deg transverse rib case. Turning the discrete ribs on the oppsite walls 60, 45, or 30 deg in the same direction with respect to the main flow increases the average Stanton number 10 to 20 percent over that in the 90 deg discrete rib case. Parallel oblique discrete ribs with α = 60, 45, and 30 deg have comparable performances and have higher overall heat transfer per unit pumping power than 90 deg discrete ribs. Crossed oblique discrete ribs perform poorly compared with 90 deg discrete ribs and are not recommended.

Introduction

Turbulent heat transfer and friction for flow in tubes, annuli, and between parallel plates with repeated ribs have been studied extensively (for example, Wilkie, 1966; White and Wilkie, 1970; Webb et al., 1971; Donne and Meyer, 1977; Han et al., 1978; Gee and Webb, 1980; Meyer, 1982; Sethumadhavan and Raja Rao, 1983). For turbine airfoil cooling, the shaped internal cooling passages are better modeled as rectangular channels with rib turbulators on two opposite walls only. Burggraf (1970) studied turbulent heat transfer and friction for flow in a square duct with transverse ribs (with α = 90 deg) on two opposite walls. With hydrodynamically fully developed flow at the duct entrance, the ribbed wall Nusselt number was 2.38 times the corresponding value for fully developed flow in a smooth duct. The smooth wall Nusselt number was 19 percent over the all-smooth wall value. The friction factor was about 8.6 times the smooth duct value. Burggraf conducted the experiments for two other entrance conditions but did not examine the rib geometry (the rib pitch, the rib height, and the angle of attack) effects.

Heat transfer in straight rectangular channels with two opposite ribbed walls and two smooth walls has been studied by Han (1984, 1988), Han et al. (1985, 1989), and Han and Park (1988). In Han (1984) and Han et al. (1985), experiments with an aluminum square duct with two ribbed walls and two smooth walls determined the effects of the rib angle of attack, the rib pitch-to-height and rib height-to-hydraulic diameter ratios on the fully developed friction factor and heat transfer coefficient. The rib angle of attack varied from 30 to 90 deg. The Reynolds number ranged from 7000 to 90,000; the rib pitch-to-height ratio and the rib height-to-hydraulic diameter ratio varied from 10 to 40 and from 0.021 to 0.063, respectively. The ribbed wall Stanton number was found to be two to three times that of the smooth square duct and the smooth wall Stanton number was also higher by about 20 to 50 percent.

In Han and Park (1988), Han (1988), and Han et al. (1989), similar experiments were conducted with square and rectangular test sections constructed of wood and acrylic sheets and heated with thin stainless steel foils. The effects of varying the rib angle of attack and the channel aspect ratio on the distribution of the local heat transfer coefficient and the friction were investigated. Results were obtained for rib angles of attack of 30, 45, 60, and 90 deg and for channel aspect ratios of 1/4, 1/2, 1, 2, and 4. For square channels, ribs with an angle of attack of 60 deg gave the highest heat transfer as well as the highest pressure drop, whereas 45 and 30 deg ribs resulted in maximum cooling for a given pumping power. For rectangular channels, the increase in the ribbed wall heat transfer was higher in a channel with a smaller aspect ratio (ribs on the narrower walls) than in a channel with a larger aspect ratio (ribs on the wider walls), for a given pumping power.

Metzger et al. (1987a, 1987b) studied the effect of varying the rib angle and length of the convective heat transfer in rib-

Contributed by the International Gas Turbine Division and presented at the ASME Winter Annual Meeting, San Francisco, California, December 10–15, 1989. Manuscript received at ASME Headquarters December 1990.

Table 1 Configurations of ribs on channel walls

Case	Rig length (cm/in.)	Rib configuration, arrays on opposite walls	Rib angle of attack, deg
1	7.62/3.0	transverse	90
2	1.52/0.6	staggered	90
3	1.52/0.6	staggered, parallel	60
4	1.52/0.6	staggered, parallel	45
5	1.52/0.6	staggered, parallel	30
6	1.52/0.6	staggered, parallel	45 and −45, alternately
7	1.52/0.6	staggered, crossed	60
8	1.52/0.6	staggered, crossed	45
9	1.52/0.6	staggered, crossed	30

roughened triangular ducts. Ribs were placed on two of the three walls of the test ducts to model the internal cooling passage at the leading edge of a turbine airfoil. The local heat transfer was determined with a coating material that melted at 43°C. They found that the heat transfer augmentation in ribbed triangular channels was significantly higher on both the ribbed and smooth walls than that in square channels. Shortening the ribs to give less flow obstruction in the corner regions did not improve the heat transfer.

The objective of this investigation is to study the turbulent heat transfer and friction for fully developed flow in a square channel with discrete turbulence promoters. The discrete ribs are staggered on two opposite walls of the channel in alternate rows of three and two ribs. The effects of replacing the transverse ribs (ribs that stretch across the width of the channel with any angle of attack) in previous investigations by short segments of the ribs on the heat transfer and friction are examined.

Airflow over a 90 deg transverse rib on a rib-roughened wall separates at the top edges of the rib. The flow reattaches in a region on the channel wall downstream of the rib. A boundary layer and a reverse flow boundary layer develop in the region of reattachment and grow in thickness in opposite directions. High heat transfer occurs in the vicinity of the reattachment region. Recirculation zones can be found adjacent to the upstream face, the downstream face, and perhaps, in some situations, the top face of the rib. In the case of an oblique rib, there is a secondary flow in a direction parallel to the rib axis. The interaction between the main flow and the secondary flow results in the vigorous mixing of the airflow near the rib and the wall and further enhances the heat transfer to the airstream.

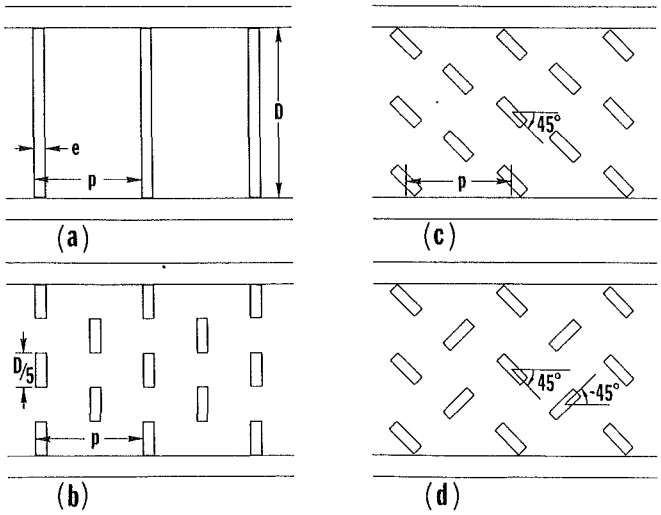

Fig. 1 Typical rib configurations: (*a*) 90 deg transverse ribs; (*b*) 90 deg discrete ribs; (*c*) 45 deg discrete ribs; (*d*) discrete ribs with α = 45 and −45 deg on alternate rows

For airflow over a staggered array of 90 deg discrete ribs, separation occurs not only at the top edges of the ribs but also at the edges at the ends of the ribs. Some of the air flowing along the wall is forced away laterally from the ends of the ribs and turns sharply as the ribs immediately downstream are encountered. This secondary flow may also interrupt the growth of the boundary layers downstream of the nearby reattachment zones. In the case of a staggered arrangement of oblique discrete ribs, this secondary flow along the wall, the secondary flow caused by the orientation of the ribs, and the separation

Nomenclature

a = coefficient in roughness functions
b = exponent in roughness functions
c_p = specific heat of air at average bulk temperature, J/(kg·K)
D = hydraulic diameter of square channel, m
dP/dx = streamwise pressure gradient in fully developed region in channel, (N/m²)/m
e = height of ribs, m
e^+ = roughness Reynolds number, equation (10)
$\bar{f}$ = friction factor for square channel with two opposite ribbed walls and two smooth walls, equation (1)
f_{ss} = friction factor for square channel with four smooth walls, equation (5)
$G(e^+, \mathrm{Pr})$ = heat transfer roughness function, equation (8)
$\overline{G}(e^+, \mathrm{Pr})$ = average heat transfer roughness function, equation (9)
$\dot{m}$ = rate of mass flow of air, kg/s
p = rib pitch, m
P = local static pressure, N/m²
$\dot{q}_r''$ = net heat flux on ribbed walls, W/m²
$\dot{q}_s''$ = net heat flux on smooth walls, W/m²
$R(e^+)$ = roughness function, equation (7)
Re_D = Reynolds number based on channel hydraulic diameter, equation (4)
$\overline{\mathrm{St}}$ = average Stanton number
St_r = Stanton number for ribbed walls in square channel with two opposite ribbed walls and two smooth walls, equation (2)
St_s = Stanton number for smooth walls in square channel with two opposite ribbed walls and two smooth walls, equation (3)
St_{ss} = Stanton number for square channel with four smooth walls, equation (6)
$(\overline{T_{wr} - T_b})$ = ribbed wall/bulk temperature difference in fully developed region in channel, K
$(\overline{T_{ws} - T_b})$ = smooth wall/bulk temperature difference in fully developed region in channel, K
$\bar{u}$ = average air velocity, m/s
x = streamwise coordinate, m
α = rib angle of attack, deg
μ = dynamic viscosity of air at average bulk temperature, N·s/m²
ρ = density of air at average bulk temperature, kg/m³
τ_w = wall shear stress, N/m²

from the ribs and the reattachment on the wall of the main flow all contribute to the heat transfer to the airstream.

Experimental Apparatus

The test apparatus is an open flow loop that consists of a settling chamber, a calibrated orifice flow meter, an entrance section, and the test section. A centrifugal blower driven by a 3.73 kW (5.0 hp) electric motor delivers air to the flow loop. The rate of mass flow of air through the flow loop is controlled by a flow diverter.

The test section is a straight, 1.52 m (5.0 ft) long, 7.62 cm (3.0 in.) by 7.62 cm (3.0 in.) square channel constructed of 0.635 cm (0.25 in.) thick aluminum plates. The interior surfaces of two opposite walls of the channel are smooth and those of the other two opposite walls are roughened with rib turbulators. The ribs, which are 4.76 mm (0.1875 in.) square brass bars, are attached to the channel walls with silicone rubber adhesive. Nine rib configurations are studied. In all nine cases, the rib height-to-channel hydraulic diameter ratio, e/D, and the rib pitch-to-height ratio, p/e, are 0.0625 and 10, respectively. Table 1 gives the lengths and orientations of the ribs in the nine cases. Discrete ribs are staggered on the walls in alternate rows of three and two ribs (see Figs. 1*a–d*). In cases 3–6, the rib arrays on the two opposite walls are parallel. In cases 7–9, the rib arrays on the two opposite walls are oriented in opposite directions with respect to the main flow.

The four channel walls are heated individually with electric heaters with wire-wound elements vulcanized between two thin layers of fiberglass-reinforced silicone rubber. Each heater has a maximum power rating of 750 W (2560 Btu/h) and has a heated area of 1.52 m (5.0 ft) by 7.62 cm (3.0 in.). The heaters are attached to the exterior surfaces of the channel walls with silicone rubber adhesive and the heaters on opposite walls are connected in parallel electrically. A 1.59 mm (0.0625 in.) thick asbestos gasket minimizes the heat transfer between adjacent channel walls.

The entrance channel has the same square cross section as that of the test section. It is constructed of 6.35 mm (0.25 in.) thick acrylic sheets. It is 1.52 m (5.0 ft) long and is mated to the test section with two flanges. The test section and the downstream half of the entrance section are insulated with 10.16 cm (4.0 in.) thick layers of fiberglass felt on all sides.

Instrumentation

The test section is instrumented with 30-gage copper-constantan thermocouples with Teflon insulation. To install the thermocouples, small holes are drilled and shallow grooves are machined on the channel walls. The junction of each thermocouple is then affixed to the bottom of a hole with silver-based paint and fast-drying epoxy. Epoxy is also applied to the shallow groove to hold the thermocouple in place. Good physical contact between the thermocouple and the channel wall is checked with an ohmmeter.

Fourteen thermocouples are installed along the axial centerline of one of the ribbed walls. Similarly, fourteen thermocouples are installed on each of the smooth walls. Six thermocouples at other locations on the test channel walls check the spanwise variation of the wall temperature.

Two additional thermocouples measure the inlet air temperature and four thermocouples the exit air temperature. A digital temperature indicator reads the thermocouple output.

Three pressure taps are installed along the axial centerline of one of the smooth walls far downstream from the test section entrance to measure the pressure drop. The distance between adjacent pressure taps is 0.457 m (18 in.). The pressures at these taps, the pressure drop across the orifice, and the gage pressure upstream of the orifice are measured with a water manometer, an inclined oil manometer, or a micromanometer.

Two variable transformers control the power input to the four heaters. Two 5-1/2 digit TRMS multimeters measure the voltage drop across each heater and the current through each heater, respectively.

Experimental Procedure

To prepare for a set of test runs, the ribs are attached to the interior surfaces of two opposite walls. The test section is then assembled and checked for air leakage. To initiate a test run, the blower is switched on. The flow diverter is adjusted to let a predetermined rate of air flow through the flow loop. The test section is heated so that the wall temperatures near the exit are about 15°C (27°F) above the exit air temperature. The power inputs to the four heaters are adjusted so that the temperatures at any axial location on the two ribbed walls and the two smooth walls are about the same.

After steady state is attained, the wall temperatures, the inlet and exit air temperatures, the voltage drop across the heaters, the current through the heaters, the pressure drop across the orifice, the gage pressure upstream of the orifice, and the local pressures are recorded. The maximum variations of some of the readings are also recorded for the uncertainty analysis of the results. The atmospheric pressure is read at the beginning and the end of a test run. A test run lasts about two hours.

The heat loss through the fiberglass insulation is determined in separate no-flow experiments. In each of these experiments, the inlet and exit of the test section are blocked and the test section is heated so that the average steady-state wall temperature is in the range of the wall temperature recorded during test runs with flow. Steady state is attained in about twelve hours. A correlation of the rate of heat input, which is also the rate of heat loss through the insulation, as a function of the average wall temperature is obtained. The correlation calculates the rate of heat loss through the insulation during a test run. For low Reynolds number runs, the rate of heat loss through the insulation can be up to 7 percent of the rate of total heat input.

Data Reduction

The friction factor is the ratio of the wall shear stress and the dynamic pressure and is determined by the measured pressure gradient and mass flow rate.

$$\bar{f} = \tau_w/[(1/2)\rho\bar{u}^2] = [(-dP/dx)D/4]/[(1/2)\rho\bar{u}^2] = (-dP/dx)D^5/[2(\dot{m}^2/\rho)] \quad (1)$$

The Stanton numbers for the ribbed walls and the smooth walls are calculated from

$$\mathrm{St}_r = \dot{q}_r'' D^2/[\dot{m}c_p(\overline{T_{wr}} - \overline{T_b})] \quad (2)$$

and

$$\mathrm{St}_s = \dot{q}_s'' D^2/[\dot{m}c_p(\overline{T_{ws}} - \overline{T_b})] \quad (3)$$

Results show that there is no difference between the temperature distributions on the two smooth walls. The heat fluxes are based on the power input to the heaters, the rate of heat loss through the insulation, the rate of streamwise heat conduction in the channel walls, and the projected heat transfer area (not including the increased rib surface area). The average wall/bulk temperature differences are determined over a section of the test channel far downstream of the entrance, where the streamwise wall temperature distributions are linear. The distribution of the bulk temperature is evaluated from an energy balance with the rate of net heat transfer to the air and the inlet bulk temperature.

The average Stanton number, $\overline{\mathrm{St}}$, is the average of the Stanton numbers for the ribbed walls and the smooth walls. The Reynolds number is defined as

$$\mathrm{Re}_D = \rho\bar{u}D/\mu = \dot{m}/(D\mu) \quad (4)$$

All fluid properties in equations (1)–(4) are based on the av-

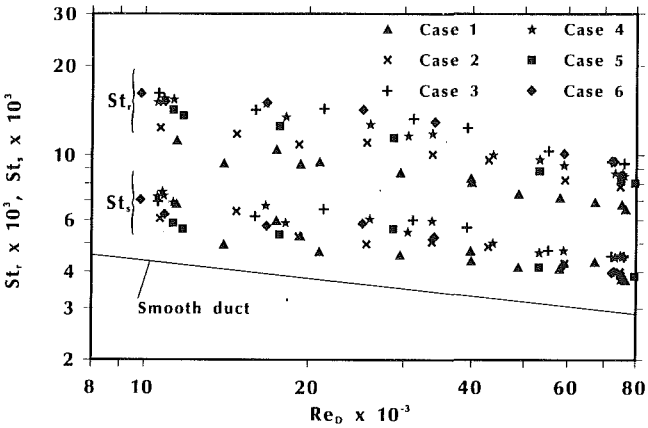

Fig. 2 Ribbed wall and smooth wall Stanton numbers as functions of Reynolds number, parallel rib cases

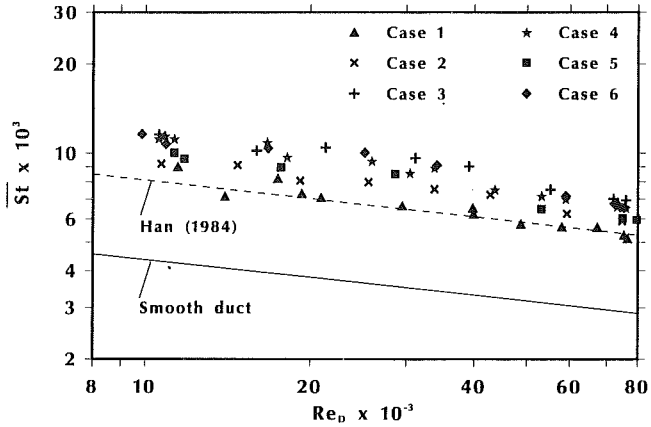

Fig. 3 Average Stanton number as a function of Reynolds number, parallel rib cases

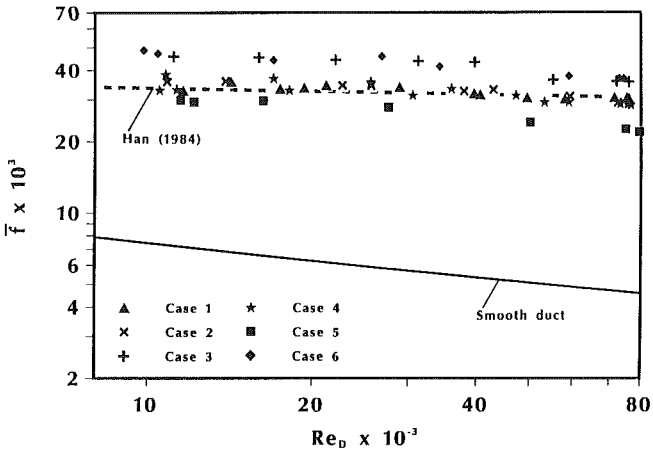

Fig. 4 Friction factor as a function of Reynolds number, parallel rib cases

erage bulk temperature. A Fortran program computes the friction factor and the Stanton numbers as functions of Reynolds number for the various rib configurations.

Based on the method of uncertainty analysis by Kline and McClintock (1953), the maximum uncertainties of the values of the Reynolds number and the Stanton numbers are ±2.9 percent and ±5.8 percent, respectively. The maximum uncertainty of the values of the friction factor is ±10.9 percent for Reynolds numbers of about 10,000 and ±6.5 percent for Reynolds numbers above 20,000. The pressure drop in the test section is small when the flow rate is low. As a result, the errors in the values of the friction factor can be quite large in the low Reynolds number cases.

The friction factor and the Stanton numbers are compared to their corresponding values for fully developed turbulent flow through a square channel with four smooth walls, which are calculated with the modified Karman–Prandtl and Dittus–Boelter equations (Han, 1984), respectively.

$$(f_{ss})^{-0.5} = 4.0 \log_{10}[\mathrm{Re}_D (f_{ss})^{0.5}] - 0.1482 \quad (5)$$

$$\mathrm{St}_{ss} = 0.02234\, \mathrm{Re}_D^{-0.2} \mathrm{Pr}^{-0.6} \quad (6)$$

To correlate the data, the roughness function, $R(e^+)$, the heat transfer roughness function, $G(e^+, \mathrm{Pr})$, and the average heat transfer roughness function, $\overline{G}(e^+, \mathrm{Pr})$, are determined with the following equations (Han, 1988):

$$R(e^+) = [(2\bar{f} - f_{ss})/2]^{-0.5} + 2.5 \ln[2(e/D)] + 2.5 \quad (7)$$

$$G(e^+, \mathrm{Pr}) = [(2\bar{f} - f_{ss})/2]^{0.5}/\mathrm{St}_r + 2.5 \ln[2(e/D)] + 2.5 \quad (8)$$

$$\overline{G}(e^+, \mathrm{Pr}) = [(2\bar{f} - f_{ss})/2]^{0.5}/\overline{\mathrm{St}} + 2.5 \ln[2(e/D)] + 2.5 \quad (9)$$

They are all functions of the roughness Reynolds number, which is defined as

$$e^+ = (e/D)\mathrm{Re}_D[(2\bar{f} - f_{ss})/2]^{0.5} \quad (10)$$

The roughness functions are correlations for the prediction of the friction factor and Stanton numbers (see Han, 1988).

Presentation of Results

The main objective of this investigation is to examine how the heat transfer and friction for airflow in a square channel are affected when transverse rib turbulators on two opposite walls of the channel are replaced by discrete ribs. Results of the Stanton numbers for the ribbed walls and the smooth walls are presented as functions of the flow Reynolds number. They are followed by the average Stanton number and friction factor results. To evaluate the performances per unit pumping power of the various rib configurations, the ratios $[(\mathrm{St}_r/\mathrm{St}_{ss})/(\bar{f}/f_{ss})^{1/3}]$ and $[(\overline{\mathrm{St}}/\mathrm{St}_{ss})/(\bar{f}/f_{ss})^{1/3}]$ are plotted versus the Reynolds number. Lastly, the friction and heat transfer results are correlated with the roughness function $R(e^+)$ and the heat transfer roughness functions $G(e^+, \mathrm{Pr})$ and $\overline{G}(e^+, \mathrm{Pr})$, respectively.

Parallel Rib Arrays. Figure 2 shows that the ribbed wall Stanton numbers in the parallel discrete rib cases are all higher than that in the 90 deg transverse rib case. Over the range of Reynolds number studied, the ribbed wall Stanton number in the 90 deg discrete rib case (case 2) is about 15 percent higher than that in the 90 deg transverse rib case (case 1). Turning the discrete ribs an angle of 60, 45, or 30 deg (cases 3, 4, and 5) or turning the discrete ribs on alternative rows angles of 45 and −45 deg (case 6) increases the value of St_r by up to an additional 30 percent. The ribbed wall Stanton numbers in the 60 and 45/−45 deg cases (cases 3 and 6) are generally higher than that in the 45 deg case (case 4), which, in turn, is higher than that in the 30 deg case (case 5).

It is believed that the secondary flow resulting from flow separation on the edges at the ends of the discrete ribs interacts with the secondary flow along the rib axes (in the oblique rib cases) and the separation and reattachment of the main flow. The vigorous mixing of the flowing air near the channel wall and ribs enhances the heat transfer to the airstream.

The presence of the ribs on the roughened walls also affects the heat transfer from the smooth walls. The smooth wall Stanton numbers in all parallel rib cases are higher than that for a square channel with four smooth walls by about 40 to 80 percent (see Fig. 2). The values of St_s in cases 2, 5, and 6 (α = 90, 30, and 45 and −45 deg on alternate rows) are slightly higher than that in case 1 (α = 90 deg). The smooth wall Stanton numbers in cases 3 and 4 (α = 60 and 45 deg) are the highest—about 20 percent higher than that in case 1. Results

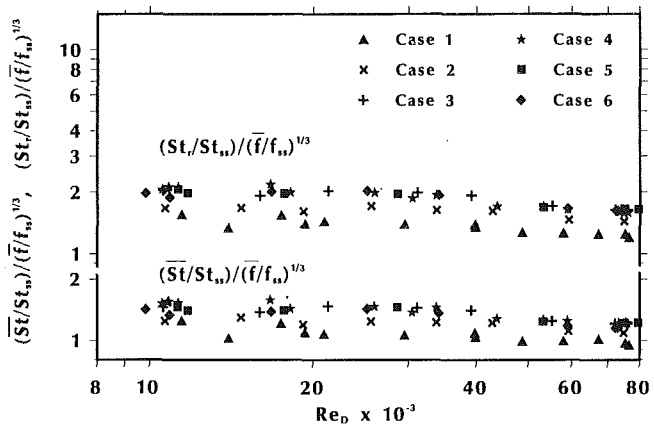

Fig. 5 Thermal performances of parallel ribs, $[(St_r/St_{ss})/(\bar{f}/f_{ss})^{1/3}]$ and $[(\bar{St}/St_{ss})/(\bar{f}/f_{ss})^{1/3}]$ as functions of Reynolds number

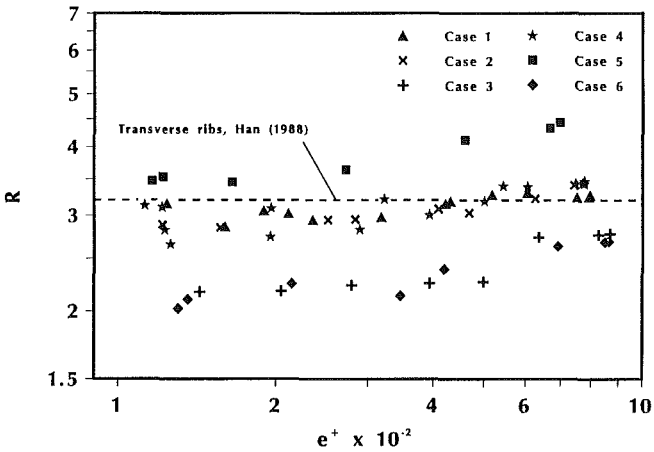

Fig. 6 $R(e^+)$ as a function of e^+, parallel rib cases

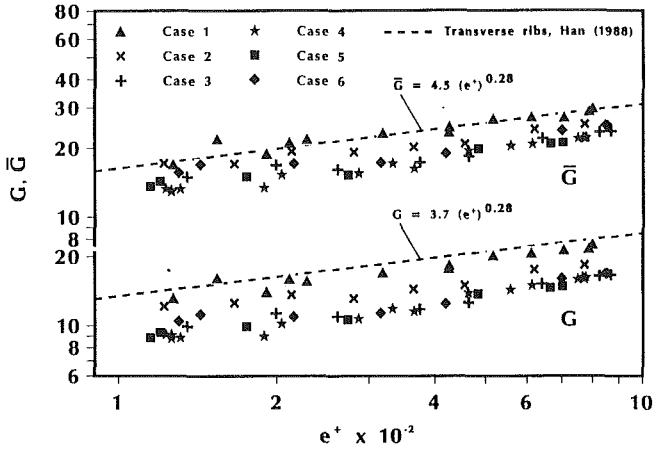

Fig. 7 $G(Pr, e^+)$ and $\bar{G}(Pr, e^+)$ as functions of e^+, parallel rib cases

Table 2 Coefficients and exponents for the functions $R(e^+)$, $G(e^+, Pr)$, and $\bar{G}(e^+, Pr)$, parallel rib cases

	$R(e^+)=a(e^+)^b$		$G(e^+, Pr)=a(e^+)^b$		$\bar{G}(e^+, Pr)=a(e^+)^b$	
Case	a	b	a	b	a	b
1	2.269	0.055	3.728	0.267	5.447	0.250
2	1.848	0.086	3.884	0.229	5.894	0.214
3	0.968	0.152	2.370	0.284	4.231	0.250
4	1.837	0.093	1.764	0.333	3.210	0.290
5	1.776	0.136	2.290	0.285	4.403	0.238
6	1.017	0.142	2.852	0.259	4.702	0.243

show that the heat transfer from the smooth walls is increased when the 90 deg transverse ribs on the roughened walls are replaced by parallel discrete ribs.

The average Stanton number results are presented in Fig. 3. For the square channel in this study, the average Stanton number is the average of the corresponding ribbed wall Stanton number and smooth wall Stanton number. Also included in Fig. 4 for comparison are the published data for fully developed flow in a square channel with 90 deg transverse ribs (Han, 1984) and the Stanton number–Reynolds number correlation for a square channel with four smooth walls.

The average Stanton number in case 1 is about two times that for airflow in a square channel with four smooth walls and compares very well with the published data from Han (1984). The average Stanton number in case 2 is about 10 to 15 percent higher than that in case 1. The average Stanton numbers in all the oblique parallel discrete rib cases (cases 3 through 6) are higher than that in the 90 deg discrete rib case (case 2).

Recall that the ribbed wall Stanton number is higher in case 6 (α = 45 and −45 deg in alternate rows) than in case 4 (α = 45 deg) and the smooth wall Stanton number is higher in case 4 than in case 6. The average Stanton numbers in the two cases do not differ significantly and are about 20 and 10 percent higher than that in case 2 at Re_D = 10,000 and 80,000, respectively. The average Stanton number in case 3 (α = 60 deg) is the highest but is only slightly higher than those in cases 4 and 6.

In Fig. 4, the friction factor in case 1 compares very well with published data and is 4.5 to 6.5 times that for airflow in a smooth square channel over the range of Reynolds number studied. The friction factors in cases 2 and 4 are only slightly higher than that in case 1 at low Reynolds numbers and are about the same as that in case 1 at high Reynolds numbers. The friction factor in case 6, however, is about 25 percent higher than that in case 4. The rib array in case 6 may have caused a portion of the air flowing near the ribbed walls to zigzag through the rows of discrete ribs, resulting in a large pressure drop in the channel. The friction factor in case 3 (α = 60 deg) is as high as that in case 6 and the friction factor in case 5 (α = 30 deg) is the lowest among all the friction factors in the parallel discrete rib cases.

Since the average Stanton numbers in cases 4 and 6 are about the same and the friction factor is higher in case 6 than in case 4, 45 deg discrete ribs should give better overall thermal performance (higher heat transfer for a given pumping power) than discrete ribs with α = 45 and −45 deg on alternate rows. This is illustrated in Fig. 5, where the ratio $[(\bar{St}/St_{ss})/(\bar{f}/f_{ss})^{1/3}]$ is plotted versus the Reynolds number. The ratio $[(\bar{St}/St_{ss})/(\bar{f}/f_{ss})^{1/3}]$ in case 4 is generally higher than that in case 6 for $10{,}000 < Re_D < 80{,}000$.

Although the average Stanton number in case 3 (α = 60 deg) is much higher than that in case 5 (α = 30 deg), the friction factor in case 3 is also much higher than that in case 5. Figure 5 shows that the overall thermal performances in the two cases are comparable to each other and to that in case 4. From a design standpoint, the thermal performances in all parallel oblique discrete rib cases are comparable to one another and are better than that in the 90 deg discrete rib case.

Figure 5 also shows that the ratios $[(St_r/St_{ss})/(\bar{f}/f_{ss})^{1/3}]$ in all the parallel oblique discrete rib cases (cases 3–6) are about the same. They are about 15 percent higher than that in case 2, which, in turn, is about 18 percent higher than that in case 1.

The roughness function, $R(e^+)$, and the heat transfer roughness functions, $G(e^+, Pr)$ and $\bar{G}(e^+, Pr)$, defined in equations (7)–(9), are presented in Figs. 6 and 7. For air at the average bulk temperature, Pr = 0.706. The values of $R(e^+)$ in cases 3 and 6 are significantly lower than those in the other cases, as a result of the higher values of $\bar{f}$ in the two cases. Oblique

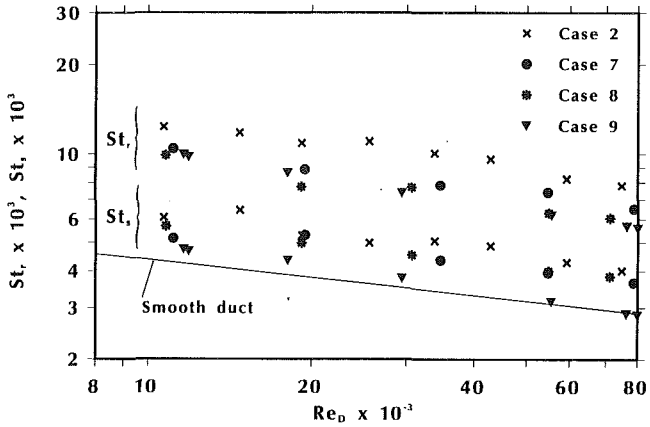

Fig. 8 Ribbed wall and smooth wall Stanton numbers as functions of Reynolds number, crossed rib cases

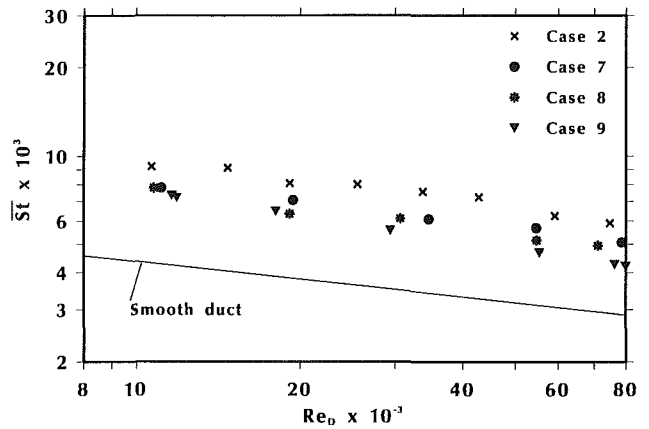

Fig. 9 Average Stanton number as a function of Reynolds number, crossed rib cases

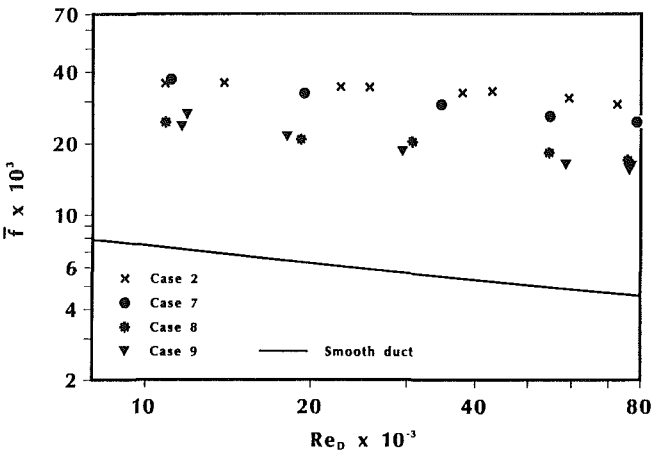

Fig. 10 Friction factor as a function of Reynolds number, crossed rib cases

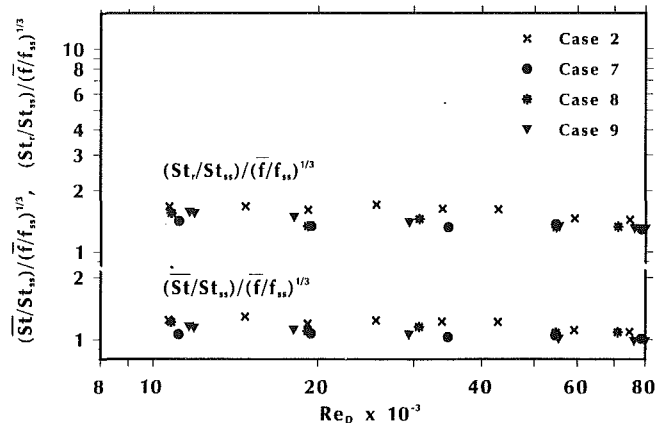

Fig. 11 Thermal performances of crossed ribs, $[(St_r/St_{ss})/(\bar{f}/f_{ss})^{1/3}]$ and $[(\overline{St}/St_{ss})/(\bar{f}/f_{ss})^{1/3}]$ as functions of Reynolds number

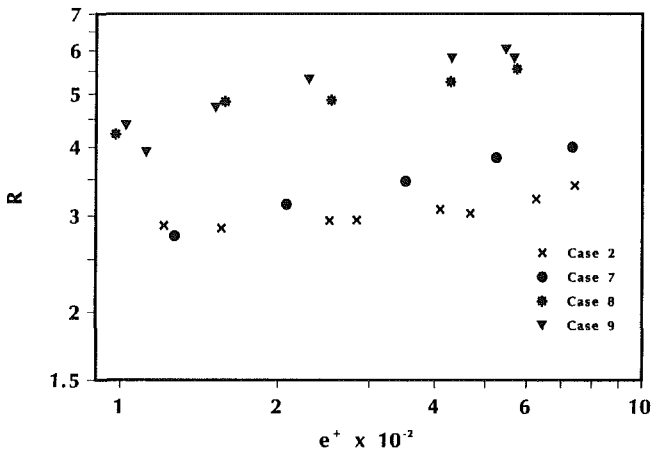

Fig. 12 $R(e^+)$ as a function of e^+, crossed rib cases

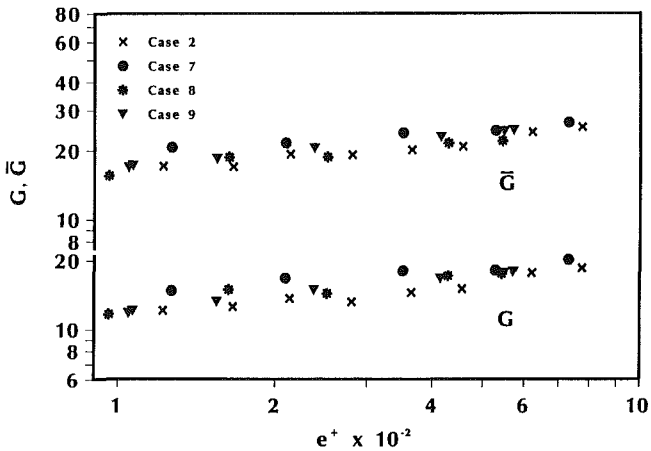

Fig. 13 $G(\mathrm{Pr}, e^+)$ and $\bar{G}(\mathrm{Pr}, e^+)$ as functions of e^+, crossed rib cases

ribs (cases 3, 4, and 5) have the lowest values of $\bar{G}(e^+, \mathrm{Pr})$ and the highest overall thermal performances among the various parallel rib configurations.

The roughness function, $R(e^+)$, and the heat transfer roughness functions, $G(e^+, \mathrm{Pr})$ and $\bar{G}(e^+, \mathrm{Pr})$, all have the form of $a(e^+)^b$. The values of the coefficient a and the exponent b based on least-squares curve fit lines through the various sets of data for the parallel rib cases are listed in Table 2. These functions are applicable to $100 < e^+ < 1000$.

With Table 2 and equations (5), (7), and (10), the friction factor, $\bar{f}$, can be predicted for given values of e/D and Re_D. Similarly, the ribbed wall Stanton number, St_r, can be predicted with Table 2 along with equations (5), (8), and (10), and the average Stanton number, $\overline{\mathrm{St}}$, with Table 2 along with equations (5), (9), and (10). The smooth wall Stanton number, St_s, can then be evaluated with the equation

$$\mathrm{St}_s = 2\overline{\mathrm{St}} - \mathrm{St}_r \tag{11}$$

Crossed Rib Arrays. In cases 7–9, the oblique ribs on the two ribbed walls are turned angles of 60, 45, and 30 deg, respectively, in opposite directions with respect to the main flow. The Stanton number, friction factor, and thermal performance results for these crossed oblique discrete rib cases

Table 3 Coefficients and exponents for the functions $R(e^+)$, $G(e^+, \text{Pr})$, and $\overline{G}(e^+, \text{Pr})$, crossed rib cases

	$R(e^+)=a(e^+)^b$		$G(e^+, \text{Pr})=a(e^+)^b$		$\overline{G}(e^+, \text{Pr})=a(e^+)^b$	
Case	a	b	a	b	a	b
7	0.994	0.213	7.026	0.158	10.404	0.140
8	2.311	0.137	4.548	0.216	6.755	0.190
9	1.595	0.210	3.981	0.237	6.326	0.214

are presented in Figs. 8–11. In each figure, corresponding results for case 2 (α = 90 deg) are included for comparison.

The Stanton numbers and the friction factors in the crossed oblique discrete rib cases are all lower than those in the 90 deg discrete rib case. Crossed oblique discrete ribs perform poorly compared with 90 deg discrete ribs (see Fig. 11) and are not recommended for the internal cooling of high-performance gas turbine blades.

Prior studies of transverse ribs (for example, Han et al., 1989, and Han and Zhang, 1991) have demonstrated that parallel oblique ribs on opposite walls enhance the heat (and mass) transfer to the cooling air more than crossed oblique ribs. The results of this investigation of discrete ribs again show that parallel oblique ribs outperform crossed oblique ribs considerably. The interaction of the main flow and secondary flow coming off the parallel ribs on two opposite walls result in counterrotating vortices in the two halves of the channel. On the other hand, in the crossed rib cases, secondary flow forces the flowing air near the two ribbed walls to rotate in the same direction. This may have caused the significant difference in the performances of corresponding parallel and crossed rib arrays.

The roughness function, $R(e^+)$, and the heat transfer roughness functions, $G(e^+, \text{Pr})$ and $\overline{G}(e^+, \text{Pr})$, for the crossed oblique rib cases are presented in Figs. 12 and 13. The values of the coefficient a and the exponent b in the functions $R(e^+)$, $G(e^+, \text{Pr})$, and $\overline{G}(e^+, \text{Pr})$ based on least-squares curve fit lines through the various sets of data are listed in Table 3. Again, these functions are applicable to $100 < e^+ < 1000$.

Concluding Remarks

Experiments study the turbulent heat transfer and friction for fully developed flow of air in a square channel with 90 deg transverse ribs, 90 deg discrete ribs, parallel and crossed oblique discrete ribs with α = 60, 45, and 30 deg, and parallel oblique discrete ribs with α = 45 and −45 deg on alternate rows. The discrete ribs are staggered on two opposite walls of the channel in alternate rows of three and two ribs. The ratios e/D and p/e are 0.0625 and 10, respectively. The Reynolds number ranges from 10,000 to 80,000. The following conclusions can be drawn:

1 The average Stanton number in the 90 deg discrete rib case is about 10 to 15 percent higher than that in the 90 deg transverse rib case.

2 Turning the discrete ribs on the two ribbed walls in the same direction with respect to the main flow (α = 30 to 60 deg) increases the average Stanton number 10 to 20 percent over that in the 90 deg discrete rib case.

3 The ribbed wall Stanton numbers in the parallel 60 and 45/−45 deg rib cases are generally higher than that in the parallel 45 deg rib case, which, in turn, is higher than that in the parallel 30 deg rib case.

4 Comparable overall thermal performances of parallel oblique discrete ribs with α = 60, 45, and 30 deg are about 20 percent higher than that of 90 deg discrete ribs.

5 The Stanton numbers and the friction factors in the crossed oblique discrete rib cases are all lower than those in the 90 deg discrete rib case. Crossed oblique discrete ribs have poor thermal performance and are not recommended for the internal cooling of gas turbine blades.

Acknowledgments

This research was supported in part by the National Science Foundation (Grant No. CBT-8713833).

References

Burggraf, F., 1970, "Experimental Heat Transfer and Pressure Drop With Two-Dimensional Turbulence Promotor Applied to Two Opposite Walls of a Square Tube," in: *Augmentation of Convective Heat and Mass Transfer*, A. E. Bergles and R. L. Webb, eds., ASME, New York, pp. 70–79.

Donne, D., and Meyer, L., 1977, "Turbulent Convective Heat Transfer From Rough Surfaces With Two-Dimensional Rectangular Ribs," *Int. J. Heat Mass Transfer*, Vol. 20, pp. 582–620.

Gee, D. L., and Webb, R. L., 1980, "Forced Convection Heat Transfer in Helically Rib-Roughened Tubes," *Int. J. Heat Mass Transfer*, Vol. 23, pp. 1127–1136.

Han, J. C., Glicksman, L. R., and Rohsenow, W. M., 1978, "An Investigation of Heat Transfer and Friction for Rib-Roughened Surfaces," *Int. J. Heat Mass Transfer*, Vol. 21, pp. 1143–1156.

Han, J. C., 1984, "Heat Transfer and Friction in Channels With Two Opposite Rib-Roughened Walls," ASME *Journal of Heat Transfer*, Vol. 106, pp. 774–781.

Han, J. C., Park, J. S., and Lei, C. K., 1985, "Heat Transfer Enhancement in Channels With Turbulence Promoters," ASME *Journal of Engineering for Gas Turbines and Power*, Vol. 107, pp. 629–635.

Han, J. C., 1988, "Heat Transfer and Friction Characteristics in Rectangular Channels With Rib Turbulators," ASME *Journal of Heat Transfer*, Vol. 110, pp. 321–328.

Han, J. C., and Park, J. S., 1988, "Developing Heat Transfer in Rectangular Channels With Rib Turbulators," *Int. J. Heat Mass Transfer*, Vol. 31, pp. 183–195.

Han, J. C., Ou, S., Park, J. S., and Lei, C. K., 1989, "Augmented Heat Transfer in Rectangular Channels With Narrow Aspect Ratios With Rib Turbulators," *Int. J. Heat Mass Transfer*, Vol. 32, pp. 1619–1630.

Han, J. C., and Zhang, P., 1991, "Effect of Rib-Angle Orientation on Local Mass Transfer Distribution in a Three-Pass Rib-Roughened Channel," ASME JOURNAL OF TURBOMACHINERY, Vol. 113, pp. 123–130.

Kline, S. J., and McClintock, F. A., 1953, "Describing Uncertainties in Single-Sample Experiments," *Mechanical Engineering*, Vol. 75, pp. 3–8.

Metzger, D. E., and Vedula, R. P., 1987a, "Heat Transfer in Triangular Channels With Angled Roughness Ribs on Two Walls," *Experimental Heat Transfer*, Vol. 1, pp. 31–44.

Metzger, D. E., Vedula, R. P., and Breen, D. D., 1987b, "Effect of Rib Angle and Length on Convection Heat Transfer in Rib-Roughened Triangular Ducts," *Proceedings of the 1987 ASME/JSME Thermal Engineering Joint Conference*, Honolulu, HI, Vol. 3, ASME, New York, pp. 327–333.

Meyer, L., 1982, "Thermohydraulic Characteristics of Single Rods With Three-Dimensional Roughness," *Int. J. Heat Mass Transfer*, Vol. 25, pp. 1043–1058.

Sethumadhavan, R., and Raja Rao, M., 1983, "Turbulent Flow Heat Transfer and Fluid Friction in Helical-Wire-Coil-Inserted Tubes," *Int. J. Heat Mass Transfer*, Vol. 26, pp. 1833–1844.

Webb, R. L., Eckert, E. R. G., and Goldstein, R., 1971, "Heat Transfer and Friction in Tubes With Repeated-Rib Roughness," *Int. J. Heat Mass Transfer*, Vol. 14, pp. 601–617.

White, L., and Wilkie, D., 1970, "The Heat Transfer and Pressure Loss Characteristics of Some Multi-start Ribbed Surfaces," in: *Augmentation of Convective Heat and Mass Transfer*, A. E. Bergles and R. L. Webb, eds., ASME, New York.

Wilkie, D., 1966, "Forced Convection Heat Transfer From Surfaces Roughened by Transverse Ribs," *Proceedings of the 2nd Int. Heat Transfer Conference*, Vol. 1, AIChE, New York.

Heat Transfer Characteristics of Turbulent Flow in a Square Channel With Angled Discrete Ribs

S. C. Lau

R. D. McMillin

J. C. Han

Turbine Heat Transfer Laboratory,
Department of Mechanical Engineering,
Texas A&M University,
College Station, TX 77843-3123

Experiments have been conducted to study the turbulent heat transfer and friction for fully developed flow of air in a square channel in which two opposite walls are roughened with 90 deg full ribs, parallel and crossed full ribs with angles of attack (α) of 60 and 45 deg, 90 deg discrete ribs, and parallel and crossed discrete ribs with $\alpha = 60$, 45, and 30 deg. The discrete ribs are staggered in alternate rows of three and two ribs. Results are obtained for a rib height-to-channel hydraulic diameter ratio of 0.0625, a rib pitch-to-height ratio of 10, and Reynolds numbers between 10,000 and 80,000. Parallel angled discrete ribs are superior to 90 deg discrete ribs and parallel angled full ribs, and are recommended for internal cooling passages in gas turbine airfoils. For $\alpha = 60$ and 45 deg, parallel discrete ribs have higher ribbed wall heat transfer, lower smooth wall heat transfer, and lower channel pressure drop than parallel full ribs. Parallel 60 deg discrete ribs have the highest ribbed wall heat transfer and parallel 30 deg discrete ribs cause the lowest pressure drop. The heat transfer and pressure drops in crossed angled full and discrete rib cases are all lower than those in the corresponding 90 deg and parallel angled rib cases. Crossed arrays of angled ribs have poor thermal performance and are not recommended.

Introduction

Rib turbulators on the surfaces of internal shaped flow passages in modern gas turbine blades enhance the heat transfer to the cooling air. Researchers have modeled these rib-roughened cooling passages as straight and/or multipass rectangular channels with two opposite ribbed walls and two smooth walls. Earlier work includes that of Burggraf (1970), who studied turbulent heat transfer and friction for flow in a square duct with 90 deg full rib arrays (ribs that stretch across the width of the channel with an angle of attack, α, of 90 deg) on two opposite walls and two smooth walls. Han (1984, 1988), Han et al. (1985, 1989), Han and Park (1988), and Han and Zhang (1989) studied the effects of varying the channel aspect ratio (0.25 to 4.0), the rib angle of attack ($\alpha = 30$, 45, 60, and 90 deg), the rib pitch-to-height ratio ($p/e = 10$ to 40), and rib height-to-channel hydraulic diameter ratio ($e/D = 0.021$ to 0.063) on the heat transfer in straight, square and rectangular channels with full ribs on two opposite walls and two smooth walls. For a square channel, although parallel 60 deg full ribs enhanced the channel heat transfer the most, they also caused the highest pressure drop. Parallel full ribs with $\alpha = 45$ and 30 deg had the best thermal performance, that is, the highest cooling rate for a given pumping power. For a rectangular channel, the increase in the ribbed wall heat transfer was higher with parallel angled full ribs on the narrower walls than with parallel angled full ribs on the wider walls, for a given pumping power. In general, parallel angled full ribs enhanced the ribbed wall heat transfer more than crossed angled full ribs.

Lau et al. (1989) conducted experiments to study the effects of replacing the aligned 90 deg full ribs on two opposite walls of a square channel with discrete ribs (five equal segments of the 90 deg full ribs staggered in alternate rows of three and two ribs, aligned rows on the opposite walls) on the turbulent heat transfer and friction for fully developed flow of air in the square channel. The rib configurations examined were: full ribs with $\alpha = 90$ deg, discrete ribs with $\alpha = 90$ deg, parallel and crossed arrays of discrete ribs (ribs on opposite walls were turned in the same direction and in opposite directions with respect to the main flow, respectively) with $\alpha = 60$, 45, and 30 deg, and parallel arrays of discrete ribs with $\alpha = 45$ and -45 deg on alternate rows. The rib height-to-hydraulic diameter ratio and the rib pitch-to-height ratio were 0.0625 and 10, respectively. The Reynolds number ranged from 10,000 to 80,000. Results showed that the average Stanton number in the 90 deg discrete rib case was about 10 to 15 percent higher than that in the 90 deg full rib case. Turning the discrete ribs on the opposite walls 60, 45, or 30 deg in the same direction with respect to the main flow increased the average Stanton number 10 to 20 percent over that in the 90 deg discrete rib case. Parallel angled discrete ribs with $\alpha = 60$, 45, and 30 deg had comparable performances and had higher overall heat transfer per unit pumping power than 90 deg discrete ribs. Crossed arrays of angled discrete ribs performed poorly compared with 90 deg discrete ribs and were not recommended.

In Lau et al. (1989), the angled discrete ribs were equal-length segments of the 90 deg full ribs (that is, the lengths of

Contributed by the International Gas Turbine Institute and presented at the 35th International Gas Turbine and Aeroengine Congress and Exposition, Brussels, Belgium June 11–14, 1990. Manuscript received by the International Gas Turbine Institute January 15, 1990. Paper No. 90-GT-254.

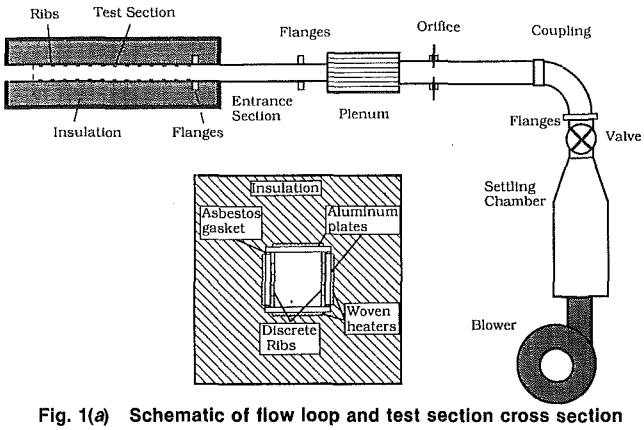

Fig. 1(*a*) Schematic of flow loop and test section cross section

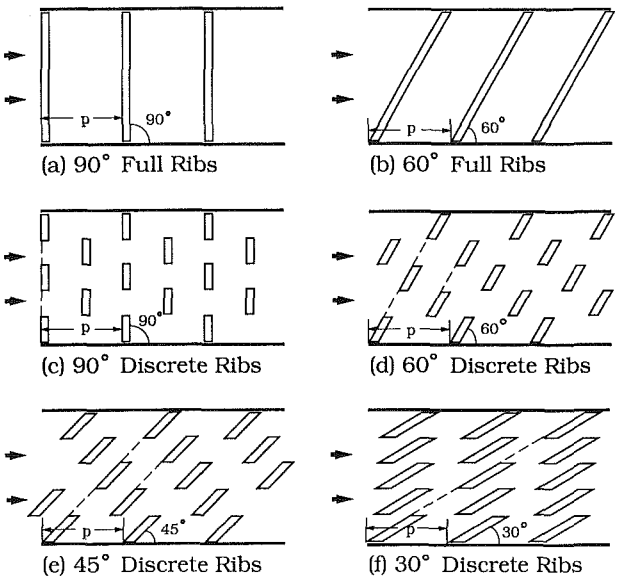

Fig. 1(*b*) Typical rib configurations

the angled discrete ribs and the 90 deg discrete ribs were the same). They were arranged in the same arrays as the 90 deg discrete rib arrays but were turned various angles equal to the angles of attack with respect to the main flow. The thermal performances of the angled discrete ribs were compared to those of the 90 deg full ribs and 90 deg discrete ribs only.

The objectives of this investigation are to study the turbulent heat transfer and friction for fully developed flow in a square channel with angled discrete ribs on two opposite walls and to compare the thermal performances of corresponding angled full ribs and angled discrete ribs. The study examines the effects on the channel heat transfer and friction of cutting the angled full ribs in prior investigations into five equal segments and staggering them in alternate rows of three and two ribs.

This study differs from that of Lau et al. (1989) in that:

1 The heat transfer and friction characteristics, and thermal performances of corresponding angled discrete ribs and angled full ribs, are compared.

2 The angled discrete ribs in this study are equal-length segments of the corresponding angled full ribs (that is, the total length of the five angled discrete ribs over each pitch is equal to the length of a corresponding angled full rib) and the ribs in each row are collinear (along an oblique line at an angle equal to the angle of attack with respect to the main flow).

3 This study compares the thermal performances of corresponding parallel and crossed angled full ribs in addition to those of corresponding parallel and crossed angled discrete ribs.

Airflow over a staggered array of angled discrete ribs on a wall separates not only at the top edges of the ribs but also at the edges at the ends of the ribs. The secondary flow near the wall resulting from flow separation at the ends of the ribs interrupts the growth of the boundary layers downstream of the nearby reattachment zones. This secondary flow around the ends of the ribs interacts with the secondary flow caused by the orientation of the ribs, and with the separation from the top edges of the ribs and the reattachment on the wall of the main flow. As a result of the vigorous mixing of the flowing

Nomenclature

a = coefficient in roughness functions
b = exponent in roughness functions
c_p = specific heat of air at average bulk temperature, J/(kg·K)
D = hydraulic diameter of square channel, m
dP/dx = streamwise pressure gradient in fully developed region in channel, $(N/m^2)/m$
e = height of ribs, m
e^+ = roughness Reynolds number, equation (8)
$\bar{f}$ = friction factor for square channel with two opposite ribbed walls and two smooth walls, equation (3)
f_{ss} = friction factor for square channel with four smooth walls
$G(e^+, \mathrm{Pr})$ = heat transfer roughness function, equation (6)
$\bar{G}(e^+, \mathrm{Pr})$ = average heat transfer roughness function, equation (7)
$\dot{m}$ = rate of mass flow of air, kg/s
p = rib pitch, m
P = local static pressure, N/m^2
$\dot{q}_r''$ = net heat flux on ribbed walls, W/m^2
$\dot{q}_s''$ = net heat flux on smooth walls, W/m^2
$R(e^+)$ = roughness function, equation (5)
Re_D = Reynolds number based on channel hydraulic diameter, equation (4)
$\overline{\mathrm{St}}$ = average Stanton number, the average of St_r and St_s
St_r = Stanton number for ribbed walls in square channel with two opposite ribbed walls and two smooth walls, equation (1)
St_s = Stanton number for smooth walls in square channel with two opposite ribbed walls and two smooth walls, equation (2)
St_{ss} = Stanton number for square channel with four smooth walls
$\overline{(T_{wr} - T_b)}$ = ribbed wall/bulk temperature difference in fully developed region in channel, K
$\overline{(T_{ws} - T_b)}$ = smooth wall/bulk temperature difference in fully developed region in channel, K
$\bar{u}$ = average air velocity, m/s
x = streamwise coordinate, m
α = rib angle of attack, deg
μ = dynamic viscosity of air at average bulk temperature, $N \cdot s/m^2$
ρ = density of air at average bulk temperature, kg/m^3
τ_w = wall shear stress, N/m^2

Table 1 Configurations of ribs on channel walls

Case	Rib Length[#] (cm)	Rib Configuration, Arrays on Opp. Walls	Rib Angle-Of-Attack
1*	7.62	full	90°
2a	8.80	full, parallel	60°
2b	8.80	full, crossed	60°
3a	10.78	full, parallel	45°
3b	10.78	full, crossed	45°
4*	1.52	discrete	90°
5a	1.76	discrete, parallel	60°
5b	1.76	discrete, crossed	60°
6a	2.16	discrete, parallel	45°
6b	2.16	discrete, crossed	45°
7a	3.05	discrete, parallel	30°
7b	3.05	discrete, crossed	30°

[#] Length of ribs are measured along the rib centerlines
* These results were reported in Lau et al. (1989)

air near the wall and the slight increase in the rib surface area, angled discrete ribs are believed to enhance the heat transfer to the airstream more than angled full ribs.

Experimental Apparatus

The test apparatus (see Fig. 1*a*) is an open air flow loop that consists of a centrifugal blower, a settling chamber, a flow diverter (to control the air flow rate), a calibrated orifice flow meter, a flow straightener, an entrance section, and the test section. The aluminum test section is a straight, 1.52-m-long channel with a square cross section of 7.62 cm by 7.62 cm. The four walls of the channel are heated individually with electric heaters. The heaters on opposite walls are connected in parallel electrically. A 1.59-mm-thick asbestos gasket minimizes the heat transfer between adjacent walls.

Full ribs or discrete ribs, which are cut from 4.76 mm by 4.76 mm square brass bars, are attached to the interior surfaces of two opposite channel walls with silicone rubber adhesive. Therefore, the rib height-to-channel hydraulic diameter ratio, e/D, in this study is 0.0625. The interior surfaces of the other two opposite walls are smooth.

Twelve rib configurations are studied: 90 deg full ribs, parallel and crossed arrays of full ribs with $\alpha = 60$ and 45 deg, 90 deg discrete ribs, and parallel and crossed arrays of discrete ribs with $\alpha = 60$, 45, and 30 deg. In all twelve cases, the rib pitch-to-height ratio, p/e, is 10; rows on opposite walls are aligned; and the first rows on both walls are at the channel entrance ($x = 0$). Discrete ribs are staggered on the walls, in alternate rows of three and two ribs (see Fig. 1*b*). Table 1 gives the lengths and orientations of the ribs in the twelve cases. In cases 2*a*, 3*a*, 5*a*, 6*a*, and 7*a*, the angled rib arrays on the two opposite walls are parallel (parallel arrays). In cases 2*b*, 3*b*, 5*b*, 6*b*, and 7*b*, the angled rib arrays on the two opposite walls are oriented in opposite directions with respect to the main flow (crossed arrays).

Up to 320 ribs are needed in each of the discrete rib cases studied. All of the ribs in each full or discrete rib case are cut individually to precisely the same length (nominal length ± 0.025 mm) with a slitting saw on a milling machine. The angled ribs are cut at an angle equal to the angle of attack such that, after the ribs are installed, the end surfaces of the ribs are parallel to the two walls with no ribs. To attach a rib onto a channel wall, a template is used to position the rib accurately. Pressure is applied on the top surface of the rib to squeeze out as much silicone rubber adhesive as possible from under the rib to ensure good metal-to-metal contact between the rib and the channel wall. The thickness of the thin silicone layer is less than 0.01 cm. The thermal resistance between the rib and the channel wall is estimated to be negligible. It takes approximately ten hours to attach all 320 discrete ribs onto the two opposite walls of the test channel.

A 1.52-m-long acrylic entrance channel provides hydrodynamically fully developed flow at the test section entrance. The test section and the downstream half of the entrance section are heavily insulated with layers of fiberglass felt.

To determine the streamwise wall temperature distributions, 42 30-gage copper-constantan thermocouples are installed along the axial centerlines of one of the ribbed walls and each of the smooth walls (at 0.25, 3.25, 6.25, 9.25, 12.25, 15.25, 16.25, 16.75, 17.25, 18.25, 21.25, 24.25, 27.25, and 30.25 times the rib pitch from the channel entrance). Six other thermocouples are installed along two off-center lines at $x/p = 16.25$, 16.75, and 17.25 on two adjacent walls to check the spanwise variations of the wall temperatures. Each of these axial lines is halfway between the centerline and an adjacent edge of a smooth wall or a ribbed wall. Results show that the variations between the temperatures at these stations along the off-center axial lines and those at corresponding adjacent stations along the axial centerlines are always smaller than the estimated uncertainty of the thermocouple readings (0.28°C). This means that the temperature of the centerline point can represent the spanwise-averaged temperature because of the high thermal conductivity of the aluminum wall.

Each thermocouple is installed in a small hole drilled on the channel wall. The junction of the thermocouple is affixed to the bottom of the hole with silver-based paint and fast-drying epoxy. An ohmmeter checks to ensure good physical contact between the thermocouple and the channel wall. Two additional thermocouples measure the inlet air temperature and four thermocouples the exit air temperature. An Omega 410B digital temperature indicator with a 0.1°C resolution reads the thermocouple output.

Three pressure taps are installed along the axial centerline of one of the smooth walls at 0.46 m, 0.91 m, and 1.37 m, respectively, from the test section entrance to determine the streamwise pressure drop. A micromanometer measures the pressures at these taps. Other U-tube and inclined manometers measure the pressure drop across the orifice and the gage pressure upstream of the orifice.

Two variable transformers control the power input to the four heaters. A Hewlett Packard 3478A multimeter and a Keithley 175 autoranging multimeter measure the voltage drop across each heater and the current through each heater, respectively.

Experimental Procedure

After the ribs are installed and the test section is assembled and checked for air leakage, the blower is switched on to let a predetermined rate of air flow through the flow loop. The test section is then heated to maintain the wall temperatures near the exit at 15°C above the exit air temperature. More power is supplied to the two ribbed wall heaters than to the two smooth wall heaters so that, at any axial location, the wall temperatures on the two ribbed walls and the two smooth walls are about the same.

After steady state is attained in about two hours, all temperatures and pressures are recorded. The maximum variations of some of the readings are also recorded for the uncertainty analysis of the results. The barometric pressure is read at the beginning and the end of a test run.

In separate no-flow experiments, the rate of heat loss through the fiberglass insulation during a test run is determined. By varying the rate of heat input to the heaters and measuring the corresponding average steady-state wall temperature, a

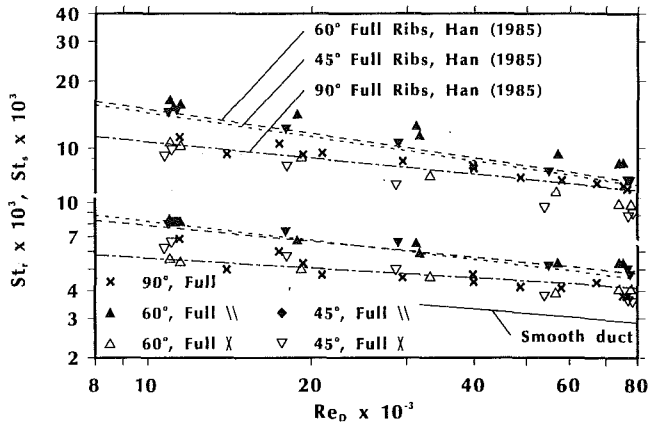

Fig. 2 Ribbed wall and smooth wall Stanton numbers as functions of Reynolds number, full rib cases

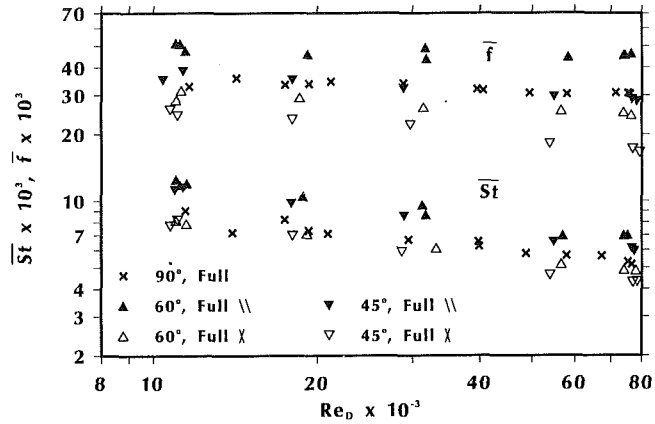

Fig. 3 Average Stanton number and friction factor as functions of Reynolds number, full rib cases

correlation between the rate of heat input, which is also the rate of heat loss through the fiberglass insulation, and the average wall temperature is obtained. The correlation estimates the rates of heat loss through the insulation at the various wall temperature measurement stations during a test run. For low Reynolds number runs, the total heat loss through the insulation can be up to 7 percent of the total heat input.

Data Reduction

The results of the ribbed wall and smooth wall heat transfer are expressed in dimensionless form as Stanton numbers for the ribbed walls and the smooth walls. They are calculated, respectively, from

$$\mathrm{St}_r = \dot{q}_r'' D^2/[\dot{m}c_p(\overline{T_{wr}} - \overline{T_b})] \quad (1)$$

and

$$\mathrm{St}_s = \dot{q}_s'' D^2/[\dot{m}c_p(\overline{T_{ws}} - \overline{T_b})] \quad (2)$$

In each of the above equations, the rate of net heat input is the measured power input to each heater minus the rate of heat loss through the insulation taking into account the rate of streamwise heat conduction in the channel walls. The heat flux is the rate of net heat input divided by the projected heat transfer area (not including the increased rib surface area). The net heat flux and the average wall/bulk temperature difference are determined over a section of the test channel far downstream of the entrance, where the streamwise wall temperature distribution is linear. The distribution of the bulk temperature is evaluated from energy balance with the rate of net heat transfer from all four walls to the air and the inlet bulk temperature. Since results show that there is no significant difference between the temperature distributions on the two smooth walls even in the parallel angled rib array cases, the smooth wall Stanton number is presented as the average of the Stanton numbers for the two smooth walls. The average Stanton number, $\overline{\mathrm{St}}$, is the average of the Stanton numbers for the ribbed walls and the smooth walls.

The friction factor and the Reynolds number are defined respectively as

$$\bar{f} = \tau_w/[(1/2)\rho\bar{u}^2] = [(-dP/dx)D/4]/[(1/2)\rho\bar{u}^2]$$
$$= (-dP/dx)D^5/[2(\dot{m}^2/\rho)] \quad (3)$$

$$\mathrm{Re}_D = \rho\bar{u}D/\mu = \dot{m}/(D\mu) \quad (4)$$

All properties of the flowing air in equations (1)–(4) are evaluated at the average bulk temperature.

The maximum uncertainties of the values of the Reynolds number and the Stanton numbers are estimated to be ±2.9 percent and ±5.8 percent, respectively (Kline and McClintock, 1953). The maximum uncertainty of the values of the friction factor is ±10.9 percent for Reynolds numbers of about 10,000 and ±6.5 percent for Reynolds numbers above 20,000. The large uncertainties of $\bar{f}$ at low Reynolds numbers are the results of the small pressure drops in the test section in the low flow rate cases.

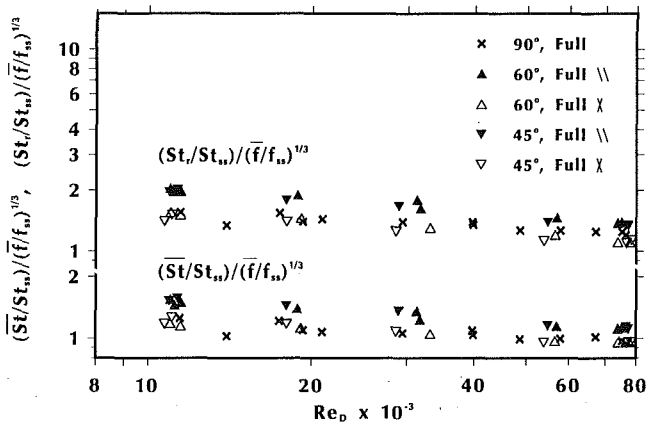

Fig. 4 Thermal performances of full ribs, $[(\mathrm{St}_r/\mathrm{St}_{ss})/(\bar{f}/f_{ss})^{1/3}]$ and $[(\overline{\mathrm{St}}/\mathrm{St}_{ss})/(\bar{f}/f_{ss})^{1/3}]$ as functions of Reynolds number

The friction factor and the Stanton numbers are compared to their corresponding values for fully developed turbulent flow through a square channel with four smooth walls, f_{ss} and St_{ss}, which are calculated with the modified Karman–Prandtl and Dittus–Boelter equations (Han, 1984), repectively.

To correlate the data, the roughness function, $R(e^+)$, the heat transfer roughness function, $G(e^+, \mathrm{Pr})$, and the average heat transfer roughness friction, $\bar{G}(e^+, \mathrm{Pr})$, are determined with the following equations (Han, 1988):

$$R(e^+) = [(2\bar{f} - f_{ss})/2]^{-0.5} + 2.5 \ln [2(e/D)] + 2.5 \quad (5)$$

$$G(e^+, \mathrm{Pr}) = [(2\bar{f} - f_{ss})/2]^{0.5}/\mathrm{St}_r + 2.5 \ln [2(e/D)] + 2.5 \quad (6)$$

$$\bar{G}(e^+, \mathrm{Pr}) = [(2\bar{f} - f_{ss})/2]^{0.5}/\overline{\mathrm{St}} + 2.5 \ln [2(e/D)] + 2.5 \quad (7)$$

In the above equations, e^+ is the roughness Reynolds number, which is defined as

$$e^+ = (e/D)\mathrm{Re}_D[(2\bar{f} - f_{ss})/2]^{0.5} \quad (8)$$

The roughness functions are correlations for the prediction of the friction factor and Stanton numbers.

Presentation of Results

This investigation examines how the heat transfer and friction for airflow in a square channel are affected when angled

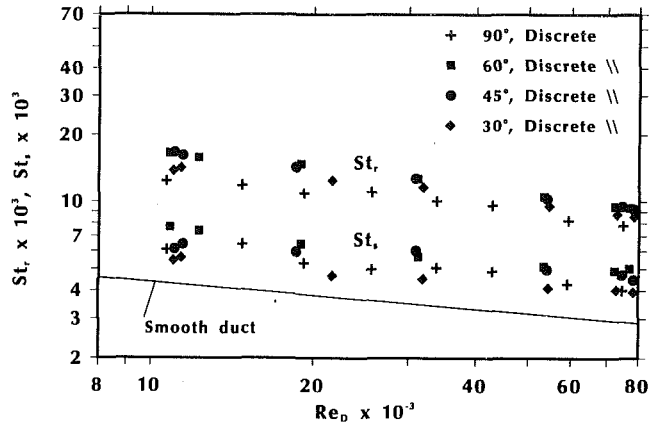

Fig. 5 Ribbed wall and smooth wall Stanton numbers as functions of Reynolds number, parallel discrete rib cases

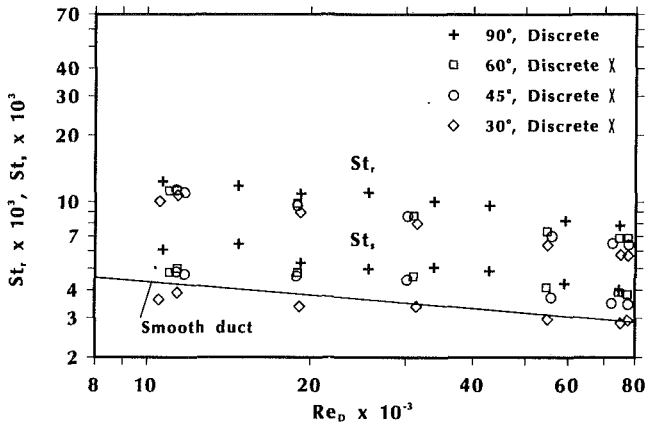

Fig. 8 Ribbed wall and smooth wall Stanton numbers as functions of Reynolds number, crossed discrete rib cases

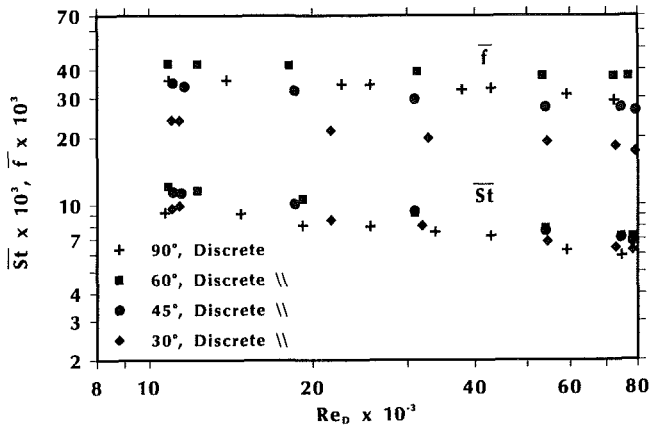

Fig. 6 Average Stanton number and friction factor as functions of Reynolds number, parallel discrete rib cases

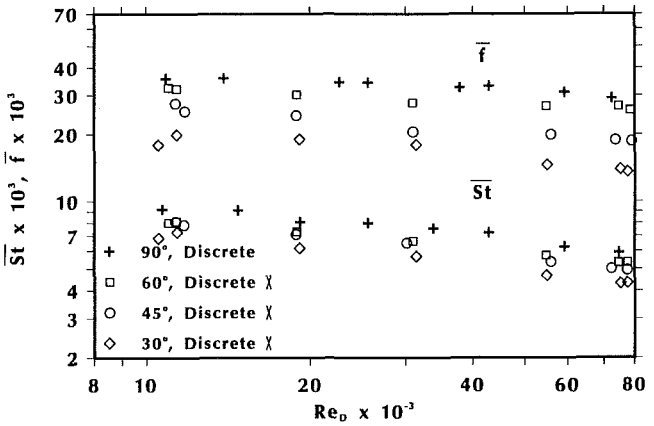

Fig. 9 Average Stanton number and friction factor as functions of Reynolds number, crossed discrete rib cases

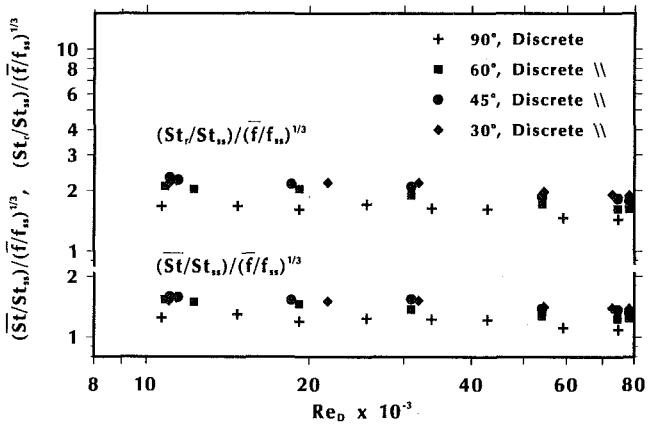

Fig. 7 Thermal performances of parallel discrete ribs, $[(St_r/St_{ss})/(\bar{f}/f_{ss})^{1/3}]$ and $[(\overline{St}/St_{ss})/(\bar{f}/f_{ss})_{1/3}]$ as functions of Reynolds number

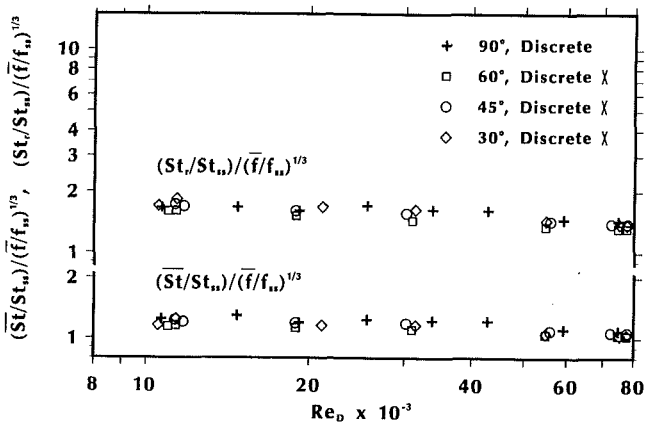

Fig. 10 Thermal performances of crossed discrete ribs, $[(St_r/St_{ss})/(\bar{f}/f_{ss})^{1/3}]$ and $[(\overline{St}/St_{ss})/(\bar{f}/f_{ss})^{1/3}]$ as functions of Reynolds number

full ribs on two opposite walls of the channel are replaced by angled discrete ribs. Heat transfer, friction, and thermal performance results for the full rib cases are presented first. They are followed by the results for the parallel and crossed discrete rib cases. Lastly, the heat transfer, friction, and thermal performances in corresponding angled full and discrete rib cases are compared and the roughness functions, $R(e^+)$, $G(e^+, \mathrm{Pr})$, and $\overline{G}(e^+, \mathrm{Pr})$, are presented.

Full Rib Arrays. Figures 2–4 show the ribbed wall and smooth wall Stanton numbers, the average Stanton number, and the friction factor, and the ratios $[(St_r/St_{ss})/(\bar{f}/f_{ss})^{1/3}]$ and $[(\overline{St}/St_{ss})/(\bar{f}/f_{ss})^{1/3}]$ as functions of the Reynolds number in the full rib cases (cases 1, 2*a*, 2*b*, 3*a*, and 3*b*, with darkened symbols for the parallel rib cases and open symbols for the crossed rib cases), respectively. Clearly, parallel 60 deg full ribs enhance the ribbed wall heat transfer more than parallel 45 deg full ribs, which, in turn, cause higher heat transfer on the ribbed walls than 90 deg full ribs. The smooth wall Stanton numbers in the parallel 60 and 45 deg full rib cases are com-

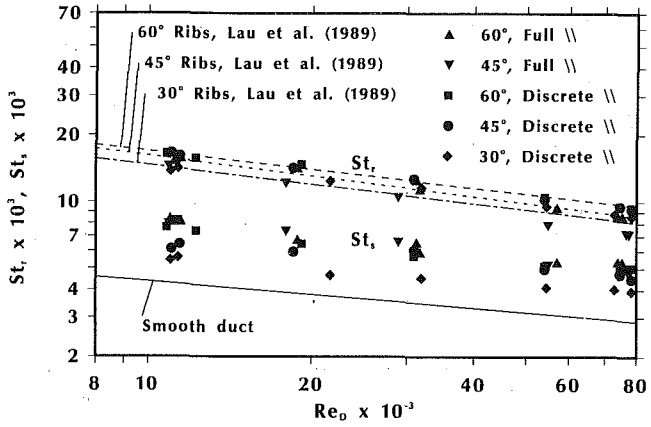

Fig. 11 Comparisons of ribbed wall and smooth wall Stanton numbers in parallel angled rib cases

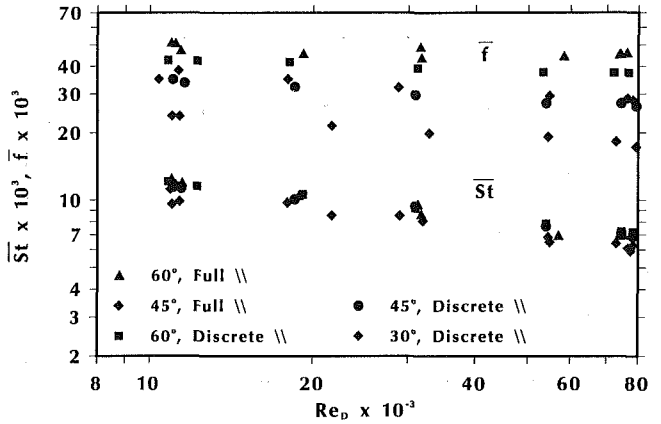

Fig. 12 Comparisons of average Stanton numbers and friction/factors in parallel angled rib cases

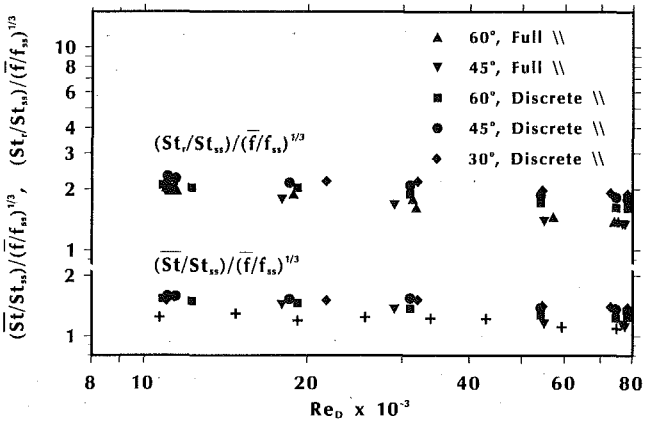

Fig. 13 Comparison of thermal performances of parallel angled ribs

parable and are considerably higher than that in the 90 deg full rib case.

Parallel 60 deg full ribs have higher overall heat transfer and pressure drop than parallel 45 deg full ribs and 90 deg full ribs. While the average Stanton number in the parallel 45 deg full rib case is much higher than that in the 90 deg full rib case, the friction factors in the two cases are comparable: $\bar{f}$ in case 3*a* is slightly higher than that in case 1 at low Reynolds numbers and slightly lower than that in case 1 at high Reynolds numbers. The thermal performances of parallel 60 and 45 deg full ribs are superior to that of 90 deg full ribs. Han et al. (1985) and Han and Park (1988) reported similar findings.

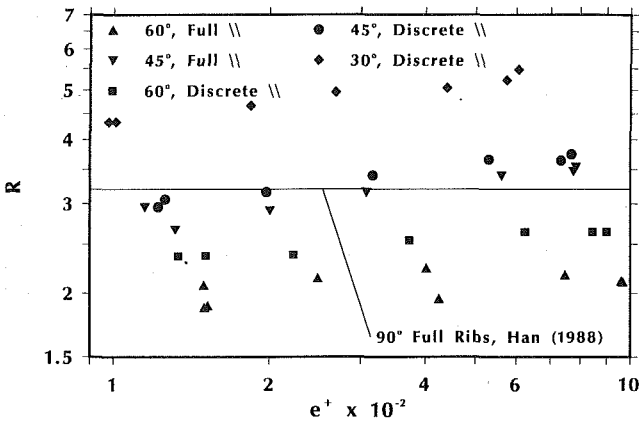

Fig. 14 $R(e^+)$ as a function of e^+, parallel angled rib cases

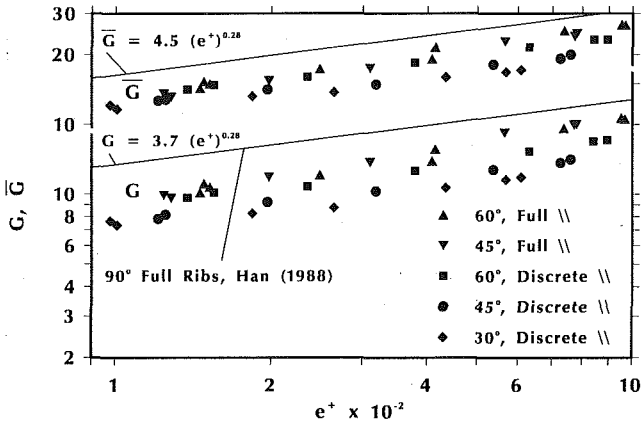

Fig. 15 $G(\mathrm{Pr}, e^+)$ and $\bar{G}(\mathrm{Pr}, e^+)$ as functions of e^+, parallel angled rib cases

The present 90 deg and parallel full rib results are compared to corresponding results from Han et al. (1985) in Fig. 2. The variations between the 90 deg and parallel 45 deg full rib results in the two studies are within the estimated experimental uncertainties. However, the ribbed wall Stanton number in the present parallel 60 deg full rib case is about 15 percent higher than that reported by Han et al. (1985). In this study, all test runs in the parallel 60 deg full rib case are repeated and the two new sets of data are consistent with each other.

Crossed 60 and 45 deg full ribs cause lower heat transfer on the ribbed walls, lower overall heat transfer, and lower pressure drop than 90 deg full ribs. Their thermal performances are only comparable to that of 90 deg full ribs.

Parallel Discrete Rib Arrays. Parallel angled discrete rib results and 90 deg discrete rib results are compared in Figs. 5, 6, and 7. Parallel 60 and 45 deg discrete ribs have higher ribbed wall heat transfer and overall heat transfer than parallel 30 deg discrete ribs, which, in turn, have higher ribbed wall heat transfer and overall heat transfer than 90 deg discrete ribs. The ribbed wall Stanton numbers in the parallel 60 and 45 deg discrete rib cases are about 32 and 18 percent higher than those in the 90 deg discrete rib case at $\mathrm{Re}_D = 10{,}000$ and 80,000, respectively. Parallel 60 deg discrete ribs cause the highest pressure drop while parallel 30 deg discrete ribs cause the lowest pressure drop. As a result, parallel 45 and 30 deg discrete ribs outperform parallel 60 deg discrete ribs in enhancing the heat transfer to the cooling air per unit pumping power.

Crossed Discrete Rib Arrays. Figures 8, 9, and 10 show that the ribbed wall Stanton numbers, the smooth wall Stanton

Table 2 Coefficients and exponents for the functions $R(e^+)$, $G(e^+, \mathrm{Pr})$, and $\overline{G}(e^+, \mathrm{Pr})$

Case	$R(e^+)=a(e^+)^b$		$G(e^+,\mathrm{Pr})=a(e^+)^b$		$\overline{G}(e^+,\mathrm{Pr})=a(e^+)^b$	
	a	b	a	b	a	b
1	2.269	0.055	3.728	0.267	5.447	0.250
2a	1.641	0.038	1.488	0.387	2.855	0.328
2b	2.395	0.078	2.514	0.340	5.096	0.260
3a	1.556	0.122	1.428	0.398	2.627	0.335
3b	1.854	0.172	3.181	0.303	4.348	0.280
4	1.848	0.086	3.884	0.229	5.894	0.214
5a	1.710	0.065	2.074	0.309	3.802	0.267
5b	2.114	0.089	3.473	0.265	6.902	0.202
6a	1.698	0.119	1.797	0.309	3.981	0.239
6b	1.913	0.154	3.049	0.269	6.080	0.207
7a	2.557	0.115	2.288	0.252	4.642	0.202
7b	3.044	0.121	2.330	0.305	5.429	0.223

numbers, the average Stanton numbers, and the friction factors in the crossed angled discrete rib cases are all lower than those in the 90 deg discrete rib cases. The thermal performances of crossed angled discrete ribs are not as good as that of 90 deg discrete ribs.

Based on the values of the ratios $[(St_r/St_{ss})/(\overline{f}/f_{ss})^{1/3}]$ and $[(\overline{St}/St_{ss})/(\overline{f}/f_{ss})^{1/3}]$ in the various parallel and crossed angled rib cases studied, parallel angled ribs (including both full and discrete ribs) perform consistently better than corresponding crossed angled ribs. Metzger and Vendula (1987), Han and Zhang (1989), Han et al. (1989), and Lau et al. (1989) all drew similar conclusions. The good thermal performances in the parallel angled rib cases may have been the results of the mixing of the main flow with the counterrotating vortices in the two opposite halves of the channel caused by secondary flow near the parallel rib arrays on the two opposite walls.

Comparisons of Full and Discrete Rib Arrays. In Figs. 11, 12, and 13, the ribbed wall heat transfer, the smooth wall heat transfer, the overall heat transfer, the overall pressure drops, and the thermal performances in the parallel angled discrete rib cases are compared to their counterparts in corresponding parallel angled full rib cases. The ribbed wall heat transfer in the parallel 60 and 45 deg discrete rib cases is about 5 to 11 percent higher than that in the parallel 60 deg full rib case and is about 14 to 31 percent higher than that in the 45 deg full rib case, over the range of Reynolds number studied (see Fig. 11). The smooth wall heat transfer in the parallel angled discrete rib cases, however, is lower than in the parallel angled full rib cases.

Included in Fig. 11 for comparison are the parallel 60, 45, and 30 deg discrete rib results from Lau et al. (1989). The ribbed wall Stanton numbers in the parallel angled discrete rib cases in this study are always as high as or slightly higher than those in corresponding discrete rib cases in the earlier study.

Figure 12 shows that 60 and 45 deg discrete ribs enhance the overall heat transfer to the cooling air slightly more than 60 and 45 deg full ribs and cause lower pressure drops than 60 and 45 deg full ribs. As a result, the values of $[(St_r/St_{ss})/(\overline{f}/f_{ss})^{1/3}]$ and $[(\overline{St}/St_{ss})/(\overline{f}/f_{ss})^{1/3}]$ in the 60 and 45 deg discrete rib cases are always higher than those in the 60 and 45 deg full rib cases (see Fig. 13). For a given pumping power, 60 deg discrete ribs enhance the ribbed wall heat transfer about 5 to 19 percent more than 60 deg full ribs, and 45 deg discrete ribs enhance the ribbed wall heat transfer about 11 to 32 percent more than 45 deg full ribs, over the range of Reynolds number studied. Because of the much lower values of $\overline{f}$, the values of $[(St_r/St_{ss})/(\overline{f}/f_{ss})^{1/3}]$ and $[(\overline{St}/St_{ss})/(\overline{f}/f_{ss})^{1/3}]$ in the 30 deg angled discrete rib case are as high as or higher than those in the 45 deg angled discrete case.

Parallel angled discrete ribs are superior to parallel angled full ribs and are recommended for internal cooling passages in gas turbine airfoils. Parallel 30 deg discrete ribs have the highest thermal performance but their performance is only slightly better than that of parallel 45 deg discrete ribs. Han et al. (1985) and Han and Park (1988) observed the same trend for angled full ribs.

The roughness functions, $R(e^+)$, $G(e^+, \mathrm{Pr})$, and $\overline{G}(e^+, \mathrm{Pr})$, are expressed as power functions of the roughness Reynolds number, e^+. Figures 14 and 15 present the roughness functions in the various parallel angled rib cases. Parallel angled discrete ribs have lower values of $G(e^+, \mathrm{Pr})$ and $\overline{G}(e^+, \mathrm{Pr})$ than parallel angled full ribs since parallel angled discrete ribs cause higher heat transfer and lower pressure drop than corresponding full ribs.

Table 2 gives the coefficients and exponents in these functions for all cases studied. With Table 2 and equations (5)–(8), the Stanton numbers and friction factor can be predicted for given values of α, e/D, and Re_D.

With Table 2 and the roughness function correlations given by Lau et al. (1989), the values of $G(e^+, \mathrm{Pr})$ and $\overline{G}(e^+, \mathrm{Pr})$ in the parallel 45 and 30 deg discrete rib cases in this study (with oblique arrays of segments of the 45 and 30 deg full ribs) are found to be consistently lower (up to 20 percent lower) than those in the parallel 45 deg and 30 deg discrete rib cases of Lau et al. (1989) (with arrays of segments of the 90 deg full ribs turned 45 and 30 deg with respect to the main flow), for $100 < e^+ < 1000$. The corresponding values of $G(e^+, \mathrm{Pr})$ and $\overline{G}(e^+, \mathrm{Pr})$ in the two parallel 60 deg discrete rib cases in the two studies, however, are within ± 5 percent of each other. Thus, the parallel 45 and 30 deg discrete rib arrays in this study have higher thermal performances than the parallel 45 and 30 deg discrete rib arrays of Lau et al. (1989).

Concluding Remarks

Based on the results of this investigation, the following conclusions can be drawn:

1 Parallel angled discrete ribs are superior to parallel angled full ribs and are recommended for internal cooling passages in gas turbine airfoils. For a given pumping power, 60 and 45 deg discrete ribs enchance the ribbed wall heat transfer about 5 to 19 percent and about 11 to 32 percent more than the corresponding angled full ribs, over the range of Reynolds number studied. Parallel 30 deg discrete ribs have the highest thermal performance but their performance is only slightly better than that of parallel 45 deg discrete ribs.

2 For $\alpha = 60$ and 45 deg, parallel discrete ribs have higher ribbed wall heat transfer, lower smooth wall heat transfer, and lower channel pressure drop than parallel full ribs. The ribbed wall heat transfer in the parallel 60 and 45 deg discrete rib cases is about 5 to 11 percent higher than that in the parallel 60 deg full rib case and is about 14 to 31 percent higher than that in the 45 deg full rib case, over the range of Reynolds number studied.

3 Parallel 60 deg discrete ribs have the highest ribbed wall heat transfer and parallel 30 deg discrete ribs cause the lowest pressure drop.

4 The parallel 45 and 30 deg discrete ribs in this study have higher thermal performances than the parallel 45 and 30 deg discrete ribs of Lau et al. (1989).

5 The Stanton numbers and the friction factors in the crossed angled full and discrete rib cases are all lower than those in the corresponding 90 deg and parallel angled rib cases. Crossed angled ribs have poor thermal performance and are not recommended.

Acknowledgments

This research was supported in part by the National Science Foundation (Grant No. CBT-8713833).

References

Burggraf, F., 1970, "Experimental Heat Transfer and Pressure Drop With Two-Dimensional Turbulence Promoter Applied to Two Opposite Walls of a Square Tube," in: *Augmentation of Convective Heat and Mass Transfer*, A. E. Bergles and R. L. Webb, eds., ASME, New York, pp. 70–79.

Han, J. C., 1984, "Heat Transfer and Friction in Channels With Two Opposite Rib-Roughened Walls," ASME *Journal of Heat Transfer*, Vol. 106, pp. 774–781.

Han, J. C., 1988, "Heat Transfer and Friction Characteristics in Rectangular Channels With Rib Turbulators," ASME *Journal of Heat Transfer*, Vol. 110, pp 321–328.

Han, J. C., Ou, S., Park, J. S., and Lei, C. K., 1989, "Augmented Heat Transfer in Rectangular Channels With Narrow Aspect Ratios With Rib Turbulators," *Int. J. Heat Mass Transfer*, Vol. 32, pp. 1619–1630.

Han, J. C., and Park, J. S., 1988, "Developing Heat Transfer in Rectangular Channels With Rib Turbulators," *Int. J. Heat Mass Transfer*, Vol. 31, pp. 183–195.

Han, J. C., Park, J. S., and Lei, C. K., 1985, "Heat Transfer Enhancement in Channels With Turbulence Promoters," ASME *Journal of Engineering for Gas Turbines and Power*, Vol. 107, pp. 629–635.

Han, J. C., and Zhang, P., 1989, "Effect of Rib-Angle Orientation on Local Mass Transfer Distribution in a Three-Pass Rib-Roughened Channel," ASME Paper No. 89-GT-98.

Kline, S. J., and McClintock, F. A., 1953, "Describing Uncertainties in Single-Sample Experiments," *Mechanical Engineering*, Vol. 75, pp. 3–8.

Lau, S. C., McMillin, R. D., and Han, J. C., 1989, "Turbulent Heat Transfer and Friction in a Square Channel With Discrete Rib Turbulators," presented at the ASME Winter Annual Meeting, San Franscisco, CA; ASME JOURNAL OF TURBOMACHINERY, Vol. 113, 1991, this issue, pp. 360–366.

Metzger, D. E., and Vendula, R. P., 1987, "Heat Transfer in Triangular Channels With Angled Roughness Ribs on Two Walls," *Experimental Heat Transfer*, Vol. 1, pp. 31–44.

A. Yamamoto
Head of Turbine Laboratory,
National Aerospace Laboratory,
Chofu, Tokyo, Japan

Y. Kondo[1]
Student,
Aoyama University,
Setagaya, Tokyo, Japan

R. Murao
Professor,
Department of Mechanical Engineering,
Aoyama University,
Setagaya, Tokyo, Japan

Cooling-Air Injection Into Secondary Flow and Loss Fields Within a Linear Turbine Cascade

In order to understand overall performance and internal flows of air-cooled turbine blade rows, flows in a model linear cascade were surveyed with secondary air injection from various locations of the blade surfaces. The secondary air interacted with the cascade passage vortices and changed the loss distribution significantly. The cascade overall loss decreased when the air was injected along the mainstream and increased when the air was injected against the mainstream from some locations of the blade leading edge. Effects on overall kinetic energy of the secondary flows and on the cascade outlet flow angle were also discussed in this paper.

Introduction

A lot of efforts have been made to increase turbine inlet gas temperature to gain better engine cycle efficiency. Turbine blades are cooled with secondary air (cooling air) so that they can withstand high-temperature gas. The cooling air is thereafter injected into the mainstream. Due to the interaction of the injected air with the mainstream, the turbine aerodynamic performance may be worsened, which may lessen the expected gain of the cycle efficiency. A lot of analytical and experimental studies have been made on the effects of cooling air; for example, by Hartsel (1972), Prust (1972, 1975), Yamamoto (1976), Tabakoff and Hamed (1975), and Suciu (1971). The first three analyze the effects as one- or two-dimensional problems of fluid mixing of the cooling air with the mainstream gas. The others present cascade experimental results. However, it has not been made clear how the injected air behaves in the cascade passages and how it causes the loss. Detailed information on such questions is needed not only from the aerodynamic point of view, but also from the thermodynamic point of view.

The main purpose of the present study is to reveal experimentally the effects of the injection on three-dimensional flows in the cascade passage and on the resultant overall performance. In the present study, in order to simulate film cooling flows, the injection was made from a total of ten slits located around the blade surfaces. The injection slits adopted here are different from the round holes that are generally used in cooled blades. The present study, therefore, does not give a general solution but will give an order of the injection effects on the loss and internal flow fields of cooled blade rows. The slits used in the present study were adopted so that the results obtained could, because of the simplicity of the injection holes, be easily analyzed by advanced computer codes recently being developed in many places. It is intended that the data thus obtained can become the preliminary verification data for the numerical analyses of cooled turbine flows.

Experimental Method and Test Condition

Figure 1 shows the linear cascade tested, which is the same as that used in the previous studies (e.g., Yamamoto and Nouse, 1989). Further details may be found from Yamamoto (1989). Figure 2 indicates locations of the injection slits using two point coordinates. The spanwise length of the slit is 95 mm and the width is 0.5 mm (see also Fig. 3). The blade has two separate air chambers inside, from each of which a slit was cut by a wire-cutting manufacturing method. The tests were made by replacing the two solid blades located nearest the center of the present six-bladed cascade with the hollow blades.

Cascade flows were surveyed with a five-hole pitot tube at four measuring planes, as shown in Fig. 3. Plane 1 is located at 34.5 percent of the cascade axial chord upstream from the blade leading edge, and plane 2 is within the cascade passage

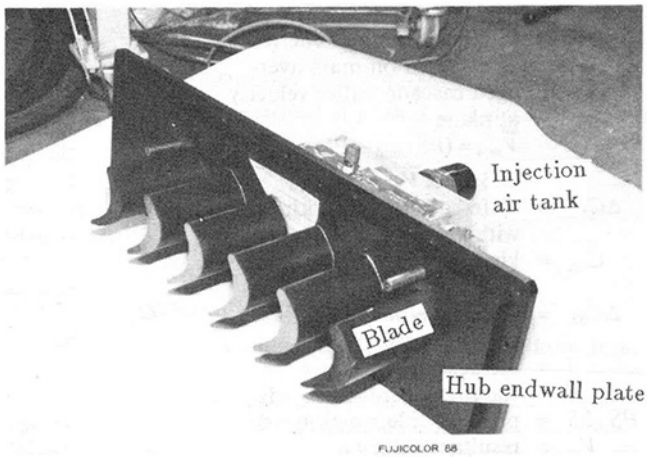

Fig. 1 Test cascade

[1]Current address: Ishikawajima-Harima Heavy Industries Co., Ltd., Tanashi, Tokyo, Japan.

Contributed by the International Gas Turbine Institute and presented at the 35th International Gas Turbine and Aeroengine Congress and Exposition, Brussels, Belgium, June 11-14, 1990. Manuscript received by the International Gas Turbine Institute January 31, 1990. Paper No. 90-GT-141.

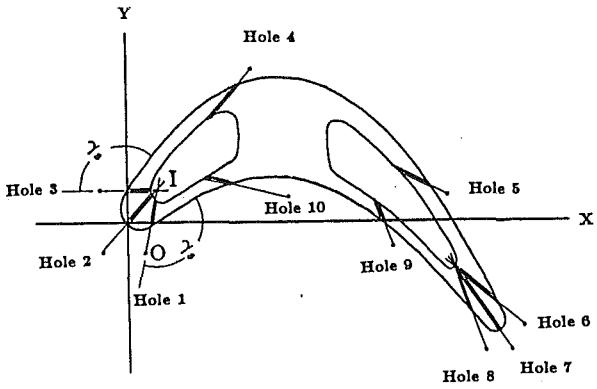

Blade coordinates (mm)

X	Yp	Ys
0.0000	0.0000	6.3292
4.0833	- 0.8167	12.2500
8.1667	2.0008	17.3542
12.2500	4.6142	21.4375
16.3333	6.5333	24.5000
20.4167	7.9625	26.3375
24.5000	8.6567	27.5625
28.5833	8.6567	27.7667
32.6667	8.0850	27.3583
36.7500	6.8600	26.1333
40.8333	4.9000	24.2142
44.9167	2.6542	21.2333
49.0000	- 0.5308	18.1708
53.0833	- 4.2875	13.0667
57.1667	- 8.6975	7.3500
61.2500	-13.2708	0.4083
65.3333	-18.1708	- 7.1458
69.4167		- 5.1083

Hole coordinates (mm)

Hole Loc.	No.	Type	I X	I Y	O X	O Y	γ_s (deg)
LE	1	a	5.34	6.32	3.35	-5.00	117
	2	b	5.34	6.32	-4.23	-5.00	90
	3	c	5.00	6.32	-5.00	6.32	125
SS	4	d	16.50	21.50	23.49	30.00	40
	5	f	51.00	10.50	61.72	5.00	30
TE	6	a	62.00	-9.00	75.36	-20.00	26
	7	b	62.00	-9.00	72.91	-25.00	90
	8	c	62.00	-9.00	67.81	-25.00	21
PS	9	d	47.50	3.00	50.35	-5.00	29
	10	f	15.50	9.30	31.08	5.00	32

a,b,c,d,f= Hollow blade type of pairing of holes

Fig. 2 Location of air-injection holes and blade coordinates

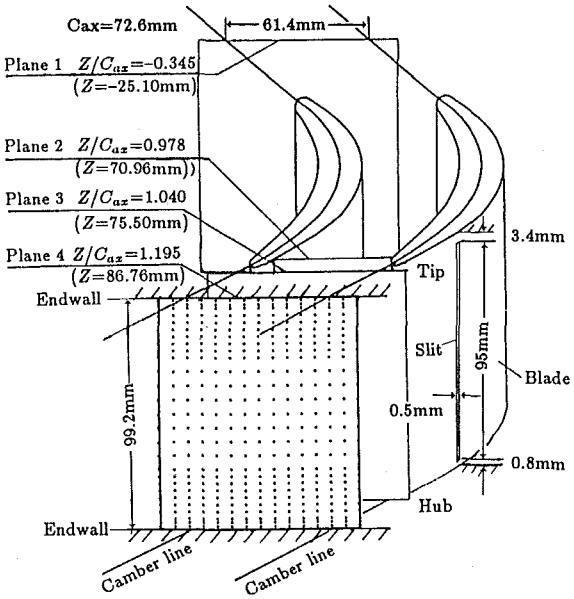

Fig. 3 Traverse measuring planes

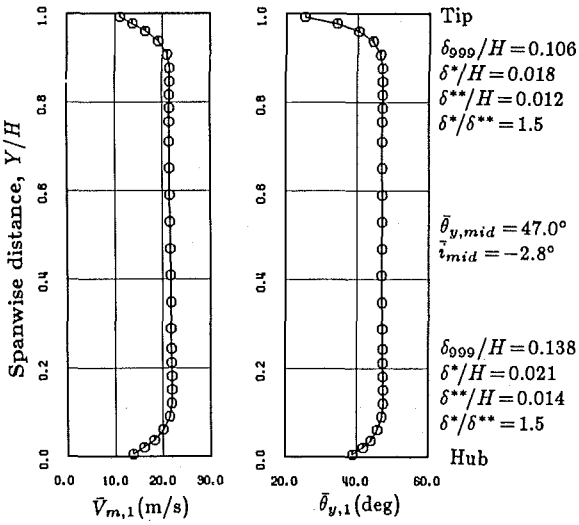

Fig. 4 Inlet velocity and angle distributions

but near the blade trailing edge (97.8 percent axial chord from the leading edge). Plane 3 is located just after the trailing edge (104 percent) and plane 4 is farther downstream of the cascade (119.5 percent). Note that injection holes 6, 7, and 8 around the trailing edge are located downstream of plane 2. The measurements were made at plane 1 without injection and then at planes 2–4 with and without injection ($\beta=0$, 0.8, and 1.7 percent). The injection flow rates were adjusted by motor-driven valves. The 0.8 and 1.7 percent injections correspond to injection velocity ratios of about 0.51 and 1.1, which are the ratio of injection velocity V_c to the mass-averaged cascade outlet velocity at plane 4 ($\overline{\bar{V}}_{m,4}$). The test Reynolds number

Nomenclature

CP_t = total pressure loss coefficient based on mass-averaged cascade outlet velocity at plane 4; $\overline{\bar{V}}_{m,4}=(Pt_{1,\text{mid}}-Pt_{,1})/(0.5\times\rho\times\overline{\bar{V}}_{m,4})$

ΔCP_t = difference of CP_t with and without injection

C_{SK} = kinetic energy coefficient of secondary flow $=(V_s/\overline{\bar{V}}_{m,4})^2$

ΔC_{SK} = difference of C_{SK} with and without injection

i = incidence

LE, TE = leading edge, trailing edge

PS, SS = pressure side, suction side

V_m = resultant velocity

$\mathbf{V}_s$ = secondary flow vector

$\Delta\mathbf{V}_s$ = difference of $\mathbf{V}_s$ with and without injection

x/L = dimensionless distance along blade surfaces from the leading edge normalized by length L of each blade surface

Y/H = dimensionless distance from the hub normalized by the cascade passage height H

Z/C_{ax} = dimensionless distance normalized by the axial blade chord C_{ax}

β = mass flow ratio of injection air against mainstream air

δ_{999} = boundary layer thickness on cascade inlet endwall

δ^* = displacement thickness of cascade inlet endwall boundary layer

δ^{**} = momentum thickness of cascade inlet endwall boundary layer

Δ = interval of contour plots

θ_y = yaw angle of flow deviated from the cascade axial direction

ρ = density

$(\ )_{,1-4}$ = number of measuring planes

$\bar{\ }$ = pitchwise mass-averaged value at each local span

$=$ = overall mass-averaged value calculated at each measuring plane

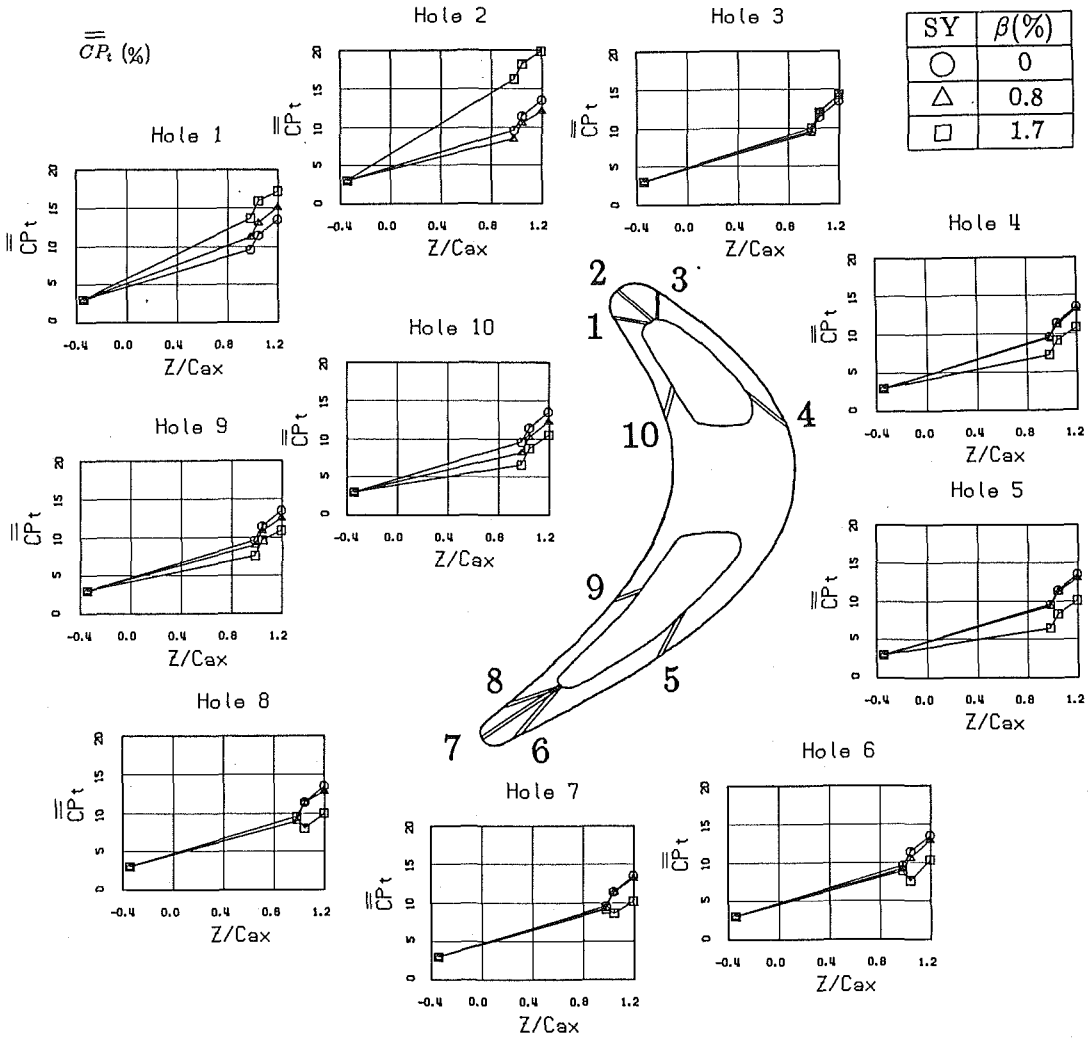

Fig. 5 Effects of air injection from various injection holes on evolution of mass-averaged total pressure loss

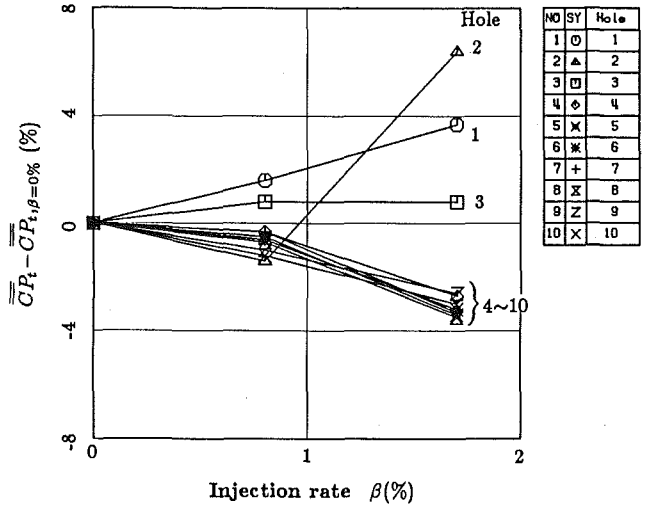

Fig. 6 Change in mass-averaged loss at plane 4 with air-injection rate

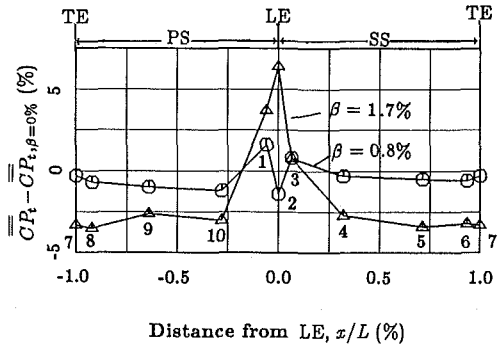

Fig. 7 Change in loss measured at plane 4 for various air-injection points

based on $\overline{\overline{V}}_{m,4}$ and the blade chord was about 1.5×10^5. The injected air is at room temperature, which is the same as the mainstream temperature. The test cascade inlet velocity and the inlet flow angle are shown in Fig. 4 with estimated values of some endwall boundary layer parameters. The test shape factors δ^*/δ^{**} suggest that the endwall boundary layers at the cascade inlet are nearly turbulent. The test incidence at the midspan is -2.8 deg.

Experimental Results and Discussion

Evolution of Overall Loss in Cascade With/Without Injection. Figure 5 shows the evolution of (overall) mass-averaged loss along the cascade passage with and without injection. Among the tests using various hollow blades, small differences arose in the loss values without injection, due possibly to misalignment of the test hollow blades and to disturbance in the

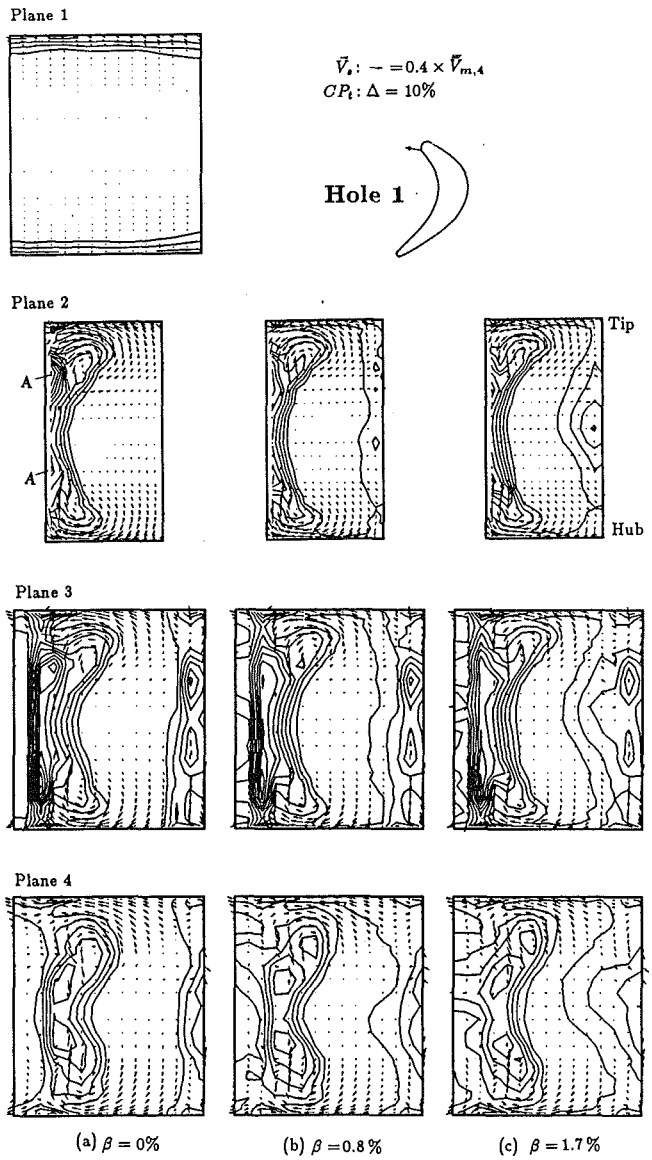

Fig 8 Secondary flows and loss with air injection from hole 1 at the pressure side of blade leading edge (β = 0, 0.8, 1.7 percent)

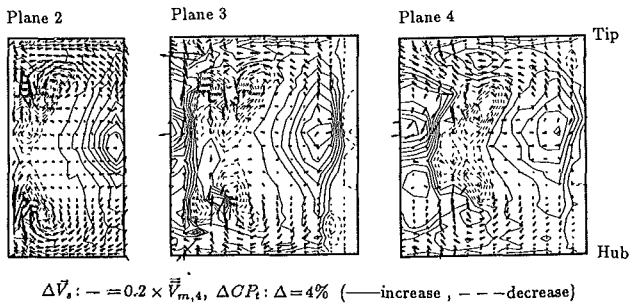

Fig. 9 Change in secondary flows and loss at β = 1.7 percent for hole 1

flowfield caused by the slits. The differences were usually small but not negligibly small compared to the loss change caused purely by injection, and could not be separated properly. To omit these differences from the following discussion, the losses of all tests without injection are averaged at each measuring plane, and the average loss is used as the basic loss without injection at the plane. Each loss shown in Fig. 5 with injection was then obtained by adding to the basic loss without injection the value of loss change caused by injection and can be calculated accurately at each plane both with and without injection.

Without injection ($\beta = 0$ percent), the overall loss increases gradually from plane 1 ($Z/C_{ax} = -0.345$) to plane 2 ($Z/C_{ax} = 0.978$), and rapidly from plane 2 to plane 3 ($Z/C_{ax} = 1.04$) due mainly to the additional trailing edge loss. Toward downstream plane 4 ($Z/C_{ax} = 1.195$), the loss increases further due to the downstream fluid mixing. For various injection configurations, the results are as follows:

(*a*) *Injection From the Blade Leading Edge* (*Holes 1, 2, or 3*). Injections from either holes 1 or 2, which are located at the pressure side of the leading edge or just at the leading edge, have strong and different effects on the overall loss evolution; for hole 1, the loss increases monotonously with increase of injection rate but for hole 2, the loss decreases once at 0.8 percent injection and increases rapidly at 1.7 percent injection. Injection from hole 3 located at the suction side of the leading edge, on the other hand, did not cause any significant effects on the loss evolution.

(*b*) *Injection From the Blade Suction Surface* (*Holes 4 or 5*). The 0.8 percent injection decreases the loss very little but the 1.7 percent injection reduces the loss significantly.

(*c*) *Injection From the Blade Trailing Edge* (*Holes 6, 7, or 8*). Since the measuring plane 2 ($Z/C_{ax} = 0.978$) is located upstream of these holes, no effects were detected at this plane. At planes 3 and 4 ($Z/C_{ax} = 1.04$ and 1.195), the loss decreases only a little at 0.8 percent injection but significantly decreases at 1.7 percent injection.

(*d*) *Injection From the Blade Pressure Surface* (*Holes 9 or 10*). The pressure surface injection decreases the loss monotonously with increase of injection rate. This is a little different from the suction surface injection, which decreases the loss very little at 0.8 percent injection.

Effects of Injection Rate and Injection Point. Figure 6 shows change of the overall loss with the injection rate. As already described in the previous section, the loss increases monotonously with increase of injection rate for hole 1. For hole 2, it decreases once at a small amount of 0.8 percent injection but increases rapidly at 1.7 percent injection. For hole 3, the loss increases a little up to 0.8 percent injection and then becomes constant. For all the other holes, 4–10, the loss decreases with increase of injection rate.

As shown in Fig. 7, leading-edge or near-leading-edge injection (from holes 1, 2, or 3), except in the case of a small amount (0.8 percent) of injection from hole 2, tends to cause an additional loss. Loss reduction due to the suction surface injection of 0.8 percent (from holes 4 and 5) seems to be somewhat smaller than that due to the pressure surface injection (from holes 9 and 10). At 1.7 percent injection, the loss reduction becomes significant, and in general it seems to become larger as the injection point moves downstream. Any injections from holes 6, 7, or 8 located around the trailing edge reduce the loss to nearly the same extent regardless of the different injection points. Loss reduction due to trailing edge injection is a well-known fact but is not especially large compared to the reduction caused by the other injections, such as from the blade surfaces.

Detailed Internal Flows

(*a*) *Injection From the Leading Edge.* Figure 8 shows the secondary flows and the loss with and without injection from hole 1. The injection increases the loss near the pressure surface. The composed vector of the inlet mainstream and the injection air from hole 1 tends to have a negative incidence

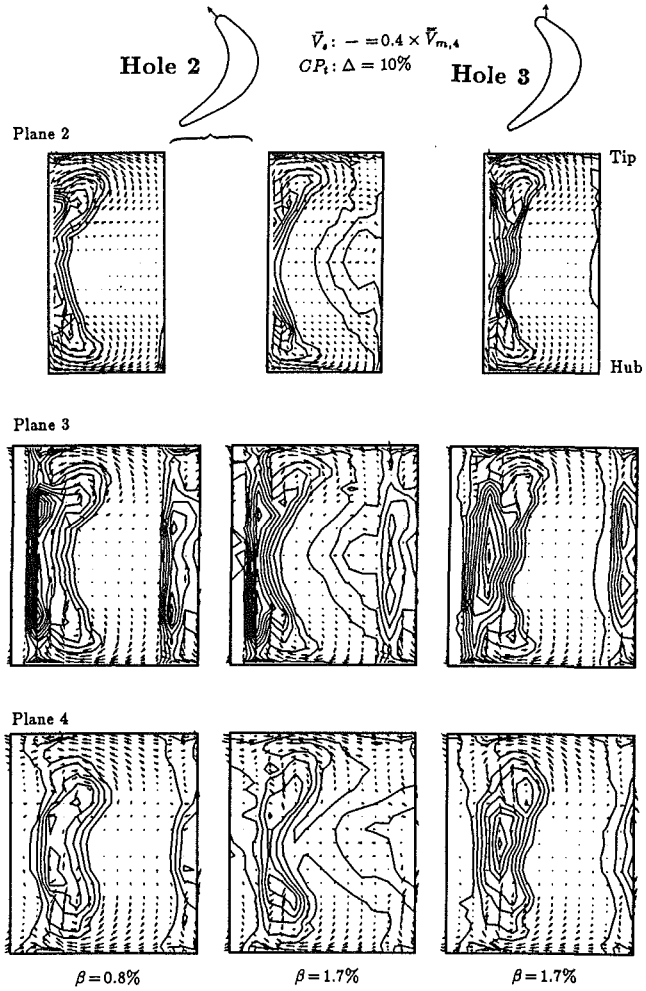

Fig. 10 Secondary flows and loss with air injection from hole 2 at the blade leading edge and from hole 3 at the suction side of blade leading edge ($\beta = 1.7$ percent)

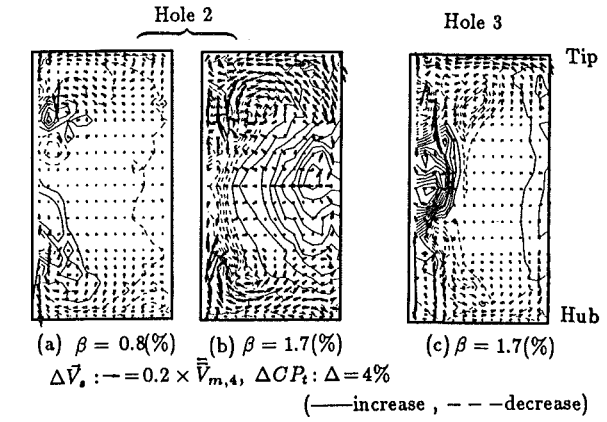

Fig. 11 Change in secondary flows and loss at plane 2 for holes 2 ($\beta = 0.8$, 1.7 percent) and 3 ($\beta = 1.7$ percent)

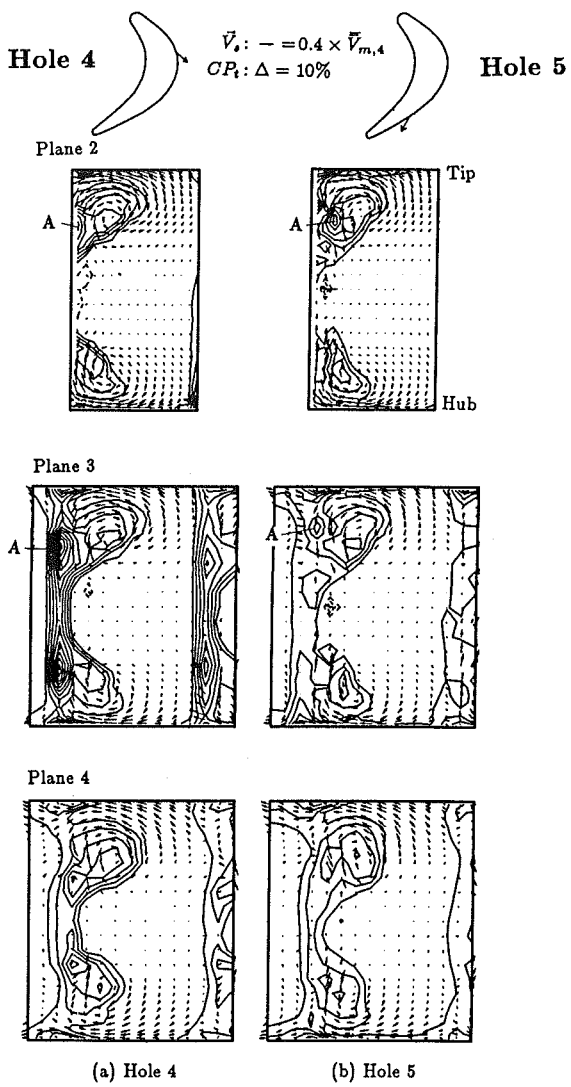

Fig. 12 Secondary flows and loss with air injection from holes 4 and 5 on the blade suction surface ($\beta = 1.7$ percent)

and tends to separate the flow from the pressure-side leading edge. The loss increase is considered to be due mainly to the interaction of the injected air with the mainstream and to the flow separation. The core loss (indicated by A) corresponds to the separation points of the passage vortices from the suction surface but seems to be reduced with the injection.

Figure 9 shows the effects of injection more clearly, where the secondary flow vectors and the loss are shown in their difference forms ($\Delta \mathbf{V}_s$ and ΔCP_t) between 0 and 1.7 percent injections. In the contour plots of ΔCP_t, solid lines indicate loss, which increases with injection, and dashed lines indicate loss, which decreases. At plane 2, a large loss-increasing area (solid lines) arises near the midspan of the pressure surface. The loss-decreasing area (dashed lines), on the other hand, exists over the suction surface except near the endwalls. The loss-increasing area seen at plane 2 becomes wider at farther downstream planes 3 and 4, while the loss-decreasing area becomes concentrated toward the midspan due to the secondary flows.

The rotational directions of the subtracted secondary flow vectors $\Delta \mathbf{V}_s$ are opposite to those of the passage vortices, which means that the vortices were weakened by the injection. The weakened vortices cause a smaller amount of the low-energy fluids to migrate onto the suction surface from the endwalls, and cause a greater amount of the low-energy fluids (from the endwalls and from the leading edge separation region) to remain on the endwalls (as seen in Fig. 8). This is the main reason that the loss decreases over the suction surface. When relating the subtracted vectors to the loss-increasing or decreasing areas, one understands that the passage vortices are very important to the mixing and loss-generation process of the injection air with the mainstream.

Figure 10 shows the results of other leading-edge injection from holes 2 or 3. For hole 2, as already found in Fig. 6, the

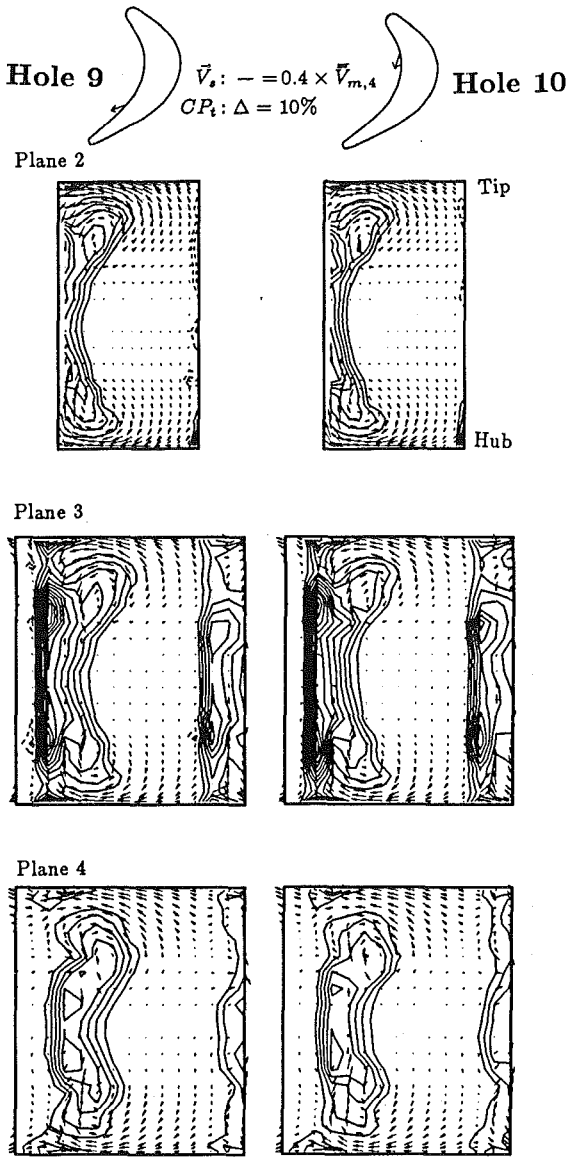

Fig. 13 Secondary flows and loss with air injection from holes 9 and 10 on the blade pressure surface ($\beta = 1.7$ percent)

overall (mass-averaged) loss decreases once at 0.8 percent injection and increases rapidly at 1.7 percent injection. These loss-decreasing and increasing mechanisms due to the hole 2 injection will be seen in detail in Fig. 10(*a*) and more clearly in Fig. 11(*a*, *b*); the 0.8 percent injection causes a loss decrease in a wide area near the pressure surface, but causes an increase at a part near the suction surface. This tendency of the loss at the 0.8 percent injection is opposite to that from hole 1. The passage vortices are a little strengthened as seen when the cascade operates at a more positive incidence. This injection in the upstream direction may suppress the occurrence of the separation from the pressure-side leading edge. At 1.7 percent injection (Fig. 11(*b*)), however, the loss increases rapidly in a large part of the cascade passage and decreases partly at the suction side, again due to the interaction and the leading-edge separation as mentioned before for injection from hole 1. The changes in the loss and in the associated secondary flows due to the injection from holes 1 or 2 are very similar to those when the cascade operated at negative incidences (Yamamoto and Nouse, 1989), where strong flow separation occurred from the whole span of the pressure-side leading edge and contributed to the changes.

Injection from hole 3 did not change the overall loss significantly as seen in Fig. 5, but did change the local loss significantly as seen now in Fig. 11(*c*); the loss increases near the midspan of the suction surface and near the pressure surface, and decreases on the suction surface close to the endwalls. The low-energy (loss) fluids that accumulated near the midspan of the suction surface and near the pressure surface are thought to occur due to the interaction of the injected air with the mainstream.

(*b*) *Injection From the Suction and the Pressure Surfaces.* As shown in Fig. 12, the injection from holes 4 or 5, which are located before and after the cascade throat, respectively, eliminates the loss on the suction surface significantly. This is because the injection along the surface adds some amounts of momentum to the low-energy fluids on the suction surface. The injected air from the upstream hole 4 passes over the low-energy fluids being driven from the endwall onto the suction surface, while the injected air from the downstream hole 5 passes below the low-energy fluids already driven onto the suction surface; clear differences can be seen in the loss distributions at plane 3 and in the locations of the local peak losses (shown by A), which correspond to low-energy fluids caused by the passage vortex separation from the suction surface.

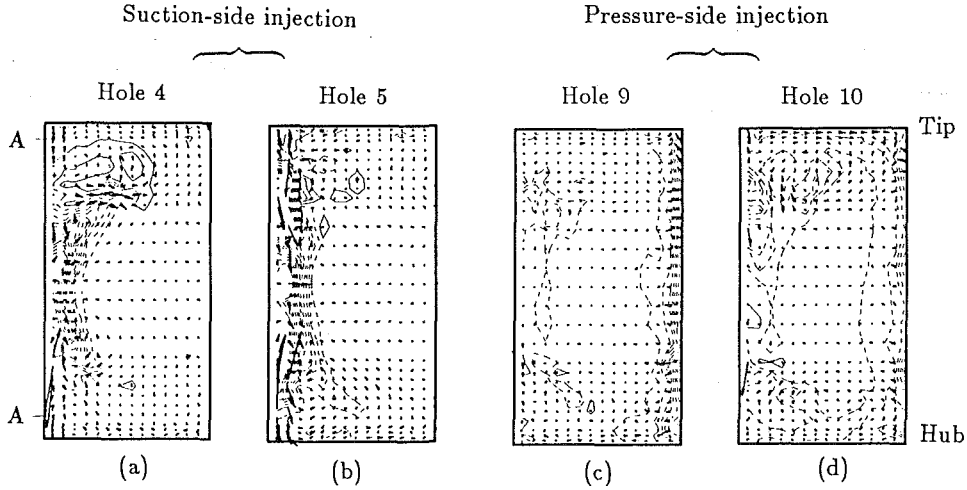

Fig. 14 Change in secondary flows and loss at plane 2 for holes 4, 5, 9, and 10 with $\beta = 1.7$ percent

As shown in Fig. 13, the pressure surface injection from holes 9 or 10 does not change the loss profiles and the secondary flows as clearly as does the suction surface injection. Figure 14, which shows difference forms, will show the effects of the suction and pressure surface injections more clearly.

Due to the well-known spanwise flows on the suction surface, the injected air is also driven toward the midspan and decreases the loss there. As shown in Fig. 14(a, b), the injected air from the upstream location of the suction surface (hole 4) becomes more concentrated toward the midspan than that from the downstream location (hole 5). This spanwise migration of the injection air should be taken into account carefully in making effective film cooling; for example, since the fluids injected from the upstream part of the suction surface can hardly reach the separated regions at the suction surface/endwall corner near the trailing edge, coolant injection not only from the suction surface in question but also from the "endwall" would be effective in cooling the separated regions. The injection from hole 9 on the rear part of the pressure surface reduces the loss over the pressure surface and partly near the suction surface, while the injection from hole 10 on the front part reduces the loss significantly near the blade surfaces and the endwalls, as seen in Fig. 14(c, d). Since the flow on the pressure surface is nearly two dimensional or tends to spread over the surface due to the passage vortex movements, the injected air can easily cover the pressure surface without accumulating at the midspan; the cooling film, therefore, could be more easily attained on the pressure surface than on the suction surface.

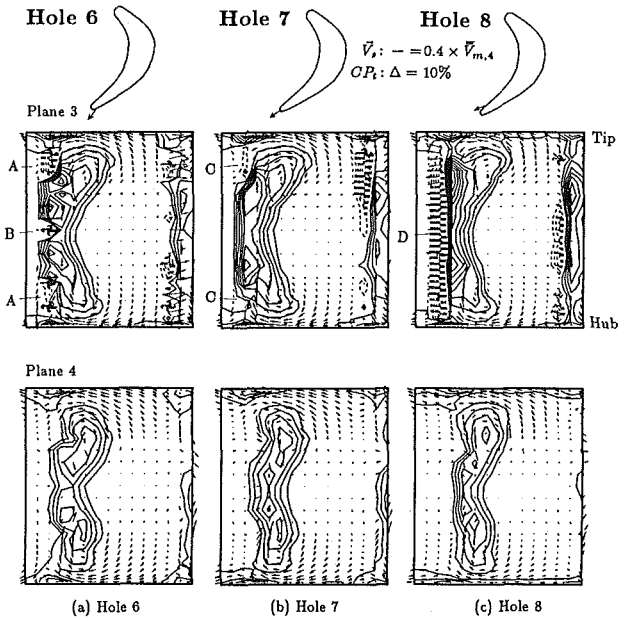

Fig. 15 Secondary flows and loss with air injection from holes 6, 7, and 8 around the blade trailing edge (β = 1.7 percent)

(c) *Injection From the Trailing Edge.* Figure 15 illustrates the results of the injection from holes 6, 7, and 8 located around the trailing edge. The injection from the suction side hole 6 introduces high-energy fluids into the separation regions at the endwall corners (indicated by A) and at the midspan (B), and eliminates the loss there. The injection from hole 7 just past the trailing edge diminishes the low-energy fluids behind the trailing edge near the endwalls as indicated by C. The pressure side injection from hole 8 increases the pressure at the pressure side of the wake (D) significantly. In spite of these differences, all the loss distributions downstream of the cascade at plane 4 are very similar to each other for the three kinds of injection; fairly thin wake profiles are shown compared to the no-injection profiles of Fig. 8(a).

Spanwise Distribution of Loss. Figure 16 shows spanwise distributions of pitchwise mass-averaged loss at the cascade upstream and downstream planes 1 and 4 for five selected injection holes: three holes 1, 2, and 3 around the leading edge, hole 4 on the suction surface, and hole 10 on the pressure surface. Three loss profiles at plane 4 correspond to injection rates of 0, 0.8, and 1.7 percent. The difference of the losses between the cascade upstream and the downstream planes 1 and 4 corresponds to the net loss, which is generated in the cascade passage. Near the endwalls, the downstream loss is lower than the upstream due to the spanwise fluid mixing.

For hole 1, the loss increases first only near the endwalls at 0.8 percent injection and then along the whole span at 1.7 percent injection. For hole 2, the loss decreases once near the endwalls at 0.8 percent injection and increases rapidly along the whole span at 1.7 percent injection. For hole 3, the loss increases a little, particularly near the midspan.

For the suction surface injection from hole 4, the loss de-

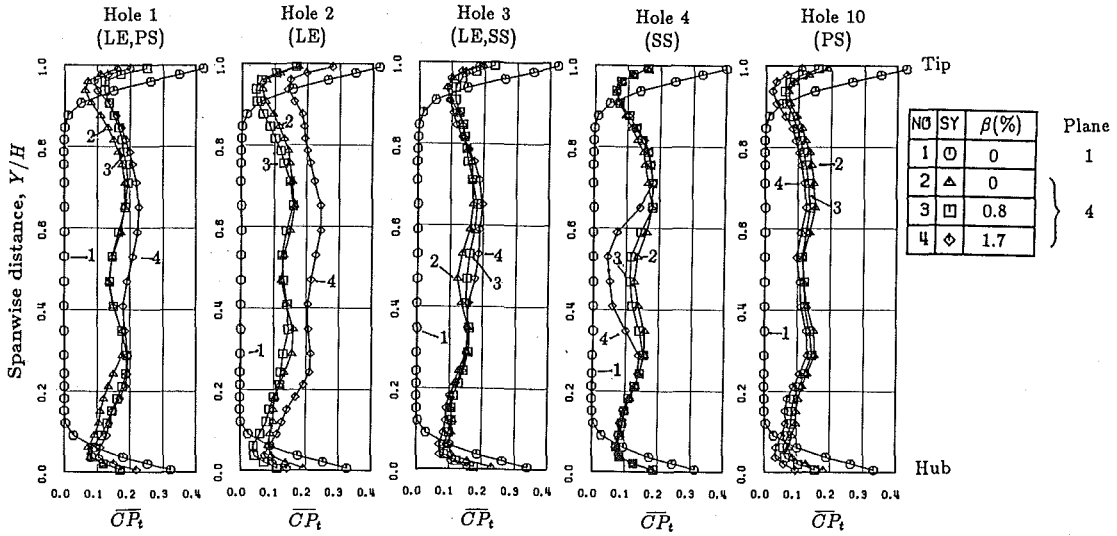

Fig. 16 Change in spanwise distribution of loss at the cascade inlet plane 1 and outlet plane 4 with air injection from various injection holes

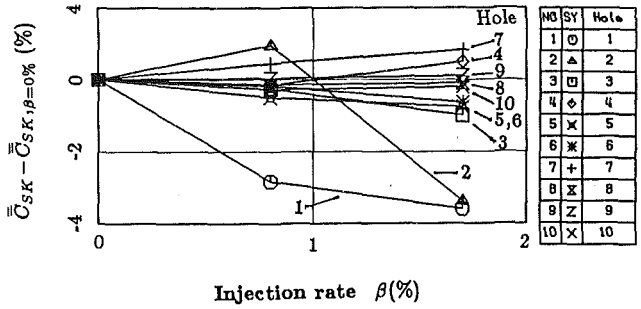

Fig. 17 Change in mass-averaged secondary kinetic energy at plane 4 with air-injection rate

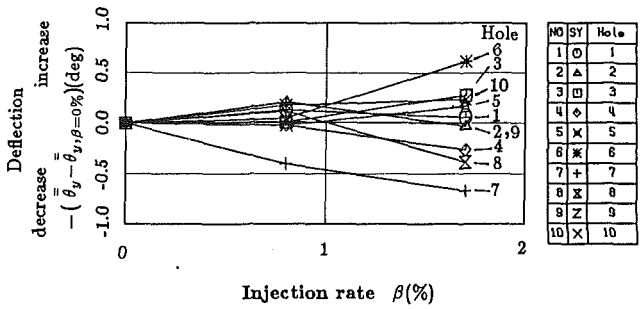

Fig. 19 Change in mass-averaged cascade outlet yaw flow angle at plane 4 with air-injection rate

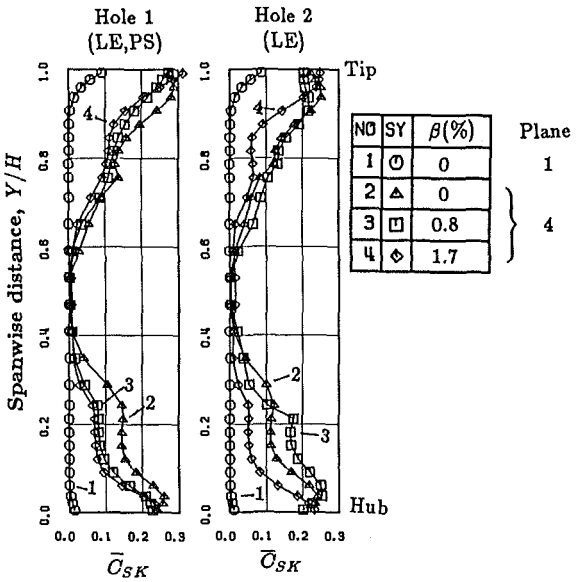

Fig. 18 Change is spanwise distribution of secondary kinetic energy at the cascade inlet plane 1 and outlet plane 4 with air injection from holes 1 and 2

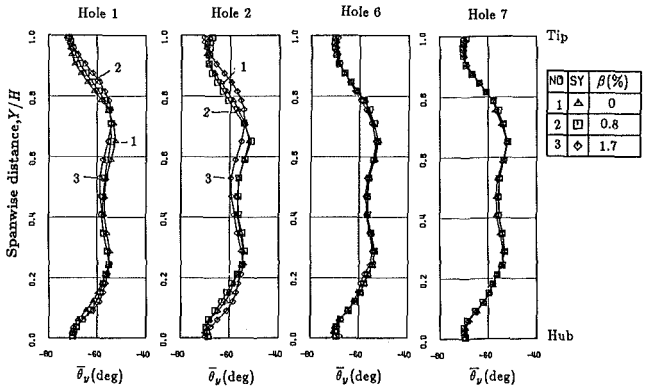

Fig. 20 Change in spanwise distribution of outlet yaw flow angle at plane 4 with air injection from holes 1, 2, 6, and 7

creases only around the midspan, while for the pressure surface injection from hole 10, the loss decreases uniformly along the whole span.

Effects on Secondary Kinetic Energy and Cascade Outlet Flow Angle. Mass-averaged kinetic energy of the secondary flows is changed by the injection, as shown in Fig. 17, which is calculated at plane 4. The change is largest in two cases of injection from holes 1 and 2, and is roughly opposite to that of the overall loss (Fig. 6). The injection from other holes, 3–10, has little effect on the kinetic energy. Figure 18 shows the local change in the kinetic energy with injection from holes 1 and 2; a large change is seen around 0.2 span apart from the endwalls where the passage vortices exist.

Figure 19 shows change in the mass-averaged cascade outlet flow angle obtained at plane 4. In the present cascade, the change due to the injection lies within about ±0.6 percent for any type of injection. The injection from the suction side of the trailing edge (hole 6) tends to increase the outlet flow angle, while the injection just past the trailing edge (hole 7) and from the pressure side of the trailing edge (hole 8) tends to decrease the angle. This tendency is opposite to what one would expect from the directions of the injections.

Figure 20 indicates spanwise local change in the cascade outlet flow angle for four types of injection: For holes 1 or 2, the local change is fairly large and reaches several degrees around the midspan, but the overall (mass-averaged) change was very small as was seen in Fig. 19. For holes 6 and 7, on the other hand, the local change is uniformly small along the span, but the mass-averaged change was relatively large as seen in Fig. 19.

Conclusions

An investigation was made on cascade overall performance and detailed internal flows of a linear cascade with secondary air injection. The main results are as follows:

1 Injection from the blade leading edge and from the pressure side of the leading edge both against the mainstream generally increases the overall loss significantly. This is due mainly to the interaction between the mainstream and the injected air, and to the resultant flow separation from the leading edge. However, it is interesting to note that a small amount of injection from the leading edge decreases the overall loss. Injection from the suction side of the leading edge against the mainstream does not increase the overall loss significantly.

2 Injection from the blade suction and pressure surfaces generally decreases the loss because of the additional momentum supplied by the injection air into the mainstream; the suction surface injection decreases the loss a little at a small amount of injection but significantly at a large amount of injection, while the pressure surface injection decreases the loss monotonously with increase of injection rate.

3 Three types of injection from the trailing edge reduce the loss to the same extent regardless of the different injection points around the trailing edge. The loss reduction is not especially large compared to the reduction caused by other injections.

4 Injection air interacts strongly and mixes with the passage vortices that are weakened or strengthened by the injection; the local loss-increasing or decreasing areas are determined by the vortex change and by the location of injection.

5 Due to the passage vortices, the injected air along the suction surface tends to migrate toward the midspan, while the injected air along the pressure surface tends to cover the pressure surface and the endwalls; the formation of cooling

film on the suction surface, therefore, should be more difficult than on the pressure surface. One should take careful account of the above tendency of the injection air in the cascade passage when designing effective cooled blades.

6 The overall change of the mass-averaged cascade outlet flow angle due to the injection was in general very small in the present linear cascade. Increase or decrease of the overall secondary kinetic energy caused by the injection from the leading edge against the mainstream is roughly opposite to that of the overall loss.

In the present study, only one loss coefficient was defined and used in the discussion. It is necessary, however, to consider the merits and demerits of the injection from various aerodynamic and thermodynamic points of view, as described by Cohen et al. (1986), on various sources of loss arising in cooled turbines.

References

Cohen, H., Rogers, G. F. C., and Saravanamuttoo, H. I. H., 1986, *Gas Turbine Theory*, 3rd ed., Longman Scientific and Technical, Longman Group UK Limited, pp. 294–301.

Hartsel, J. E., 1972, "Prediction of Effects of Mass-Transfer Cooling on the Blade-Row Efficiency of Turbine Airfoils," AIAA Paper No. 72-11.

Prust, H. W., Jr., 1972, "An Analytical Study of the Effect of Coolant Flow Variables on the Kinetic Energy Output of a Cooled Turbine Blade Row," AIAA Paper No. 72-12.

Prust, H. W., Jr., 1975, "Two-Dimensional Cold-Air Cascade Study of a Film-Cooled Turbine Stator Blade, II — Experimental Results of Full Film Cooling Tests," NASA TM X-3153.

Suciu, S. N., 1971, "High Temperature Design Considerations," *High Temperature Turbines*, AGARD-CP-73-71.

Tabakoff, W., and Hamed, A., 1975, "Theoretical and Experimental Study of Flow Through Turbine Cascades With Coolant Flow Injection," AIAA Paper No. 75-843.

Yamamoto, A., 1976, "Two-Dimensional Aerodynamic Performance of Cascade Blade With Secondary-Air Injection From the Blade Trailing-Edges — An Analytical Method and Results," National Aerospace Laboratory TR-469 [in Japanese].

Yamamoto, A., 1989, "Experimental Study on Three Dimensional Flow and Loss Mechanisms in Axial-Flow Turbine Blade Rows," Dr.Eng. dissertation, University of Tokyo [in Japanese].

Yamamoto, A., and Nouse, H., 1989, "Effects of Incidence on Three-Dimensional Flows in a Linear Turbine Cascade," ASME JOURNAL OF TURBOMACHINERY, Vol. 110, pp. 486–496.

Heat Transfer and Aerodynamics of a High Rim Speed Turbine Nozzle Guide Vane Tested in the RAE Isentropic Light Piston Cascade (ILPC)

S. P. Harasgama

E. T. Wedlake

Royal Aerospace Establishment,
Propulsion Department,
Pyestock, Farnborough
Hampshire, GU14 0LS, United Kingdom

Detailed heat transfer and aerodynamic measurements have been made on an annular cascade of highly loaded nozzle guide vanes. The tests were carried out in an Isentropic Light Piston test facility at engine representative Reynolds number, Mach number, and gas-to-wall temperature ratio. The aerodynamics indicate that the vane has a weak shock at 65–70 percent axial chord (midspan) with a peak Mach number of 1.14. The influence of Reynolds number and Mach number on the Nusselt number distributions on the vane and endwall surfaces are shown to be significant. Computational techniques are used for the interpretation of test data.

Introduction

Improvements in the performance and thrust-to-weight ratio of aero gas turbine power plants require advances in turbomachinery efficiency, increases in pressure ratio, and the ability to run the combustor at ever-increasing temperatures. As a result, the modern high-pressure (HP) turbine stage operates in a very hostile pressure and temperature environment. Most HP turbines have a considerable amount of cooling in order to sustain an adequate service life. Efficiency improvements have been brought about by improved design methodologies, which combine high-quality experimental correlations and three-dimensional computational fluid dynamic techniques.

The present nozzle guide vane design was undertaken using an inviscid three-dimensional (3D) time-marching code (Denton, 1976, 1983). Detailed design features of the HP turbine stage are described by Kingcombe et al. (1989). The nozzle guide vane (NGV) incorporates radial work distribution to offload the root and tip, thereby obtaining more work in the midspan region, which is the most efficient. The vane has also been designed with compound lean of the trailing edge. These two design features should result in reducing the amount of secondary flow in the NGV passage. Figure 1 shows details of the NGV.

Current work at RAE is targeted at establishing a high-quality data base on NGV aerodynamics and heat transfer, especially in the area of NGV endwall heat load distribution. Testing of the NGV ring was performed in the ILPC at a range of Reynolds and Mach number. Details of the ILPC test facility have been reported by Brooks et al. (1985). There have been several investigations of NGV aerofoil heat transfer and the behavior of suction and pressure surface Nusselt/Stanton number variations has been well catalogued. The characteristics of endwall heat transfer are not generally well defined. Early work on endwall heat transfer concentrated on linear vane cascades, which do not correctly represent the growth of inner and outer wall boundary layers. This also meant that the radial pressure gradient within the NGV cascade was not modeled. The work by Graziani et al. (1979), Gaugler and Russell (1983), among others, was not representative of engine conditions in terms of Reynolds number, Mach number, or gas-to-wall temperature ratio. York et al. (1983) conducted a very thorough evaluation of heat transfer to endwalls on a steady-state hot rig but chose to test a linear cascade system under the NASA HOST (Hot Section) program (Gladden and Simoneau, 1988); even here the full nondimensional engine conditions were not

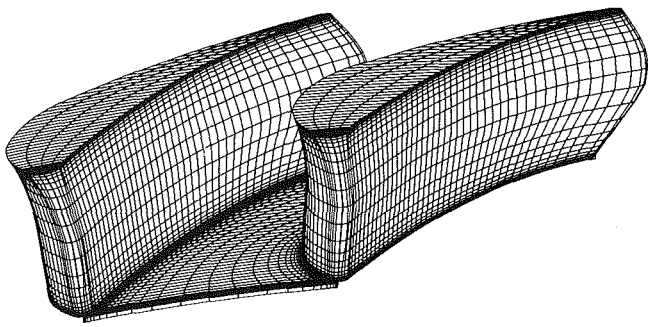

Fig. 1 Vane detail and computational grid

Contributed by the International Gas Turbine Institute and presented at the 35th International Gas Turbine and Aeroengine Congress and Exposition, Brussels, Belgium, June 11–14, 1990. Manuscript received by the International Gas Turbine Institute January 11, 1990. Paper No. 90-GT-41.

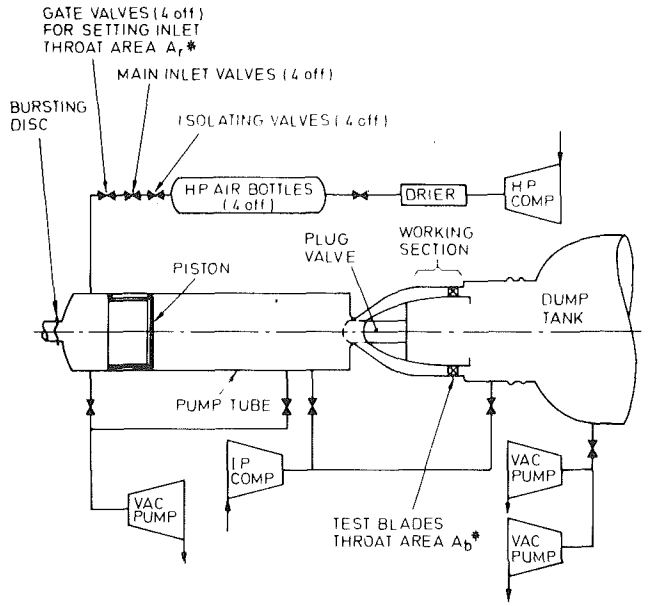

Fig. 2 ILPC test facility

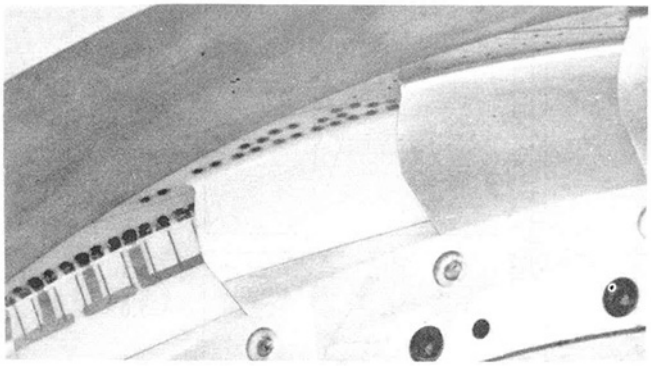

Fig. 3 Vane instrumentation

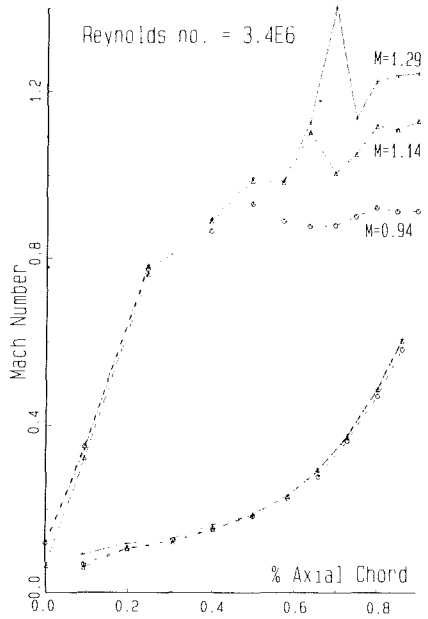

Fig. 4 Effect of increasing M on vane

simulated. Some work was also attempted on annular configurations under HOST but did not appear to be definitive.

More recent work by Boyle and Russel (1990) using thermochromic liquid crystals has shown detailed information on the pattern of heat transfer on NGV endwalls. Reynolds numbers from 7.3E4 to 4.95E5 were covered with various different inlet boundary layer thicknesses. Boyle and Hoose (1989) measured heat transfer within an NGV passage and a curved duct and showed that the distributions are similar but that stronger secondary flows in the duct cause higher Stanton numbers than in the vane passage. Both papers concentrate on linear cascades operating at relatively low velocities and low inlet turbulence. What has been shown by the various authors is that endwall heat transfer is dominated by the horseshoe vortex generated at the leading edge and subsequently by the evolution of secondary flow within the NGV passage. Generally, high heat transfer is found close to the leading edge and also near the pressure side trailing edge region.

Therefore, a requirement exists for data on the heat transfer to turbine NGV operating at the correct engine parameters. The present paper reports on the aerodynamics and heat transfer of a highly loaded NGV operating at the correct engine nondimensional parameters of Reynolds number, Mach number, and gas-to-wall temperature ratio utilizing a fully annular vane ring. Both experimental results and computational analyses are presented.

Test Facility

The ILPC (Fig. 2) is derived from the short duration isentropic light piston tunnels pioneered at Oxford University (Schultz and Jones, 1973). The facility operates by compressing air with a light piston, which raises its pressure and temperature to a required level. Subsequently a valve is opened rapidly and the air is discharged over the set of test vanes/blades. The compression time of the facility is 1.0 s with a run time of 0.5 s when operating at a gas-to-wall temperature ratio of 1.5.

The NGV are manufactured from machinable glass (MACOR),[1] which has a low thermal diffusivity. Thin film heat transfer gages are painted onto the surface of the NGV and monitor the surface temperature during the run time of the ILPC. Derivation of the heat transfer coefficients from the surface temperature–time history is obtained by solving the one-dimensional transient heat conduction equation (Schultz and Jones, 1973). This solution is implemented via an analogue electrical circuit with a transfer function similar to the conduction equation (Oldfield et al., 1982). The output of the heat transfer circuit is then digitized on a DEC PDP-11/24 minicomputer. The present tests included thin film gages at 10, 50, and 90 percent spanwise locations with 12 on the suction side and 9 on the pressure side at each spanwise location. There were 35 gages on the inner wall and 39 gages on the outer wall. With this level of instrumentation it was possible to obtain a fairly accurate distribution of vane surface and endwall heat transfer. Accuracy of the present heat transfer data is within ±5 percent based upon isothermal wall conditions.

The NGV aerodynamics were measured with surface static pressure tappings. The inlet total pressure was measured with a rake of five pitot probes. Local surface isentropic Mach numbers could then be determined. The surface static pressures were monitored using the Scanivalve-ZOC[2] electronic data acquisition system. The response of the pressure tappings/pitot probe and Scanivalve system was around 5 ms, which was adequate to obtain a sufficient number of readings during the 0.5 s run time. The NGV was equipped with tappings at 5, 10, 15, 50, 85, 90, and 95 percent span with 13 on the suction side and 11 on the pressure side, at each spanwise location. The inner platform was instrumented with 47 pressure tappings and the outer platform contained 60 pressure tappings. The ac-

[1]MACOR: Trademark of Corning Glass, Corning, NY, USA.
[2]Scanivalve ZOC: Trademark of Scanivalve Corp., San Diego, CA, USA.

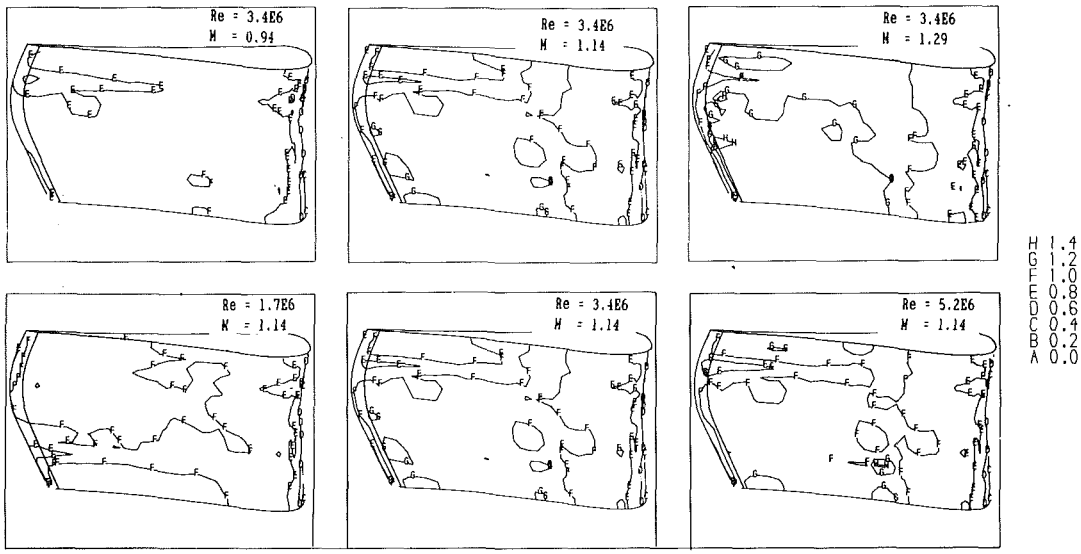

Fig. 5 Suction side Mach number

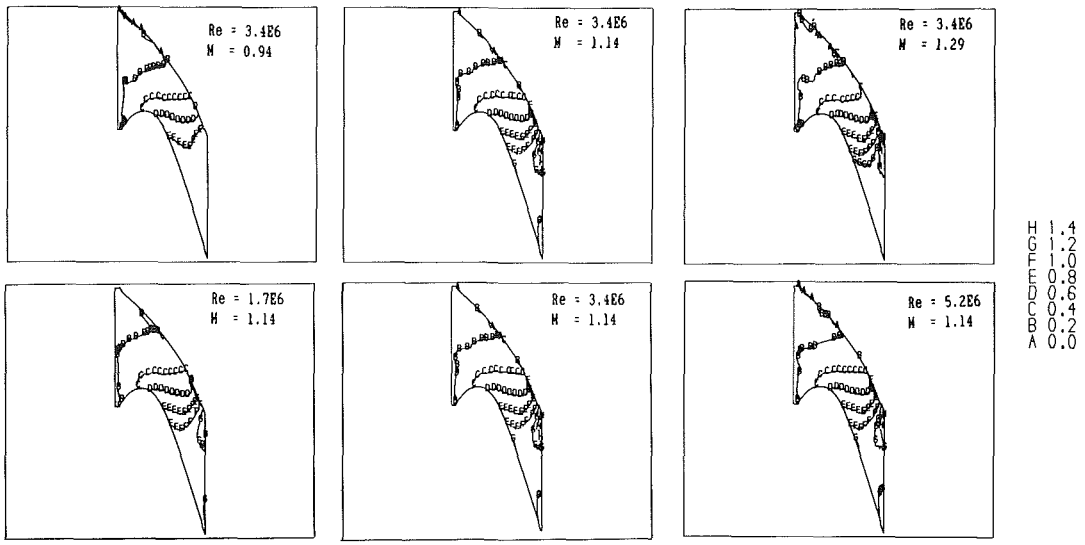

Fig. 6 Hub Mach number

curacy of the derived isentropic Mach number is placed at better than 0.1 percent for Mach numbers greater than 0.1, and at 10 percent for Mach numbers below 0.1. Figure 3 shows the instrumented NGV ring.

In performing the experiments, great care was taken to establish run-to-run repeatability. For all tests the exit Mach number was held to within 2 percent and exit Reynolds number to within 1 percent of the target value. Repeatability was found to be excellent with a maximum scatter band of 5 percent on Nusselt number and Mach number. The High Rim Speed Turbine (HRST) nozzle guide vane design value for the Reynolds number was 3.4E6 while design Mach number was 1.14, both being based on exit hub static pressure. At the design Reynolds number the NGV was operated at three exit Mach numbers of 0.94, 1.14, and 1.29. The vane was also tested at Reynolds numbers of 1.7E6, 3.4E6, and 5.2E6 at design Mach number. In all cases a turbulence grid was placed 4.5 axial chords upstream of the NGV leading edge giving an inlet turbulence of 6.5 percent as measured with a hot-wire anemometer. The gas-to-wall temperature ratio was held to 1.5, representative of modern day high-temperature turbines. Further details of the vane ring, instrumentation, operating conditions, and computations are given by Harasgama (1987).

Aerodynamic Results

Midspan Mach number distributions for the vane surfaces are shown on Fig. 4 for varying exit Mach number. It can be seen that at design exit Mach number (1.14) there is a weak shock at 65 percent axial chord. At the high exit Mach number condition (1.29) the shock is considerably stronger and peaks at 1.40. Pressure side aerodynamics are little influenced by changes in exit Mach number because the vane passage is choked.

The suction side isentropic Mach number distributions for all running conditions are shown on Fig. 5. It should be noted that the Mach numbers at the vane root are higher than those at the vane tip because radial equilibrium dictates a lower hub static pressure. These distributions indicate that the vane aerodynamics are not significantly influenced by changes in exit Reynolds number. However, changes in exit Mach number do change the distributions. In the case of highest exit Mach number, most of the vane root to midspan section is operating at a Mach number of 1.2–1.3.

Hub and casing Mach number distributions are shown in Figs. 6 and 7. Here also, the inner platform Mach numbers exceed those on the outer due to the radial equilibrium criteria.

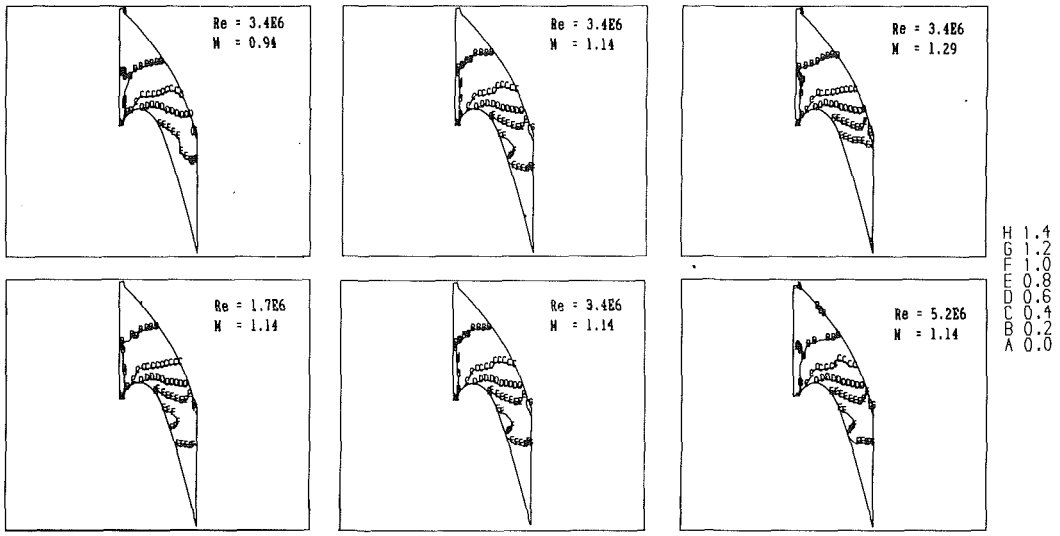

Fig. 7 Casing Mach number

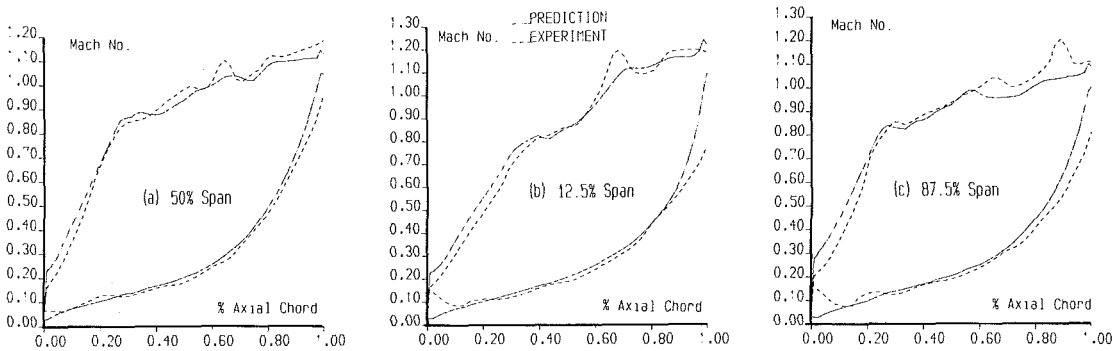

Fig. 8 Predicted and experimental Mach number

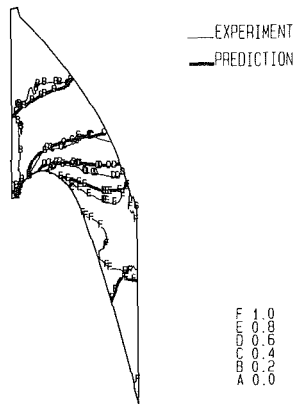

Fig. 9 Predicted and experimental Mach number on casing

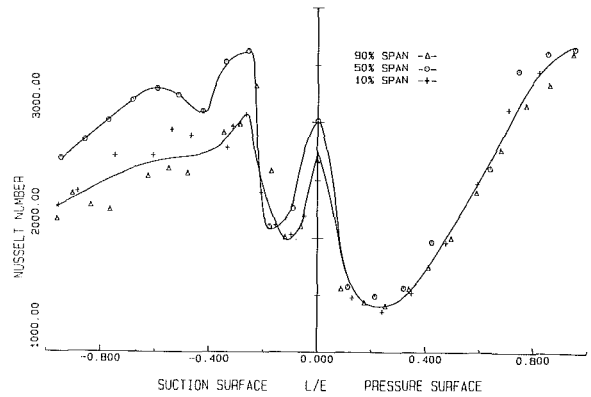

Fig. 10 Spanwise variation of heat load, Re = 3.4E6 and M = 1.14

Again, the influence of Reynolds number is only marginal. When operating at the high Mach number condition, the inner platform indicates a peak Mach number of 1.4 near the trailing edge region, while the outer platform only reaches 1.0.

The predictions of NGV aerodynamics were performed using a 3D inviscid flow solver (Denton, 1976, 1982). The code was run with 67 axial, 17 radial, and 17 blade-blade grid points. The 3D solution was run on an FPS-164 array processor attached to a VAX-11/780 computer. The computations took approximately eight hours CPU on the FPS-164. The solution was run with no inlet boundary layer in order to achieve a purely inviscid result. All computations were performed at the design Reynolds number and Mach number. The vane surface Mach number predictions are compared with experimental results in Fig. 8(*a*, *b*, & *c*). It can be seen that agreement between experiment and computation is very good in the midspan section (Fig. 8*a*). The weak shock at 65 percent axial chord is captured even though the predicted magnitude is slightly lower. The computations also show good agreement at 12.5 and 87.5 percent span. There is some disparity at 87.5 percent span around the 90 percent axial chord position where the experiment shows a high Mach number of 1.25. This is experimental interpolation error because there were no tappings after approximately 85 percent axial chord due to the thin trailing edge. The casing endwall Mach number distribution for experiment and computation is shown in Fig. 9; again the comparisons are very good. These results clearly validate the 3D

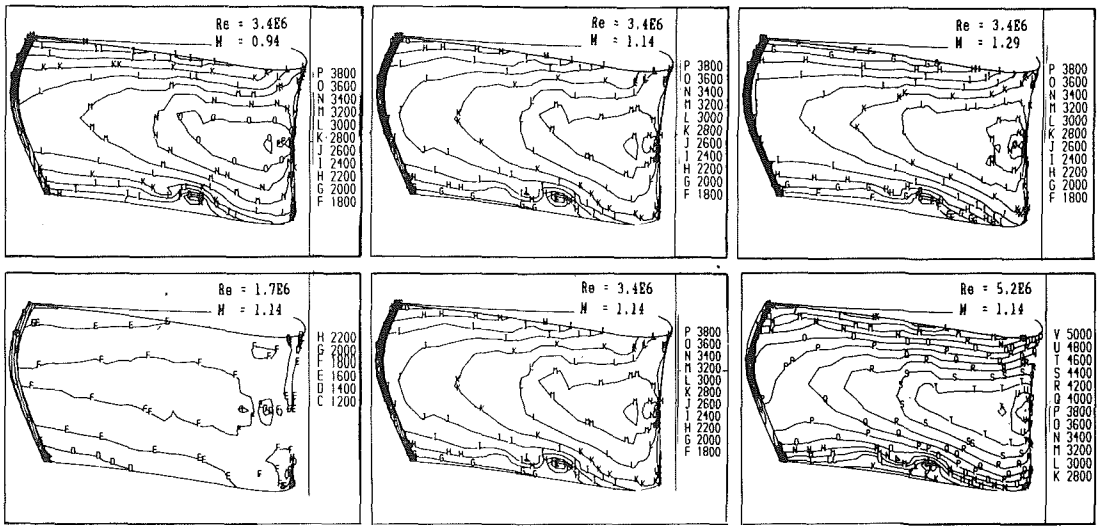

Fig. 11 Suction side Nusselt number

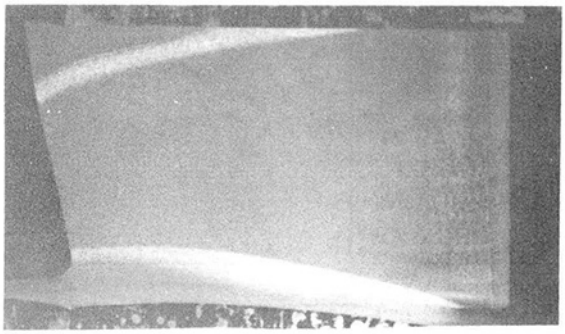

Fig. 12 Suction side flow visualization

inviscid code as a fast and accurate method for the aerodynamic design of turbine components. Any discrepancies may be attributed to viscous blockage effects, the relatively low grid resolution used for this prediction, and the numerical damping in the time-marching code.

Nusselt number distributions on the vane aerofoil surfaces for 10, 50, and 90 percent are shown in Fig. 10, at the design operating conditions. These data indicate that the Nusselt numbers at the root and tip are lower than those at midspan by some 20–30 percent. It should be noted that the thin film gages on the vane are approximately 10 mm long in the spanwise direction and would effectively integrate the data over its length. Hence, at each location the results represent an average over ±10 percent span about their nominal locations.

Nusselt number contours overlaid onto a 3D view of NGV suction side are presented in Fig. 11. It can be seen that there is a significant effect of the secondary flow on the heat transfer distributions. The midspan Nusselt numbers are consistently higher than elsewhere for all operating conditions. This is due to the endwall boundary layer migrating over the suction side caused by the secondary flow in the vane passage. This boundary layer will therefore be relatively thick with reduced enthalpy due to heat transfer taking place on the endwall before reaching the suction surface. Flow visualization performed on a similar vane in the ILPC (Fig. 12) indicates that the secondary flow is higher near the outer wall due to the radial pressure acting toward the turbine axis.

Variation of Reynolds number causes the Nusselt numbers over the entire surface to increase while the opposite happens for increasing Mach number. These results are in agreement with the work of previous authors, and recent work utilizing liquid crystal heat transfer measurements (Jones et al., 1989) shows similar distributions on the suction surfaces of turbine vanes. The pressure side Nusselt number distributions are not significantly affected by the running conditions. As Fig. 10 indicates, there is very little spanwise variation of Nusselt number on the pressure side. The highest heat transfer is located near the trailing edge due to the prolonged zone of transition, which will require a cooled design for an engine configuration.

Endwall heat transfer is affected by the inlet boundary layer, aerodynamic loading, and geometry of the vane passage. The present tests show that there are considerable differences in the inner and outer wall Nusselt numbers both in magnitude and distribution. Figure 13 shows the hub Nusselt numbers for all operating conditions. The low Reynolds number condition was run first and indicates high heat transfer at the leading edge of the vane/platform intersection. Unfortunately, some of the heat transfer gages near the leading edge were damaged at the higher Reynolds number conditions and this has led to a loss of resolution in this area. It is considered that had this not occurred, then all other conditions would also indicate high heat transfer in this region. As Reynolds number is increased the area of highest heat transfer moves from the pressure surface corner into the center of the vane passage. This feature also occurs when Mach number is increased. The results show that the Nusselt number increases with increasing Reynolds number and decreases with increasing Mach number as is the case on the aerofoil surfaces. The movement of the "hot patch" is caused by the different boundary layer growths upstream and within the vane passage due to changing Reynolds/Mach number. This, along with the radial pressure gradient, causes the horseshoe vortex to migrate toward the suction surface earlier, thereby starting the new endwall boundary layer earlier on in the vane passage. Low values of heat transfer are evident close to the suction side of the passage after about 60–70 percent axial chord. This is thought to be generated by the low-energy boundary layer moving across from the pressure side to the suction side, which has also been reported by Goldstein and Spores (1988).

Outer platform Nusselt numbers are presented in Fig. 14. The distributions are quite different from those on the inner wall. There is no evidence of high heat transfer at the leading edge due to the formation of the horseshoe vortex. It is possible that the radial pressure gradient has caused the vortex to be moved just off the surface, which would explain the absence of high heat transfer in the region. Some previous exploratory studies (York et al., 1981) on an annular cascade have also failed to locate high heat transfer on the casing/leading edge region. Flow visualizations performed on a similar vane in the

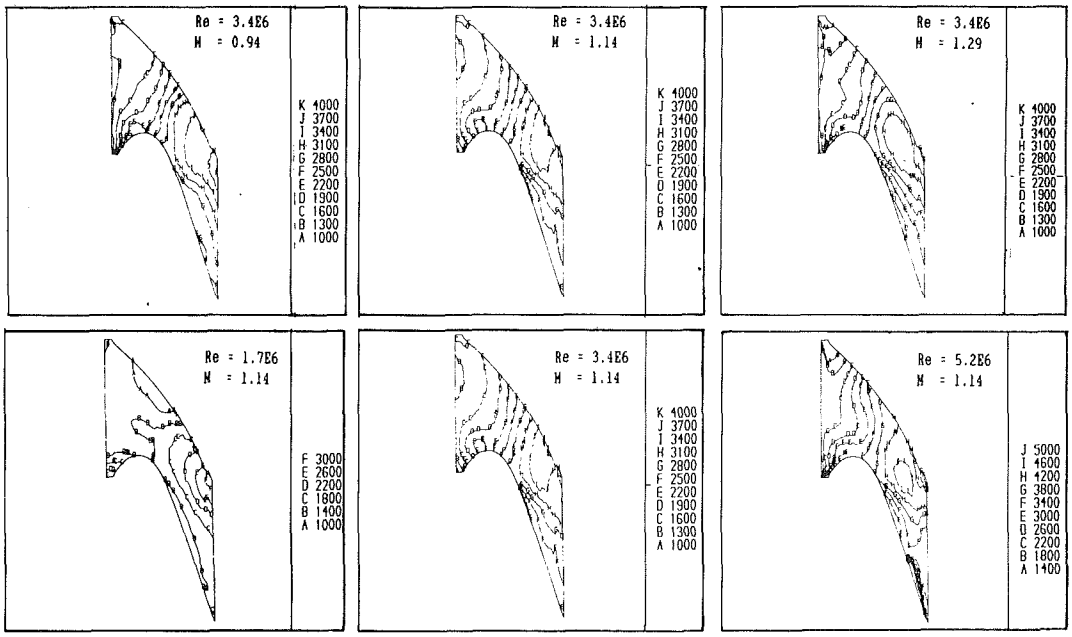

Fig. 13 Hub Nusselt number

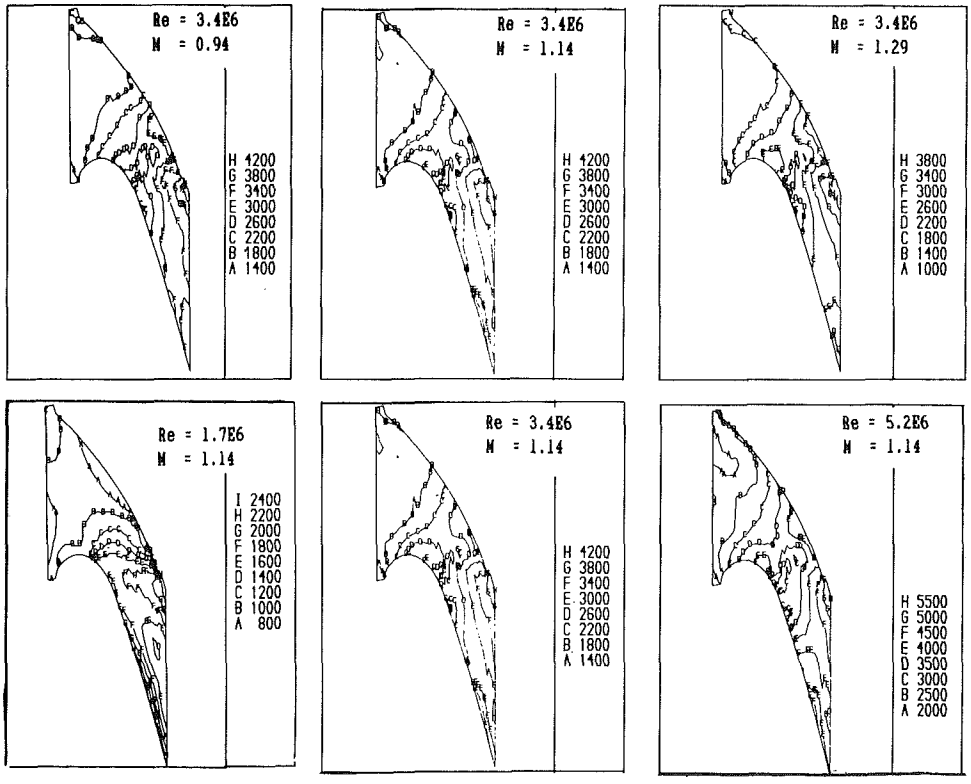

Fig. 14 Casing Nusselt number

Fig. 15 SS/casing flow visualization

ILPC show a considerable amount of secondary flow (Fig. 15). The Nusselt number distributions indicate the presence of high heat transfer near the pressure side trailing edge region for all running conditions. This is caused by the horseshoe vortex stripping off the incoming boundary layer and the start of a new boundary layer immediately downstream, as indicated by the flow visualization in Fig. 15. As the Reynolds number is increased the Nusselt number follows suit. Also, a new region of high heat transfer appears at approximately 50 percent axial chord near the pressure side and, at the highest Reynolds number, extends across most of the platform. This feature also

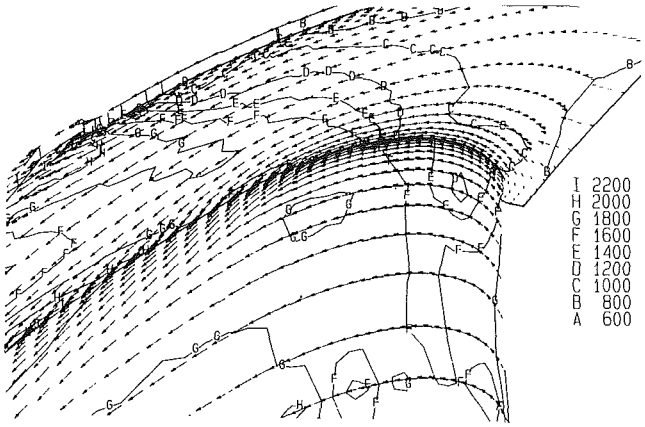

Fig. 16 SS/casing predicted flow vectors and experimental Nusselt number

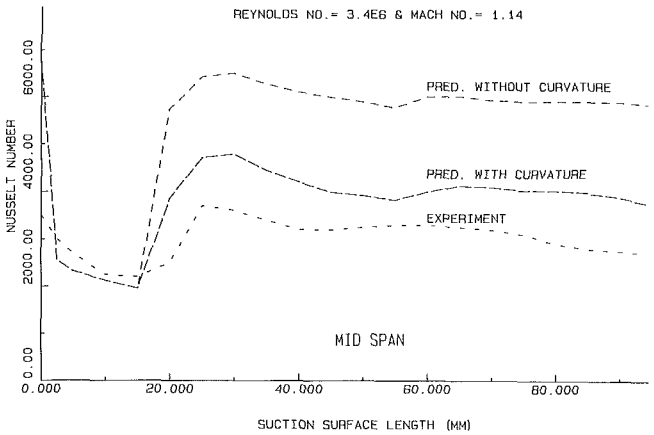

Fig. 17 Experimental and predicted Nusselt number

occurs as the Mach number is increased, although in this case the heat transfer is reduced in magnitude.

A 3D Navier–Stokes flow solver (Dawes, 1986) has been used to calculate the secondary flows within the NGV passage. The code was run with 25 radial, 83 axial, and 23 blade-to-blade grid points. The mixing length turbulence model is utilized with near-wall Van Driest damping and a laminar sublayer model is also incorporated. The STAN5 code was run on inner and outer annuli from 15 axial chords upstream to the vane leading edge and the predicted boundary layers used as input to the 3D Navier–Stokes code. Figure 16 is a perspective view of the outer wall and suction surface with computed flow vectors and experimental Nusselt number contours. The comparison with the flow visualization of Fig. 15 is very good. The prediction captures the migration of endwall fluid onto the suction surface and shows that the "break" in the Nusselt number distribution ties up with the position at which the endwall flow first reaches the suction surface. This is also corroborated by the flow visualization.

The midspan Nusselt numbers on the suction surface at design operation have been predicted using a modified version of the STAN5 boundary layer code (Crawford and Kays, 1976). The code has been modified as recommended by Gaugler (1981) for calculating the onset and length of transition due to free-stream turbulence. The inlet turbulence level was set to 6.5 percent and the mixing length model was used with Van Driest damping in the near wall region. Results are presented in Fig. 17 for the experiment and predictions with and without suction surface curvature. It will be noted that the experimental values are around 50 percent below the computation done with zero curvature. The computation with curvature shows closer agreement with the experimental result, the disparity being around 25 percent. This is to be expected because convex curvature tends to suppress shear stress in the boundary layer leading to lower heat transfer (Simon et al., 1982). Transition location (Seyb, 1972) and length (Chen and Thyson, 1971) are quite well predicted in this case.

Conclusions

Detailed heat transfer and aerodynamics measurements have been made on a fully annular ring of nozzle guide vanes at engine representative operating conditions. The main conclusions may be summarized as follows:

- Vane surface aerodynamics indicate that the suction side is operating at the designed Mach numbers and that agreement with 3D inviscid computations is very good.
- Detailed Mach number distributions are presented on the hub and casing endwalls. These indicate higher Mach numbers on the hub as dictated by radial equilibrium criteria. Again, agreement with the 3D inviscid solution is very good.
- Nusselt number distributions on the aerofoil surfaces show the presence of secondary flows on the suction side. Pressure side heat transfer indicates a prolonged transition with the highest heat load at the trailing edge. Flow visualizations also show that secondary flow on the suction side is higher at the casing than at the hub due to the radial pressure gradient.
- Inner platform Nusselt number distributions are strongly dependent on Reynolds number and Mach number. The area of high heat transfer near the pressure side trailing edge moves into the center of the platform with increasing Reynolds number and Mach number.
- Nusselt number distribution on the outer platform is also dependent on Reynolds and Mach numbers. As Reynolds and Mach numbers are increased a new region of high heat transfer appears close to the pressure side at approximately 50 percent axial chord. This region spreads across most of the platform for the high Mach number and Reynolds number condition.
- Analysis using a 3D viscous flow solver shows good agreement with endwall/suction side flow visualizations. Predicted flow vectors agree with the migration of endwall fluid onto the vane suction surface as indicated by experimentally derived Nusselt number distributions.
- Heat transfer calculations with the STAN5 finite difference, boundary layer code show convex curvature to have a major effect on the suction side. Predictions incorporating surface curvature are around 25 percent higher than experiment. Transition location and length are quite well predicted. Further work is required to obtain more accurate predictions of heat transfer.

Acknowledgments

Thanks are due to Mr. K. J. Walton who maintained the test rig and to the late Professor D. L. Schultz and the heat transfer group at Oxford University whose help has been invaluable.

References

Boyle, R. J., and Hoose, K. V., 1989, "Endwall Heat Transfer in a Vane Cascade Passage and in a Curved Duct," ASME Paper No. 89-GT-90.

Boyle, R. J., and Russell, L. M., 1990, "Experimental Determination of Stator Endwall Heat Transfer," ASME JOURNAL OF TURBOMACHINERY, Vol. 112, pp. 547–558.

Brooks, A. J., Colbourne, D. E., Wedlake, E. T., Jones, T. V., Oldfield, M. L. G., Schultz, D. L., and Loftus, P. J., 1985, "The Isentropic Light Piston Cascade Facility at RAE Pyestock," in: *Proceedings—AGARD Conference on Heat Transfer and Cooling in Gas Turbines*, May, Bergen, Norway, AGARD-CP-390.

Chen, K. K., and Thyson, N. A., 1971, "Extension of Emmons' Spot Theory to Flows on Blunt Bodies," *AIAA J.*, Vol. 9, No. 5.

Crawford, M. E., and Kays, W. M., 1976, "STAN5: A Program for Numerical Computations of Two Dimensional Internal and External Boundary Layers," NASA CR-2742.

Dawes, W. N., 1986, "A Numerical Method for the Analysis of Three-Dimensional Viscous Compressible Flow in Turbine Cascades: Application to Secondary Flow Development in a Cascade With and Without Dihedral," ASME Paper No. 86-GT-145.

Denton, J. D., 1976, "Extension of the Finite Area Time Marching Method to Three-Dimensions," Von Karman Institute for Fluid Mechanics, Lecture Series 84.

Denton, J. D., 1983, "An Improved Time-Marching Method for Turbomachinery Flow Calculation," ASME *Journal of Engineering for Power*, Vol. 105, pp. 514–524.

Gaugler, R. E., 1981, "Some Modifications to, and Operational Experience With, the Two-Dimensional, Finite-Difference Boundary Layer Code, STAN5," ASME Paper No. 81-GT-89.

Gaugler, R. E., and Russell, L. M., 1983, "Comparison of Visualized Turbine Endwall Secondary Flows and Measured Heat Transfer Patterns," NASA Technical Memorandum TM-83016.

Gladden, H. J., and Simoneau, R. J., 1988, "Review and Assessment of the Database and Numerical Modeling for Turbine Heat Transfer," in: *Towards Improved Durability in Advanced Aircraft Engine Hot Sections*, D. E. Sokolowski, ed., ASME, New York.

Goldstein, R. J., and Spores, R. A., 1988, "Turbulent Transport on the Endwall in the Region Between Adjacent Turbine Blades," ASME *Journal of Heat Transfer*, Vol. 110, pp. 862–869.

Graziani, R. A., Blair, M. F., Taylor, J. R., and Mayle, R. E., 1979, "An Experimental Study of Endwall and Airfoil Surface Heat Transfer in a Large Scale Turbine Blade Cascade," ASME Paper No. 79-GT-99.

Harasgama, S. P., 1987, "Heat Transfer and Aerodynamic Characteristics of the High Rim Speed Turbine Vane as Tested in the ILPC," RAE Technical Report TR87055.

Jones, T. V., Harvey, N. W., Ireland, P. T., and Wang, Z., 1989, "Detailed Heat Transfer Measurements in Nozzle Guide Vane Passages in Linear and Annular Cascades in the Presence of Secondary Flows," presented at the AGARD Conference on Unsteady Aerodynamic Phenomena & Secondary Flows in Turbomachines, Luxembourg, Aug. 28–Sept. 1.

Kingcombe, R. C., Harasgama, S. P., Leversuch, N. P., and Wedlake, E. T., 1989, "Aerodynamic and Heat Transfer Measurements on Blading for a High Rim-Speed Transonic Turbine," ASME Paper No. 89-GT-228.

Oldfield, M. L. G., Burd, H. J., and Doe, N. G., 1982, "Design of Wide Bandwidth Analogue Circuits for Heat Transfer Instrumentation in Transient Wind Tunnels," in: *Heat and Mass Transfer in Rotating Machinery*, D. E. Metzger, ed., Hemisphere Pub. Corp., New York.

Schultz, D. L., Jones, T. V., and Hendley, A. D., 1973, "On the Flow in an Isentropic Light Piston Tunnel," ARC, R&M 3731.

Schultz, D. L., and Jones, T. V., 1973, "Heat Transfer Measurements in Short Duration Hypersonic Facilities," AGARD-AG-165.

Seyb, J., 1972, "The Role of Boundary Layers in Axial Flow Turbomachines and Prediction of Their Effects," AGARD-AG-164.

Simon, T. W., Moffat, R. J., Johnston, J. P., and Kays, W. M., 1982, "Turbulent Boundary Layer Heat Transfer Experiments: Convex Curvature Effects Including Introduction and Recovery," NASA CR-3510.

York, R. E., Hylton, L. D., Mihelc, M. S., and Turner, E. R., 1981, "Experimental Investigations of Turbine Endwall Heat Transfer," Final reports I–III, Aero Propulsion Labs., Wright Patterson Air Force Base, AFWAL-TR-81-2077.

York, R. E., Hylton, L. D., and Mihelc, M. S., 1984, "An Experimental Investigation of Endwall Heat Transfer and Aerodynamics in a Linear Vane Cascade," ASME *Journal of Engineering for Gas Turbines and Power*, Vol. 106, pp. 159–167.

Navier-Stokes Analysis of Turbine Blade Heat Transfer

R. J. Boyle
NASA Lewis Research Center,
Cleveland, OH 44135

Comparisons with experimental heat transfer and surface pressures were made for seven turbine vane and blade geometries using a quasi-three-dimensional thin-layer Navier-Stokes analysis. Comparisons are made for cases with both separated and unseparated flow over a range of Reynolds numbers and free-stream turbulence intensities. The analysis used a modified Baldwin-Lomax turbulent eddy viscosity model. Modifications were made to account for the effects of: (1) free-stream turbulence on both transition and leading edge heat transfer; (2) strong favorable pressure gradients on relaminarizations; and (3) variable turbulent Prandtl number on heat transfer. In addition, the effect on heat transfer of the near-wall model of Deissler is compared with the Van Driest model.

Introduction

Accurate predictions of turbine blade heat transfer are important, especially as turbine inlet temperature increases. One approach to predicting blade heat transfer is to use a boundary layer analysis such as the STAN5 analysis of Crawford and Kays (1976). However, this approach cannot be used to predict heat transfer beyond the point of separation. Also, because of the necessity of specifying a starting condition with boundary layer analyses, the heat transfer predictions in the leading edge region may be in error. An alternate approach to predicting turbine blade heat transfer, especially useful when separation occurs, is the use of Navier-Stokes analysis. Both two- and three-dimensional Navier-Stokes analyses have been developed. A quasi-three-dimensional analysis was developed by Chima (1986), and a three-dimensional analysis was described by Chima and Yokota (1988). Davis et al. (1988) discussed the prediction of compressor cascade performance using a two-dimensional Navier-Stokes analysis. Hah (1989) and Yang et al. (1985) give heat transfer predictions for a turbine rotor and vane, respectively. The emphasis in these analyses has been on obtaining accurate aerodynamic results. This paper discusses the results of turbine blade heat transfer predictions using the quasi-three-dimensional, thin-layer Navier-Stokes analysis developed by Chima (1986). The modifications described by Chima et al. (1987) were used.

The analysis developed by Chima incorporated the Baldwin and Lomax (1978) turbulence model. This model has several attractive features from a computational standpoint. However, the model does not account for several factors known to influence turbine blade heat transfer. Among these factors are: (1) the effect of free-stream turbulence on leading edge heat transfer and on the location of transition, (2) the effect of boundary layer relaminarization on heat transfer, and (3) the effect of a variable turbulent Prandtl number. The turbulence model was modified to include models for these various effects. Also, the near-wall damping model of Deissler (1955) was compared with Van Driest's model.

The solution procedures for Navier-Stokes analyses differ from boundary layer analyses in several respects. Before alternate models can be evaluated, it is necessary to verify that other factors do not cloud the comparisons. In boundary layer analyses all of the solution domain is confined to the boundary layer region. For Navier-Stokes analyses, however, only a small fraction of the blade-to-blade grid may be within the boundary layer regions. Also, the boundary layer analyses are marching-type analyses, while Navier-Stokes analyses require the solution of the entire flow field in an iterative manner. One purpose of this paper is to show results for different grid and iteration parameters to demonstrate the values needed so that comparisons are independent of these parameters.

The appropriateness of the heat transfer models is shown by comparisons with experimental data. Comparisons were made for each of the three blade rows in the stage-and-a-half data of Dring et al. (1986a-d), which consisted of a summary report and three volumes of tabulated data. Comparisons were also made with the experimental data for the two stators of Hylton et al. (1983), as well as with the data of Hippensteele et al. (1986, 1985) for a stator and rotor. These sources of data result in comparisons over a wide range of Reynolds numbers and turbulence intensities. The Navier-Stokes analyses have the ability to calculate heat transfer when there is separation. Therefore, comparisons are made for cases with attached flows and for cases with separated flows. With respect to the thermal modeling there are three objectives. The first is to show that the accepted models for boundary layer analyses are appropriate for Navier-Stokes analyses as well. The second is to choose a model that gives reasonably good agreement for the cases examined. Since improved models for turbine blade heat transfer are continually being developed, it is not the purpose of this paper to demonstrate that a particular model gives good agreement with data for every case. However, to demonstrate the aspects of the Navier-Stokes heat transfer predictions it is necessary to choose a reasonably accurate model. The third objective is to show the effects of various

Contributed by the International Gas Turbine Institute and presented at the 35th International Gas Turbine and Aeroengine Congress and Exposition, Brussels, Belgium, June 11-14, 1990. Manuscript received by the International Gas Turbine Institute January 10, 1990. Paper No. 90-GT-42.

assumptions on turbine blade heat transfer. Since some of these assumptions show better agreement than the base-case model, a recommendation is made for the appropriate prediction methodology.

Description of Analysis

Basic Flow Analysis. The analysis used the flow solver developed by Chima, which is for either inviscid or viscous quasi-three-dimensional flow, wherein the variation of the stream sheet thickness is accounted for. The variation in stream sheet thickness is determined from a hub-to-shroud flow analysis using a program such as MERIDL (Katsanis and McNally, 1977). The viscous analysis of Chima (1986) employs the thin-layer Navier–Stokes assumptions, wherein the streamwise derivatives of the viscous terms are neglected. A four-stage Runge–Kutta algorithm with residual smoothing and variable time steps is used. The equations used are given by Chima (1986). The heat transfer predictions are dependent on an effective viscosity, μ_{eff}, and an effective Prandtl number, Pr_{eff}. These quantities are given by:

$$\mu_{\text{eff}} = \mu_{\text{laminar}} + \mu_{\text{turbulent}} = \rho(\nu + \epsilon_M) \tag{1}$$

$$\text{Pr}_{\text{eff}} = \frac{1 + \left(\frac{\epsilon_M}{\nu}\right)}{1/\text{Pr} + \left(\frac{\epsilon_M}{\nu}\right)/\text{Pr}_t} \tag{2}$$

The following description focuses on the calculation of $\mu_{\text{turbulent}}$, and the turbulent Prandtl number, Pr_t.

Baldwin–Lomax Turbulence Model. This model is a two-layer algebraic eddy viscosity model. The eddy viscosity is found from:

$$\mu_t = \begin{cases} (\mu_t)_{\text{inner}} & \text{if } y \le y_{\text{crossover}} \\ (\mu_t)_{\text{outer}} & \text{if } y > y_{\text{crossover}} \end{cases} \tag{3}$$

where $y_{\text{crossover}}$ is given by the minimum value of y for which $(\mu_t)_{\text{inner}} = (\mu_t)_{\text{outer}}$. The inner and outer values are:

$$(\mu_t)_{\text{inner}} = \rho(\kappa y(1 - e^{-y^+/A^+}))^2 |\omega| \tag{4}$$

$$(\mu_t)_{\text{outer}} = C_{\text{outer}} \rho F_{\text{WAKE}} F_{\text{KLEB}} \tag{5}$$

$A^+ = 26$, and $C_{\text{outer}} = 0.0269$. F_{WAKE} is given by:

$$F_{\text{WAKE}} = \min(y_{\max} F_{\max}, 0.25 y_{\max} v_{\text{DIF}}^2 / F_{\max}) \tag{6}$$

The quantities $y_{\max}$ and $F_{\max}$ are found from:

$$F(y) = y|\omega|(1 - e^{-y^+/A^+}) \tag{7}$$

$y_{\max}$ is the y value for which $F(y)$ is a maximum. F_{KLEB} is given by:

$$F_{\text{KLEB}} = [1 + 5.5(0.3y/y_{\max})^6]^{-1} \tag{8}$$

The term v_{DIF} is given by:

$$v_{\text{DIF}} = (\sqrt{v_\theta^2 + v_m^2})_{\max} - (\sqrt{v_\theta^2 + v_m^2})_{\min} \tag{9}$$

Except for wakes, the second term is zero.

When $(\mu_t)_{\text{MAX IN PROFILE}}/\mu_\infty \ge 14$, transition occurs. μ_∞ is the free-stream molecular viscosity. The turbulent Prandtl number $\text{Pr}_t = 0.9$.

Turbulent Prandtl Number Model. As an alternative to the constant Pr_t used in the Baldwin–Lomax model, Crawford and Kays (1975) give Pr_t as a function of the distance from the wall. This model is referred to as the Kays and Moffat model, and expresses Pr_t as:

$$\text{Pr}_t = \left[\frac{0.5}{\text{Pr}_{t\infty}} + \frac{0.2\epsilon_M \text{Pr}}{\nu\sqrt{\text{Pr}_{t\infty}}} - 0.04\left(\frac{\epsilon_M \text{Pr}}{\nu}\right)^2 \left(1.0 - e^{-(5\nu/\epsilon_M/Pr/\sqrt{\text{Pr}_{t\infty}})}\right)\right]^{-1} \tag{10}$$

The recommended value for $\text{Pr}_{t\infty}$ is 0.86. Figure 1 shows the variation of Pr_t with distance from the wall, y^+, for a flat plate boundary layer. Pai and Whitelaw (1971) used a linear variation in Pr_t with a value of 1.75 at the wall and decreasing to 0.5 at the edge of the boundary layer. The model of Kays and Moffat was used because Pr_t varied smoothly into the commonly used free-stream value.

Eddy Viscosity Model. In the near-wall region the most commonly used eddy viscosity model is the Van Driest model. This model is incorporated into the Baldwin–Lomax model, and is given by equation (4). Other models have been proposed for the near-wall region (White, 1974). One of these is Deissler's (1955), where the eddy viscosity is given as:

Nomenclature

A = area
A^+ = damping coefficient
C = chord
C_f = friction factor
C_p = specific heat at constant pressure
d = leading edge diameter
k = thermal conductivity
l = length scale
m = meridional direction
Nu = Nusselt number
P = pressure
P^+ = pressure gradient = $(\nu U_e^3/\rho)(C_f/2)^{3/2}\partial P/\partial s$
Pr = Prandtl number
Q = dynamic head = $\rho U^2/2$
Re = unit Reynolds number, subscript gives length
r = radius
s = surface distance
s^+ = normalized surface distance = $(sU_e/\nu)\sqrt{C_f/2}$
St = Stanton number = $k|\partial T/\partial y|_w/[(\rho U)_{IN} C_p(T'_{IN} - T_w)]$
T = temperature
T_u = turbulence intensity
U = inviscid velocity
v = velocity in flow solution
x = axial direction
Y = pressure coefficient = $(P'_{IN} - P)/Q_{IN}$
y = perpendicular distance from surface
y^+ = normalized surface distance = $(yU_e/\nu)\sqrt{C_f/2}$
γ_t = intermittency factor
δ = full boundary layer thickness
ϵ_M = eddy viscosity
η = direction outward from blade
θ = momentum thickness
κ = Von Karman's constant = 0.4
λ = momentum thickness pressure gradient parameter
μ = dynamic viscosity
ν = kinematic viscosity
ξ = direction around blade
ρ = density
ϕ = ratio of axial velocity to mean blade speed
ω = vorticity = $\partial v/\partial y$

Subscripts

e = edge of boundary layer
EX = exit
f = end of transition
i = start of transition
IN = inlet
m = meridional
s = distance along blade
t = turbulent
x = axial
w = wall
θ = tangential direction or momentum thickness

Superscript

$'$ = total conditions

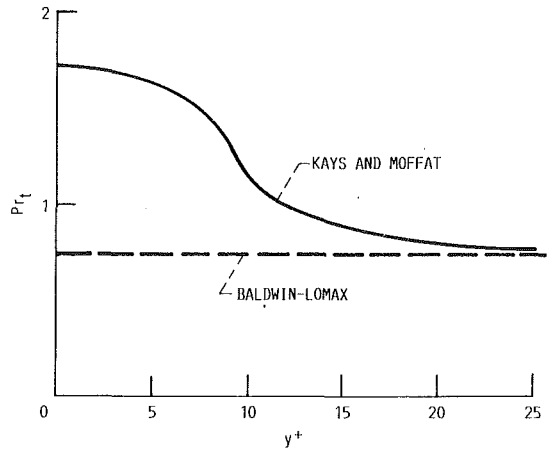

Fig. 1 Variation of turbulent Prandtl number with distance from the wall for flow over a flat plate

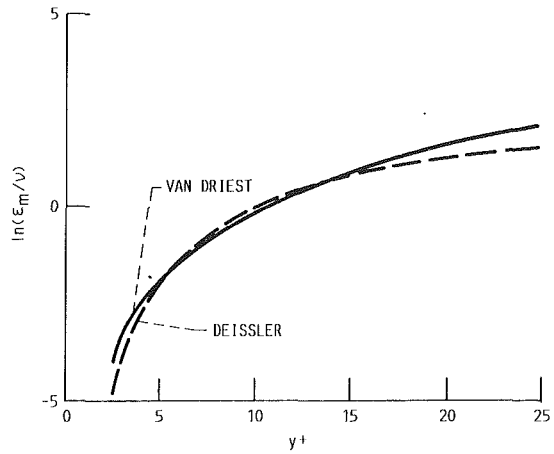

Fig. 2 Comparison of Van Driest and Deissler eddy viscosity model in near-wall region

$$\epsilon_M = n^2 vy(1 - e^{-n^2 vy/\nu}) \tag{11}$$

where $n = 0.124$. The form of equations (4) and (11) is very different. Away from the wall, the eddy viscosity becomes proportional to $y^2|\omega|$ in the Van Driest model. In Deissler's model the ratio of eddy to molecular viscosity is proportional to the Reynolds number based on distance from the wall. Figure 2 shows the similarity of the two models for a flat plate boundary layer.

Near-Wall Damping Model. In the Baldwin–Lomax model $A^+ = 26$, while in both the Kays and Moffat (1975) and the Cebeci–Smith (1974) turbulent boundary layer models A^+ is a function of the free-stream pressure gradient, P^+. The Kays and Moffat model gives:

$$A^+ = 25/(C_{KM}P^+ + 1) \tag{12}$$

$C_{KM} = 30.2$ for $P^+ \leq 0.0$, otherwise $C_{KM} = 20.6$. The Cebeci–Smith model gives:

$$A^+ = 26/\sqrt{(11.8P^+ + 1)} \tag{13}$$

Figure 3 gives the damping coefficient as a function of the pressure gradient for the three models. The greatest differences among the models occur for favorable pressure gradients. When $A^+ \to \infty$, the boundary layer completely relaminarizes. The Kays and Moffat model shows complete relaminarization occurring at lower favorable pressure gradients than the Cebeci–Smith model.

Crawford and Kays (1976) recommend that a lag equation be used for the pressure gradient value used to determine the damping coefficient. They recommended the form suggested by Jones and Launder (1969):

$$dP^+/ds^+ = -(P^+ - P^+_{eq})/C \tag{14}$$

Here P^+_{eq} is equilibrium value for the pressure gradient, and C has a recommended value of 4000. The streamwise distance between nodes in a Navier–Stokes analysis is much greater than the marching distance used in a boundary layer analysis. This can result in large point-to-point variations in the pressure gradient. The lag equation smooths out these variations, and was always used when A^+ was allowed to vary.

Free-stream Turbulence Model. The strong favorable free-stream pressure gradients near the leading edge result in laminar flow, even with high free-stream turbulence. The free-stream turbulence increases the laminar heat transfer. The model of Smith and Kuethe (1966) was incorporated into the analysis to account for this effect. The equation for the turbulent viscosity is:

$$\epsilon_M = 0.164 yTu_\infty U_\infty \tag{15}$$

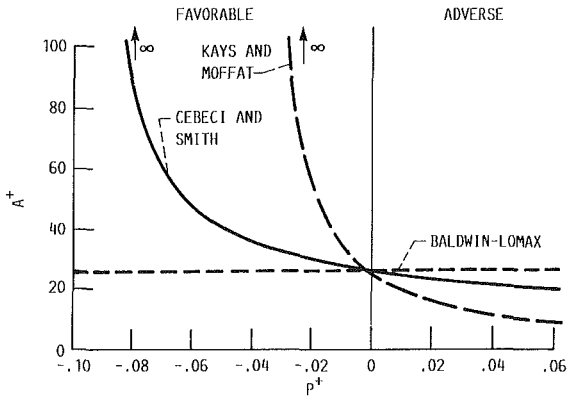

Fig. 3 Comparison of Kays and Moffat, Cebeci-Smith, and Baldwin-Lomax damping coefficients models as a function of pressure gradient

This equation was developed for the heat transfer analysis of cylinders in crossflow, and here U_∞ refers to the upstream velocity. One difficulty with applying this model in a computational scheme is that the eddy viscosity increases continually with the distance from the blade. The model of Forrest (1977) can be used to overcome this difficulty. This model gives:

$$\epsilon_M = C_F l Tu_\infty U_\infty \tag{16}$$

where the mixing length, l, is defined as

$$l = \min(\kappa y, \quad 0.086\delta) \tag{17}$$

Since one of the attractive features of the Baldwin–Lomax turbulence model is that boundary layer parameters are not calculated, the model of Forrest was implemented by calculating the mixing length l in the same manner as in the Baldwin–Lomax model. This was done by letting $l = \kappa y$ when the Baldwin–Lomax eddy viscosity was calculated from the inner formulation. When the outer formulation was used, the mixing length in Forrest's model was either held constant at the crossover value or set to zero. The coefficient C_F is found from:

$$C_F = \min(0.1875|\lambda|/(0.25|\lambda| + 0.01), \ 0.75) \tag{18}$$

where

$$\lambda = \frac{\theta^2}{\nu}\frac{dU_e}{ds} \tag{19}$$

The calculation of ϵ_M due to free-stream turbulence was modified from the original form in that it was applied only when the flow was laminar. Otherwise, the analysis would give sig-

nificantly increased heat transfer due to free-stream turbulence even for fully turbulent flow.

The momentum thickness is not calculated directly. Rather, Twaites' method, as given by White (1974), is used. The momentum thickness at a distance s_1 along the blade surface is given by:

$$\theta^2(s_1) = \frac{0.45\nu}{U_e^6(s_1)} \int_0^{s_1} U_e^5 ds \tag{20}$$

The origin in this calculation is taken as the geometric stagnation point.

Transition Model. In the Baldwin-Lomax transition model, the pressure gradient does not affect transition, except insofar as it affects the vorticity. Perhaps more importantly, the effect of free-stream turbulence is also not accounted for. The choice of transition models to be included in the calculation procedure was limited to those that explicitly accounted for the effects of both free-stream turbulence and pressure gradient. The model of Dunham (1972) was chosen. This model gives the start of transition $\mathrm{Re}_{\theta i}$ as:

$$\mathrm{Re}_{\theta i} = (0.27 + 0.73e^{-80Tu})\,(550 + 680/(1-D)) \tag{21}$$

with D given as a function of the pressure gradient parameter λ:

$$D = \min(21\lambda - 100Tu,\ 0.75) \tag{22}$$

where λ is given by equation (19). Comparisons for a range of λ and Tu values showed Dunham's model to give lower $\mathrm{Re}_{\theta i}$ values than the model of Seyb (1977). Dunham's model gave nearly the same values when compared with the model of Abu-Ghannam and Shaw (1980). Dunham's model was chosen for implementation over the other models because the pressure gradient enters in a linear fashion, and is less likely to result in oscillations in the transition location as the calculations progress.

Even the approximate calculation of the momentum thicknesses can cause difficulties, especially near the stagnation point. The edge velocity, U_e is calculated from the local static and free-stream total pressures. If stagnation occurs other than at the geometric stagnation point, $U_e \to 0$ and $\theta \to \infty$. Consequently, transition would occur at this point. To prevent this, transition was not allowed to occur within a small fraction (about 10 percent) of the surface distance from the stagnation point.

Transition length is determined from the Dhawan and Narasimha (1958) model. The end of transition is given by:

$$\mathrm{Re}_{Sf} = \mathrm{Re}_{Si} + c\mathrm{Re}_{Si}^{0.8} \tag{23}$$

The coefficient c has a value of 5.0 for a transition length between 25 and 75 percent intermittency. For the full intermittency range between 0 and 99 percent, the coefficient c increases by a factor of 3.36. The intermittency factor γ_t of Abu-Ghannam and Shaw (1980) is used:

$$\gamma_t = 1 - e^{-4.65((\mathrm{Re}_S - \mathrm{Re}_{Si})/(\mathrm{Re}_{Sf} - \mathrm{Re}_{Si}))^3} \tag{24}$$

Calculation Procedure

The GRAPE code of Sorenson (1980) was used to generate C-grids for the analysis. The location of the intersection of grid lines with the inner and outer boundaries was controlled to give minimum shear in regions of interest. For example, it was often desired to have near-normal grids on the rearward portion of the suction surface. However, because of the large amount of turning, a near-normal grid could not be generated over the entire blade surface and still maintain grid-line periodicity on the outer boundary. Fortunately, the presence of sheared grid lines did not appear to affect the flow solutions adversely.

The thick trailing edges made it necessary to use trailing edge cusps. Without a cusp, there was a large loss in total pressure in the trailing edge region, even for the inviscid calculations. Inviscid calculations were used to determine the shape of the cusp. The cusp shape was adjusted to give no net loading over the cusp region beyond the physical end of the turbine blade.

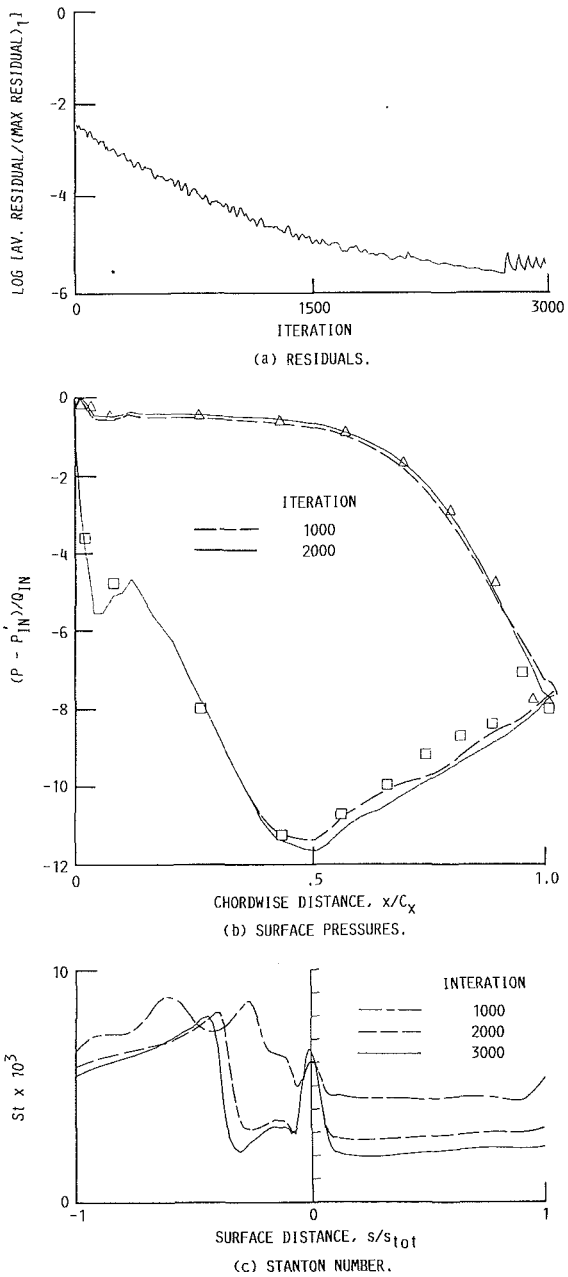

Fig. 4 Convergence history for a sample case

After the Euler solution was obtained, the Navier–Stokes solution was calculated for the same blade geometry, but with $y^+ \approx 1$ for the first node from the wall. For the Euler calculation the spacing of the first node from the wall increased about an order of magnitude to avoid an unacceptably large total pressure loss.

Steady state was reached in 3000 to 5000 time cycles. Residuals were reduced by at least two orders of magnitude. Figure 4 shows the convergence history as well as pressure distributions and heat transfer results for a typical case. Reductions in residuals by two orders of magnitude were needed for converged heat transfer results, but fewer cycles were needed for pressure.

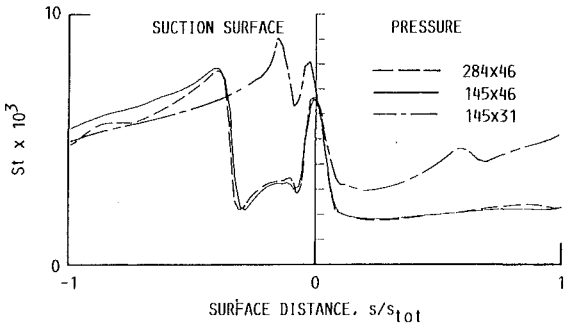

Fig. 5 Comparison of Stanton number distribution for different grids

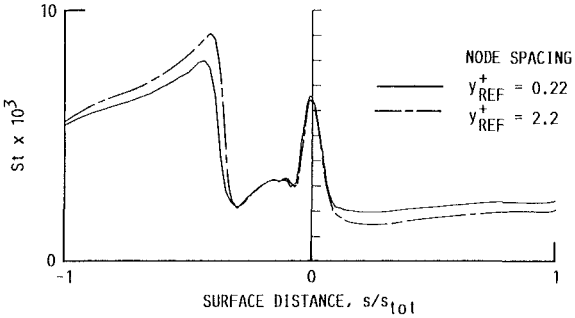

Fig. 6 Effect of first node spacing on surface heat transfer

Figure 5 shows converged results for three different grids. Grids of 145 × 46, 284 × 46, and 145 × 31 were used. The coarser grid in the ξ direction, 145 × 46, gave satisfactory agreement with the finer grid, 284 × 46, in this direction. However, the results were sensitive to the number of grid lines in the η direction. The number of grid lines in the ξ direction was determined by the desire to resolve the surface pressure distribution. When strong surface pressure gradients were encountered, a large number of ξ grid lines were used.

Figure 6 shows heat transfer results as a function of the distance of the first node from the wall, y_1^+, expressed in terms of y_{REF}^+. This value is calculated prior to the viscous calculation, where $y_{REF}^+ = (y_1 U_e/\nu)\sqrt{C_f/2}$. The value of C_f is obtained from a flat plate correlation: $C_f/2 = 0.0287\ (sU_e/\nu)^{-0.2}$, to give:

$$y_{REF}^+ = 0.17 y_1 \mathrm{Re}^{0.9}/s^{0.1} \tag{25}$$

The largest value of the unit Reynolds number, typically the one based on exit conditions, gives the largest value for y_{REF}^+. This, in turn, gives a conservative estimate of y_1^+. y_{REF}^+ is only slightly affected by the choice of s, and s can be taken as the chord. When $s \to 0$, near the stagnation point, so does U_e, and y_{REF}^+ remains finite. Figure 6 shows that y_1^+ values approximately equal to one are sufficient. Since y^+ is related to the normalized temperature by the Prandtl number, sensitivity to y^+ reflects the sensitivity to normalized temperature.

The Navier–Stokes and Euler solutions took approximately 250 and 200 seconds on a Cray X-MP for 3000 time cycles using a 145 × 46 grid.

Predictions were made with a specified wall temperature approximately equal to the average of the experimental wall temperatures. Varying the wall temperature showed no change in the heat transfer as long as the analytic gas-to-wall temperature difference was equal to or greater than the experimental one. It was felt that it was appropriate to compare heat transfer calculated assuming constant wall temperature with experimental data generated from nominally constant heat flux conditions. In the experiments there was some lateral conduction within the blade surface, which changes the boundary condition from one of constant flux to one with more slowly varying temperature. If calculations are made using specified wall flux, comparisons of heat transfer coefficients may not adequately verify a code's ability to predict heat transfer. If the Reynolds number is sufficiently high, and the specified heat flux sufficiently low, the gas temperatures adjacent to the wall will not change significantly from the no-heat-flux case. Under these conditions, comparisons of heat transfer coefficients will show good agreement, independent of how far the first grid point is from the wall.

The temperature gradient at the wall accounted for the nonorthogonality of the grid lines, and was evaluated using a three-point formula:

$$\frac{\partial T}{\partial y} = \frac{\xi_m \eta_\theta/r - \eta_m \xi_\theta/r}{\sqrt{\eta_m^2 + (\eta_\theta/r)^2}} \frac{(-3T_1 + 4T_2 - T_3)}{2} \tag{26}$$

Comparisons With Data

In the comparisons that follow, a prediction that gave good agreement for a number of cases is given by the solid curve. This model incorporates Dunham's transition model, and the Smith and Kuethe free-stream turbulence augmentation effect. In addition to this curve, other curves are shown in each figure to illustrate the effects of various parameters on blade heat transfer. A further discussion of the appropriate heat transfer model will occur after the results for all the comparisons have been presented. Conclusions based on one set of data may not be appropriate for another set, and the appropriate model is a best fit model to all the data.

Stator Results

Low-Speed Cascade Tests. Figure 7 compares predicted and experimental results for the stator of Dring et al. (1986a-d) Figure 7(*a*) shows reasonably good agreement between the analysis and the experimental pressure distribution. The pressures are slightly higher on the rearward portion of the suction surface. The pressure gradient, though, is accurately predicted. The pressure gradient is more important than the small differences in level in predicting the heat transfer.

Figure 7(*b*) shows heat transfer comparisons at design Reynolds number, and low free-stream turbulence. The transition model is very sensitive to the free-stream turbulence at low turbulence intensities. This can be seen by comparing the prediction at a turbulence level of 1.5 percent with the prediction of no free-stream turbulence. The Baldwin–Lomax transition model gave a reasonably accurate prediction of suction surface transition for this case. It was observed that this model predicted transition when the suction surface pressure gradient became positive, and was somewhat accurate only when the free-stream turbulence level was low.

Figure 7(*c*) shows the effect of a variation in the free-stream turbulence on the transition location for the same Reynolds number as in Fig. 7(*b*), but at higher free-stream turbulence. One curve assumes $Tu = Tu_\infty$, and the other assumes $Tu = Tu_\infty U_\infty/U_e$. Since the suction surface pressure is near a minimum at transition, the second assumption results in transition occurring farther back on the suction surface. Dunham suggested that the turbulence intensity be taken as the average of two values, which are closely approximated by these two values. Consequently, these two curves represent the range of turbulence intensities for use in the transition model. Also shown in this figure is a fully turbulent prediction.

Stanton numbers at an intermediate Reynolds number for two Tu_∞ values are shown in Figs. 7(*d*) and 7(*e*). Figure 7(*d*) shows that the shorter transition length agrees better with the rapid rise in heat transfer. Figure 7(*e*) shows the effect of a variable Pr_t to be relatively small, even though Fig. 1 shows Pr_t to be twice as large at the wall for the variable Pr_t as-

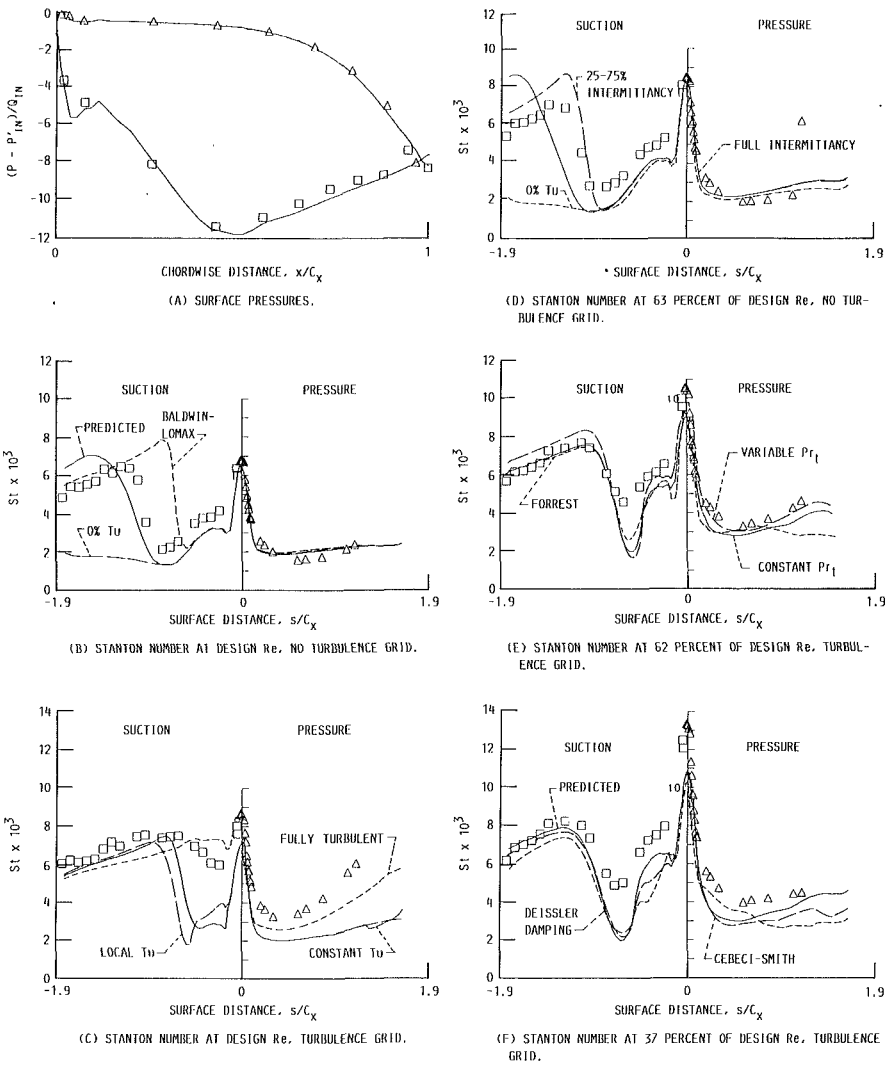

Fig. 7 Pressure distribution and Stanton numbers for stator 1 of Dring et al.

sumption. Figure 7 (f) shows that the effects of both Deissler's near-wall turbulence model and the Cebeci–Smith relaminarization model are also relatively small for the lowest Reynolds number with an upstream turbulence grid.

Transonic Cascade Tests. Figure 8 gives comparisons for the Mark II stator of Hylton et al. Figure 8(a) shows that because of the rapid rise in suction surface pressure near midchord, a grid with 271 circumferential lines was needed to predict surface pressures accurately. Due to the large adverse suction surface pressure gradient the flow separated, and boundary layer analyses could not be used downstream of the separation. Figure 8(b) shows heat transfer comparisons for the two grid densities and for a case where the measured wall temperatures were used for the boundary conditions. This case, which used the 271 × 53 grid, shows that the variation in wall temperature did not account for the overshoot in predicted heat transfer. Even though the overshoot was large, it was very narrow. It appears that the thermal modeling is incorrect immediately after separation, or perhaps there was some smoothing of the experimental data due to conduction. The 146 × 53 grid gives results in better agreement with the heat transfer data, though not with the surface pressure data.

Figure 8(c) shows that the Baldwin–Lomax transition criterion is less satisfactory than Dunham's model for pressure surface transition using the 146 × 53 grid. Figure 8(d) shows that neglecting the effect of free-stream turbulence at Tu = 8.3 percent underpredicts the heat transfer in the leading edge region. Figure 8(e) shows that using a variable Pr_t increased the predicted heat transfer slightly, and did not agree better with the data for either pressure or suction surfaces. Figures 8(b–e) show reasonably good agreement between the predicted and experimental suction surface heat transfer downstream of separation. This shows the usefulness of the Navier–Stokes approach for turbine blade heat transfer.

Comparisons are shown in Fig. 9 for similar conditions as shown in Fig. 8 for the Mark II stator. Figure 9(a) shows good agreement in surface pressures for the C3X stator of Hylton et al. There is no indication of separation for the higher solidity C3X stator. Figure 9(b) shows an accurate heat transfer prediction for the case with low Re and pressure ratio of 0.582, except on the rear portion of the pressure surface. This figure also shows that the effect of Deissler's near-wall turbulence model is relatively small. A prediction with Tu_∞ reduced to 5 percent is also shown, and is in somewhat better agreement with the data. This is shown because the turbulence may have decayed somewhat between the measuring station and the leading edge of the blade. Figure 9(c) gives comparisons at high Re, where free-stream turbulence effects on heat transfer are expected to be large. Forrest's model for free-stream turbulence effects is very close to the data in the leading edge region. This model agrees with the data better than the Smith and Kuethe model.

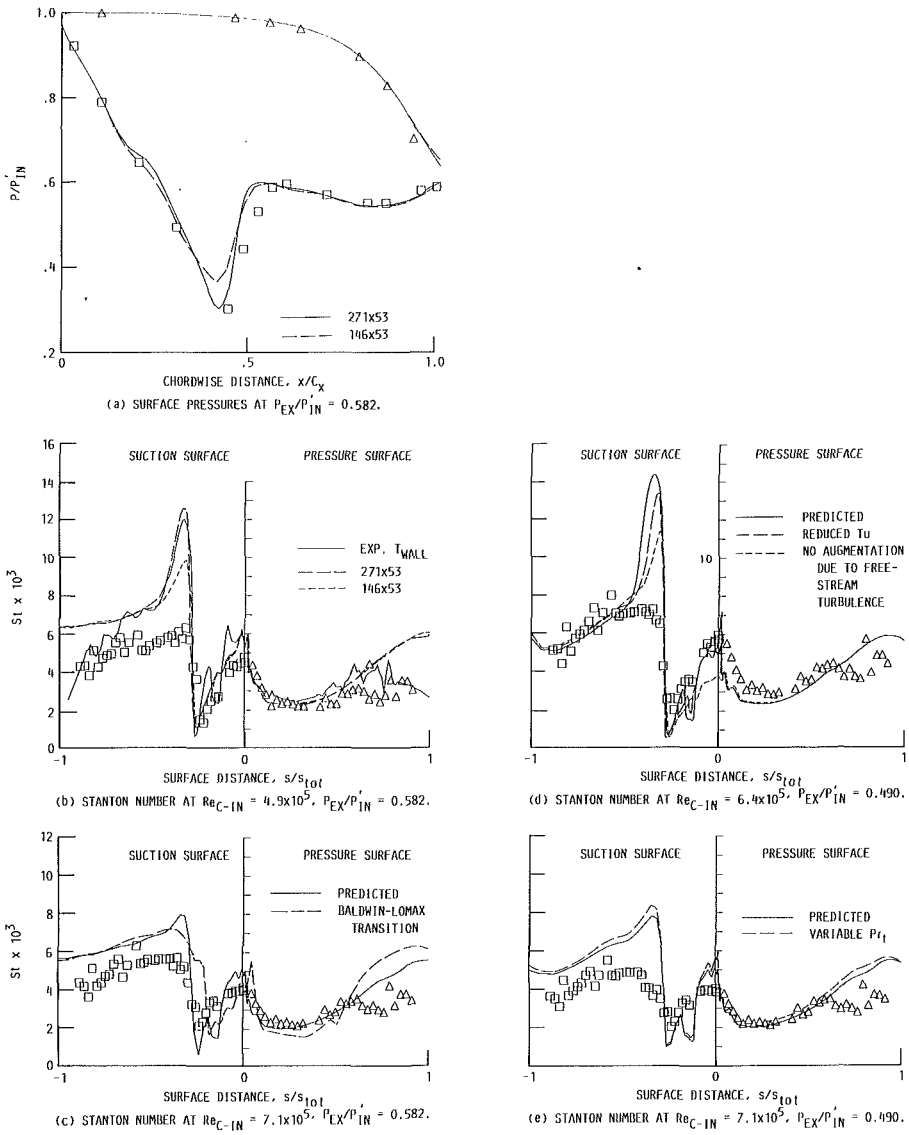

Fig. 8 Pressure distribution and Stanton numbers for Mark II stator of Hylton et al.

A comparison of the peak experimental heat transfer in the leading edge region for several different geometries showed that the slope of the Frossling number, $(\mathrm{Nu}/\sqrt{\mathrm{Re}_d})$, versus the turbulence intensity parameter, $(Tu\sqrt{Re_d})$, was about 0.012. Calculations were done for two different geometries over a range of turbulence intensities for both the Smith and Kuethe model and the model of Forrest. Calculations were done with three different assumptions for each model. The assumptions were that the turbulent viscosity due to free-stream turbulence was zero in the outer region; that it was held constant at the crossover value; and that it varied in the outer region. There was some variation in the predicted slope, $(\Delta(\mathrm{Nu}/\sqrt{\mathrm{Re}_d})/\Delta(Tu\sqrt{\mathrm{Re}_d}))$, depending on the geometry chosen. There was consistency in terms of the results for the different implementation assumptions for each model. Forrest's model gave best agreement in terms of the desired slope. When the turbulent viscosity in the outer region was limited to the crossover value, the slope was somewhat less than the experimental one. When the turbulent viscosity was allowed to vary in the outer region, the slope was as great or slightly higher than the experimental one. The model of Smith and Keuthe resulted in a slope much greater than the experimental one except when the turbulent viscosity was neglected in the outer region.

Figure 9(*d*) shows good agreement with the heat transfer data at the low Re and pressure ratio of 0.490. The figure also shows that the A^+ model had little effect on the heat transfer. Figure 9(*e*) shows a fully turbulent calculation to agree better with the data than a model with transition for the high Re and low pressure ratio case. The improved agreement occurs in the leading edge region, and just prior to suction surface transition.

Linear Cascade Tests. Figure 10(*a*) compares surface pressures for the vane data of Hippensteele et al. Figure 10(*b*) compares heat transfer results at design Reynolds number and low turbulence intensity for two transition lengths and for the Baldwin–Lomax transition criteria. In contrast to Fig. 7(*d*), the longer transition length agrees better with the data. However, either transition length in Dunham's model agrees better than the Baldwin–Lomax criterion. Figure 10(*c*) shows that the free-stream turbulence model of Forrest agrees with the heat transfer data better than the model of Smith and Kuethe at high *Tu*. Figure 10(*d*) shows a longer transition length than the data for the low Re–low *Tu* case. Since even the suction surface transitioned near the rear of the vane, any turbulence generated within the passage would move transition forward. Increasing *Tu* to 3 percent in the predictor gave the correct suction surface transition. Figure 10(*e*) shows that, even with

the high *Tu*, suction surface transition is delayed to the near midchord as a result of the low Reynolds number.

Rotor Results

Large Scale Rotor. Figure 11 compares pressure distributions and heat transfer results for three different values of flow coefficient, ϕ. Changing ϕ changes the inlet flow angle. There is good agreement in pressure distribution between the analysis and data for all three ϕ values. Changing inlet flow angles gives different pressure distribution, with different boundary layer growth rates, which in turn affect the blade heat transfer. When $\phi = 0.68$, the flow is more tangential, resulting in a greater adverse pressure gradient along the pressure surface. When $\phi = 0.96$, the flow angle is reduced from the design case. This in turn gives a less favorable gradient along the suction surface.

Heat transfer comparisons are shown for three ϕ values at design Reynolds number, and for $\phi = 0.78$ at a low Re. Since the test occurred in a rotating rig, the rotor, being behind the stator, was always in a high turbulence environment. The effect of augmenting the viscosity to account for free-stream turbulence is shown in Fig. 11(*b*). Figure 11(*d*) shows that a constant value of A^+ gives the best prediction on the suction surface. It was observed that for high *Tu* cases neglecting relaminarization often gave the best agreement with the data for the pressure surface. Since high free-stream turbulence causes laminar boundary layers to become turbulent, it may also inhibit relaminarization of turbulent boundary layers. Figure 11(*f*) shows that a fully turbulent boundary layer calculation gives a reasonably accurate prediction for the entire blade surface. However, because this model does not account for the level of free-stream turbulence, the leading edge region heat transfer may in some cases be in error. The heat transfer prediction for the low Reynolds number case in Fig. 11(*g*) is accurate, except for the prediction of transition. The underprediction of pressure surface heat transfer again suggests that relaminarization is not appropriate in a high *Tu* environment.

Large-Scale Exit Vane. The exit vane of the tests of Dring et al. had a shape similar to the rotor. Therefore, comparisons for this blade row are included with other rotor results. Figure 12 compares surface pressure and heat transfer predictions. The analysis underpredicts the heat transfer even for the turbulent assumption on the rearward portion of the suction surface. While only one prediction is shown in Fig. 12, several other cases were run with other assumptions for Pr_t, A^+, and

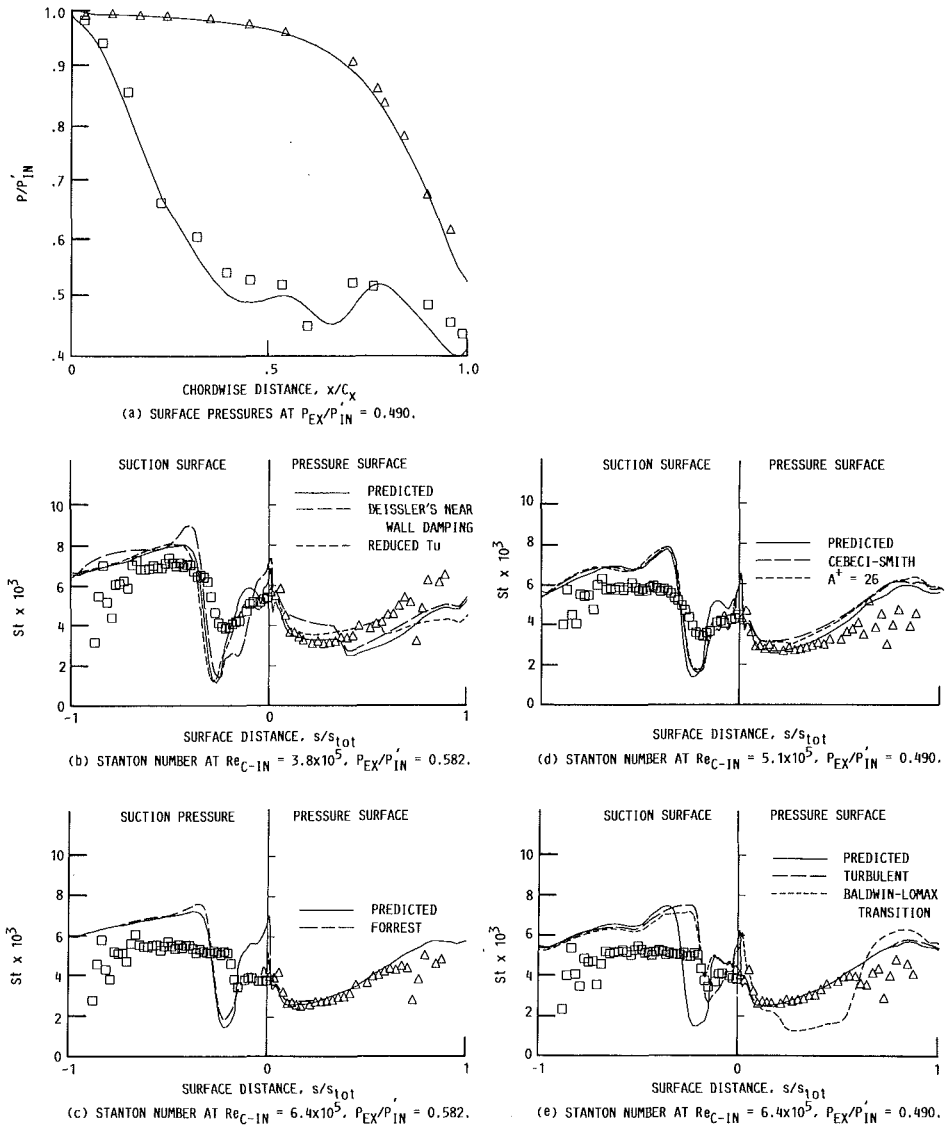

Fig. 9 Pressure distribution and Stanton numbers for C3X stator of Hylton et al.

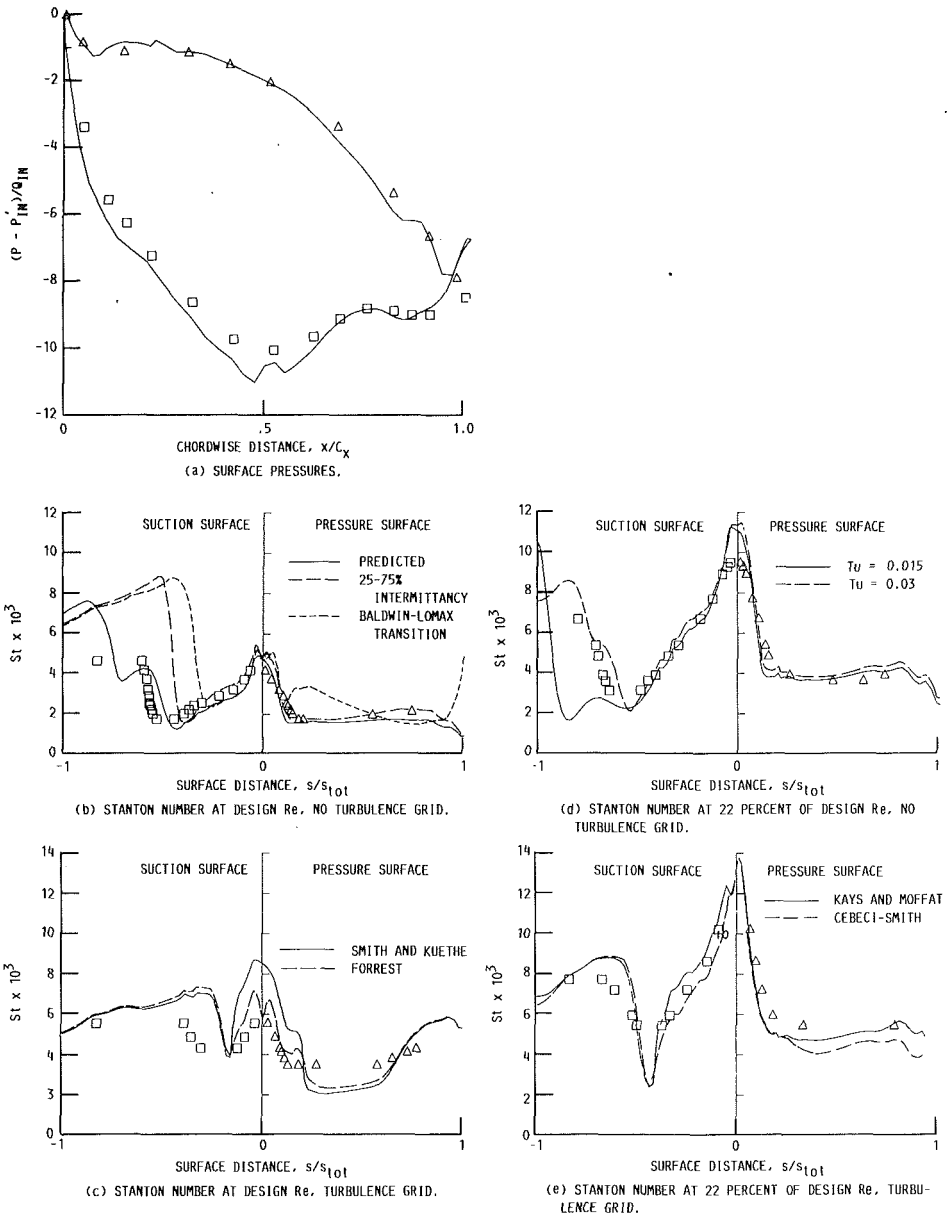

Fig. 10 Pressure distribution and Stanton numbers for stator of Hippensteele et al.

the near-wall damping model. No case gave heat transfer results that agreed with the data on the rear portion of the suction surface. It appears that the thermal modeling is in error, or perhaps there are three-dimensional flow effects. The fully turbulent boundary layer prediction shown by Dring et al. also underpredicted this heat transfer.

Linear Cascade Rotor. The rotor tested by Hippensteele, Russell, and Torres showed pressure surface separation. Figure 13(*a*) gives comparisons of surface pressures. While there is reasonably good agreement between the analysis and experimental surface pressures, the analysis shows a stronger suction surface adverse pressure gradient than might be inferred from the data.

The tests were done in a low free-stream turbulence environment. Consequently, transition occurred toward the rear of the blade on the suction surface. Figure 13(*b*) shows an early prediction of suction surface transition at the highest Reynolds number. This was probably the result of an overly strong suction surface adverse pressure gradient. At the lower Reynolds numbers, Figs. 13(*b*, *c*) Re_θ was not large enough to initiate transition at this point on the blade. This figure shows only a small effect on suction surface transition when the free-stream turbulence is assumed to vary with the local free-stream velocity.

On the pressure surface separation occurred near the leading edge. At all Reynolds numbers the pressure surface heat transfer reached a second peak as a result of separation. Because this occurred close to the leading edge, θ, calculated from equation (20), was too small to initiate transition in this region. Best agreement with the pressure surface data was achieved when the Navier–Stokes analysis was used to indicate transition. Once a negative wall friction was calculated, the flow was assumed to be fully turbulent. This assumption gave the location of a transition-like increase in heat transfer only slightly downstream of separation. The higher heat transfer along most of the pressure surface compared with the suction surface was predicted. The analysis predicted an increase in heat transfer at separation. The increase was from a lower laminar level, and, in contrast to the experimental data, the heat transfer did

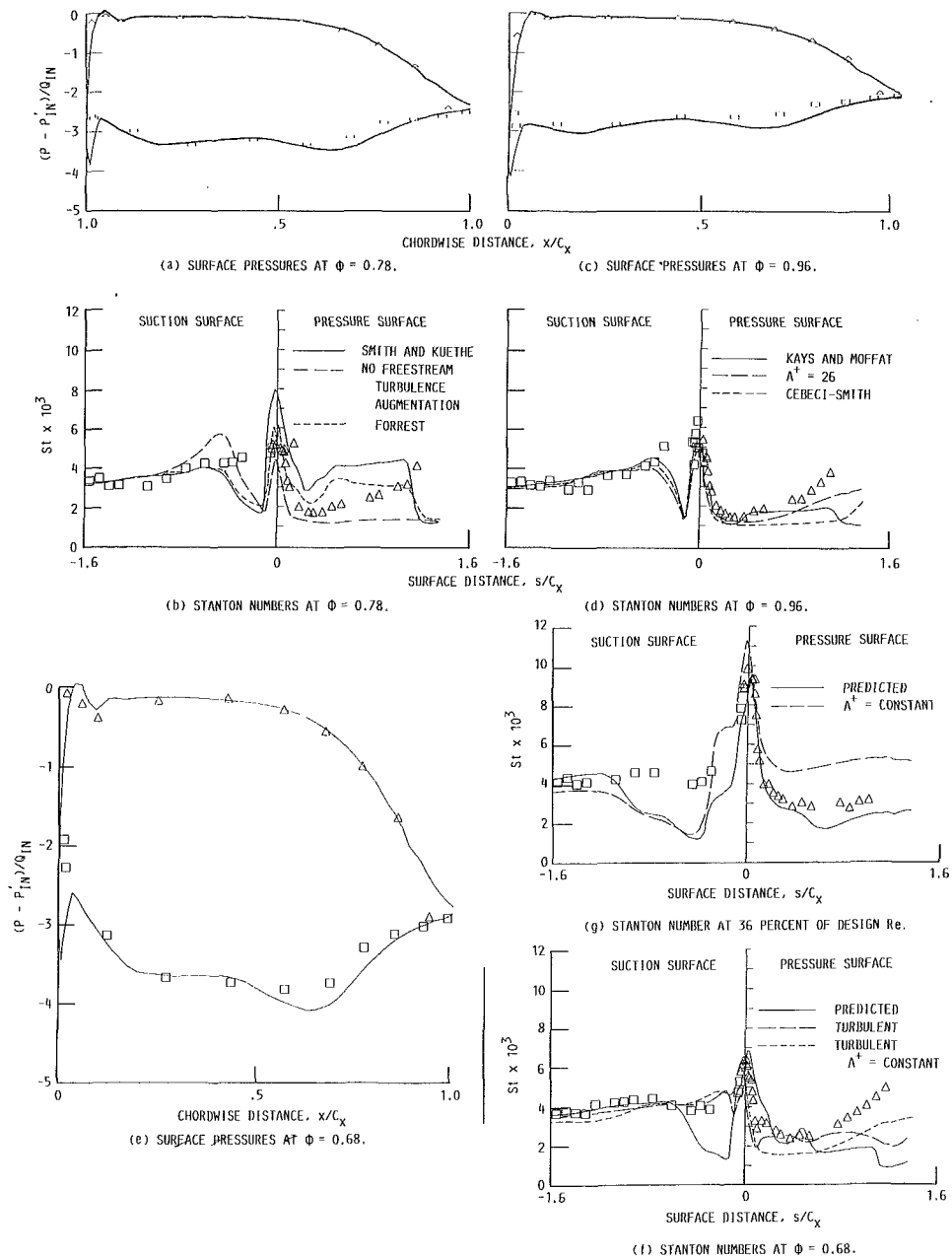

Fig. 11 Pressure distribution and Stanton numbers for rotor of Dring et al.

not reach the leading edge level. The results in Fig. 8 showed that a denser grid changed the heat transfer predictions at separation. For the rotor case, however, the heat transfer did not change with a denser grid.

Choice of Heat Transfer Model. The results in Figs. 7–13 show that the choice of heat transfer model is somewhat dependent on the flow field environment. When both the Reynolds number and *Tu* are high, a fully turbulent model gives accurate predictions. When the Reynolds number is low, even if *Tu* is high, transition must be accounted for. Dunham's transition model gives accurate predictions, and the actual level of free-stream turbulence, even if it is low, should be used. When the turbulence level is low, but not known, a value of at least 2 percent should be used. When the turbulence level is low, and especially if the Reynolds number is also low, a negative skin friction should be used to switch to fully turbulent flow. This should not be done in the immediate region of the stagnation point so as to avoid spurious transition. At stagnation the sign of the shear stress is indeterminate. The transition criterion in the Baldwin–Lomax model is less accurate, principally because it fails to account for free-stream turbulence. The data comparisons did not indicate a strong preference for either the 0 to 99 percent intermittency model or the 25 and 75 percent one. Both gave reasonably accurate results.

The choice of relaminarization model also was dependent on the free-stream turbulence environment. With high *Tu* it did not appear appropriate to increase A^+ when the pressure gradient was strongly favorable. Since high free-stream turbulence causes a laminar boundary to become turbulent, it also may inhibit relaminarization of a turbulent boundary layer. Otherwise the Kays and Moffat model appeared slightly favorable, perhaps only from a computational standpoint, to the Cebeci–Smith model.

Not only did Deissler's near-wall turbulence model give similar results to the widely used VanDriest model for a flat plate

boundary layer, the results were nearly the same for the heat transfer after separation occurred.

Using a variation in Pr_t instead of a constant value did not result in significantly different heat transfer results. However, there was some indication that at low Reynolds numbers a variable Pr_t would give higher heat transfer rates.

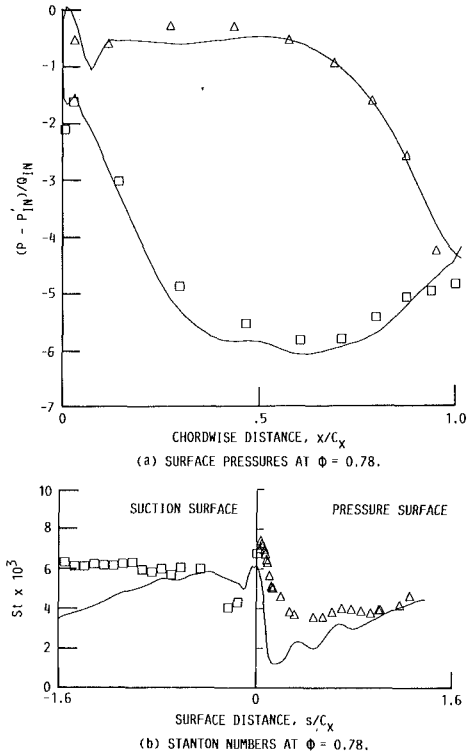

Fig. 12 Pressure distribution and Stanton numbers for second stator of Dring et al.

The model of Forrest for the heat transfer augmentation in laminar flow was in better agreement with the data. If the model of Smith and Kuethe is used, best agreement with the data is achieved when the coefficient used in their model is reduced by about 50 percent. A reduction of this magnitude is consistent with the observations made by O'Brien and VanFossen (1985).

Conclusions

Comparisons with experimental data showed good agreement in terms of surface pressures for the several different turbine blades. When the surface pressure changed abruptly, grids of high density were required. Otherwise, a grid size of 145 × 46 was adequate.

Reductions in residuals of at least two orders of magnitude were required in order to achieve converged heat transfer predictions. Convergence was slower for the pressure surface heat transfer than for the suction surface heat transfer. Use of the GRAPE code to generate grids proved satisfactory.

The ability of the thin-layer Navier–Stokes analysis to predict turbine blade heat transfer accurately downstream of separations demonstrates the utility of this approach. After separation, a fully turbulent prediction agrees well with the data. The degree of agreement between the analysis and the experimental data is primarily determined by the choice of model for transition. The Navier–Stokes results should be used to change the calculation procedure from laminar to turbulent when separation is indicated.

References

Abu-Ghannam, B. J., and Shaw, R., 1980, "Natural Transition of Boundary Layers—The Effects of Turbulence, Pressure Gradients, and Flow History," *J. Mech. Engr. Science*, Vol. 22, No. 5, pp. 213–228.

Baldwin, B. S., and Lomax, H., 1978, "Thin-Layer Approximation and Algebraic Model for Separated Turbulent Flows," AIAA Paper No. 78-257.

Cebeci, T., and Smith, A. M. O., 1974, *Analysis of Turbulent Boundary Layers*, Academic Press, New York.

Chima, R. V., 1986, "Development of an Explicit Multigrid Algorithm for

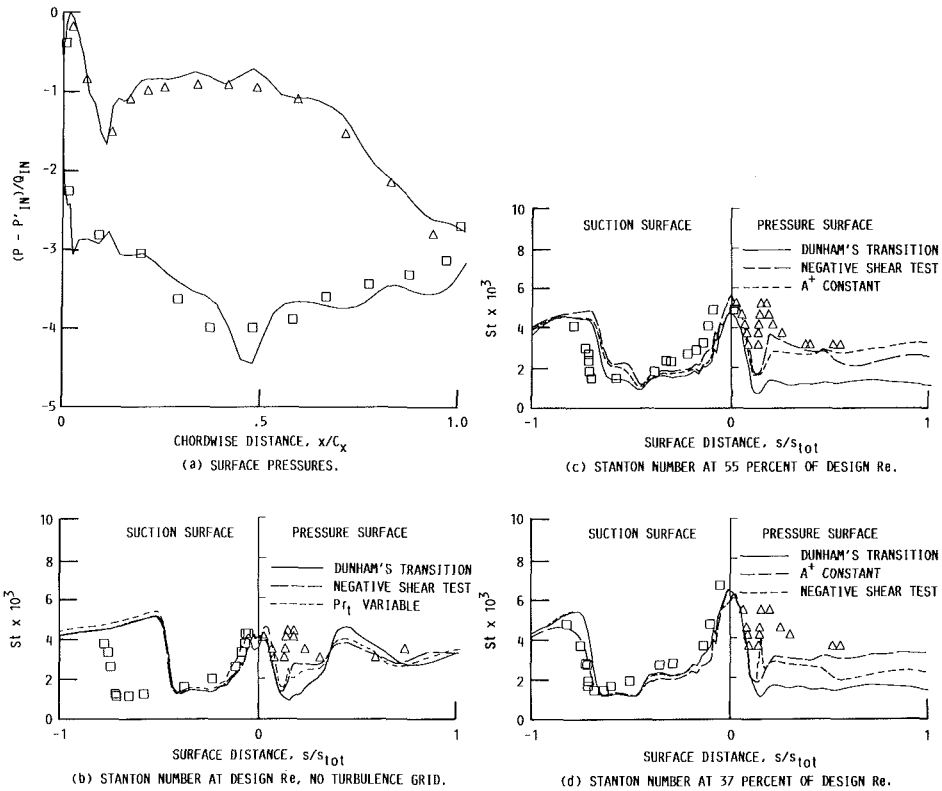

Fig. 13 Pressure distribution and Stanton numbers for rotor of Hippensteele et al.

Quasi-Three-Dimensional Viscous Flows in Turbomachinery," AIAA Paper No. 86-0032; NASA TM-87128.

Chima, R. V., Turkel, E., and Schaffer, S., 1987, "Comparison of Three Explicit Multigrid Methods for the Euler and Navier–Stokes Equations," AIAA Paper No. 87-0602; NASA TM-88878.

Chima, R. V., and Yokota, J. W., 1988, "Numerical Analysis of Three-Dimensional Viscous Internal Flows," AIAA Paper No. 88-3522; NASA TM-100878.

Crawford, M. E., and Kays, W. M., 1976, "STAN5—A Program for Numerical Computation of Two-Dimensional Internal and External Boundary Layer Flows," NASA CR 2742.

Davis, R. L., Hobbs, D. E., and Weingold, H. D., 1988, "Prediction of Compressor Cascade Performance Using a Navier–Stokes Technique," ASME JOURNAL OF TURBOMACHINERY, Vol. 110, pp. 520–531.

Deissler, R. G., 1955, "Analysis of Turbulent Heat Transfer, Mass Transfer, and Friction in Smooth Tubes at High Prandtl and Schmidt Numbers," NACA Report 1210.

Dhawan, S., and Narasimha, R., 1958, "Some Properties of Boundary Layer Flow During Transition From Laminar to Turbulent Motion," *J. Fluid Mechanics*, Vol. 3, pp. 418–436.

Dring, R. P., Blair, M. F., Joslyn, H. D., Power, G. D., and Verdon, J. M., 1986a, "The Effects of Inlet Turbulence and Rotor/Stator Interactions on the Aerodynamics and Heat Transfer of a Large-Scale Rotating Turbine Model. Pt. I—Final Report," NASA CR 4079.

Dring, R. P., Blair, M. F., and Joslyn, H. D., 1986b, "The Effects of Inlet Turbulence and Rotor/Stator Interactions on the Aerodynamics and Heat Transfer of a Large-Scale Rotating Turbine Model. Pt. II—Heat Transfer Data Tabulation—15% Axial Spacing," NASA CR 179467.

Dring, R. P., Blair, M. F., and Joslyn, H. D., 1986c, "The Effects of Inlet Turbulence and Rotor/Stator Interactions on the Aerodynamics and Heat Transfer of a Large-Scale Rotating Turbine Model. Pt. III—Heat Transfer Data Tabulation—65% Axial Spacing," NASA CR 179468.

Dring, R. P., Joslyn, H. D., and Blair, M. F., 1986d, "The Effects of Inlet Turbulence and Rotor/Stator Interactions on the Aerodynamics and Heat Transfer of a Large-Scale Rotating Turbine Model. Pt. IV—Aerodynamic Data Tabulation," NASA CR 179469.

Dunham, J., 1972, "Predictions of Boundary Layer Transition on Turbomachinery Blades," AGARD-AG-164.

Forrest, A. E., 1977, "Engineering Predictions of Transitional Boundary Layers," AGARD-CP-224.

Hah, C., 1989, "Numerical Study of Three-Dimensional Flow and Heat Transfer Near the Endwall of a Turbine Blade Row," AIAA Paper No. 89-1689.

Hippensteele, S. A., Russell, L. M., and Torres, F. J., 1985, "Local Heat-Transfer Measurements on a Large Scale-Model Turbine Blade Airfoil Using a Composite of a Heater Element and Liquid Crystals," ASME *Journal of Engineering for Gas Turbines and Power*, Vol. 107, pp. 953–960.

Hippensteele, S. A., Russell, L. M., and Torres, F. J., 1986, "Use of a Liquid-Crystal, Heater-Element Composite for Quantitative, High-Resolution Heat Transfer Coefficients on a Turbine Airfoil, Include Turbulence and Surface Roughness Effects," in: *Pressure and Temperature Measurements*, J. H. Kim and R. J. Moffat, eds., ASME FED-Vol. 44/HTD-Vol. 58, pp. 105–120; NASA TM-87355.

Hylton, L. D., Mihelc, M. S., Turner, E. R., Nealy, D. A., and York, R. E., 1983, "Analytical and Experimental Evaluation of the Heat Transfer Distribution Over the Surfaces of Turbine Vanes," NASA CR 168015.

Jones, W. P., and Launder, B. E., 1969, "On the Prediction of Laminarescent Turbulent Boundary Layers," ASME Paper No. 69-HT-13.

Katsanis, T., and McNally, W. D., 1977, "Revised FORTRAN Program for Calculating Velocities and Streamlines on the Hub-Shroud Midchannel Stream Surface of an Axial-, Radial-, or Mixed-Flow Turbomachine or Annular Duct, Vol. I—User's Manual," NASA TN D-8430.

Kays, W. M., and Moffat, R. J., 1975, "The Behavior of Transpired Boundary Layers," in: *Studies in Convection, Vol. 1: Theory, Measurement, and Application*, B. E. Launder, ed., Academic Press, London.

O'Brien, J. E., and VanFossen, G. J., 1985, "The Influence of Jet-Grid Turbulence on Heat Transfer From the Stagnation Region of a Cylinder in Crossflow," ASME Paper No. 85-HT-58.

Pai, B. R., and Whitelaw, J. H., 1971, "The Prediction of Wall Temperature in the Presence of Film Cooling," *Int. J. Heat Mass Transfer*, Vol. 14, pp. 409–426.

Seyb, N. J., 1977, "The Role of Boundary Layers in Axial Flow Turbomachines and the Prediction of Their Effects," AGARD-CP-224.

Smith, M. C., and Kuethe, A. M., 1966, "Effects of Turbulence on Laminar Skin Friction and Heat Transfer," *Physics of Fluids*, Vol. 9, pp. 2337–2344.

Sorenson, R. L., 1980, "A Computer Program to Generate Two-Dimensional Grids About Airfoils and Other Shapes by the Use of Poisson's Equation," NASA TM-81198, 1980.

White, F. M., 1974, *Viscous Fluid Flow*, McGraw-Hill, New York.

Yang, R. J., Weinberg, B. C., Shamroth, S. J., and McDonald, H., 1985, "Turbine Vane External Heat Transfer—Vol. II. Numerical Solutions of the Navier–Stokes Equations for Two- and Three-Dimensional Turbine Cascades With Heat Transfer," NASA CR 174828.

Heat Transfer Measurements and Calculations in Transitionally Rough Flow

M. H. Hosni

H. W. Coleman

R. P. Taylor

Thermal & Fluid Dynamics Laboratory,
Mechanical and Nuclear Engineering
Department,
Mississippi State University,
Mississippi State, MS 39762

Experimental data on a rough surface for both transitionally rough and fully rough turbulent flow regimes are presented for Stanton number distribution, skin friction coefficient distribution, and turbulence intensity profiles. The rough surface is composed of 1.27-mm-dia hemispheres spaced in a staggered array four base diameters apart on an otherwise smooth wall. Special emphasis is placed on the characteristics of heat transfer in the transitionally rough flows. Stanton number data are reported for zero pressure gradient incompressible turbulent boundary layer air flow for nominal free-stream velocities of 6, 12, 28, 43, 58, and 67 m/s, which give x-Reynolds numbers up to 10,000,000. These data are compared with previously published rough surface data, and the classification of a boundary layer flow into transitionally rough and fully rough regimes is explored. Moreover, a new heat transfer model for use in the previously published discrete element prediction approach is presented. Computations using the discrete element model are presented and compared with data obtained from two different rough surfaces. The discrete element predictions for both surfaces are found to be in substantial agreement with the data.

Introduction

Heat transfer and skin friction can be significantly larger for a turbulent flow over a rough surface compared with an equivalent turbulent flow over a smooth surface. Many surfaces of engineering interest are rough in the aerodynamic sense. Turbine blades, re-entry vehicles, ship hulls, atmospheric flows, and piping networks are examples of systems in which surface roughness can play an important role in heat transfer and skin friction. The primary application that motivated the work reported in this paper is the external convective heat transfer for gas turbine blades.

Taylor (1990) measured and statistically classified the surface roughness on a number of first-stage in-service turbine blades from TF-39 and F-100 aeroengines. He found the blades to be very rough and to have a wide variation in both the height and character of the roughness at different points around the blades. Figure 1 shows a summary of Taylor's results for the average height measurements. Considering that the thickness of the boundary layer is on the order of 1 mm, the roughness values shown in the figure represent conditions ranging from extremely rough to modestly rough. In another related work, Taylor (1989) reported roughness measurements on the Space Shuttle Main Engine (SSME) fuel turbine blades and boundary layer computations for conditions that are considered to be representative of the conditions in the SSME turbine. He found that the blades had rms roughness heights on the order of 15 μm, which resulted in a computed Stanton number increase of about 100 percent in the nominally 0.5-mm-thick boundary layer.

In light of such potentially significant effects, there is a continuing interest in the development of fundamental engineering understanding of the influence of surface roughness on fluid flow and heat transfer. In parallel, there is an interest in the development of accurate predictive models for heat transfer and fluid mechanics in turbulent flow over rough surfaces.

The work reported here is concerned with heat transfer in the transitionally rough turbulent boundary layer. Experiments are reported for the incompressible flow of air over a rough surface for nominal free-stream velocities of 6, 12, 28, 43, 58, and 67 m/s, which give an x-Reynolds number range up to 10,000,000. The surface is roughened with 1.27-mm-dia hemispherical elements spaced 4 diameters apart in a staggered array. Data are presented for Stanton number distribution, skin friction coefficient distribution, and turbulent intensity profiles. These data are discussed and compared with previously published data. Special emphasis is placed on the nature of heat transfer in the transitionally rough flows. Computations using the previously published (Taylor et al., 1984, 1985) discrete element prediction approach are presented and compared with the data. Furthermore, the classification of a boundary layer flow into transitionally rough and fully rough regimes is explored.

Background

General. The experimental study of roughness effects on

Contributed by the International Gas Turbine Institute and presented at the 35th International Gas Turbine and Aeroengine Congress and Exposition, Brussels, Belgium, June 11–14, 1990. Manuscript received by the International Gas Turbine Institute January 10, 1990. Paper No. 90-GT-53.

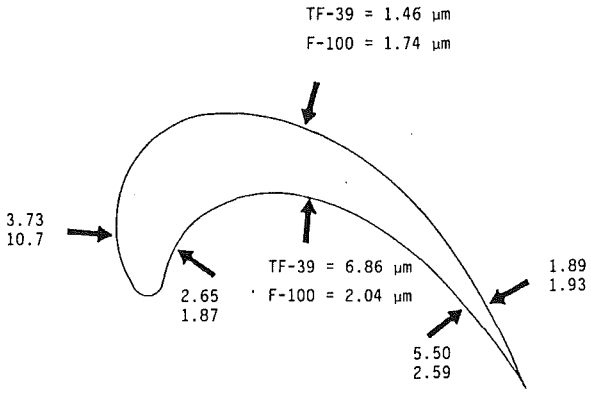

Fig. 1 Profilometer trace locations and average roughness heights for aeroengine turbine blade as reported by Taylor (1990)

fluid flow has its origin with the classic work of Nikuradse (1933). Since the 1930s, much of the work on the investigation of surface roughness effects has been directed toward fluid dynamics behavior. Moreover, most of the roughness-influenced data taken over the years have been on ill-defined rough surfaces. Much less work has been done in the field of heat transfer. The work of Nunner (1956) is one of the first experimental studies on the heat transfer behavior of a rough surface. He used his experimental results for air flow through rough pipes to establish a single empirical relationship between the increase in Nusselt number due to roughness and the increase in the friction coefficient. The other early rough wall heat transfer studies for internal flows are summarized by Sood and Johnson (1969) and by Norris (1971).

A series of experimental studies at Stanford University (Healzer, 1974; Pimenta, 1975; Coleman, 1976; Ligrani, 1979) has reported data sets that contain heat transfer and skin friction distributions and velocity, temperature, and Reynolds stress profiles. However, these data sets are for a single rough surface, which was comprised of spheres of a single size packed in the most dense array. Holden (1983) reported heat transfer and skin friction distribution measurements on well-defined surface roughness on cones for hypersonic flow conditions.

Characterization of Transitionally Rough Flow. Nikuradse (1933), based on his experimental results of skin friction coefficient distributions from sand-roughened pipe flows, identified three regimes of *fully developed flow*: aerodynamically smooth, transitionally rough, and fully rough flow. Aerodynamically smooth flow is flow over a surface that has the same resistance as flow over an ideal smooth surface at the same Reynolds number. The aerodynamically smooth regime, thus, is characterized by the skin friction coefficient depending on the Reynolds number of the gross flow only and being independent of roughness shape, size, density, etc. In contrast, for a fully rough flow the skin friction coefficient depends solely on the character of the roughness and is entirely independent of the Reynolds number of the gross flow. The regime of flow between aerodynamically smooth and fully rough is known as transitionally rough. It is characterized by the dependence of the skin friction coefficient on both flow Reynolds number and roughness character.

The flow regime delimiter Nikuradse chose to measure the state of the flow with respect to the three regimes was the roughness Reynolds number,

$$\mathrm{Re}_{k_s} = u^* k_s / \nu \tag{1}$$

where u^* is the friction velocity and k_s is the size of the sand grains. His reported limits for the three regimes for fully developed pipe flow were:

aerodynamically smooth	$\mathrm{Re}_{k_s} < 5$
transitionally rough	$5 < \mathrm{Re}_{k_s} < 55$–$70$
fully rough	$\mathrm{Re}_{k_s} > 55$–70

Following Nikuradse's work, Schlichting (1936) conducted experiments in a *fully developed* rectangular channel flow with

Nomenclature

A = plate surface area
C_D = roughness element drag coefficient (equation (16))
C_f = skin friction coefficient $= 2\tau_W/\rho U_\infty^2$
C_p = free-stream specific heat
$d(y)$ = local roughness element diameter
h = convective heat transfer coefficient
H = time mean static enthalpy
$H_{o,\infty}$ = free-stream total enthalpy
K = thermal conductivity
k_s = sandgrain roughness
ℓ_m = mixing length
L = roughness element spacing
Nu_d = roughness element Nusselt number (equation (17))
P = pressure
Pr = Prandtl number
q_c = conductive heat loss rate
q_r = radiative heat loss rate
r = recovery factor
R_τ = roughness parameter $= \tau_R/\tau_T$
Re_d = Reynolds number based on local roughness element diameter
Re_{k_s} = Reynolds number based on sandgrain roughness
Re_x = Reynolds number based on x
Re_{δ_2} = momentum thickness Reynolds number $= \rho U_\infty \delta_2/\mu$
St = Stanton number $= h/\rho C_p U_\infty$
T = temperature
T_o = free-stream total temperature
T_r = recovery temperature
T_R = roughness element temperature $= T_w$
T_w = wall temperature
u = mean axial velocity
U_∞ = free-stream velocity
$(UA)_{\mathrm{eff}}$ = overall conductance for q_c calculation
u' = longitudinal velocity fluctuation
$\overline{u'v'}$ = Reynolds shear stress factor
$\overline{v'h'}$ = turbulent heat flux factor
u^* = friction velocity $= U_\infty\sqrt{C_f/2}$
v = mean normal velocity
W = plate heater power
x = longitudinal coordinate measured from nozzle exit plane
y = coordinate normal to surface
α = thermal diffusivity
β_x = blockage factor
β_y = blockage factor
δ = boundary layer thickness
δ_2 = momentum thickness
Δ_2 = enthalpy thickness
ϵ = plate surface emissivity
κ = Karman constant
μ = dynamic viscosity
ν = kinematic viscosity
ρ = density
σ = Stefan–Boltzmann constant
τ = viscous shear stress
τ_R = apparent wall shear stress due to form drag on roughness elements
τ_T = total wall shear stress

Subscripts

bar = barometric
t = turbulent
wb = wet bulb

the upper surface rough and the remaining sides smooth. He studied the effects of roughness size, shape, and density on the flow resistance using well-defined roughness elements. He related his skin friction results to Nikuradse's results through definition of an equivalent sand grain roughness. He proposed the use of the equivalent sand grain roughness, k_s, as a measure of the flow resistance character of a rough surface. It was Schlichting's stated purpose to use this parameter as a means of extrapolating a set of experimental resistance data to other Reynolds numbers based on Nikuradse's data set.

The equivalent sand grain roughness concept of Schlichting and the roughness Reynolds number of Nikuradse as the delimiter for classification of flow regimes have been extensively used since the 1930s for both fully developed and developing flows. Many workers have in fact related their experimental data to that of Schlichting by implicitly introducing the equivalent sand grain roughness into their data reduction. Recently Coleman et al. (1983, 1984) showed that Schlichting had made erroneous assumptions during his data reduction, which had significant effects on the results he reported. They showed that his skin friction results were too large by amounts ranging up to 73 percent and that his reported values of k_s were too high by amounts ranging from 26 to 555 percent.

Pimenta (1975) studied the effects of roughness on the structure of rough wall turbulent boundary layers using the Stanford rough surface comprised of spheres of a single size (1.27-mm-dia) packed in the most dense array. He suggested an alternative method as a measure of the state of boundary layer flow over rough surfaces. He identified the flow regimes based on certain similarity characteristics of the flow. He stated that for his surface the flow characteristics (integral parameters) were all independent of Reynolds number in the fully rough flow regime:

$$\mathrm{St} = f(\Delta_2/r) \tag{2}$$

$$C_f = g(\delta_2/r) \tag{3}$$

where r was the radius of the spherical roughness elements. Pimenta in equation (2) expressed his conclusion in functional form that the Stanton number data versus enthalpy thickness collapsed to a single curve for fully rough flow. Similarly, he concluded that his friction coefficient data versus momentum thickness for the fully rough state collapsed to a single curve as expressed by equation (3).

Pimenta also investigated the Reynolds stress tensor components in fully rough and transitionally rough boundary layers. He found that the near-wall distribution of u'^2 profiles showed different behavior for the fully rough and transitionally rough states. In the transitionally rough regime, u'^2 profiles showed qualitative characteristics similar to the smooth wall state, with a near-wall peak present. In the fully rough regime, the peak in u'^2 was lowered, moved away from the wall, and spread over a larger portion of the boundary layer. He pointed out that the distinctive difference in the near-wall profiles of u'^2 may offer a new and more definitive measure of distinguishing between transitionally rough and fully rough behaviors. In introducing the new set of measures for identification of rough surface flow states, he emphasized that his conclusions were based only on the data taken from the single rough surface comprised of spheres packed in the most dense array.

In experiments using the same surface, Ligrani (1979) used an artificially thickened boundary layer to achieve larger momentum thicknesses, and his conclusions agreed with those of Pimenta. He concluded that at fully rough conditions the skin friction coefficient was a function only of boundary layer momentum thickness, while transitionally rough skin friction coefficients depend on momentum thickness and on flow Reynolds number. He also observed the distinct difference in the near-wall peak from u'^2 profiles taken at transitionally rough and fully rough conditions as was reported by Pimenta.

Over the past decade or so, a predictive approach called the discrete element method, which does not use the equivalent sand grain roughness concept, has been used by several groups of researchers (Finson, 1975, 1982; Adams and Hodge, 1977; Finson and Wu, 1979; Finson and Clark, 1980; Lin and Bywater, 1980; Coleman et al., 1983; Taylor et al., 1985). This method was suggested by Schlichting (1936) in the same paper that the equivalent sand grain roughness was proposed. He proposed that the flow resistance of a rough surface be divided into two components: (1) that due to the form drag on the element, and (2) that due to viscous shear on the smooth surface area between the roughness elements.

The discrete element method in effect abandons the concept of sand grain roughness and thereby abandons the roughness Reynolds number as the delimiter for aerodynamically smooth, transitionally rough, and fully rough conditions. Taylor et al. (1985) suggested that the ratio of the apparent shear stress due to the roughness elements to the total apparent shear stress ($R_\tau = \tau_R/\tau_T$) be used to distinguish between aerodynamically smooth, transitionally rough, and fully rough regimes. They proposed, based on data available at the time and their calculations of τ_R and τ_T using their discrete element model, the divisions:

$R_\tau < 0.05$–0.10	aerodynamically smooth
0.05–$0.1 < R_\tau < 0.80$–0.90	transitionally rough
$R_\tau > 0.80$–0.90	fully rough

Scaggs et al. (1988) investigated the effects of surface roughness on turbulent pipe flow friction factors using eleven different rough surfaces, nine of which had uniform roughness elements and two of which were roughned nonuniformly. Based on their data and the corresponding calculations of τ_T and τ_R made using their discrete element model, they proposed that a value of R_τ about 0.6 might be considered as an appropriate boundary between the transitionally rough and fully rough flow regimes.

Discrete Element Method

The basic idea of the discrete element approach is to treat the roughness as a collection of individual entities and to account for blockage, form drag, and heat transfer on the element. The discrete element scheme used is formulated for roughness elements with three-dimensional shapes (as opposed to transverse ribs) for which the element cross section can be approximated as circular at every height y. This scheme includes the physical effects of roughness on the flow field by considering the blockage effects of the roughness elements, the drag forces that the roughness elements exert on the field, and the local heat transfer between the roughness elements and the fluid. The steady (Reynolds-averaged), two-dimensional turbulent boundary layer equations presented here are for flow over a rough surface with roughness elements of uniform shape and spacing as derived by Taylor et al. (1984). The discrete element boundary layer equations and boundary conditions are

$$\frac{\partial}{\partial x}(\rho\beta_x u) + \frac{\partial}{\partial y}(\rho\beta_y v) = 0 \tag{4}$$

and

$$\beta_x \rho u \frac{\partial u}{\partial x} + \beta_y \rho v \frac{\partial u}{\partial y} = -\frac{\partial}{\partial x}(\beta_x P) + \frac{\partial}{\partial y}\left[\beta_y\left(\mu \frac{\partial u}{\partial y} - \overline{\rho u' v'}\right)\right] - \frac{1}{2}\rho C_D d(y)\frac{u^2}{L^2} \tag{5}$$

and

$$\beta_x \rho u \frac{\partial H}{\partial x} + \beta_y \rho v \frac{\partial H}{\partial y} = \frac{\partial}{\partial y}\left[\beta_y\left(\frac{K}{C_p}\frac{\partial H}{\partial y} - \overline{\rho v' h'}\right)\right]$$

$$+u\frac{\partial}{\partial x}(\beta_x P)+\beta_y\frac{\partial u}{\partial y}\left(\mu\frac{\partial u}{\partial y}-\overline{\rho u'v'}\right)$$
$$+\frac{1}{2}\rho C_D\frac{d(y)}{L^2}u^3+\pi\frac{K\mathrm{Nu}_d}{L^2}(T_R-T) \quad (6)$$

Examination of equations (5) and (6) shows that empirical models for $-\overline{\rho u'v'}$, $-\overline{\rho v'h'}$, and the roughness element drag coefficient C_D and Nusselt number Nu_d are necessary for closure.

The blockage parameters β_x and β_y and the element shape descriptor $d(y)$ require no empirical fluid mechanics input as they are determined solely from the geometry of the rough surface. Taylor et al. (1984) have shown for uniform three-dimensional roughness elements with circular cross section that

$$\beta_x=\beta_y=1-\frac{\pi d^2}{4L^2} \quad (7)$$

The boundary conditions for the discrete element approach for rough wall flows are identical to those for smooth wall flows. The wall location ($y = 0$) is the smooth surface on which the roughness elements occur. At $y = 0$, $u = v = 0$ and $H = H_w$. As $y\to\infty$, $u\to U_\infty$ and $H\to H_\infty$.

The "wall shear stress" is defined as the sum of the shear and drag forces on the wall in the mean flow direction divided by the plan area of the wall. The corresponding skin friction coefficient is then

$$C_f=\frac{(\beta_y)_w\mu\left.\frac{\partial u}{\partial y}\right|_w+\frac{1}{2}\frac{1}{L^2}\int_0^\infty(\rho d C_D u^2)dy}{\frac{1}{2}\rho_\infty U_\infty^2} \quad (8)$$

and the Stanton number is

$$\mathrm{St}=\frac{-(\beta_y)_w\frac{K}{C_p}\left.\frac{\partial H}{\partial y}\right|_w+\frac{\pi}{L^2}\int_0^\infty[K\mathrm{Nu}_d(T_R-T)]dy}{\rho_\infty U_\infty(H_w-H_{o,\infty})} \quad (9)$$

These definitions for C_f and St can be formulated from physical reasoning. However, they also arise naturally from equations (4)–(6) in the formulation of the integral boundary layer equations using the discrete element model.

In order to solve equations (4), (5), and (6), turbulence models for $-\overline{\rho u'v'}$ and $-\overline{\rho v'h'}$ and roughness models for C_D and Nu_d are required. Because of its wide acceptance and proven predictive capability for boundary layer flows over smooth surfaces, the Prandtl mixing length model with van Driest damping and a constant turbulent Prandtl number is used for turbulence closure. Thus

$$-\overline{\rho u'v'}=\rho\ell_m^2\left(\frac{\partial u}{\partial y}\right)\left|\frac{\partial u}{\partial y}\right| \quad (10)$$

where

$$\ell_m=0.40y[1-\exp(-y^+/26)];\ \ell_m<0.09\delta \quad (11)$$

$$\ell_m=0.09\delta;\ \text{otherwise} \quad (12)$$

and

$$-\overline{\rho v'h'}=\frac{\mu_t}{\mathrm{Pr}_t}\frac{\partial H}{\partial y} \quad (13)$$

where

$$\mathrm{Pr}_t=0.9 \quad (14)$$

Taylor et al. (1984), and also Lin and Bywater (1980), chose to formulate the roughness element C_D and Nu_d models as functions of the local element Reynolds number

$$\mathrm{Re}_d=u(y)d(y)/\nu \quad (15)$$

which includes roughness element size and shape information through $d(y)$. The *general shape* of the drag coefficient and Nusselt number versus Reynolds number curves of Zukauskas (1972) were used as starting points to determine the final expressions for C_D and Nu_d through comparison with calibration data sets from well-defined rough surfaces. As discussed by Taylor et al. (1984), the C_D model that gave the best overall agreement was

$$\log C_D=-0.125\log(\mathrm{Re}_d)+0.375 \quad (16)$$

The C_D model has been tested for values of Re_d up to about 25,000 (Taylor et al., 1984; Scaggs et al., 1988).

Taylor et al. also developed a $\mathrm{Nu}_d=f(\mathrm{Re}_d, \mathrm{Pr})$ model for Reynolds numbers up to $\mathrm{Re}_d=1000$ using the heat transfer data on the single rough surface from the Stanford series of tests. They chose the 27 m/s experimental run by Pimenta (1975) to calibrate their model.

In our current effort, a modified Nu_d model was formulated using that of Taylor et al. (1984) as a starting point. The new model is

$$\mathrm{Nu}_d=1.7\ \mathrm{Re}_d^{0.49}\mathrm{Pr}^{0.4} \quad (17)$$

This model has been tested up to $\mathrm{Re}_d\approx 2200$ using several experimental runs from multiple rough surfaces including the Stanford rough surface.

Experimental Apparatus and Measurement Procedures

The experiments were performed in the Turbulent Heat Transfer Test Facility (THTTF), which is shown schematically in Fig. 2. Complete descriptions of the facility and its qualification are presented by Coleman et al. (1988). This facility is a closed-loop wind tunnel with a free-stream velocity range of 6 to 67 m/s. The temperature of the circulating air is controlled with an air to water heat exchanger and a cooling water loop. Following the heat exchanger the air flow is conditioned by a system of honeycomb and screens.

The bottom wall of the 2.4-m-long test section consists of 24 electrically heated flat plates, which are abutted together to form a continuous flat surface. These precision machined test plates are roughened with 1.27-mm-dia hemispherical elements spaced 4 diameters apart in a staggered array, as shown in Fig. 3. The measured average surface roughness on the "smooth" wall portion of the plates is less than 1.6 μm and the allowable step (or mismatch) between any two plates is 0.013 mm. The heating system is under active computer control and any desired set of plate temperatures can be maintained within the limits of the power supply. For example, the plate temperature can be maintained at any temperature, ± 0.1°C, between 50°C and 2°C above the free-stream air temperature, which is typically 30°C. To minimize the conduction losses, the side rails that support the plates are heated to approximately the same temperature as the plates.

The top wall can be adjusted to maintain a constant free-stream velocity. An inclined water manometer with resolution

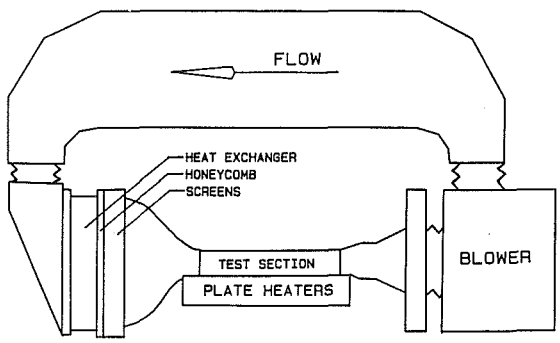

Fig. 2 Schematic of the turbulent heat transfer test facility (THTTF)

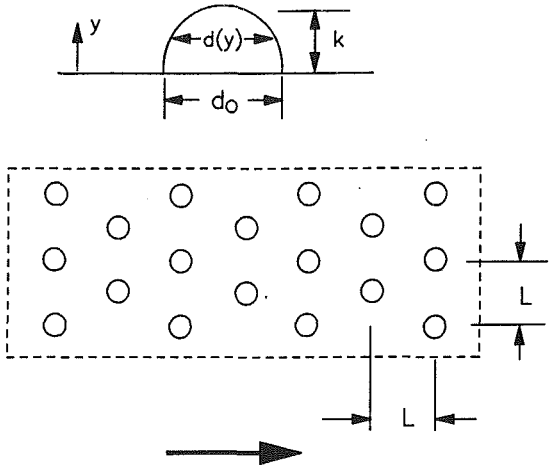

Fig. 3 Surface roughness geometry

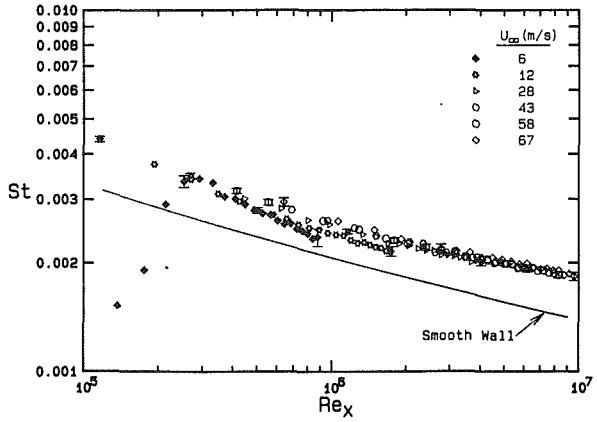

Fig. 4 Composite plot of THTTF Stanton number data for the L/d_o = 4 surface versus x-Reynolds number

of 0.06 mm is used to measure the pressure gradient during top wall adjustment. Static pressure taps are located in the side wall adjacent to each plate. The pressure tap located at the second plate is used as a reference, and the pressure difference between it and each other tap is minimized. For example, the maximum pressure difference for the 42 m/s case was 0.30 mm of water.

The boundary layer is tripped at the exit of the 19:1 area ratio inlet nozzle with a 1 mm × 12 mm wooden strip. This trip location is immediately in front of the heated surface.

Before proceeding with rough surface testing with the THTTF, a series of smooth wall qualification tests were performed to insure the fitness of the test rig and the correctness of the instrumentation, data acquisition system, and data reduction procedures (Coleman et al., 1988). Measurements in the nozzle exit plane showed the mean velocity to be uniform within about 0.5 percent and the free-stream turbulence intensity to be less than 0.3 percent. Measurements 1.1 m downstream of the nozzle exit showed the spanwise variation of momentum thickness to be less than ±5 percent. Profiles of mean temperature and velocity were in good agreement with the usual "laws-of-the-wall." Stanton number data for the constant wall temperature cases were in excellent agreement with the data of Reynolds et al. (1958), which is the definitive data set on which the usual Stanton number correlations are based. The THTTF smooth wall data fall within the data scatter of this definitive data set.

Stanton Number Determination. The data reduction expression for the experimentally determined Stanton number is

$$\mathrm{St} = \frac{W - q_r - q_c}{A\rho C_p U_\infty (T_w - T_o)} \tag{18}$$

The power, W, supplied to each plate heater is measured with a precision wattmeter. The radiation heat loss, q_r, is estimated using a gray body enclosure model where the emissivity of the nickel-plated aluminum is estimated as $\epsilon = 0.11$. The conductive heat loss, q_c, is calculated using an experimentally determined plate conductance, $(UA)_{\mathrm{eff}}$, which includes both side rail and back losses. The conduction losses are minimized by actively heating the side rails. Both q_r/W and q_c/W are generally in the 0.5–1 percent range. The plate area, A, is determined from the length and width dimensions. The density and specific heat are determined from property data for moist air using the measured values of barometric pressure and wet and dry bulb temperatures in the tunnel. The free-stream velocity is measured using a pitot probe and specially calibrated precision pressure transducers. The free-stream and plate temperatures are measured using specially calibrated thermistors. The free-stream total temperature, T_o, is computed using the measured free-stream recovery temperature, T_r, and a recovery factor for the free-stream thermistor probe of $r = 0.86$ (Eckert and Goldstein, 1976). All fluid properties are evaluated at the free-stream static temperature.

The experimentally determined Stanton number is then a function of the 13 measured variables and reference parameters

$$\mathrm{St} = \mathrm{St}(W, \epsilon, A, T_w, T_r, T_{\mathrm{rail}}, (UA)_{\mathrm{eff}}, T_{wb}, P_{\mathrm{bar}}, C_{p_{\mathrm{air}}}, C_{p_{\mathrm{water}}}, U_\infty, r) \tag{19}$$

The uncertainty in the experimentally determined Stanton number was estimated based on the ANSI/ASME *Standard on Measurement Uncertainty* (1986) following the procedures of Coleman and Steele (1989). Precision errors associated with all measured variables used to determine the Stanton number were found to be negligible compared to the corresponding bias errors except for the 6 m/s run. Investigation showed that at low free-stream velocities—$U_\infty \leq 6$ m/s for the rough wall tests—the heat transfer coefficients are relatively low and the time constant of the THTTF is thus increased. At these conditions the time constant of the THTTF is large enough so that the relatively long period variations in facility line voltage to the test plate heater circuits and in the temperature of the incoming make-up water for the heat exchanger loop affect the ability to hold a tight steady-state condition. Observations of the St results for previous smooth wall runs at low U_∞ and the three rough wall U_∞ = 6 m/s runs produced a 95 percent confidence estimate of a precision limit in St of about 3 percent for these conditions. The 3 percent precision limit contribution was combined by root-sum-square with the estimated bias limit to obtain the overall uncertainty in St. For the Stanton number data in this paper, the overall uncertainty, as discussed in detail by Coleman et al. (1988), ranged from about 2 percent to 5 percent, depending on flow conditions.

Results and Discussion

Stanton number data obtained on a rough surface at both transitionally rough and fully rough states are presented for nominal free-stream velocities of 6, 12, 28, 43, 58, and 67 m/s. The rough surface is composed of 1.27-mm-dia hemispheres spaced in a staggered array 4 base diameters apart as shown in Fig. 3. Figure 4 shows a composite plot of the Stanton data for this surface. The uncertainty intervals on selected points indicate the estimated uncertainties in the experimentally determined Stanton number. The figure reveals that the Stanton number for this rough surface is greater than that for a smooth surface with an equivalent free stream by up to about 40 percent. Moreover, the data do not all collapse to a single curve

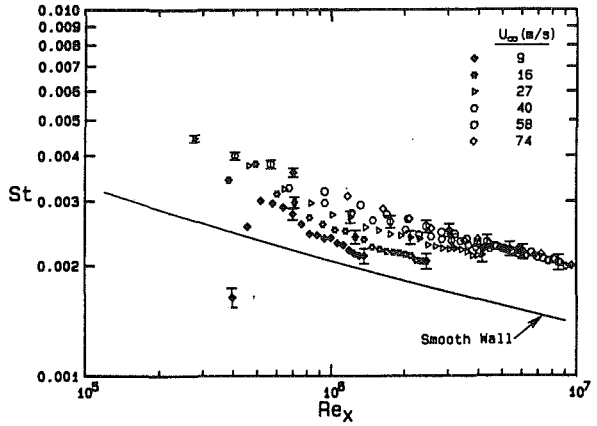

Fig. 5 Composite plot of Stanton number data versus Re_x for the Stanford surface

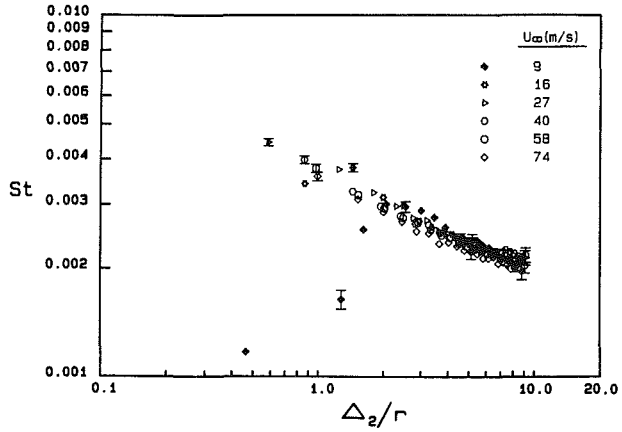

Fig. 6 Composite plot of Stanton number data for the Stanford surface versus enthalpy thickness normalized by the roughness element radius

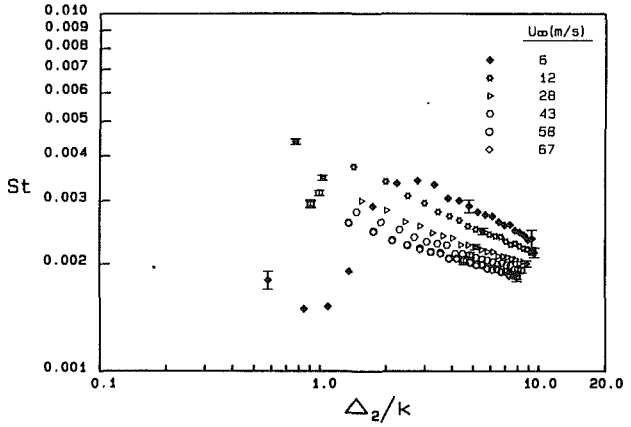

Fig. 7 Composite plot of THTTF Stanton number data for the L/d_o = 4 surface versus enthalpy thickness normalized by the roughness element height (which corresponds to the roughness element radius)

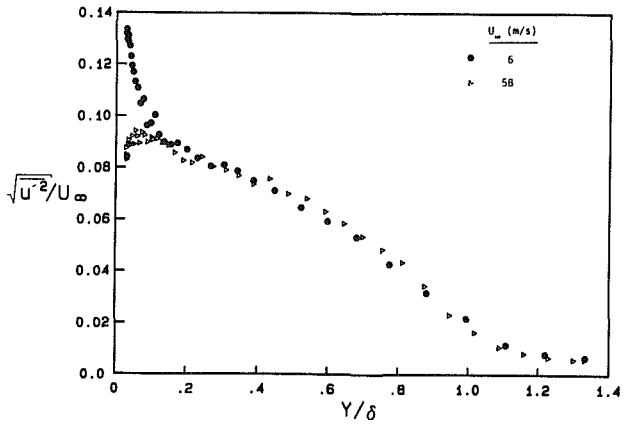

Fig. 8 Comparison of the axial turbulence intensity profiles in transitionally rough and fully rough flow regimes for the L/d_o = 4 surface

in St versus Re_x coordinates as is the case for a smooth wall. The data for free-stream velocities of 6 and 12 m/s are clearly on different tracks. However, as the free-stream velocity increases, the data collapse to a single curve within the data uncertainty.

Figure 5 shows Stanton number data sets reported by Healzer (1974) and Pimenta (1975) for constant wall temperature, zero pressure gradient turbulent boundary layer flows over the Stanford surface plotted in St versus Re_x coordinates. These data exhibit similar behavior to those for the THTTF rough surface in that the data for the highest free-stream velocities appear to collapse together in these coordinates. However, for this surface the data for U_∞ = 27 m/s fall below the higher U_∞ data rather than collapsing together with them. Neither Healzer nor Pimenta stressed the apparent approach of the St data to a single curve versus Re_x as U_∞ increased. Rather, they postulated such behavior in St versus Δ_2/r coordinates.

Figure 6 shows the zero pressure gradient Stanton number data sets from the Stanford surface plotted versus Δ_2/r, where Δ_2 is the enthalpy thickness and r is the radius of the spherical roughness elements. As discussed previously, Pimenta (1975) concluded that, for the Stanford surface, Stanton data plotted in these coordinates fell on a single curve for boundary layers that were considered to be in the fully rough regime. Based on this conclusion and on the indications from his fluid mechanics data, he classified the 9 and 16 m/s runs as transitionally rough and the 27, 40, 58, and 74 m/s runs as fully rough.

Figure 7 shows the THTTF Stanton number data plotted versus Δ_2/k for free-stream velocities of 6, 12, 28, 43, 58, and 67 m/s (k is the roughness height and corresponds to the sphere radius, r, used in the original Stanford surface data presentations). As shown, as the free-stream velocity increases the data approach a single curve with the data for 58 m/s and 67 m/s essentially coinciding. If Pimenta's criterion based on St versus Δ_2/k behavior is used, the boundary layer on this surface would be considered to be in the fully rough regime only for the free-stream velocities of 58 and 67 m/s and in the transitionally rough regime for 6, 12, 28, and 43 m/s.

The second approach to distinguish between the transitionally rough and fully rough regimes proposed by Pimenta was to look for distinctive behavior of the $\overline{u'^2}$ profile near the wall. Figure 8 shows the profiles of $(\overline{u'^2})^{1/2}/U_\infty$ versus y/δ for the THTTF 6 and 58 m/s runs. The 6 m/s profile shows a behavior that is very similar to the profile over a smooth surface with a near-wall peak. According to Pimenta, this is an indication that the boundary layer is in the transitionally rough regime. For 58 m/s, the profile is typical of a fully rough boundary layer as described by Pimenta. The peak in $(\overline{u'^2})^{1/2}/U_\infty$ has moved farther from the wall and is broader. Observation of the $(\overline{u'^2})^{1/2}$ profiles led to the conclusion that the 6 and 12 m/s runs were transitionally rough, while those for 28 m/s and above were fully rough.

In Fig. 9. the Stanton number data sets for the Stanford surface reported by Healzer (1974) and Pimenta (1975) are compared with calculations made with the discrete element method discussed previously. The calculations for free-stream velocities of 9, 16, 27, 40, and 58 m/s are in excellent agreement with Pimenta's data. For the free-stream velocity of 74 m/s, the discrete element model predicts Healzer's data to almost within the data uncertainty of ±0.0001 St units. The data for

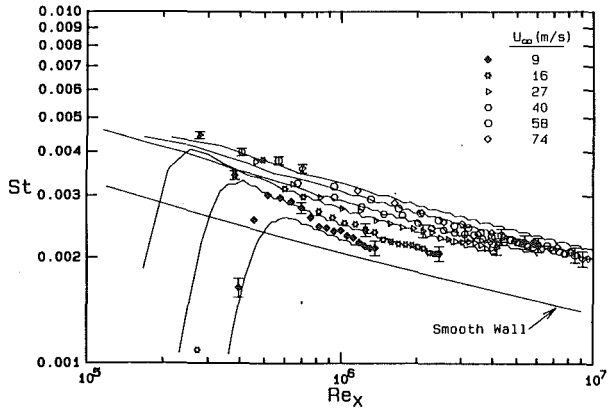

Fig. 9 Comparison of predictions using the discrete element method with the Stanford Stanton number data

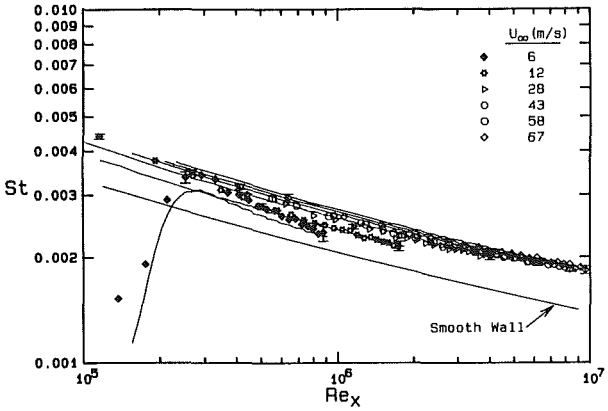

Fig. 10 Comparison of predictions using the discrete element method with the THTTF Stanton number data

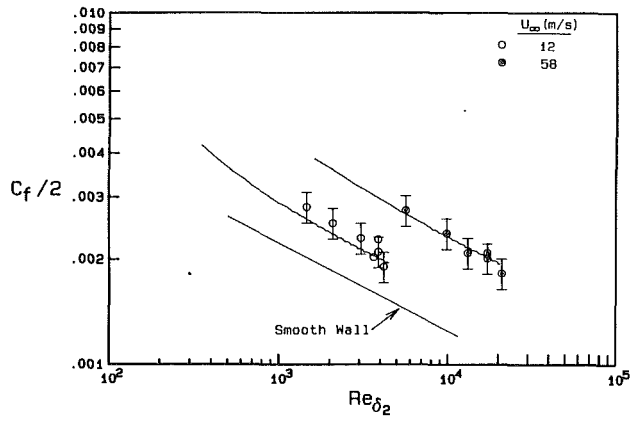

Fig. 11 THTTF skin friction coefficient distributions versus momentum thickness Reynolds number compared with the predictions from the discrete element method

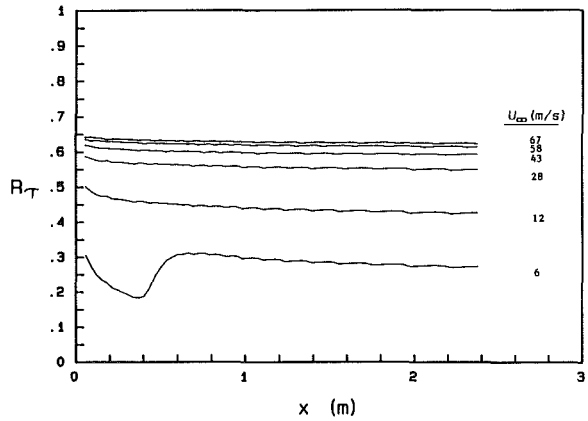

Fig. 12 Distribution of R_τ versus x computed with the discrete element method for the THTTF runs

9 and 16 m/s were in the transitionally rough regime, according to Pimenta, while the 27, 40, 58, and 74 m/s results were in the fully rough regime. In Fig. 10, the THTTF Stanton number data sets are compared with predictions made with the discrete element method for free-stream velocities of 6, 12, 28, 43, 58, and 67 m/s. As shown, the discrete element method predicts each data set extremely well, irrespective of any transitionally rough and fully rough classifications.

Measurements of the skin friction coefficient were made at free-stream velocities of 12 and 58 m/s to obtain data in both transitionally rough and fully rough regimes. Figure 11 shows a plot of skin friction coefficient versus Reynolds number based on momentum thickness, Re_{δ_2}. The error bars represent the estimated ± 10 percent uncertainty in C_f, while the curves represent the predictions using the discrete element model. Comparison of the data and predictions shows that the agreement is excellent, with the predictions matching the data within the ± 10 percent uncertainty.

The agreement between the calculations and the data sets for both heat transfer and fluid mechanics over such a range of free-stream velocities for the two different surfaces is certainly encouraging. The fact that the two surfaces were manufactured differently and had different characteristics and the discrete element model was able to predict each data set so closely is noteworthy. The ability of the discrete element model to predict the data sets from these two different surfaces over both the transitionally rough and fully rough flow regimes indicates that the roughness model incorporates a significant portion of the physics of the interactions between the roughness elements and the flow.

Figure 12 shows a plot of R_τ versus x calculated using the discrete element model for all of the THTTF runs. As was discussed previously, the ratio $R_\tau = \tau_R/\tau_T$ is an alternative measure proposed by Taylor et al. (1984) for classification of aerodynamically smooth, transitionally rough, and fully rough regimes. Based on the limit between transitionally and fully rough flow regimes suggested by Scaggs et al. (1988) of R_τ about 0.6, the 6 and 12 m/s results would definitely be classified as transitionally rough, while the 28 m/s run (with $R_\tau \approx 0.56$) would fall in the upper range of transitionally rough and the 43, 58, and 67 m/s runs (with $R_\tau \approx 0.60$–0.65) would be classified in the fully rough state.

Summary

Experimental data on a rough surface at both transitionally rough and fully rough states are presented for Stanton number distribution, skin friction coefficient distribution, and turbulent intensity profiles. Special emphasis is placed on the characteristics of heat transfer in flows that would be classified as transitionally rough. The Stanton number data are compared with previously published data, and the classification of a boundary layer flow into transitionally rough and fully rough regimes is explored. Futhermore, computations using the previously published (Taylor et al., 1984, 1985) discrete element prediction approach are presented and compared with data from two different rough surfaces. The discrete element predictions for both rough surfaces are found to be in substantial agreement with the data. Such agreement between the calculations and the data sets over a wide range of free-stream velocities for two different surfaces and for both transitionally rough and fully rough flow regimes is encouraging since it indicates that the discrete element method with the current

roughness models for C_D and Nu_d incorporates a significant portion of the physics of the interactions between the roughness elements and the flow.

Acknowledgments

This work was supported by the U.S. Air Force Office of Scientific Research (Research Grant AFOSR-86-0178), and the experimental apparatus was acquired under grant AFOSR-85-0075. The authors gratefully acknowledge the interest and encouragement of Capt. Hank Helin of AFOSR and also the expert help of Mr. James Garner in the experimental effort reported herein.

References

Adams, J. C., and Hodge, B. K., 1977, "The Calculation of Compressible Transitional Turbulent and Relaminarizational Boundary Layers Over Smooth and Rough Surfaces Using an Extended Mixing-Length Hypothesis," AIAA Paper No. 77-682.

ANSI/ASME, 1986, *Measurement Uncertainty*, PTC 19.1-1985 Part 1.

Coleman, H. W., 1976, "Momentum and Energy Transport in the Accelerated Fully Rough Turbulent Boundary Layer," Ph.D. Dissertation, Mech. Eng. Dept., Stanford University (also Report No. HMT-24).

Coleman, H. W., Hodge, B. K., and Taylor, R. P., 1983, "Generalized Roughness Effects on Turbulent Boundary Layer Heat Transfer," AFATL-TR-83-90.

Coleman, H. W., Hodge, B. K., and Taylor, R. P., 1984, "A Reevaluation of Schlichting's Surface Roughness Experiment," ASME *Journal of Fluids Engineering*, Vol. 106, pp. 60–65.

Coleman, H. W., Hosni, M. H., Taylor, R. P., and Brown, G. B., 1988, "Smooth Wall Qualification of a Turbulent Heat Transfer Test Facility," TFD-88-2, Mechanical and Nuclear Engineering Department, Mississippi State University.

Coleman, H. W., and Steele, W. G., 1989, *Experimentation and Uncertainty Analysis for Engineers*, Wiley, New York.

Eckert, R. G., and Goldstein, R. J., 1976, *Measurements in Heat Transfer*, 2nd ed., McGraw-Hill, New York.

Finson, M. L., 1975, "A Reynolds Stress Model for Boundary Layer Transition With Applications to Rough Surfaces," AFOSR-TR-76-0322.

Finson, M. L., and Wu, P. K. S., 1979, "Analysis of Rough Wall Turbulent Heating With Applications to Blunted Flight Vehicles," AIAA Paper No. 79-008.

Finson, M. L., and Clark, A. S., 1980, "The Effects of Surface Roughness Character on Turbulent Reentry Heating," AIAA Paper No. 80-1459.

Finson, M. L., 1982, "A Model for Rough Wall Turbulent Heating and Skin Friction," AIAA Paper No. 82-0199.

Healzer, J. M., 1974, "The Turbulent Boundary Layer on a Rough, Porous Plate: Experimental Heat Transfer with Uniform Blowing," Ph.D. Dissertation, Mech. Eng. Dept., Stanford University (also Report No. HMT-18).

Holden, M. S., 1983, "Studies of Surface Roughness Effects in Hypersonic Flow," Calspan Report No. 7018-A-2, Advanced Technology Center, Buffalo, NY.

Ligrani, P. M., 1979, "The Thermal and Hydrodynamic Behavior of Thick, Rough-Wall, Turbulent Boundary Layers," Ph.D. Dissertation, Mech. Eng. Dept., Stanford University (also Report No. HMT-29).

Lin, T. C., and Bywater, R. J., 1980, "The Evaluation of Selected Turbulence Models for High-Speed Rough Wall Boundary Layer Calculations," AIAA Paper No. 80-0132.

Nikuradse, J., 1933, "Stromungsgesetze in Rauhen Rohren," VDI-Forchungsheft 361 (also "Laws of Flow in Rough Pipes," NACA TM 1292).

Norris, R. H., 1971, "Some Simple Approximate Heat Transfer Correlations for Turbulent Flow in Ducts With Surface Roughness," *Augmentation of Convective Heat and Mass Transfer*, ASME, New York.

Nunner, W., 1956, "Heat Transfer and Pressure Drop in Rough Tubes," VDI Forschungsheft, No. 455, Series B, Vol. 22, pp. 5–39; English translation, 1956, A.E.R.E. Library/Transactions 786.

Pimenta, M. M., 1975, "The Turbulent Boundary Layer: An Experimental Study of the Transport of Momentum and Heat with the Effect of Roughness," Ph.D. Dissertation, Mech. Eng. Dept., Stanford University (also Report No. HMT-21).

Reynolds, W. C., Kays, W. M., and Kline, S. J., 1958, "Heat Transfer in the Turbulent Incompressible Boundary Layer, Parts I, II, and III," NASA Memos 12-1-58W, 12-2-58W, and 12-3-58W.

Scaggs, W. F., Taylor, R. P., and Coleman, H. W., 1988, "Measurement and Prediction of Rough Wall Effects on Friction Factor—Uniform Roughness Results," ASME *Journal of Fluids Engineering*, Vol. 110, pp. 385–391.

Schlichting, H., 1936, "Experimentelle Untersuchungen Zum Rauhigkeits-Problem," *Ingenieur-Archiv.*, Vol. VII, No. 1, pp. 1–34 (also "Experimental Investigation of the Problem of Surface Roughness," NACA TM 832).

Sood, N. S., and Jonsson, V. K., 1969, "Some Correlations for Resistances to Heat and Momentum Transfer in the Viscous Sublayer at Rough Walls," ASME *Journal of Heat Transfer*, Vol. 91, pp. 488–494.

Taylor, R. P., Coleman, H. W., and Hodge, B. K., 1984, "A Discrete Element Prediction Approach for Turbulent Flow Over Rough Surfaces," Mech. and Nuc. Eng. Dept., Mississippi State University, Report No. TFD-84-1.

Taylor, R. P., Coleman, H. W., and Hodge, B. K., 1985, "Prediction of Turbulent Rough-Wall Skin Friction Using a Discrete Element Approach," ASME *Journal of Fluids Engineering*, Vol. 107, pp. 251–257.

Taylor, R. P., 1989, "Skin Friction and Heat Transfer Predictions for Turbulent Boundary Layer Flow Over Rough Surfaces," Mech. and Nuc. Eng. Dept., Mississippi State University, Aug.

Taylor, R. P., 1990, "Surface Roughness Measurements on Gas Turbine Blades," ASME JOURNAL OF TURBOMACHINERY, Vol. 112, pp. 175–180.

Zukauskas, A., 1972, "Heat Transfer From Tubes in Crossflow," *Advances in Heat Transfer*, Academic Press, New York.

The Effect of Incident Wake Conditions on the Mean Heat Transfer of an Airfoil

K. Dullenkopf

A. Schulz

S. Wittig

Lehrstuhl und Institut für Thermische Strömungsmaschinen, Universität Karlsruhe (T.H), D-7500 Karlsruhe, Federal Republic of Germany

The flow phenomena of wakes shed by upstream blade rows is a well-known problem in turbomachinery, which influences blade forces, vibrations, losses, and heat transfer. With respect to the heat load to turbine blades, this problem becomes even more complex because of the interaction between wake, potential flow, and the boundary layer along the surface of the airfoil. Experimentally evaluated mean heat transfer coefficients obtained under different unsteady initial conditions are reported. The heat transfer measurements have been carried out in the cascade test facility at the ITS in Karlsruhe, using a rotating bar wake generator placed upstream of the cascade to simulate the wake passing process. The variation of the wake parameters includes different wake passing frequencies, cascade inlet Reynolds numbers, and wake inclination angles. In addition, the relevant parameters of the unsteady wake have been measured by means of a fixed hot-wire anemometer using the ensemble-average technique. The results are compared to those from the literature for the wake of a cylinder in crossflow. They also serve as experimental base for parallel theoretical analyses.

Introduction

Common design methods for turbomachines based on computer codes, correlations, or experimental results are often still limited to steady-state flow conditions. In order to predict the performance of axial-flow turbomachines, it is necessary to understand how the unsteady nature of the flow inside a turbomachine affects the performance of specific components. The periodic change in the inflow conditions caused by the relative motion of adjacent blade rows has three major effects. The first and probably least important is the potential flow interaction. As described by several authors, potential flow interaction occurring upstream and downstream of the blade is weak and its decay rate is high. In some cases it is necessary to take care of the secondary flow vortices, especially in low aspect ratio stages (Binder, 1985). The majority of research work concerning unsteady turbomachinery flow concentrates on the effects of wakes shed by upstream blades or obstructions to the performance of turbomachinery components. Not taking into account the investigations on unsteady compressor aerodynamics, several groups are performing experimental and theoretical research work in the field of unsteady effects in turbine flows (Doorly et al., 1985; Doorly, 1988; Hodson, 1985; Addison and Hodson, 1990a, 1990b; Dunn et al., 1989; Dring et al., 1986). The major part of the published results describes the interaction between a wake flow and the boundary layer on the suction side of a turbine blade. The experimental tests have been conducted either in turbines (Dunn, 1985, 1986; Dring et al., 1986; Hodson, 1985; Guenette et al., 1989; Stöcker, 1987; Stöcker et al., 1983) or in laboratory simulations (Doorly et al., 1985; Pfeil and Pache, 1977; Wittig et al., 1988). Most of the available data concern forced transition, caused by wake impact. This behavior of the boundary layer has, in addition to other effects, a significant influence on the heat load of a turbine blade. Many investigators—the groups at Calspan, Oxford, or Cambridge, for example—are using fast responding sensors in order to obtain the real time history of the boundary layer/wake interaction. Our complementary approach to studying the problem is to evaluate a broad database of time mean results under different inflow conditions. Quite often the knowledge about the time average of the heat load to a turbine blade is sufficient for design-relevant statements. The periodic high-frequency variation of the free-stream temperature and the heat transfer is damped at the blade surface and right below the surface because of the thermal inertia of the blade material. The time mean values, instead, can be largely affected by periodic wake impact to the boundary layer. Based on all the information, no attempt was made in the present study to perform high-frequency measurements, and we confined our efforts to conduct time mean heat transfer measurements using a technique proposed by Turner (1971) and approved by us several years ago (Wittig et al., 1985, 1988). This experimental study alone will not lead to a complete understanding of the complex phenomena within the boundary layer during the interaction with a wake, but based on the results several theoretical analyses were initiated.

It is the common opinion that the wake impact causes an unsteady laminar-to-turbulent transition. These zones of transition move downstream and propagate with a certain factor forming a growing region of turbulent flow and high "tur-

Contributed by the International Gas Turbine Institute and presented at the 35th International Gas Turbine and Aeroengine Congress and Exposition, Brussels, Belgium, June 11–14, 1990. Manuscript received by the International Gas Turbine Institute January 20, 1990. Paper No. 90-GT-121.

bulent'' heat transfer. Following this model, the time-averaged heat transfer along the surface is composed of an intermittent laminar and turbulent boundary layer and the related heat transfer. As stated by several authors, the time-averaged conditions for the boundary layer and the heat transfer may be obtained from the following equation:

$$\overline{h} = (1-\gamma)h_{\text{lam}} + \gamma h_{\text{tur}} \tag{1}$$

Mayle and Dullenkopf (1990) presented a model based on the theory of turbulent spots, which accounts for wake-induced and natural transition and shows excellent agreement with the experimental results. Other approaches to solve the problem have been proposed by Doorly (1988), LaGraff et al. (1989), or Addison and Hodson (1990a) interpreting the results of time-resolved measurements obtained by means of high-frequency response sensors.

The time-averaged data of the experimental investigation as presented in this paper were used to improve and test the model of Mayle and Dullenkopf. Complementary to the heat transfer measurements, hot-wire measurements were conducted to monitor the characteristics of the wake flow entering the cascade. These measurements were compared to published correlations (Schlichting, 1982; Pfeil and Eifler, 1975; Van Dresar, 1987) in order to validate the applicability of steady-state results for a cylinder in crossflow.

Experimental Apparatus

Test Section. The linear cascade test facility of the Institute for Thermal Turbomachinery (ITS) was used for both the heat transfer and hot-wire measurements presented in this paper. The cascade, consisting of five blades, is incorporated into the hot gas test facility of the ITS, as already described (Wittig et al., 1985, 1987). The air supply system has a maximum capacity of 2.5 kg/s at a pressure of 1.5 bar. An oil-fired combustion chamber provides the capability to heat the test gas. Directly following the combustion chamber, a settling duct with mixers and meshes reduces the turbulence level and equalizes temperature and velocity profiles. In a circular to rectangular nozzle the air flow is accelerated to the cascade inlet velocity. In order to vary the turbulence level of the inflow, grids of different mesh sizes can be installed. Before entering the cascade, the air passes the rotating wake generator. Instead of a squirrel cage type, preferred by Pfeil and Pache (1977), Liu and Rodi (1989), or Priddy and Bayley (1988), the basic design concept of our wake generator is similar to the one used at Oxford by LaGraff et al. (1989) or Doorly et al. (1985).

Details on the total arrangement of the test section including the wake generator and the cascade are given in Fig. 1. A stainless steel disk is equipped with bars that pass the side walls through adjustable slots along a track parallel to the entrance plane of the cascade. The axis of the disk is located outside of the test section in a sealed housing. Special care was taken

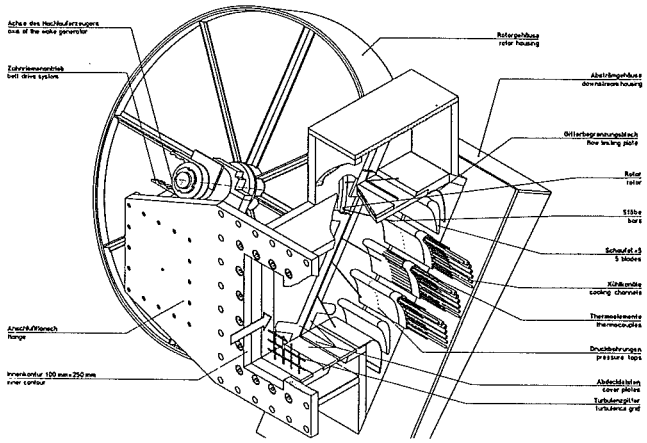

Fig. 1 Heat transfer test rig with rotating wake generator

to avoid flow disturbances by the slots at the measurement plane. Comprehensive tests, including flow visualization, were performed to guarantee that the flow is two dimensional at midplane.

The actual design is matched to the turbine, with special emphasis on the aerodynamic drag of the bars, as investigated in preliminary studies (Wittig et al., 1988). The layout of the wake generator in combination with the cascade allows numerous variations in the flow conditions in order to simulate a wide range of turbine designs as described later. The geometric arrangement in a cross section at midplane is shown in Fig. 2, containing some data on the size, the important velocity components, and angles for the cascade and the bars.

Hot-Wire Instrumentation. For a correct interpretation of the heat transfer results, it is necessary to know about the wake conditions entering the cascade. On the other hand, the present investigation was performed to check whether data from steady-state wake measurements of a cylinder in crossflow can be transformed to our conditions at the inlet plane of the cascade. The hot-wire anemometer is best suited for these measurements because of its capability to give an "analog" signal of the instantaneous flow velocity. Hence, the frequency resolution of the system depends on the sampling frequency of the analog to digital converter (ADC).

The hot-wire probe was located at midspan between two blades on the cascade inlet plane, as shown in Fig. 3. The probe is connected to a constant temperature anemometer bridge. After passing a signal conditioner the signal of the bridge is fed to a plug-in 12 bit ADC card at a personal computer, which handles the data acquisition. When the measurements were performed, only the utilization of a single hot wire was possible because of the limited capacity of the ADC in the PC. Only in the single-channel configuration are the maximum sample

Nomenclature

a = axial distance
$b_{1/2}$ = half width of the wake
c = absolute velocity
c_d = drag coefficient
d = diameter of the bars
d_w = relative duration of the wake $= \tau_w/\tau$
f_w = wake frequency
h = heat transfer coefficient
l = chord length of the airfoil
Re = Reynolds number based on chord length and velocity of the inflow
s/l = dimensionless surface coordinate
T = temperature
u = circumferential velocity
v = velocity
v_{def} = velocity deficit
w = velocity relative to the bar
x = propagation length of the wake
y = coordinate normal to the wake centerline
α = angle between velocities u and w
β = angle between velocities c and w
γ = angle between velocities u and c
γ = intermittency
τ = wake-passing period
τ_w = wake duration time

Superscripts

$\overline{\ }$ = time-averaged quantity
$\tilde{\ }$ = ensemble-averaged quantity
$'$ = random fluctuating quantity

Subscripts

fl = periodic fluctuating quantity
m = maximum
w = quantity of wake
∞ = quantity outside wake

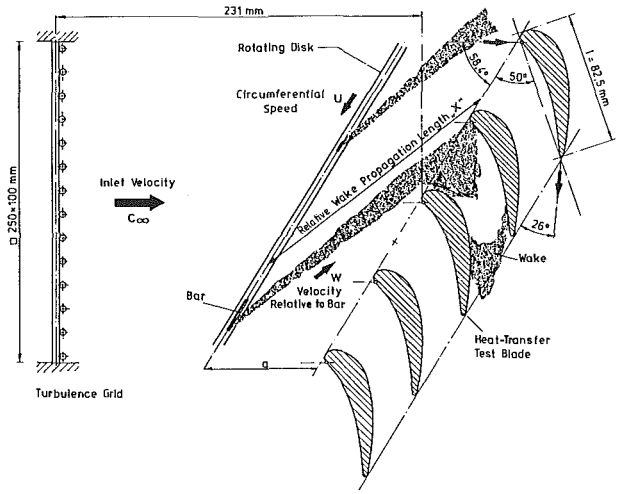

Fig. 2 Geometric arrangement

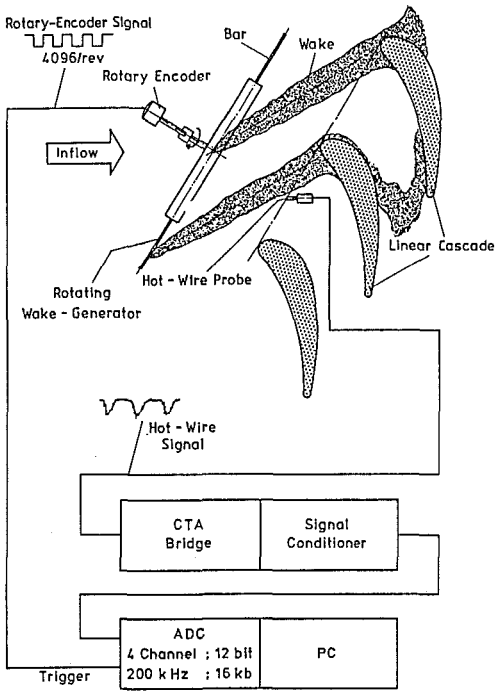

Fig. 3 Hot-wire position and data acquisition

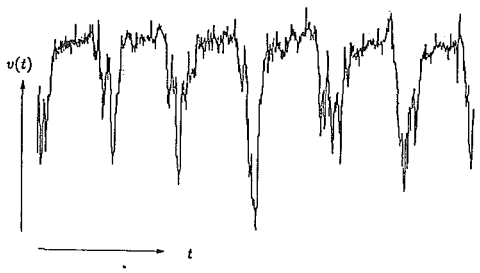

Fig. 4 Instantaneous hot-wire signal (typical record)

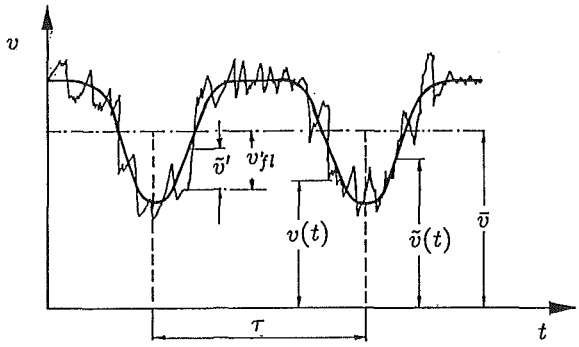

Fig. 5 Parameters of the signal analysis

frequency of 200 kHz and the full memory size of 16 kb available. This capacity is required to arrive at a sufficient temporal resolution of the velocity deficit in the wake passing the probe. A sample frequency of 200 kHz guarantees at least 50 data points in the wake even under the most unfavorable conditions. Because of the limited capacity of the PC the data were transferred to a Micro-VAX and further processing of the data was performed on the minicomputer.

A typical record of the instantaneous velocity signal with the wake generator rotating at the inflow (Fig. 4) demonstrates the characteristic shape with the velocity drop when the wake passes the sensor. The analysis of this unsteady random signal indicates that its behavior is not ergodic; hence the time-averaged value $\bar{v}$ is not equal to the ensemble-average $\tilde{v}(t)$.

$$\bar{v} = \frac{1}{T}\int_0^T v(t)\,dt \tag{2}$$

$$\tilde{v}(t) = \frac{1}{n}\sum_{j=1}^{n} v_j(t) \tag{3}$$

Evaluating only the time mean values of the hot-wire signal would characterize the flow conditions insufficiently because that procedure would lead to a mean velocity $\bar{v}$, as marked in Fig. 5 with a thin line.

Moreover using the well-known approach

$$v' = \bar{v} - v(t) \tag{4}$$

to determine the turbulent fluctuation would give a value composed of a periodic fraction, a fraction resulting from the mixing in the wake and the free-stream turbulence level. The important parameters like the time-dependent velocity $v(t)$ composed of the periodically variable component $\tilde{v}(t)$ and the stochastic velocity fluctuations $\tilde{v}'$ as shown schematically in Fig. 5 have to be calculated with an ensemble-averaging analysis.

Figure 6 demonstrates the technique used to calculate the time-dependent mean velocity according to the following equation:

$$\tilde{v}(t_i) = \frac{1}{m}\sum_{j=1}^{m} v_j(t_i) \tag{5}$$

The distribution of the turbulent fluctuating component over one spacing, as schematically drawn in Fig. 7, is evaluated by means of the following equation:

$$\tilde{v}'^2(t_i) = \frac{1}{m-1}\sum_{j=1}^{m} (v_j(t_i) - \tilde{v}(t_i))^2 \tag{6}$$

As indicated in the previous figures, the averaging procedure is performed over one period τ, which depends on the circumferential speed and the number of bars on the disk. Therefore, the whole dataset of 16 kb has to be separated into regions with length τ containing one wake passing the sensor. Additionally the center of the individual wakes was adjusted to the center of the regions in order to guarantee the correct determination of the wake parameters after the superposition. An extensive software procedure was employed for the analysis. With respect to the accuracy it was not possible to use a trigger signal from the rotary encoder or a calculated value of τ as a reference because the observed variations in the position of the wake center would influence the shape of the mean velocity, the wake width, and above all the turbulence distribution within

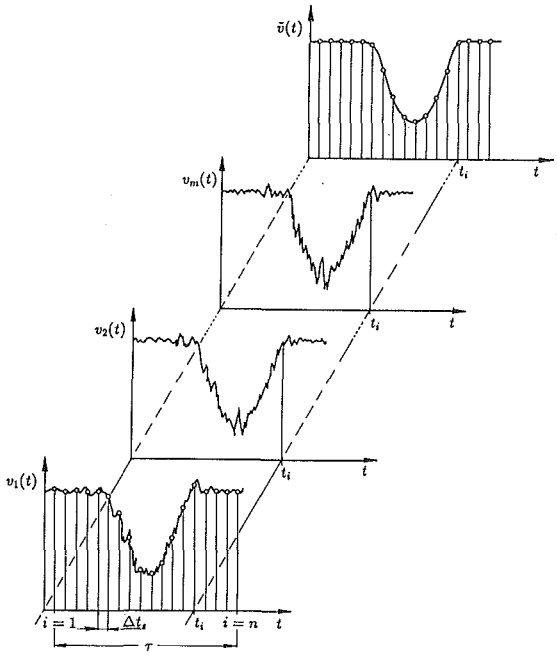

Fig. 6 Ensemble-average technique

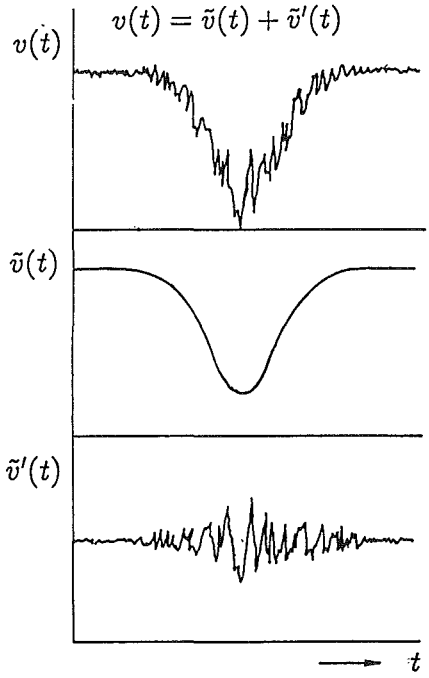

Fig. 7 Ensemble-averaged turbulence distribution

the wake. The averaged values presented later in the paper were calculated from about 100 measured individual wakes obtained from series of consecutive measurements and a subsequent combination at the computer. As an example Fig. 8 presents the shape of the mean velocity distribution and an individual wake.

Heat Transfer Instrumentation. The technique applied to obtain the time mean heat transfer coefficients $\bar{h}$ is based on a calculated temperature distribution in the cross section of the test blade by means of a finite element code, similar to the approach applied by Turner (1971) and used by us in earlier studies (Wittig et al., 1985, 1987, 1988). As marked in Fig. 1, the inner blade of the cascade is used for the heat transfer measurements. It has seven cooling channels and is supplied

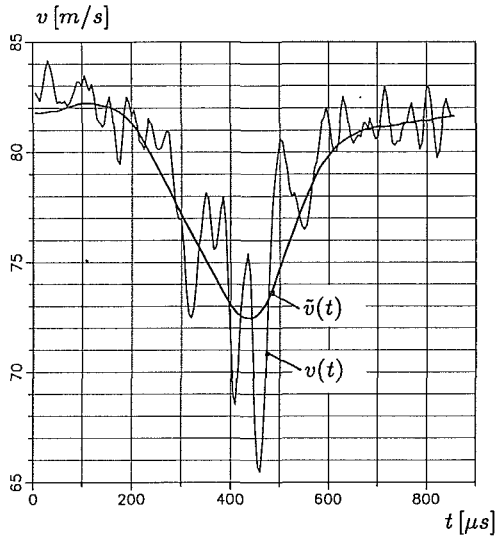

Fig. 8 Superposition of an ensemble-averaged and an individual velocity signal in the wake

with water of a temperature-controlled circuit with an average temperature of about 18°C. In the present test series, the combustion chamber was not used to heat the test gas. Therefore, the inlet air temperature is the compressor exit temperature of about 60°C. The blade is equipped with 32 thermocouples on the surface at midspan to determine the boundary conditions of the finite element code. The heat transfer within the cooling channels is determined from the mass flux and the temperature difference of the cooling fluid between entrance and exit. The resulting temperature field can be used to evaluate the local mean heat transfer coefficients from the gradients of the temperature distribution. A detailed description of the instrumentation, the data acquisition, and the data processing is given by Schulz (1986).

Experimental Results

Both the hot-wire and heat transfer measurements have been carried out in the test section as described in the previous section. The design of the wake generator in combination with the cascade allows a variety of different inflow conditions. Besides the inlet velocity and turbulence level, the circumferential speed of the wake generator can be changed from 0 to 6500 rpm, thus modeling a broad bandwidth of wake inclination angles with respect to the cascade. Obviously the velocity, relative to the bars and the wake frequency, is changed at the same time. Keeping the relative speed constant, the wake frequency can be varied by the number of bars installed in the disk. The present design allows the use of 4, 7, 14, or 28 bars. Another possibility to control the wake width and depth is to change the distance between the cascade and the track of the bars in 6 discrete steps from 60 mm to 112 mm or to install bars of different diameter. In the past, bar diameters of 1.5 mm and 3 mm were used, but our interest was concentrated on the 1.5 mm bars because in this case the drag and the size of the wake correspond well with a frequently studied airfoil (Wittig et al., 1988).

Wake-Flow Results. In the present paper, only some typical results of the hot-wire measurements are presented. It should be kept in mind that a single-wire arrangement was used, which was oriented in the inflow direction. Therefore, only the magnitude of the velocity was detected, not the direction. The velocity and turbulence distributions presented in the following figures were calculated using equations (5) and (6). In Fig. 9 the velocity distribution $\tilde{c}$ and turbulence intensity $\tilde{T}u$ are plot-

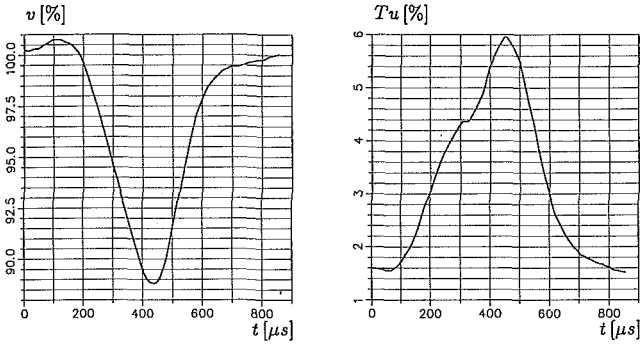

Fig. 9 Velocity and turbulence distribution (absolute frame)

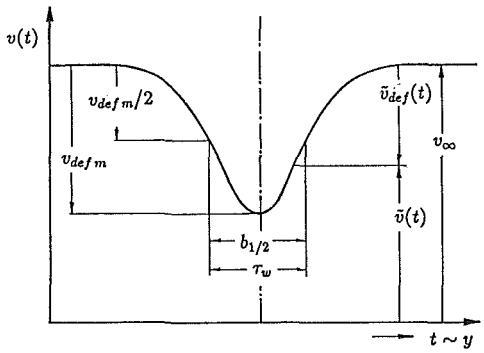

Fig. 10 Wake quantities

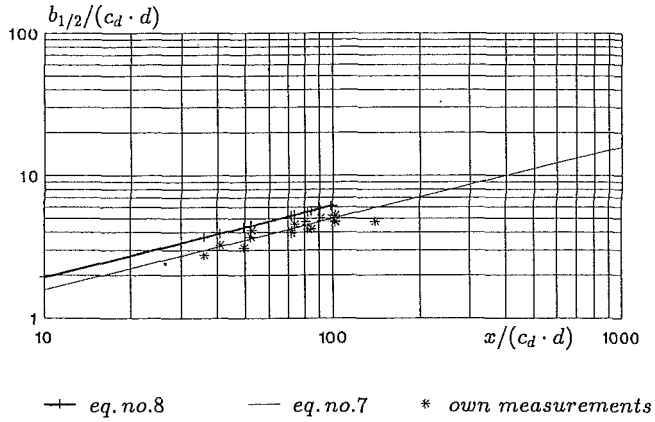

Fig. 11 Comparison of the wake width

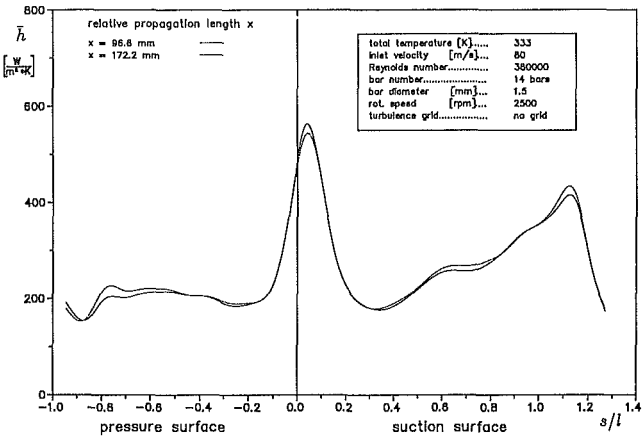

Fig. 12 Variation of the wake width

ted over one period τ. The turbulence intensity distribution presented in the figure is related to the local velocity.

Figure 9 shows an ensemble-averaged velocity and turbulence distribution in the stationary frame plotted over one period. The timespan in this case was 860 μs with 2500 rpm and 28 bars installed in the disk. The velocity was normalized with the undisturbed inlet velocity c_∞—in this case 80 m/s—leading to the expected shape of the distribution. In comparison to the velocity deficit, the flow region affected by the turbulence of the wake is expanded. In this context an interesting detail was observed. Comparing the distributions of the turbulence intensity for 7 bars and 28 bars, measured under identical inflow conditions and circumferential speed of the disk, the turbulence level Tu_∞ shows a remarkable difference between the two cases. Although the wakes in the 28 bars case do not merge in the inflow, the turbulence level between successive wakes does not drop to the undisturbed free-stream level of approximately 0.75 percent. This behavior of the turbulence cannot be observed if only 7 bars are installed to the disk. The turbulence intensity with 28 bars remains at a level almost twice the free-stream level. This effect is not limited to specific inflow conditions. If the relative wake duration $d_w = \tau_w/\tau$ exceeds a certain level, the turbulence intensity between the wakes stays at an increased value. In the near future an investigation will be performed to scrutinize the influence of this phenomenon on the resulting heat transfer to the blade.

The results concerning the wake width obtained from a large number of different test conditions were compared with measurements and correlations published by Reichardt (1942), Schlichting (1982), Pfeil and Eifler (1975), and Van Dresar (1987), which were derived from measurements in the wake of fixed cylinders in crossflow. In contrast, we have been performing our measurements with a fixed hot wire recording a moving wake that passes the probe location. As a consequence, a transformation to the relative frame was necessary for comparison with the wake flow parameters recorded in the stationary frame. The relevant values for the wake formation are the relative velocity w to the bar and the propagation length x in the relative frame. The wake width $b_{1/2}$ as defined in Fig. 10 was used as an indicator for the similarity.

The increase in wake width based on the mean velocity distribution in the relative frame is shown as a function of x in Fig. 11. The results of our own measurements are shown along with two theoretical curves. Equation (7) was used by Schlichting (1982) and Van Dresar (1987) to compare with their own measurements and the data of Reichardt (1942), whereas Pfeil and Eifler (1975) used equation (8) to fit their measurements for $x/d < 100$

$$b_{1/2} = 1/2 \cdot (x c_d d)^{1/2} \tag{7}$$

$$b_{1/2} d = 0.308 \sqrt{c_d} (x/d)^{1/2} \tag{8}$$

Our own measurements seem to match the trend quite well, especially if all the uncertainties of the measurement and the transformation are taken into account. The data show good agreement with the theoretical values from equation (7) whereas equation (8) predicts a higher trend. As far as the wake width is concerned it can be concluded that the transformation of steady-state results leads to good agreement with the performed measurements.

Heat Transfer Results. The temperature measurements from the heat transfer tests are used to calculate local heat transfer coefficients $\bar{h}$ on the whole surface of the blade. In the plots 172 data points are connected by means of a cubic Spline algorithm to smooth the distributions. The local heat transfer coefficients are plotted versus the nondimensionalized surface coordinate s/l. Where s/l equals 0 it characterizes the design stagnation point, whereas $s/l = -1.0$ and $s/l = 1.2$ are the coordinates of the trailing edge on pressure and suction surface, respectively. Figure 12 shows the distributions of the heat transfer coefficients at an inlet velocity of 80 m/s that corresponds

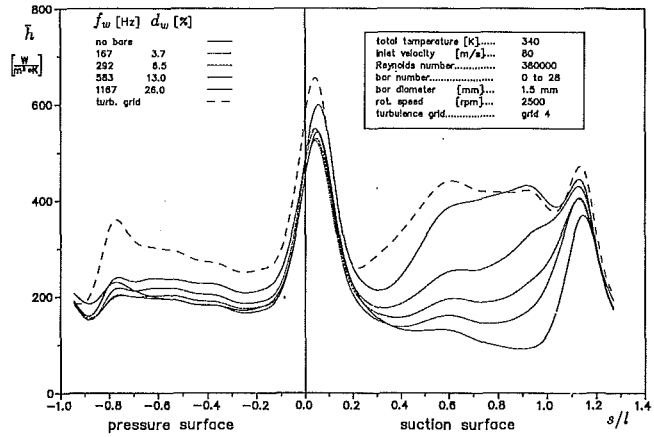

Fig. 13 Variation of the wake frequency, Re = 3.8×10^5

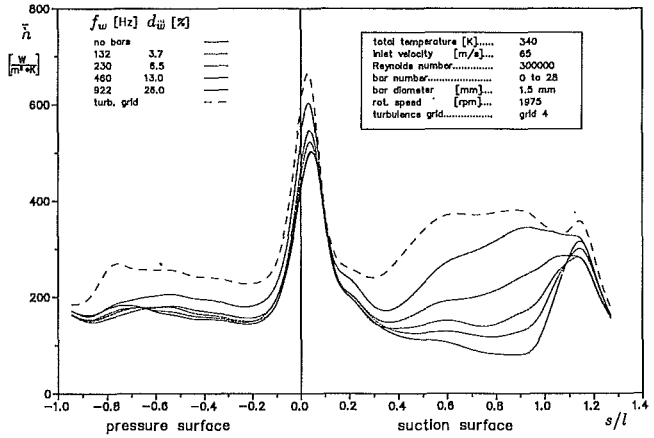

Fig. 14 Variation of the wake frequency, Re = 3.0×10^5

to a Reynolds number of 3.8×10^5 based on the chord length of the blade. The wake generator was equipped with 14 bars and rotated at 2500 rpm. To demonstrate the influence of the axial distance a between the wake-generating bars and the cascade two results are plotted: one with $a = 60$ mm, the other with $a = 107$ mm. The resulting change factor in the relative propagation length x of the wake in this case was 1.78. Assuming that the relation $\Delta b_{1/2} \sim \Delta x^{1/2}$ is valid, it would lead to an increase in the wake width by a factor of 1.34. The corresponding difference between the two distributions is weak as expected and it is covered by the uncertainty of the measurement.

A considerably more significant effect to the heat transfer is demonstrated in the following figures. In Fig. 13 the general inflow conditions are the same as in the previous. Six distributions of the heat transfer coefficient are plotted representing the conditions: no bars, 4 bars, 7 bars, 14 bars, 28 bars, and the fully turbulent case with a grid produced turbulence level of 8 percent. The other important parameters are indicated in the figure. As expected there is a distinct influence of the wakes to the heat transfer on the suction side. Starting with the high values in the vicinity of the stagnation point a strong decrease of the heat transfer can be observed following the increase in the laminar boundary layer thickness. At s/l of approximately 0.2 the boundary layer starts to react sensitively to a disturbance caused by wakes. The exact starting point varies depending on the wake frequency. Downstream from this location the heat transfer coefficients increase to the point where the natural transition occurs, and reaches the turbulent values. The slope of the different distributions can be related to the wake frequency or to the relative wake duration d_w. To emphasize this, both values are included in the following figures. The behavior of the boundary layer and consequently the distribution of the local heat transfer coefficient may be explained by the growth of a turbulent region moving downstream to the trailing edge. According to the theory of Mayle and Dullenkopf (1990) the turbulent region and the wake in the free stream outside the boundary layer act independently after the wake triggers the transition at a specific position on the surface. The resulting time mean distribution of the local heat transfer coefficient, as shown in the figure, is composed of an intermittent laminar and turbulent time fraction, whereas the turbulent fraction increases over the surface length. This leads to the distinct elongated shape of the transitional zone. Although the wake frequency is moderate and the relative wake duration does not exceed 33 percent the heat transfer coefficients in the following figure almost reach the fully turbulent values.

The pressure surface of the test blade does not show a similar behavior. The overall effect of the wakes is considerably less significant and the increase in the local heat transfer remains more or less constant over the major part of the surface. This

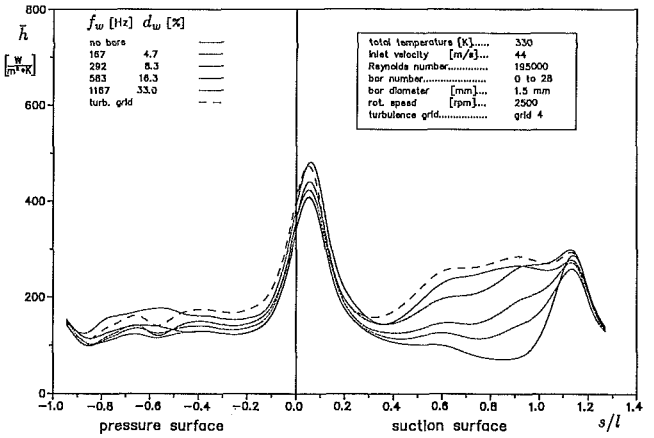

Fig. 15 Variation of the wake frequency, Re = 1.9×10^5

indicates that the local intermittency is approximately constant on the pressure side. The magnitude of the rise seems to depend on the relative wake duration $d_w = \tau_w/\tau$. Because we have focused our interest in the past on the dominant effect, the knowledge about the boundary layer/wake interaction on the pressure side is not as detailed as the one concerning the suction side processes. The "linear" behavior of the pressure side boundary layer on our blade is probably not representative and therefore the results cannot be generalized.

In order to demonstrate the independence of the phenomena described with respect to certain flow conditions, the following figures present heat transfer data obtained under different Reynolds numbers and wake conditions. Again, the number of bars varies from 0 to 28 according to the previous figure. In Figs. 13 and 14 the flow Reynolds number and the rotational speed of the bars were simultaneously reduced to keep the inclination angle of the wakes constant. In Fig. 15, however, only the flow Reynolds number was reduced, which produced a smaller wake inclination angle and a greater propagation length before interaction.

The reason for the differences in the shape of the curves in Fig. 14 in comparison to the others can be found in the fact that a second test blade was used. Therefore, the discrepancy especially in the vicinity of the stagnation point is due to the machining, but the general characteristic of the blade had not changed.

In the last figure of this series, a simple comparison is presented to distinguish whether the wake frequency f_w or the wake duration d_w is the relevant parameter for the development of the boundary layer and the heat transfer along the blade surface. Figure 16 contains two measurements: the first one, performed with 28 bars at 1250 rpm, and the second with 14

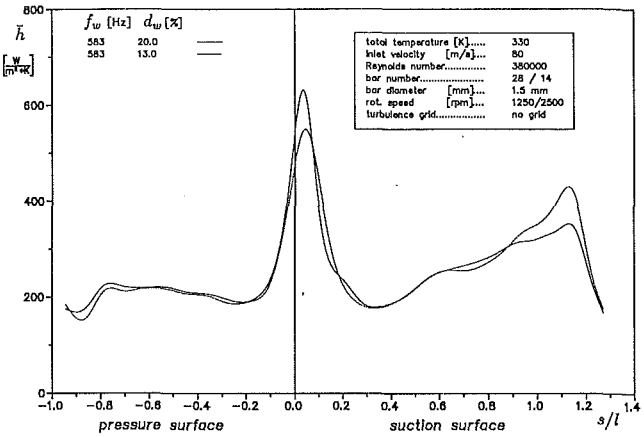

Fig. 16 Constant wake frequency, Re = 3.8×10^5

bars but 2500 rpm. Again the inflow conditions are 80 m/s and the bar diameter is 1.5 mm in both cases. The wake frequency stays constant but the relative wake duration changes from 20 to 13 percent caused by the different wake propagation length and inclination angle. For the interpretation of the results it is important to know that the obvious discrepancy in the leading edge region is caused by the grinding procedure of the blade as already mentioned. In the most interesting region, the transitional zone of the suction side, the h values are almost identical, indicating that the wake frequency is one of the dominant factors for the development of the unsteady boundary layer and consequently for the resulting mean heat transfer.

Conclusion

Measurements of unsteady wake flow have been presented, obtained by means of a fixed hot-wire anemometer using the ensemble-average technique. The results are compared to those from the literature for the wake width of a cylinder in crossflow showing good agreement.

Experimentally evaluated mean heat transfer coefficients obtained under different unsteady initial conditions are reported. The heat transfer as well as the hot-wire measurements have been carried out in the cascade test facility at the ITS in Karlsruhe using a rotating bar wake generator placed upstream of the cascade to simulate the wake passing process. The variation of the wake parameters includes different wake passing frequencies, cascade inlet Reynolds numbers, and different wake inclination angles. The results demonstrate the strong effect of unsteady wakes on the suction side boundary layer and heat transfer. The temporary laminar and turbulent condition in the boundary layer leads to an elongated transitional zone where the wake frequency is a dominant factor for the mean heat transfer.

Acknowledgment

The authors are indebted to Prof. R. E. Mayle from Rensselaer Polytechnic Institute, Troy, New York, who spent several weeks as a visiting professor at the ITS, for his helpful discussions. The work was supported in part by funds from the Bundesministerium für Forschung und Technologie and industrial sponsors through the AG TURBO (working group high-temperature gas turbine).

References

Addison, J. S., and Hodson, H. P., 1990a, "Unsteady Transition in an Axial-Flow Turbine: Part I—Measurements on the Turbine Rotor," ASME JOURNAL OF TURBOMACHINERY, Vol. 112, pp. 206–214.

Addison, J. S., and Hodson, H. P., 1990b, "Unsteady Transition in an Axial-Flow Turbine: Part II—Cascade Measurements and Modeling," ASME JOURNAL OF TURBOMACHINERY, Vol. 112, pp. 215–221.

Ashworth, D., and LaGraff, J., 1989, "Measurement and Modeling of Turbulent Spot Growth on a Gas Turbine Blade," AIAA Paper No. 89-0328.

Binder, A., 1985, "Turbulence Production Due to Secondary Vortex Cutting in a Turbine Rotor," ASME *Journal of Engineering for Gas Turbines and Power*, Vol. 107, pp. 1039–1046.

Doorly, D. J., Oldfield, M. L. G., and Scrivener, C. T. J., 1985, "Wake-Passing in a Turbine Rotor Cascade," AGARD-CP-390, pp. 7.1–7.18.

Doorly, D. J., 1988, "Modeling the Unsteady Flow in a Turbine Rotor Passage," ASME JOURNAL OF TURBOMACHINERY, Vol. 110, pp. 27–37.

Dring, R. P., Blair, M. F., Joslyn, H. D., Power, G. D., and Verdon, J. M., 1986, "The Effects of Inlet Turbulence and Rotor–Stator Interactions on the Aerodynamics and Heat Transfer of a Large-Scale Rotating Turbine Model: I—Final Report," NASA Contractor Report No. 4079.

Dunn, M. G., 1985, "Turbine Heat Flux Measurements: Influence of Slot Injection on Vane Trailing Edge Heat Transfer and Influence of Rotor on Vane Heat Transfer," ASME *Journal of Engineering for Gas Turbines and Power*, Vol. 107, pp. 76–83.

Dunn, M. G., 1986, "Heat-Flux Measurements for the Rotor of a Full-Stage Turbine: Part I—Time-Averaged Results," ASME JOURNAL OF TURBOMACHINERY, Vol. 108, pp. 90–97.

Dunn, M. G., George, W. K., Rae, W. J., Woodward, S. H., Moller, J. C., and Seymour, J. P., 1986, "Heat-Flux Measurements for the Rotor of a Full-Stage Turbine: Part II—Description of Analysis Technique and Typical Time-Resolved Measurements," ASME JOURNAL OF TURBOMACHINERY, Vol. 108, pp. 98–107.

Dunn, M. G., Seymour, P. J., Woodward, S. H., George, W. K., and Chupp, R. E., 1989, "Phase-Resolved Heat-Flux Measurements on the Blade of a Full-Scale Rotating Turbine," ASME JOURNAL OF TURBOMACHINERY, Vol. 111, pp. 8–19.

Evans, R. L., 1974, "Turbulence and Unsteadiness Measurements Downstream of a Moving Blade Row," ASME Paper No. 74-GT-73.

Guenette, G. R., Epstein, A. H., Giles, M. B., Haimes, R., and Norton, R. J. G., 1989, "Fully Scaled Transonic Turbine Rotor Heat Transfer Measurements," ASME JOURNAL OF TURBOMACHINERY, Vol. 111, pp. 1–7.

Hodson, H. P., 1985, "Measurements of Wake-Generated Unsteadiness in the Rotor Passages of Axial Flow Turbines," ASME *Journal of Engineering for Gas Turbines and Power*, Vol. 107, pp. 466–476.

LaGraff, J. E., Ashworth, D. A., and Schultz, D. L., 1989, "Measurement and Modeling of the Gas Turbine Blade Transition Process as Disturbed by Wakes," ASME JOURNAL OF TURBOMACHINERY, Vol. 111, pp. 315–322.

Liu, X., and Rodi, W., 1989, "Measurements of Unsteady Flow Over and Heat Transfer From a Flat Plate," ASME Paper No. 89-GT-2.

Mayle, R. E., and Dullenkopf, K., 1990, "A Theory for Wake Induced Transition," ASME JOURNAL OF TURBOMACHINERY, Vol. 112, pp. 188–195.

Pfeil, H., and Eifler, J., 1975, "Messungen im turbulenten Nachlauf des Einzelzylinders," *Forsch. Ing.-Wes.*, Vol. 41, No. 5, pp. 137–168.

Pfeil, H., and Pache, W., 1977, "Messungen von Strömungsgrenzschichten unter Turbomaschinenbedingungen," *Zeitschrift für Flugwissenschaft und Weltraumforschung 1*, Vol. 4, pp. 267–277.

Priddy, W. J., and Bayley, F. J., 1988, "Turbulence Measurements in Turbine Blade Passages and Implications for Heat Transfer," ASME JOURNAL OF TURBOMACHINERY, Vol. 110, pp. 73–79.

Reichardt, H., 1942, "Gesetzmässigkeiten der freien Turbulenz," *VDI-Forschungsheft 414*.

Schlichting, H., 1982, *Grenzschicht-Theorie*, G. Braun, Karlsruhe, Federal Republic of Germany.

Schulz, A., 1986, "Zum Einfluss hoher Freistromturbulenz, intensiver Kühlung und einer Nachlaufströmung auf den äusseren Wärmeübergang einer konvektiv gekühlten Gasturbinenschaufel," Dissertation, Institut für Thermische Strömungsmaschinen, Universität Karlsruhe, Federal Republic of Germany.

Stöcker, U., 1983, "Temperaturfeld und örtlicher Wärmeübergang bei instationären Strömungsvorgängen an einer gekühlten Turbinenlaufschaufel," *Fortschr.-Ber. VDI-Z*, Vol. 7, No. 80.

Stöcker, U., Kühl, W., and Koschel, W., 1983, "Über den Einfluss instationärer Strömungsvorgänge auf die Wärmeübergangsverteilung an einer Turbinenlaufschaufel," *VDI-Berichte*, No. 487, pp. 191–199.

Turner, A. B., 1971, "Local Heat Transfer Measurements on a Gas Turbine Blade," *Journal of Mechanical Engineering Science*, Vol. 13, No. 1, pp. 1–12.

Van Dresar, N. T., 1987, "The Effect of Incident Wake Flow on Blunt-Body Transfer Rates," PhD Dissertation, Rensselaer Polytechnic Institute, Troy, New York.

Van Dresar, N. T., Mayle, R. E., 1987, "A Quasi-Steady Approach of Wake Effects on Leading Edge Heat Transfer Rates," in: *Heat Transfer in Gas Turbine Engines*, D. E. Metzger, ed., ASME HTD-Vol. 87, pp. 1–10.

Wittig, S., Schulz, A., Bauer, H. J., and Sill, K. H., 1985, "Effects of Wakes on the Heat Transfer in Gas Turbine Cascades," AGARD-CP-390, pp. 6.1–6.13.

Wittig, S., Dullenkopf, K., Schulz, A., and Hestermann, R., 1987, "Laser-Doppler Studies of the Wake-Effected Flow Field in a Turbine Cascade," ASME JOURNAL OF TURBOMACHINERY, Vol. 109, pp. 170–176.

Wittig, S., Schulz, A., Dullenkopf, K., and Fairbank, J., 1988, "Effects of Free-Stream Turbulence and Wake Characteristics on the Heat Transfer Along a Cooled Gas Turbine Blade," ASME Paper No. 88-GT-179.

D. E. Paxson
Mem. ASME

R. E. Mayle
Mem. ASME

Mechanical Engineering Department,
Rensselaer Polytechnic Institute,
Troy, NY 12181

Laminar Boundary Layer Interaction With an Unsteady Passing Wake

An investigation was conducted to study the unsteady effects of a moving wake as it passes over a laminar boundary layer in a stagnation region. Arguments are presented showing that in this region, the wake-induced unsteadiness may be treated, for the most part, as an inviscid, unsteady free stream, which impresses itself on the boundary layer flow. As a result, the boundary layer equations remain valid and, for relatively small oscillations, a solution to the equations may be obtained using standard perturbation techniques. A related experiment is then described and the results are examined in light of this analytical approach.

Introduction

Since their introduction in the middle of this century, gas turbines have experienced rapid and dramatic improvements in performance. Not only are the engines lighter and more powerful, they are also cleaner and more fuel efficient. Many of these advancements have been the direct results of an increased knowledge of the fluid mechanical and heat transfer processes that occur within the various parts of the engine. Even with the great strides made, however, a great deal remains to be learned about the complex flows occurring within these machines.

One prominent area of study concerns the interaction between upstream and downstream turbine airfoils. Of particular interest are the wakes, created by the upstream airfoils, through which the downstream airfoils must pass. These wakes produce an incident flow, which is periodically unsteady in both the mean values and the turbulence levels. Such a situation is depicted schematically in Fig. 1. The free-stream unsteadiness has a large effect on the boundary layer flow about the downstream airfoils. In the past, however, this fact was largely disregarded and calculations of heat load and aerodynamics were based upon a steady-state, mass-averaged incident flow and, as a result, predictions were largely in error (see for example Dunn et al., 1986). For this reason, particular attention is now being paid to the investigation of wake-induced unsteadiness.

In general, the number of unsteady boundary layer experiments that have been performed is relatively small compared to the simpler steady type. Of those that have been done, nearly all involve unsteadiness which is either: (1) periodic in a regular manner, (2) varying only in the magnitude of the free-stream flow, or (3) free of vorticity in the free-stream flow. Wake-induced unsteadiness fits into none of these categories. Although ensemble-averaged measurements may show regular periodicity, the random turbulence present in the wake does not. In addition, a passing wake with its associated mean velocity defect must alter not only the magnitude but also the direction of the free-stream flow. Finally, the passing wake is highly vortical due to both the random turbulent eddies and the mean shear of the velocity defect. Thus, the study of wake-induced unsteadiness is relatively unique.

Some experiments have been performed that have investigated the wake-induced unsteady boundary layer. Pfeil et al. (1983), as well as Liu and Rodi (1989), measured the velocity distributions on a flat plate. Pfeil et al. found that the impinging wakes created transition zones, which propagated down the plate, creating an intermittent flow in the boundary layer. Others, notably Evans (1978) and Hodson (1983), obtained unsteady velocity measurements on large-scale airfoils. Evans

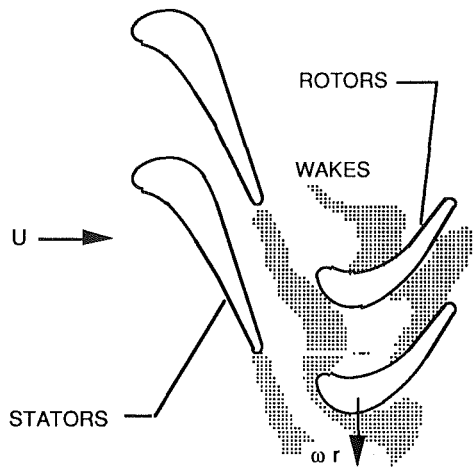

Fig. 1 Stator-rotor interaction schematic

Contributed by the International Gas Turbine Institute and presented at the 35th International Gas Turbine and Aeroengine Congress and Exposition, Brussels, Belgium, June 11–14, 1990. Manuscript received by the International Gas Turbine Institute January 23, 1990. Paper No. 90-GT-120.

obtained detailed boundary layer measurements at several positions along the suction side of a single-stage compressor stator blade, while Hodson measured the velocity characteristics just outside the boundary layer of the rotor in a large-scale air turbine. Evans showed that over the first 30 percent of the chord, the flow alternated between periods of laminar and turbulent flow, much as that found by Pfeil et al. Both he and Hodson showed that the primary oscillation period in the boundary layer corresponded directly to the upstream rotor wake passing period. Both of these investigations, however, addressed boundary layers that were transitional and/or turbulent even in the steady state.

This paper addresses the problem of wake-induced, unsteady flow on a nontransitional laminar boundary layer. First, a theory is presented for laminar boundary layer. flow with an unsteady passing wake in the main flow. Then an experiment, which examined wake-induced unsteadiness in the stagnation region boundary layer of a bluff body, is described and its results presented in light of the theory.

Theory

The basic method of attack for most unsteady flow analyses consists of modeling the unsteadiness of the flow as a perturbation on the basic steady flow solution. By requiring the perturbations to be small, it is possible to develop an approximate system of governing differential equations that are simpler than the original time-dependent equations. The first equation of this system is nonlinear and identical to that for the unperturbed steady state flow (such as that solved by Blasius, 1908). Subsequent equations are linear and represent the time-dependent corrections due to the perturbations. A definitive work using this approach was presented by Lighthill (1954) who studied the response of skin friction and heat transfer coefficient on various bodies exposed to a sinusoidal perturbation in the magnitude of the free-stream velocity.

Although wake-induced unsteadiness is far more complex than a simple sinusoidal oscillation, the question arises as to whether or not a similar perturbation approach to solution might still be valid. For the approach to be valid, two conditions must be satisfied. First, the viscous effects within the wake must be negligible during the interaction such that the boundary layer equations are still appropriate. Specifically, the mean velocity defect and turbulence of the wake must manifest themselves as forcing functions on the affected boundary layer. Second, the fluctuations induced by the passing wake, whether random or periodic, must be small. The second condition is nearly always met in the gas turbine environment, where the mean velocity deficit and the turbulence intensity of the wakes at the interaction distance are generally less that 10 to 20 percent. However, the first condition needs to be examined.

Consider first the wake-perturbed mean velocity field as viewed from the boundary layer on a surface. If the width of the wake is large compared to the time-averaged boundary layer thickness, then the viscous effects from the surface cannot diffuse through the wake as it passes over the surface. Also, if the decay length of the wake is large compared to the characteristic length of the surface it is passing over, then the viscous effects within the wake itself may be neglected during the interaction. Since both of these criteria are met for wake-airfoil interactions in gas turbine flows, the mean flow in the wake may be considered as an unsteady, inviscid (though rotational) flow with respect to the boundary layer development on the surface.

Consider now the turbulence in the wake relative to the boundary layer. The larger eddies in the wake contain most of the turbulent energy, while the smallest are responsible for the dissipation of energy through viscosity. The larger energy bearing eddies are characterized by the integral length scale of the turbulence. In the gas turbine, this length scale is of the order of the trailing edge thickness of the wake-producing airfoil plus the momentum thicknesses of the suction and pressure side boundary layers at the trailing edge. In most cases, it can be shown that this is nearly an order of magnitude greater than the laminar boundary layer thickness on the forward portion of the airfoil. Therefore, even these eddies may be considered inviscid relative to the boundary layer development. That is, like the mean wake flow, they simply impress a time-varying, albeit complex, free-stream flow on the boundary layer.

Turning to the smallest eddies of the wake flow, those responsible for the dissipation of turbulent energy, the length scale appropriate to these eddies is the Kolmogorov scale. This can be shown to be of the order $L(\mathrm{Re}_L Tu)^{-3/4}$, where L is the integral length scale, Re_L is the Reynolds number based on this length scale $\bar{U}_\infty L/\nu$, and Tu is the turbulence intensity. For typical engine Reynolds numbers, wake length scales, and turbulence levels, it is found that the Kolmolgorov length scale in the wake is comparable to the boundary layer thickness. Thus, the smallest eddies cannot be considered inviscid relative to the developing laminar boundary layer flow; however, since they contain very little of the turbulent energy, they would not be expected to severely affect the flow.

From the above analysis then, it appears that the wake may be treated as an unsteady, inviscid, rotational incident flow. It also appears that the unsteady disturbance caused by the wake may be analyzed using a small perturbation analysis. Considering this so, the external tangential velocity about a body may be expressed in the form

Nomenclature

A_n = Fourier coefficient
d = diameter of wake-generating rod
L = integral length scale
R = leading edge radius of bluff body
Re_L = Reynolds number based on turbulence length scale
t = time
Tu = turbulence level
u = streamwise velocity within the boundary layer
$\bar{U}_\infty$ = incident velocity
U_ϕ = tangential velocity outside of the boundary layer
v = transverse velocity within the boundary layer
x = direction of main flow
y = transverse direction (normal to surface)
δ = boundary layer thickness
ϵ = perturbation parameter
η = dimensionless distance from the surface
ν = kinematic viscosity
ϕ = angle from stagnation
ω = frequency
ω_r = dimensionless (or reduced) frequency

Subscripts

d = pertaining to the wake defect
i = index of ensemble-averaged quantities
max = maximum values
ss = steady state
w = pertaining to the wake
1 = pertaining to first-order corrections

Superscripts

$\bar{}$ = time averaged
$\tilde{}$ = ensemble averaged
$'$ = random fluctuations

$$U_\phi(x,\ t) = \bar{U}_{\phi ss}(x) + \tilde{U}_\phi(x,\ t) + U'_\phi(x,\ t), \tag{1}$$

where $\bar{U}_{\phi ss}$ is the steady component, $\tilde{U}_\phi$ is the periodic component from the ensemble-averaged flow of the passing wake, and U'_ϕ is the random component arising from the turbulence. Since the second two terms on the right-hand side are supposedly small compared to the first, equation (1) may be rewritten as

$$U_\phi(x,\ t) = \bar{U}_{\phi ss}(x) + \epsilon[\tilde{U}_{\phi 1}(x,\ t) + U'_{\phi 1}(x,\ t)], \tag{2}$$

In this equation ϵ is small and of the size

$$\epsilon \sim \frac{\tilde{U}_{\phi \max}}{\bar{U}_{\phi ss}} \text{ or } \frac{\sqrt{\tilde{U}^2_{\phi max}}}{\bar{U}_{\phi ss}}, \tag{3}$$

where $\tilde{U}_{\phi \max}$ is the maximum absolute value of the ensemble-average periodic fluctuation, and $\sqrt{\tilde{U}'^2_{\phi \max}}$ is the maximum ensemble-averaged root mean square value of the random fluctuations. Consequently, $\tilde{U}_{\phi 1}$ and $U'_{\phi 1}$ are functions of the same order as $\bar{U}_{\phi ss}$. Similarly, the velocity components in the boundary layer may be expressed in the forms

$$u(x,y,t) = \bar{u}_{ss}(x,y) + \epsilon[\tilde{u}_1(x,y,t) + u'_1(x,y,t)] \tag{4}$$

and

$$v(x,y,t) = \bar{v}_{ss}(x,y) + \epsilon[\tilde{v}_1(x,y,t) + v'_1(x,y,t)]. \tag{5}$$

Equations (2), (4), and (5) may be substituted into the time-dependent boundary layer equations, which may then be grouped according to powers of ϵ. The order ϵ^o equations are simply those for steady flow, e.g.,

Continuity:

$$\frac{\partial \bar{u}_{ss}}{\partial x} + \frac{\partial \bar{v}_{ss}}{\partial y} = 0 \tag{6}$$

Momentum:

$$\bar{u}_{ss}\frac{\partial \bar{u}_{ss}}{\partial x} + \bar{v}_{ss}\frac{\partial \bar{u}_{ss}}{\partial y} = \bar{U}_{\phi ss}\frac{d\bar{U}_{\phi ss}}{dx} + \nu\frac{\partial^2 \bar{u}_{ss}}{\partial y^2} \tag{7}$$

Conditions:

$$\bar{u}_{ss} = \bar{v}_{ss} = 0 \text{ at } y = 0 \qquad \bar{u}_{ss} = \bar{U}_{\phi ss} \text{ at } y = \delta. \tag{8}$$

The ϵ^1 equations can be ensemble averaged and the resulting equations subtracted from the originals. This results in two more sets of equations. One pertains to the regular ensemble-averaged velocity fluctuations, the other to the random fluctuations. They have the forms:

Regular Fluctuations:

Continuity:

$$\frac{\partial \tilde{u}_1}{\partial x} + \frac{\partial \tilde{v}_1}{\partial y} = 0 \tag{9}$$

Momentum:

$$\frac{\partial \tilde{u}_1}{\partial t} + \bar{u}_{ss}\frac{\partial \tilde{u}_1}{\partial x} + \tilde{u}_1\frac{\partial \bar{u}_{ss}}{\partial x} + \tilde{v}_1\frac{\partial \bar{u}_{ss}}{\partial y} + \bar{v}_{ss}\frac{\partial \tilde{u}_1}{\partial y} = \frac{\partial \tilde{U}_{\phi 1}}{\partial t} + \frac{d\bar{U}_{\phi ss}\tilde{U}_{\phi 1}}{dx} + \nu\frac{\partial^2 \tilde{u}_1}{\partial y^2} \tag{10}$$

Conditions:

$$\tilde{u}_1 = \tilde{v}_1 = 0 \text{ at } y = 0 \qquad \tilde{u}_1 = \tilde{U}_{\phi 1} \text{ at } y = \delta \tag{11}$$

Random Fluctuations:

Continuity:

$$\frac{\partial u'_1}{\partial x} + \frac{\partial v'_1}{\partial y} = 0 \tag{12}$$

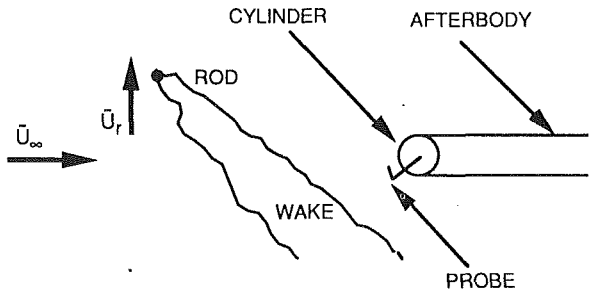

Fig. 2 Unsteady wake schematic

Momentum:

$$\frac{\partial u'_1}{\partial t} + \bar{u}_{ss}\frac{\partial u'_1}{\partial x} + u'_1\frac{\partial \bar{u}_{ss}}{\partial x} + v'_1\frac{\partial \bar{u}_{ss}}{\partial y} + \bar{v}_{ss}\frac{\partial u'_1}{\partial y} = \frac{\partial U'_{\phi 1}}{\partial t} + \frac{d\bar{U}_{\phi ss}U'_{\phi 1}}{dx} + \nu\frac{\partial^2 u'_1}{\partial y^2} \tag{13}$$

Conditions:

$$u'_1 = v'_1 = 0 \text{ at } y = 0 \qquad u'_1 = U'_{\phi 1} \text{ at } y = \delta \tag{14}$$

Equations (9) and (10) are identical to those of Lighthill, who obtained a solution for the case when the perturbation of the external flow is a simple sinusoid, namely

$$\tilde{U}_\phi(x,\ t) = \bar{U}_{\phi ss}(x)(1 + \epsilon e^{i\omega t}). \tag{15}$$

His solution yields boundary layer oscillations that have one component that is in phase with the free stream and one that is not. The out-of-phase component is small if the frequencies are low, and grows as the frequency increases. Specifically, the parameter that multiplies the out-of-phase component is

$$\omega_r = \frac{\omega\delta^2}{\nu}, \tag{16}$$

where δ is the boundary layer height and ω is the frequency of the free-stream fluctuations. This parameter is a ratio of the characteristic free-stream frequency ω to that of the boundary layer δ^2/ν (i.e., inverse of the time for diffusion through the boundary layer). Lighthill showed that flows with $\omega_r << 40$ had a low-frequency behavior, while those with $\omega_r >> 40$ had a high-frequency behavior. For low frequencies (i.e., $\omega_r << 40$), an interesting result may be obtained by ensemble averaging equations (2) and (4), and then dividing one by the other. This yields the equation

$$\frac{\bar{u}_{ss} + \tilde{u}}{\bar{U}_{\phi ss} + \tilde{U}_\phi} \approx \frac{\bar{u}_{ss}}{\bar{U}_{\phi ss}}\left[1 + \epsilon\left(\frac{\tilde{u}_1}{\bar{u}_{ss}} - \frac{\tilde{U}_{\phi 1}}{\bar{U}_{\phi ss}}\right)\right], \tag{17}$$

where the fact that ϵ is small has been used. Since $\tilde{u}_1/\bar{u}_{ss}$ and $\tilde{U}_{\phi 1}/\bar{U}_{\phi ss}$ are of the same order and in phase, their difference should remain small at all times. Thus the term that multiplies ϵ is small (and of course, ϵ is small), which suggests that the nondimensional, time-dependent, ensemble-averaged velocity distribution is nearly the same as that in steady flow. As will be shown later, this is indeed the case.

Since equation (10) is linear, and Lighthill's solution is for sinusoidal free-stream oscillations, it is possible to extend his ideas to the periodic unsteadiness of the wake. Expanding the unsteady mean velocity $U_\phi(x,\ t)$ in a Fourier series

$$U_\phi(x,\ t) = \sum_{n=0}^{\infty} A_n(x)e^{i\omega_n t} \tag{18}$$

and recognizing that solutions of a linear differential equation may be added, or superposed, to obtain another solution, the wake-induced periodic laminar boundary layer flow about a body satisfying the requirements stated above (e.g., a turbine blade) may be obtained as an infinite superposition of Lighthill's solutions.

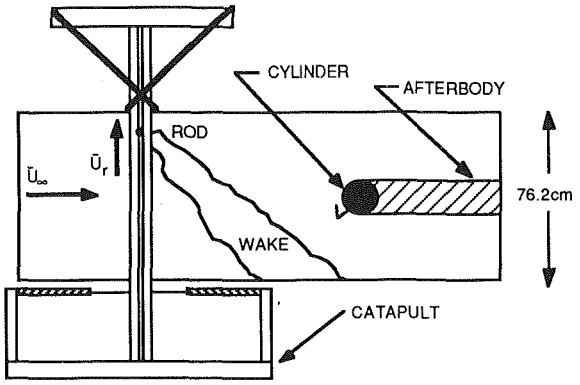

Fig. 3 Test section

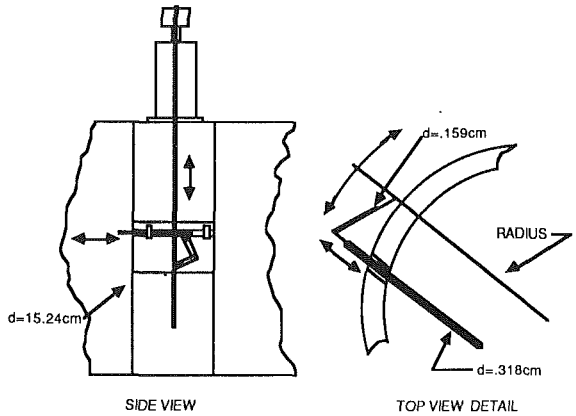

Fig. 4 Probe and traverse detail

Solution to equation (13) is much more difficult since a model of the random free-stream fluctuations is not known; however, if the arguments presented above are valid, then in principle, they are solvable. Although random, the fluctuations induced by the turbulence can be approximated by a Fourier integral (not a series). If this is done then the same approach as that for the regular perturbations is possible, with the series replaced by an integral. This, of course, is a very difficult task. Even without formal solution, though, speculation as to the behavior of these fluctuations may be made. It was pointed out earlier that only the eddies with large characteristic times would be expected to affect the boundary layer flow. The higher frequency eddies have too little energy to have an influence. This being the case, it is suspected that the nature of the boundary layer fluctuations would be qualitatively similar to the lower frequency solutions presented by Lighthill. This will be shown to be nearly true.

Experimental Equipment and Techniques

The geometry of the experiment is shown schematically in Fig. 2. The experiment utilized a large-scale, low-speed setup to model the flow over the leading edge of a typical gas turbine airfoil. A small-diameter moving rod was used to simulate the upstream stator wake. Downstream, a bluff body with a cylindrical forward portion simulated the airfoil's leading edge. The cylindrical section was equipped with a specially designed boundary layer probe to measure the flow quantities. Measurements were made using ensemble-averaging techniques in order to obtain detailed unsteady flow information.

The wind tunnel facility was an open circuit type composed of a blower, a plenum chamber, a nozzle that led into the test section, and the test section itself. The blower was a large centrifugal fan with an attached throttling device at the inlet to regulate the flow. The plenum chamber contained a series of screens, baffles, and honeycomb that served to filter, distribute, straighten, and reduce turbulence in the flow before it entered the nozzle. The nozzle was a two-to-one elliptic contraction and provided a uniform stream to the test section. For these experiments, its velocity was maintained at a nominal 10.7 m/s, which provided an incident flow Reynolds number of 110,000 based on the leading edge diameter of the bluff body. The flow was uniform with an average variation in velocity of approximately 1.0 percent of the centerline value and had a turbulence level of approximately 0.5 percent. The entire tunnel, along with the associated data acquisition instrumentation, was housed within a room equipped with a large air conditioning unit, which maintained a constant temperature environment for the experiments at a nominal 18°C with a variation of less than ±1°C.

The test section is shown in Fig. 3. It was a rectangular duct 45.7 cm high by 76.2 cm wide. It had a small gap formed in the top and sides to accommodate the movement of the 2.54-cm-dia wake-generating rod. A simple "crossbow"-like catapult mechanism was used to "shoot" the rod across the flow. The rod was attached to a bearing wheeled cart, which rode in a track above the test section. The bottom of the rod was guided by a second track below the test section. The cart and rod arrangement was propelled by two springs whose length could be adjusted to change the cart velocity. For this experiment the velocity was 10.0 m/s, nearly that of the incident flow. On the opposite side of the test section a set of rubber shock cords was arranged in a crossed fashion to "catch" the rod. A return system allowed an operator to retrieve the rod while remaining on the launch side. Upon entering the test section, the rod made contact with a trigger switch, which was wired to the computer data acquisition system.

The test body was made from a circular test cylinder and a parallel-sided afterbody, both of which completely spanned the height of the test section. The afterbody was a simple rectangular structure whose upstream end fit snugly around the cylinder. When in space, the afterbody left only the forward half of the cylinder exposed to the flow. This created a simple bluff body with a cylindrical leading edge. The test cylinder, shown in a detailed cutaway in Fig. 4, was a 15.2-cm-dia hollow aluminum structure comprised of three sections. The two large outer pieces supported a smaller center section, which housed the probe and a traverse mechanism.

Velocity measurements in the boundary layer of the test cylinder were made using a special miniature hot-wire probe as shown in Fig. 4. The sensor was a 5 μm tungsten wire welded between two 6.4-mm-long needles. These needles, the only nonsensor portion of the probe extending into the flow, tapered from a diameter of 0.38 mm to 0.076 mm at the sensor and were bent so that the probe would not interfere with the flow. The probe was inserted in a hole through the cylinder wall and attached to an external traverse device by a rod and bell-crank mechanism. The entire traverse mechanism except for the computer-controlled traverse device and the probe head was contained within the cylinder. Even though the boundary layer traverses were always conducted in one direction, all of the linkages were very carefully designed and manufactured to keep backlash to a minimum and prevent the probe from rocking as it was moved in and out of the cylinder. Calibration tests showed that the relation between the probe and traverse device movement was linear within 2 cm from the surface of the cylinder. Measurements at different angular positions around the cylinder were obtained by rotating the entire test cylinder assembly.

The hot wire was calibrated in a separate facility against a Pitot tube. At the very low velocities, a method utilizing Roshko's (1976) results for vortex shedding from a cylinder was

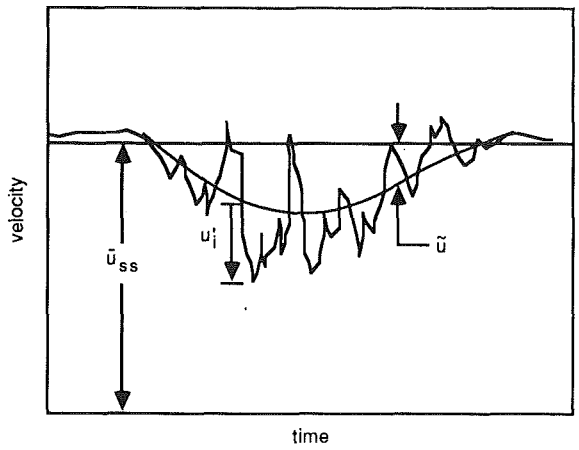

Fig. 5 Velocity trace in the boundary layer

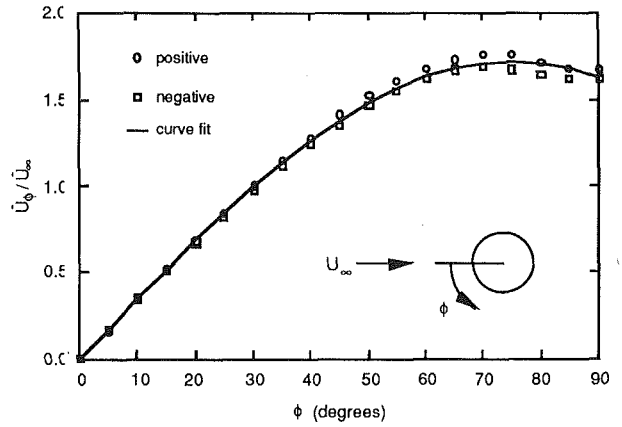

Fig. 6 Bluff-body external velocity distribution

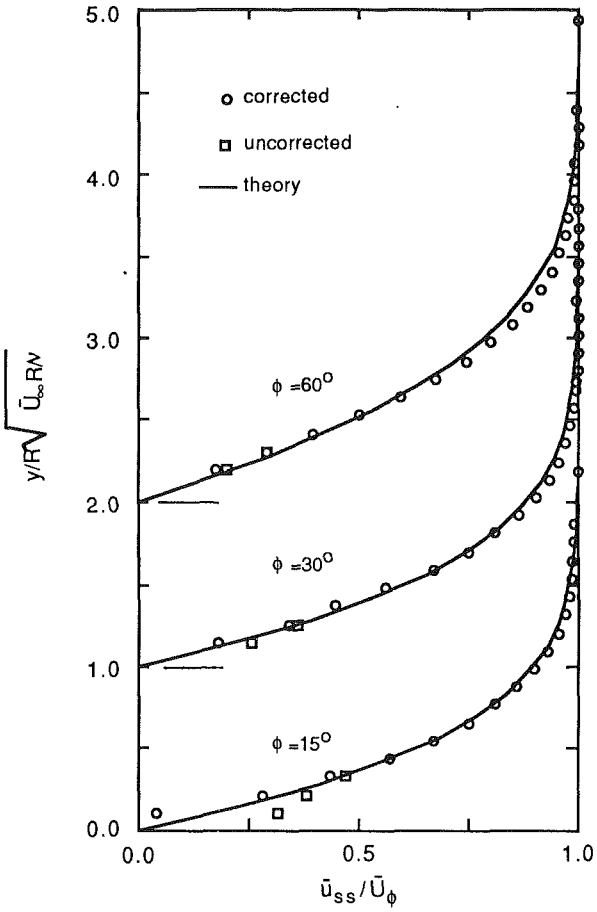

Fig. 7 Steady velocity profiles at positive angles

used. Near the wall, it was found that a "wall correction" had to be applied to the data. The correction according to Zemskaya et al. (1979) was used. As a result, the measured velocities are accurate to within 2 percent, except for those nearest the wall, where a correction of as much as $(u_{\text{meas.}} - u_{\text{act.}})/U_\phi = 0.06$ has been applied.

A small static pressure tap was also installed on the surface of the cylinder. Using this tap, a pressure, and hence, outer tangential velocity distribution could be obtained over the forward half of the cylinder.

Data Acquisition and Sampling Procedures

The data acquisition system included a TSI model 1051 anemometer, model 1052 signal linearizer, model 1057 signal conditioner, model 1047 averaging circuit, and model 1015c correlator. Also, an Apple IIgs computer equipped with a 12-bit A-D converter was used. An input line to the computer came from the trigger mechanism on the catapult described above. The data acquisition software sampled at a rate of 10 kHz for approximately 180 ms. The sampled signal was actually an a-c component of the velocity. A high pass filter set at 2 Hz passed the wake-generated time varying signal with virtually no attenuation. For each test point, the number of launches, N, was always 100. Tests conducted with $N = 300$ showed virtually no difference in the mean velocity measurements but, as may be expected, cleaner rms distributions. Since the distributions were not significantly different, however, an ensemble average of 100 tests was considered satisfactory. All velocity measurements were obtained at ± 15, ± 30, and ± 60 deg from stagnation. For each of these angles unsteady data were obtained in at least four positions within the boundary layer.

As shown in Fig. 5, the absolute time-dependent velocity has three components, i.e.,

$$U_i(t) = \bar{u}_{ss} + \tilde{u}(t) + u_i'(t). \tag{19}$$

Here, $\bar{u}_{ss}$ is the conventionally averaged steady-state velocity, $\tilde{u}(t)$ is the time-dependent ensemble-average velocity offset, and $u_i'(t)$ is the fluctuating component. The ensemble-average velocity fluctuation is thus obtained from the relation

$$\tilde{u}(t) = \frac{1}{N}\sum_{i=1}^{N} u_i(t), \tag{20}$$

where $u_i(t)$ is the ith sample of the instantaneous offset taken at time t after trigger (i.e., launch of the catapult), and N is the total number of samples (launches). Also from the figure it is seen that

$$\tilde{U}(t) = \bar{u}_{ss} + \tilde{u}(t), \tag{21}$$

and

$$u_i'(t) = u_i(t) - \tilde{u}(t). \tag{22}$$

Furthermore, some algebra will show that the mean square of the fluctuations is given by

$$\tilde{u}'^2(t) = \frac{1}{N}\sum_{i=1}^{N} u_i^2(t) - \tilde{u}(t)^2. \tag{23}$$

With each launch of the catapult the computer updated the time-dependent, ensemble-averaged distribution of both the velocity and the rms fluctuations.

Results and Discussion

Steady-State Boundary Layer. The external tangential velocity distribution $\bar{U}_\phi/\bar{U}_\infty$ calculated using Bernoulli's equation

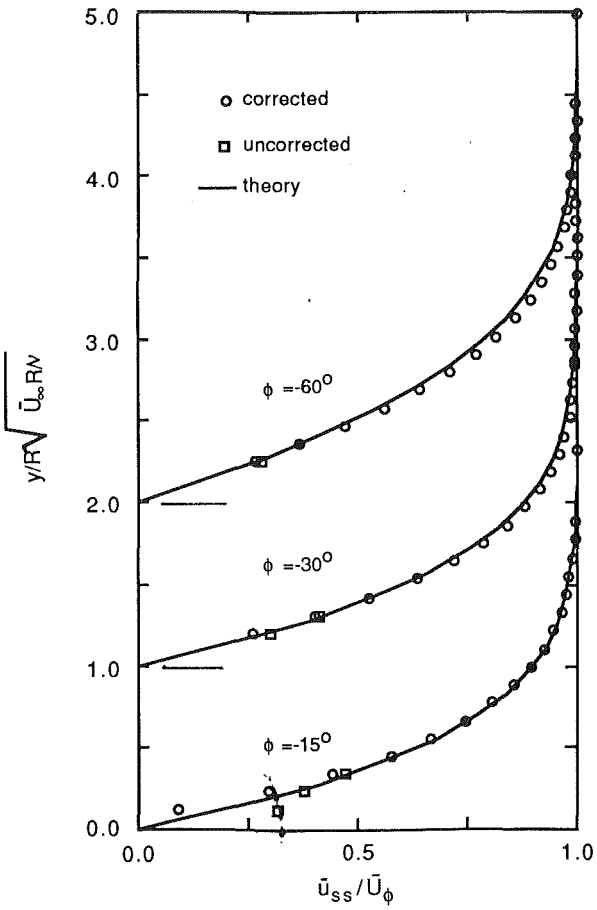

Fig. 8 Steady velocity profiles at negative angles

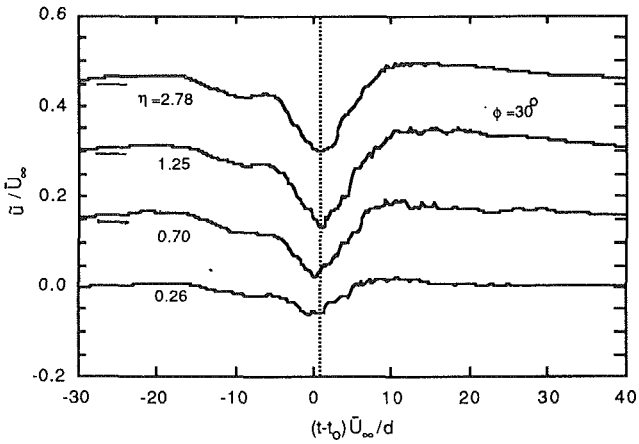

Fig. 9 Unsteady velocity profile at $\phi = 30$ deg

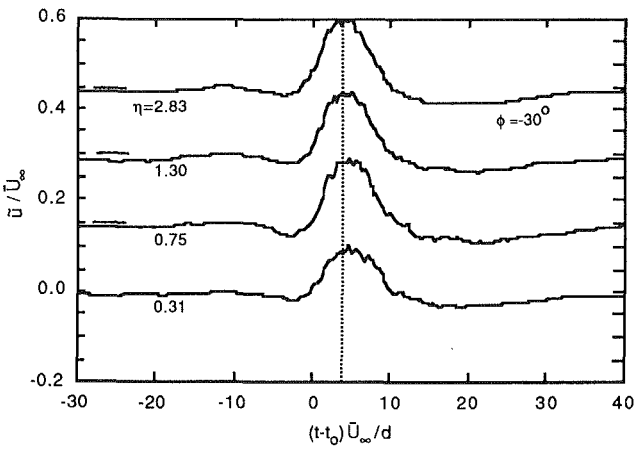

Fig. 10 Unsteady velocity profile at $\phi = -30$ deg

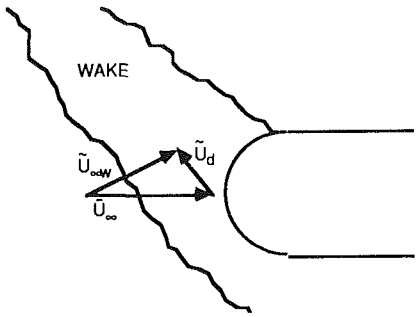

Fig. 11 Wake-induced angle of attack

and the measured pressure distribution is shown in Fig. 6 as a function of angle from stagnation. In this figure the velocity at negative angles is shown reflected into the positive axis. As seen, the flow is nearly symmetric. A curve fit obtained using a fifth-order polynomial provides

$$\frac{\bar{U}_\phi}{\bar{U}_\infty} = 2.019\ \phi - 0.429\ \phi^3 + 0.012\ \phi^5 \qquad (24)$$

where ϕ is the angle in radians. In the present notation, the positive angles are those on the side first affected by the wake.

The steady-state data are shown in Figs. 7 and 8 together with the theoretical velocity profiles obtained from Blasius' (1908) solution using the free-stream velocity distribution given in equation (24) above. In both figures the ordinate is the normalized distance from the surface according to Blasius where R is the radius of the leading edge. Profiles at different angles are shown shifted on the ordinate by a value of 1.0. In addition, the figures show both the corrected and uncorrected values where they apply. The agreement is excellent.

Unsteady Boundary Layer Velocity Profiles. The measured time-dependent ensemble-averaged velocity offsets for the angles ±30 deg are shown in Figs. 9 and 10. These are typical of those measured at the other angles, although slight variations in both shape and magnitude did exist (the interested reader is referred to Paxson, 1989). The abscissa in each plot is a dimensionless time $(t-t_0)\bar{U}_\infty/d$, where d is the diameter of the upstream wake generating rod, $\bar{U}_\infty$ is the steady free-stream velocity, and t_0 is the time required for the centerline of the undisturbed wake to reach the stagnation point position of the bluff body. In each figure, there are four separate plots representing positions in the boundary layer ranging from very near the wall to the outer edge. Each plot is displaced from the previous one, along the ordinate, by an amount 0.15. The slight raggedness is a result of ensemble averaging only 100 data samples.

As seen in these figures, and the same can be said for all angles, whether positive or negative, the data closest to the wall display the smallest response to the passing wake. This result was expected since the fluid motion near the wall is severely damped by viscosity. In addition, the response to the wake appears to occur at the same time throughout the boundary layer. That is, a minimum near the edge of the boundary layer is coincident with a minimum near the wall, which implies that the boundary layer virtually adjusts instantaneously to the free-stream variations. In the context of the perturbation solution discussed in the Theory section, this corresponds to Lighthill's low-frequency behavior. Specifically, using the estimate of δ from either Fig. 7 or 8, and an estimate of the

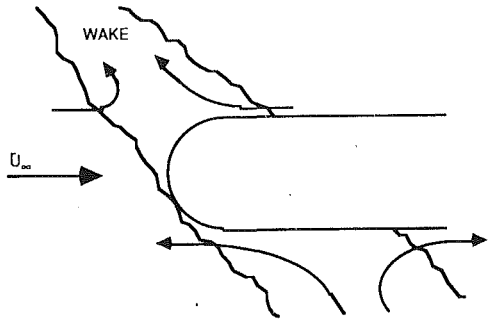

Fig. 12 Wake cutting effect

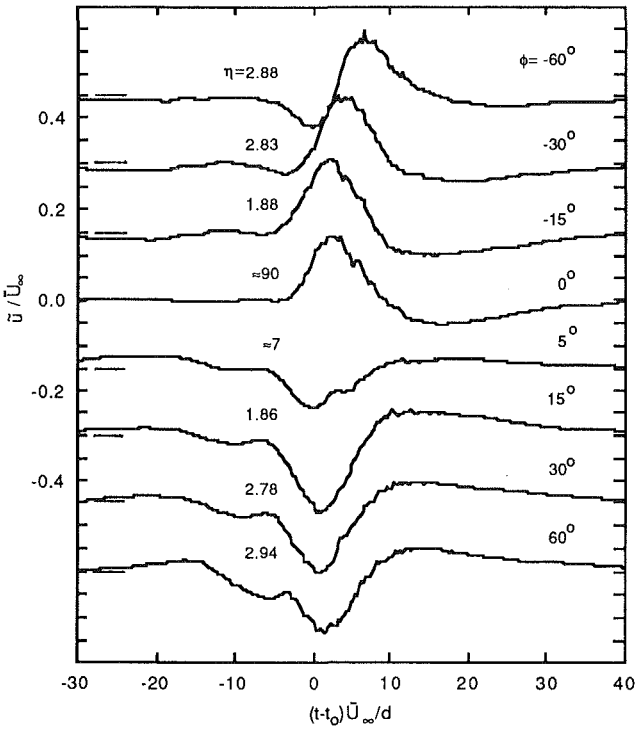

Fig. 13 Unsteady boundary layer edge-velocity traces

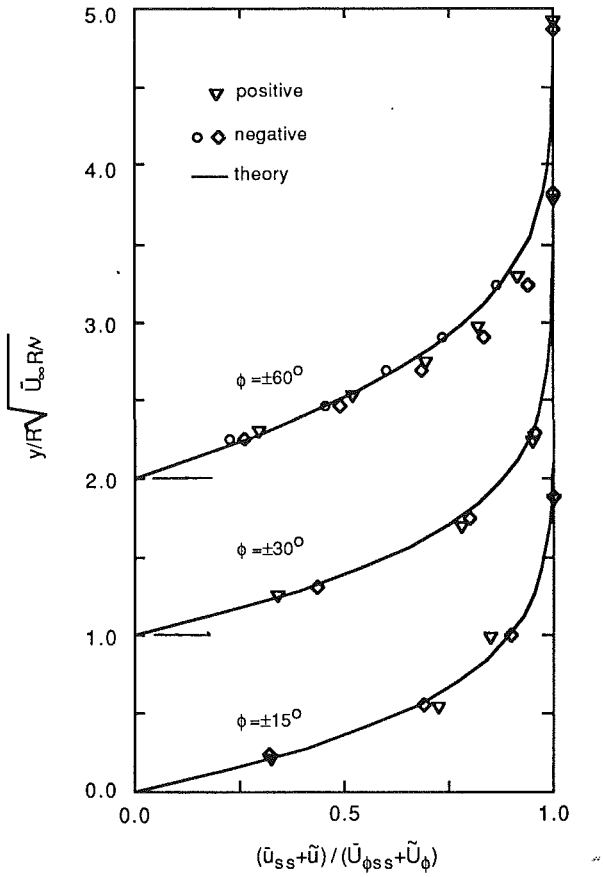

Fig. 14 Unsteady velocity profiles at maximum excursion

wake passing period from either Fig. 9 or 10, the value of ω_r in equation (16) is roughly 0.71, which is small (according to Lighthill's analysis). Hence, to the first order of approximation

$$\frac{\tilde{u}_{ss}+\tilde{u}}{\tilde{U}_{\phi ss}+\tilde{U}_{\phi}} \approx \frac{\tilde{u}_{ss}}{\tilde{U}_{\phi ss}} \tag{25}$$

Despite the fact that the wake creates a defect in the longitudinal free-stream velocity, it is noted that the profiles for -30 deg show an increase in velocity as a result of the passing wake. This seems somewhat paradoxical at first, but may be explained by considering the time-dependent incident flow caused by the wake. In particular, consider the velocity triangle in Fig. 11 where $\tilde{U}_\infty$ is the steady-state free-stream velocity, $\tilde{U}_d$ is the unsteady wake velocity defect, and $\tilde{U}_{\infty w}$ is the resulting unsteady free-stream velocity. As the wake passes over the forward portion of the test body, it causes a simple shift in the main flow direction. The shift is such as to produce a time varying positive angle of attack on the body, which displaces the stagnation toward the positive (lower) side of the body. From Fig. 6, it is seen that this will decrease the free-stream velocity for the positive angles and increase it for the negative. This change occurs in addition to that caused by the time-varying magnitude of the "incident" velocity. A calculation using the unsteady streamwise and lateral velocity components measured for the wake without the body, together with the measured steady outer tangential velocity of the cylinder, produced time-varying free-stream velocities that qualitatively agreed with those shown in Figs. 9 and 10. The calculation is admittedly an oversimplification of the actual flow phenomenon, for it assumed that the local change in flow direction caused by the passing wake applies throughout the flow field. Furthermore, it does not account for the rather large distortion of the wake flow caused by the presence of the bluff body.

Another partial cause for the observed shape of the velocity traces involves the "cutting" of the wake by the bluff body. This effect imposes a "jet-like" flow on the lower surface (positive angles) and a "sink-like" flow on the upper surface. The behavior is sketched in Fig. 12. For positive angles, the jet-like behavior tends to accelerate, then decelerate the fluid. For negative angles, the effect is just the opposite. Here, the sink-like behavior tends first to decelerate the boundary layer flow, then accelerate it as the wake is convected downstream. Although the acceleration associated with the positive angles was not observed in the experiment, the deceleration was clearly found. This may be seen in Fig. 13, where the velocity–time traces from the outermost position sampled are presented. The behavior corresponding to the negative angles (i.e., sink flow) is clearly seen in the figure, most notably at $\phi = -60$ deg.

The absolute maximum value of the offset, $\tilde{U}_{\phi \max}$, was found to be in the range of 15 to 20 percent of the external velocity (compare Figs. 6 and 13). Hence, the first-order correction to the linearized perturbation equations of motion presented in the Theory is roughly 20 percent. This is not a particularly small value; however, it will be seen that perturbation approach is, apparently, still valid.

It was shown that the undisturbed boundary layer velocity profiles are laminar and well matched to existing theory. Furthermore, it has been proposed that despite the rather intense turbulence levels in the wake, the boundary layer experiences

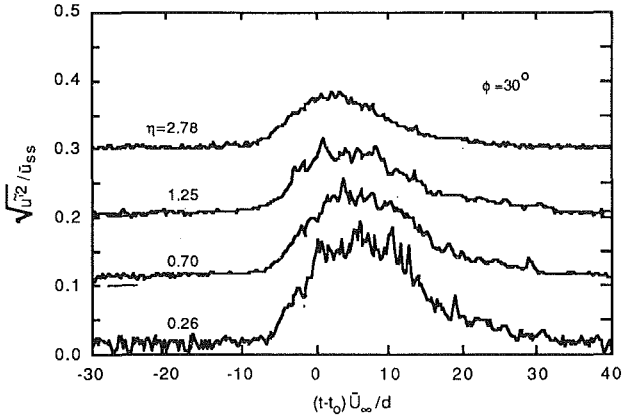

Fig. 15 Unsteady velocity fluctuations at $\phi = 30$ deg

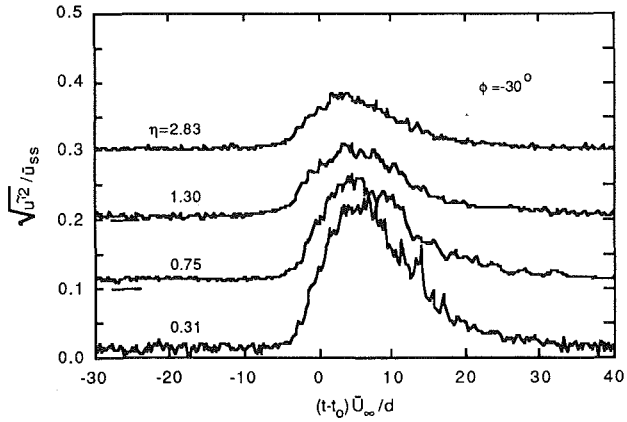

Fig. 16 Unsteady velocity fluctuations at $\phi = -30$ deg

only inviscid, irrotational perturbations of the external flow. This supposition gave rise to equation (17), which states that the nondimensionalized steady and unsteady velocity profiles should be identical. These profiles are plotted in Fig. 14 where, for each angle, the unsteady measurements within the boundary layer at maximum excursion from the mean are shown (dashed vertical lines in Figs. 9 and 10). At $\phi = -60$ deg, data at the maximum excursion in both the positive and negative directions are plotted. For any position, the plotted points correspond to data obtained at the same time. Despite the intense disturbance of the passing wake, it appears that the profile remains virtually the same as in the undisturbed case. This not only implies that the boundary layer remains laminar, but that it may be treated as a quasi-steady flow with a mean flow corresponding to that impressed by the time-varying mean wake flow.

Unsteady Boundary Layer Velocity Fluctuations. Since the ensemble-averaged velocity profiles are quite laminar in form, the ensemble-averaged velocity fluctuations in the boundary layer should not be referred to as turbulence. Although the flow is indeed highly irregular in an instantaneous sense, the fluctuations are simply that—fluctuations caused by a highly irregular, time-varying free stream. The root-mean-squares of the these fluctuations are presented in Figs. 15 and 16 for $\phi = \pm 30$ deg. Again, the results for the other angles are similar but differ slightly in magnitude. In each figure the fluctuations have been nondimensionalized by the local steady-state mean velocity at that position and angle. For each angle, the data are displaced vertically from the next by 0.10. As the wake passes, an abrupt rise in the fluctuation level is seen as might be expected. In addition, the fluctuation levels are highest near

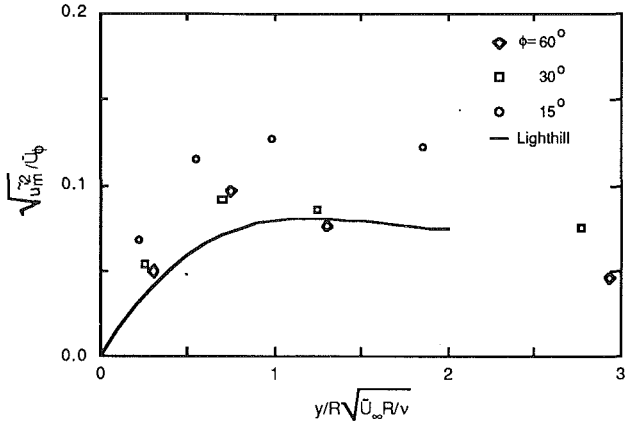

Fig. 17 Maximum rms fluctuation distribution for positive angles

the wall and diminish at farther distances. This is simply due to the fact that the local velocity drops abruptly in the vicinity of the wall. That is, even though the absolute level of the fluctuations decreases somewhat near the wall, the local velocity by which it is scaled decreases much faster, making the relative level higher. Although not shown, it was found that the maximum absolute fluctuations at the outermost positions remained nearly constant for all angles. This supports the idea that the turbulence in the wake is largely unaffected by the presence of the bluff body.

Figure 17 shows the maximum rms values for the positive angles. These values have been scaled by the external velocity, $\bar{U}_\phi$. The data are plotted as functions of the nondimensional distance from the wall, η. For comparison purposes Lighthill's in-phase solution for $\phi = 30$ deg is shown as a solid line. In this case, the maximum experimental rms value at the outer edge of the boundary layer has been used to determine the parameter ϵ. It is seen that the behavior is qualitatively very similar to the results obtained in the experiment. This result, like the mean velocity data, strongly suggests that a perturbation approach to solution of the equations of motion is a valid one.

Conclusions

The unsteady velocity measurements in an accelerating laminar boundary layer on the forward portion of a bluff-body confirmed the argument that a perturbation approach to the unsteady equations of motion is valid for this situation. That is, that the relevant perturbation parameter ϵ is small. Specifically, it was found to have a value of approximately 15–20 percent.

It was also found that the boundary layer concept remains applicable. That is, the periodic and random free-stream fluctuations induced by the wake may be treated as essentially inviscid and the effects of viscosity remain confined to a region near the surface of the body.

The perturbation approach allowed the unsteady boundary layer equations of motion to be linearized and separated into periodic and random sets by ensemble averaging. It was shown that the regular periodic equations may be solved as a superposition of simpler sinusoidal equations using the method of Lighthill, and that for typical gas turbine wake–airfoil interactions with a reduced frequency $\omega_r << 40$,

$$\frac{\bar{u}_{ss} + \tilde{u}}{\bar{U}_{\phi ss} + \tilde{U}_\phi} \approx \frac{\bar{u}_{ss}}{\bar{U}_{\phi ss}}.$$

This condition was experimentally confirmed as well.

Although a solution of the equations for the random motion was not obtained, it was argued that the fluctuations would

also behave qualitatively like those of Lighthill. This was experimentally shown to be nearly so.

Acknowledgment

The authors would like to express their gratitude to Dr. John Adamczyk of the NASA Lewis Research Center for his support of this work.

References

Blasius, H., 1908, "Grenz Schichten in Flüssigkeiten mit kleiner Reibung," *Z. Math. u. Phys.*, Vol. 56, pp. 1-37; English Translation, NACA TM 1256.

Dunn, M. G., Martin, H. L., and Stanek, M. J., 1986," Heat Flux and Pressure Measurements and Comparison With Prediction for a Low-Aspect-Ratio Turbine Stage," ASME JOURNAL OF TURBOMACHINERY, Vol. 108, pp. 108-115.

Evans, R. L., 1978, "Boundary Layer Development on an Axial-Flow Compressor Stator Blade," ASME *Journal of Engineering for Power*, Vol. 100, pp. 287-293.

Hodson, H. P., 1983, "The Development of Unsteady Boundary Layers on the Rotor of an Axial-Flow Turbine," AGARD-CP351, Copenhagen.

Hodson, H. P., 1985, "Measurements of Wake Generated Unsteadiness in the Rotor Passages of Axial Flow Turbines," ASME *Journal of Engineering for Gas Turbines and Power*, Vol. 107, pp. 467-476.

Lighthill, M. J., 1954, "The Response of Laminar Skin Friction and Heat Transfer to Fluctuations in the Freestream Velocity," *Proceedings of the Royal Society of London*, Vol. 224, June, pp. 1-23.

Liu, X., and Rodi, W., 1989, "Measurements of Unsteady Flow Over and Heat Transfer From a Flat Plate," ASME Paper No. 89-GT-2.

Paxson, D. E., 1989, "An Investigation of the Steady and Unsteady Near Wake and Its Effect on a Laminar Boundary Layer," Ph.D. Thesis, Rensselaer Polytechnic Institute, Troy, NY.

Pfeil, H., Herbst, R., and Schröder, T., 1983, "Investigation of the Laminar-Turbulent Transition of Boundary Layers Disturbed by Wakes," ASME *Journal of Engineering for Power*, Vol. 105, pp. 130-137.

Roshko, A., 1976, "On the Drag and Shedding Frequency of Two-Dimensional Bluff Bodies," NACA TN 3169.

Zemskaya, A. S., Levitskiy, V. N., Repik, Ye.U., and Sosedko, Yu.P, 1979, "The Effect of Proximity of the Wall on Hot-Wire Readings in Laminar and Turbulent Boundary Layers," *Fluid Mechanics—Soviet Research*, Vol. 8, No. 1, pp. 133-141.

More on the Turbulent-Strip Theory for Wake-Induced Transition

R. E. Mayle
Department of Mechanical Engineering,
Rensselaer Polytechnic Institute,
Troy, NY 12181
Mem. ASME

K. Dullenkopf
Lehrstuhl und Institut für Thermische
Strömungsmaschinen,
Universität Karlsruhe (T.H.),
D-7500 Karlsruhe, Germany

A theory for transition from laminar to turbulent flow with an unsteady, periodic passing of turbulent wakes in the free stream has recently been presented by the authors. The theory considers a time-averaged transitional flow caused by the formation and propagation of turbulent strips along the surface. To apply the theory, however, both the origin and a quantity related to the production rate of these turbulent strips must be known. In this paper, after a brief review of the theory, a dimensional analysis of the problem is presented and data from experiments re-examined in light of the result. From this, an expression for the time-averaged intermittency is obtained, which may be used to calculate the time-averaged distributions of various boundary layer quantities for wake-induced transitional flow.

Introduction

Unsteady flows in gas turbines caused by wakes from upstream airfoils or obstructions, such as shown in Fig. 1, have recently received much attention. The reason is simple. Only recently have data from new full- and large-scale (rotating) compressor and turbine facilities been compared back-to-back to (nonrotating) cascade tests. Results of these comparisons have shown large time-averaged discrepancies in predicted losses and surface heat loads. On the suction surface, modern measurement techniques and data acquisition systems (see Hodson, 1984, Ashworth et al., 1985, Doorly et al., 1985, Doorly, 1988, Dring et al., 1986, Dunn, 1986, Dunn et al., 1986, LaGraff et al., 1989, and Wittig et al., 1988) have allowed one to determine that part of the discrepancy is caused by an improper account of laminar–turbulent transition. In particular, it has been shown that the transition, as a result of the unsteady passing of wakes from the upstream airfoils, is unsteady and cannot be predicted using steady-flow boundary layer analysis.

Quickly on the heels of these experimental results, models for unsteady transition have been proposed by several investigators; namely, Doorly (1988), Sharma et al. (1988), Addison and Hodson (1990), Mayle and Dullenkopf (1989), and Hodson (1989). While Sharma, Addison and Hodson, and Hodson were mainly concerned with the effect of transition on loss and showed that the time-averaged loss depended on the reduced frequency, Doorly and Mayle and Dullenkopf were mostly concerned with its effect on the time-averaged heat load distribution. Much earlier, however, Walker (1974) described a model for unsteady transition on compressor blades, which depended on the unsteady formation and collapse of separation bubbles, and Pfeil and Herbst (1979), after conducting an innovative set of experiments, qualitatively described the model for wake-induced transition that is generally accepted as correct today.

In particular, Pfeil and Herbst and later Pfeil et al. (1983) examined the laminar–turbulent transition of a flat-plate boundary layer disturbed by passing wakes. They measured the steady and unsteady velocity components in the flow along a plate positioned downstream of a rotating cylinder of circular spokes aligned parallel to the leading edge of the plate. Besides presenting information about the time-averaged growth of the boundary layer, they showed that the wakes caused the boundary layer to become turbulent during their "impingement" on the plate. This, they pointed out, formed wake-induced transition zones, which propagated down the plate at a velocity less than the wake-passing velocity. Although not formally stated, they implied that the time-averaged condition of the boundary layer may be obtained from

$$\tilde{f} = (1-\tilde{\gamma})f_L + \tilde{\gamma} f_T \tag{1}$$

where f is a boundary-layer flow related quantity such as surface shear stress or heat flux, f_L is its laminar value, f_T is its fully turbulent value, and $\tilde{\gamma}$, the time-averaged intermittency, is the fraction of time the flow is turbulent. The latter varies between zero for laminar flow and unity for fully turbulent flow. It should also be noted that they found regions of natural transition occurring between those induced by the wake implying that the two types of transition can occur independently of one another, as shown in Fig. 2. In this figure, x_{tw} is the "origin" of wake-induced transition while x_{tn} is that for natural transition.

Doorly used the intermittency concept and assumed that the high turbulence content of the wake produces a turbulent patch in an otherwise laminar boundary layer during each passing. To obtain the time-observed flow, they used equation (1) and an intermittency determined by computing the temporal position of the wake adjacent to the surface. The intermittency,

Contributed by the International Gas Turbine Institute and presented at the 35th International Gas Turbine and Aeroengine Congress and Exposition, Brussels, Belgium, June 11–14, 1990. Manuscript received by the International Gas Turbine Institute January 23, 1990. Paper No. 90-GT-137.

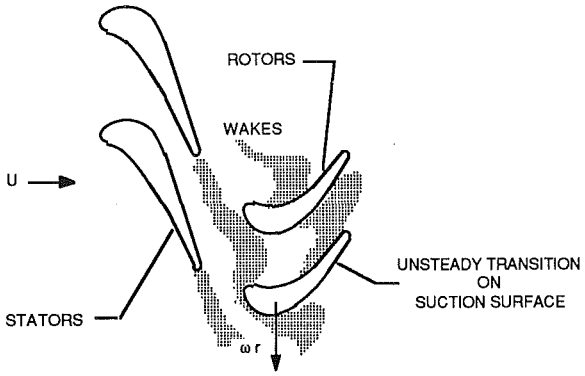

Fig. 1 Unsteady wake propagation through blade row

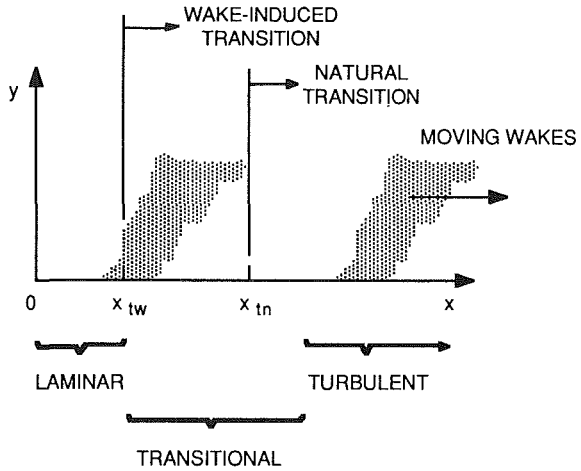

Fig. 2 Combined wake-induced and natural transition on a surface

therefore, depended on the propagation and growth of the wake around the airfoil. A comparison to time-averaged heat-flux measurements showed only a qualitative agreement.

Mayle and Dullenkopf (1990) proposed a model, based on Emmons' (1951) turbulent spot theory, that considered a coalescence of turbulent spots into turbulent "strips," as shown in Fig. 3, which then propagated and grew along the surface within the laminar boundary layer. They assumed that once the turbulent strip is formed by the wake its propagation and growth are independent of the wake. As a result, their theory predicts a wake-induced intermittency distribution without any need to calculate the wake position. From their expression for intermittency and equation (1), the surface heat flux or shear stress distribution and, by integration of the shear stress distribution, the time-averaged loss caused by wake-induced and natural transitional flow on the surface can be obtained.

Assuming that the turbulent spots produced naturally (natural transition) and by the periodic passing of wakes imbedded in the free stream (wake-induced transition) are independent, Mayle and Dullenkopf found that the time-averaged intermittency $\tilde{\gamma}$ is given by

$$\tilde{\gamma}(x) = 1 - [1 - \gamma_n(x)][1 - \tilde{\gamma}_w(x)] \tag{2}$$

where γ_n and $\tilde{\gamma}_w$ are the intermittency distributions for natural and wake-induced transition. The tilde refers to a time-averaged quantity over the wake passing period.

An expression for γ_n was obtained by Dhawan and Narasimha (1958) who showed that the intermittency distribution through natural transition is well represented by

$$\gamma_n(x) = 1 - \exp\left[-0.412\left(\frac{x - x_{tn}}{x_{75} - x_{25}}\right)^2\right] \tag{3}$$

where x is the distance along the surface, x_{tn} is the location of natural transition, and x_{25} and x_{75} are the x positions where γ = 0.25 and 0.75, respectively. The quantity $x_{75} - x_{25}$ is a characteristic length for transition, which may be obtained from correlations (see, for example, Sharma et al., 1988).

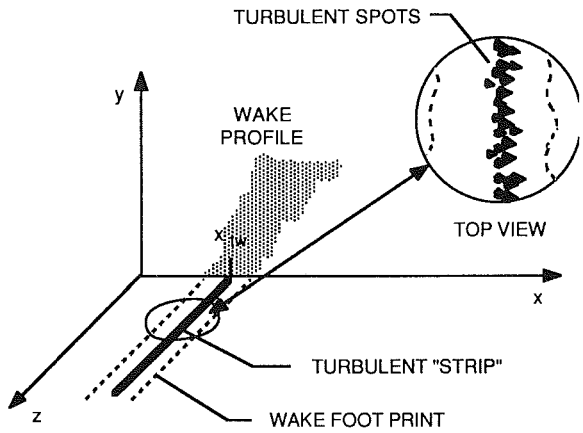

Fig. 3 Formation of turbulent strips from turbulent spot coalescence

The expression for $\tilde{\gamma}_w$ was that obtained by Mayle and Dullenkopf, namely,

$$\tilde{\gamma}_w(x) = 1 - \exp\left[-b\left(\frac{\tau_w}{\tau}\right)\left(\frac{x - x_{tw}}{U_s}\right)\right] \tag{4}$$

where b is a quantity proportional to the production rate of turbulent strips and their angle of spread, x_{tw} is the origin of the turbulent strips, τ_w is the residence time of the wake over any position on the surface within one wake-passing period τ, and U_s is the turbulent-strip propagation velocity (taken here

Nomenclature

b = a modified turbulent-strip production strength
c = airfoil chord
h = heat transfer coefficient
L = integral length scale of wake turbulence
n = number of rotating spokes or bars
Tu = turbulence level in wake
u' = rms of the wake turbulence
U = free-stream or incident velocity
U_s = local spot- or strip-propagation velocity
ΔU = wake deficit
x = coordinate on surface in streamwise direction
x_t = transition position
β = wake angle to surface
γ = intermittency
$\tilde{\gamma}$ = time-averaged intermittency
ν = kinematic viscosity
τ = wake-passing period
τ_w = resident time of wake over location x_{tw}
ω = wake-passing frequency
ω_r = reduced frequency

Subscripts

L = fully laminar
n = quantity related to natural transition
T = fully turbulent
w = quantity related to wake-induced transition

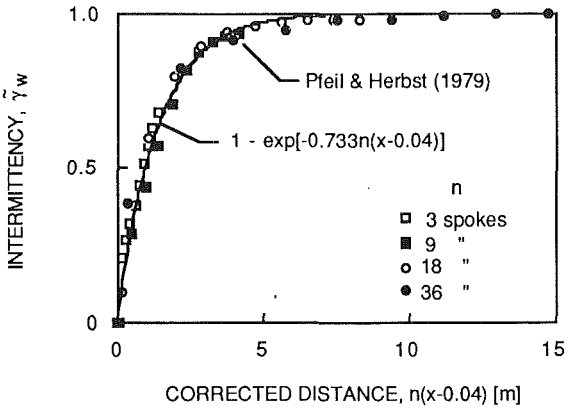

Fig. 4 Flat-plate wake-induced intermittency data of Pfeil and Herbst (1979) and comparison to theory

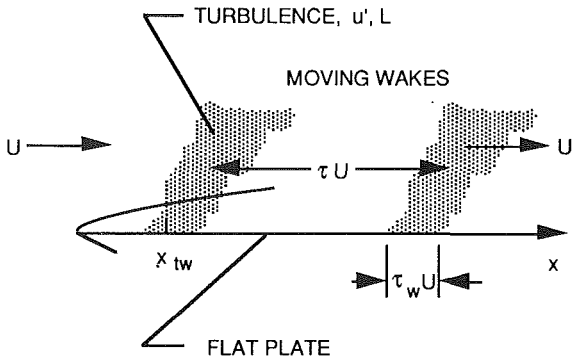

Fig. 5 Wake-induced transition on a flat plate

for simplicity as constant). Measurements indicate that $U_s \approx 0.6$–$0.8\ U$ where U is the local free-stream velocity. In general, it is expected that both b and x_{tw} are functions of the wake strength. Obviously, if the wake is very weak, i.e., the velocity deficit and turbulence are small, spot production caused by the wake will be less, spot coalescence into turbulent strips will not occur, and transition will be more natural-like.

A comparison of equation (4) with the data of Pfeil and Herbst (1979), Dring et al. (1986), and Wittig et al. (1988) showed excellent agreement. Figure 4 shows the comparison made with Pfeil and Herbst's data and is a reproduction of Mayle and Dullenkopf's Fig. 7. However, the comparison also provided the unexpected result that the quantity b/U_s was nearly independent of the test situation and roughly equal to 57 m^{-1}. This result is either fortuitous or a consequence of a common scaling in all three experiments. The present work was undertaken to investigate this situation.

In the following, the wake-induced transition problem is examined from a dimensional analysis standpoint and the important dimensionless parameters defined. A dimensionally correct functional expression is then written for the quantity b/U_s and the data from the experiments of Pfeil and Herbst, Dring et al., and Wittig et al. used to approximate the functional. This provides a new looking and extremely simple expression for the time-averaged wake-induced intermittency, which does not involve the quantity b/U_s. Finally, this expression is compared to data both previously published and newly presented herein.

Some Considerations Using Dimensional Analysis

Consider an unsteady wake-induced transitional boundary layer as shown in Fig. 5. For simplicity, a flat plate is being considered rather than an airfoil and only wake-induced transition will be assumed to occur. The important quantities of the problem appear to be U, the free-stream velocity, ν, the kinematic viscosity, τ, the wake-passing period, τ_w, the residence time of the wake, equal to the wake width divided by $U\cos\beta$, where β is the wake angle, ΔU, the wake deficit, u', the characteristic velocity of turbulence in the wake, and L, the characteristic length scale of turbulence. Here, it is assumed that the wake drifts with the free stream. For two-dimensional wakes, the quantity $\tau_w \Delta U$ is independent of position on the plate, but will depend on the wake generator (see Schlichting, 1979). Of course, the wake width $\tau_w U$ will increase as the wake moves downstream, and both the deficit and turbulence will decrease. Since there are no other dynamic quantities, the fluid density and viscosity have already been combined to form the kinematic viscosity.

The dimensionless parameters of the problem are then $U^2\tau_w/\nu$, a Reynolds number based on the wake width, $\Delta U/U$, τ_w/τ, β, Tu, the turbulence level in the wake, and $u'L/\nu$, the turbulence Reynolds number. These are six independent parameters of which any combination may be used and, with the exception of $\Delta U/U$, β and Tu may be looked at as either a ratio of length scales or time scales. From dimensional analysis considerations, one then has

$$(b/U_s)^{-1} = (\text{Length Scale}) \times F(U^2\tau_w/\nu,\ \Delta U/U,\ \tau_w/\tau,\ \beta,\ Tu,\ u'L/\nu)$$

where F is a function of the dimensionless parameters of the problem as listed.

To obtain this relation rigorously from experiments, one should pick a length scale, say τU, and then plot $\tau U(U_s/b)$ versus all the parameters. Its success, of course, depends on the completeness of the data set. In many cases, however, a good guess can be made. For example, since b/U_s was nearly the same for all the tests examined, b/U_s cannot depend on τ because only τ changed when the number of rotating elements were changed in Pfeil and Herbst's and Wittig's et al. tests. In fact, this is why τ_w rather than τ was used to define the first dimensionless quantity listed in F. Also, it is not clear why b/U_s should depend on the wake angle unless a width normal to the wake is used rather than as done here $\tau_w U$. So, it appears that one might have

$$(b/U_s)^{-1} = (\text{Length Scale}) \times F(U^2\tau_w/\nu,\ \Delta U/U,\ Tu,\ u'L/\nu)$$

where the length scale multiplying F must be independent of τ (i.e., the length scale τU picked as an example above is no good).

The parameters listed in the argument of F and several length scales were calculated for each of the experiments conducted by Pfeil and Herbst, Dring et al., and Wittig et al. With the exception of the turbulence length scale, there was enough information to obtain reasonable values for most of the quantities. In this regard, the results from Pfeil and Eifler (1975) were used to supplement Pfeil and Herbst's data. In all cases, due regard was given to the relative motion between the wake generator, be it bars or airfoils, and the test surface. For the results using airfoils, the quantities were calculated using both the incident (reported here) and the local free-stream velocity at the beginning of transition and, although the numbers were different, the conclusions remain unchanged. The turbulence length scale was obtained by using the measurements of Van Dresar and Mayle (1988) in the wake of a cylinder and scaling them according to the diameter of the wake generating bars for Pfeil and Herbst and Wittig et al. tests. For Dring et al., the measurements were scaled using the sum of the calculated momentum thicknesses on the pressure and suction side of the first vane and its trailing edge thickness. These calcultions are somewhat questionable and should be viewed only as estimates. The results are shown in Table 1.

The main point is that all but $\tau_w U$ vary by a factor of two or more, which indicates that F is independent of $U^2\tau_w/\nu$, $\Delta U/U$, Tu, and $u'L/\nu$ if $\tau_w U$ is used as the length scale multiplying F. The values of $(b/U_s)(\tau_w U)$ are

Table 1

Quantity	b/U_s, m^{-1}	$U^2\tau_w/\nu$	$\Delta U/U$	Tu, percent	$u'L/\nu$	$\tau_w U$, mm	L, mm
Pfeil and Herbst	66	31,800	0.14	12	245	28	1.8
Dring et al.	56	72,500		12	1432	34	5.6
Wittig et al.	57*	141,600	0.06	6	525	34	2.1

* This differs from the value of 49 reported previously because more accurate, unsteady wake measurements showed that τ_w/τ was different from that reported.

	$(b/U_s)(\tau_w U)$
Pfeil and Herbst	1.85
Dring et al.	1.90
Wittig et al.	1.94

which provides $(b/U_s)^{-1} \approx \tau_w U/1.9$, i.e., $F \approx$ const $\approx 1/1.9$. This is interesting, because it implies (see theoretical development in previous paper) that the wake in all of these experiments was so intense that it caused a turbulent strip to be immediately formed when it reached x_{tw} and that the formation of any other strips within the wake foot print, see Fig. 3, were suppressed. Evidence that this is possible has been presented by Pfeil and Herbst. Evidence that it doesn't always happen has been presented by Addison and Hodson. In this regard, more work is required.

Substituting the above result for b/U_s into equation (4), one obtains the following relatively simply expression for the time-averaged wake-induced intermittency:

$$\tilde{\gamma}_w(x) = 1 - \exp\left[-1.9\left(\frac{x - x_{tw}}{U\tau}\right)\right] \tag{5}$$

where U is the incident velocity and τ is the wake-passing period. Expressing τ in terms of the wake-passing frequency ω and introducing a chord length c, an equation incorporating the reduced frequency ω_r is obtained:

$$\tilde{\gamma}_w(x) = 1 - \exp\left[-0.302\omega_r\left(\frac{x - x_{tw}}{c}\right)\right] \tag{6}$$

where $\omega_r = \omega c/U$. From this it is seen that the time-averaged loss for wake-induced transitional flow on a surface will depend only on the reduced frequency ω_r, as found by Sharma and Hodson, and the beginning of transition x_{tw}/c.

Comparisons to Experiments

The experimental data of Pfeil and Herbst, Dring et al., and Wittig et al. have been previously presented in Fig. 4 in this paper and Figs. 8 and 10 of our previous paper. In each of these figures, the data are plotted as time-averaged intermittency versus streamwise distance. At this point, it is perhaps best to recollect that Pfeil and Herbst measured the time-dependent velocities in a transitional boundary layer on a 0.7-m-long flat plate positioned in a wind tunnel behind a rotating cylinder cascade. The data presented in Fig. 4 were obtained using their measured shape factors for 0, 3, 9, 18, 36, and 90 spokes in the cascade. On the other hand, Dring et al. obtained the time-averaged heat transfer on a first-stage rotor in a large-scale turbine facility, while Wittig et al. measured the time-averaged heat transfer on an airfoil in a full-scale, stationary cascade with an unsteady wake generator of 4, 7, and 14 rotating bars placed upstream. In both of these cases, the data presented were obtained using their reported values of Stanton numbers or heat transfer coefficients.

All these data are presented again in Fig. 6. In this figure, however, the wake-induced intermittency factor $\tilde{\gamma}_w(x)$ is plotted against a streamwise distance scaled by $U\tau$ as suggested by equation (5). For the data of Dring et al. and Wittig et al., where natural transition also occurred, the wake-induced intermittency was obtained by using equations (2) and (3) to eliminate γ_n. The curve in the figure corresponds to the theory

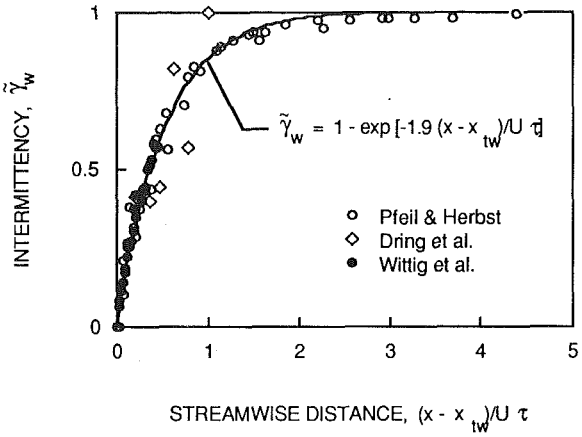

Fig. 6 Comparison between theory and experiments

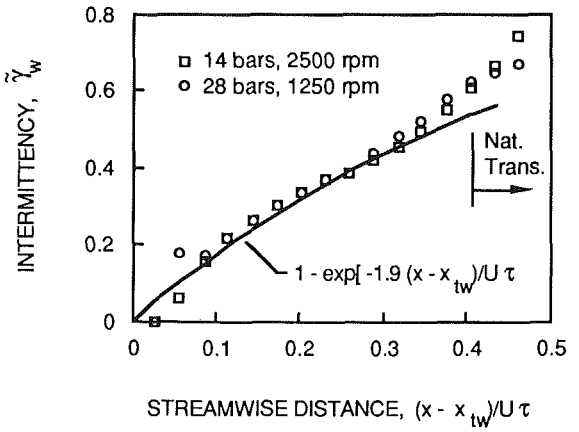

Fig. 7 Intermittency distributions for tests having same τ but different τ_w/τ and comparison to theory

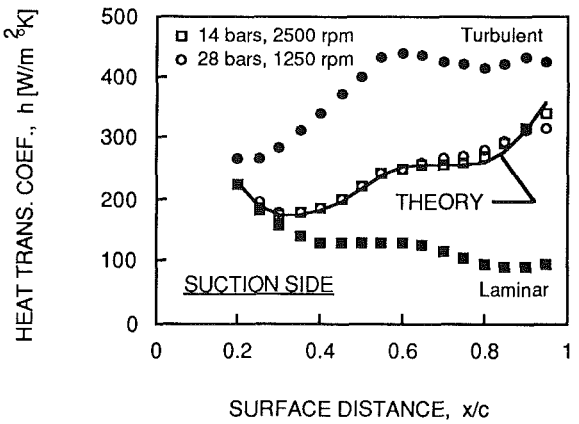

Fig. 8 Predicted and measured time-averaged heat transfer distributions for unsteady transition

with $b/U_s = 1.9/\tau_w U$, namely equation (5). The agreement is truly remarkable considering the differences in test configurations and conditions.

A further comparison is shown in Fig. 7 where data for two different tests are shown. These tests were conducted at the Institut für Thermische Strömungsmaschinen using the same test facility and flow conditions under which the data reported above were obtained. In fact, the data shown in this figure for 14 bars are identical to those shown in Fig. 6. The data shown for 28 bars, however, are for a rotational speed half that for the test with 14 bars. According to equation (5), since τ is the

same for both tests, the results should be the same. Measurements of τ_w/τ for these tests provided $(\tau_w/\tau)_{14} = 0.72\,(\tau_w/\tau)_{28}$. Hence, equation (4) with b/U_s constant would have erroneously predicted two different distributions for the time-averaged wake-induced intermittency. The data used to obtain Fig. 7 are presented in their original form in Fig. 8. Here, the heat transfer coefficient distributions on the suction side of the test airfoil are plotted against the streamwise distance normalized by the airfoil's chord for the two tests. In addition, the results for fully turbulent and laminar flow (see previous paper for details), together with the prediction using equations (1), (2), (3), and (5) (with $f \equiv \dot{h}$) are also shown. This is a good illustration of how well one may now evaluate the time-averaged heat transfer coefficient for unsteady boundary-layer transition caused by a periodic passing of a turbulent wake in the mainstream flow.

Conclusions

In a continuing effort to understand unsteady wake-induced transitional flows, a dimensional analysis of the problem provided a functional relation for the production of turbulent strips in the laminar boundary layer by the passing wakes, b/U_s. Upon calculating the various dimensionless parameters of the problem and length scales using published data it was found that $b/U_s \approx 1.9/\tau_w U$, which, in turn, provided the following expression for the time-averaged wake-induced intermittency.

$$\tilde{\gamma}_w(x) = 1 - \exp\left[-1.9\left(\frac{x - x_{tw}}{U\tau}\right)\right].$$

Comparisons of this expression to data showed very good agreement. In addition, this expression allows one to calculate the local time-averaged conditions in an unsteady, transitional boundary-layer flow.

Acknowledgments

This work was conducted while the first author was at the Institut für Thermische Strömungsmaschinen, Universität Karlsruhe as a Visiting Professor and Scientist funded by the Sonderforschungsbereich N. 167. This author is truly grateful to his host, Professor S. Wittig, for his hospitality and continual support.

References

Addison, J. S., and Hodson, H. P., 1990, "Unsteady Transition in an Axial-Flow Turbine: Part 1—Measurements on the Turbine Rotor; Part 2—Cascade Measurements and Modeling," ASME JOURNAL OF TURBOMACHINERY, Vol. 112, pp. 206–221.

Ashworth, D. A., LaGraff, J. E., Schultz, D. L., and Grindrod, K. J., 1985, "Unsteady Aerodynamic and Heat Transfer Processes in a Transonic Turbine Stage," ASME *Journal of Engineering for Gas Turbines and Power*, Vol. 107, pp. 1011–1030.

Dhawan, S., and Narasimha, R., 1958, "Some Properties of Boundary Layer Flow During Transition From Laminar to Turbulent Motion," *Journal of Fluid Mechanics*, Vol. 3, pp. 418–436.

Doorly, D. J., Oldfield, M. L. G., and Scrivener, C. T. J., 1985, "Wake-Passing in a Turbine Rotor Cascade," *Heat Transfer and Cooling in Gas Turbines*, AGARD-CP-390, pp. 7-1 to 7-18.

Doorly, D. J., 1983, "Modeling the Unsteady Flow in a Turbine Rotor Passage," ASME JOURNAL OF TURBOMACHINERY, Vol. 110, pp. 27–37.

Dring, R. P., Blair, M. F., Joslyn, H. D., Power, G. D., and Verdon, J. M., 1986, "The Effects of Inlet Turbulence and Rotor/Stator Interactions on the Aerodynamics and Heat Transfer of a Large-Scale Rotating Turbine Model," NASA Contractor Rept. 4079, Vol. 1.

Dunn, M. G., 1986, "Heat-Flux Measurements for the Rotor of a Full-Stage Turbine: Part I—Time-Averaged Results," ASME JOURNAL OF TURBOMACHINERY, Vol. 108, pp. 90–97.

Dunn, M. G., George, W. K., Rae, W.J., Woodward, S. H., Moller, J.C., and Seymour, P. J., 1986, "Heat-Flux Measurements for the Rotor of a Full-Stage Turbine: Part II—Description of Analysis Technique and Typical Time-Resolved Measurements," ASME JOURNAL OF TURBOMACHINERY, Vol. 108, pp. 98–107.

Emmons, H. W., 1951, "The Laminar-Turbulent Transition in a Boundary Layer—Part 1," *Journal of the Aeronautical Sciences*, Vol. 18, pp. 490–498.

Hodson, H. P., 1984, "Boundary Layer and Loss Measurements on the Rotor of an Axial-Flow Turbine," ASME *Journal of Engineering for Gas Turbines and Power*, Vol. 106, pp. 391–399.

Hodson, H. P., 1989, private communication.

LaGraff, J. E., Ashworth, D. A., and Schultz, D. L., 1989, "Measurement and Modeling of the Gas Turbine Blade Transition Process as Disturbed by Wakes," ASME JOURNAL OF TURBOMACHINERY, Vol. 111, p. 315–322.

Mayle, R. E., and Dullenkopf, K., 1990, "A Theory for Wake-Induced Transition," ASME JOURNAL OF TURBOMACHINERY, Vol., 110, pp. 18?-195.

Pfeil, H., and Eifler, J., 1975, "Turbulenzverhältnisse hinter rotierenden Zylindergittern," *Forsch. Ing.-Wes.*, Vol. 41, No. 5, pp. 137–145.

Pfeil, H., and Herbst, R., 1979, "Transition Procedure of Instationary Boundary Layers," ASME Paper No. 79-GT-128.

Pfeil, H., Herbst, R., and Schröder, T., 1983, "Investigation of the Laminar-Turbulent Transition of Boundary Layers Disturbed by Wakes," ASME *Journal of Engineering for Power*, Vol. 105, pp. 130–137.

Schlichting, H., 1979, *Boundary Layer Theory*, McGraw-Hill, New York.

Sharma, O. P., Renaud, E., Butler, T. L., Milsaps, K., Dring, R. P., and Joslyn, H. D., 1988, "Rotor-Stator Interaction in Multi-stage Axial-Flow Turbines," AIAA Paper No. 88-3013.

Van Dresar, N., and Mayle, R. E., 1988, "Stagnation Transfer Rates for an Incident Flow With High Turbulence Intensities," ASME Paper 88-HT-**, to be published in JOURNAL OF TURBOMACHINERY.

Walker, G. J., 1974, "The Unsteady Nature of Boundary Layer Transition on an Axial Compressor Blade," ASME Paper No. 74-GT-135.

Wittig, S., Schulz, A., Dullenkopf, K., and Fairbank, J., 1988, "Effects of Free-Stream Turbulence and Wake Characteristics on the Heat Transfer Along a Cooled Gas Turbine Blade," ASME Paper No. 88-GT-179.

Effects of Vortices With Different Circulations on Heat Transfer and Injectant Downstream of a Single Film-Cooling Hole in a Turbulent Boundary Layer

P. M. Ligrani
Associate Professor.

C. S. Subramanian
Adjunct Research Professor.

D. W. Craig
Graduate Student.

P. Kaisuwan
Graduate Student.

Department of Mechanical Engineering,
Naval Postgraduate School,
Monterey, CA 93943-5000

Results are presented that illustrate the effects of single embedded longitudinal vortices on heat transfer and injectant downstream of a single film-cooling hole in a turbulent boundary layer. Attention is focused on the changes resulting as circulation magnitudes of the vortices are varied from 0.0 to 0.15 m^2/s. Mean temperature results are presented that show how injectant is distorted and redistributed by vortices, along with heat transfer measurements and mean velocity surveys. Injection hole diameter is 0.952 cm to give a ratio of vortex core diameter to hole diameter of about 1.5–1.6. The free-stream velocity is maintained at 10 m/s, and the blowing ratio is approximately 0.5. The film-cooling hole is oriented 30 deg with respect to the test surface. Stanton numbers are measured on a constant heat flux surface with a nondimensional temperature parameter of about 1.5. Two different situations are studied: one where the injection hole is beneath the vortex downwash, and one where the injection hole is beneath the vortex upwash. For both cases, vortex centers pass well within 2.9 vortex core diameters of the centerline of the injection hole. To quantify the influences of the vortices on the injectant and local heat transfer, the parameter S is used, defined as the ratio of vortex circulation to injection hole diameter times mean injection velocity. When S is greater than 1.0–1.5, injectant is swept into the vortex upwash and above the vortex core by secondary flows, and Stanton number data show evidence of injectant beneath the vortex core and downwash near the wall for x/d only up to 33.6. For larger x/d, local Stanton numbers are augmented by the vortices by as much as 23 percent relative to film-cooled boundary layers with no vortices. When S is less than 1.0–1.5, some injectant remains near the wall beneath the vortex core and downwash where it continues to provide some thermal protection. In some cases, the protection provided by film cooling is augmented because of vortex secondary flows, which cause extra injectant to accumulate near vortex upwash regions.

Introduction

Embedded vortices cause significant perturbations to local wall heat transfer distributions, as well as to distributions of film injectant along with the accompanying thermal protection, in many components of high-temperature engines. In the present study, such perturbations are quantified as dependent upon vortex strength. This information is a necessary for designers of high-temperature engine components since the strengths of embedded longitudinal vortices vary significantly, especially in turbine blade passages of gas turbine engines. However, the interactions resulting from these vortex disturbances to surrounding injectant and boundary layer fluids are so complex that numerical models to predict these flows are currently unavailable. Consequently, experiments are needed to elucidate physical behavior.

Of other experimental studies, Blair (1974) measured heat transfer on an endwall film-cooled using a slot inclined at a 30 deg angle. The large vortex located in the corner between the endwall and the suction surface of their cascade was believed to cause significant variations of measured heat transfer and film cooling effectiveness. Goldstein and Chen (1985, 1987) studied the influence of flows originating near the endwall on blade film cooling from one and two rows of holes. A triangular region was found on the convex side of the blade where coolant was swept away from the surface by the passage vortex.

Ligrani et al. (1989a) examined the influences of embedded

Contributed by the International Gas Turbine Institute and presented at the 35th International Gas Turbine and Aeroengine Congress and Exposition, Brussels, Belgium, June 11–14, 1990. Manuscript received by the International Gas Turbine Institute January 11, 1990. Paper No. 90-GT-45.

longitudinal vortices on film cooling from a single row of film-cooling holes in turbulent boundary layers. Blowing ratios ranged from 0.47 to 0.98, and free-stream velocities were 10 m/s and 15 m/s. The results of this study showed, first, that film coolant is greatly disturbed and local Stanton numbers are altered significantly by the secondary flows within vortices, and second, that the spanwise position of the vortex with respect to film-cooling holes is very important. To clarify further the interactions between vortices and wall jets, Ligrani and Williams (1990) then examined the effects of an embedded vortex on injectant from a single film-cooling hole in a turbulent boundary layer. Attention was focused on the effect of spanwise position of the vortices with respect to film injection holes. The ratio of vortex circulation to injection velocity times hole diameter was 3.16, and the ratio of vortex core size to injection hole diameter was 1.58. The main conclusion of this study is that injection hole centerlines must be at least 2.9–3.4 vortex core diameters away from the vortex center in the lateral direction to avoid significant alterations to wall heat transfer and distributions of film coolant.

In the present study, interactions between a single longitudinal embedded vortex and injectant from a single film-cooling hole are again studied. As for the Ligrani and Williams (1990) study, a single hole is chosen because interactions with injectant from neighboring holes are not present, allowing a clearer understanding of the interactions of interest. To provide a basis of comparison, the same boundary layer flow, injection hole geometry, blowing ratio, and injection temperature are employed.

The investigation extends results presented by Ligrani and Williams (1990) since attention is focused on the changes to wall heat transfer and injectant distributions that result as vortex circulation is altered. Two different situations are considered. For the first, the vortex upwash passes above the centerline of the injection hole such that the vortex center passes 0.87 vortex core diameters away in the positive spanwise direction. For the second, the vortex downwash passes above the centerline of the injection hole such that the vortex center passes 1.67 vortex core diameters away in the negative spanwise direction. Vortices are generated using a half-delta wing placed on the wind tunnel test surface, and vortex circulation is varied by changing the angle of attack of the delta wing.

Experimental Apparatus and Procedures

In order to isolate the interactions between the film injectant and the embedded vortices, measurements are made on a flat plate in a zero pressure gradient. Wind tunnel speed is 10 m/s and temperature differences are maintained at levels less than 30°C to maintain constant property conditions. With this approach, many of the other effects present in high-temperature engines are not considered (curvature, high free-stream turbulence, variable properties, stator/blade wake interactions, shock waves, compressibility, rotation, etc.) since these may obscure and complicate the interaction of interest.

Detailed measurements are made in spanwise/normal planes at different streamwise locations in order to elucidate the development and evolution of flow behavior. In order to match the experimental conditions found in many practical applications, the boundary layer, embedded vortex, and wall jet are all turbulent. The nondimensional injection temperature parameter θ is maintained at about 1.5 for all heat transfer tests to maintain this parameter at a value similar to ones existing in gas turbine components.

Wind Tunnel and Coordinate System. The wind tunnel is open-circuit, subsonic, and located in the laboratories of the Department of Mechanical Engineering of the Naval Postgraduate School. A centrifugal blower is located at the upstream end, followed by a diffuser, a header containing a honeycomb and three screens, and then a 16 to 1 contraction ratio nozzle. The nozzle leads to the test section, which is a rectangular duct 3.05 m long and 0.61 m wide, with a topwall having adjustable height to permit changes in the streamwise pressure gradient.

A schematic showing the test section and coordinate system is presented in Fig. 1 from Ligrani and Williams (1990). The vortex generator base plate is shown to be located 0.48 m downstream of the boundary layer tip. The left edge of this base plate (looking downstream) is the base edge refered to in Table 1 as a location reference. The downstream edge of the single injection hole is then 0.60 m farther downstream from

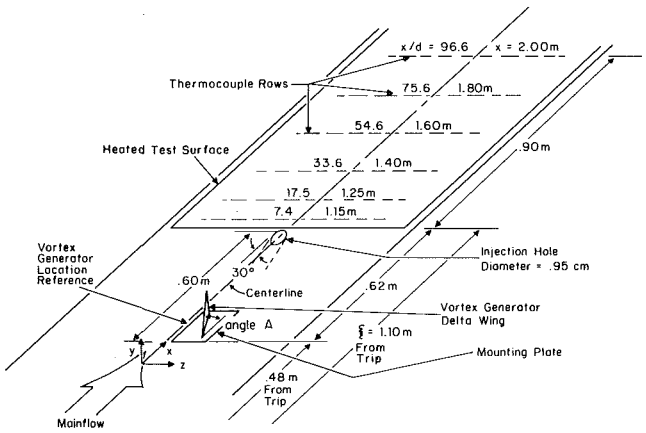

Fig. 1 Coordinate system and schematic of wind tunnel test section

Nomenclature

A = vortex generator delta wing angle of attack
c = average vortex core radius
d = injection hole diameter
m = blowing ratio = $\rho_c U_c / \rho_\infty U_\infty$
S = nondimensional circulation = $\Gamma / U_c * d$
St = Stanton number with vortex and film injection
St_o = baseline Stanton number, no vortex, no film injection
St_f = Stanton number with film injection and no vortex
T = temperature
U = mean velocity
X = streamwise distance from boundary layer trip
x = streamwise distance from downstream edge of film-cooling hole
Y = distance normal to the surface
Z = spanwise distance from test surface centerline
Γ = circulation of streamwise vorticity
θ = nondimensional injection temperature = $(T_{rc} - T_{r\infty})/(T_w - T_{r\infty})$
ξ = unheated starting length
ρ = density

Subscripts

c = injectant at exits of injection holes
o = total condition
r = recovery condition
w = wall
y = normal direction
z = spanwise direction
∞ = free stream

Table 1 Vortex generator spanwise positions for different vortex strengths

Vortex	Vortex Generator Angle A (degrees)	Spanwise Z Locations of the Generator Base Edge for Vortex Spanwise Position e	Spanwise Z Locations of the Generator Base Edge for Vortex Spanwise Position h
r	18	0.00	+3.80
w	15	-0.51	+3.29
x	12	-1.53	+2.27
y	8	-3.56	+0.24
z	4	-4.07	-0.27

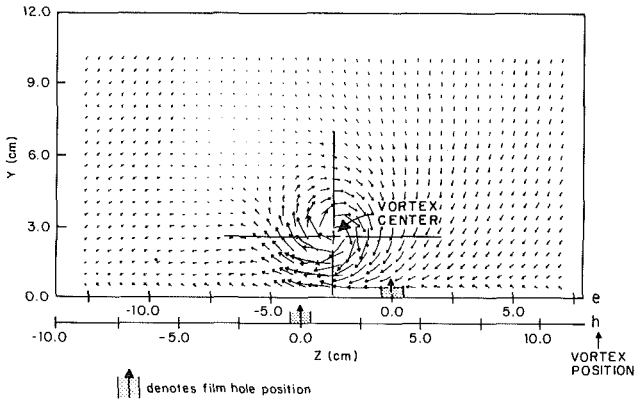

Fig. 2 Film-cooling injection locations with respect to vortex center and secondary flow vectors ($x/d \sim 0.0$) for vortex positions *e* and *h*

this base plate. The surface used for heat transfer measurements is then located a short distance farther downstream. With this surface at elevated temperature, an unheated starting length of 1.10 m exists, and the direction of heat transfer is then from the wall to the gas. Thermocouple row locations along the test surface are also labeled in Fig. 1. In regard to the coordinate system, Z is the spanwise coordinate measured from the test section centerline, X is measured from the upstream edge of the boundary layer trip, and Y is measured normal to the test surface. x is measured from the downstream edge of the injection holes and generally presented as x/d.

Injection System. The 0.952-cm-diam injection hole is inclined at an angle of 30 deg with respect to the test surface, and located on the spanwise centerline ($Z = 0.0$ cm). Air for the injection system originates in a 1.5-hp DR513 Rotron Blower capable of producing 30 cfm at 2.5 psig. From the blower, air flows through a regulating valve, a Fisher and Porter rotometer, a diffuser, and finally into the injection heat exchanger and plenum chamber. The exchanger provides means to heat the injectant above ambient temperature. The plenum connects to the plexiglass injection tube, which is 8 cm long with a length/diameter ratio of 8.4. With no vortex present, boundary layer displacement thickness at the injection location is $0.28d$. Injection system performance was checked by measuring discharge coefficients, which compared favorably with earlier measurements.

Mean Velocity Components. Three mean velocity components are measured using a five-hole pressure probe with a conical tip manufactured by United Sensors Corporation. Celesco transducers and Carrier Demodulators are used to sense pressures when connected to probe output ports. Following Ligrani et al. (1989b), corrections are made to account for spatial resolution and downwash velocity effects. The same automated traverse used for injectant surveys is used to obtain surveys of secondary flow vectors, from which mean streamwise vorticity contours are calculated. These devices, measurement procedures employed, as well as data acquisition equipment and procedures used, are further detailed by Ligrani et al. (1989c).

Stanton Number Measurements. The heat transfer surface is designed to provide a constant heat flux over its area. The surface next to the airstream is stainless steel foil painted flat black. Immediately beneath this is a liner containing 126 thermocouples, which is just above an Electrofilm Corp. etched foil heater rated at 120 V and 1500 W. Located below the heater are several layers of insulating materials including several Lexan sheets, foam insulation, styrofoam, and balsa wood. Surface temperature levels and convective heat transfer rates are controlled by adjusting power into the heater using a Standard Electric Co. variac, type 3000B. To determine the heat loss by conduction, an energy balance was performed. Radiation losses from the top of the test surface are estimated analytically. The thermal contact resistance between thermocouples and the foil top surface are estimated on the basis of outputs of the thermocouples and measurements from calibrated liquid crystals on the surface of the foil. This difference is then correlated as a function of heat flux through the foil.

Mean Temperature Measurements. Copper-constantan thermocouples are used to measure temperatures along the surface of the test plate, the free-stream temperature, as well as temperature distributions, which are correlated to injection distributions. For the distributions, a thermocouple is traversed over spanwise/normal planes (800 probe locations) using an automated two-dimensional traversing system, which may also be placed at different streamwise locations. Selected thermocouples are calibrated using a temperature-regulated bath.

Experimental Uncertainties. Uncertainty estimates are based upon 95 percent confidence levels, and determined following procedures described by Kline and McClintock (1953) and Moffat (1982). Typical nominal values of free-stream recovery temperature and wall temperature are 18.0 and 40.0°C, with respective uncertainties of 0.13 and 0.21°C. The free-stream density, free-stream velocity, and specific heat uncertainties are 0.009 kg/m^3 (1.23 kg/m^3), 0.06 m/s (10.0m/s), and 1 J/kgK (1006 J/kgK), where typical nominal values are given in parenthesis. For convective heat transfer, heat transfer coefficient, and heat transfer area, 10.5 W (270 W), 1.03 W/m^2 K (24.2 W/m^{2}K), and 0.0065 m^2 (0.558 m^2) are typical uncertainties. The uncertainties of St, St/St$_o$, m, and and x/d are 0.000086 (0.00196), 0.058 (1.05), 0.025 (0.50), and 0.36 (41.9).

Additional Experimental Details. Additional details on the experimental apparatus and procedures employed are given by Craig (1989), Kaisuwan (1989), Ligrani et al. (1989a), Ligrani and Williams (1990), and Ortiz (1987).

Generation and Control of Vortex Characteristics

The device used to generate the vortices is a half-delta wing with 3.2 cm height and 7.6 cm base. With this device, vortices are produced with secondary flow vectors such as the ones shown in Fig. 2. The wing is attached to a base plate and rotated about a pivot point to give different generator angles, which, in turn, result in different vortex circulation magnitudes. As vortex circulation becomes larger, secondary flow velocities between the vortex center and wall increase and the amount of spanwise vortex drift increases as the vortices are convected downstream. Thus, as the delta wing angle of attack increases (with constant pivot point location), vortices are located at more negative Z locations at any particular x/d.

Table 2 Characteristics of embedded vortices (spanwise vortex position *h*), symbols for Fig. 9

Fig. 9 Symbols	Vortex Labels	Vortex Generator Angle (degrees)	Max. Streamwise Vorticity (1/s)	Circulation (m**2/s)	S	2c/d
●	r	18	746	.144	3.03	1.61
△	w	15	668	.113	2.38	1.56
◆	x	12	537	.079	1.67	1.52
◇	y	8	304	.039	0.82	1.48
▲	z	4	159	.017	0.35	1.49
O	no vortex	0	000	.000	0.00	---

Table 3 Characteristics of embedded vortices (spanwise vortex position *e*), labels for Fig. 5, symbols for Fig. 10

Fig. 10 Symbols	Fig. 5 Labels	Vortex Generator Angle (degrees)	Max. Streamwise Vorticity (1/s)	Circulation (m**2/s)	S	2c/d
●	r	18	832	.151	3.17	1.58
△	w	15	691	.121	2.55	1.49
◆	x	12	534	.089	1.88	1.51
◇	y	8	323	.051	1.08	1.46
▲	z	4	154	.014	0.29	1.55
O	no vortex	0	000	.000	0.00	---

Because the principal objective of the present study is to examine the influences of vortex circulation, and because significant changes occur as spanwise positions of vortices with respect to injection holes are varied (Ligrani and Williams, 1990), the present study requires that the same portion of the vortex be located over the injection hole as the vortices pass. Thus, in order to obtain systematic results as circulation is changed, the spanwise starting locations of the vortices are altered by changing the spanwise position of the vortex generator delta wing. This is done so that the distances between the centerline of the middle injection hole and vortex centers (located at local vorticity maxima) are always maintained about constant as the vortices pass this injection hole. With this arrangement, streamwise vorticity measurements at $x/d = 41.9$ show that the centers of the different strength vortices are within ± 0.1 cm of $Y = 3.0$ cm, and within ± 0.5 cm of $Z = -3.6$ cm. Vortex generator spanwise positions used to attain this requirement are then given in Table 1. Two sets of spanwise positions are listed, labeled *e* and *h*.

As shown in Fig. 2, with spanwise position *e*, the vortex *downwash* passes over the injection hole, and the vortex center is at -2.5 cm or -1.67 core diameters relative to the centerline of the injection hole. With spanwise position *h*, injection emerges beneath the vortex *upwash* and the vortex center is located $+1.3$ cm or $+0.87$ core diameters away from the centerline of the injection hole. For both cases, $Z = 0.0$ locates the centerline of the middle injection hole and the centerline of the test surface. Core diameter characterizes the sizes of the vortices, and is determined here for vortices undisturbed by injectant using procedures described later in this section. Secondary flow vectors in Fig. 2 were measured just downstream of the injection hole with the vortex at position *e*. The horizontal axis is then shifted in the figure so that the centerline of the middle hole is appropriately oriented with respect to the vortex center for both vortex spanwise positions *e* and *h*.

Tables 2 and 3 give vortex characteristics as determined from measurements at $x/d = 41.9$ when $m = 0.5$ injection is employed. These two tables present data for spanwise vortex positions *h* and *e*, respectively. In these two tables and in Table 1, vortices with different circulation magnitudes are labeled *r*, *w*, *x*, *y*, and *z*, where a particular label applies to a particular generator delta wing angle. The same vortex labels are then used for both vortex spanwise positions (*e* and *h*) and whether or not injection is employed, which is important because vortex characteristics are often altered slightly by injectant.

Circulation magnitudes in Tables 2 and 3 are calculated by integrating streamwise vorticity with respect to spanwise/normal plane area. Local streamwise vorticity is equal to $\partial U_z/\partial y - \partial U_y/\partial z$, which is applied in finite difference form to secondary flow vector distributions. To minimize the influences of background noise, the integration is performed assuming that all vorticity values less than a threshold are equal to zero. The same numerical threshold of 76.0 (1/s) is used for all measurement points, chosen as the value equal to 10 percent of the maximum vorticity of vortex *r* with no injection (Craig, 1989). From data in Tables 2 and 3, increases of vortex circulation with vortex generator angle are apparent.

Also given in Tables 2 and 3 is *c*, the vortex core radius. This quantity is determined as one half of the sum of average core radii in the *Y* and *Z* directions (as measured from vortex centers). These radii are determined for the area that encompasses all vorticity values greater than or equal to 40 percent of peak velocity (at the center) for a particular vortex. The choice of 40 percent was made to give a good match to core radii determined at the locations of maximum secondary flow vectors (Craig, 1989). The area enclosed by secondary flow maxima is important because, for ideal Rankine vortices, it corresponds to the vortex core, which contains *all* vorticity. Secondary flow vector maxima are not used to determine core size as this gives results that are less accurate than the 40 percent threshold approach (Craig, 1989). $2c/d$ then gives the ratio of vortex core diameter to injection hole diameter. Core sizes are about the same even though peak vorticity varies. $2c/d$ is then about 1.5–1.6 for vortices, *r*, *w*, *x*, *y*, and *z* in Tables 2 and 3.

Also contained in Tables 2 and 3 is parameter *S*, which is discussed in the next section.

Heat Transfer and Injectant Distributions

In this section, baseline heat transfer data are first discussed. The discussion then focuses on the interactions of the vortices with injectant from a single film-cooling hole. For this part, addressed are the influences of the vortices on: (1) local heat transfer variations, and (2) injectant distributions. Here, data are presented for two different situations, one where the vortices are located at spanwise position *e* and one where the vortices are located at spanwise position *h*.

Baseline Data. Baseline data with no film injection already exist for similar test conditions (Ligrani et al., 1989a). Repeated measurements of spanwise-averaged Stanton numbers show good agreement (maximum deviation is 5 percent) with the correlation from Kays and Crawford (1980) for turbulent heat transfer to a flat plate with unheated starting length and constant heat flux boundary condition. Local and spanwise-averaged Stanton numbers with injection at a blowing ratio of 0.5 (and no vortex) also show agreement with earlier results (Ligrani and Williams, 1990). Further checks on measurement apparatus and procedures were made by measuring spatial variations of Stanton numbers along the test surface with different strengths vortices (and no injection). These data are also consistent with other results in the literature (Ligrani et al., 1989a).

Stanton Number Ratios for Z/d = 0.0 as Dependent Upon Vortex Circulation. Figures 3 and 4 present St/St_o Stanton number ratios measured at $Z/d = 0.0$. Here, St_o is the baseline Stanton number measured in a turbulent boundary layer with a two-dimensional mean flow field when no vortex or film

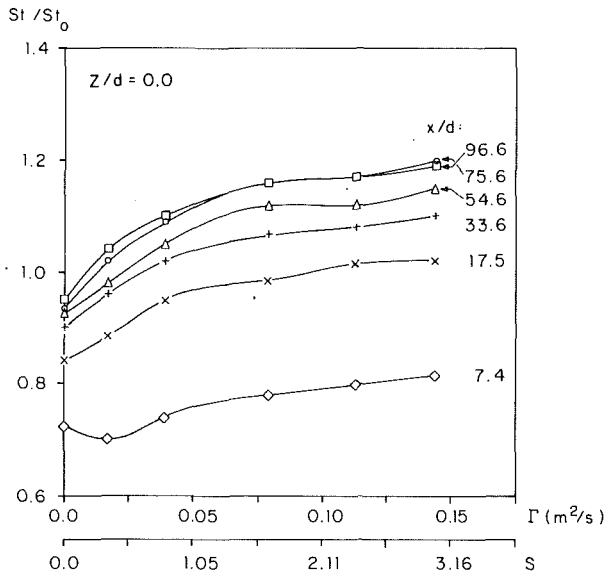

Fig. 3 Stanton number ratios as dependent upon dimensional and nondimensional vortex circulation, spanwise vortex position, *h*; vortex upwash passes over the injection hole. Vortex characteristics in Table 2.

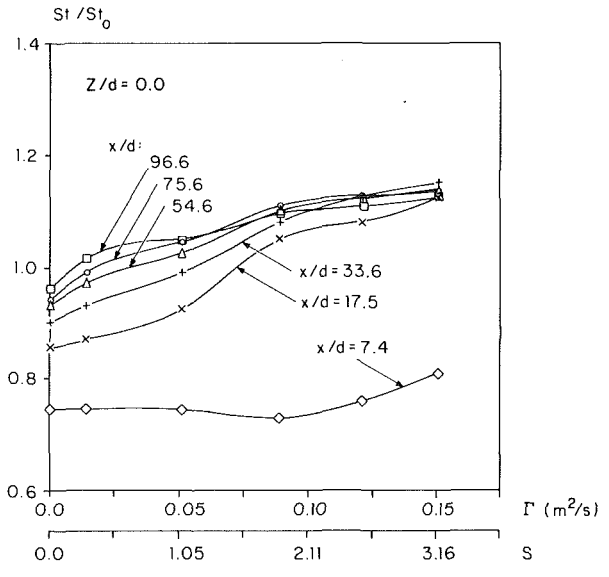

Fig. 4 Stanton number ratios as dependent upon dimensional and nondimensional vortex circulation, spanwise vortex position *e*; vortex downwash passes over the injection hole. Vortex characteristics in Table 3.

cooling is present. St is then the Stanton number with a vortex and film injection, except when circulation Γ equals 0.0, in which case St/St_o values represent flow behavior under the influence of the injectant only. St_f is used later in this paper and represents the Stanton number with film injection and no vortex. Data at $Z/d = 0.0$ are presented because this is where injectant from the single hole ordinarily provides the best protection along the test surface when no vortex is present. Improved local protection from the injectant film is indicated by local Stanton number ratios, which are less than 1.0.

The St/St_o ratios in Figs. 3 and 4 are given as dependent upon dimensional circulation as well as on nondimensional circulation parameter S. This parameter is used to quantify the influences of vortices with different circulations on injectant and is defined as

$$S = \Gamma / U_c * d$$

As such, this quantity gives a measure of the ratio of vortex strength to injection jet strength (Ligrani et al., 1991). For all cases of the present study, U_c and d are not changed as the blowing ratio m is maintained constant at about 0.5 and injection geometry is not altered. For data in Figs. 3 and 4, S then ranges from 0.0 to 3.17, where values for individual vortices are listed in Tables 2 and 3.

The data in Figs. 3 and 4 are for spanwise vortex positions h and e, respectively. With both spanwise vortex positions, St/St_o magnitudes when S is greater than 0.0 are different from those when S equals 0.0. This means that all vortices examined influence local heat transfer behavior at $Z/d = 0.0$, including the weakest vortices with circulations of 0.014–0.017 m^2/s. The only exception is evident with $x/d = 7.4$. Otherwise, St/St_o values generally increase at a particular x/d as S increases from 0.0 to 3.16. When $x/d = 7.4$, Stanton number ratios are about constant with S because the injectant rather than the vortex is dominating local heat transfer behavior. This is because: (1) The vortices may be pushed off the surface slightly as they pass above injection locations, and (2) the vortices have not had the time to redistribute and thereby deplete injectant near the wall in quantities significant enough to diminish local protection. With additional downstream development, higher St/St_o evidence diminished protection at $Z/d = 0.0$ resulting from the redistribution and rearrangement of injectant away from the wall by vortex secondary flows. As vortex circulation then increases, the protection from film injection disappears more rapidly as the film is convected downstream. This is indicated by St/St_o increases with x/d at particular values of S greater than the increases with x/d when $S = 0.0$.

A comparison of data in Figs. 3 and 4 shows significant St/St_o differences as S and x/d vary. For both cases, the most important St/St_o increases occur as x/d increases from 7.4 to 17.5. In Fig. 3 (position h), St/St_o values continue to increase with x/d. However, in Fig. 4 (position e), St/St_o values increase with x/d up to 33.6. For larger x/d and magnitudes of S greater than about 1.5, additional increases are not apparent. Another important difference between data in Figs. 3 and 4 is evident for S values less than about 1.5. With the exception of St/St_o data for $x/d = 7.4$, St/St_o magnitudes for position h (Fig. 3) are greater than those for position e (Fig. 4). Such differences result because of different interactions between the vortices and injectant as the spanwise position of the vortex is changed with respect to the film injection hole.

Attention is now focused on data in Fig. 3 for vortex position h when $x/d \geq 17.5$. For each value of x/d within this range, two distinct types of St/St_o behavior are evident. The first type is present as S increases from 0.0 to 1.0–1.5. Here, St/St_o distributions increase with nondimensional vortex circulation. The second type is present for larger S values where St/St_o distributions at particular x/d show little variation with S. The former behavior results because injectant is being swept in the negative Z direction by vortex secondary flows. As less and less injectant remains near $Z/d = 0.0$, the protection provided by the injectant diminishes and local heat transfer rates increase. Because $S < 1.0$ vortices are too weak to redistribute the injectant away from the wall, injectant is merely pushed along the wall to accumulate to the sides of vortex downwash regions and beneath vortex cores.

For values of S greater than 1.0–1.5 in Fig. 3, almost all of the injectant is swept away from the wall into vortex upwash regions and above vortex cores by secondary flows (Kaisuwan, 1989). Consequently, the vortices, rather than the injectant, are playing the dominant role in influencing near-wall boundary layer behavior and wall heat transfer variations at $Z/d = 0.0$. At a particular values of x/d with this situation, Fig. 3 shows that St/St_o values show little variation with S. However, if data are viewed as S is held constant, St/St_o values increase steadily for x/d up to 75.6. Such changes result because of the gradient of wall heat transfer that exists beneath vortex cores

between upwash and downwash regions. This gradient moves in the negative spanwise direction as the vortices are convected downstream such that higher St/St_o are located at $Z/d = 0.0$ as x/d increases. These higher St/St_o result because of the proximity of vortex downwash regions to $Z/d = 0.0$, which convect free-stream fluid close to the wall to produce a boundary layer that is locally thinned. The negative spanwise motion of the vortices occurs initially because of interactions with the jet and then, afterward, because of secondary flows beneath vortex cores.

In Fig. 4, St/St_o ratios are presented for $Z/d = 0.0$ when the injectant emerges beneath the vortex downwash at position *e*. As for results in Fig. 3, vortices, rather than the injectant, provide the greatest influence on local heat transfer variations when $S > 1.0$–1.5 and $x/d \geq 17.5$. Over this range of conditions, injectant is swept away from the wall by secondary flows immediately downstream of $x/d = 7.4$. The thermal protection ordinarily provided by the injectant is thus decimated as x/d increases from 7.4 to 17.5, as indicated by significantly higher St/St_o values fo the latter position. With additional downstream development, injectant then accumulates in upwash regions and above vortex cores where injectant heat sink and insulating benefits are useless. Because of significant turbulent diffusion in these portions of the vortices, temperature differences with respect to the free stream decrease rapidly with x/d.

When $S < 1.0$–1.5, St/St_o values in Fig. 4 are generally less than 1.0, at least for $x/d \leq 54.6$. Under these conditions, significant amounts of injectant are present near the wall, which influence local heat transfer rates. Here, as for position *h*, significant interactions between the injectant and the vortices are occurring, and St/St_o variations with S and x/d occur largely because injectant is being redistributed along the wall by vortex secondary flows.

Effects of Vortex Circulation on Distributions of Film Injectant for Position e. Figure 5 quantifies the distortion and rearrangement of injectant by different strength vortices for spanwise vortex position *e*. These data are given for $x/d = 41.9$ when a blowing ratio 0.5 is employed. Data are presented for vortices *r*, *w*, *x*, *y*, *z*, and for no vortex, where vortex properties and figure labels are given in Table 3. The results for position *e* are chosen for presentation because rearrangement of injectant is more severe when the vortex *downwash* passes over the injection hole than for some other vortex spanwise positions (Ligrani et al., 1989a; Ligrani and Williams, 1990).

Measured secondary flow vectors are superimposed on each part of Fig. 5 to illustrate how their magnitudes and distributions relate to the reorganization of injectant by the different vortices. The same scaling for secondary flow vectors is used for all parts of the figure. Procedures to determine injectant distributions were developed by Ligrani et al. (1989a) and later also used by Ligrani and Williams (1990). In these studies and the present one, injectant distributions are qualitatively correlated to mean temperature distributions. To do this, injectant is heated to 50°C without providing any heat to the test plate. Thus, because the injectant is the only source of thermal energy (relative to free-stream flow), higher temperature (relative to free-stream temperature) generally indicate greater amounts of injectant. The temperature field in Fig. 5 is therefore given as $(T_o - T_\infty)$, and as such, shows how injectant accumulates and is rearranged mostly as a result of convective processes from the boundary layer and vortex secondary flows. These temperature variations are different from ones that would exist if the wall were heated because of different distributions of turbulent diffusion of injectant heat. However, in spite of this, a good qualitative indication of injectant distributions is obtained because, compared to convection, turbulent diffusion

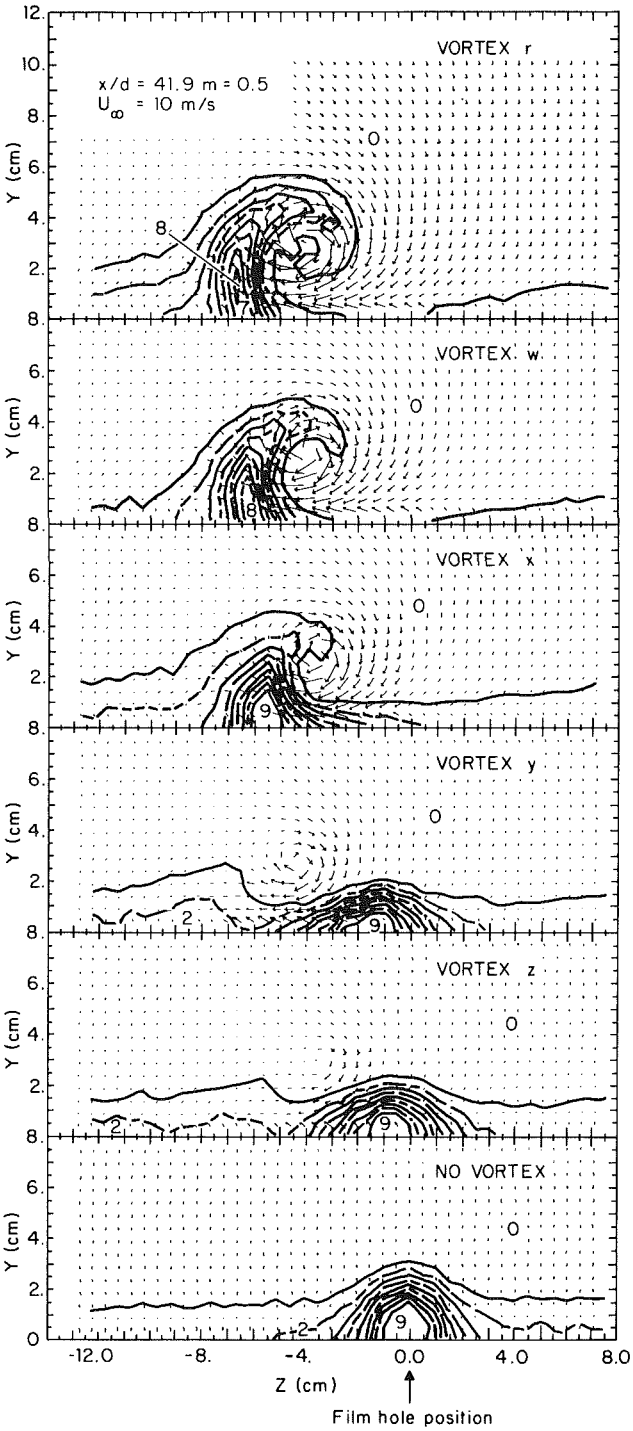

$T_o - T_\infty$ (DEGREES CELCIUS) RANGES

0.	< 0.5	5.	$1.50 - 1.75$
1.	$0.5 - 0.75$	6.	$1.75 - 2.00$
2.	$0.75 - 1.00$	7.	$2.00 - 2.25$
3.	$1.00 - 1.25$	8.	$2.25 - 2.50$
4.	$1.25 - 1.50$	9.	> 2.50

Fig. 5 Mean temperature field $(T_o - T_\infty)$ showing distributions of film injectant with secondary flow vectors. Spanwise vortex position *e*; vortex downwash passes over the centerline injection hole. Labels in Table 3.

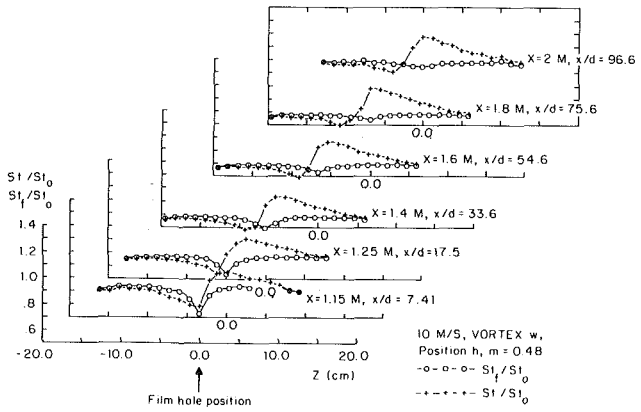

Fig. 6 Streamwise development of Stanton number ratios with film cooling with and without vortex *w*. Spanwise vortex position *h*; vortex upwash passes above injection hole. Vortex characteristics in Table 2.

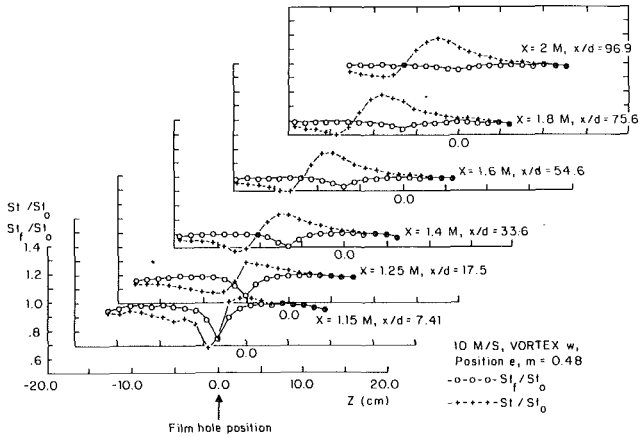

Fig. 7 Streamwise development of Stanton number ratios with film cooling with and without vortex *w*. Spanwise vortex position *e*; vortex downwash passes above injection hole. Vortex characteristics in Table 3.

is of secondary importance in organizing relative positions of injectant concentrations.

The data in Fig. 5 directly correlate with St/St_o distributions in Fig. 4 for $x/d = 33.6$ and 54.6. When no vortex is present, St/St_o values are lowest and results in Fig. 5 show that injectant is centered over $Z/d = 0.0$. As S increases to 0.29 and 1.08 for vortices z and y, respectively, the bulk of the injectant is still located near the wall, but progressively farther away from $Z/d = 0.0$ as circulation increases. The somewhat abrupt increase in St/St_o that occurs as S increases from 1.08 to 1.88 (vortex x) the corresponds to a drastic change in the injectant distributions. With vortex x, injectant is no longer in the proximity of the downwash, but is swept up and away from the wall into the vortex upwash region. As S increases further to 2.55 and 3.17 for vortices w and r, this trend continues as significantly greater amounts of injectant collect into upwash regions and above vortex cores. The disturbance is greatest when S equals 3.17 where secondary flows are so intense that portions of injectant are swept around the entire circumference of the vortex core. Corresponding St/St_o values for $x/d \geq 17.5$ and $S > 1.0$–1.5 in Fig. 4 are then nearly invariant with S because little injectant is present near the wall, and because the same portion of the vortex downwash remains near $Z/d = 0.0$ as the vortices are convected downstream.

Streamwise Development of Local Stanton Number Ratios and Film Injectant Distributions, Vortex W. Figures 6 and 7 are presented to illustrate the streamwise development of St/St_o and St_f/St_o for one particular vortex strength. In this case, results are given for vortex w ($S = 2.38$–2.55) for x/d ranging from 7.41 to 96.9. The two ratios are plotted together on each set of graphs so that St/St_o values can be compared to St_f/St_o ratios to indicate magnitudes of local perturbations provided to film-cooled boundary layers by the vortices.

Ratios for position h are given in Fig. 6 and for position e in Fig. 7. In both cases, St/St_o are generally higher than St_f/St_o near vortex downwash regions at larger Z, and St/St_o are generally lower than St_f/St_o at smaller Z in the vicinity of vortex upwash regions. Between these two regions, St/St_o gradients exist along the length of the test surface because of the streamwise persistence and coherence of the vortices. Thus, regardless of which of the two positions of the vortices relative to the injection location is considered, the same overall qualitative trends are present for $x/d \geq 33.6$.

With the upwash passing above the injection hole, results at $x/d = 7.41$ in Fig. 6 provide evidence that some of the film is lifted slightly off the surface since the St/St_o local minimum is slightly higher than the St_f/St_o local minimum from the film only. With the downwash passing above the hole, results in Fig. 7 at $x/d = 7.41$ show a St/St_o minimum that is lower than the St_f/St_o minimum. This evidences an increase in the protection provided by the injectant as it is pushed toward the surface by downwash secondary flows just downstream of the injection location. This is further illustrated by the $x/d = 5.2$ results in Fig. 8, which shows the streamwise development of injectant distributions for vortex w at spanwise position e.

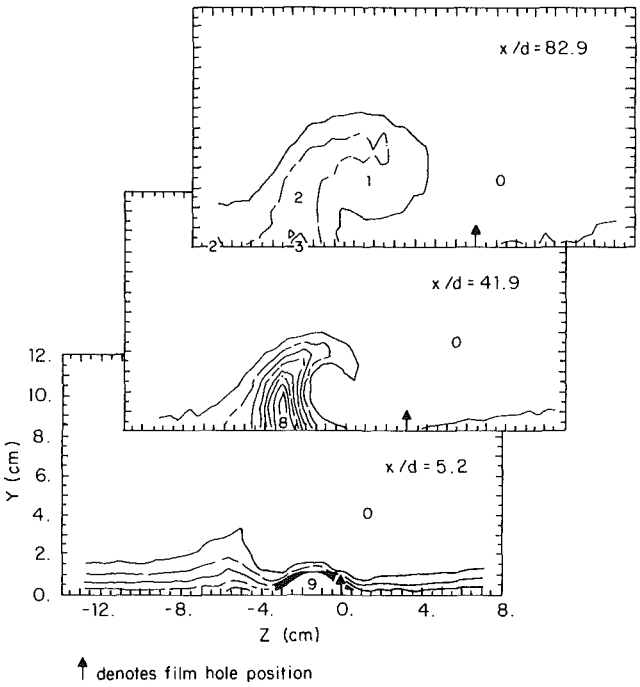

Fig. 8 Streamwise development of mean temperature field ($T_o - T_\infty$) showing distributions of film injectant for vortex *w*. Spanwise vortex position *e*; vortex downwash passes above injection hole. Vortex characteristics in Table 3. Same contour levels as Fig. 5.

When $x/d \geq 33.6$, little evidence of the injectant is present except for St/St_o values beneath upwash regions, which may be lowered slightly because of accumulation of injectant. Results in Fig. 8 for vortex position e correlate this conclusion since results for x/d equal to 41.9 and 82.9 show accumulation of injectant at the same locations as the lowered St/St_o.

Surveys of Stanton Number Ratios With Film Injection as Dependent Upon Nondimensional Vortex Circulation Parameter S. Figures 9 and 10 present surveys to illustrate the influences of the different strength vortices on the streamwise development of St/St_o and St_f/St_o. Symbols are listed in Tables

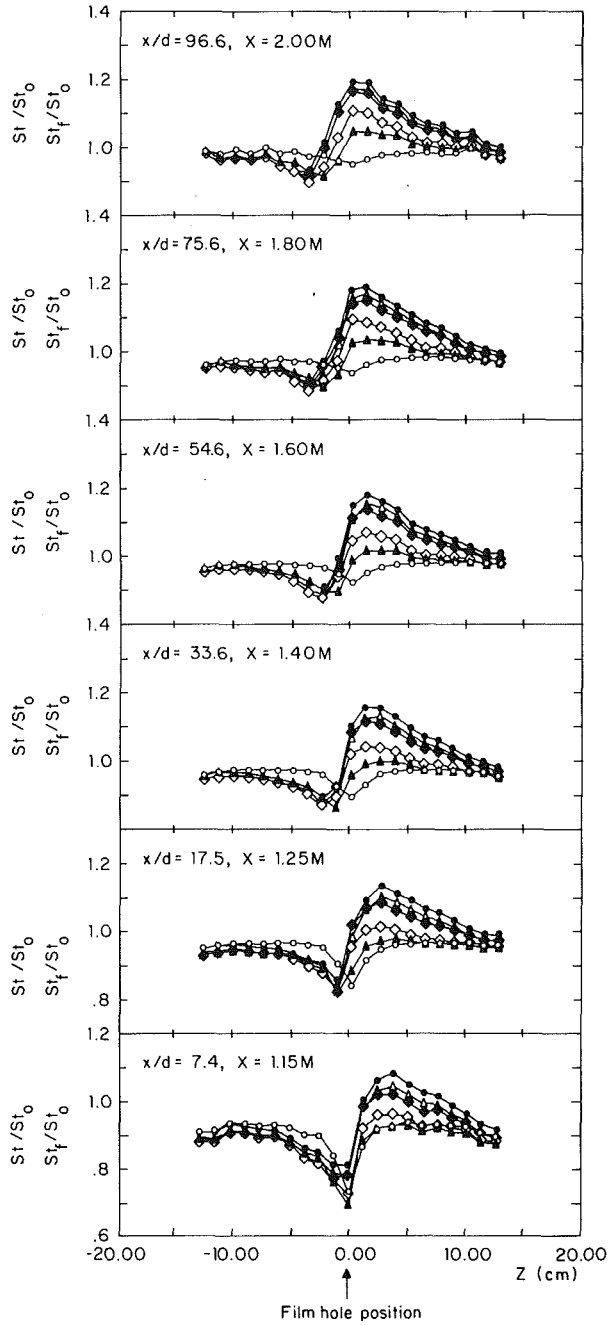

Fig. 9 Stanton number ratios with film cooling for different vortex strengths. Spanwise vortex position *h*; vortex upwash passes above injection hole. Free-stream velocity = 10 m/s, *m* = 0.48. Symbols in Table 2.

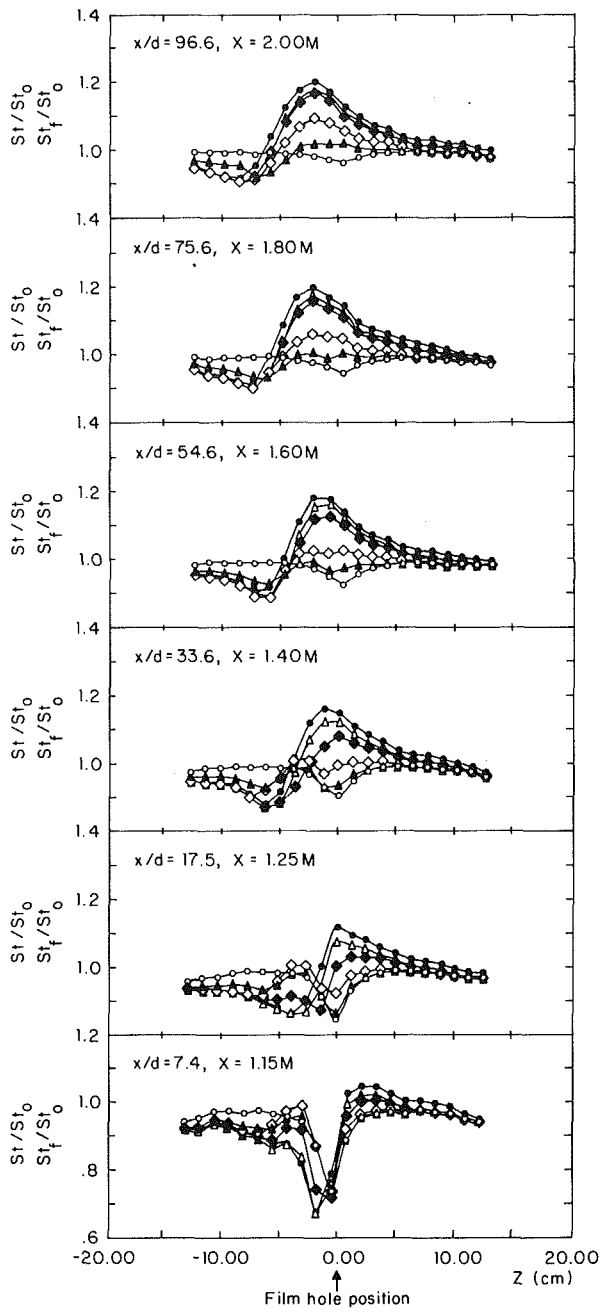

Fig. 10 Stanton number ratios with film cooling for different vortex strengths. Spanwise vortex position *e*; vortex downwash passes above injection hole. Free-stream velocity = 10 m/s, *m* = 0.48. Symbols in Table 3.

2 and 3, respectively. Results in Fig. 9 were obtained for vortex spanwise position *h* and those in Fig. 10 were obtained using spanwise position *e*. Each figure has six separate parts for x/d of 7.4, 17.5, 33.6, 54.6, 75.6, and 96.6. In each part, St/St_o data are given for vortices *r*, *w*, *x*, *y*, and *z*, along with St_f/St_o data for no vortex. Comparison of these data thus shows how St/St_o change with vortex strength relative to St_f/St_o.

Results for $x/d = 7.4$ in Fig. 9 evidence significant and complicated interactions between the vortices and the injectant. Near $Z/d = 0.0$, where the injectant nominally provides protection, St/St_o values are either about the same or slightly higher than St_f/St_o depending on whether the injectant is relatively undisturbed by the vortices or redistributed away from the wall by upwash secondary flows. The former situation results when $S \leq 0.82$ for vortices *y* and *z*. The latter occurs with stronger vortices *r*, *w*, and *x*. At *Z* larger than 0.0, local St/St_o beneath downwash regions generally increase with *S*.

Results for $x/d = 17.5$ in Fig. 9 show the same general qualitative trends as when $x/d = 7.4$, except for St/St_o minima near $Z = 0.0$, which show almost no variation with *S*. The positions of these minima are shifted about 1 cm away from the nominal location of injectant at this streamwise location because of vortex secondary flows near the wall.

St/St_o distributions in Fig. 10 for vortex position *e* are significantly different from those in Fig. 9. Such behavior further illustrates the importance of the spanwise positions of vortices as they pass above film injection locations (Ligrani and Williams, 1990). With position *h* (Fig. 9), injectant is abruptly swept away from the wall by vortex upwash regions as x/d increases from 7.4 to 33.6 when $S > 1.0$–1.5. With spanwise

position e (Fig. 10) and the same S, the film is initially swept in the spanwise direction and then beneath the vortex core, and redistribution of injectant is more vigorous than with position h. Because injectant is then spread over a larger surface area with position e, interactions with the vortices are more complex.

At $x/d = 7.4$, results in Fig. 10 for position e, the most important changes due to the vortices occur near $Z/d = 0.0$. When $S \geq 1.88$, minimum St/St_o are lower in magnitude and shifted about 2 cm with respect to minimum St_f/St_o. With weaker vortices, St/St_o distributions at $Z/d = 0.0$ as well as for larger Z/d closely follow distributions resulting from the presence of the injectant only. At Z locations ranging from -2.0 cm to -7.0 cm, contorted St/St_o distributions evidence complicated interactions resulting in St/St_o values that generally decrease with increasing S.

St/St_o values beneath downwash regions for $x/d = 17.5$ and $x/d = 33.6$ are significantly greater than those for $x/d = 7.4$ in Fig. 10. This is because local heat transfer variations are strongly affected by behavior in the near-wall portions of boundary layer regions where injectant initially accumulates. Some downstream development is then required before enough injectant is disturbed and swept away from the wall by vortex secondary flows to cause high St/St_o. Downwash regions for $x/d = 17.5$ and $x/d = 33.6$ are located at Z values greater than -1.0 to -3.0 cm. Here, heat transfer rates generally increase with vortex strength. At locations beneath upwash regions located at Z ranging from -1.0 cm to -10.0 cm, St/St_o distributions for $S \leq 1.08$ show different behavior than when $S \geq 1.88$. Lower St/St_o are present with the stronger vortices because of injectant accumulation in upwash regions. Less injectant collects in this area with the weaker vortices since they do not have the vitality to rearrange injectant from initial positions beneath vortex downwash regions.

St/St_o data for $x/d \geq 54.6$ for position e (Fig. 10) and for $x/d \geq 33.6$ for position h (Fig. 9) show qualitative trends that are similar to each other. In both cases, St/St_o values generally increase with S in downwash regions. In upwash regions, St/St_o data are noticeably lower than St_f/St_o data on the left-hand portions of Figs. 9 and 10. Here, different data sets follow the same quantitative magnitudes regardless of the value of S.

Summary and Conclusions

Results are presented that illustrate the effect of single embedded longitudinal vortices on heat transfer and injectant downstream of a single film-cooling hole in a turbulent boundary layer. Attention is focused on the changes resulting as circulation magnitudes of the vortices are varied from 0.0 to 0.15 m^2/s. The ratio of vortex core diameter to hole diameter is about 1.5–1.6, and the blowing ratio is approximately 0.5. The film-cooling hole is oriented 30 deg with respect to the test surface. Stanton numbers are measured on a constant heat flux surface with a nondimensional temperature parameter θ of about 1.5. Two different situations are studied: one where the injection hole is beneath the vortex downwash (position e), and one where the injection hole is beneath the vortex upwash (position h). For both cases, vortices pass well within 2.9 vortex core diameters of the centerline of the injection hole.

The most important general conclusion is that the magnitude of parameter S determines whether perturbations to local heat transfer and injectant distributions are significant, where S is defined as the ratio of vortex circulation to injection hole diameter times mean injection velocity. S is varied from 0 to 3.17. When S is greater than 1.0–1.5 with $2c/d = 1.5$–1.6 and $m = 0.5$, injectant is swept into the vortex upwash and above the vortex core by secondary flows. Enough injectant is then depleted near the wall beneath the core and downwash to significantly reduce the protection nominally provided by film cooling, and St/St_o data show evidence of injectant beneath the vortex core and downwash near the wall for x/d only up to 17.5 for position h and 33.6 for position e. For larger x/d with such situations, the vortices cause local Stanton numbers in the film-cooled boundary layers to be augmented by as much as 23 percent relative to film-cooled layers with no vortices. Loss of film protection corresponds to St/St_o values greater than 1.0.

When S is less than 1.0–1.5, some injectant may remain near the wall beneath vortex core and downwash regions where it continues to provide some thermal protection. With the weakest vortices studied ($S = 0.29$–0.35), evidence of injectant is evident for x/d values as large as 75.6.

In some cases, the protection provided by film cooling is augmented because of the vortex when secondary flows cause extra injectant to accumulate in one area. This occurs over the entire range of x/d studied, especially for stronger vortices with $S > 1.0$–1.5. It is particularly noticeable near upwash regions, especially for position e, when the vortex downwash passes over the injection hole location. Here, St/St_o may be reduced as much as 14 percent compared to values when no vortex is present.

Acknowledgments

This study was supported, in part, by the Aero-Propulsion Laboratory of Wright Patterson Air Force Base, MIPR Number FY 1455-88-N0608. Dr. R. B. Rivir was program monitor. Some of the facilities used were purchased using funds from the Naval Postgraduate School Foundation Research Program.

References

Blair, M. F., 1975, "An Experimental Study of Heat Transfer and Film Cooling on Large-Scale Turbine Endwalls," ASME *Journal of Heat Transfer*, Vol. 96, pp. 524–529.

Craig, D. W., 1989, "Effects of Vortex Circulation on Injectant From a Single Film-Cooling Hole and a Row of Film-Cooling Holes in a Turbulent Boundary Layer, Part 1: Injection Beneath Vortex Downwash," M. S. Thesis, Department of Mechanical Engineering, Naval Postgraduate School, Monterey, CA.

Goldstein, R. J., and Chen, H. P., 1985, "Film Cooling on a Gas Turbine Blade Near the Endwall," ASME *Journal of Engineering for Gas Turbines and Power*, Vol. 107, pp. 117–122.

Goldstein, R. J., and Chen, H. P., 1987, "Film Cooling of a Turbine Blade With Injection Through Two Rows of Holes in the Near-Endwall Region," ASME JOURNAL OF TURBOMACHINERY, Vol. 109, pp. 588–593.

Kaisuwan, P., 1989, "Effect of Vortex Circulation on Injectant From a Single Film-Cooling Hole and a Row of Film Cooling Holes in a Turbulent Boundary Layer, Part 2: Injection Beneath Vortex Upwash," M. S. Thesis, Department of Mechanical Engineering, Naval Postgraduate School, Monterey, CA.

Kays, W. M., and Crawford, M. E., 1980, *Convective Heat and Mass Transfer*, 2nd ed., McGraw-Hill, New York.

Kline, S. J., and McClintock, F. A., 1953, "Describing Uncertainties in Single-Sample Experiments," *Mechanical Engineering*, Vol. 75, pp. 3–8.

Ligrani, P. M., Ortiz, A., Joseph, S. L., and Evans, D. L., 1989a, "Effects of Embedded Vortices on Film-Cooled Turbulent Boundary Layers," ASME JOURNAL OF TURBOMACHINERY, Vol. 111, pp. 71–77.

Ligrani, P. M., Singer, B. A., and Baun, L. R., 1989b, "Spatial Resolution and Downwash Velocity Corrections for Multiple-Hole Pressure Probes in Complex Flows," *Experiments in Fluids*, Vol. 7, No. 6, pp. 424–426.

Ligrani, P. M., Singer, B. A., and Baun, L. R., 1989c, "Miniature Five-Hole Pressure Probe for Measurement of Mean Velocity Components in Low Speed Flows," *Journal of Physics E—Scientific Instruments*, Vol. 22, No. 10, pp. 868–876.

Ligrani, P. M., and Williams, W. W. 1990, "Effects of an Embedded Vortex on Injectant From a Single Film-Cooling Hole in a Turbulent Boundary Layer," ASME JOURNAL OF TURBOMACHINERY, Vol. 112, pp. 428–436.

Ligrani, P. M., Subramanian, C. S., Craig, D. W., and Kaisuwan, P., 1991, "Effects of Vortices With Different Circulations on Heat Transfer and Injectant Downstream of a Row of Film-Cooling Holes in a Turbulent Boundary Layer," ASME *Journal of Heat Transfer*, Vol. 113, pp. 79–90.

Moffat, R. J., 1982, "Contributions to the Theory of Single-Sample Uncertainty Analysis," ASME *Journal of Fluids Engineering*, Vol. 104, pp. 250–260.

Ortiz, A., 1987, "The Thermal Behavior of Film Cooled Turbulent Boundary Layers as Affected by Longitudinal Vortices," M. E. Thesis, Department of Mechanical Engineering, Naval Postgraduate School, Monterey, CA.

Film-Cooling Effectiveness Downstream of a Single Row of Holes With Variable Density Ratio

A. K. Sinha

D. G. Bogard

M. E. Crawford

Mechanical Engineering Department,
University of Texas at Austin,
Austin, TX 78712

Film-cooling effectiveness was studied using a row of inclined holes that injected cryogenically cooled air across a flat, adiabatic test plate. The density ratio of the coolant to mainstream varied from 1.2 to 2.0. Surface temperatures were measured using a unique surface thermocouple arrangement free of conduction errors. Temperatures were obtained along the jet centerline and across a number of lateral locations. By independently varying density ratio and blowing rate, scaling of adiabatic effectiveness with mass flux ratio, velocity ratio, and momentum ratio was determined. Depending on the momentum flux ratio, the jet either remains attached to the surface, detaches and then reattaches, or is fully detached. For attached jets, the centerline effectiveness scaled with the mass flux ratio. However, for detached-reattached jets, a consistent scaling was not found although the general distribution of the centerline effectiveness scaled with momentum flux ratio. Laterally averaged effectiveness was found to be dependent on density ratio and momentum flux ratio. Decreases in density ratio and increases in momentum flux ratio were found to reduce the spreading of the film cooling jet significantly and thereby reduce laterally averaged effectiveness.

Introduction

High-performance propulsion gas turbine engines require cooling of the turbine airfoil (blade or vane) to protect the airfoil from thermal stress fields created by exposure to hot combustion gases. In the blade (or vane) cooling process, compressor bleed air is introduced into the hollow core of each blade and is channeled and then dumped through the blade surface via rows of holes located in the vicinity of the leading edge of the blade and at other high thermally loaded locations along the suction and pressure surfaces. The heat transfer process can be locally analyzed as a heat exchanger configuration, requiring information about both the internal and external convection processes. This research addresses the external convection process, called film cooling, whereby the coolant exiting the rows of holes is designed to create an enthalpy-absorbing film in the vicinity downstream of injection.

Studies of film cooling have, for the most part, focused on the geometric and fluid mechanical variables that control heat transfer as the hot combustion gases form a boundary-layer-like flow over the surface and as the wall shear layer interacts with the cooling jets emerging at various locations along the surface. Parameters that govern the flow field of the jets-in-crossflow interaction and its associated surface heat transfer are both geometric: hole shape, angle, spacing, and pattern; and fluid mechanical: coolant-to-crossflow ratios of density (*D.R.*), velocity (*V.R.*), mass flux (*M*), and momentum flux (*I*). These ratios are defined as

$$D.R. = \frac{\rho_j}{\rho_\infty} \quad V.R. = \frac{V_j}{V_\infty} \quad M = \frac{\rho_j V_j}{\rho_\infty V_\infty} \quad I = \frac{\rho_j V_j^2}{\rho_\infty V_\infty^2} \tag{1}$$

where the subscripts ∞ and j refer to the fluid states of the crossflow in the far field and of the injectant at the location where it emerges into the crossflow.

In film-cooling applications the wall heat flux, q'', is usually defined using an analogy to convective heat transfer with high-speed flows, whereby an adiabatic wall temperature replaces the far-field temperature of the crossflow,

$$q'' = h(T_w - T_{aw}) \tag{2}$$

In equation (2) h is the convective heat transfer coefficient in the presence of film cooling; T_w is the airfoil wall temperature; and T_{aw} is the adiabatic wall temperature. The heat transfer coefficient is often assumed to be that which would exist for the same boundary layer hydrodynamics but no injection (dry wall conditions), although it will deviate from the no-injection value in the near-hole region. This leaves a majority of the film-cooling research, to date, focused on the adiabatic wall temperature, and how it depends on geometric and fluid mechanical parameters.

The adiabatic wall temperature as a function of distance downstream of injection must be experimentally determined for a given film-cooling geometry and crossflow hydrodynamics. The data are generally presented nondimensionally in terms of film effectiveness, defined as

$$\eta = \frac{(T_{aw} - T_\infty)}{(T_j - T_\infty)} \tag{3}$$

Thus, the effectiveness parameter represents the three temperature potentials associated with a film-cooling process.

Contributed by the International Gas Turbine Institute and presented at the 35th International Gas Turbine and Aeroengine Congress and Exposition, Brussels, Belgium, June 11–14, 1990. Manuscript received by the International Gas Turbine Institute January 11, 1990. Paper No. 90-GT-43.

The literature abounds with adiabatic film-cooling effectiveness data under conditions that represent varying degrees of compromise with those found in a gas turbine engine. Up through the late 1960s most of the literature reports effectiveness distributions associated with slot injection, porous injection, and from a single hole, mostly carried out at a density ratio near 1.0. The study reported herein focuses on the effects of density ratio on the adiabatic film cooling effectiveness distribution. To date, the primary open-literature studies of density ratio effects have been carried out primarily at the University of Minnesota in the U.S.A. and at the University of Nottingham in the U.K.

The first in a series of research reports from the University of Minnesota began with Goldstein et al. (1968) reporting the effectiveness results from a circular hole. This was followed by a study of Goldstein et al. (1970) that contrasted the single hole results with that from a row of holes. A study of the accompanying heat transfer coefficient distributions for the Minnesota effectiveness data was reported by Eriksen and Goldstein (1974). Pedersen et al. (1977) presented the first open-literature study of the effects of density ratio on film cooling. Their primary test surface geometry utilized holes angled 35 deg from the surface, directed in the downstream direction, with three-diameter hole spacing, but with holes half the diameter of the previous Minnesota single-row studies. Also, unlike the previous Minnesota studies, their data were acquired using the mass transfer technique. Predictably, this touched off significant questioning of the applicability of the heat/mass transfer analogy, mostly in regard to whether the molecular and/or turbulent Lewis number needed to be at or near unity, and subsequent studies in various laboratories have since substantiated the validity of the mass transfer technique. The Pedersen study was an extensive investigation into the effects of *V.R.*, *M*, and *I* on effectiveness over a range of *D.R.* Their data showed that beyond about 10 hole diameters, the centerline effectiveness maximizes for a *V.R.* of about 0.5–0.6, over a *D.R.* range from 0.8 to 4.0. Goldstein et al. (1974) present a limited amount of effectiveness data with *D.R.* variation to show that higher film-cooling effectiveness can be achieved at larger blowing ratio when the *D.R.* is greater than unity. Their geometry was a surface with 35 deg holes spaced three diameters apart. Momentum ratio was varied from 0.02 to 8.0. Ito et al. (1978) report the effect of curvature on effectiveness with *D.R.* varied from 0.75 to 2.0, with a surface geometry of 35 deg holes spaced three diameters apart, and with *M* varied from 0.2 to 3.0.

Studies at the University of Nottingham have been carried out focusing primarily on a *D.R.* of 2.0, using mass transfer studies to acquire effectiveness data. Foster and Lampard (1980) acquired both effectiveness and concentration profile data, and primarily studied the influence of injection angle (35, 55, and 90 deg) and row spacing (1.25–3.0 diameters) on effectiveness for a range of *M* from 0.5 to 2.5. Their data, where appropriate, were checked and favorably compared with Pedersen et al. (1977). Data for the effect of a second row of holes, with spacing downstream of 10 to 40 diameters, and with both 35 and 90 deg injection were presented by Afejuku et al. (1980). This was followed by a companion two-row study by the same three authors (Afejuku et al., 1983). Experiments for determining the effect of density ratio on heat transfer coefficient associated with film cooling were reported by Ammari et al. (1989). The *D.R.* was varied from baseline at 1.0 to 1.5 with *M* varied from 0.5 to 2.0 and injection angles of 35 and 90 deg.

Bergeles et al. (1977) at the Imperial College, London, report data at a *D.R.* of 0.85 for a row of holes at injection angle 35 deg and three-diameter spacing, for a range of *M* from 0.2 to 1.0 using a mass transfer technique. The research was a part of a wider study that included both single-hole injection and single-row injection, with the primary emphasis on surface pressure profiles and effectiveness in the near-hole region downstream of injection.

A series of studies have been recently carried out at Oxford University to study the effect of density ratio on film cooling. Forth et al. (1985) carried out a study of *D.R.* effects on film cooling from a single 30 deg row of holes with three-diameter hole spacing. This research was similar in content to that reported by Forth and Jones (1988), both of which present studies of the scaling parameters for the effect of density ratio on heat transfer. The latter study included three injection geometries, a row of 30 deg slots, a row of 30 deg holes, and a double row of 30 deg holes. Both studies show that there exist two regimes of injection: weak injection describing film-cooling flow that emerges and stays attached to the surface; and strong injection describing film-cooling flows with high enough momentum to lift from the surface and penetrate into the mainstream. The momentum flux parameter *I* was found to scale the weak injection data, whereas *V.R.* scaled the strong injection data. Teekaram et al. (1989) studied the effect of *D.R.* on film cooling heat transfer using two methods to achieve the density difference between the injectant and mainstream. The first was by changing the temperature ratio of the injectant to crossflow fluid, and the second was by using foreign gas injection. For both cases, the wall boundary condition was isothermal. For the experiments density ratios of 1.25 and 1.67 were used, and *M* was varied from 0.1 to 1.2, with injection from a row of 30 deg holes spaced 2.5 diameters apart. The results of their isothermal effectiveness measurements were similar to those of their previous investigations.

In the present study, measurements of surface temperature have been used to determine effectiveness distributions on the surface for density ratio range from 1.2 to 2.0. Conduction errors in surface temperature measurements have been eliminated by using a unique experimental design. The mass flux parameter, *M*, for the experiments has been varied from 0.25 to 1.0. The density ratio variation, in conjunction with vari-

Nomenclature

D = diameter of injection hole
$D.R.$ = jet to mainstream density ratio = ρ_j/ρ_∞
h = heat transfer coefficient
I = jet-to-mainstream momentum flux ratio = $\rho_j V_j^2/\rho_\infty V_\infty^2$
L = length of injection tube
M = mass flux ratio or blowing rate = $\rho_j V_j/\rho_\infty V_\infty$
q'' = wall heat flux
T_w = wall temperature
T_{aw} = adiabatic wall temperature
T_j = temperature of injected fluid
V_j = average jet velocity at the exit based on volume flow rate and cross-sectional area of the hole
V_∞ = mainstream velocity
$V.R.$ = jet to mainstream velocity ratio = V_j/V_∞
X = downstream distance from trailing edge of hole
Y = vertical distance measured from the test surface
Z = lateral distance measured from the axis of the hole
η = local adiabatic film cooling effectiveness
η_c = centerline adiabatic film cooling effectiveness
$\bar{\eta}$ = laterally averaged adiabatic film cooling effectiveness
ρ_j = density of secondary fluid at exit of injection hole
ρ_∞ = density of mainstream fluid

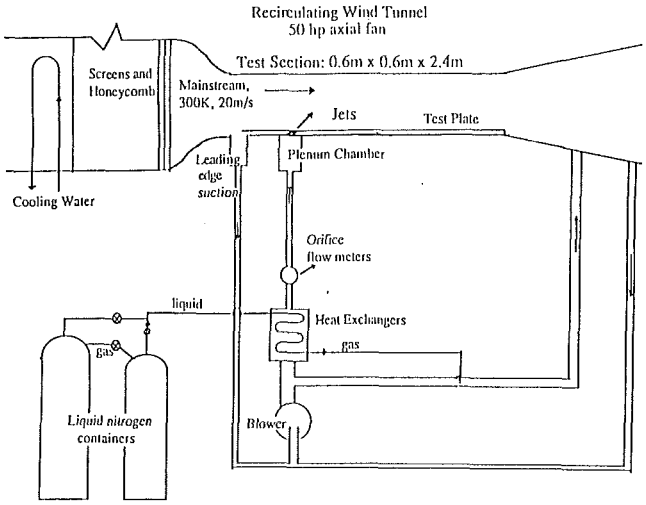

Fig. 1 Schematic of film-cooling test facility

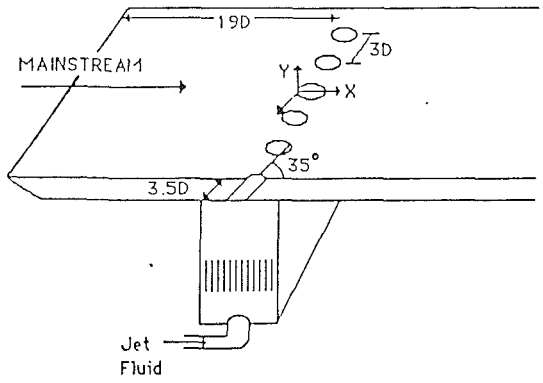

Fig. 2(*a*) Film-cooling test geometry and coordinate system

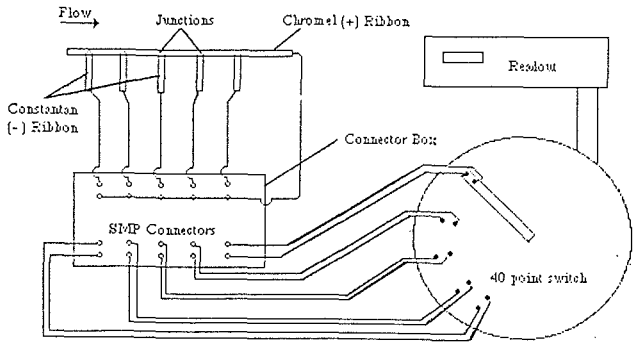

Fig. 2(*b*) Electrical schematic of thermocouple instrumentation with accessories

ation of M, has yielded a significant momentum flux range for the tests, thereby allowing examination of the effects on effectiveness of velocity ratio, mass flux ratio, and momentum flux ratio.

Experimental Facility and Instrumentation

Experiments were conducted in the closed-loop wind tunnel facility shown schematically in Fig. 1. A comprehensive description of this facility was given by Pietrzyk et al. (1990). The secondary flow loop in this facility uses cryogenic cooling of the injectant to obtain different density ratios between the jets and the mainstream. The test plate was modified for this study to reduce conduction problems associated with adiabatic wall temperature measurements.

Figure 2(*a*) shows the geometry of the new test plate. A new test plate was installed in the facility to reduce conduction errors. The test plate was constructed from extruded polystyrene foam (Styrofoam), which has a thermal conductivity ($k = 0.027$ W/m·K) significantly lower than the previous test plate. An analysis of conduction errors using a three-dimensional conduction heat transfer code indicated negligible conduction errors for the new test plate. In the new test plate the jets issued from a row of 7 holes, each 1.27 cm in diameter and spaced 3 diameters apart laterally. Each hole was inclined at 35 deg from the surface and the injectant passage had an L/D of 1.75.

The test plate was instrumented with thin ribbon thermocouples for measurement of adiabatic surface temperatures. The large surface area of the ribbon relative to its very small cross-sectional area essentially eliminates thermocouple conduction errors. The chromel and constantan ribbons were 38 μm thick and 1.5 mm wide. The diameter of the junctions was approximately 0.4 mm. The ribbons were glued to the surface with epoxy. Junctions for the thermocouples were made by spot welding negative (constantan) ribbons to a single positive (chromel) ribbon. An electrical schematic of the configuration is shown in Fig. 2(*b*).

Thermocouple junctions were positioned on the test surface in order to obtain both the centerline and lateral effectivenesses. There were 12 junctions along the centerline between 1 and 60 diameters from the trailing edge of the hole. At five different streamwise locations (1, 3, 6, 10, and 15 diameters) five junctions spanned the lateral direction from the axis to the dividing line between the holes.

Operating Conditions. The streamwise development of the boundary layer on the plate was documented by Pietrzyk et al. (1990). For all experiments the free-stream velocity was 20 m/s ±1 percent and the free-stream turbulence was about 0.2 percent. The variation in the free-stream velocity was found to be less than ±0.5 percent in both spanwise and vertical directions, which was less than the precision uncertainty of the mean velocity (±1 percent). The total mass flow rate was measured using a calibrated, sharp-edged orifice plate in the secondary flow loop. Velocity measurements at the exit of each hole verified equal distribution of the flow through all holes. The total mass flow rate of the jets was determined with a precision of ±0.7 percent. The mass flux ratio was held constant within ±4 percent during experiments. Jet temperatures were varied from 150 K for $D.R.$ = 2.0 to 250 K for $D.R.$ = 1.2 while the mainstream was held at 300 K. Maximum variation of density ratio during the runs was ±3 percent. The uncertainty on density ratio was lower (±0.5 percent) as the temperatures were measured to within an accuracy of ±0.1 K.

Film-cooling parameters were varied systematically over a range of density ratios. Blowing rates were selected so that each of the parameters, M, $V.R.$, and I would be held constant as $D.R.$ varied. A list of the experimental conditions is presented in Table 1.

Results and Discussion

Centerline Effectiveness. Present measurements of centerline effectiveness, η_c, are compared with those obtained by Pedersen et al. (1979) in Fig. 3. The data of Pedersen et al. were selected for comparison since the foreign gas technique they used to deduce η_c is free of conduction errors. At low values of I, the present results correspond well with results of Pedersen et al. As the blowing rate (and consequently I) increases, η_c measured in the present study decreases at a greater rate than that of Pedersen et al. Data to be discussed later in this section show that at larger momentum flux ratios the jet begins to detach from the surface and this detachment causes

Table 1 Range of experimental parameters

Case No.	Density Ratio	Mass Flux Ratio	Velocity Ratio	Momentum Flux Ratio
1	1.2	0.25	0.208	0.05
2	1.2	0.50	0.42	0.208
3	1.2	0.60	0.50	0.30
4	1.2	0.78	0.65	0.50
5	1.2	1.00	0.83	0.83
6	1.6	0.57	0.35	0.20
7	1.6	0.80	0.50	0.40
8	1.6	0.90	0.56	0.50
9	1.6	1.00	0.625	0.625
10	2.0	0.50	0.25	0.125
11	2.0	0.80	0.40	0.32
12	2.0	1.00	0.50	0.50

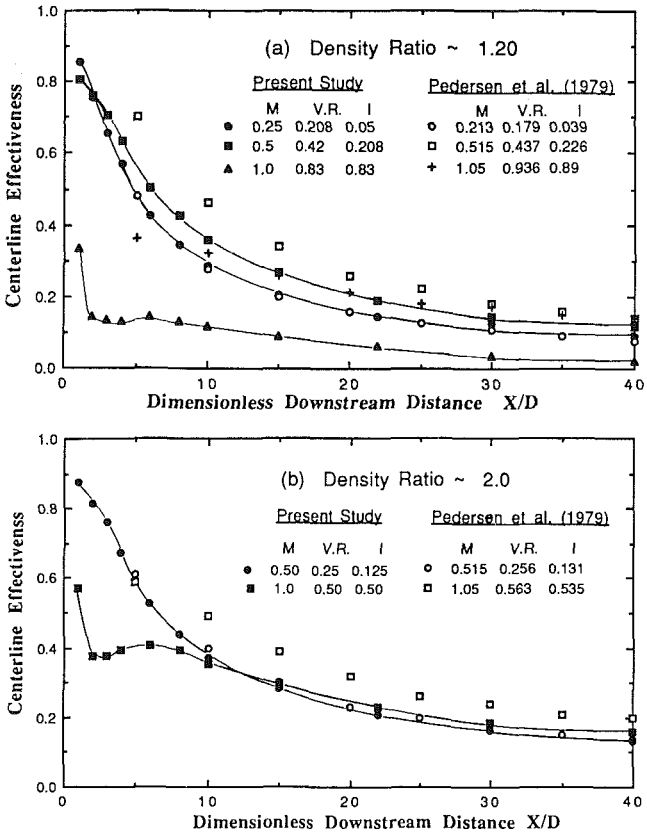

Fig. 3 Comparison with mass-transfer analogy data by Pedersen et al. (1979) for (*a*) low density ratio and (*b*) high density ratio

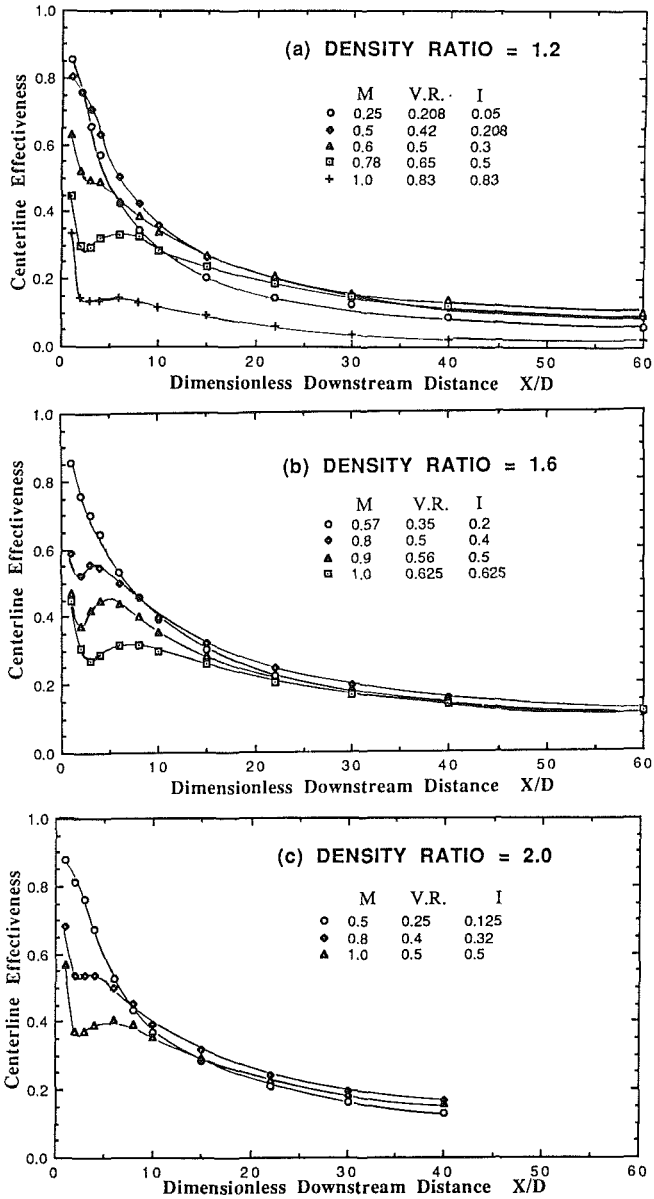

Fig. 4 Centerline effectiveness distributions over a range of film cooling parameters at constant density ratios, (*a*) *D.R.* = 1.2, (*b*) *D.R.* = 1.6, and (*c*) *D.R.* = 2.0

a sudden drop in η_c. Evidently detachment occurs at a smaller momentum flux ratio in the present study. This earlier detachment may be attributed to the short holes ($L/D = 1.75$) used in this study compared to long holes ($L/D \sim 40$) used by Pedersen et al. For a small L/D the effective injection angle of the jet would be expected to be somewhat greater, which would results in liftoff of the jets at a smaller value of momentum flux ratio.

The effect of increasing the mass flux ratio, and consequently the velocity and momentum flux ratios, at the same density ratio can be seen from Figs. 4(*a*) (*D.R.* = 1.2), 4(*b*) (*D.R.* = 1.6), and 4(*c*) (*D.R.* = 2.0). A consistent trend is evident in each of these figures with a greater rate of decrease in η_c immediately downstream of the hole as the blowing ratio increases. For higher blowing ratios, η_c increases again to a peak value between $X/D = 3$ and $X/D = 6$. This increase in η_c suggests that the jets have detached and then reattached to the wall. These results indicate that the flow pattern following injection can assume any one of three different forms: It can remain attached, it can detach and then reattach, or it can lift off completely.

Near the hole, the highest values of η_c were obtained for cases when the jets remain fully attached; this occurs when the momentum flux ratio is very low. However, due to the relatively low mass flux, and consequently low energy flux, the effectiveness falls off steeply for these cases. Comparing the η_c distribution for $M = 0.25$ and $M = 0.5$ at *D.R.* = 1.2 in Fig. 4(*a*), the increase in the mass flux causes the effectiveness to fall off at a slower rate for attached jets. With increasing momentum flux ratio the jet detaches from the surface. Figure 4 shows that detachment clearly occurs for $I > 0.3$. However, the detached jet reattaches within $X/D = 6$ causing increased η_c at this point. Moreover, the reattachment location occurs

farther downstream with increase in momentum flux ratio. After reattachment η_c decreases downstream at a slower rate than for jets that remain attached. The slower decrease in η_c is probably due to the higher mass flux ratio for the detached-reattached jets.

Increasing the momentum flux ratio beyond $I = 0.7$ results in complete detachment of the jet, which results in low values of η_c for the entire downstream region. A sharp decrease in η_c immediately downstream of the hole exit was observed for these cases too. Although the energy flux is very high for these jets, effective cooling of the surface is minimized as the cold jet does not come in contact with the surface.

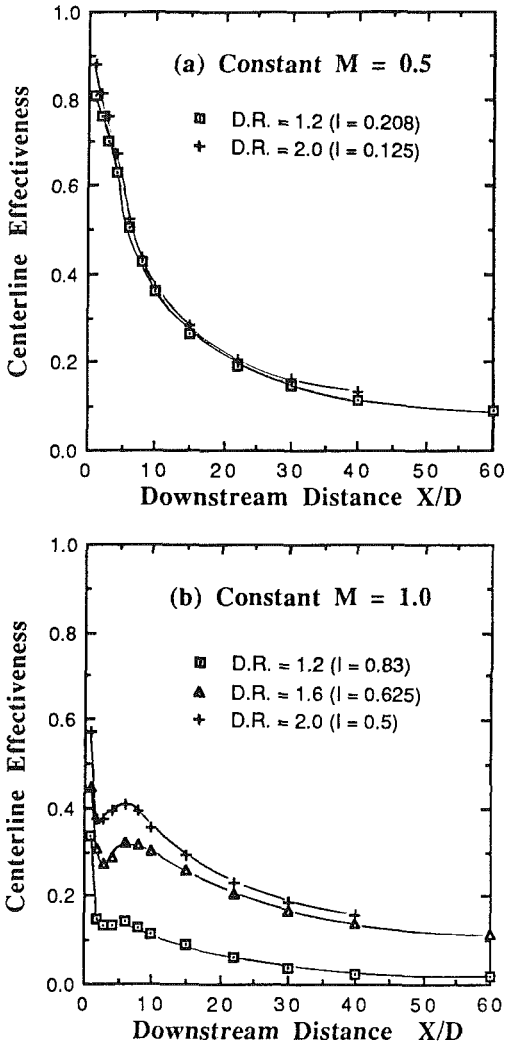

Fig. 5 Effect of density ratio at constant mass-flux ratios: (*a*) $M = 0.5$ and (*b*) $M = 1.0$

To establish that the effectiveness distributions for attached flows depend on the mass flux, the η_c distributions at different density ratios but the same mass flux ratio were compared. Results for two mass flux ratios are presented in Fig. 5. At $M = 0.5$ the jets remain attached and the η_c distributions for two widely different density ratios ($D.R. = 1.2$ and 2.0) were essentially the same. However, for $M = 1.0$ the jets detached for all density ratios examined resulting in significantly different levels of η_c for different density ratios.

Distributions of η_c for a range of density ratios at a constant velocity ratio of $V.R. = 0.5$ are shown in Fig. 6. Distinct differences in trends for η_c at different density ratios are clearly evident in Fig. 6. These differences appear to be due primarily to different degrees of detachment ranging from a very slight detachment at $D.R. = 1.2$ to a distinct detachment-reattachment at $D.R. = 2.0$.

Distributions of η_c for a range of density ratios at a constant momentum flux ratio are shown in Fig. 7. For a constant momentum flux ratio of $I = 0.2$, Fig. 7(*a*), the jets remain attached and the distribution of η_c is similar for $D.R. = 1.2$ and $D.R. = 1.6$. However, comparing these results with the constant mass flux results presented in Fig. 5(*a*) shows that the η_c distributions correlate better with mass flux ratio when the jets remain attached. At a constant momentum flux ratio of $I = 0.3$, Fig. 7(*b*), the jets have evidently just barely detached. The trends of the η_c distributions for $D.R. = 1.2$ and $D.R. = 2.0$ are very similar, but η_c for $D.R. = 1.2$ is slightly lower than for $D.R. = 2.0$. Finally, for a constant momentum flux ratio of $I = 0.5$, Fig. 7(*c*), there is a clear detachment and reattachment that occurs for all density ratios. The level of η_c is consistently lower for $D.R. = 1.2$ compared to the higher density ratios. The similarity in the trends of the η_c distributions evident in each of Figs. 7(*a*), 7(*b*), and 7(*c*) in-

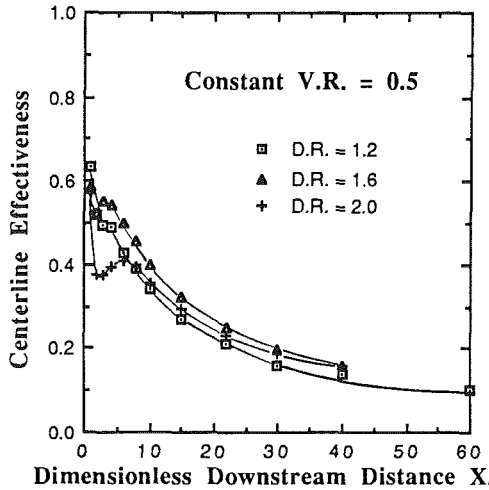

Fig. 6 Effect of density ratio at a constant velocity ratio, $V.R. = 0.5$

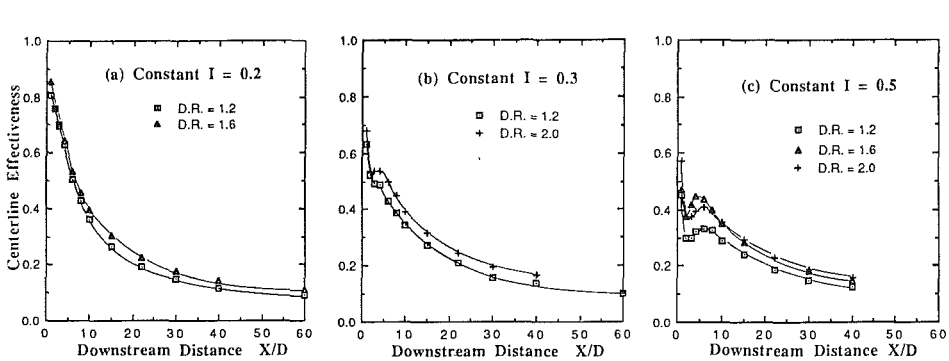

Fig. 7 Effect of density ratio at constant values of momentum flux ratios, (*a*) $I = 0.2$, (*b*) $I = 0.3$, and (*c*) $I = 0.5$

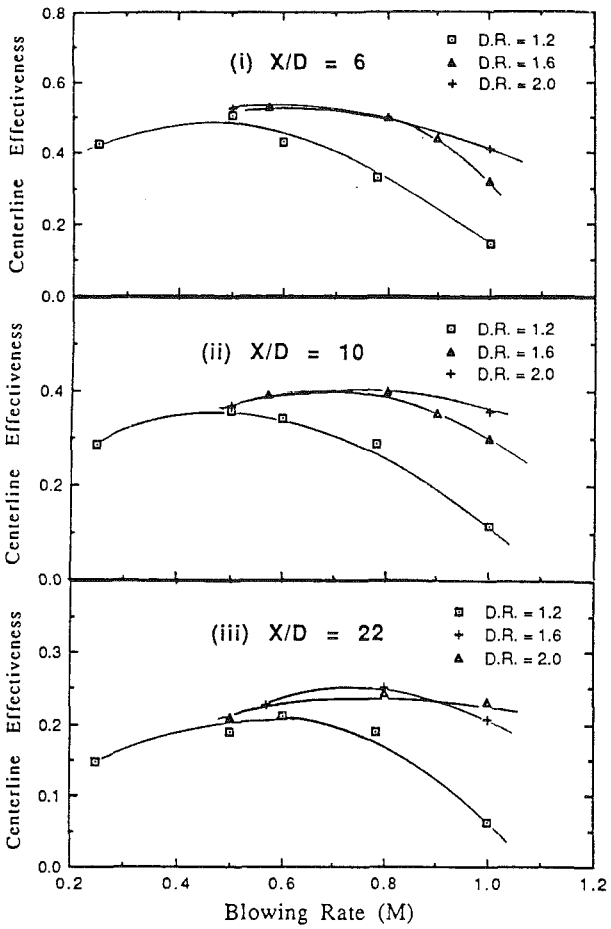

Fig. 8(*a*) Effect of mass-flux ratio (*M*) on centerline effectiveness at fixed downstream locations, (*i*) *X/D* = 6, (*ii*) *X/D* = 10, and (*iii*) *X/D* = 22

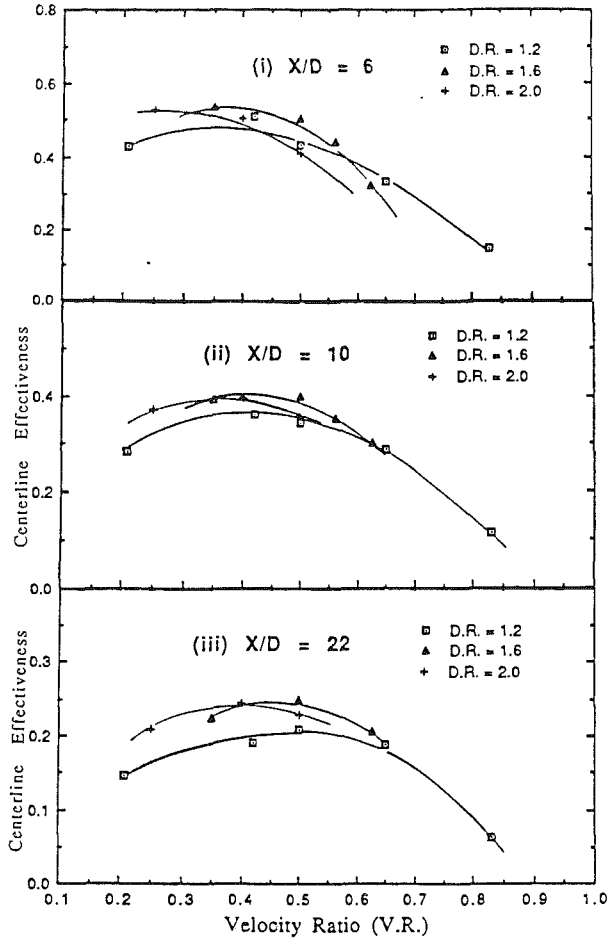

Fig. 8(*b*) Effect of velocity ratio (*V.R.*) on centerline effectiveness at fixed downstream locations, (*i*) *X/D* = 6, (*ii*) *X/D* = 10, and (*iii*) *X/D* = 22

dicates that detachment-reattachment of the jet scales with the momentum flux ratio. The reduced levels of η_c for lower density ratios may be attributed to the lower mass flux ratio for lower density ratio jets at the same momentum flux ratio.

Changes in η_c at X/D = 6, 10, and 22 for different density ratios and as a function of M, $V.R.$ and I are presented in Fig. 8. At low values of M, Fig. 8(*a*) shows that η_c values for different density ratios collapse to a single curve. With increasing M there are progressive branch-offs between the data sets of different density ratios. The collapse of η_c values at low values of M occurs when the jets remain attached, in which case the mass flux dictates the cooling on the plate. From the trends present in Fig. 8, it is clear that the local effectiveness at first increases and then decreases with increase in any of the three parameters M, $V.R.$, or I. However, the consistent trends that occur as a function of I, Fig. 8(*c*), indicate that the effects of the changing density ratio are best scaled by the momentum flux ratio. The high density data sets ($D.R.$ = 1.6, 2.0) more or less collapse on a line when plotted against I. Points corresponding to $D.R.$ = 1.2 are lower but the shape is similar. As the downstream distance increases, the maximum effectiveness occurs for higher values of I. This may be due to increasing reattachment distance with increasing momentum flux.

Laterally Averaged Effectiveness. Using the lateral distribution of η measured at discrete locations ranging from X/D = 1 to 15, the laterally averaged effectiveness, $\overline{\eta}$, was determined for a range of operating conditions. Results for $\overline{\eta}$ are presented in Fig. 9 as a function of X/D and for density ratios ranging from $D.R.$ = 1.2 to 2.0. The characteristics of the $\overline{\eta}$ distributions shown in Fig. 9 are distinctly different from the characteristics of the η_c distributions shown in Fig. 4. For low blowing ratio $\overline{\eta}$ is maximum near the hole and montonically decreases with distance from the hole. As the momentum flux ratio increases above I = 0.3, $\overline{\eta}$ is low immediately behind the hole and increases to a maximum about 10 diameters downstream of the hole. Results presented below show that this occurs because the lateral spreading of the injected fluid over the wall is strongly dependent on the momentum flux ratio.

The effect of momentum flux ratio on the jet spreading over the wall is clearly evident in Fig. 10, which shows the lateral distribution of η for a range of I with a constant density ratio of $D.R.$ = 2.0. At X/D = 1 the width of high η values was found to decrease considerably as I increases from 0.125 to 0.5. Recall that at I = 0.5 the centerline distribution of η_c indicates that the jet initially detaches from the wall but reattaches downstream. The rapid decrease in η in the lateral direction is consistent with the view that the jet is detached from the wall at this point. Farther downstream at X/D = 15 the lateral distributions of η are much the same for the range of momentum flux ratios investigated. At this point downstream the large momentum flux jets have reattached to the wall and the average effectiveness is similar to that of the jets with lower momentum flux.

Scaling of $\overline{\eta}$ at X/D = 10 with respect to M, $V.R.$, and I is shown in Fig. 11. Immediately obvious from this figure is that none of the parameters collapse $\overline{\eta}$ values for different density ratios. Figure 11(*a*) shows that, at a blowing ratio of M = 0.5, $\overline{\eta}$ is twice as large for $D.R.$ = 2.0 as for $D.R.$ =

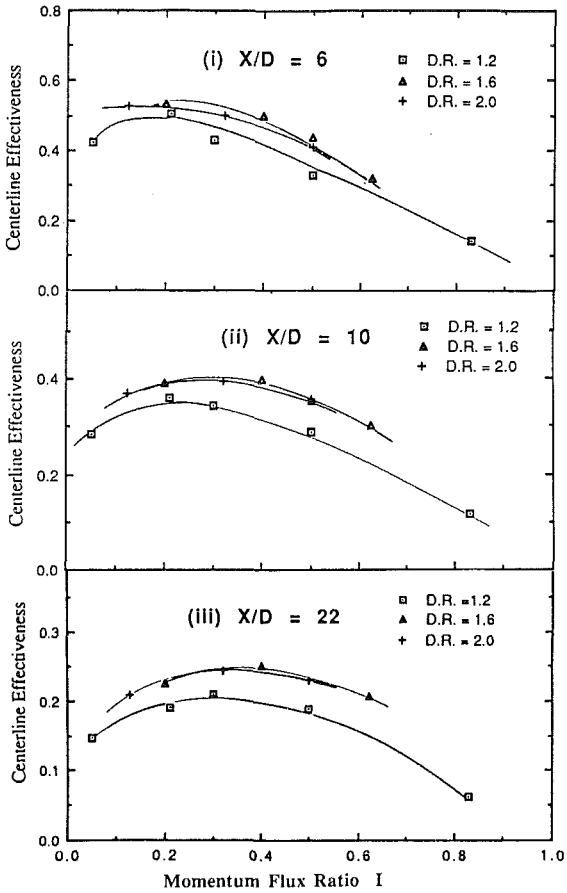

Fig. 8(*c*) Effect of momentum flux ratio (*I*) on centerline effectiveness at fixed downstream locations, (*i*) *X/D* = 6, (*ii*) *X/D* = 10, and (*iii*) *X/D* = 22

1.2. This is in constrast to the centerline effectiveness, which was the same for the high and low density ratio. The distributions of $\bar{\eta}$ with respect to velocity ratio, Fig. 11(*b*), and with respect to momentum flux ratio, Fig. 11(*c*), have similar trends for the higher density ratios, but the $D.R. = 1.2$ distributions are distinctly different and values for $\bar{\eta}$ are significantly lower. Similar results were obtained by Pedersen et al. (1977) who noted a monotonic increase of $\bar{\eta}$ with increasing density ratio for $M = 0.5$.

The previous results indicate that there is less spreading of the jet at the lower density ratio. A direct indication of the reduced spreading is shown in Fig. 12, which shows the lateral distribution of η with different density ratios at constant M, and in Fig. 13, which shows the lateral distribution of η with different density ratios at constant I. For a constant $M = 0.5$, Fig. 12 shows that at the centerline η is the same for $D.R. = 2.0$ and $D.R. = 1.2$, but the decrease in η in the lateral direction is much more rapid for $D.R. = 1.2$. The more rapid decrease in η in the lateral direction might be attributed to the larger momentum flux ratio for $D.R. = 1.2$. The lateral distribution of η for a constant momentum flux ratio of $I = 0.3$ is shown in Fig. 13. Although the lateral distribution is similar for high and low density ratios, the level of η is consistently lower for low density ratio. In this case the lower levels of η might be attributed to the lower mass flux ratio at $D.R. = 1.2$. Consequently, whether the mass flux ratio or the momentum flux ratio is held constant, $\bar{\eta}$ is smaller for lower density ratios.

Conclusions

In general the effect of variable density ratio on η_c and $\bar{\eta}$ cannot be scaled with mass flux ratio, velocity ratio, or momentum flux ratio. For low blowing rates with the cooling jets remaining attached to the wall, η_c scales with the mass flux ratio. At higher blowing rates the detachment and reattachment of the cooling jets become important. This detachment-reattachment of the jets scales with the momentum flux ratio. For constant momentum flux ratio, jets with higher density ratio

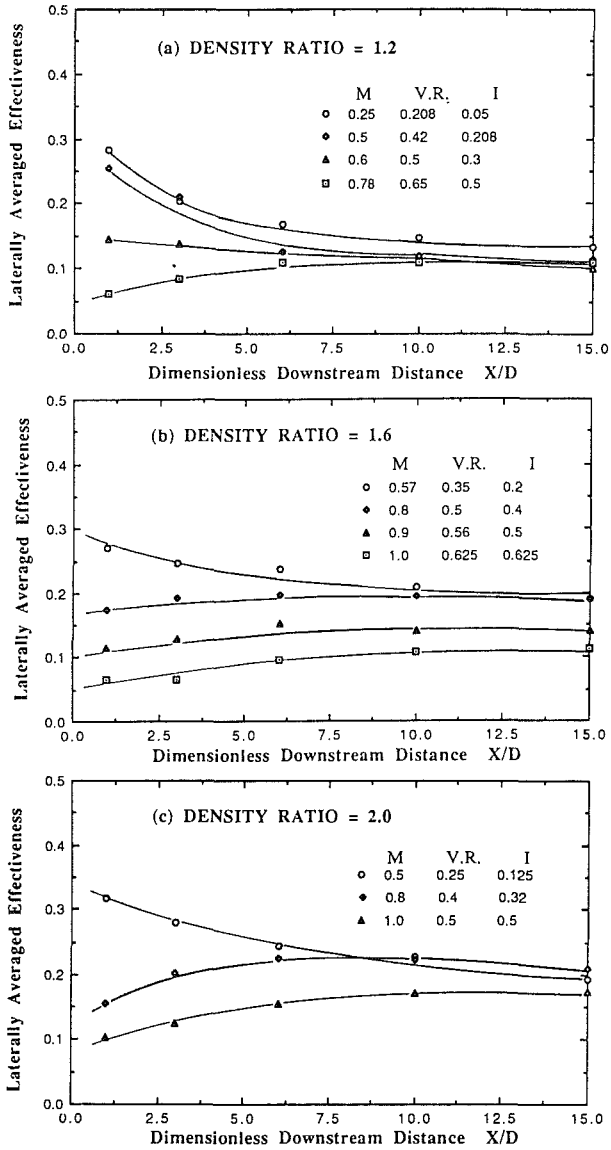

Fig. 9 Laterally averaged effectiveness distributions over a range of film cooling parameters at constant density ratios, (*a*) *D.R.* = 1.2, (*b*) *D.R.* = 1.6, and (*c*) *D.R.* = 2.0

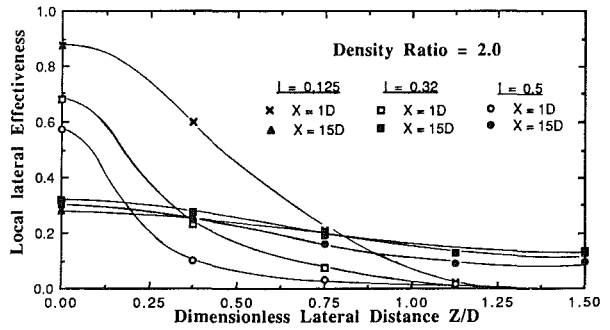

Fig. 10 Local lateral effectiveness distributions at two different streamwise locations (*X/D* = 1 and *X/D* = 15) for *D.R.* = 2

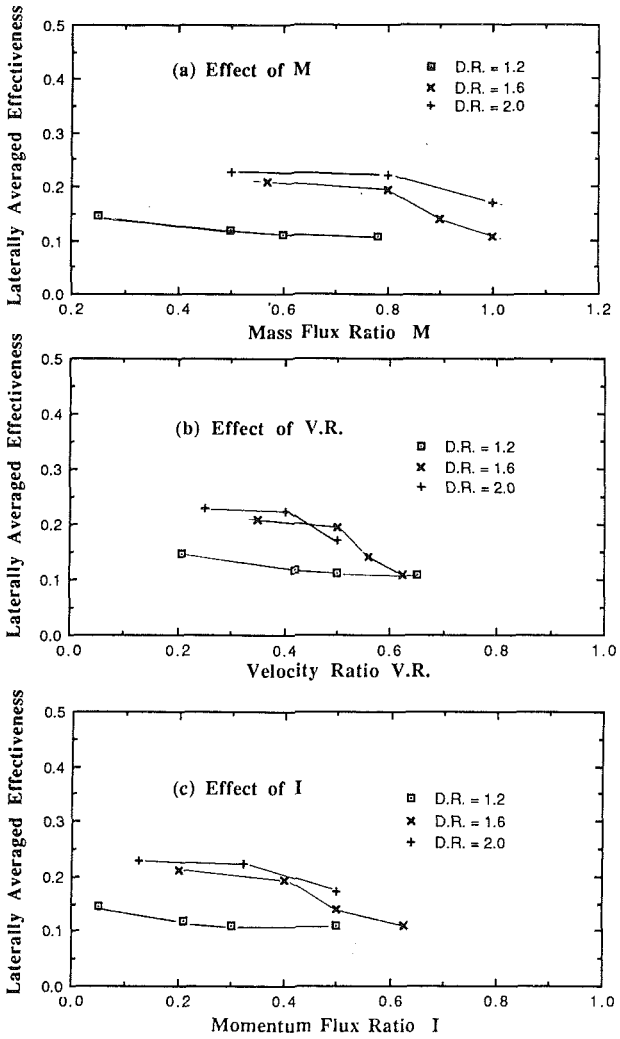

Fig. 11 Effect of: (*a*) mass-flux ratio, (*b*) velocity ratio, and (*c*) momentum flux ratio on laterally averaged effectiveness at $X/D = 10$

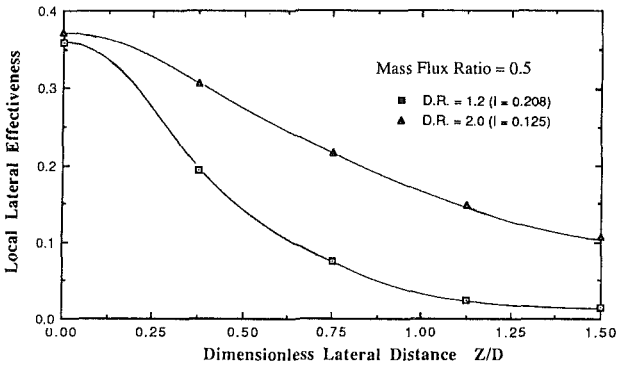

Fig. 12 Local lateral effectiveness distributions at $X/D = 10$ for different density cases corresponding to mass flux ratio $M = 0.5$

will have higher mass flux ratio, which results in greater η_c values. Laterally averaged effectiveness is strongly dependent on the lateral spreading of the cooling jet. Decreases in density ratio and increases in momentum flux ratio were found to reduce the spreading of the film cooling jet significantly and thereby reduce laterally averaged effectiveness.

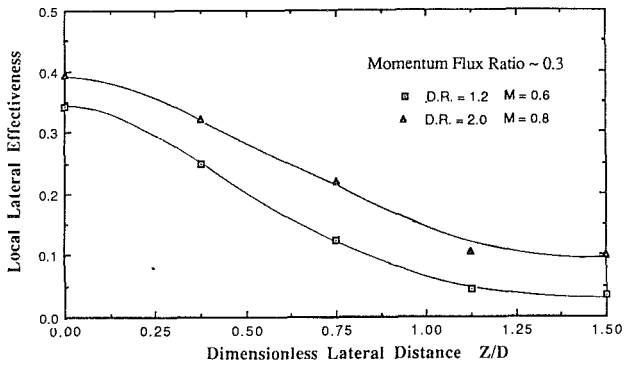

Fig. 13 Local lateral effectiveness distributions at $X/D = 10$ for different density cases corresponding to momentum flux ratio $I = 0.3$

Acknowledgments

The authors gratefully acknowledge Garrett Engine Division of the Allied-Signal Aerospace Company for support of this research. We would also like to thank Mr. David Dotson and Mr. Kenneth Leonore for their assistance in construction of the facilities and processing the experimental data.

References

Afejuku, W. O., Hay, N., and Lampard, D., 1980, "The Film Cooling Effectiveness of Double Rows of Holes," ASME *Journal of Engineering for Power*, Vol. 102, pp. 601–606.

Afejuku, W. O., Hay, N., and Lampard, D., 1983, "Measured Coolant Distributions Downstream of Single and Double Rows of Film Cooling Holes," ASME *Journal of Engineering for Power*, Vol. 105, pp. 172–177.

Ammari, H. D., Hay, N., and Lampard, D., 1989, "The Effect of Density Ratio on the Heat Transfer Coefficient From a Film Cooled Flat Plate," ASME Paper No. 89-GT-200.

Bergeles, G., Gosman, A. D., and Launder, B. E., 1977, "Near-Field Character of a Jet Discharged Through a Wall at 30° to a Mainstream," *AIAA Journal*, Vol. 15, pp. 499–504.

Eriksen, V. L., and Goldstein, R. J., 1974, "Heat Transfer and Film Cooling Following Injection Through Inclined Circular Tubes," ASME *Journal of Heat Transfer*, Vol. 96, pp. 239–245.

Forth, C. J. P., Loftus, P. J., and Jones, T. V., 1985, "The Effect of Density Ratio on the Film Cooling of a Flat Plate," *AGARD Conference Proc. CP 390*, Paper 10.

Forth, C. J. P., and Jones, T. V., 1988, "Scaling Parameters in Film Cooling," *Proc. 8th International Heat Transfer Conference*, Vol. 3, pp. 1271–1276.

Foster, N. W., and Lampard, D., 1980, "The Flow and Film Cooling Effectiveness Following Injection Through a Row of Holes," ASME *Journal of Engineering for Power*, Vol. 102, pp. 584–588.

Goldstein, R. J., Eckert, E. R. G., and Ramsey, J. W., 1968, "Film Cooling With Injection Through Holes: Adiabatic Wall Temperatures Downstream of a Circular Hole," ASME *Journal of Engineering for Power*, Vol. 90, pp. 384–395.

Goldstein, R. J., Eckert, E. R. G., Eriksen, V. L., and Ramsey, J. W., 1970, "Film Cooling Following Injection Through Inclined Circular Tubes," *Israel Journal of Technology*, Vol. 8, pp. 145–154.

Goldstein, R. J., Eckert, E. R. G., and Burggraf, F., 1974, "Effects of Hole Geometry and Density on Three-Dimensional Film Cooling," *International Journal of Heat and Mass Transfer*, Vol. 17, pp. 595–605.

Ito, S., Goldstein, R. J., and Eckert, E. R. G., 1978, "Film Cooling of a Gas Turbine Blade," ASME *Journal of Engineering for Power*, Vol. 100, pp. 476–481.

Pedersen, D. R., Eckert, E. R. G., and Goldstein, R. J., 1977, "Film Cooling With Large Density Differences Between the Mainstream and the Secondary Fluid Measured by the Heat-Mass Transfer Analogy," ASME *Journal of Heat Transfer*, Vol. 99, pp. 620–627.

Pietrzyk, J. R., Bogard, D. G., and Crawford, M. E., 1990, "Effects of Density Ratio on the Hydrodynamics of Film Cooling," ASME JOURNAL OF TURBOMACHINERY, Vol. 112, pp. 437–443.

Teekaram, A. J. H., Forth, C. J. P., and Jones, T. V., 1980, "The Use of Foreign Gas to Simulate the Effects of Density Ratios in Film Cooling," ASME JOURNAL OF TURBOMACHINERY, Vol. 111, pp. 57–62.

Gas Turbine Film Cooling: Flowfield Due to a Second Row of Holes

A. K. Sinha

D. G. Bogard

M. E. Crawford

University of Texas at Austin,
Austin, TX 78712

Flowfield measurements with relevance to gas turbine film cooling were carried out behind a second row of holes located 40 hole diameters downstream of a first row and staggered with respect to it. The effects of the thicker boundary layer and that of injection from the first row were examined. Experiments were carried out for jet-to-mainstream density ratios of 1 and 2 and results compared to those obtained by Pietrzyk et al. (1989, 1990) behind the first row. Results show that the dominant structures identified in the flowfield downstream of the first row were also present behind the second row. Due to the thicker boundary layer, though, the mean flowfield and the turbulence and shear stress fields were altered. One of the significant results was that the thicker boundary layer enables the jets to penetrate deeper into the mainstream.

Introduction

Higher efficiency in gas turbine engines can be achieved by increasing the turbine entry temperature. For current technology, the maximum temperature is significantly below the stoichiometric temperature with its limit set by requiring an acceptable blade lifetime. Film cooling is a turbine blade cooling technique in which the blade surface is protected from high-temperature mainstream gases by releasing a coolant through the blade surface. In this cooling technique, air bled from the compressor is introduced into the hollow core of the blade and is channeled and then dumped through the blade surface via one or more rows of holes near high thermally loaded locations on the blade's suction and pressure surfaces.

Film-cooling studies have been extensively reported in the literature. However, a significant portion of the research has concentrated on determining how variation of design parameters improves the effectiveness of reducing heat transfer to the wall. Studies have been conducted for multiple-row injection but their numbers pale in comparison to those done for single-row injection. Although the essential characteristics of the thermal and velocity fields can be understood from single-row (or for that matter single hole) injection, studies of multiple-row injection assume importance from a design point of view. For a successful engine design, the effects of interaction between jets in different rows have to be understood to eliminate regions of high thermal stress from the entire blade surface. The usefulness of film-cooling data in the literature is limited due to a lack of understanding of the physical mechanisms associated with the film-cooling jet-mainstream interaction. Some of the results for multiple-row cooling data are reviewed here.

Contributed by the International Gas Turbine Institute and presented at the 35th International Gas Turbine and Aeroengine Congress and Exposition, Brussels, Belgium, June 11–14, 1990. Manuscript received by the International Gas Turbine Institute January 11, 1990. Paper No. 90-GT-44.

Afejuku et al. (1983) measured the coolant distributions downstream of double rows of film cooling holes using a foreign gas mixture to obtain the density difference between the jet and the mainstream. They varied the row spacings from 10 to 40 diameters and the second row was staggered with respect to the first. They made concentration measurements both on and above the surface. One of their major conclusions was that an increased momentum flux from the upstream film affects the control of the trajectory of the jets from the downstream row. Muska et al. (1975) conducted an experimental investigation to verify the validity of a model by Sellers (1963) that assumes that the overall film cooling effectiveness from several rows can be calculated from data or correlations for a single row of holes. For blowing rates from 0.1 to 1.3 and row spacings from 16.7 diameters to 25 diameters, the additive model was found to provide good agreement between the predicted and measured film effectiveness for flat plate configurations. Mayle and Camarata (1975) presented adiabatic film effectiveness and heat transfer measurements with injection of secondary air through arrays of holes in a flat plate into a turbulent boundary layer. Within the hole pattern, they found the heat transfer coefficient to increase significantly with increase in mass-flux ratio or density ratio. Their measured film effectiveness distributions due to the staggered multihole pattern did not compare favorably with those predicted by a model based on the superposition of point heat sinks.

Jabbari and Goldstein (1978) investigated film cooling and heat transfer following injection through two staggered rows of holes. They found that the film-cooling effectiveness at locations beyond about 30 hole diameters downstream of the injection was laterally uniform. The heat transfer coefficient was found to be within a few percent of that without injection at low blowing rates, but increased rapidly as the blowing rate increased above unity. Afejuku et al. (1980) studied film-cooling effectiveness from two rows of holes with variable row

spacing, two injection angles, and both a staggered and in-line hole configuration. They concluded, as have other researchers, that staggered was preferable to in-line injection, and that angled injection was preferable to normal injection. They also investigated varying the blowing ratio between the first and second row of holes. Jubran and Brown (1985) conducted experiments to study the film-cooling effectiveness of two rows of holes inclined in streamwise and spanwise directions. They examined the effects of hole row spacings. Combinations of inclinations were also studied in presence of pressure gradients and turbulence.

There are almost no data in the open literature describing the flowfield resulting from film-cooling injection and consequent interaction of two or more rows of holes. Yavuzkurt et al. (1980) made detailed measurements of the three velocity components and six Reynolds stresses on a full-coverage surface and its recovery region using a triple-wire hot-wire anemometer system. Pietrzyk et al. (1989, 1990) made detailed measurements of the three velocity components and six Reynolds stresses of the flowfield downstream of a single row of 35 deg jets laterally spaced 3 diameters apart using laser-Doppler velocimetry. The present study, an extension of the Pietrzyk studies, examines the flowfield behind a second row of holes, staggered with respect to the first row, and located 40 diameters downstream of the first row. The density ratio effects are simulated by cooling the jets with respect to the mainstream. A detailed comparison of the flowfield behind the second staggered row with that existing behind the first row in terms of different fluid mechanical structures has been made.

Facility and Instrumentation

Experiments were conducted using a closed-loop recirculating wind tunnel and a secondary flow loop, which provides cryogenically cooled air for controlling the jet-to-mainstream density ratio. A schematic of the experimental setup is shown in Fig. 1, and details of the test facility and the streamwise development of the boundary layer on the test plate are documented by Pietrzyk et al. (1989). Film coolant was provided by the secondary injection system. In that system a blower directed air through a set of four finned heat exchangers arranged in series where liquid nitrogen, supplied by a pressurized dewar, was used as the coolant in the exchangers. Exhausted dry nitrogen gas leaving the exchangers was used to drive the LDV seeders. The cold air stream was then directed into the two injection plenum chambers, one for each row of injection holes. The total flow rate of air leaving the heat exchanger and the flow rate diverted to the second row of holes were monitored by separate calibrated sharp-edged orifice plate flow meters.

Figure 2 shows the geometry of the film-cooled test plate, in which the bottom of the plate formed the top surface of each plenum. The first row had 11 injection holes that were 1.27 cm in diameter, spaced 3 diameters apart laterally. The

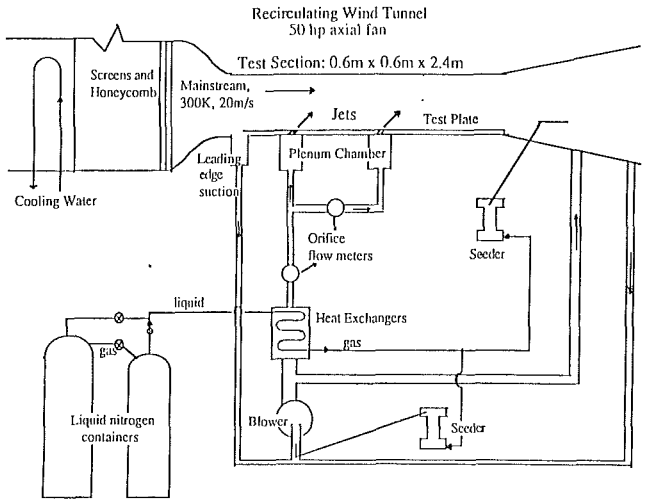

Fig. 1 Schematic of experimental test facility

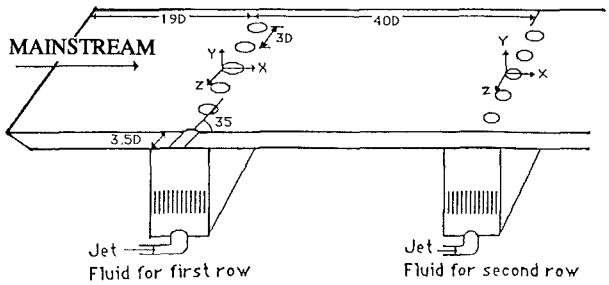

Fig. 2 Film cooling test geometry and coordinate system

second row was 40 diameters downstream of the first row, with the hole array staggered with respect to the first row and containing 12 holes. Both rows had holes inclined at 35 deg from the surface, and the injectant passages had an L/D of 3.5. The test plate and plenum chamber were constructed of a glass-reinforced plastic material (commercially known as Extren) because of its low thermal conductivity ($k = 0.58$ W/m·K) and low thermal expansion coefficient ($\alpha = 1.4 \times 10^{-5}$/K). The surface roughness of the plate was measured by a micrometer screw gage and found to be less than 3.5 mil (0.09 mm), which corresponds to a y^+ of 5 for flat plate, unblown flow.

Laser-Doppler Velocimeter. Velocity measurements were made with a three-component laser-Doppler velocimeter (LDV). The TSI 9100-10 LDV system was extensively modified to allow accurate measurements of the mean lateral velocity component (W) and turbulence quantities involving W. The system was modified by adding a second optical axis oriented 30 deg from the first axis. Off-axis collection reduced the length of the

Nomenclature

D = injection hole diameter
$D.R.$ = density ratio, jet to mainstream $= \rho_j/\rho_\infty$
H = shape factor
I = momentum flux ratio $= \rho_j U_j^2/\rho_\infty U_\infty^2$
k = thermal conductivity
M = mass flux ratio or blowing rate $= \rho_j U_j/\rho_\infty U_\infty$
L = length of injection hole
TL = turbulence level $= \sqrt{(u_{rms}^2 + v_{rms}^2 + w_{rms}^2)/3}$
U_∞ = free-stream velocity
U = mean velocity component in the free-stream direction (X)
V = mean velocity component perpendicular to the test surface (Y)
W = mean velocity component in the lateral direction (Z)
$u_{rms}, v_{rms}, w_{rms}$ = fluctuating components of velocity
$\overline{uv}, \overline{uw}, \overline{vw}$ = turbulent shear stresses
$V.R.$ = velocity ratio $= U_j/U_\infty$
X = downstream distance from the leading edge of the hole
Y = vertical distance measured from the test surface
Z = lateral distance measured from the axis of the hole
α = coefficient of thermal expansion
ρ_j = density of jet fluid at injection location
ρ_∞ = density of mainstream

probe volume to 300 μm. Coincident data (instantaneous measurements of three velocity components on the same particle), necessary to determine the turbulence shear stresses, were obtained by establishing a 10 μs coincidence window. A computer-controlled traverse was used to position the LDV probe volume precisely. The signal from the LDV was processed by three TSI counter signal processors. An HP-1000 microcomputer system, interfaced with the signal processors and the motion control system for the traverse table, was used for data acquisition. Dry particle generators (Pietrzyk, 1989) were used to provide 1 μm TiO_2 particles to independently seed the free stream and the jets in equal concentrations to avoid bias errors.

The precision errors involved with the LDV measurements were estimated from repeatability tests in the lateral portion of the jet mainstream interaction, near the trailing edge of the hole. The three mean velocity components and the six turbulent stresses were determined from a sample size of 2048 discrete measurements, with sampling time of about 60 seconds. The precision uncertainties were less than ± 0.01 for normalized mean velocity components U/U_∞, V/V_∞, and W/W_∞, less than ± 0.005 for normalized rms velocity components u_{rms}/U_∞, v_{rms}/U_∞, and w_{rms}/U_∞, and less than ± 0.001 for normalized shear stresses $\overline{uv}/U_\infty^2$, $\overline{uw}/U_\infty^2$ and $\overline{vw}/U_\infty^2$.

Operating Conditions

For all experiments the free-stream velocity was 20.0 m/s $\pm$ 1 percent and the free-stream turbulence was less than 0.2 percent. The variation in the free-stream velocity was less than the precision uncertainty of the mean velocity measurement (± 1 percent). A heat exchanger located between the blower and the wind tunnel contraction maintained the free-stream temperature at 298.0 $\pm$ 0.5 K. The total mass flow rate of the jets was determined with a precision of ± 0.7 percent. The uncertainty of mass flow rate through the jets of the second row was higher, at a level of $\pm$ 1 percent. The mass-flux ratio varied as much as ± 4 percent due to variations in the flow rate caused by the accumulation of frost in the secondary flow loop. For the high-density ($D.R. = 2$) experiment, the plenum chambers were maintained at 150 $\pm$ 5 K. The jet-to-mainstream density ratio hence varied by ± 3 percent.

Experimental Plan

The three-dimensional flowfield was mapped for two experiments: (*i*) $D.R. = 1.0$, $M = 0.5$, $I = 0.25$, and (*ii*) $D.R. = 2.0$, $M = 1.0$, $I = 0.5$. Both these tests correspond to a velocity ratio of 0.5. For both experiments, the three mean velocities and the six turbulent stresses were measured, and the results presented in this paper are nondimensionalized using the mainstream velocity. Data were taken for a region extending from 1 diameter upstream of the leading edge of the second row of holes to 30 and 20 diameters downstream for density ratios 1.0 and 2.0, respectively. Measurements were taken from the wall vertically to the free stream, and from the jet centerline laterally to the centerline between the jets. A grid of 115 measurement points was used across vertical-lateral (Y-Z) planes. Measurements of these Y-Z plane cross sections were made at several different streamwise locations. Vertical profiles along the jet centerline ($Z/D = 0$) were taken at numerous stations between $X/D = -1$ and $X/D = 20$ to 30 with each profile containing 15–25 points.

Results and Discussion

This section contains a description of the flowfield downstream of the second row of holes and a detailed comparison with that obtained by Pietrzyk (1989) for injection through a single row for the same film cooling parameters, i.e., blowing rate and density ratio. In this study the blowing ratio is such that the velocity ratio is constant as the density is varied. The salient structures present downstream of a single row of holes will be presented briefly before examining the effects of the first row of holes on the second row.

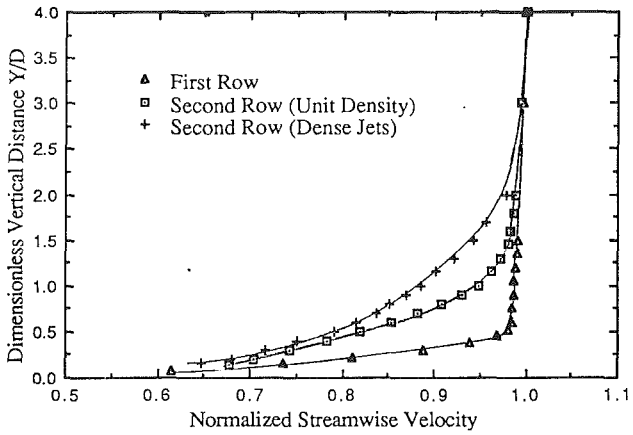

Fig. 3 Normalized streamwise velocity profiles in the boundary layer upstream of the first and second rows ($X/D = -1$) with secondary injection for unit density and dense jets

Description of Flowfield Following Single-Row Injection. Pietrzyk (1989) found that the dominant structures in the flowfield for single-row injection were a shear layer over the top of the jet due to velocity differences between the jet fluid and the mainstream, longitudinal vortices that form at the lateral edges of the hole and continue downstream of the hole, and a shear layer within the jet downstream of the hole. He also found that for density ratios of unity and two, the mean velocity and turbulence fields in the hole exit plane scaled with the velocity ratio. The turbulence in the region above the hole was found to be very anisotropic. The strength of the longitudinal vortices was found to scale with the velocity ratio, and with increasing distance downstream of the hole, the size of the vortices increased and their angular velocity decreased. The vertical movement of the vortex center was away from the wall. Elevated levels of $\overline{vw}$ shear stress were found to be associated with these vortices. The distance the jet penetrated into the mainstream was found to scale with the momentum flux ratio. Far downstream of the holes the flow relaxed to standard turbulent boundary layer.

Initial Conditions. Figure 3 presents normalized streamwise velocity profiles of the boundary layer taken one diameter upstream of injection from the first and second rows of holes. These approaching boundary layer profiles are taken at the relative location $Z = 0$, corresponding to the jet centerline for each row. The profiles upstream of the second row are for injectant from the first row corresponding to $M = 0.5$ and $M = 1.0$, and $V.R. = 0.5$ for both cases. The two second-row profiles both have a shape factor, H, of about 1.5, typical of a turbulent boundary layer, and a boundary layer thickness significantly thicker than that in front of the first row. Because the second row is staggered with respect to the first, the boundary layer thickness for the second row was found to vary from a minimum at the hole centerline to a maximum at the dividing line between the holes, although no distinct jets are observed by a distance of 35 diameters for the momentum ratios considered. The effect on boundary layer thickness of dense injection at a $V.R.$ of 0.5 compared to unit density injection is pronounced.

Mean Velocity Field. This section compares on a mean velocity component basis the interaction of the second row of injectant with the crossflow to that of the first row. Two factors will alter the second row hydrodynamics. The first is the pres-

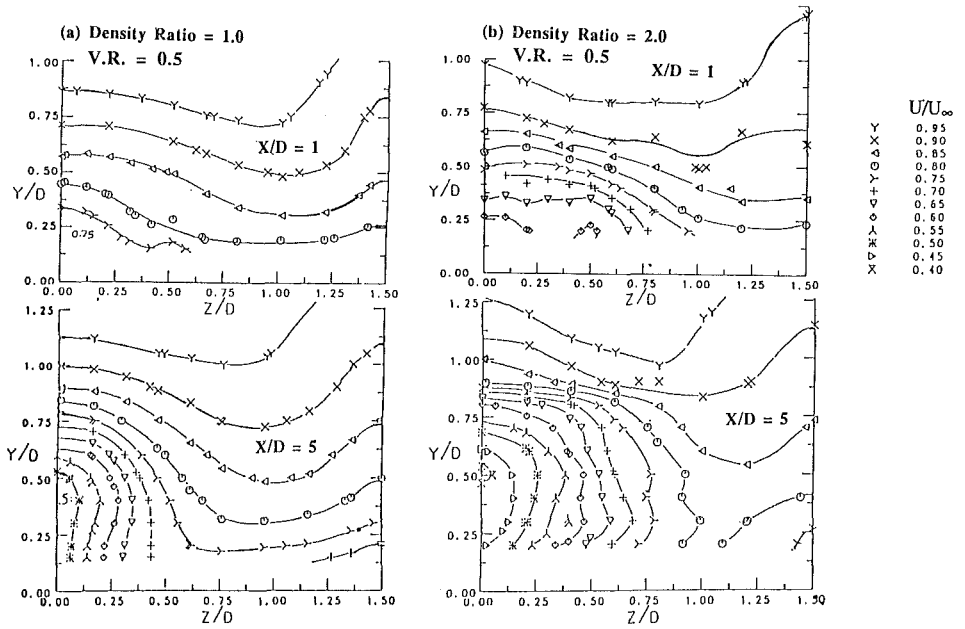

Fig. 4 Normalized streamwise velocity contours (U/U_∞) in vertical lateral planes at $X/D=1$, 5 downstream of the second row for (*a*) unit density jets and (*b*) dense jets

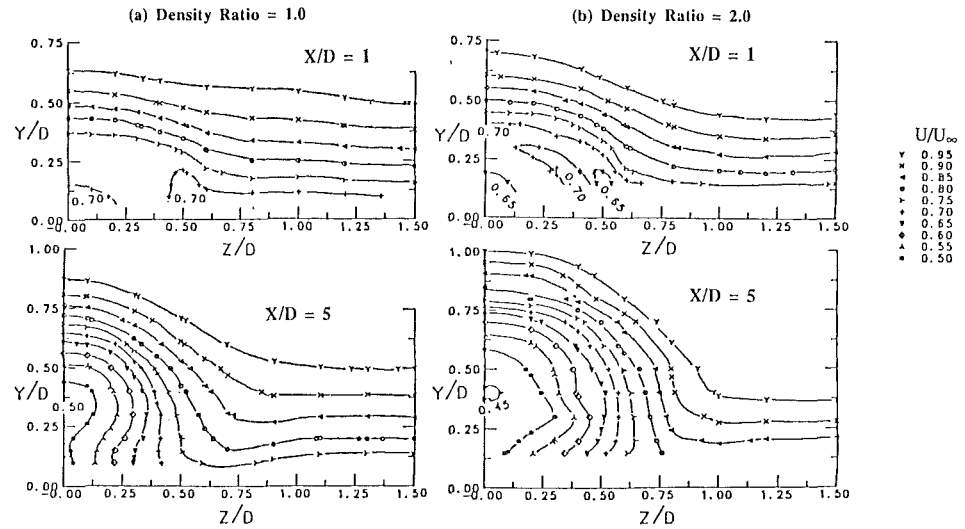

Fig. 5 Normalized streamwise velocity contours (U/U_∞) in vertical lateral planes at $X/D=1$, 5 downstream of the first row for (*a*) unit density jets and (*b*) dense jets (Pietrzyk, 1989)

ence of a much thicker approaching boundary layer, and the second is the potential existence of flow structures, e.g., vorticity and three dimensionality, that would not be present upstream of the first row. The following section considers effects on the turbulence field.

The normalized streamwise mean velocity contours for the second row for unit density and large density jets are presented in Figs. 4(*a*) and 4(*b*), respectively, and their counterparts for single row injection are presented in Figs. 5(*a*) and 5(*b*). The normalized velocity data are presented as vertical-lateral planes in Y–Z space at fixed X/D locations of 1.0 and 5.0, representing the very near field as the jet emerges. In the figure the $Z/D=0$ location corresponds to the jet centerline, and the 1.5 value is the symmetry line between adjacent holes spaced 3 diameters apart. The effect of the second row being staggered with respect to the first can be observed from the streamwise velocity contours in Fig. 4. As the centerline between two holes of the second row lies at the axis of a hole in the first row, injection from the latter results in the boundary layer thickness at this location being significantly greater than that without injection.

In Figs 4 and 5, as the jet exits from the hole, it is bent toward the wall by the mainstream. This can be seen in the concentration of concentric contours near $Z/D=0$ to $Z/D=0.5$, the edge of the injection hole. The second-row concentrations of contours in Fig. 4 extend farther up from the surface than their first-row counterparts in Fig. 5, suggesting that the jets penetrate deeper into the mainstream behind the second row than the first.

Figure 6 presents selected mean velocity contours of 0.5 and 0.75 at $X/D=5$ in the Y–Z plane for unit and dense jets. In Fig. 6(*a*), the second-row jet penetration is more clearly seen. An interesting observation can be made regarding the difference in the shapes of the 0.5 level contours for the first and second rows. As the vertical mixing for the first-row jet is hampered by the high-momentum mainstream, the jet spreads out more in the lateral direction. Figure 6(*b*) presents a comparison of two mean streamwise velocity contours for dense and unit density jets for the second row, which indicates that the boundary layer thickness is about 25 percent greater for the dense jets than the unit density jets in the near hole region.

This is another indication that there is deeper penetration of the dense jets into the mainstream than the unit density jets.

There are two reasons for the increased jet penetration. First, the boundary layer from the approaching flow for the case density ratio two is larger than that for unit density case, causing smaller diversion of the jet. Second, the higher density ratio for the same velocity ratio results in twice the momentum flux ratio of the unit density case. Momentum flux ratio has been identified as the key parameter determining penetration distance (Thole et al., 1990). Due to the greater mass flux (and consequently energy flux) for the large density jet, the interaction region in the lateral direction is much more spread out.

Velocity profiles along the jet centerline at different streamwise positions for first and second rows are shown in Fig. 7.

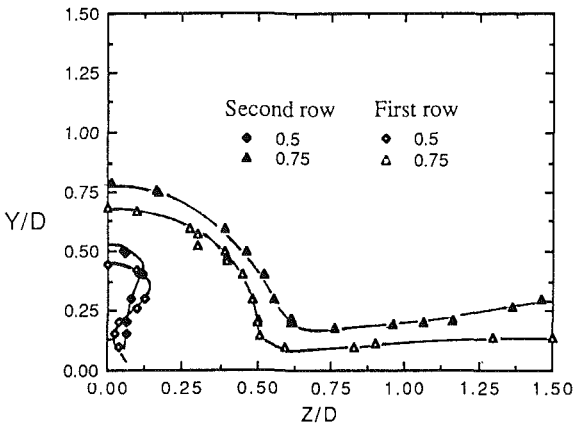

Fig. 6(*a*) Comparison of mean velocity contour levels ($V/V_\infty = 0.5$ and 0.75) for first and second row for unit density jets ($X/D = 5$)

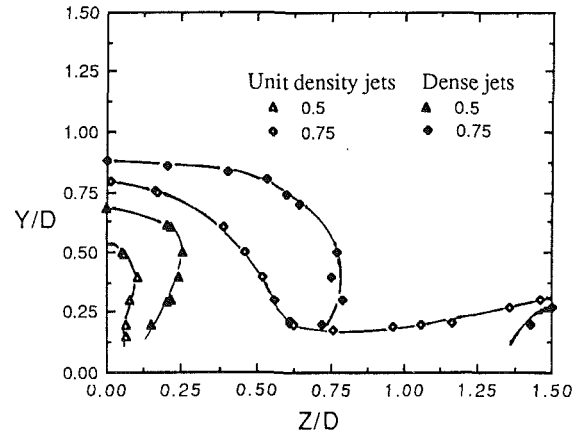

Fig. 6(*b*) Comparison of mean velocity contour levels ($V/V_\infty = 0.5$ and 0.75) for second row for unit density and dense jets ($X/D = 5$)

They show the deeper penetration for the second row jets, due to a much thicker approaching boundary layer at this location. The jets exiting from the second row are diverted less by the approaching flow than those coming out from the first row, due to the greater momentum defect of the approaching flow at the second row as compared to the first.

The formation of the longitudinal vortices in the vertical-lateral plane at $X/D = 5$ for the second row is shown in Fig. 8. The vectors in the figure represent magnitude and direction of the combined V and W velocity components in the Y–Z plane. At the top of the figure is a vector representing the magnitude of the corresponding normalized U component, showing that the absolute velocities associated with the vortices are very small compared to the streamwise component. The top of the vortex and the side of the vortex nearest the mainstream is evident from the horizontal- and downward-angled vectors in the region over the wall, near the lateral edge of the hole, $Z/D = 0.5$. The location of the center of the vortex and the magnitude of the angular velocities associated with it at this streamwise station are about the same for the first and the second rows.

Turbulence Field. The turbulence field surrounding and downstream of the second row of holes is presented in terms of turbulence level contours and $\overline{uv}$ shear stress contours in the X–Y plane in Figs. 9–12, and in terms of Y–Z contours at two X/D stations in Figs. 13–14. The figures provide a comparison of unit density and density ratio two turbulence fields. In general the fields behind the second row were found to be strikingly similar to those behind the first row.

For second-row injection, as with first-row injection, the different shear layers existing in the flowfield were found to be large sources of turbulence. Figures 9 and 10 present contours of the turbulence levels in the vertical plane along the centerline downstream of the second row and first row of holes, respectively, for unit density and dense jet injection. The turbulence levels over the top of the jet, within the jet, and downstream of the jet were found to be much the same for the second row of holes compared to the first. For the first row of holes the high turbulence level regions downstream of the hole were slightly narrower in the vertical direction, which may be due to the narrow region of large velocity gradient evident in Fig. 7. Also, for $D.R. = 1.0$, there was a slightly higher turbulence level, 12 percent compared to 10 percent, downstream of the first row of holes.

Normalized $\overline{uv}$ shear stresses in the vertical plane along the jet centerline for the second row of holes and the first row of holes are presented in Figs. 11 and 12, respectively, for unit density and dense jet injection. Again, the characteristics for the second row are very similar to those for the first row. The slight difference between the two again occurs downstream of the holes where the high turbulence regions for the first row

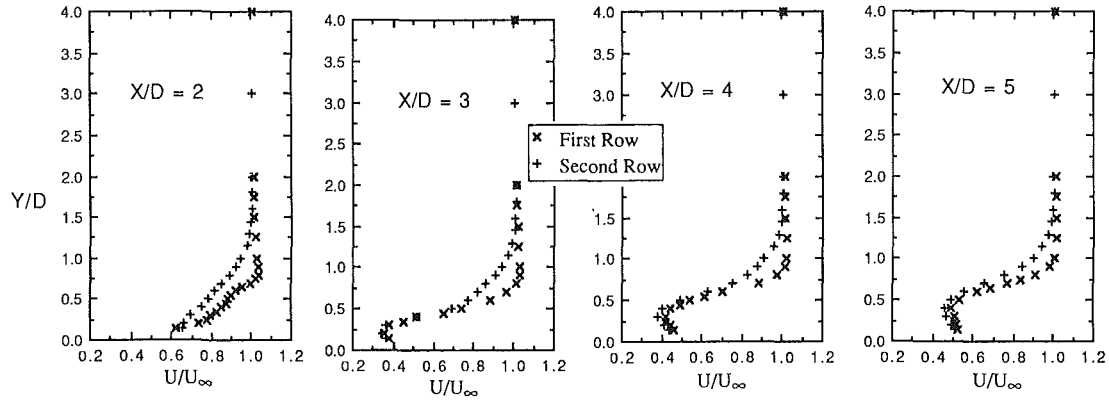

Fig. 7 Normalized mean velocity profiles at different streamwise stations ($X/D = 2$, 3, 4, and 5) along the jet centerline for first and second row for unit density jets

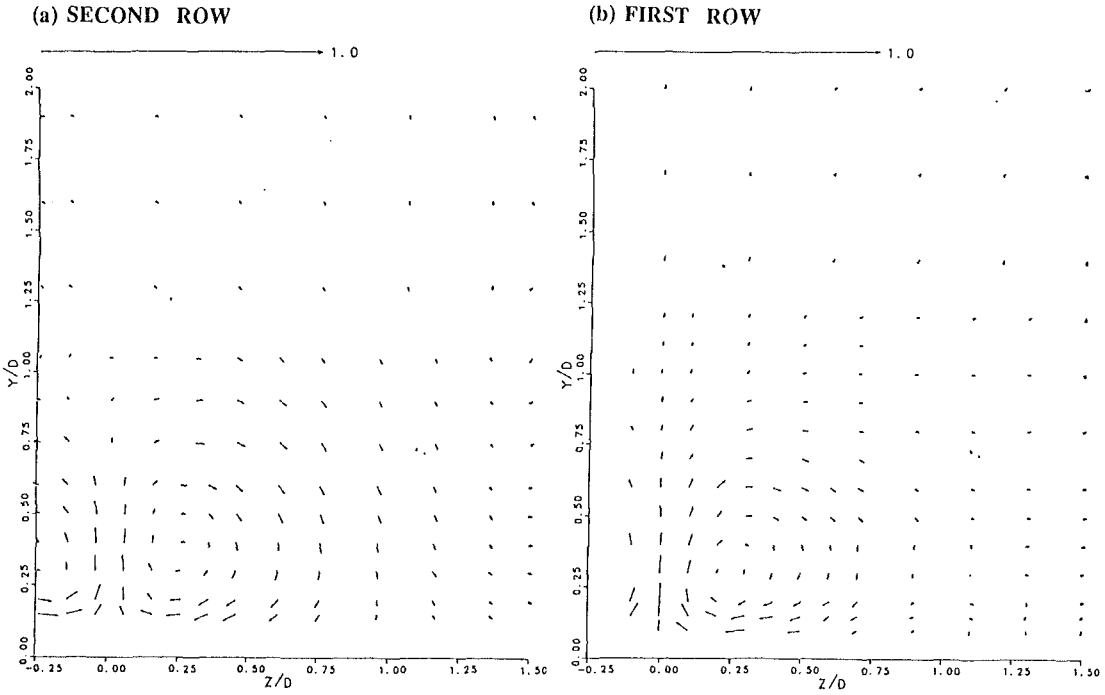

Fig. 8 Normalized velocity vectors (V/U_∞, W/U_∞) in the vertical lateral plane at $X/D = 5$ downstream of the (*a*) second row and (*b*) first row (Pietrzyk, 1989) for unit density jets

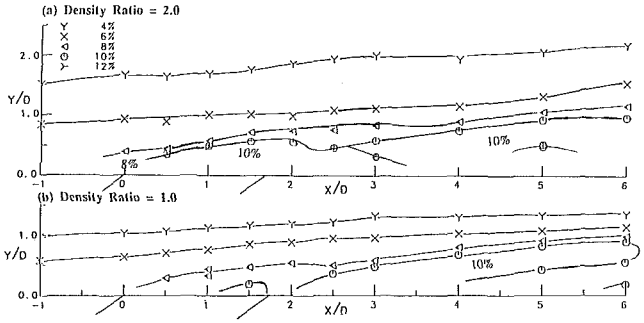

Fig. 9 Turbulence level contours in the vertical plane along the jet centerline ($Z/D = 0$), in the near-hole region downstream of the second row of holes for (*a*) dense jets and (*b*) unit density jets

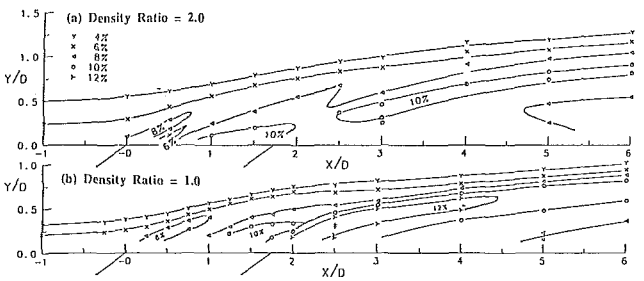

Fig. 10 Turbulence level contours in the vertical plane along the jet centerline ($Z/D = 0$), in the near hole region downstream of the first row of holes for (*a*) dense jets and (*b*) unit density jets (Pietrzyk, 1989)

of holes are found to be at slightly higher levels and narrower in the vertical direction.

The high levels of $\overline{uv}$ shear stresses are evident in the regions where the shear layers formed. In general, the correspondence between the regions of high shear stress and turbulence level was quite good for the second row of holes. For unit density jets, the largest magnitude of $\overline{uv}/U_\infty^2$ measured was -0.006, whereas that for the first row was -0.007. Even though the magnitudes of the highest stress are somewhat similar, the region over which this occurs is much larger and stretched for the first row than the second. It can be hence concluded that

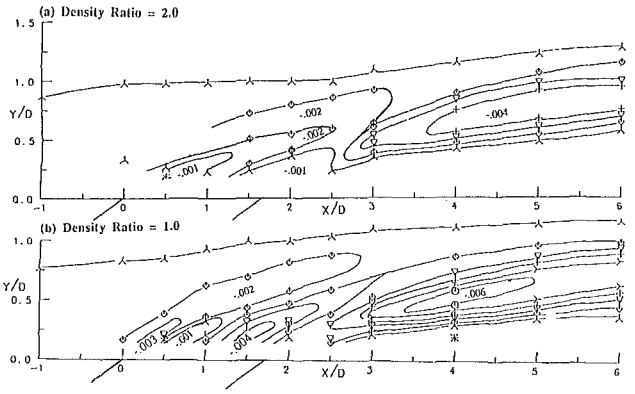

Fig. 11 Contours of normalized *uv* shear stress ($\overline{uv}/U_\infty^2$) in the vertical plane along the jet centerline ($Z/D = 0$), in the near hole region downstream of the second row of holes for (*a*) dense jets and (*b*) unit density jets

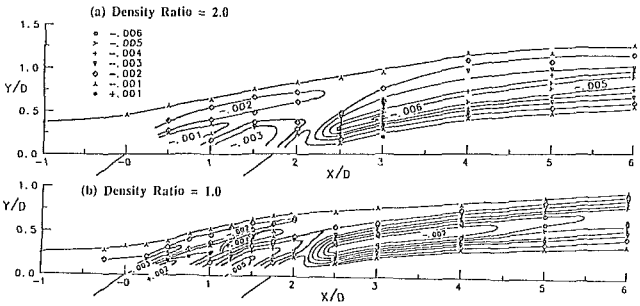

Fig. 12 Contours of normalized *uv* shear stress ($\overline{uv}/U_\infty^2$) in the vertical plane along the jet centerline ($Z/D = 0$), in the near hole region downstream of the first row of holes for (*a*) dense jets and (*b*) unit density jets (Pietrzyk, 1989)

the shear layer over the jet downstream of the first row is stronger than that in front of the second row. The same observation is made for the dense jets too. The difference in the strength of the shear layer is the cause of higher turbulence associated with the first row of holes. This shear layer is formed because of the large difference between the mainstream velocity

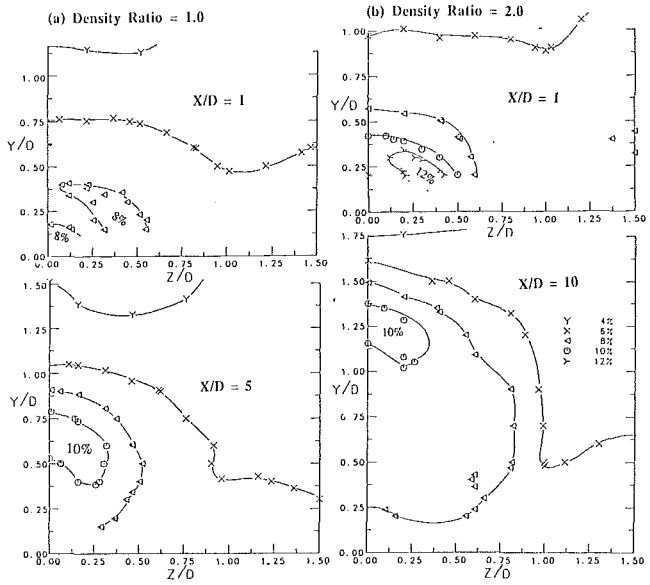

Fig. 13 Turbulence level contours in the vertical lateral planes downstream of the second row for (*a*) unit density jets at *X/D* = 1, 5 and (*b*) dense jets at *X/D* = 1, 10

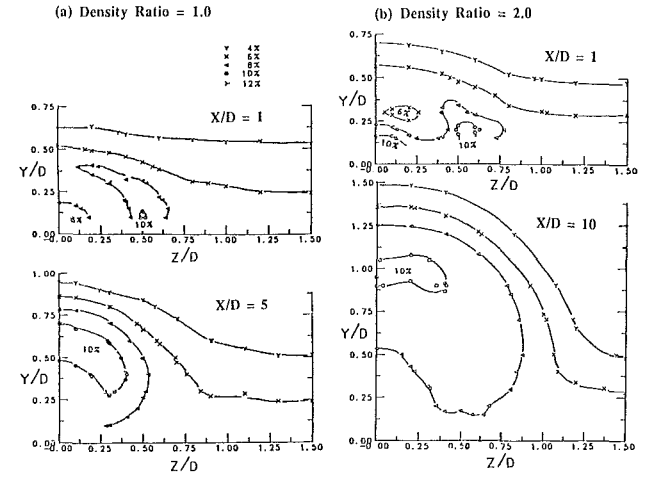

Fig. 14 Turbulence level contours in the vertical lateral planes downstream of the first row for (*a*) unit density jets at *X/D* = 1, 5 and (*b*) dense jets at *X/D* = 1, 10 (Pietrzyk, 1989)

and that occurring within the jet ($V.R. = 0.5$). The levels of velocities in the jet are only slightly lower for the second row than the first. After the first row however the velocity gradients are much stronger due to the smaller boundary layer. These steeper gradients cause the shear layer downstream of the first row to be stronger.

Contours of turbulence levels in vertical lateral Y–Z planes for single and two-row injection are presented in Figs. 13 and 14, respectively. The most important results shown in these two figures is that there is a striking similarity between contours for the first and second row of holes. The magnitude and location of the maximum turbulence level, TL, of 10 percent is the same for both cases. However, the 4 percent TL occurs at a much higher location for the second row due to thicker boundary layer. The higher contour levels consistently extend further in the vertical direction for the second row of holes indicating greater penetration by the jets for the second row of holes. At $x/D = 1$, the TL at the lateral edge of the hole is higher for the first row (10 percent) than the second (8 percent). For the dense jets at $x/D = 1$ higher turbulence levels were observed for the second row (12 percent) than the first at the lateral edge (10 percent). The turbulence field at $x/D = 10$ appears strikingly similar for the first and second rows for dense jets. From the lateral contours it can be concluded that the turbulence field is highly inhomogeneous.

Conclusions

The study considered the fluid mechanics associated with injection from a second row of film-cooling holes whose approaching boundary layer was influenced by a first row of film-cooling holes located 40 diameters upstream. It was found that all the dominant fluid mechanical structures present behind the first row of film-cooling holes are also present downstream of a staggered second row. The differences were mainly in the strength of these structures primarily caused by a much thicker approaching boundary layer at the second row of holes. The thicker boundary layer at the second row resulted in greater penetration of the jets into the mainstream. The boundary layer due to high-density jets was greater than that for unit density jets for the same velocity ratio. The reduced momentum of the cross stream due to thicker boundary layer resulted in reduced velocity gradients in the shear layers and consequently the levels of turbulence generated were slightly lower for the second row. To obtain the same level of film cooling, the momentum flux ratio downstream of the second row should be smaller than that downstream of the first. It must be noted, however, that in an actual turbine blade the temperature of the free stream will be less at the second row than the first, and there will be significant effects of pressure gradient on the boundary layer.

Acknowledgments

The authors gratefully acknowledge Garrett Engine Division of the Allied-Signal Aerospace Company for support of this research. We would also like to thank Dr. Joe Pietrzyk for his assistance in parts of the experiments.

References

Afejuku, W. O., Hay, N., and Lampard, D., 1980, "Film Cooling Effectiveness of Double Rows of Holes," ASME *Journal of Engineering for Power*, Vol. 102, pp. 601–606.

Afejuku, W. O., Hay, N., and Lampard, D., 1983, "Measured Coolant Distributions Downstream of Single and Double Rows of Film Cooling Holes," ASME *Journal of Engineering for Power*, Vol. 105, pp. 172–177.

Jabbari, M. Y., and Goldstein, R. J., 1978, "Adiabatic Wall Temperature an Heat Transfer Downstream of Injection Through Two Rows of Holes," ASME *Journal of Engineering for Power*, Vol. 100, pp. 303–307.

Jubran, B., and Brown, A., 1985, "Film Cooling From Two Rows of Holes Inclined in the Streamwise and Spanwise Directions," ASME *Journal of Engineering for Gas Turbines and Power*, Vol. 107, pp. 84–91.

Mayle, R. E., and Camarata, F. J., 1975, "Multihole Cooling Film Effectiveness and Heat Transfer," ASME *Journal of Heat Transfer*, Vol. 97, pp. 534–538.

Muska, J. F., Fish, R. W., and Suo, M., 1975, "The Additive Nature of Film Cooling for Rows of Holes," ASME Paper No. 75-WA/GT-17.

Pietrzyk, J. R., 1989, "Experimental Study of Dense Jets With a Crossflow for Gas Turbine Applications," Ph.D. Dissertation, Univ. of Texas at Austin.

Pietrzyk, J. R., Bogard, D. G., and Crawford, M. E., 1989, "Hydrodynamics Measurements of Jets in Crossflow for Gas Turbine Film Cooling Applications," ASME JOURNAL OF TURBOMACHINERY, Vol. 111, No. 2, pp. 139–145.

Pietrzyk, J. R., Bogard, D. G., and Crawford, M. E., 1990, "Effects of Density Ratio on the Hydrodynamics of Film Cooling," ASME JOURNAL OF TURBOMACHINERY, Vol. 112, pp. 437–443.

Sellers, J. P., 1963, "Gaseous Film Cooling With Multiple Injection Stations," *AIAA J.*, Vol. 1, pp. 2154–2156.

Thole, K. A., Sinha, A. K., Bogard, D. G., and Crawford, M. E., 1990, "Mean Temperature Measurements of Jets in Crossflow for Gas Turbine Film Cooling Application," to be presented at the 3rd International Symposium on Transport Phenomena and Dynamics of Rotating Machinery, Honolulu, HI, Apr.

Yavuzkurt, S., Moffat, R. J., and Kays, W. M., 1980, "Full-Coverage Film Cooling. Part 1. Three-Dimensional Measurements of Turbulence Structure," *J. Fluid Mechanics*, Vol. 101, pp. 129–158.

Velocity and Temperature Profiles for Stagnation Film Cooling

R. E. Mayle
Mem. ASME

A. Anderson

Department of Mechanical Engineering,
Rensselaer Polytechnic Institute,
Troy, NY 12180

Experiments were conducted for film cooling through rows of slanted holes into the stagnation region of a two-dimensional blunt body with a circular leading edge. The rows were located at ±15 deg +44 deg from stagnation. The holes in each row were spaced four hole diameters apart and were angled 30 deg to the surface in the spanwise direction. Detailed velocity and temperature measurements were obtained downstream of injection. Measurements were taken for three secondary-to-incident flow mass flux ratios at various streamwise and spanwise positions. The results show large initial spanwise variations and indicate that the injected secondary flow at high mass flux ratios actually leaves the surface. In addition, it was found that the aerodynamic loss caused by injection increases linearly with the mass injected and that for a given hole pattern, there is an optimum blowing rate at which the injected fluid from one row of holes does not interfere with that from the other.

Introduction

It is now rather common to film cool the leading edge of airfoils in the first stage of a gas turbine engine. Usually, the air used to form the protective cool layer of air between the hot mainstream gas and the leading edge is injected through numerous holes after passing through an internal cooling channel in the leading edge of the airfoil. Considering a simple one-dimensional heat transfer model of the leading edge, it is easily shown that most of the overall cooling effect results from the convective heat pickup in the holes and not from the film. In this sense, the film provides a bonus cooling effect. However, as the turbine inlet temperature continued to rise through the years, designers depended more on the film's effect to maintain the required leading edge metal temperatures and now it has become imperative to predict the films effectiveness with accuracy. In addition, since the leading edge boundary layer is drastically altered by the film, its condition immediately after injection is required to predict the subsequent boundary layer development along the airfoil.

Most film cooling investigations have been concerned with injection through a slot or rows of holes on a flat or mildly curved surface under a variety of mainstream conditions. Metzger and Fletcher (1969), Goldstein (1971), Ericksen and Goldstein (1974), Mayle et al. (1977), and Ito et al. (1977) are representative samples. In general, the conditions under which these investigations were conducted are rather simple and for the simplest, if the conditions immediately after injection are known, an analytical solution can be obtained as shown by Mayle and Kopper (1976).

In contrast, film cooling on the leading edge of an airfoil is much more complex. By injecting fluid into the stagnation region, one must now consider the additional effects of high acceleration, thin boundary layers, and coolant injection at angles nearly opposite to the main flow direction. The latter is the result of trying to drill holes into the leading edge of an airfoil. Discharge coefficients for injection into a stagnation region were determined by Tillman and Jen (1984) and Tillman et al. (1985) for a large variety of injection geometries and blowing rates. Hanus and L'Ecuyer (1977) obtained spanwise-averaged Stanton numbers for a single row of holes on the leading edge of a turbine vane with injection at different mass flux ratios, row locations, and coolant hole injection angles. Luckey et al. (1977) measured the local Stanton number for various mass flux ratios by using a circular cylinder to model the leading edge region. This work was later extended by Luckey and L'Ecuyer (1981) to include 2, 3, and 5-row injection configurations. In each case, large spanwise variations in the surface heat flux were detected, the pattern of which varied with mass flux ratio. Recently, Camci and Arts (1985) measured heat transfer in and downstream of the leading edge region under typical engine conditions. A somewhat different approach to the problem was taken by Wadia and Nealy (1985), whose measurements include the heat transferred on the coolant side and in the holes as well as on the film-cooled side of the leading edge.

Using a flat-sided model with a circular leading edge (as in the present study), Sasaki et al. (1976) and Mick and Mayle (1986) measured the local film effectiveness distributions for various injection mass flux ratios both within the injection pattern and to distances far downstream of injection. Mick and Mayle also measured the corresponding local heat transfer distributions. Again, large spanwise variations were detected and the mass flux ratio that provided the highest protection near the leading edge was found not to produce the highest protection farther downstream. In addition, Mick and Mayle determined that using a high blowing rate can actually be detrimental to the overall cooling effectiveness of the leading edge.

The present work was undertaken as an extension of that done by Mick and Mayle (1986). In particular, the streamwise

Contributed by the International Gas Turbine Institute and presented at the ASME Winter Annual Meeting, San Francisco, California, December 10–15, 1989. Manuscript received at ASME Headquarters December 1990.

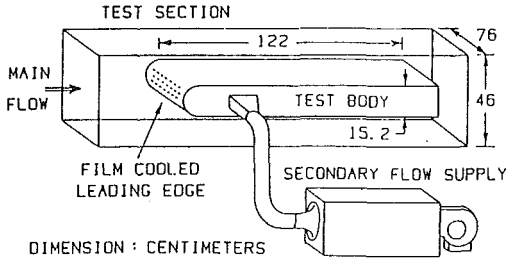

Fig. 1 Test facility

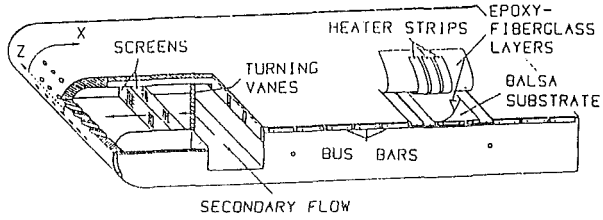

Fig. 2 Leading edge film cooling test body

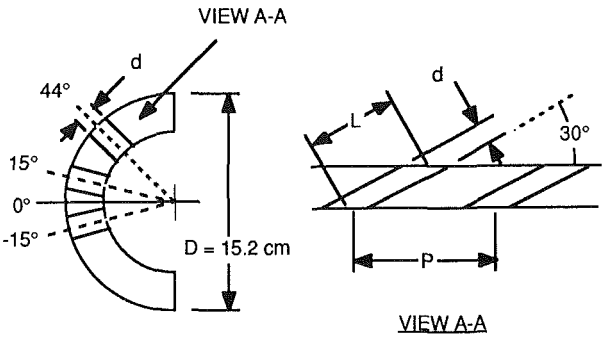

Fig. 3 Injection hole geometry

velocity and temperature distributions in the flow field were measured. Although measurements of the normal and spanwise components of velocity and the various turbulence quantities were not obtained, it is hoped that the new information, together with the film effectiveness and heat transfer measurements reported earlier, will help those who wish to model film cooling numerically on the leading edge of a gas turbine airfoil. The interested reader may also wish to see a related paper by Bellows and Mayle (1986) who investigated the flow on a similar model but without leading edge injection.

Experimental Apparatus

The primary air system was a low-speed, open-circuit wind tunnel with a straight, rectangular test section 46 cm high by 76 cm wide. The incident flow velocity in the test section was nominally maintained at 9.8 m/s and was uniform to within one-half of one percent. Air leaving the test section entered the laboratory, mixed with the surrounding air and circulated back to the inlet of the tunnel's centrifugal fan. An air conditioner in the room with its sensor placed in the tunnel automatically controlled the air temperature to within 1°C.

The secondary air system supplied air to the leading edge film holes. This air could be heated uniformly by a series of Nichrome wire grids strung across the flow in a heater section of the system. An insulated duct carried this heated air to a plenum inside the test model. Its temperature was measured by two thermocouples centrally located in two of the holes on either side of the hole pattern. The secondary-air mass flow rate was measured using a calibrated nozzle at the exit of the heater section.

The test model spanned the entire width of the test section as shown in Fig. 1 and was held in position by steel rods passing through it and each side wall of the test section. It was centered between the top and bottom walls and could be pivoted about the front rod to position the stagnation line at the model's midplane on the leading edge.

The test body and film hole geometry were the same as Mick and Mayle's. The test body had a cylindrical, semicircular leading edge with a 7.6-cm radius, which smoothly joined two parallel, flat, 1.22-m-long surfaces as shown in Fig. 2. It was constructed mostly of wood and had a composite, constant-heat-flux surface attached on a 13-mm-thick balsa wood substrate. For this series of tests, however, the surface was never heated. Nevertheless, it was virtually an adiabatic surface such that the attached thermocouples could be used to measure the distribution of adiabatic wall temperatures. The plenum in the forward portion of the model uniformly distributed the secondary flow from an inlet in the model's side to the leading edge holes. This was accomplished by turning and diffusing the flow through numerous, thin turning vanes designed according to Salter (1946). Measurements of the centerline velocity for each hole indicated that the flow through all holes in a row was the same to within ±8 percent for the rows closest to stagnation and ±3 percent for the furthest row.

The film hole geometry is shown in Fig. 3. Rows of circular holes were located at ±15 deg and at +44 deg from the stagnation line. This configuration is equivalent to a four-row, symmetric injection scheme since the row that would exist at −44 deg does not affect the results above the stagnation line. Because of its proximity to the stagnation line, however, the same cannot be said about the row at −15 deg. Each hole had

Nomenclature

C_f = skin friction coefficient
d = injection hole diameter
D = leading edge diameter
I = average secondary-to-incident momentum flux ratio
L = length of injection hole
M = average secondary-to-incident mass flux ratio
P = pitch of holes in row
Re_D = Reynolds number based on the incident velocity and leading edge diameter
T = temperature
T_{aw} = adiabatic wall temperature
T_s = secondary or injected air temperature
T_∞ = mainstream or incident air temperature
u = streamwise velocity component
U = local free-stream velocity
U_s = average secondary air exit velocity
U_∞ = incident air velocity
x = streamwise distance measured from stagnation
y = distance normal to the surface
z = spanwise distance
δ_1 = displacement thickness
δ_2 = momentum thickness
Δ_2 = enthalpy thickness
η = adiabatic film effectiveness
ρ_s = secondary or injected air density
ρ_∞ = mainstream or incident air density
τ = wall shear stress

a diameter of $d = 1.52$ cm and was angled at 30 and 90 deg to the surface in the spanwise and streamwise directions, respectively. There were seven holes spaced four diameters apart, $P/d = 4$, in each row. The holes in each row were shifted one-half pitch in the spanwise direction from those in the previous row, forming what is normally called a staggered array of holes. The hole-to-leading edge diameter ratio was $d/D = 0.1$ and the hole length-to-diameter ratio was $L/d = 4$.

The surface temperatures were measured using a total of 118 0.075-mm thermocouples bonded in the surface. Their leads ran in opposite directions along the surface for a short distance to minimize heat loss and then through the surface. A number of thermocouples were attached to the back of the surface in order to determine the conduction loss through the model's surface. All the thermocouples were placed within the central spanwise portion of the test body with some thermocouple positions duplicated across the span. Although data from all the thermocouples were recorded, only those where velocity and temperature profiles were measured were used for checking the temperature near the surface as measured by the boundary layer probe. These results were found to be in excellent agreement once the thermocouple conduction losses were taken into account. A more detailed account of the thermocouple positions and analysis can be found in Mick (1983).

Surface pressure taps were installed in the model at the location of each row of holes in order to measure the secondary-air exit pressure. Pressure taps were also provided on the top and bottom of the model and along its span to align the model.

The velocity measurements were obtained with a TSI 1051 hot-wire anemometer system with a single, 3.8-μm tungsten wire probe. Temperature measurements were taken using the same probe by switching the unit from a constant-temperature operating mode to a resistance-thermometer mode. This was handled by a computer, which also controlled the probe traverse device and collected the data. With this arrangement the velocity and temperature measurements could be taken at exactly the same locations, but, of course, not simultaneously. In fact, a small time between measurements was scheduled to allow the wire to reach its new equilibrium state. The hot wire was calibrated in a heated jet tunnel specifically constructed for the purpose and the results correlated according to

$$u = B_0 + B_1 \left(\frac{E}{\Delta T}\right)^2 + B_2 \left(\frac{E}{\Delta T}\right)^3 + B_3 \left(\frac{E}{\Delta T}\right)^4$$

where E is the wire voltage, ΔT is the wire-to-air temperature difference, and the B_i's are calibration constants.This expression is inverse of that used by Taslim et al. (1978), which has the form $E/\Delta T = fnc(u)$. Theirs was found to be generally acceptable but required a time-consuming iteration to solve for the velocity. Surprisingly, neither expression explicitly includes the effects of fluid property changes with temperature such as the modified version of King's law proposed by Bradshaw (1971); however, both equations were more accurate than Bradshaw's. Apparently, the temperature dependence is simply confined to the quantity ΔT. To reduce probe interference, all measurements were made using the probe inclined 45 deg into the flow. This was done by plugging the probe into a 45 deg adapter attached to the vertical probe stem such that the wire was held parallel to the surface and perpendicular to the mainstream flow direction. The errors in measuring velocity and temperature are estimated to be about 10 cm/s and 0.2°C, respectively.

An energy balance was performed for each mass flux ratio as a check on the experimental methods. The total influx of energy from one pitch of holes was compared to the energy contained in the thermal boundary layer at the various streamwise measurement locations. When corrections were made for losses to radiation and conduction through the model's surface, which varied along the surface from 3 to 10 percent of the injected energy, the energy in the boundary layer was found to be within 14 percent of that injected for the three mass flux ratios.

Test Conditions

The tests were conducted with an incident air flow velocity of 9.8 m/s at a temperature of 18°C and with a turbulence level of 0.4 percent.This provided an incident flow Reynolds number of 100,000. The secondary air temperature was maintained approximately 30°C above the mainstream, which yields a secondary-to-mainstream density ratio, ρ_s/ρ_∞, of 0.91. Tests at correct engine density ratios are presently being conducted. All measurements were acquired during a steady-state period of operation, which was normally attained after about three hours.

Measurements were obtained at three secondary-to-incident mass flux ratios, $M = (\rho U)_s/(\rho U)_\infty$, of 0.38, 0.64, and 0.97. These values are based on the average mass flow injected through only the two upper rows of holes at +15 deg and +44 deg even though air was always injected through all of the rows. On this basis, the present results may be compared directly to other symmetric four-row injection schemes having the same mass flux ratio. The flow split between the three rows of holes was determined by measuring the centerline velocity in each hole and forming a ratio between the average centerline velocity in each row. The ratio of the flow in the row at +44 deg to that at +15 deg was found to be 2.97, 2.44, and 1.72 for $M = 0.38$, 0.64, and 0.97, respectively. These flow splits result from the different exit pressures at each row caused by the mainstream flow around the leading edge, and are expected to be similar to those for leading edge film cooling of a gas turbine airfoil. The flows from the rows of holes at ±15 deg were always within 10 percent of each other.

Velocity and temperature profiles were measured at the streamwise positions of $x/d = 9$, 16, 27, and 52, where x is measured from stagnation, and at the spanwise positions of $z/P = 0$, 0.25, 0.50, 0.75, and 1.00. The spanwise distance z was measured from the obtuse lip of the center hole in the most downstream row. In addition, for $M = 0.64$, measurements were taken at $x/d = 42$ and 70, and at $z/P = 0.125$, 0.375, 0.625, and 0.875 for $x/d = 9$. The measurements at $z/P = 0$ and 1.0 were taken to check spanwise periodicity even though the surface measurements of Mick and Mayle indicated a periodic situation exists for this model. In the present study, comparisons of the momentum and enthalpy thicknesses at $z/P = 0$ and 1.0 were found to agree to within 10 and 13 percent, respectively.

Results

The velocity profiles at $x/d = 9$ are shown in Figs. 4(*a*, *b*, *c*) for the mass flux ratios of 0.38, 0.64, and 0.97, respectively. Here u is the streamwise velocity component and U is the local free-stream velocity. Although only the streamwise component of velocity has been measured, it is no more than 3 percent less than the actual velocity at any of the positions reported here. This estimate was obtained from the results of Mick and Mayle, which show, at $x/d = 9$ and downstream, that the largest spanwise migration of the flow caused by injection is for $M = 0.97$ and its angle is about 13 deg from the streamwise direction. The corresponding temperature profiles are shown in Figs. 5(*a, b, c*). In contrast to the usual method of displaying these profiles using the local adiabatic wall and free-stream temperature difference, $T_{aw} - T_\infty$, to normalize the temperature, the secondary air and free-stream temperature difference, $T_s - T_\infty$, has been used. This helps in comparing the results at various spanwise locations.

As might be expected from such an injection scheme, the resulting flow is by no means two dimensional. Large spanwise

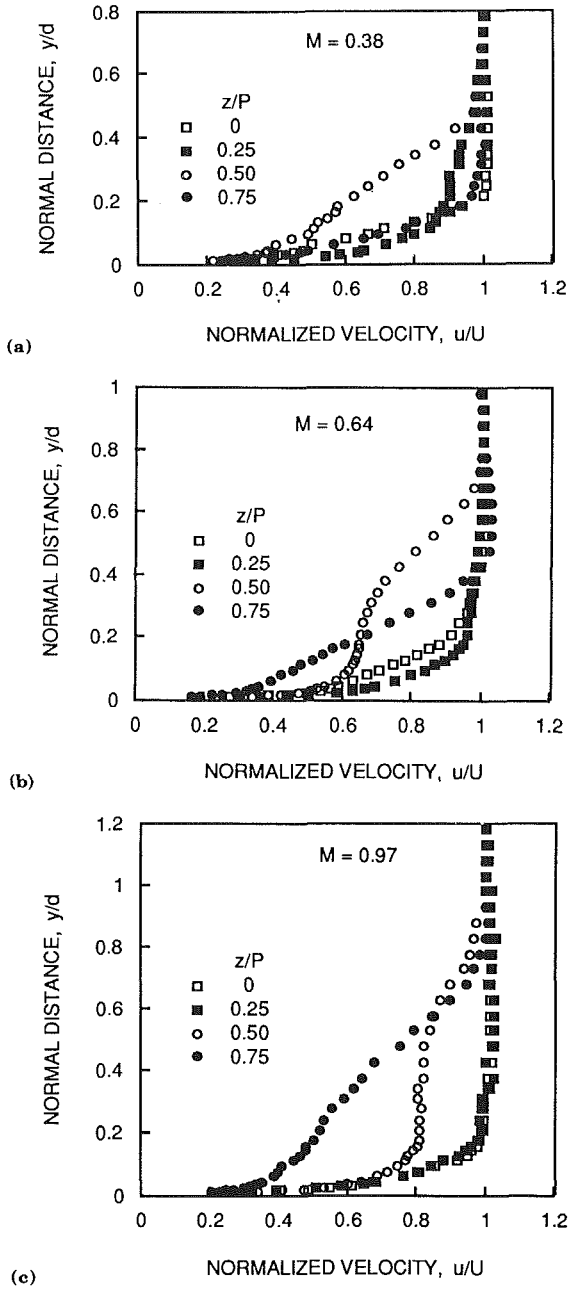

Fig. 4 Velocity profiles for (*a*) $M = 0.38$, (*b*) $M = 0.64$, and (*c*) $M = 0.97$

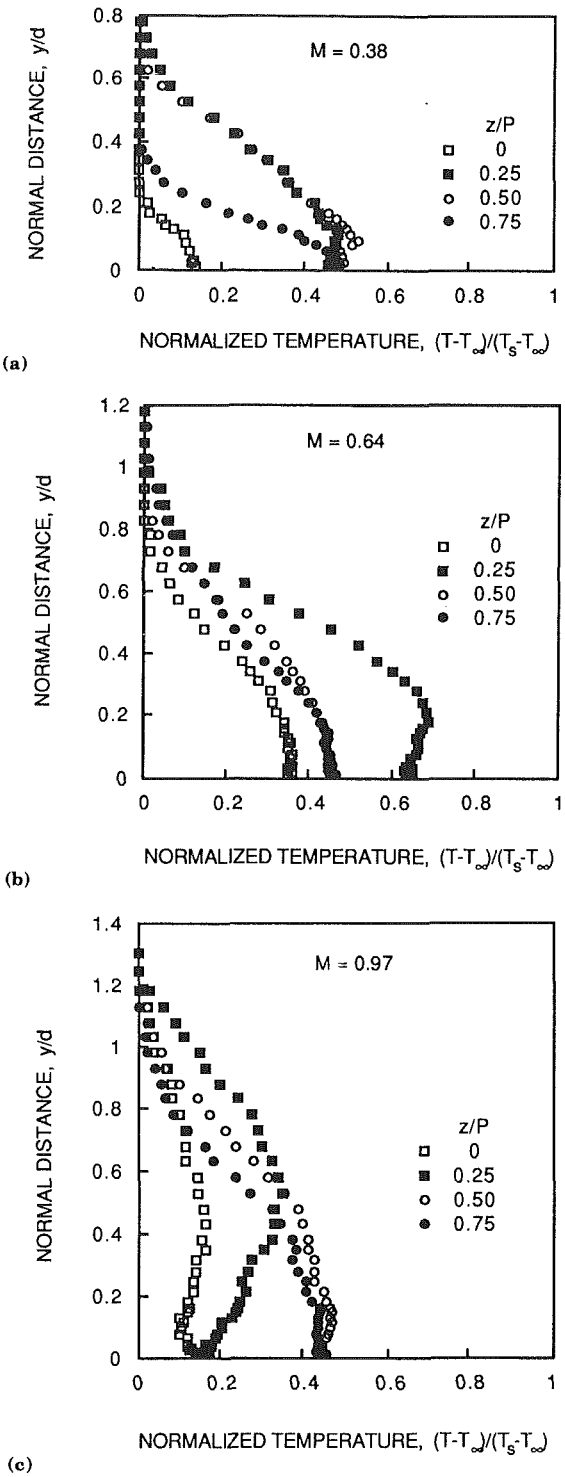

Fig. 5 Temperature profiles for (*a*) $M = 0.38$, (*b*) $M = 0.64$, and (*c*) $M = 0.97$

variations in both the velocity and temperature distributions are found at this streamwise position. Note that $x/d = 9$ corresponds to a position of 4.7 hole diameters downstream of the last row of holes, which is about one hole diameter down on the flat portion of the model. At some spanwise locations, namely at $z/P = 0.5$ and 0.75, the injected flow produces a noticeable momentum deficit. This is a result of injection in the spanwise direction, which, of course, adds no streamwise momentum to the flow. At the lower blowing rates, the injected fluid remains near the wall, while at the highest most of the fluid is injected into the flow away from the surface letting the mainstream air move under the jets. The latter is revealed by maximum temperature differences within the flow. In any case, the effect of increasing the blowing rate from 0.38 to 0.97 is to thicken the boundary layer from about $0.8d$ to $1.2d$. Consequently, the secondary flow penetrates into the flow about one hole diameter, which is about three times the boundary layer thickness on the leading edge. The latter, as measured by Bellows and Mayle (1986), is about $0.3d$. Hence, leading edge injection completely changes the nature of the flow from that which would have existed without injection. This, in turn, also affects the boundary layer development further downstream.

Spanwise distributions of displacement, momentum, and enthalpy thicknesses at $x/d = 9$ are provided in Figs. 6(*a*, *b*, *c*). These thicknesses are defined as follows:

$$\delta_1 = \int_0^\infty \left(1 - \frac{\rho u}{\rho_\infty U}\right) dy \text{ (displacement thickness)}$$

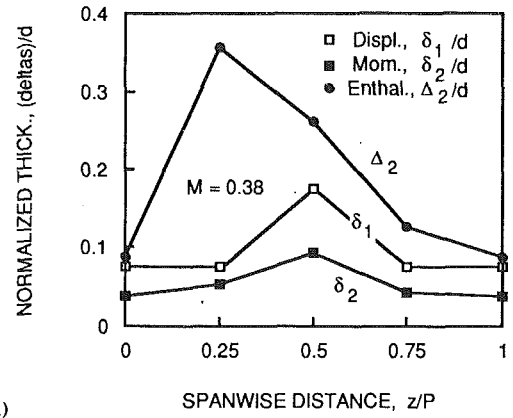

(a)

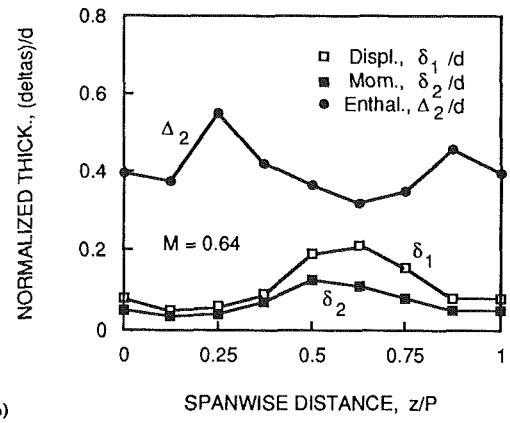

(b)

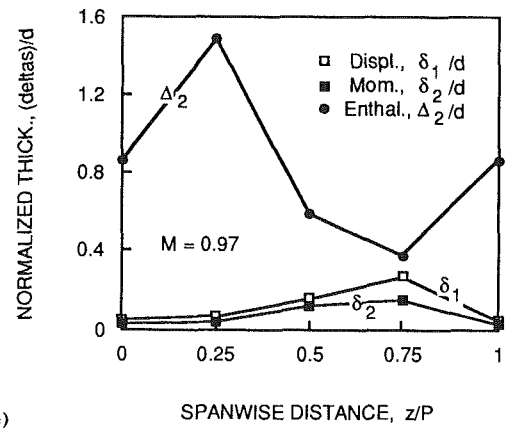

(c)

Fig. 6 Displacement, momentum, and enthalpy thickness distributions at x/d = 9 for (*a*) M = 0.38, (*b*) M = 0.64, and (*c*) M = 0.97

$$\delta_2 = \int_0^\infty \left(\frac{\rho u}{\rho_\infty U}\right)\left(1-\frac{u}{U}\right) dy \text{ (momentum thickness)}$$

and

$$\Delta_2 = \int_0^\infty \left(\frac{\rho u}{\rho_\infty U}\right)\left(\frac{T-T_\infty}{T_{aw}-T_\infty}\right) dy \text{ (enthalpy thickness)}$$

The corresponding distributions of the skin friction coefficients, $C_f = 2\tau/\rho_\infty U^2$ where τ is the wall shear stress, are presented in Fig. 7. These were obtained from Clauser plots by fitting the velocity profiles to the law of the wall. In Fig. 8, the spanwise distributions of the adiabatic wall effectiveness η at x/d = 9 for the three blowing rates are shown. The adiabatic wall effectiveness was obtained from

$$\eta = \left[\frac{T-T_\infty}{T_s-T_\infty}\right]_{y/d=0} = \frac{T_{aw}-T_\infty}{T_s-T_\infty}$$

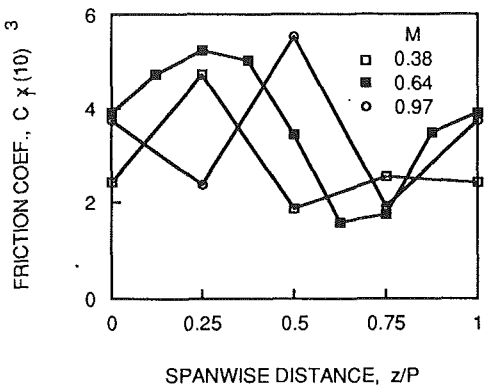

Fig. 7 Skin friction coefficient distributions at x/d = 9

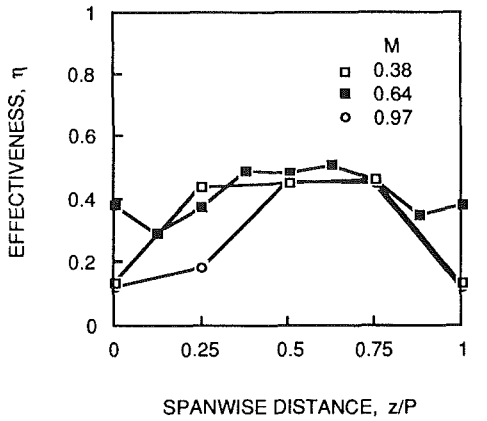

Fig. 8 Adiabatic wall effectiveness distributions at x/d = 9

after fitting the data near the wall with a cubic equation in y. This results by expanding the temperature as a a function of distance away from the wall, using $(\partial T/\partial y)_{y=0} = 0$ and the energy equation.

As the mass flux is increased, the maximum in the displacement and momentum thicknesses, Figs. 6(*a*, *b*, *c*), shifts to the right (direction of injection) indicating that the jet penetrates the mainstream flow farther before turning into the streamwise direction. The skin friction coefficient is a minimum at these locations and the adiabatic wall effectiveness is a maximum. For M = 0.64, the enthalpy thickness distribution is more or less constant compared to those for the other mass flux ratios, as is the effectiveness. This is because the flow from the second row of holes at 44 deg is injected between that from the first row (see Mick and Mayle), whereas for both M = 0.34 and 0.97 the injected flows from the two rows of holes interfere with each other. For M = 0.97, the jets from the last row actually leave the surface completely and move more than one spanwise pitch to a position nearly behind the next hole in the row producing a maximum in Δ_2 at z/P = 0.25. Therefore, to gain the maximum effectiveness from a leading edge film cooling scheme, one must consider the spanwise placement of the holes relative to the injected flow rate, or more correctly stated, relative to the injected momentum flux ratio.

The spanwise-averaged momentum thickness at x/d = 9, normalized using the hole diameter, is plotted against the mass flux ratio in Fig. 9. The momentum thickness without blowing was found by Bellows and Mayle to be about 0.6 mm or δ_2/d = 0.04. A simple momentum balance for injection of a secondary flow in the spanwise direction provides an increase in the momentum thickness caused by blowing to be $\Delta\delta_2/d \propto M(d/P)$. By fitting the data shown in Fig. 9, the proportionality constant for the present configuration is 0.17.

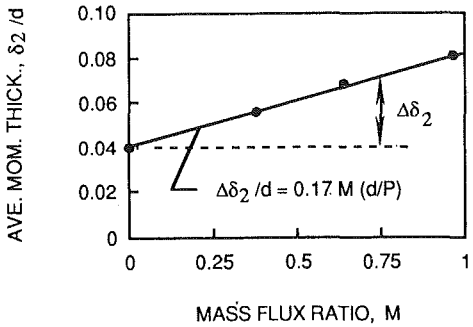

Fig. 9 Spanwise-averaged momentum thickness at $x/d = 9$ versus the mass flux ratio

Table 1

M	δ_1/d	δ_2/d	Δ_2/d	$C_f x10^3$
0.38	0.25	0.19	0.99	4.0
0.64	0.25	0.19	1.08	3.8
0.97	0.28	0.21	1.44	3.7

Although not shown here, the velocity and temperature profiles farther downstream are more two dimensional. The velocity profiles are characteristically turbulent while the temperature profiles are similar to that predicted by Wieghardt (1946). The spanwise-averaged thickness and skin friction coefficients at $x/d = 52$ are presented in Table 1. Except for the enthalpy thickness the results do not change much with blowing rate. Interested readers are referred to Anderson (1985) for details.

Streamwise distributions of the spanwise-averaged adiabatic wall effectiveness $\bar{\eta}$ are shown in Fig. 10. The lines represent the results of Mick and Mayle. In general, the two sets of data agree reasonably well, although the effectiveness from this study tends to be slightly lower at the upstream locations. The cause is most likely that in the upstream region ($x/d < 30$), heat is conducted from the interior plenum of the test body through the insulating balsa wood substrate to the surface, and this heat must be conducted to the air. Therefore a temperature difference must exist between the wall and the air above it, so this study's results, being based on air temperature near the wall, will be lower than the previous study's based on wall temperatures. Nevertheless, the trends are the same. While the effectiveness for the two lower blowing rates is highest close to injection, it is highest farther downstream for the two higher blowing rates. This is relatively easy to understand considering the results discussed above. For $M = 0.38$, the secondary fluid is injected near the surface, but there isn't enough mass to sustain a high effectiveness. On the other hand, for $M = 0.97$, the secondary fluid is injected into the mainstream flow away from the wall, which yields an initially low effectiveness, but because a large amount is injected the effectiveness decreases little downstream. Besides, for both $M = 0.38$ and 0.97, the fluid from one row of holes interferes with that from the other. Thus, based on film effectiveness, it appears that the intermediate blowing rate of $M = 0.64$ is an optimum. However, as shown by Mick and Mayle (Fig. 9), the designer of a leading edge cooling scheme must beware of basing a design on film effectiveness alone since the effect of injection on the heat transfer coefficients is significant. In fact, they found that near the holes $M = 0.34$ provided the best protection, while farther downstream $M = 0.64$ was the best. Since the penetration of the secondary flow into the mainstream depends on the momentum flux and not mass flux, one should expect this situation to change for higher density ratios. In fact, for engine conditions, one should expect higher mass flux ratios to be better.

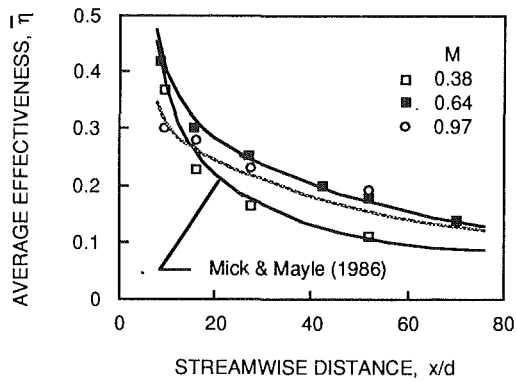

Fig. 10 Streamwise variations of the spanwise-averaged film effectiveness

Conclusions

The velocity and temperature profiles presented herein indicate that for high blowing rates, the jets of the injected secondary flow separate from the surface immediately. Since the main part of the jet is off the surface, much of its beneficial effect is lost, negating the advantage of the greater amount of mass being injected. For the lower mass flux ratios, the injected fluid remains close to the surface and so improves the adiabatic wall effectiveness. However, and obviously, if the blowing rate is too low, the benefit of better flow characteristics will be lost to the lack of a sufficient amount of secondary fluid. Therefore, as found here, an intermediate mass flux ratio provides the best film effectiveness. In addition, it was found at $M = 0.64$ that the flow from one row of holes did not interfere with the other. Hence, a designer must separately take into account the optimum blowing rate for maintaining the coolant near the wall and the optimum placement of the holes for that blowing rate.

In any case, the boundary layer thickness with leading edge injection, about one hole diameter in size, is much larger than that without and is highly three dimensional. Since most present-day design systems take neither one of these effects into account to predict heat loads on airfoils with leading edge film cooling, a re-evaluation of these design systems is in order.

Finally, it was found that the aerodynamic loss caused by injecting secondary fluid in the stagnation region in the spanwise direction is directly proportional to the mass flux ratio. This is in agreement with theory. In particular, it was found that the loss, expressed as an increase in momentum thickness, was $\Delta\delta_2/d = 0.17M(d/P)$.

Acknowledgments

The work reported in this paper was sponsored by Pratt & Whitney Group, United Technologies Corporation, East Hartford, CT.

References

Anderson, A. T., 1985, "Velocity and Temperature Profiles in Leading-Edge Film Cooling of Gas Turbine Blades," Master's Thesis, Rensselaer Polytechnic Institute, Troy, NY.

Bellows, W. J., and Mayle, R. E., 1986, "Heat Transfer Downstream of a Leading Edge Separation Bubble," ASME JOURNAL OF TURBOMACHINERY, Vol. 108, pp. 131–136.

Bradshw, P., 1971, *An Introduction to Turbulence and Its Measurement*, Pergamon Press, New York.

Camci, C., and Arts, T., 1985, "Experimental Heat Transfer Investigation Around the Film-Cooled Leading Edge of a High Pressure Gas Turbine Rotor Blade," ASME *Journal of Engineering for Gas Turbines and Power*, Vol. 107, pp. 1016–1021.

Ericksen, V. L., and Goldstein, R. J., 1974, "Heat Transfer and Film Cooling Following Injection Through Inclined Circular Tubes," ASME *Journal of Heat Transfer*, Vol. 96, pp. 239–245.

Goldstein, R. J., 1971, "Film Cooling," *Advances in Heat Transfer*, Vol. 7, Academic Press, New York.

Hanus, G. J., and L'Ecuyer, M. R., 1977, "Leading Edge Injection for Film Cooling of Turbine Vanes," *Journal of Energy*, Vol. 1, pp. 44–49.

Ito, S., Goldstein, R. J., and Eckert, E. R. G., 1977, "Film Cooling of a Gas Turbine Blade," Paper No. 03, presented at the 1977 Tokyo Joint Gas Turbine Congress.

Luckey, D., and L'Ecuyer, M. R., 1981, "Stagnation Region Gas Film Cooling—Spanwise Angled Injection From Multiple Rows of Holes," NASA CR 165333.

Luckey, D., Winstanley,D., Hanus, G. J., and L'Ecuyer, M. R., 1977, "Stagnation Region Gas Film Cooling for Turbine Blade Leading Edge Applications," *Journal of Aircraft*, Vol. 14, No. 5, pp. 494–501.

Mayle, R. E., and Kopper, K. C., 1976, "Adiabatic Wall Effectiveness of a Turbine Boundary Layer With Slot Injection," ASME *Journal of Heat Transfer*, Vol. 98, No. 2, pp. 240–244.

Mayle, R. E., Kopper, F. C., Blair, M. F., and Bailey, D. A., 1977, "Effect of Streamline Curvature on Film Cooling," ASME *Journal of Engineering for Power*, Vol. 99, pp. 77–82.

Metzger, D. E., and Fletcher, D. D., 1969, "Surface Heat Transfer Immediately Downstream of Flush, Non-tangential Injection Holes and Slots," AIAA Paper No. 69-523.

Mick, W. J., 1983, "An Experimental Study of Stagnation Region Film Cooling for Application to Gas Turbine Airfoils," Master's Thesis, Rensselaer Polytechnic Institute, Troy, N.Y.

Mick, W. J., and Mayle, R. E., 1988, "Stagnation Film Cooling and Heat Transfer Including Its Effect Without the Hole Pattern," ASME JOURNAL OF TURBOMACHINERY, Vol. 110, pp. 66–72.

Salter, C., 1946, "Experiments on Thin Turning Vanes," ARC RM 2469.

Sasaki, M., Takahoru, K., Sakata, K., and Kumagai, T., 1976, "Study on Film Cooling of Turbine Blades," *Bulletin Japan Soc. Mech. Engrs.*, Vol. 19, No. 137, pp. 1344–1352.

Taslim, T. E., Kline, S. J., and Moffat, R. J., 1978, "Calibration of Hot-Wires and Hot-Films for Velocity Fluctuations," Mechanical Engineering Department, Stanford University, Stanford, CA, Report TMC-4.

Tillman, E. S., and Jen, H. F., 1984, "Cooling Airflow Studies at the Leading Edge of a Film-Cooled Airfoil," ASME *Journal of Engineering for Gas Turbines and Power*, Vol. 106, pp. 214–221.

Tillman, E. S., Hartel, E. O., and Jen, H. F., 1985, "The Prediction of Flow Through Leading Edge Holes in a Film Cooled Airfoil With and Without Inserts," ASME *Journal of Engineering for Gas Turbines and Power*, Vol. 107, pp. 92–98.

Wadia, A. R., and Nealy, D. A., 1985, "Development of a Design Model for Airfoil Leading Edge Film Cooling," ASME Paper No. 85-GT-120.

Wieghardt, K., 1946, "Hot-Air Discharge for De-icing," AAF Translation No. F-TS919-Re, Air Material Command (or see Mayle and Kopper, 1976).

Effect of Acceleration on the Heat Transfer Coefficient on a Film-Cooled Surface

H. D. Ammari

N. Hay

D. Lampard

Department of Mechanical Engineering,
University of Nottingham,
Nottingham, United Kingdom

Results are presented of an experimental investigation into the influence of mainstream acceleration on the heat transfer coefficient downstream of injection through a row of 35 deg holes in a flat plate. A mass transfer analogue technique was used, with two uniform acceleration parameters, K $(=\nu(du_\infty/dx)/u_\infty^2)$, of 1.9×10^{-6} and 5.0×10^{-6} in addition to the zero acceleration baseline case. Two injectants, air and carbon dioxide, were employed to give coolant-to-mainstream density ratios of 1.0 and 1.52, respectively. The blowing rate varied from 0.5 to 2.0. The heat transfer coefficient beneath the film decreased progressively as the acceleration increased, with maximum reductions from the zero acceleration datum case of about 27 percent. In the presence of acceleration, the heat transfer coefficient at a given blowing rate was dependent on the density ratio, an increase in the density ratio leading to a decrease in the heat transfer coefficient. An empirical correlation of the data over most of the range of densities and blowing rates of the experiments has been developed.

Introduction

The high-temperature environment of gas turbine nozzle vanes and rotor blades may necessitate the use of film cooling to protect the exposed surfaces. In film cooling, relatively cool air bled from the compressor is injected onto the blade surface via one or multiple rows of holes.

For heat transfer calculations, the cooling effect is customarily expressed in terms of a heat transfer coefficient, h_f, defined as

$$h_f = q_f/(T_{aw} - T_w)$$

and a film cooling effectiveness, η_{aw}, defined as

$$\eta_{aw} = (T_\infty - T_{aw})/(T_\infty - T_c)$$

where q_f is the wall heat flux, T_w and T_{aw} are the temperatures of the wall and adiabatic wall, respectively, and T_∞ and T_c are the mainstream and coolant temperatures.

In gas turbine practice, large pressure and temperature gradients may be present over film-cooled areas. An appreciation of their influence on the heat transfer coefficient under cooling films, h_f, is vital for heat flux calculations, and, hence, for proper cooling system design. The effect of mainstream pressure gradient in particular has received little attention.

Hartnett et al. (1961) and Warren and Metzger (1972), both blowing via an angled flush slot, found that the effect of low acceleration was weak. In the latter study, an appreciable decrease in the heat transfer coefficient was observed at low blowing rates when the favorable pressure gradient was sufficiently strong for retransition of the turbulent boundary layer to laminar state in the absence of injection. As the blowing rate increased toward unity, the depressed heat transfer coefficients increased toward their fully turbulent values.

Jabbari and Goldstein (1978), using a staggered double row geometry, found that the centerline and spanwise-averaged heat transfer coefficients normalized by those without injection were not affected significantly by acceleration when the blowing rate was less than one. At higher blowing rates, a reduction of about 10 percent was found close to the injection point. This reduction extended farther downstream as the blowing rate increased. The suppression of injection-induced turbulence by mainstream acceleration was suggested as a possible cause.

Liess (1975) gave the suppression of the development of streamwise vortices by the mainstream acceleration as the possible reason for the fall in the spanwise-averaged heat transfer coefficients he found downstream of a single row of 35 deg inclined holes. Hay et al. (1984) used an identical injection angle, and, additionally, normal injection. They reported large

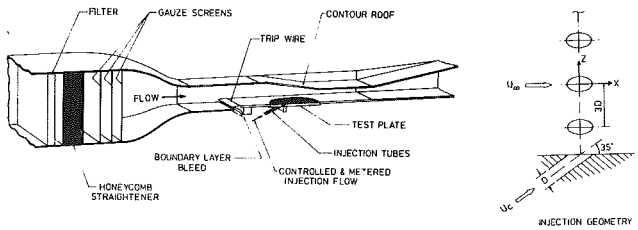

Fig. 1 Wind tunnel arrangement and injection geometry

Contributed by the International Gas Turbine Institute and presented at the 35th International Gas Turbine and Aeroengine Congress and Exposition, Brussels, Belgium, June 11–14, 1990. Manuscript received by the International Gas Turbine Institute January 5, 1990. Paper No. 90-GT-8.

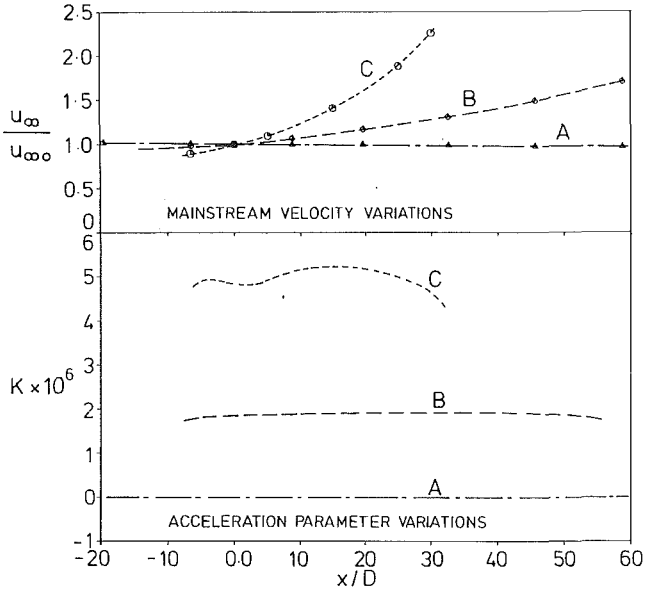

Fig. 2 Variation of mainstream velocity and acceleration parameter in the absence of injection

reductions in the heat transfer coefficient under the film when the blowing rates were low or the acceleration was strong.

By contrast, Kruse (1985) found acceleration effects to be weak for single-row injection at 10, 45, and 90 deg. He also examined the effect of adverse pressure gradient, concluding that this too had only a weak effect on the heat transfer coefficient. This is in agreement with the results of Hay et al. (1984) for a slightly stronger deceleration.

Thus, although it is generally agreed that acceleration reduces the heat transfer coefficient under a cooling film, there is conflicting evidence regarding the strength of the effect. Further, the effect of variation of the jet-to-mainstream density ratio appears not to have been considered in combination with mainstream acceleration.

In this paper, systematic work is presented on the effect of acceleration on the cooling film heat transfer coefficient for injection through a row of 35 deg holes. Density ratios of 1.0 and 1.52 have been used employing air and carbon dioxide injection with a mass transfer analogue technique.

Experimental Technique and Approach

The mass transfer technique employed uses a swollen polymer surface and laser holographic interferometry (Macleod and Todd, 1973). The technique provides high-resolution results over the whole surface under study.

The test surface is coated with a silicone rubber polymer swollen to equilibrium in a swelling agent. The uniform concentration of the swelling agent over the surface simulates an isothermal wall condition. Exposure of the swollen coating to the film cooling flows results in evaporation of the swelling agent such that the recession in the polymer coating thickness is proportional to the local mass transfer coefficient (Macleod and Todd, 1973). The coating recession is measured by laser holographic interferometry, which yields a fringe pattern from which the heat transfer coefficient is deduced. For a more comprehensive description of the technique see Hay et al. (1982).

The heat transfer coefficient, h, measured by the present analogous mass transfer technique when the mass-transferring agent is absent from both the mainstream and coolant flows, corresponds to h_f (Ammari et al., 1990).

Apparatus and Test Conditions

The experiments were conducted in a subsonic, low turbulence, open-circuit wind tunnel (Fig. 1). A description of the tunnel and its test section is given elsewhere (Ammari et al., 1989). Contoured roofs were fixed to the top wall of the test section in order to produce the required uniform accelerations.

The injection geometry is shown in Fig. 1. Two gas injectants were used: air drawn from the same supply as the mainstream and carbon dioxide fed from pressurized bottles. The injectant was regulated, controlled, and metered, then passed through a plenum chamber containing a straightener and gauze screens before entering the injection tubes.

Steady-state, isothermal conditions prevailed during all tests. The experimental main parameters and operating conditions were:

- Injection hole diameter = 2.30 mm
- Hole spacing to diameter ratio = 3.0
- Injection hole streamwise inclination = 35 deg
- Number of injection holes = 7
- Mainstream velocity at the injection location = 25 m/s, giving a Reynolds number, $Re_D = 3.8 \times 10^3$ for all cases considered.
- The mainstream intensity of turbulence was 0.68 percent.
- The approaching boundary layer was fully developed, two dimensional, and turbulent.
- In absence of acceleration the boundary layer displacement thickness to hole diameter ratio, δ^*/D, at the injection location was 0.40.
- The flow within the injection tube exits was fully developed

Nomenclature

D = injection hole diameter
h = heat transfer coefficient
$\bar{h}$ = lateral average heat transfer coefficient
I = momentum flux ratio $= \rho_c u_c^2/\rho_\infty u_\infty^2$
K = acceleration parameter $= \nu(du_\infty/dx)/u_\infty^2$
M = blowing rate (mass flux ratio $= \rho_c u_c/\rho_\infty u_\infty$)
q = heat flux
Re = Reynolds number
s = distance between centers of injection holds
Tu = turbulence intensity
u = velocity component in x direction
u' = time-averaged rms fluctuating velocity in x direction
x = downstream distance from injection hole center
y = vertical distance from the test surface
z = lateral distance from injection hole center
α = injection inclination to the streamwise direction
δ = thickness of boundary layer
δ^* = boundary layer displacement thickness
η = effectiveness
ν = kinematic viscosity
ρ = density

Subscripts

aw = adiabatic wall
c = coolant
D = injection hole diameter
f = injection
MF = moderate favorable pressure gradient
o = zero injection
oMF = zero injection, moderate favorable pressure gradient
oSF = zero injection, strong favorable pressure gradient
SF = strong favorable pressure gradient
∞ = mainstream
∞o = mainstream conditions at the hole center
∞x = local mainstream conditions

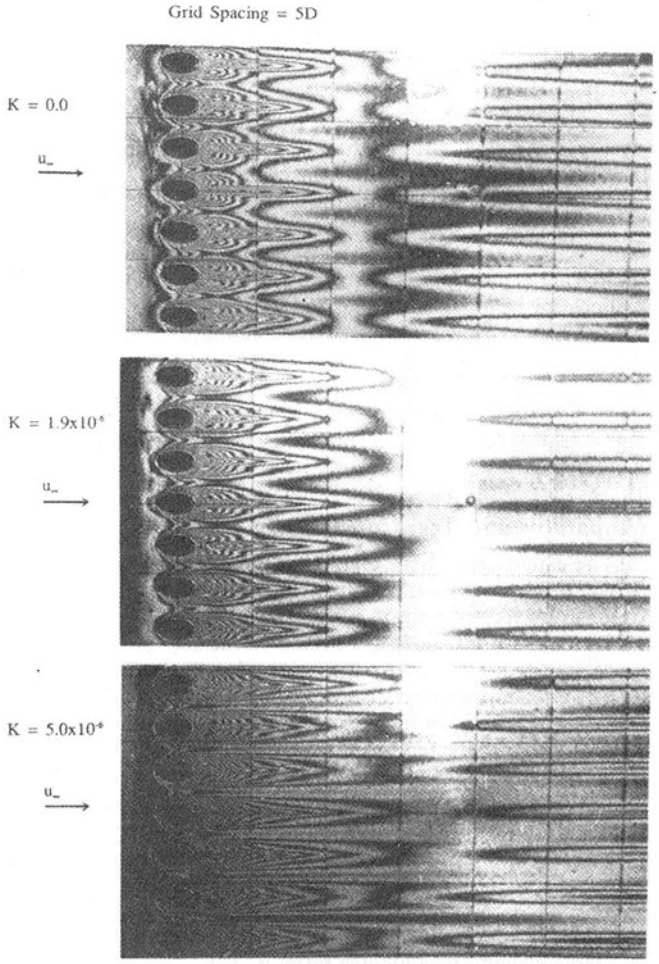

Fig. 3 Interference fringes giving contours of constant mass (heat) transfer coefficient for air injection at $M = 1$

and turbulent during all tests. The maximum tube-to-tube variation of injected flow was less than one percent.

- Density ratio = 1.0 and 1.52
- Blowing rate = 0.5, 1.0, 1.5, and 2.0

The variation of the mainstream velocity, u_∞, normalized by the mainstream velocity at the point of injection, $u_{\infty o}$, and that of the pressure gradient parameter K are shown in Fig. 2 as a function of the dimensionless distance x/D.

The dimensionless distances covered by effectively constant acceleration were as follows:

Case (A), $K \approx 0.0$, $-5 \le x/D \le 60$,
Case (B), $K \approx 1.0 \times 10^{-6}$, $-5 \le x/D \le 50$, and
Case (C), $K \approx 5.0 \times 10^{-6}$, $-5 \le x/D \le 30$.

For Case (A) the test section roof was flat.

Although the acceleration of $K = 5 \times 10^{-6}$ produced considerable thinning of the boundary layer and thickening of the viscous sublayer, particularly far downstream, the distance subjected to strong acceleration was not sufficient for flow relaminarization (Ammari, 1989).

It has been shown that, for zero pressure gradient in the presence of injection, a large change in the approach boundary layer condition (from thick, turbulent to thin, transitional) produces no measurable change in the cooling film heat transfer coefficient (Hay et al., 1984). It would seem logical to assume that the heat transfer coefficients under films injected into regions with nonzero pressure gradients are similarly insensitive to approach boundary layer conditions. In the current work, therefore, no attempt was made to keep the approach boundary later thickness constant when the acceleration was varied.

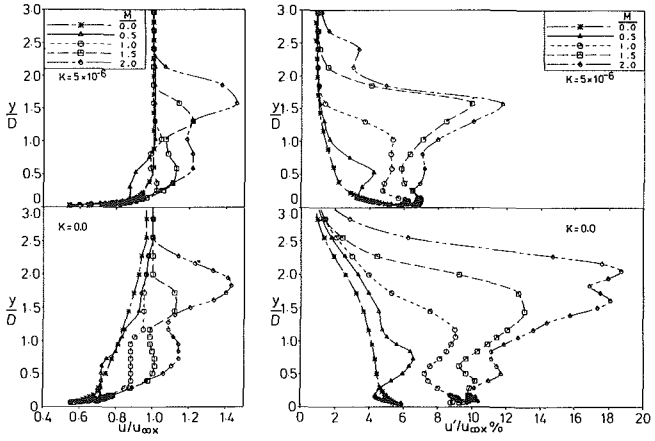

Fig. 4 Mean velocity and turbulence intensity profiles at $x/D = 5$

Applicability of the present technique for the measurement of heat transfer coefficient without injection as well as with foreign gas injection has been validated by Ammari et al. (1989).

Uncertainty analysis was carried out according to the method of Kline and McClintock (1953). The uncertainty on the heat transfer coefficient ratio with and without injection, h/h_o, was estimated to be ± 4.0 percent in the near field ($x/D < 10$) and ± 5.0 percent in the far field ($x/D > 10$). The uncertainties associated with the laterally averaged heat transfer coefficient, $\bar{h}/h_o$, were rather larger, ± 7.9 percent and ± 9.4 percent in the near and far fields, respectively. Uncertainty on the absolute mass transfer coefficient was ± 6.7 percent, so that the uncertainties on the ratios $\bar{h}_{MF}/\bar{h}$ and $\bar{h}_{SF}/\bar{h}$ in the presence of favorable pressure gradients were even larger at ± 9.4 percent and ± 8.2 percent, respectively, in the near field, and ± 13.4 percent and ± 12.4 percent, respectively, in the far field, since the analysis was dependent on division of two averaged absolute heat transfer coefficient values. Bias domination of the error of the absolute coefficients would result in a much reduced error in the ratio. However, no clear evidence of a bias has been found so far.

Results and Discussion

The results are presented as ratios of local and laterally averaged heat transfer coefficients with and without injection, and also as the ratio of laterally averaged heat (mass) transfer coefficient under the film in the presence of the favorable pressure gradient to that with zero pressure gradient conditions at the same location and blowing rate. In this way, both the effect of injection on the boundary layer, and the factor by which the heat transfer coefficients are altered by the imposition of a favorable pressure gradient, are quantified.

Mainstream Acceleration. The interference fringes mapping constant mass transfer contours (Fig. 3) provide a clear picture of the variation in the structure of jet–mainstream mixing due to acceleration. The three interferograms shown are all for a blowing rate of unity at three different pressure gradients: zero (A), moderate favorable (B), and strong favorable (C). The tests were run for equal times (12 min) and at temperatures of 27°–29°C, so the fringe patterns provide a direct comparison of heat transfer coefficients.

The figure shows that the lateral spread of the jets downstream of the holes is reduced by the acceleration, most notably in case (C). Close to the injection site, the jet flows seem to be more compact and therefore more independent of each other. This behavior has also been observed by Foster (1976) for 90 deg injection with $s/D = 3$. He measured jet concentrations at $x/D = 4.25$ and $z/D = 0.0$–1.5 above a film-cooled wall at zero and strong favorable ($K = 8.5 \times 10^{-6}$) pressure gra-

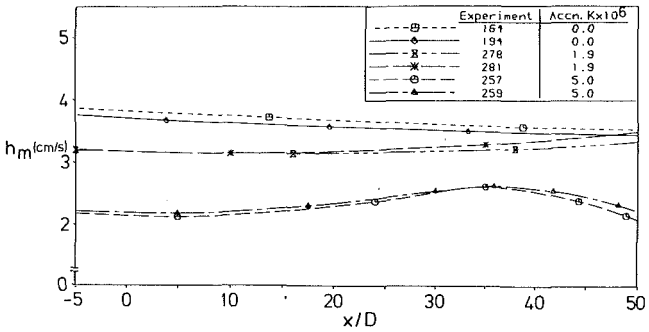

Fig. 5 Variation of mass transfer coefficients in the absence of injection

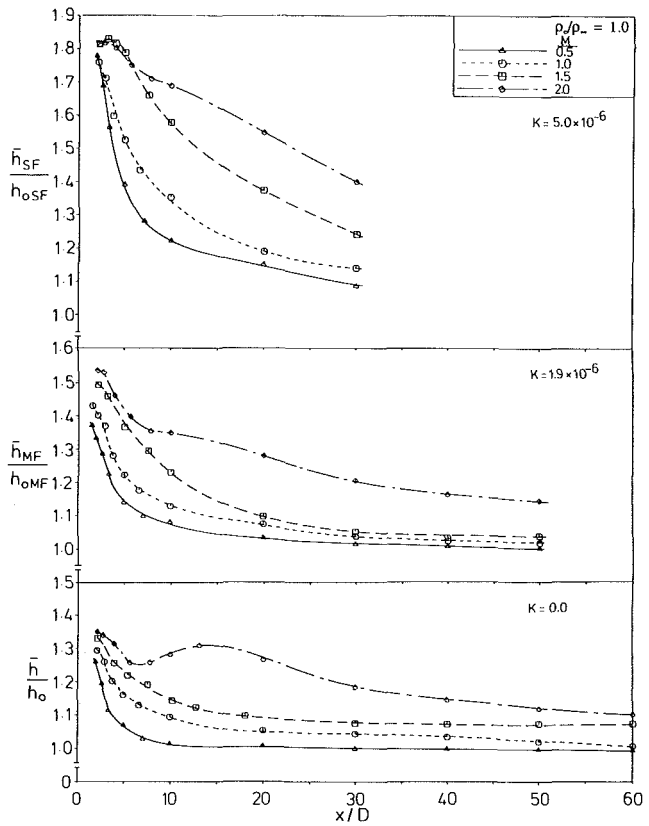

Fig. 6 Streamwise variation of the laterally averaged heat transfer coefficient at unity density ratio

dients. A reduction in the lateral spread of jets issuing from staggered rows of holes aligned at 45 deg with $s/D=8$ was also reported by Launder and York (1974) for an acceleration parameter of 2.0×10^{-6}.

The pattern of the mass transfer contours is generally similar at all accelerations. The peak in the local mass (heat) transfer coefficient corresponding to the maximum coating shrinkage downstream of the hole centerline happens at the same position, about $x/D=2.4$. Thus, separation may have occurred even at $K=5.0\times10^{-6}$, with reattachment at almost a fixed location.

Similar behavior to that in Fig. 3 was seen at the other blowing rates used in this study.

To demonstrate the response of the injectant jets to the acceleration, the centerline turbulence intensity (longitudinal velocity fluctuations only) and mean velocity profiles of air injection at $x/D=5$ with and without acceleration of $K=5\times10^{-6}$ are plotted in Fig. 4. The most striking acceleration effect is the amount by which the injection-introduced turbulence is reduced. The effect of acceleration on the tur-

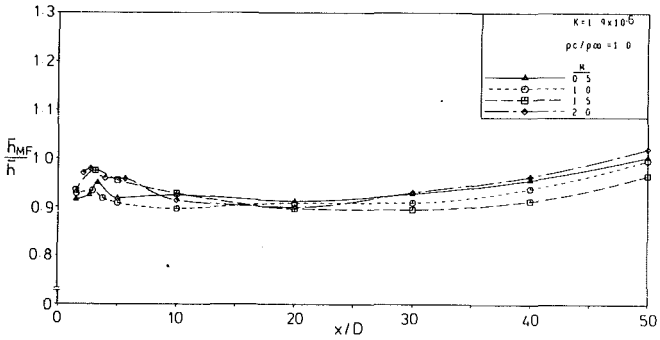

Fig. 7 Ratio of the laterally averaged heat transfer coefficient under a cooling film subjected to moderate acceleration to that for zero acceleration

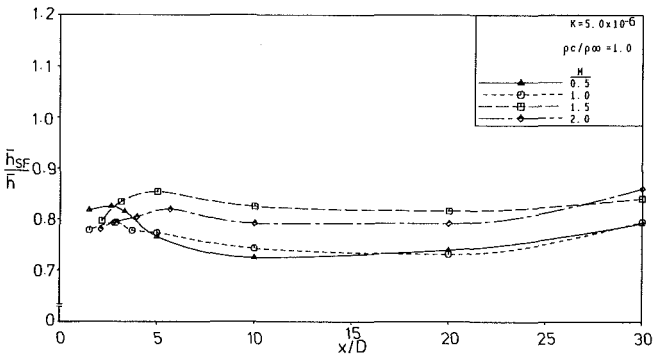

Fig. 8 Ratio of the laterally averaged heat transfer coefficient under a cooling film subjected to strong acceleration to that for zero acceleration

bulence intensities is larger than on the mean velocities. The peaks appearing in the turbulence intensity profiles correspond to the edges of the jet core where intensive jet–mainstream mixing takes place.

As M increases, jet penetration and turbulence intensity increase. The favorable pressure gradient reduces turbulence intensities, and gives slightly lower jet trajectories. The latter effect may arise at least in part from the thinner approaching boundary layer, with its reduced momentum deficit.

The reduction in turbulence intensity in the noninjected boundary layer is accompanied by a progressive drop in heat transfer coefficient, as seen in Fig. 5. These results are in agreement with the findings of Back et al. (1970), who reported heat transfer rates considerably below expected magnitudes for turbulent flow when K was above $2\text{–}3\times10^{-6}$.

Injection gives rise to increased heat transfer coefficients; see Fig. 6. The accelerated flow cases follow a generally similar pattern to that for zero pressure gradient. After the initial peak associated with injection, the heat transfer coefficient ratio falls to a value dependent upon the blowing rate. Higher blowing gives increased heat transfer coefficients.

Under moderate acceleration, the suppression of turbulence by the pressure gradient results in the heat transfer coefficients almost returning to the noninjected boundary level for the three lowest blowing rates. The heat transfer coefficient ratios for the strongest pressure gradient are still falling steeply at the end of the constant acceleration region, and it seems plausible that they too would approach noninjected levels given sufficient development length. The presentation of heat transfer coefficient data as a ratio to noninjected levels, as here, gives a picture of the effect of injection on the boundary layer, but the comparison of values at different pressure gradients is not useful because of their dependence on the initial boundary layer. It has been noted earlier that the heat transfer coefficient under the film is relatively insensitive to this, so to gain a clearer impression of the effect of the pressure gradients on

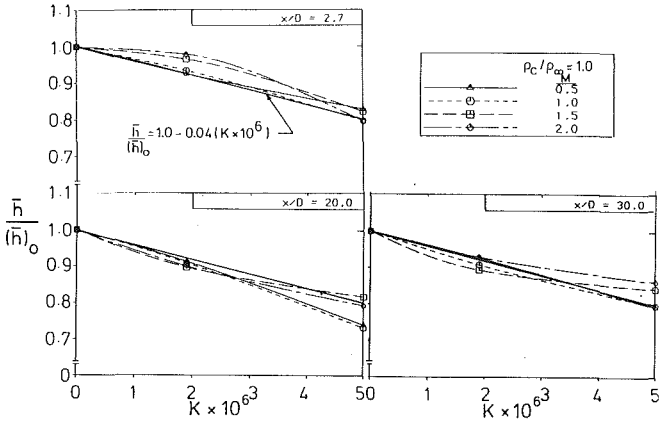

Fig. 9 Correlation of the laterally averaged heat transfer coefficient with acceleration parameter

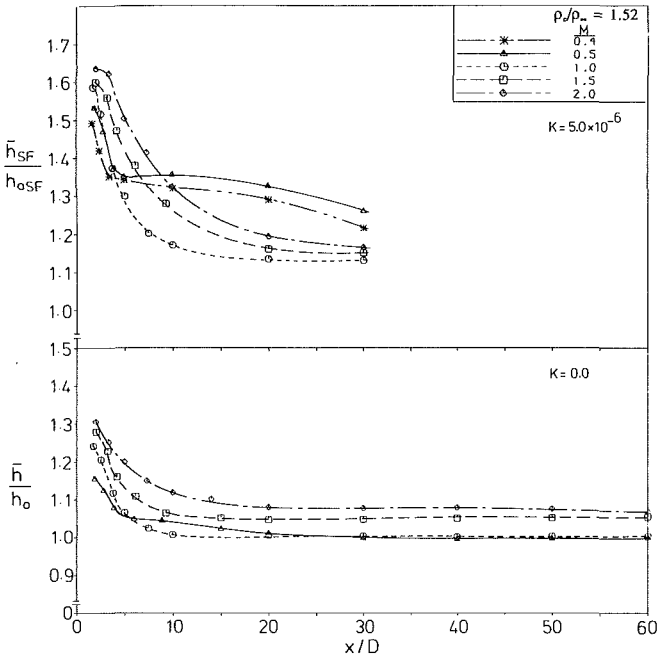

Fig. 10 Streamwise variation of the laterally averaged heat transfer coefficient at a density ratio of 1.52

the film heat transfer coefficients, the data are presented also as a ratio of the spanwise-averaged value under a pressure gradient to that at the same location with no pressure gradient; see Figs. 7 and 8.

Figure 7 shows that the moderate pressure gradient depresses the film heat transfer coefficient for all blowing rates by between about 5 and 10 percent over the first 25 diameters after injection. A progressive recovery to zero pressure gradient levels then occurs. Even close to the injection point, $\bar{h}_{MF}$ is reduced by 3 to 8 percent of that for zero acceleration, $\bar{h}$. Caution should be exercised in attributing this solely to the effect of the pressure gradient on the injection process itself. The holograms of Fig. 3 show the initial mixing region to be modified in the presence of pressure gradients. It is probable that this owes much to the variations between the approaching boundary layers.

The increase in the uncertainty due to the combination of data from different runs means that no credible trend can be extracted from the observed small variations with blowing rate.

The reduction in the spanwise-averaged heat transfer coefficient in the presence of a moderate pressure gradient is in general agreement with observations of Liess (1975) and Hay et al. (1984) for a similar configuration with mild pressure gradients.

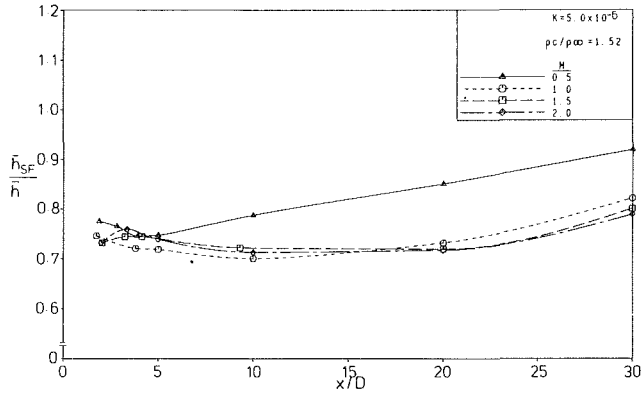

Fig. 11 Ratio of the laterally averaged heat transfer coefficient under a cooling film subjected to strong acceleration to that for zero acceleration; density ratio = 1.52

As the patterns of interference fringes of equirecession at zero and favorable pressure gradient conditions do not differ greatly (see Fig. 3), the trends of the ratios of local and lateral average heat transfer coefficients downstream of injection were found to be generally similar.

In the presence of strong favorable pressure gradient ($K = 5.0 \times 10^{-6}$), a more definite variation of the reduced cooling film heat transfer coefficient with blowing rate M is observed (Fig. 8). In general, the strong mainstream acceleration appears to lower significantly the heat transfer coefficient all the way downstream, particularly at lower M's . This behavior was also observed by Hay et al. (1984). The lateral average heat transfer coefficient is now reduced by about 20 percent and falls further, by 27 percent, for low blowing, at locations further downstream, before commencing a slight recovery. At higher blowing rates, $\bar{h}_{SF}$ ranges between 80 percent of the value for the zero pressure gradient close to the injection point to 86 percent far downstream.

An increase in $\bar{h}_{SF}/\bar{h}$ with M may be expected since at $K = 5.0 \times 10^{-6}$ the boundary layer is very thin ($\delta/D \approx 0.6$ at $x/D = 5$), and the emerging jets readily penetrate it and encounter the high mainstream velocity.

The jet trajectory at a given M therefore tends to be lower for this case than for the zero or moderate pressure gradient cases. The thinner boundary layer also mixes less with the jets, leaving tighter structures. The heat transfer coefficients will therefore tend to reflect the jet behavior more directly, and hence will respond to factors, such as M, that influence it. It should be noted, however, that although the differences in the values of $\bar{h}_{SF}/\bar{h}$ resulting from varying M now reach as much as 10 percent, this is still within the uncertainties associated with the curves themselves.

To examine the correlation of the heat transfer coefficient with acceleration parameter, the average coefficients at the various pressure gradients, each normalized by that at zero pressure gradient, have been plotted against K for a range of fixed downstream positions in Fig. 9. A roughly linear variation with K is seen, with only a weak and inconsistent dependence upon M. Dispersion from the fitted line is small, within about ± 7 percent, at all downstream positions.

Acceleration and Density Ratio. The tests with $\rho_c/\rho_\infty = 1.52$ at $K = 5.0 \times 10^{-6}$ showed the same general trends as those at $K = 0.0$ (Fig. 10). The laterally averaged ratio $\bar{h}_{SF}/h_{oSF}$ for $M \geq 1.0$ increases significantly with M in the vicinity of the holes, and decays monotonically with x/D. Now, however, $M = 0.5$ yields a heat transfer coefficient for the region $x/D > 5$, which is well in excess of those at higher blowing rates. Closer inspection of the zero pressure gradient curves in Fig. 10 shows that the $M = 0.5$ curve lies above that for $M = 1$ over a short distance. A further test at $M = 0.4$ was conducted under strong

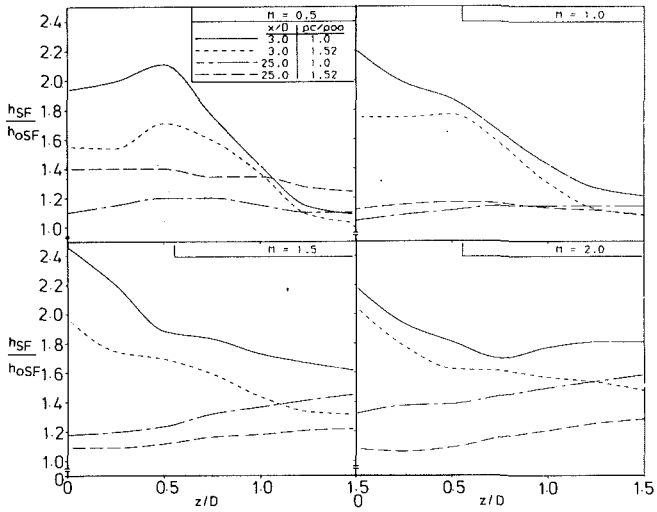

Fig. 12 Effect of density ratio on the local heat transfer coefficient under strong acceleration, $K = 5 \times 10^{-6}$

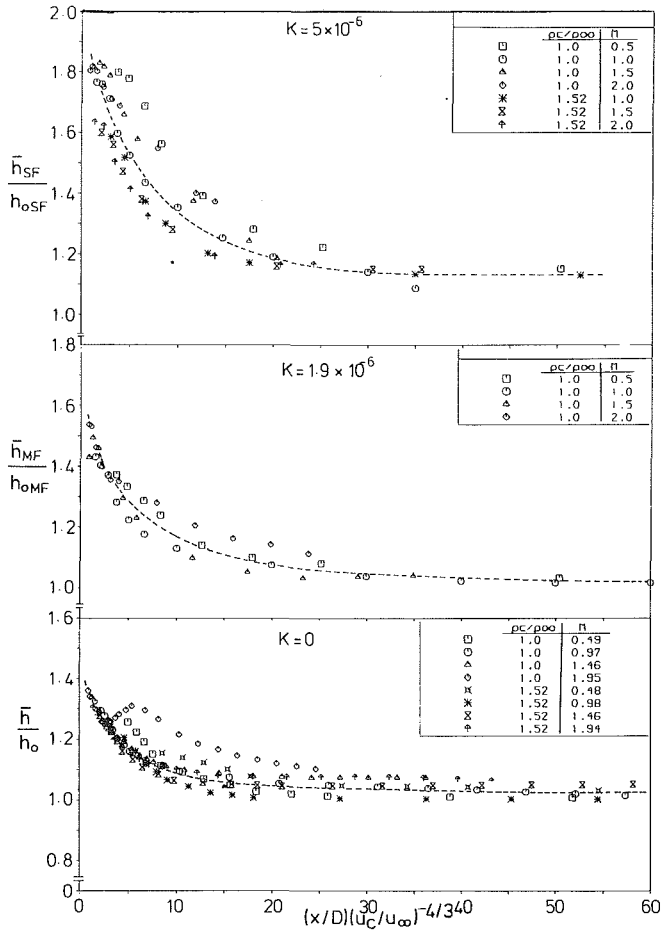

Fig. 13 Correlations of laterally averaged heat transfer coefficient for three mainstream accelerations

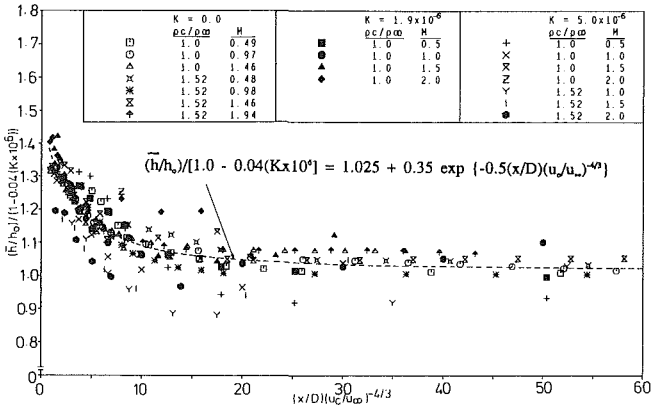

Fig. 14 Correlation of $\bar{h}/h_o$ data of $0.0 \le K \le 5 \times 10^{-6}$ at two density ratios

pressure gradient conditions, and this produced lower values than for $M = 0.5$.

This behavior is consistent with the occurrence of jet liftoff at a blowing rate slightly greater than 0.5, corresponding to a momentum flux ratio, I, of 0.16. This is in fair agreement with the approximate limit of 0.1 given by Forth and Jones (1986) who recognized the need to develop separate correlations for predominantly attached and predominantly separated film cooling flows. These they identify as weak and strong injection regimes. It is evident that the bulk of the present work has been conducted with strong injection, with the single exception of the 0.5 blowing rate, high density ratio case, where reattachment occurs within the first 5 diameters.

The attached jets mix less with the mainstream, giving higher velocities close to the wall and, hence, increase heat transfer coefficients. The effect appears much more pronounced under strong acceleration than under zero pressure gradient conditions in Fig. 10 partly because of normalization by the non-injected heat transfer coefficients. Because the normalizing factor is very low for the strong acceleration (see Fig. 5), a change in heat transfer coefficient in this case appears proportionately larger than for the zero gradient case.

To clarify the effect of the pressure gradient on the film, the heat transfer coefficients normalized by their corresponding zero pressure gradient values, $\bar{h}_{SF}/\bar{h}$, are given as a function of x/D with M as parameter in Fig. 11. The curves for $1.0 \le M \le 2.0$ with CO_2 injection have the same form as those with air injection (Fig. 8), but are less sensitive to blowing parameter. Reductions in heat transfer coefficient for most downstream distances are about the same as for the two lowest air-injection blowing rates, but are rather higher close to the injection point at around 25 percent.

The most striking feature in Fig. 11 is the difference in behavior at the lowest blowing rate. Although the reduction in heat transfer coefficient close to the injection point is the same as for other blowing rates, this is not sustained. The heat transfer coefficient climbs progressively toward its zero pressure gradient levels.

The influence of varying the density ratio from 1.0 to 1.52 at constant acceleration $K = 5.0 \times 10^{-6}$ on the heat transfer coefficient is shown in Fig. 12. The data are presented as lateral distributions of the local heat transfer coefficient for M ranging from 0.5 to 2.0 at $x/D = 3$, and $x/D = 25$.

At $x/D = 3$, and for $0.5 \le M \le 2.0$, a substantial decrease in the heat transfer coefficient ratio h_{SF}/h_{oSF} of around 20 percent occurs when ρ_c/ρ_∞ is increased by 52 percent. As stated in Ammari et al. (1990) for $K = 0$, this behavior is due to the denser injectant gas having a low momentum at a fixed value of the blowing rate.

At $x/D = 25$, the difference between h_{SF}/h_{oSF} at high and low density ratios is a maximum at $M = 2$, and is near zero at $M = 1$. For the higher blowing rates, the lower density ratio gives the higher heat transfer coefficient.

For $M = 0.5$, an increase in density ratio from 1 to 1.52 is accompanied by a change in injection regime from strong to weak, as I decreases from 0.25 to 0.16. An increase in h_{SF}/h_{oSF} results from this change of flow regime. A similar, although smaller, increase was observed at $K = 0.0$ (Ammari et al., 1990). Recently, measurements of turbulence intensity at density ratios of 1.0 and 2.0 have been reported by Pietrzyk et al. (1990). Using an injection geometry identical to that used

here, and a blowing rate of 0.5, they found that the turbulence intensity for unity density ratio was initially slightly higher, but decayed quite rapidly with distance. The intensity for the higher density ratio fell only slowly. Although these measurements were made at zero pressure gradient, it seems likely that the same effect would occur under acceleration, and that the sustained high heat transfer coefficients seen at high density ratio and low blowing rate reflect a similarly sustained high turbulence intensity.

Close to a hole, a peak in the heat transfer coefficient for $M=0.5$ is observed at about $z/D=0.5$ at both density ratios. This is characteristic of low trajectory jets at zero pressure gradient conditions (Eriksen and Goldstein, 1974), where the centerline value of the heat transfer coefficient is lower than the value near the edge of the jet. As M was increased, the peak moved to the centerline and remained there.

Far downstream from a hole, the relatively high values of h_{SF}, at the edges of a jet for $M=0.5$ at both density ratios, moved to the midposition between the holes, $z/D=1.5$, as the blowing rate increased. This effect is due to jet spreading, interaction with adjacent jets, and the induced streamwise vortices.

The results are seen to be consistent with those found at zero mainstream pressure gradient (Ammari et al., 1990) although the strong mainstream acceleration seems to enhance the influence of density ratio.

The effect of an acceleration of $K=5.0\times10^{-6}$ on the heat transfer coefficient at density ratios above unity is shown to differ only slightly in manner and magnitude to the effect at density ratio of one. An acceleration of 1.9×10^{-6} would, therefore, be expected to conform to the same pattern.

Correlating Parameters. It has been shown by Ammari et al. (1990) that, at zero mainstream acceleration, the heat transfer data, including those with a density ratio of 1.52, correlated reasonably well with the velocity ratio parameter, $(x/D)(u_c/u_\infty)^{-4/3}$, in the strong injection regime.

Since most of the present heat transfer data lie in the strong injection regime, and the general behavior of the cooling film heat transfer coefficient under favorable and zero pressure gradients is similar (see Figs. 6 and 10), it seems logical that the pressure gradient data should correlate with the zero pressure gradient correlating parameter, $(x/D)(u_c/u_\infty)^{-4/3}$. This is clearly shown to be so in Fig. 13, where a reasonable collapse of the pressure gradient heat transfer data is achieved.

An attempt to collapse all the experimental data excluding those at u_c/u_∞ of 2 is shown in Fig. 14. The correlation incorporates the scaling parameter, $(x/D)(u_c/u_\infty)^{-4/3}$, and the linear relationship derived at unity density ratio to describe the effect of acceleration. The scatter, however, is seen to be large particularly for the high density ratio in the presence of acceleration.

Concluding Comments

The present results support earlier conclusions that the effect of acceleration of moderate strength is weak, with around 10 percent reduction in heat transfer coefficient being recorded. Under strong acceleration, up to 25 percent reduction may occur, but the magnitude is more dependent on the blowing rate. The heat transfer coefficient has also been shown to be related to the turbulence intensity within the film.

The existence of weak and strong injection regimes has again been demonstrated. Although the effect of density ratio variation at a fixed blowing rate is generally not great, it has a key role in determining the weak-strong injection regime transition as this is momentum-ratio dependent. The precise value at which transition occurs is likely to depend on details of injection geometry and velocity distribution, and may contribute to a lack of close consensus regarding acceleration effects.

Conclusions

1 Mainstream acceleration suppresses injection-induced turbulence, and hence reduces the heat transfer coefficient.

At unity density ratio, the overall average reduction in the averaged coefficients, $\bar{h}$, was about 8 percent under moderate acceleration, and fell from about 25 to 20 percent under strong acceleration as the blowing rate increased.

At a fixed blowing rate, the spanwise average coefficients normalized by the corresponding zero acceleration values, $\bar{h}/(\bar{h})_o$, decrease almost linearly as the acceleration parameter, K, increases.

Blowing rate had a negligible effect on the heat transfer coefficients ratio at the lower acceleration. At the higher acceleration, increased injection weakened the effect of the acceleration on the coefficients ratio.

2 When the injectant-to-mainstream density ratio was 1.52, the imposition of a strong mainstream acceleration ($K=5\times10^{-6}$) had a similar effect on the film heat transfer coefficients as for unity density ratio, at least where the influence of M was quite weak ($M<1.5$). A substantial overall reduction in $\bar{h}/(\bar{h})_o$ of about 27 percent was present for $M>0.5$.

3 The effect on the heat transfer coefficient of raising the density ratio from 1.0 to 1.52 under strong acceleration was also similar to that at zero pressure gradient. The decrease in the coefficients reached 20 percent at some downstream positions for the large blowing rates.

4 Empirical evidence shows the heat transfer coefficient data in the presence of acceleration and with a density ratio of 1.52 to scale reasonably well with $(x/D)(u_c/u_\infty)^{-4/3}$, the data-correlating parameter for zero acceleration. An initial attempt at an overall correlation, to include effects of both acceleration and density ratio variation, gave

$$\bar{h}/h_o=[1.0-0.04(K\times10^6)][1.025+0.35\exp\{-0.15(x/D)(u_c/u_\infty)^{-4/3}\}]$$

The scatter becomes large for the data at the higher density ratio in the presence of acceleration.

References

Ammari, H. D., 1989, "The Heat Transfer Coefficient on Film Cooled Surfaces," Ph.D. thesis, University of Nottingham, United Kingdom.

Ammari, H. D., Hay, N., and Lampard, D., 1989, "Simulation of Cooling Film Density Ratios in a Mass Transfer Technique," ASME Paper No. 89-GT-200.

Ammari, H. D., Hay, N., and Lampard, D., 1990, "The Effect of Density Ratio on the Heat Transfer Coefficient From a Film-Cooled Flat Plate," ASME JOURNAL OF TURBOMACHINERY, Vol. 112, pp. 444-450.

Back, L. H., Cuffel, R. F., and Massier, P. F., 1970, "Laminarization of a Turbulent Boundary Layer in Nozzle Flow-Boundary Layer and Heat Transfer Measurements With Wall Cooling," ASME *Journal of Heat Transfer*, Vol. 92, pp. 333-334.

Eriksen, V. L., and Goldstein, R. J., 1974, "Heat Transfer and Film Cooling Following Injection Through Inclined Circular Holes," ASME *Journal of Heat Transfer*, Vol. 96, pp. 239-245.

Forth, C. J. P., and Jones, T. V., 1986, "Scaling Parameters in Film-Cooling," *Proceedings of the 8th Int. Heat Transfer Conference*, pp. 1271-1276.

Foster, N. W., 1976, "Film Cooling of Gas Turbine Blades," Ph.D. thesis, University of Nottingham, United Kingdom.

Hartnett, J. P., Birkebak, R. C., and Eckert, E. R. G., 1961, "Velocity Distributions, Temperature Distributions, Effectiveness and Heat Transfer in Cooling of a Surface With a Pressure Gradient," *Int. Developments in Heat Transfer*, Pt. IV, ASME, New York, pp. 682-689.

Hay, N., Lampard, D., and Saluja, C. L., 1982, "Application of the Swollen Polymer Technique to the Study of Heat Transfer on Film Cooled Surfaces," *Proceedings of the 7th International Heat Transfer Conference*, Munich, Vol. 4, pp. 503-508.

Hay, N., Lampard, D., and Saluja, C. L., 1984, "Effects of the Condition of the Approach Boundary Layer and of Mainstream Pressure Gradients on the Heat Transfer Coefficient on Film-Cooled Surfaces," ASME *Journal of Engineering for Power*, Vol. 107, pp. 99-104.

Jabbari, M. Y., and Goldstein, R. J., 1978, "Effect of Mainstream Acceleration on Adiabatic Wall Temperature and Heat Transfer Downstream of Gas Injection," presented at the 6th Int. Heat Transfer Conf., Toronto, Canada.

Kline, S. J., and McClintock, F. A., 1953, "Describing Uncertainties in Single Sample Experiments," *Mechanical Engineering*, pp. 3–8.

Kruse, H., 1985, "Effects of Hole Geometry, Wall Curvature and Pressure Gradient on Film Cooling Downstream of a Single Row," AGARD-CP-390, Paper No. 8.

Launder, B. E., and York, J., 1974, "Discrete-Hole Cooling in the Presence of Free Stream Turbulence and Strong Favourable Pressure Gradient," *Int. J. Heat Mass Transfer*, Vol. 17, pp. 1403–1409.

Liess, C., 1975, "Experimental Investigation of Film Cooling With Injection From a Row of Holes for the Application to Gas Turbine Blades," ASME *Journal of Engineering for Power*, Vol. 97, pp. 21–27.

Macleod, N., and Todd, R. B., 1973, "The Experimental Determination of Wall Fluid Mass-Transfer Coefficients Using Plasticised Polymer Surface Coatings," *Int. J. Heat Mass Transfer*, Vol. 16, pp. 485–503.

Pietrzyk, J. R., Bogard, D. G., and Crawford, M. E., 1990, "Effects of Density Ratio on the Hydrodynamics of Film Cooling," ASME JOURNAL OF TURBOMACHINERY, Vol. 112, p. 437.

Warren, J. M., and Metzger, D. E., 1972, "Heat Transfer With Film Cooling in the Presence of a Laminarizing Mainstream," ASME Paper No. 72-HT-11.

The Influence of Curvature on Film Cooling Performance

S. G. Schwarz
Department of Mechanical Engineering,
Tulane University,
New Orleans, LA 70118

R. J. Goldstein

E. R. G. Eckert

Department of Mechanical Engineering,
University of Minnesota,
Minneapolis, MN 55455

The effects of injection rate and strength of curvature on film cooling performance of gas injected through a row of holes on a convex surface are studied. Comparisons are made to film cooling of concave and flat surfaces. Three different relative strengths of curvature (ratio of radius of curvature to radius of injection hole), two density ratios (0.95 and 2.0), and a wide range of blowing rates (0.3 to 2.7) are considered. A foreign gas injection technique (mass transfer analogy) is used. The strength of curvature was controlled by varying the injection hole diameter. At low blowing rates, film cooling is more effective on the convex surface than on a flat or a concave surface. The cross-stream pressure gradient present in curved flows tends to push the jet into the convex wall. As the injection rate is increased, normal and tangential jet momentum promote liftoff from the convex surface, thereby lowering performance. In contrast, previous studies show that on a concave surface, tangential jet momentum, flow instabilities, and blockage improve performance on a concave surface as blowing rate is increased.

Introduction

The desire to increase the performance of modern gas turbine engines has led to higher turbine inlet temperatures. Advances in the development of rotor materials have not kept up with the ever-increasing thermal requirements. Cooling techniques have, therefore, been developed to protect the rotor blades from their extremely hot environment. Film cooling is one such method. It involves injecting a coolant gas, usually bled from the turbine compressor, through holes in the surfaces of the hollow blades. This coolant travels along the airfoil's outer surfaces, protecting them from the hot mainstream.

A quantitative understanding of how well a given film cooling geometry in a particular gas turbine engine will perform can only be achieved by testing the actual engine. This can be quite expensive. Realizing this, researchers in film cooling over the past 25 years have tried to gain a more fundamental understanding of how various jet geometries behave in simplier flows (e.g., injection along a flat plate). The importance of understanding how jets interact with the main flow under idealized conditions such as these cannot be understated. Investigations into the effects of injection rate, coolant-to-mainstream density ratio, injection hole geometry, and condition and size of the main flow boundary layer on the performance of film cooled flat surfaces under controlled conditions have given excellent qualitative information about how to approach the more complex flows and geometries in gas turbine engines. A comprehensive review of works through 1971 studying two- and three-dimensional injection along flat surfaces is presented by Goldstein (1971).

For a given injection system geometry, two parameters of particular importance in film cooling of flat surfaces are the blowing rate and density ratio. The condition of the approaching flow also influences the film cooling effectiveness. Mainstream parameters such as the displacement thickness at the point of injection over the injection hole diameter (δ_o^*/D) can also be significant.

Due to the shape of turbine passages, the flow through them experiences very strong streamline curvature. This curvature can produce phenomena not present in conventional flows over flat surfaces. Bradshaw (1973) discusses flows over curved surfaces in an excellent review. Two-dimensional flow through curved turbine blade passages is accelerated into the center of curvature by a pressure gradient normal to the blade surfaces. The centripetal acceleration of the fluid is determined by the force created by the cross-stream pressure gradient, enabling the streamlines to be essentially parallel to the curved surfaces. For a given density ratio, film cooling jets, which have a lower mean velocity than the neighboring main flow, will tend to travel in a smaller radius of curvature. Consequently, low-speed jets will be drawn away from concave (pressure) walls and into convex (suction) walls. The reverse is true of high-speed jets. Additionally, the pressure gradient creates an unstable flow on the concave wall, which manifests itself in increased turbulence intensity and Taylor–Görtler vortices (Tani, 1962). These phenomena have the potential to influence film cooling performance on curved surfaces.

Studies over the past 20 years have considered film cooling of constant radius of curvature surfaces and more practical variable curvature turbine blade designs. Lander et al. (1972) studied staggered, two-row injection over the convex surface of a turbine cascade using actual combustor gases for the main flow. A density ratio typically found in gas turbine applications (1.89) was used, but blowing rates were low (between 0.31 and 1.05). Nicolas and Le Meur (1974) compared two-dimensional

Contributed by the International Gas Turbine Institute and presented at the 35th International Gas Turbine and Aeroengine Congress and Exposition, Brussels, Belgium, June 11–14, 1990. Manuscript received by the International Gas Turbine Institute January 5, 1990. Paper No. 90-GT-10.

film cooling of flat, convex, and concave walls. Particular attention was paid to streamwise pressure gradient. Convex and concave data were compared to flow over a flat plate where the streamwise pressure gradient was forced to have similar characteristics by means of a contoured opposite wall. The data were taken at fairly high blowing rates (1.0 to 2.0). Folayan and Whitelaw (1976) measured effectiveness for step-down slot cooling of concave, convex, and flat surfaces in a mass transfer experiment using a foreign gas injection technique. Mayle et al. (1977) investigated low blowing rates (0.5 to 0.9) through a slot on convex, concave, and flat surfaces.

Ito et al. (1978) conducted the first tests of film cooling on curved surfaces for a wide range of blowing rates (0.2 to 2.98). A foreign gas injection technique was used to measure impermeable wall concentrations downstream of injection through a row of holes along the pressure (concave) and suction (convex) sides of a turbine blade in a cascade.

Ko et al. (1984) measured centerline effectiveness close to the injection holes at a low blowing rate along a convex surface using a foreign gas injection technique. Injection was very near the onset of curvature, where the pressure gradient might be strong. Within the same research group, Ko et al. (1986) compared the effectiveness of film cooling convex and concave surfaces.

Furuhama and Moffat (1983) explored full (13 rows of holes) and partial (6 and 2 rows) coverage film cooling over a convex surface at a blowing rate of 0.4. Other blowing rates were investigated by Furuhama et al. (1983), but the effectiveness could only be obtained from further calculation of the results. In the former study, performance was consistently higher than the flat plate results of Crawford et al. (1976). The jets, which had a low velocity compared to the free stream, are forced into the convex wall by the cross-stream pressure gradient.

Individually, most of the aforementioned studies have shown a significant effect of surface curvature and injection rate on film cooling performance. For three-dimensional (discrete hole) injection, convex surfaces were generally easier to cool than flat or concave at low injection rates, while the opposite was true when more coolant was used. On convex and flat surfaces, increased injection improved performance to a point. Further increase, however, resulted in a reduction in film cooling effectiveness. The blowing rate at which the effectiveness is at a maximum is one focus of the present investigation.

The present study investigates experimentally the effects of strength of convex curvature on the film cooling performance. It also compares these findings to the turbine cascade work of Ito et al. (1978) and the flat surface work of Pedersen et al. (1977). Strength of curvature can be defined in many ways, each of which could be the subject of separate studies. This work will look at the effects of the radius of surface curvature as compared to the injection hole diameter ($2r/D$). To control this parameter, the hole diameter, rather than the surface curvature, is varied, because varying the latter would also result in changes in δ_o^*/r, whose effects on film cooling performance are not known at present.

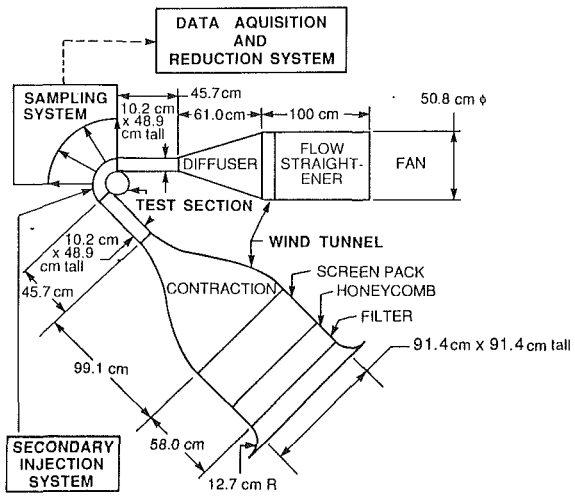

Fig. 1 Experimental apparatus—schematic

Apparatus and Procedure

The experimental apparatus (Fig. 1) consists of five major components: the wind tunnel, the test section, the secondary injection system, the sampling system, and the data acquisition and reduction system. It is essentially the same as that used by Schwarz and Goldstein (1989), the only exception being that effectiveness measurements are made on the convex wall rather than the concave.

The convex working surface has a radius of curvature of

Nomenclature

C_2 = mass concentration of tracer in injected gas
C_{iw} = mass concentration of tracer in gas adjacent to impermeable wall
D = injection hole diameter (0.160 cm, 0.216 cm, and 0.333 cm, in the present study)
I = momentum flux ratio = $\rho_2\mu_2^2/\rho_\infty u_\infty^2$
M = blowing rate = $\rho_2\mu_2/\rho_\infty u_\infty$
n_D = number of injection holes
r = radius of curvature of wall
Re_2 = Reynolds number of secondary flow = $\rho_2 u_2 D/\mu_2$ for injection through a row of holes or $\rho_2 u_2 s/\mu_2$ for injection through a slot
s = equivalent slot thickness of row of injection holes ($Z_D s = (\pi/4)D^2$)
μ_{av} = average streamwise fluid velocity in wind tunnel
u_2 = average velocity of secondary gas through the injection holes
u_∞ = main flow velocity at the outside edge of the boundary layer at the point of injection
x = streamwise distance from downstream edge of injection hole
y = perpendicular distance from convex or concave wall
z = lateral distance from injection hole centerline
Z_D = lateral spacing of injection holes center to center ($3D$ in the present study)
α = angle of jet axis to tangent to wall (35 deg in the present study)
δ_o^* = boundary layer displacement thickness without injection at $x = 0$
η = local impermeable wall effectiveness = C_{iw}/C_2
η_c = centerline impermeable wall effectiveness (i.e., at $z = 0$)
$\bar{\eta}$ = laterally averaged (over z) impermeable wall effectiveness
Θ_o = boundary layer momentum thickness without injection at $x = 0$
μ_2 = dynamic viscosity of the secondary (injected) gas
μ_∞ = dynamic viscosity of the main flow gas
ξ = slot injection parameter = $[x/Ms][\mathrm{Re}_2(\mu_2/\mu_\infty)]^{-1/4}$
ρ_2 = density of the secondary (injected) gas
ρ_∞ = density of the main flow gas

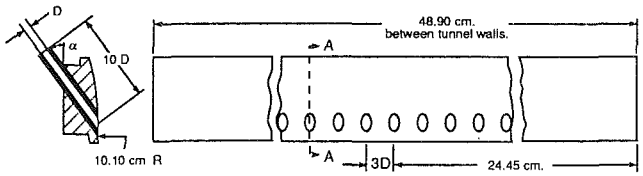

Section A-A

Convex Injection Hole Sets

n_D	D[cm]	α[°]
29	0.160	35
23	0.216	35
15	0.333	35

Fig. 2 Convex injection plate

10.10 cm and is 135 deg long in the streamwise direction. The cross section of the test section is 48.9 cm (between plane end walls) by 10.2 cm (normal to the curved walls). The convex surface has a flanged slot milled the entire height. In the slot, one of three injection plates can be inserted (Fig. 2). Each injection plate is made of aluminum and has holes drilled through it at an angle of 35 deg to the working surface. Stainless steel tubes of either 0.160 cm, 0.216 cm, or 0.333 cm i.d. are epoxied into these holes. The tubes are all ten i.d. long. The centers of the injection holes are located at 45 deg after the onset of curvature. The holes were spaced three i.d. apart center to center. The three different hole diameters allowed for a study of the effect of the ratio $2r/D$ on the film cooling effectiveness. The outer surface of the injection plate is turned down to the radius of curvature of the working surface. Sampling taps are installed at various locations downstream of injection by drilling holes through the convex injection tank and epoxying 0.061 cm i.d., stainless steel inserts in these holes. The convex wall is sanded smooth.

Effectiveness measurements along the convex wall of the test section are made using a foreign gas injection technique. Air mixed with either helium or Freon-12 is injected through the row of film cooling holes in the curved surface. Samples are lightly drawn off at the wall and stored in sampling containers to be measured for foreign gas content using a gas chromatograph. Measurements of main flow tunnel velocity are also made. Blowing rate, density ratio, and local impermeable wall effectiveness are measured to within 1.4, 0.1, and 5.7 percent, respectively. A detailed uncertainty analysis can be found from Schwarz (1986).

The operating conditions are listed in Table 1. The density ratios obtained are nominally 0.95 and 2.0 for helium tracer and Freon-12 injection, respectively. Detailed velocity profiles, and a description of how they were obtained, can be found in Schwarz (1986).

Results

Figure 3 shows local impermeable wall effectivenesses for helium tracer injection (density ratio of 0.95) over the convex wall plotted against both x/D and $z/3D$ at a blowing rate of 0.68. Trends are similar to those found in flat plate studies (Goldstein et al., 1970; Pedersen et al., 1977; Kadotani and Goldstein, 1979). At this blowing rate, the centerline effectiveness is quite high immediately after the injection holes, and it trails off farther downstream. The jets of relatively low momentum tend to remain close to the surface, hence providing good performance just after injection. Mixing with the mainstream dilutes the coolant gas farther downstream, thereby lowering effectiveness. Midline ($z/3D = 0.5$) effectiveness, on the other hand, starts off near zero, and gradually increases as the jet travels downstream. Very close to injection, but halfway between two holes, the jets' influence is not felt at the wall. As the jets travel downstream, they spread, covering a wide lateral portion of the convex surface.

Table 1 Nominal operating conditions

	Convex	Concave S&G (1989)
T_∞	24°C	24°C
u_{av}	40 m/s	40 m/s
u_∞	59 m/s	32 m/s
δ_o^*	0.11 cm.	0.41 cm.
Θ_o	0.09 cm.	0.29 cm.
ρ_2/ρ_∞	0.95 or 2.0	0.95 or 2.0
M	0.3 to 2.7	0.3 to 2.7
$2r/D$	+61, +94, or +126	−59, −89, or −111
r	20.32 cm.	10.10 cm.

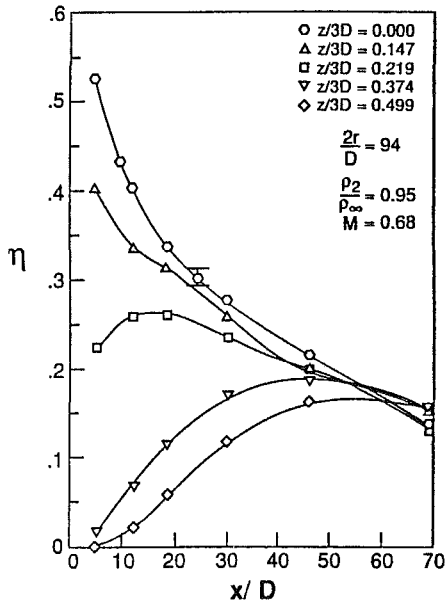

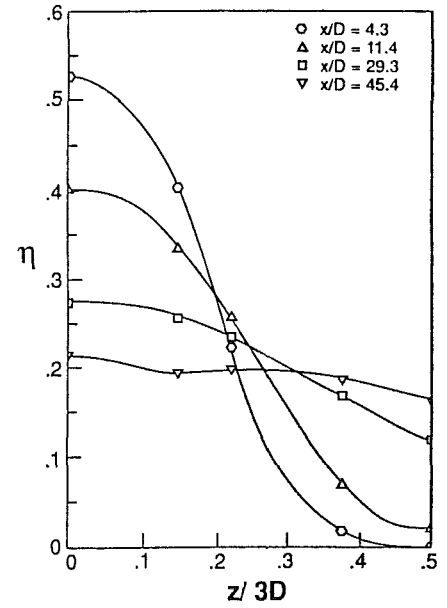

Fig. 3 Film cooling of a convex surface—local effectiveness

The effect of blowing rate on centerline effectiveness can be seen in Fig. 4. Very near the injection hole ($x/D = 2.64$), centerline effectiveness is very high at the lowest blowing rate studied, and it decreases dramatically with increased injection. At higher blowing rates, the jets lift off the surface immediately after they leave the holes, resulting in poor performance even at low x/D. Farther downstream, at low blowing rates, increased injection causes a gradual improvement in centerline

performance; the jets spread, blocking the main flow from the surface, causing more of the jet to come in contact with the surface, thereby gradually increasing effectiveness.

Jet liftoff is revealed visually in Fig. 5. Carbon dioxide–water vapor jets, photographed from the side, show that at a blowing rate of 1.6, the jets are completely off the surface.

The lateral variation in local effectiveness is large when compared to that on a concave surface. Figure 6 (Schwarz and Goldstein, 1989) shows that local effectiveness profiles plotted versus $z/3D$ are virtually flat after 10 diameters from injection on the concave wall. On the convex wall (Fig. 3) significant variation is found as far as 30 diameters from injection. The greater lateral mixing found on the concave wall is attributed to concave flow instabilities. In contrast, on the convex surface at blowing rates of 0.4 and 0.8, the top views in the flow visualization (Fig. 5) reveal that the jets along the convex surface are quite distinct and retain their lateral position as far as 20 diameters from injection (the white lines on the surface

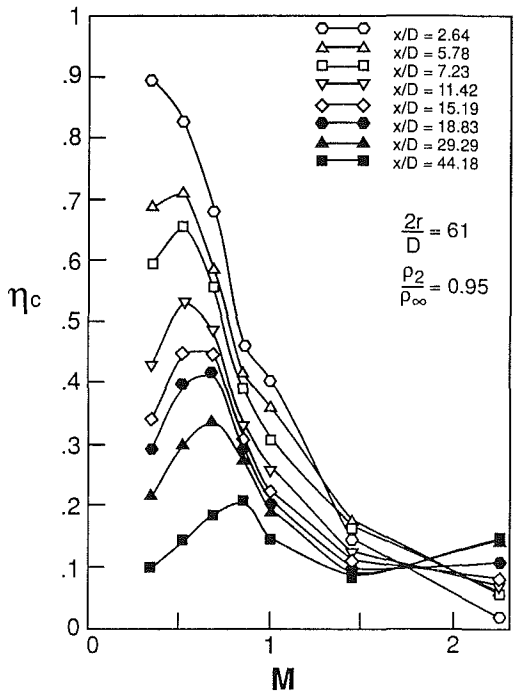

Fig. 4 Film cooling of a convex surface—centerline effectiveness

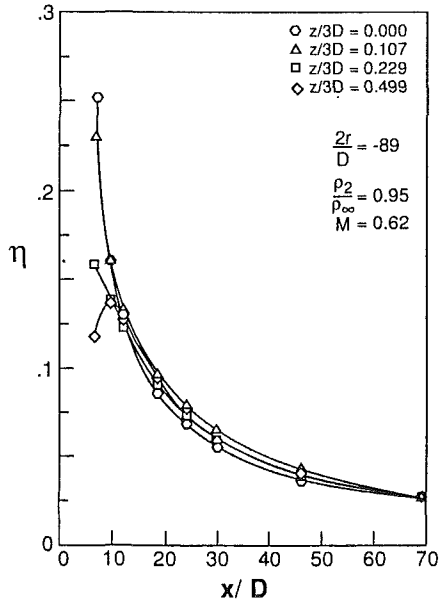

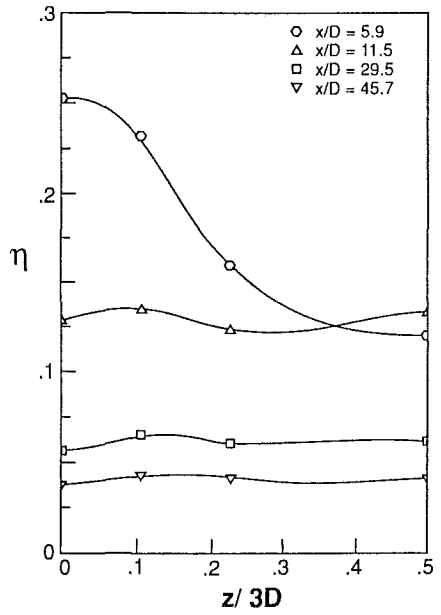

Fig. 6 Film cooling of a concave surface—local effectiveness

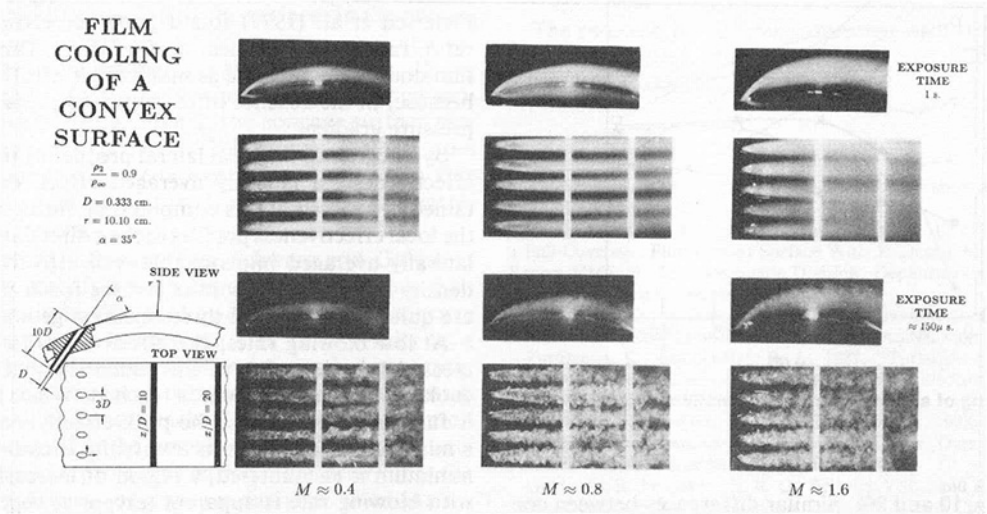

Fig. 5 Film cooling of a convex surface—flow visualization

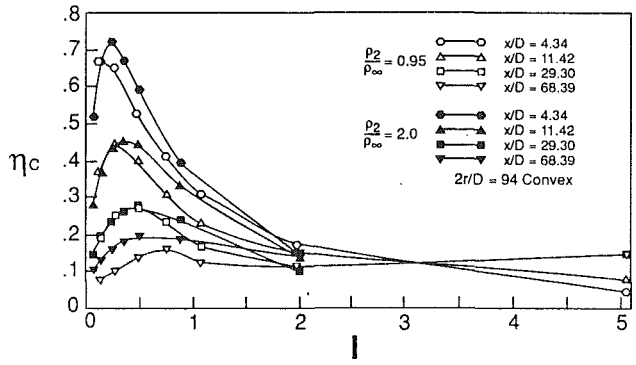

Fig. 7 Film cooling of a convex surface—momentum flux ratio effects

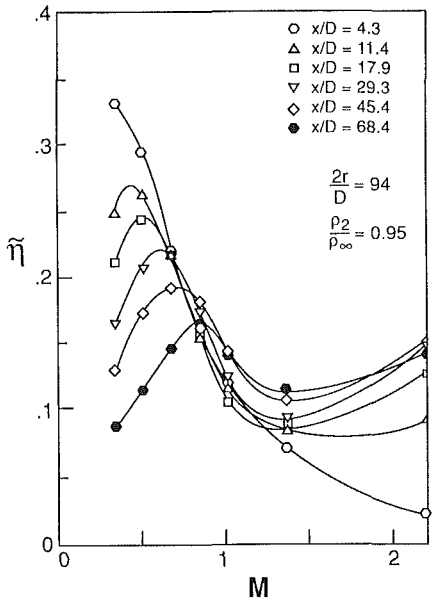

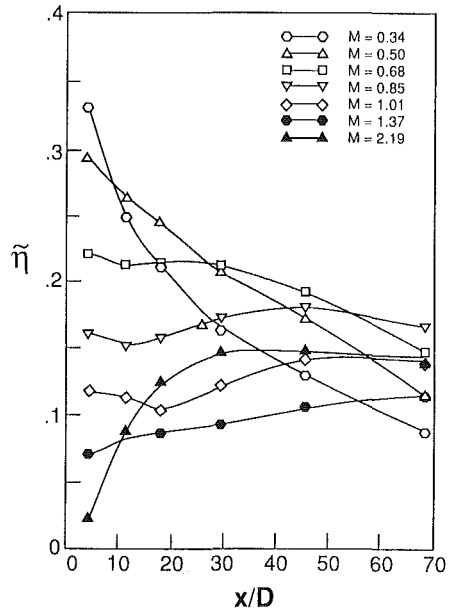

Fig. 8 Film cooling of a convex surface—laterally averaged effectiveness

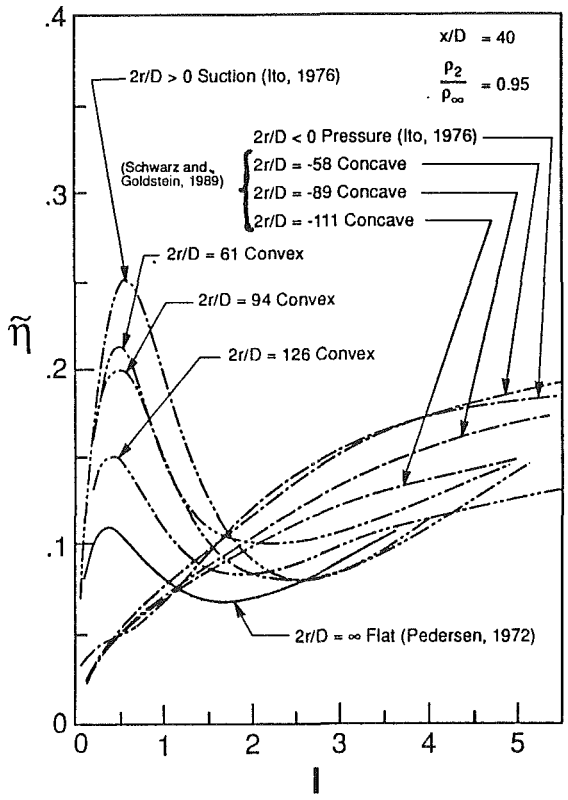

Fig. 9 Film cooling of convex, concave, and flat surfaces—strength of curvature comparison

represent x/D = 10 and 20). Similar differences between concave and convex flows were observed by Ko et al. (1986).

The blowing rate at which the centerline performance is best is larger for higher density injection. The momentum flux ratio where this occurs, however, is nearly the same for the two density ratios (Fig. 7). In fact, the centerline effectiveness correlates fairly well with any momentum flux ratio.

It is reasonable to assume that centerline performance is closely tied to jet liftoff. Figure 7 indicates that momentum flux ratio is the cause of the jets leaving the convex surface. The normal component of momentum of the jets ($I\sin^2\alpha$) obviously pulls the jets away from the surface. Any increase in the tangential component of the momentum flux ratio ($I\cos^2\alpha$) must result in a corresponding increase in the radius of curvature of the jet trajectory because its centripetal acceleration is determined by the cross-stream pressure gradient force. Therefore, a larger momentum flux ratio will improve the chances for jet liftoff. For film cooling on flat surfaces, Pedersen et al. (1977) found good correlation with velocity ratio, rather than momentum flux ratio. Tangential momentum does not contribute as much to jet liftoff on flat surfaces because, in the absence of curvature, there is no cross-stream pressure gradient.

By integrating the local lateral profiles of impermeable wall effectiveness, a laterally averaged effectiveness can be obtained. The integral was computed by fitting a cubic spline to the local effectiveness profiles in the z direction. Figure 8 shows laterally averaged impermeable wall effectiveness with low-density injection on a convex surface for $2r/D$ = 94. (Trends are quite similar for all three injection geometries studied.)

At low blowing rates, the effectiveness improves, with increased injection, due to the added thermal capacity of the coolant, until a maximum is reached. When the blowing rate is further increased past the peak-effectiveness blowing rate, a minimum effectiveness is eventually encountered. After this minimum is encountered, a region of increasing effectiveness with blowing rate is apparent (except at very small x/D). At these larger blowing rates, the amount of coolant added is so

large, both in thermal mass and volume, that the jets have merged and blocked the mainstream from the surface. Also increased dilution of the mainstream boundary layer improves performance. Similar trends are found at a density ratio of 2.0 (Schwarz, 1986); however, the peak-effectiveness blowing rates are higher. Rather, for convex and flat surfaces, it is the peak-effectiveness momentum flux ratio that is fairly constant with density ratio, as can be seen in Fig. 9. This further supports the conclusion drawn from Fig. 7 that jet liftoff is strongly influenced by momentum flux ratio.

Figure 9 also provides some insight into the influence of relative strength of surface curvature on laterally averaged effectiveness. Data are extracted and reduced from the present convex study, the concave study of Schwarz and Goldstein (1989), and the flat and variable curvature turbine blade surfaces of Pedersen et al. (1977) and Ito et al. (1978), respectively.

Increased convex curvature (lower $2r/D$) enhances effectiveness at low injection rate. Beyond a momentum flux ratio of 2, the strength of convex curvature seems to have little effect. In the study by Folayan and Whitelaw (1976), where the actual radius of curvature was varied, and a step-down slot geometry was used, performance also improved with stronger curvature.

Laterally averaged effectiveness is substantially higher on a convex wall than on a flat surface at low injection rates. This is because, at low blowing rates, the effects of cross-stream pressure gradient greatly overshadow the effects of the normal and tangential momentum of the jet, thereby pushing the jets into the convex wall.

On the concave wall, the striking result is the small influence curvature has on effectiveness at low-momentum flux ratio ($I < 1.5$). As the rate of injection is increased, strong concave curvature is found to cause a slight improvement over the weaker curvature.

At $x/D = 40$, concave curvature has better performance at high blowing rates than a flat surface. Lateral mixing helps effectiveness here, promoting blockage (Schwarz and Goldstein, 1989) as occurs with slot injection. At low injection rates, concave instabilities work to dilute the jet, impeding performance when compared to flat surface flows. The cross-stream pressure gradient on the concave wall is another factor that degrades effectiveness, working to move the jets away from the surface.

Ito et al. (1978) found that when $I\cos^2\alpha$ is of the order unity, film cooling effectiveness values on convex, flat, and concave surfaces were similar. Above this value, a concave surface had a higher effectiveness, and a convex surface had a lower effectiveness. At lower I, the reverse is true. Data for the flat wall of Pedersen et al. (1977) and the pressure and suction surfaces of the turbine blade of Ito et al. (1978) support this. Figure 9 shows that film cooling of the surfaces in the present study all exhibit nearly identical performance at a momentum flux ratio of somewhere between 1.5 and 2. Since $\alpha = 35$ deg in the present study, $I\cos^2\alpha = 1$ when $I = 1.5$. When momentum flux ratio is greater than 2, the concave surface performs better than the convex. The convex surface does substantially better than the concave at low-momentum flux ratio. The results of the present study are in reasonable agreement with earlier results.

It should be noted, however, that Schwarz and Goldstein (1989) found that mass flux ratio has a greater influence than momentum flux ratio on film cooling effectiveness of concave surfaces. An increase in momentum flux ratio results in a corresponding increase in tangential and normal momentum. On the concave surface, these two momenta have opposing effects, which tend to cancel each other when the injection angle is near 45 deg. It is the amount of coolant, which acts as a thermal sink and a protective barrier, that determines the film cooling effectiveness on concave surfaces when the injection angle is near 45 deg.

Conclusions

Several factors have been found to influence the performance of film cooling through a row of holes on a curved surface. Some of these are peculiar to curved flows; others are also present in flows along flat surfaces.

Tangential Momentum of Jets. Increasing the relative tangential momentum of the jets, $I\cos^2\alpha$, reduces effectiveness on the convex surface, and improves it on the concave. The radius of curvature of the jet trajectory is increased, pulling it away from a convex wall and pushing it into a concave wall.

Normal Momentum of Jets. The normal momentum of the jets, $I\sin^2\alpha$, works to degrade effectiveness on all surfaces: convex, flat, and concave. As it is increased, the jets tend to lift away from the wall. The influence of normal momentum decreases with increasing x/D.

Mass Added. Increasing the blowing rate increases the thermal mass available to absorb heat from the mainstream. Also, at higher blowing rates, the fact that a very large mass of coolant is injected into the mainstream causes adjacent jets to merge far downstream of injection. This shields the surface from the main flow, hence improving effectiveness. These phenomena are present in both curved and flat flows. When coupled with the instabilities present on the concave surface, blockage is promoted to the point that row of holes injection can be correlated with the parameter ξ (Schwarz and Goldstein, 1989) typically reserved for slot or multirow injection geometries.

Concave Instabilities. Lateral profiles of local effectiveness are much flatter on the concave surface than on the convex. This is attributed to lateral mixing caused by the unstable concave flow. It results in slotlike behavior for row of holes injection. Coupled with the mass added, concave instabilities promote blockage as blowing rate is increased.

Cross-Stream Pressure Gradient. This occurs in all curved flows. A high pressure is at the concave wall, and a low pressure is at the convex. This tends to move film cooling jets into a convex wall and away from a concave. The strength of the pressure gradient is determined by the main flow geometry, not blowing rate. However, the other factors are blowing rate dependent, so cross-stream pressure gradient's relative influence is affected by the mass flux ratio. At low blowing rates, where the tangential and normal momentum are weak, the convex surface is easier to cool than a flat surface, which has better performance than a concave.

Acknowledgments

The research herein was conducted with the support of the Air Force Office of Scientific Research (Contract Number F49620-85-C-0049).

References

Bradshaw, P., 1973, "Effects of Streamwise Curvature on Turbulent Flow," AGARDOgraph No. 169.

Crawford, M. E., Kays, W. M., and Moffat, R. J., 1976, Heat Transfer to a Full-Coverage, Film Cooled Surface With 30 Degree Slant-Hole Injection," Report HMT-25, Thermosciences Division, Department of Mechanical Engineering, Stanford University, CA.

Folayan, C. O., Whitelaw, J. H., 1976, "The Effectiveness of Two-Dimensional Film-Cooling Over Curved Surfaces," ASME Paper No. 76-HT-31.

Furuhama, K., and Moffat, R. J., 1983, "Turbulent Boundary Layer and Heat Transfer on a Concave Wall With Discrete Hole Injection," ASME-H-43 for meeting 3/20-24/1983.

Furuhama, K., Moffat, R. J., and Frota, M. N., 1983, "Heat Transfer and Turbulence Measurements of a Film-Cooled Flow Over a Convexly Curved Surface," ASME Paper No. 83-Tokyo-IGTC-16.

Goldstein, R. J., Eckert, E. R. G., Eriksen, V. L., and Ramsey, J. W., 1970, "Film Cooling Following Injection Through Inclined Circular Tubes," *Israel J. Technology*, Vol. 8, pp. 145–154.

Goldstein, R. J., 1971, "Film Cooling," *Advances in Heat Transfer*, Academic Press, New York.

Ito, S., Goldstein, R. J., and Eckert, E. R. G., 1978, "Film Cooling of a Gas Turbine Blade," ASME *Journal of Engineering for Power*, Vol. 100, p. 476–481.

Kadotani, K., and Goldstein, R. J., 1979, "Effect of Mainstream Variables on Jets Issuing From a Row of Inclined Round Holes," ASME *Journal of Engineering for Power*, Vol. 101, pp. 298–304.

Ko, S.-Y., Xu, J.-Z., Yao, Y.-Q., and Tsou, F.-K, 1984, "Film Cooling Effectiveness and Turbulence Distribution of Discrete Holes on a Convex Surface," *Int. J. Heat Mass Transfer*, Vol. 27, pp. 1551–1557.

Ko, S.-Y., Yao, Y.-Q., Xia, B., and Tsou, F.-K., 1986, "Discrete-Hole Film Cooling Characteristics Over Concave and Convex Surfaces," *Heat Transfer 1986, Proceedings of the Eighth International Heat Transfer Conference*, San Francisco, CA.

Lander, R. D., Fish, R. W., and Suo, M., 1972, "External Heat-Transfer Distribution on Film Cooled Turbine Vanes," *J. Aircraft*, Vol. 9, pp. 707–714.

Mayle, R. E., Kopper, F. C., Blair, M. F., and Bailey, D. A., 1977, "Effect of Streamwise Curvature on Film Cooling," ASME *Journal of Engineering for Power*, Vol. 99, pp. 77–82.

Nicolas, J., and Le Meur, A., 1974, "Curvature Effects on a Turbine Blade Cooling Film," ASME Paper No. 74-GT-156.

Pedersen, D. R., Eckert, E. R. G., and Goldstein, R. J., 1977, "Film Cooling With Large Density Differences Between the Mainstream and the Secondary Fluid Measured With the Heat-Mass Transfer Analogy," ASME *Journal of Heat Transfer*, Vol. 99, pp. 620–627.

Schwarz, S. G., 1986, "Film Cooling of Curved Surfaces," PhD Thesis, University of Minnesota, Minneapolis, MN.

Schwarz, S. G., and Goldstein, R. J., 1989, "The Two-Dimensional Behavior of Film Cooling Jets on Concave Surfaces," ASME JOURNAL OF TURBOMACHINERY, Vol. 111, pp. 124–130.

Tani, I., 1962, "Production of Longitudinal Vortices in the Boundary Layer Along a Concave Wall," *J. Geophysical Research*, Vol. 67, pp. 3075–3080.

G. W. Jumper

W. C. Elrod

Air Force Institute of Technology,
Dayton, OH

R. B. Rivir

Aero Propulsion and Power Laboratory,
Wright Patterson AFB, OH 45433

Film Cooling Effectiveness in High-Turbulence Flow

The mechanisms influencing film cooling effectiveness on a flat plate in high free-stream turbulence using a single row of 30 deg slant-hole injectors are examined. The primary area of focus is the area within 40 diameters downstream of injection. Of interest are blowing ratios for optimum film cooling effectiveness within 10 diameters downstream of injection, and the decay of film cooling effectiveness down the plate. Film cooling flow Reynolds numbers, Re, from 24,700 to 86,600 and free-stream turbulence intensities from 14 to 17 percent were examined. Changes in Reynolds number or free-stream turbulence broadened and increased the blowing ratios for optimum film cooling effectiveness. In comparison with tests conducted at 0.5 percent free-stream turbulence, higher free-stream turbulence causes a faster decay in film cooling effectiveness, or a reduction in the effective cooling length, and a reduction of the level of cooling effectiveness at the higher Reynolds numbers.

Introduction

The use of film cooling for a surface exposed to a high-temperature gas flow is substantially more effective than using convective cooling applied to the back side of the surface. Even though it has been employed for a number of years, there is a lack of understanding of the influence of various parameters of the main flow stream on the effectiveness of film cooling. Current gas turbine film cooling data bases for heat transfer or cooling effectiveness distribution have been generated in conventional wind tunnels with low free-stream turbulence levels (Tu = 0.4 to 2 percent). These data are represented by the work of Han and Mehendale (1986), and Goldstein et al. (1968). In general, the influence of free-stream Tu would be expected to become important when the level of free-stream fluctuations becomes comparable to the fluctuations in the film cooling flow. The local Tu level in a film cooling flow is typically on the order of 10–20 percent (Rivir et al., 1987). Launder and York (1974) found no influence of 4 percent Tu for uniform flow. Brown and Saluja (1979) report a loss in cooling effectiveness for increases in Tu from 2–9 percent. Brown and Minty (1975) also found a loss of cooling effectiveness for Tu levels of 2–8 percent. Ko and Liu (1980) report a loss in cooling effectiveness with increases in Tu correlating the loss with a turbulent mixing coefficient. The variation of Tu scale from experiment to experiment in the literature makes comparison of turbulence/effectiveness data difficult to access. The Tu scales for this study are given by MacMullin et al. (1989). The range of the scale of the Tu is a parameter that remains to be effectively quantified for film cooling. The work of Blair (1983) showed the heat transfer coefficient, without film cooling, to increase dramatically as free-stream turbulence increased to levels up to 6 percent for Tu scales comparable to the boundary layer thickness.

In turbomachinery the turbulence level in the flow passing through the blades is much higher than the 6 to 7 percent that can be generated by placing a grid in the flow of an experimental facility. Wall jets, the free jet, and the jet grid that can establish free-stream turbulence levels of 10 percent or more have been used by MacMullin et al. (1989), Moffat and Maciejewski (1985), and Young and Han (1989), to investigate heat transfer from a flat plate in this extended range. Figure 1, taken from MacMullin et al. (1989), summarizes the current turbulent heat transfer results. It is shown that at a Reynolds number ($Re_{x'}$) of 10^6 the heat transfer coefficient for a turbulence level of 17 percent in the wall jet is 1.8 times that of the fully turbulent relationship of Kays and Crawford (1980). This paper will present results of an investigation of the effectiveness of film cooling under the same 14–17 percent free-stream turbulence conditions obtained in the wall jet facility.

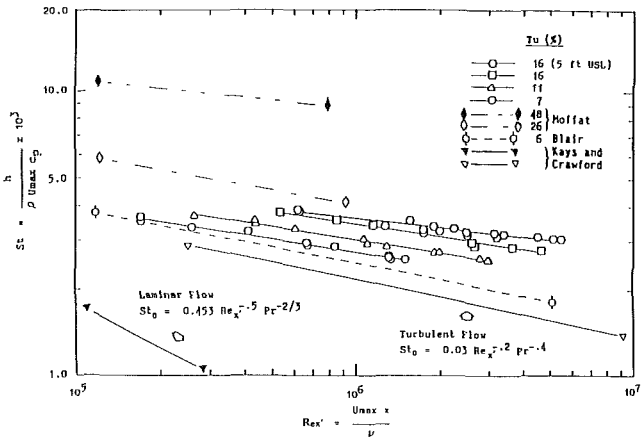

Fig. 1 Effects of high free-stream turbulence on heat transfer

Contributed by the International Gas Turbine Institute and presented at the ASME Winter Annual Meeting, San Francisco, California, December 10–15, 1989. Manuscript received at ASME Headquarters December 1990.

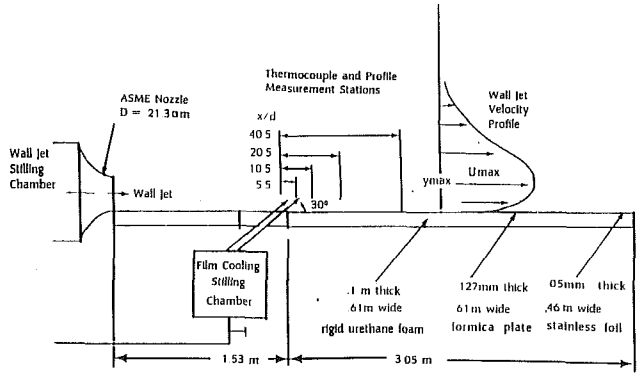

Fig. 2 Wall jet schematic

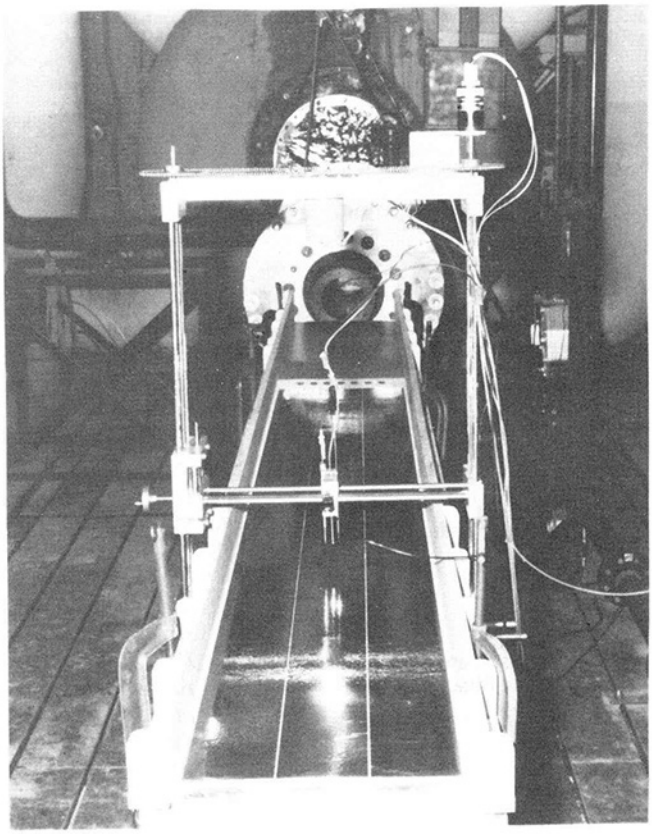

Fig. 3 Wall jet facility with film cooling test section

Apparatus

The wall jet, the flat plate with film cooling, and the instrumentation traverse assembly are shown in Figs. 2 and 3. The flat plate test section consisted of an electrically heated thin film surface 3.05 m long with a 1.52 m unheated starting length. The film cooling injectors consisted of five 2.54 cm diameter injectors with a l/d of 6. The injectors, which have a pitch-to-diameter ratio of 2, are inclined at an angle of 30 deg and are located at the end of the unheated starting length. The following 3.05 m surface is instrumented with 42 copper constantan thermocouples of 0.127 mm diameter to provide the plate temperature distribution. The thermocouple locations on the plate are shown in Fig. 4. The heat transfer, velocity, and temperature profiles of this configuration of the test section without film cooling are given by MacMullin et al. (1989). The heat transfer and cooling characteristics were obtained at x/d locations of 5.5, 10.5, 20.5, and 40.5 for the configuration of Fig. 4.

Film Cooling Model

A simple two-dimensional, two layer model as shown in Fig. 5 can give an insight on the effect of free-stream turbulence on film cooling effectiveness. The flow is divided into a laminar sublayer and a turbulent layer. In the laminar sublayer the mechanism of heat transfer is random collision of molecules and in the turbulent layer the mechanism is from the interaction of eddies. For film cooling an adiabatic surface, the flow of heat is from the warmer turbulent layer in toward the plate into the cooler film, which is adjacent to the plate.

The Stanton number for the wall jet flow over a flat plate

Nomenclature

A = area, m^2
C_p = specific heat at constant pressure, W-s/kg-°C
C_f = coefficient of friction $= 2\tau_p/(\rho_m U^2_{max})$
C = const
C'' = const
D = inside diameter of ASME nozzle, cm
d = outside diameter or dimension, cm
h = heat transfer coefficient, W/m^2-°C
k = thermal conductivity, W/m-K
l = length of film cooling injector, cm
M = blowing ratio $= (\rho_f U_f/\rho_\infty U_\infty)$
Pr = Prandtl number $= \mu C_p/k$
q = heat flux per unit area, W/m^2
Re = Reynolds number $= \rho U d/\mu$
$Re_{x'}$ = Reynolds number $= \rho U x'/\mu$
St = Stanton number $= h/(U_{max}\rho C_p)$
Tu = longitudinal turbulence intensity $= (U'^2)^{0.5}/U_{max}$
U = mean velocity component in x direction, m/s
USL = configuration of test section: unheated starting length attached between nozzle and heated section
U_{max} = maximum U on the y axis at a specified location on the plate
x = distance from film cooling injectors, cm
x' = distance from ASME nozzle, cm
y = vertical distance from plate, cm
y^+ = nondimensional distance from plate, defined by equation (2)
y_{max} = distance above plate where U is a maximum, cm
w = lateral distance, cm
δ = conventional boundary layer thickness, cm
δ_{sl} = laminar sublayer thickness, cm
η = film cooling effectiveness, equation (7)
μ = viscosity, kg/m-s
ν = kinematic viscosity, m^2/s
ρ = density, kg/m^3
τ_p = shear stress at plate, N/m^2

Subscripts

aw = adiabatic wall condition, evaluated at the plate
f = evaluated at the film cooling temperature, T_f
o = evaluated at the film cooling injection station
p = evaluated at the plate
sl = laminar sublayer boundary
x' = evaluated at a distance from the nozzle along the x axis
∞ = reference datum for a calculation, usually at y_{max}

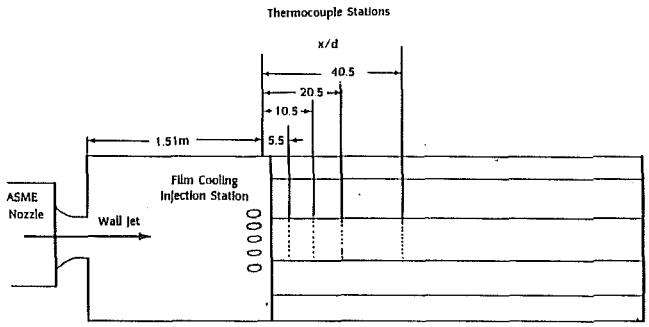

Fig. 4 Thermocouple schematic

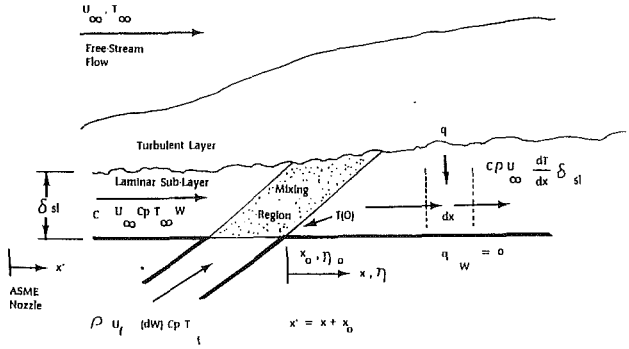

Fig. 5 Two-layer model

with an unheated starting length may be written as (MacMullin et al., 1989)

$$\mathrm{St} = 0.0125\mathrm{Re}_{x'}^{-0.1003}\mathrm{Pr}^{-0.4} \quad (1)$$

which includes the effect of the 17 percent Tu level at the film injector location. The nondimensional y^+ is given by

$$y^+ = y\sqrt{g_c\tau_p/\rho}/\nu = (yU_\infty\sqrt{C_f/2})/\nu \quad (2)$$

where C_f is the coefficient of friction.

Previous measurements on this wall jet (MacMullin et al., 1989) showed that a modified Reynolds analogy could be used to describe the wall jet flow. Combining the modified Reynolds analogy and equation (1), the friction coefficient is

$$C_f/2 = (0.0125\mathrm{Re}_{x'}^{-0.1003}\mathrm{Pr}^{-0.4})/(1.18 + 1.3\mathrm{Tu}/100) \quad (3)$$

Substituting into equation (2), with $y = \delta_{sl}$ at $y^+ = 30$

$$(\delta_{sl}Ux'/x'\nu) \times \sqrt{((0.0125\mathrm{Re}_{x'} - 0.1003\mathrm{Pr}^{-0.4})/(1.18 + 1.3\mathrm{Tu}/100))} = 30 \quad (4)$$

or

$$\mathrm{St}/\delta_{sl} = (C_0(\rho U_\infty)^{0.85})/x'^{0.15} \quad (5)$$

Writing an energy balance for the differential control volume in Fig. 5, dx long and δ_{sl} high

$$C(\rho U_\infty)(\delta_{sl}wdT/dx)dx = qwdx \quad (6)$$

With q flowing into the control volume and $T = T_{aw}$, on substituting into equation (5), separating variables, and integrating:

$$\eta/\eta_0 = (T - T_\infty)/(T_{(0)} - T_\infty) = \exp(-C''\mathrm{Re}_x^{0.85}(1 - (x_{(0)}/x'^{0.85})) \quad (7)$$

This model allows a prediction of the behavior of cooling effectiveness with Reynolds number to be made. If at least two data points are known, then one can solve for C'' and the film cooling effectiveness at $x = 0$, assuming perfect mixing occurs in the mixing region. If ρU_∞ increases in equation (5), then the heat transfer coefficient, h, will also increase and the sublayer thickness will decrease. This will have the effect of increasing the decay in film cooling effectiveness as the Reynolds number increases in equation (7). Increased turbulence intensity decreases the film cooling effectiveness down the plate as a result of the faster mixing, which results in the large increases in heat transfer (equation (1)) and skin friction (equation (3)).

Experimental Results

The purpose of the investigation was to assess the importance and the effect of the interaction of high free-stream turbulence (14–17 percent) with a film cooling flow, which likewise has a local turbulence level of 15–20 percent. Existing data bases have reported film cooling effectiveness values and effective cooling lengths from experiments with free-stream levels of 0.4 to 2 percent. In the current data base the high turbulence levels of the cooling film dominate the heat transfer and the flow structure near the plate. This can be observed from the flow visualization by Rivir et al. (1987) in which the free-stream turbulence was raised from 1 to 4 percent with virtually no change in the film cooling turbulence structure. We would expect a strong interaction with the cooling film as the free-stream turbulence levels are raised to a level comparable to that in the film. The issues to be addressed then are whether the Reynolds number dependence, the value of the film cooling effectiveness versus x/d, and the optimum blowing ratios used in turbine design data bases are valid.

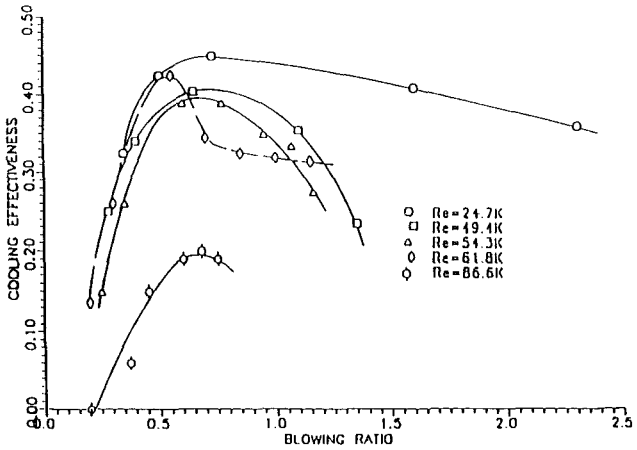

Fig. 6 Cooling effectiveness at x/d = 5.5

Optimum Blowing Ratio. The optimum density-velocity ratio or blowing ratio (M) was reported by Han and Mehendale (1986) to be 0.5 to 0.7 at a Re = 20,000. Other turbine investigations have reported optimum ratios down to 0.3. The observed high-turbulence blowing ratio dependence is illustrated in Figs. 6–8. At an x/d of 5.5 (Fig. 6), this optimum blowing ratio ranges from 0.5 to 0.7, with Re = 24,700. Progressing downstream in x/d to 10.5 and 20.5 (Figs. 7 and 8), the maximum becomes much broader at the low Reynolds numbers extending to 1.5 and 2, respectively. With increase of Reynolds number, cooling effectiveness is attenuated and the optimum blowing ratio for a Reynolds number of 86,600 has stayed at 0.5 to 0.6. Limitations in both pressure and flow rate restricted the range of data that could be collected at an x/d of 40.5. Although the x/d = 40.5 data have not been included, at 40.5 x/d the trend to broaden and suppress appears to continue.

Reynolds Number Dependence and Effective Cooling Length. The low Reynolds number behavior is illustrated in

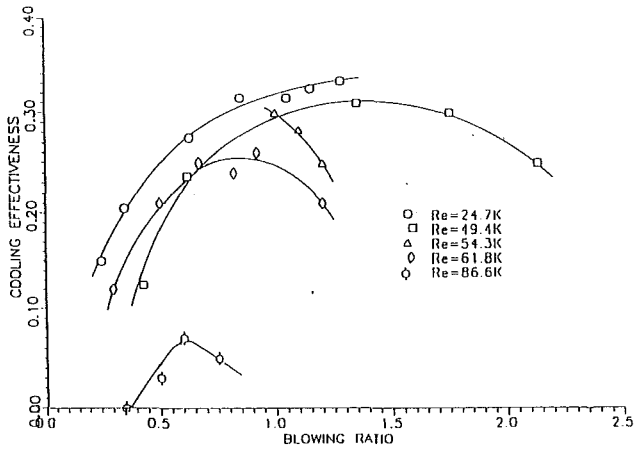

Fig. 7 Cooling effectiveness at x/d = 10.5

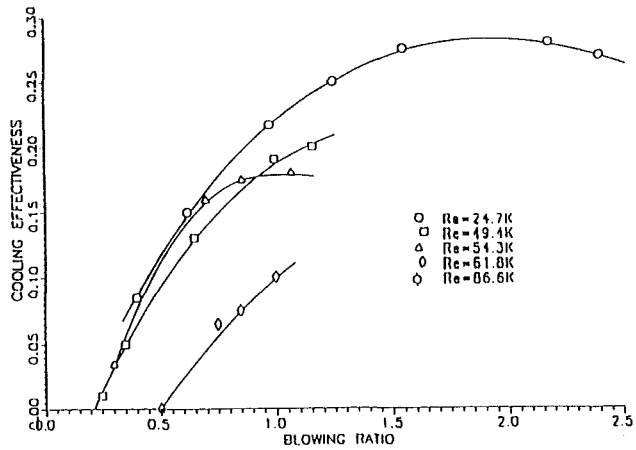

Fig. 8 Cooling effectiveness at x/d = 20.5

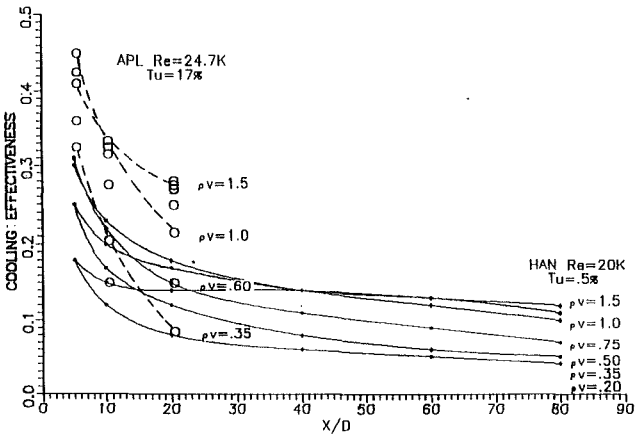

Fig. 9 Comparison of low Reynolds number flows

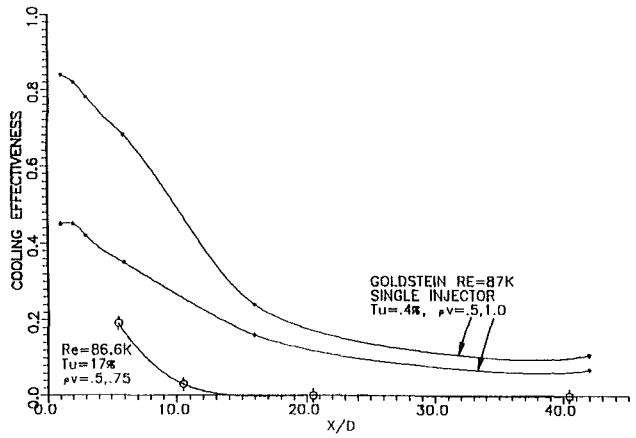

Fig. 10 Comparison of high Reynolds number flows

Table 1 Tabulated data for Fig. 9

x/d	Cooling effectiveness	Blowing ratio
5.5	0.450	0.73
	0.425	0.50
	0.410	1.60
	0.360	2.30
	0.325	0.35
10.5	0.333	1.28
	0.325	1.15
	0.310	1.05
	0.275	0.63
	0.205	0.35
	0.150	0.25
20.5	0.280	2.18
	0.275	1.55
	0.270	2.40
	0.250	1.25
	0.2150	0.62
	0.085	0.40

Fig. 9 where the high turbulence data at Re of 24,700 are superimposed on the single row data of Han and Mehendale (1986), which had a free-stream Tu level of 0.5 percent. Blowing ratios from 0.2 to 2.3 have been tabulated in Table 1 and plotted in the figure with curves through the experimental data for nominal blowing ratios of 1.5, 1.0, 0.6, and 0.35. The decrease of the cooling effectiveness for the high blowing ratio ($M > 1$) data compared to the lower blowing ratio data is attributed to lift-off of the cooling flow. The high Tu blowing ratio data, $\rho v \leq 1$, show higher cooling effectiveness values than the low-turbulence data at low x/d values. The rate of decrease, $d\eta/d(x/d)$, for the high Tu data is much larger in the range $10 < x/d < 20$ for all values of $\rho v_\infty \leq 1$. This indicates that the high free-stream Tu promotes mixing with the cooling flow and reduces its effectiveness. However, the $M = 0.35$ data appear to be greater than for the low-turbulence data. More extensive high Tu data should be obtained in the low Reynolds number range, particularly at $x/d \geq 20$.

A change of the distance for which film cooling is effective is shown in Fig. 10, which compares Goldstein et al. (1968), Re = 87,000, single injector, Tu = 0.4 data for blowing ratios of 0.5 and 1.0 with the high Tu curves for blowing ratios of 0.5 and 0.75. There was no measurable difference for the high Tu = 0.5 and 0.75 data at high Re. The high Tu cooling effectiveness data go to zero at an x/d of 14 as shown in the figure whereas the low Tu data maintain some effectiveness out beyond x/d = 40. Figure 11 illustrates the effect of Reynolds number on film cooling effectivness for low and high free-stream turbulence at a blowing ratio of 0.5. At low free-stream turbulence, 0.4 percent, the cooling effectiveness is relatively insensitive to Reynolds number but decreases with x/d. This indicates an interaction of the film with the free stream so as to increase film temperature with distance downstream. This reduces cooling effectiveness but leaves the film intact in the range of Reynolds numbers and x/d shown. The high turbulence, 14–17 percent, data show two effects: (1) The cooling effectiveness at middle Reynolds numbers (40,000) is reduced by at least one third at each x/d due to increased interaction between free stream and film, thus increasing the film temperature, and (2) the cooling film is destroyed by aggressive mixing with the turbulent layer. The first effect also appears

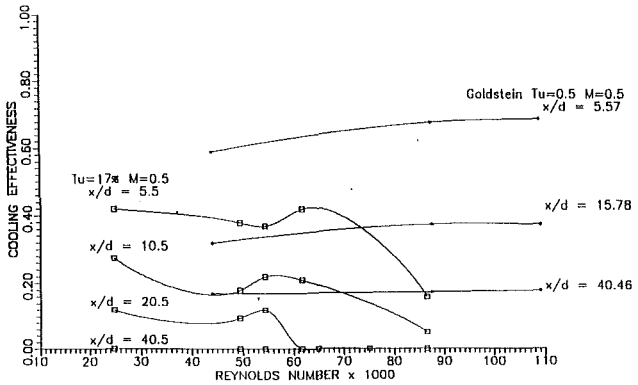

Fig. 11 Reynolds number effects of high turbulence

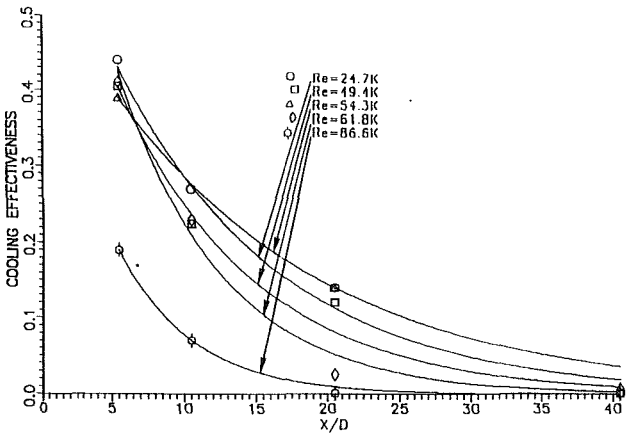

Fig. 12 Comparison of model and experiment for $M = 0.6$

to be insensitive to Reynolds number but the second effect produces a large reduction of cooling effectiveness with increase of Reynolds number. In addition, the second effect is influenced by distance from the cooling injection point, such that the reduction of effectiveness with increase of Reynolds number occurs at lower Reynolds numbers with increase of x/d. The cooling effectiveness totally disappeared for the high Tu data by an x/d of 40.5.

Comparison of Data Against the Theoretical Model. The theoretical model provides an estimate of the decay of cooling effectiveness of the film away from the injector. Two measured values are required to establish a theoretical curve. The model results for Re of 86,600, 61,800, 54,300, 49,400, and 24,700 are compared against the experimental measurements in Fig. 12. The data decrease approximately exponentially with x/d. The data presented are for a blowing ratio of 0.6. Although retaining the exponential decay characteristic, the effect of changing blowing ratio is to shift the curves. The turbulence intensity did not specifically appear in the St relation of equation (1) since this relation was developed for a fixed turbulence intensity of 17 percent; the turbulence intensity remains approximately constant for the wall jet after x/D greater than 10 (MacMullin et al., 1989). The turbulence intensity varied from 14 to 17 percent for the predicted region downstream of the injection point of the film cooling.

Conclusions

The turbulence levels of 14–17 percent resulted in significant reductions in the effective film cooling length compared to data bases with turbulence levels of 1/2 percent. At high Tu the cooling films are decreased with increase in x/d greater than 20.5 for all blowing ratios ranging from 0.2 to 2.1, with the film effectively destroyed by an x/d of 40 for low Reynolds numbers and by x/d of 20 for high Reynolds (86,600) numbers. The Reynolds number dependence of effectiveness showed no additional reduction in effectiveness and destruction of the film that is not observed in low free-stream turbulence data bases as the Reynolds number increases. The optimum blowing ratios for the high turbulence levels were found to be much broader and higher than is reported for the low turbulence data bases. It is clear that the use of low turbulence data bases is inadequate for high turbulence applications and that high turbulence results in a significant shortfall of cooling lengths as well as the heat removed.

References

Blair, M. F., 1983, "Influence of Free-Stream Turbulence on Turbulent Boundary Layer Heat Transfer and Mean Profile Development, Parts I & II," ASME *Journal of Heat Transfer*, Vol. 105, pp. 34–47.

Brown, A., and Minty, A. G., 1975, "The Effects of Mainstream Turbulence Intensity and Pressure Gradient on Film Cooling Effectiveness for Cold Air Injection Slits of Various Ratios," ASME Paper No. 75-WA/HT-17.

Brown, A., and Saluja, C. L., 1979, "Film Cooling From Three Rows of Holes on Adiabatic Constant Heat Flux and Isothermal Surfaces in the Presence of Variable Free-Stream Velocity Gradients and Turbulence Intensity," ASME Paper No. 79-GT-24.

Goldstein, R. J., Eckert, R. G., and Ramsey, J. W., 1968, "Film Cooling With Injection Through Holes: Adiabatic Wall Temperatures Down Stream of a Circular Hole," ASME *Journal of Engineering for Power*, Vol. 90, pp. 384–395.

Han, J. C., and Mehendale, A. B., 1986, "Flat Plate Film Cooling With Steam Injection Through One Row and Two Rows of Inclined Holes," ASME JOURNAL OF TURBOMACHINERY, Vol. 108, pp. 137–144.

Kays, W. M., and Crawford, M. E., 1980, *Convective Heat and Mass Transfer*, 2nd ed., McGraw-Hill, New York, pp. 76, 172, 176, 211–217.

Ko, Shao-Yen, and Liu, Deng-Ying, 1980, "Experimental Investigations on Effectiveness, Heat Transfer Coefficient, and Turbulence of Film Cooling," *AIAA Journal*, Vol. 18, No. 8, pp. 907–913.

Launder, B. E., and York, J., 1974, "Discrete-Hole Cooling in the Presence of Free Stream Turbulence and Strong Favorable Pressure Gradient," *International Journal of Heat and Mass Transfer*, Vol. 17, pp. 1403–1409.

MacMullin, R., Elrod, W. C., and Rivir, R. B., 1989, "Free Stream Turbulence From a Circular Wall Jet on a Flat Plate Heat Transfer and Boundary Layer Flow," ASME JOURNAL OF TURBOMACHINERY, Vol. 111, pp. 78–86.

Moffat, R., and Maciejewski, P. K., 1985, "Heat Transfer With Very High Free-Stream Turbulence," NASA Grant NAG3-522, *Proceedings of the 1985 Turbine Engine Hot Section Technology Conference*, NASA Conference Publication 2405, pp. 203–215.

Rivir, R., Roqumore, W., and McCarthy, J., 1987, "Visualization of Film Cooling Flows Using Laser Sheet Light," Paper No. AIAA-87-1914.

Young, C. D., and Han, J. C., 1989, "The Influence of Jet-Grid Turbulence on Turbulent Boundary Layer Flow and Heat Transfer," Texas A&M University Contractor Report-RF 5734, Mar.

Film Cooling in the Presence of Mainstream Pressure Gradients

A. J. H. Teekaram

C. J. P. Forth

T. V. Jones

University of Oxford,
Department of Engineering Science,
Oxford, United Kingdom

Film cooling in the presence of mainstream pressure gradients typical of gas turbines has been studied experimentally on a flat plate. This paper describes measurements of the spanwise-averaged effectiveness and heat transfer coefficient for an inclined slot and a single row of holes in the presence of favorable, zero, and adverse pressure gradients. Acceleration parameters of $K=2.62\times10^{-6}$ and -0.22×10^{-6} were achieved at the point of injection where the free-stream unit Reynolds number was held constant at $Re/m=2.7\times10^{7}$. The flow was accelerated to high Mach number and results are analyzed using a superposition model of film cooling, which included the effects of viscous energy dissipation. The experimental results show that the effects of pressure gradient differ between the geometries and a discussion of these results is included. The unblown turbulent boundary layers with pressure gradient were also studied. Experiments were performed using the Isentropic Light Piston Tunnel, a transient facility that enables conditions representative of those in the engine to be attained.

Introduction

Research to date at Oxford has investigated the separate effects of injection rate, injection geometry, and injection-to-mainstream density ratios on film cooling on a flat plate with zero pressure gradient (Smith, 1974; Loftus, 1982; Forth, 1985). The use of foreign gas to simulate the coolant-to-mainstream density ratio under zero pressure gradient has also been studied (Teekaram et al., 1989). The present work is an extension of these studies to include an experimental investigation of blade representative pressure gradients on film-cooling performance.

Since only limited studies have been made in this particular area of research, the literature on the subject is rather sparse. A comprehensive review of the reported work (Teekaram, 1989) shows the effect of pressure gradient on the film-cooling effectiveness to differ between geometries. This review includes the work of such authors as Hartnett et al. (1961), Seban and Back (1962), Pai and Whitelaw (1969), Liess (1975), Launder and York (1974), Kruse (1985), and Hay et al. (1985). For two-dimensional slot injection, the influence of favorable pressure gradients is a small decrease in the effectiveness at a given point relative to zero pressure gradient values. For example, Hartnett et al. (1961) report little change in the measured boundary layer temperature profiles despite large differences in the measured velocity profiles. The acceleration parameters used were of order $K=0.86\times10^{-6}$ and 2.75×10^{-6}. The general findings of Pai and Whitelaw (1969) at $K=1.0\times10^{-6}$, 1.82×10^{-6}, and 3.30×10^{-6} showed in addition that the small influence of pressure gradient is dependent on the distance from the slot and coolant-to-gas velocity and density ratios. The reported studies in adverse pressure gradients for a slot are contradictory, but again the observed differences with respect to zero pressure gradient are small.

For three-dimensional hole injection, no consistent view emerges concerning the influence of pressure gradient on the effectiveness. The use of mainstream pressure gradients does however appear to have a strong influence on the behavior of the cooling jets in the vicinity of injection. There are a few results on the effect of mainstream pressure gradients on the heat transfer coefficient with film cooling. Hay et al. (1985) report a substantial decrease in the heat transfer coefficient in the presence of a strong favorable pressure gradient for three-dimensional hole injection. The acceleration parameter was varied from 5×10^{-6} at the point of injection to a nearly constant value of 2×10^{-6} at $X/D\geq20$. The decrease in the heat transfer coefficient was attributed to relaminarization of the turbulent boundary layer, particularly at low mass flux ratios. With a mild favorable pressure gradient of $K=1.0\times10^{-6}$, which was nearly constant over the test surface, Hay et al. also reported a decrease in the heat transfer coefficient relative to zero pressure gradient values at a given position for mass flux ratios below 0.5. In the presence of a mild adverse pressure gradient ($K=-0.85\times10^{-6}$) there was no significant effect on the heat transfer coefficient at a given position when compared to zero pressure gradient values.

The present paper reports on experimental results obtained under isothermal wall conditions for a 30 deg inclined slot and a single row of 30 deg holes in the presence of a strong favorable and a mild adverse pressure gradient. Both the isothermal effectiveness and the heat transfer coefficient are measured in all cases. The results are compared with the zero pressure gradient results of Forth (1985), for similar cooling geometries and at the same experimental conditions. Since many of the data are acquired in high flow velocities, a superposition model, which includes the effects of viscous dissipation due to Jones (1989), is used to interpret the film-cooling results. The effect

Contributed by the International Gas Turbine Institute and presented at the 35th International Gas Turbine and Aeroengine Congress and Exposition, Brussels, Belgium, June 11-14, 1990. Manuscript received by the International Gas Turbine Institute January 19, 1990. Paper No. 90-GT-334.

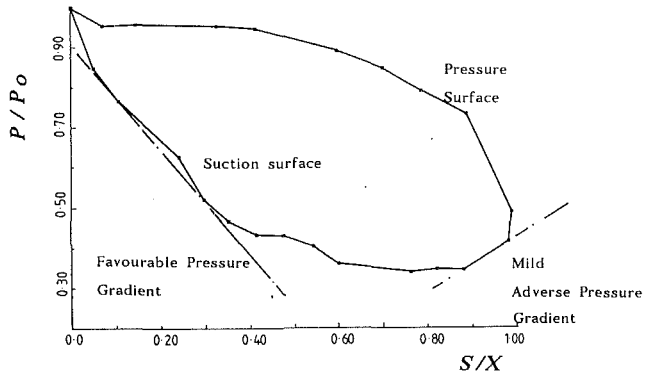

Fig. 1 A typical turbine blade pressure distribution (Johnson, 1988)

of mainstream pressure gradients on the unblown turbulent boundary layer is also investigated to establish a baseline heat transfer level for the film-cooling experiments.

Superposition Model of Film Cooling With Viscous Dissipation

The film-cooling process has been described by a superposition model in past work at Oxford for cases where the wall is isothermal. This model, which is based on the superposition of temperature fields, has been developed and validated for incompressible flow. The theory is extended to include the effect of viscous energy dissipation. As described by Jones (1989), a total temperature field in the presence of film cooling with dissipation may be represented as

$$T(x, y) = T_{aw}(x, y) + T_1(x, y)[T_w - T_{r1}] + T_2(x, y)[T_{ti} - T_{t\infty}] \quad (1)$$

T_{aw} is a nonhomogeneous solution to the temperature field with dissipation when the coolant is at the free-stream total temperature, and there is zero heat transfer to the surface at the point of interest on the isothermal wall. Under these conditions the isothermal wall temperature equals the local recovery temperature, T_{r1}. T_1 is the homogeneous solution to the temperature field in the absence of dissipation when the coolant is at free-stream temperature and there is unit difference between this and the wall temperature. T_2 is similarly defined as a homogeneous solution when the wall is at the free-stream total temperature and the difference between the coolant and the free stream is unity. The fluid dynamics is considered to be constant for all these cases and fluid properties independent of the thermal boundary conditions are assumed. Differentiating with respect to y using Fourier's conduction law $\dot{q} = -k(\partial T/\partial y)$ and setting $y = 0$ gives

$$\dot{q}/k = 0 + \alpha(x)[T_w - T_{r1}] + \beta(x)[T_{ti} - T_{t\infty}] \quad (2)$$

$(\partial T_{aw}/\partial y) = 0$ since this is the adiabatic wall condition for which the heat transfer is zero at a point on the isothermal wall. Equation (2) is rearranged to give the unit Nusselt number

$$\mathrm{Nu}_m = \dot{q}/k(T_{r1} - T_w) = \alpha(x) + \beta(x)\theta \quad (3)$$

α and β are functions of the free-stream and injection fluid dynamics and are independent of the thermal boundary conditions. This, therefore, is the superposition description with dissipation where $\theta = (T_{t\infty} - T_{ti})/(T_{r1} - T_w)$.

In the present study, T_{r1} is approximated to be close to the free-stream recovery temperature $T_{r\infty}$, which is obtained in the absence of injection. For moderate blowing rates, this approximation is justified, since in the vicinity of injection $\mathrm{M} \approx 0.5$ and the effects of dissipation will be small; thus $T_{r1} \approx T_{t\infty} \approx T_{r\infty}$. Far downstream T_{r1} is expected to tend to the free-stream recovery temperature without injection and again the approximation is justified. This simplification is most appropriate for large values of $T_{r\infty} - T_w$.

For a given Reynolds number, equation (3) can be divided by the unblown local unit Nusselt number to give

$$\mathrm{Nu}_m/\mathrm{Nu}_o = A(x) + B(x)\theta \quad (4)$$

The superposition model therefore predicts that for a given flowfield, there is a linear dependence of the Nusselt number on θ. For a constant flowfield to be maintained, the free-stream and injection temperatures must be held constant. θ is varied by changing the wall temperature. A and B are, respectively, the intercept and slope of the Nusselt number versus θ plot.

To compare the effects of pressure gradient on the film-cooling performance, the nondimensional quantities A and B are examined. A quantifies the local ratio of the heat transfer coefficient relative to the zero injection value produced by the mixing of the two flows when the coolant is at the free-stream total temperature. When the coolant total temperature is not equal to the free-stream value, $-B/A$ quantifies the fraction of the difference between these temperatures that the local adiabatic wall temperature differs from the local recovery temperature. Thus a result of the superposition theory with dis-

Nomenclature

a = speed of sound, m/s
D = hole diameter or slot width, m
k = thermal conductivity, W/mK
Nu_m = unit Nusselt number, m^{-1}
$\dot{q}$ = heat transfer rate per unit area, W/m
S = blade surface distance from leading edge, m
T = temperature, K
u = velocity, m/s
X = distance from injection, m
α, β = film-cooling parameters in the superposition model, m^{-1}
μ = dynamic viscosity, $\mathrm{Ns/m}^2$
ρ = density, $\mathrm{kg/m}^3$
A, B = film-cooling parameters in the superposition model
G = mass flux ratio = $\rho_i u_i/\rho_\infty u_\infty$
K = acceleration parameter = $(\nu/u_\infty^2)du_\infty/dx$
M = Mach number = u_∞/a_∞
Nu = Nusselt number = $\dot{q}x/k_{t r\infty}(T_{r\infty} - T_w)$
Re = Reynolds number = $\rho_\infty u_\infty x/\mu_\infty$
Re'_x = integral Reynolds number = $(1/\mu)\int_0^x \rho_\infty u_\infty dx$
St = Stanton number = $h/\rho_\infty u_\infty c_p$
η_{iso} = effectiveness = $(T_{r\infty} - T_{\mathrm{awiso}})/(T_{t\infty} - T_{ti})$
θ = $(T_{t\infty} - T_{ti})/(T_{r\infty} - T_w)$

Subscripts

awiso = adiabatic isothermal wall
i = injection
iso = isothermal
M.A.P.G = mild adverse pressure gradient
o = without injection
r = recovery
S.F.P.G. = strong favorable pressure gradient
t = total
w = wall
Z.P.G. = zero pressure gradient
∞ = free stream

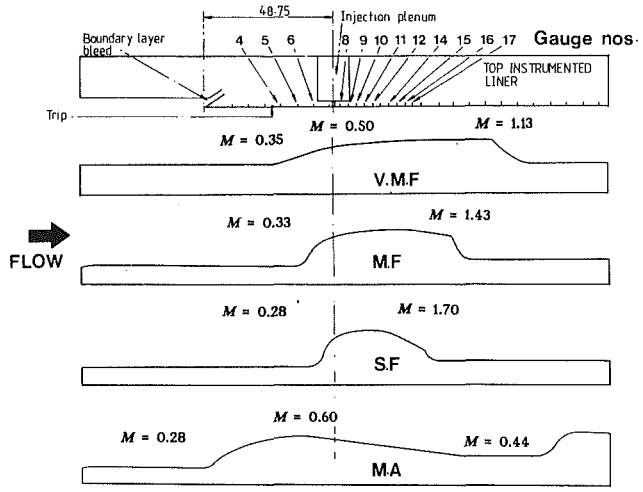

Fig. 2 Profiles of pressure gradient nozzles

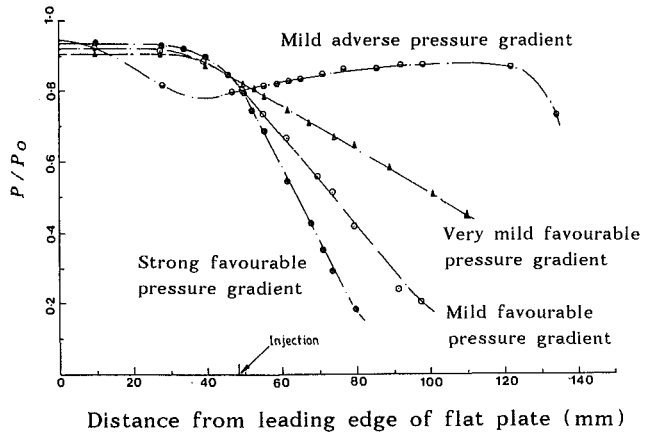

Fig. 3 Measured mainstream pressure distributions

sipation is the manner in which the film-cooling effectiveness is defined:

$$\eta_{\text{iso}} = -B/A = \frac{1}{\theta_{\text{awiso}}} = \frac{T_{r\infty} - T_{\text{awiso}}}{T_{t\infty} - T_{ti}} \tag{5}$$

T_{awiso} is a particular value of the isothermal wall temperature for which the heat transfer rate is zero at a point. The effects of dissipation are thus taken into account in the present experiments if the cooling effectiveness is defined as in equation (5). In the event that injection itself takes place at high Mach number, then $T_{r\infty}$ should be replaced by T_{r1}.

Pressure Gradient Nozzle Design

In order to simulate turbine conditions in the flat plate experiment, the surface distance was similar to that on a blade. Thus similarity was satisfied merely by matching free-stream Reynolds number and Mach number or pressure ratio along the nozzle. For the purposes of the present study, four mainstream pressure gradients were employed: [*a*] a strong favorable pressure gradient (S.F.), [*b*] a mild favorable pressure gradient (M.F.), [*c*] a very mild favorable (V.M.F.), and [*d*] a mild adverse (M.A.). Contoured nozzles to reproduce the desired pressure gradient were designed from the measured nondimensional pressure distribution around several turbine blades. Figure 1 shows a typical distribution determined around a turbine blade in a two-dimensional cascade at Oxford under engine representative Mach numbers and Reynolds number (Johnson, 1988). The maximum favorable pressure gradient occurs on the leading section of the blade suction surface where

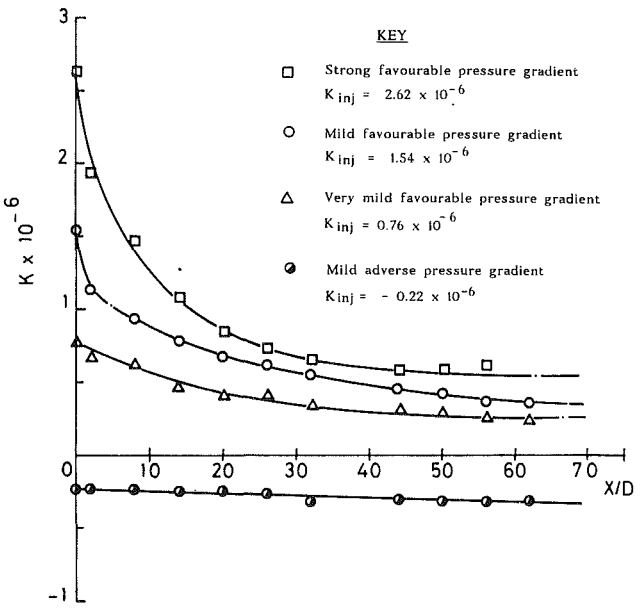

Fig. 4 Variation of the acceleration parameter *K* with *X/D* from the point of injection

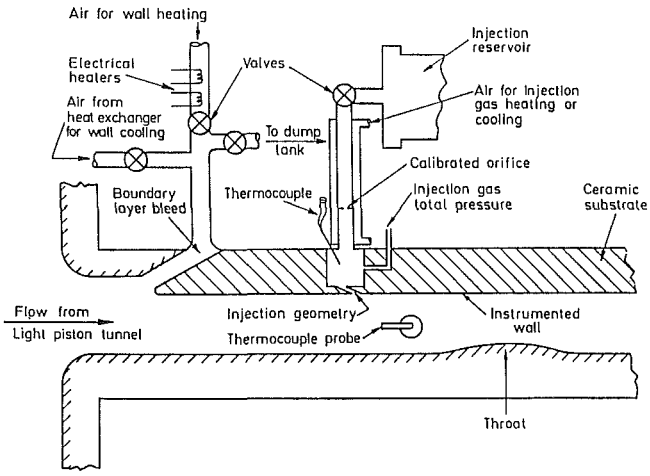

Fig. 5 Schematic of the working section of the Isentropic Light Piston Tunnel

the flow accelerates rapidly from subsonic to supersonic conditions. At $X/S \geq 0.89$ a mild adverse pressure gradient exists.

The profiles of each nozzle are shown in Fig. 2 and these impose the desired pressure gradient upstream and downstream from the proposed point of injection on the test surface. The inlet Mach number is shown in all cases and the Mach number at the point of injection was maintained nominally at a value of 0.5. Nozzles [*a*]-[*c*] were designed to produce a linear variation of P/P_o with X/S as this approximated the leading part of the suction surface as shown in Fig. 1 For a M.A.P.G., a 7 deg diverging nozzle was employed. The results of the measured mainstream pressure gradients are presented in Fig. 3 and these showed agreement with the designed pressure distributions.

Figure 4 shows the values of the acceleration parameter K for each pressure gradient. With a S.F.P.G., the maximum value of $K = 2.62 \times 10^{-6}$ was achieved at the injection holes. At this value, relaminarization of the turbulent boundary layer is not expected.

Experimental Facility and Test Conditions

Results were obtained using the Isentropic Light Piston Tun-

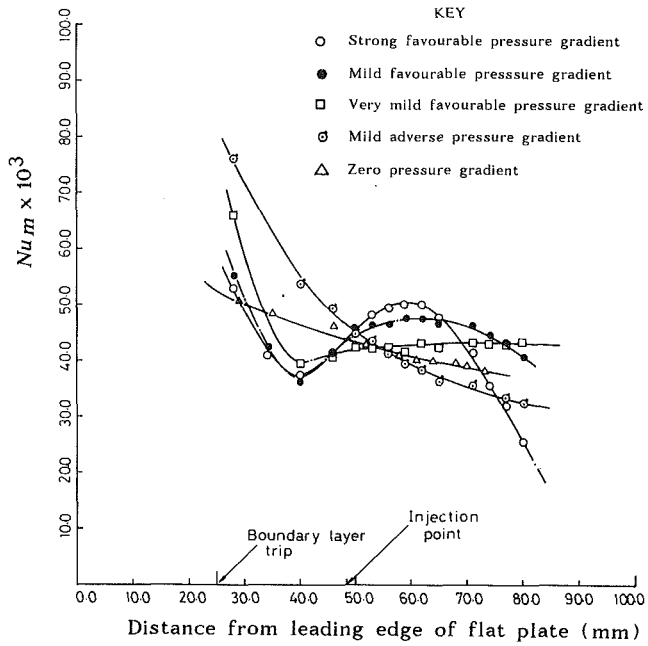

Fig. 6 Effect of mainstream pressure gradients on the Nusselt number for zero injection

Table 1

Free-stream total temperature $T_{t\infty}$	Injection total temperature T_{ti}	$T_{ti}/T_{t\infty}$
365 K	300 K	0.82
280 K	340 K	1.21

nel, a transient facility in which the test gas was compressed in a tube by an air-driven piston before flowing through the working section at constant pressure and temperature (Jones et al., 1973). A schematic of the working section is shown in Fig. 5. Surface temperatures were measured using thin film platinum resistance thermometers from which spanwise-averaged heat transfer rates were computed using established transient techniques. A comprehensive treatment of their characteristics and use is given by Schultz and Jones (1973). The instrumented flat plate was either preheated or precooled by forced convection using air that was electrically heated or cooled using a liquid nitrogen heat exchanger. A wall temperature range of 280 K $< T_w <$ 350 K was obtainable. The boundary layer was tripped at $x = 25$ mm from the leading edge of the flat plate in all cases.

Preliminary experiments were conducted to establish the effect of pressure gradient on the turbulent boundary layer without injection. The unit Reynolds number and Mach number at the proposed point of injection were 2.7×10^7/m and 0.5, respectively.

Film-cooling results were obtained for a S.F.P.G. and a M.A.P.G. The geometries tested were a 30 deg inclined slot, length-to-width ratio of 5.0, nominal width 0.5 mm and a single row of 30 deg holes, spacing-to-diameter ratio of 2.5, with nominal diameter 0.5 mm. The unit Reynolds number and Mach number at the point of injection were the same as for the unblown heat transfer experiments. The coolant and free-stream temperatures were fixed as in Table 1 and results were obtained in the region $2 \leq X/D \leq 62$ for a range of mass flux ratios at two temperature ratios.

The absolute uncertainty in the basic measurement of the heat transfer rate was approximately ±3 percent of the unblown levels, being due to the uncertainty in the thermal product of the model material (machinable glass ceramic). Free-stream and coolant total temperature uncertainties are approximately ±1 K. The errors in the reported values of A and

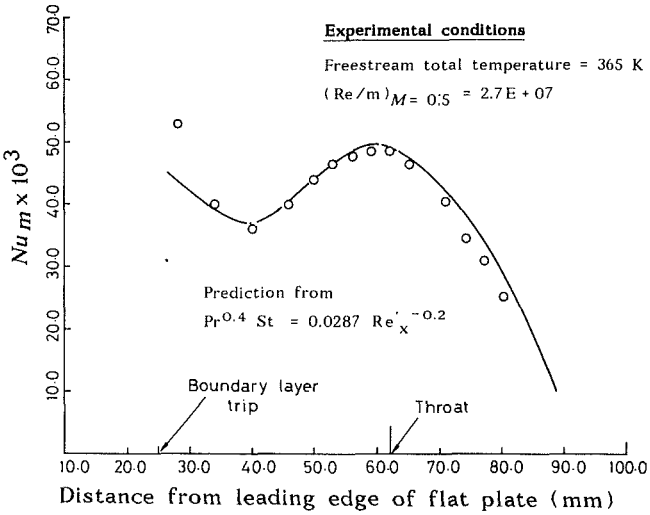

Fig. 7 Strong favorable pressure gradient results and a comparison with equation (6)

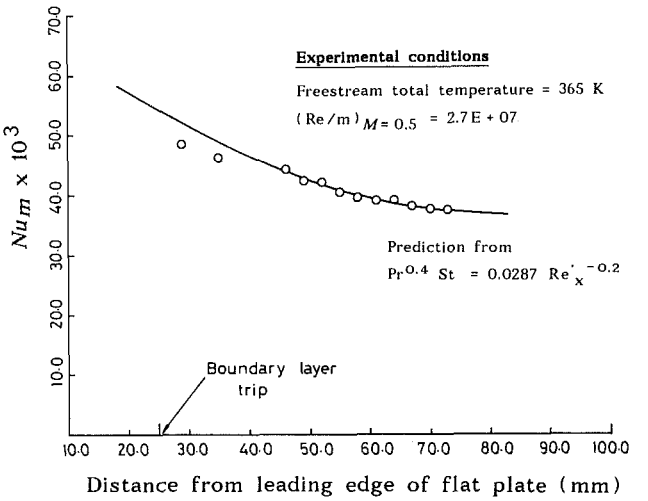

Fig. 8 Zero pressure gradient results and a comparison with equation (6)

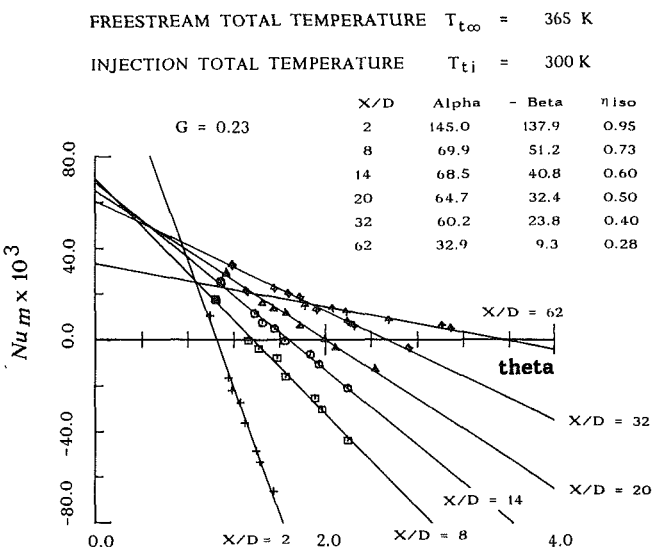

Fig. 9 30 deg slot data: linearity of the Nusselt number with θ for a strong favorable pressure gradient at $T_{ti}/T_{t\infty} = 0.82$

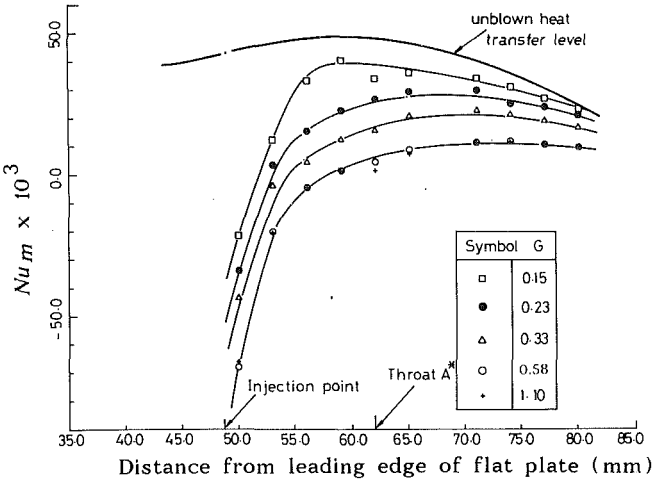

Fig. 10 30 deg slot data: effect of injection on the Nusselt number at $\theta = 1.3$, $T_{ti}/T_{t\infty} = 0.82$ for a strong favorable pressure gradient

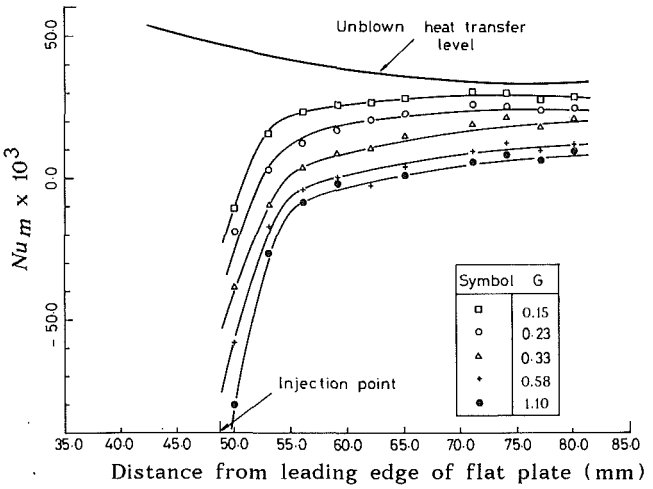

Fig. 11 30 deg slot data: effect of injection on the Nusselt number at $\theta = 1.3$, $T_{ti}/T_{t\infty} = 0.82$ for a mild adverse pressure gradient

B arise due to the small random errors in the linear plots of Fig. 9. For given X/D, i.e., a given heat transfer gage, the systematic error in A is eliminated as it is a ratio and only the random error of ±3 percent is relevant. The errors in the slope B are similar. The absolute error in the effectiveness arises due to temperature measurements only and are of order ±4 percent. The absolute error in the Nusselt number in Figs. 10–13 is ±5 percent.

Heat Transfer Results With Pressure Gradient for Zero Injection

Figure 6 shows the effect of mainstream pressure gradients on the unit Nusselt number. The unit Nusselt number is defined in terms of the local free-stream recovery temperature. In all cases the unit Nusselt number falls initially with distance and for the favorable pressure gradients rises again at the throat subsequently falling in the supersonic region. Figures 7 and 8 show a comparison of the results for a strong favorable and zero pressure gradient with predictions using the following correlation of Kays and Crawford (1980):

$$\mathrm{St}\ \mathrm{Pr}^{0.4} = 0.0287\ \mathrm{Re}_x'^{\,-0.2} \tag{6}$$

from which the unit Nusselt number can be obtained. In general there has been good agreement of the data with predictions for all pressure gradients investigated.

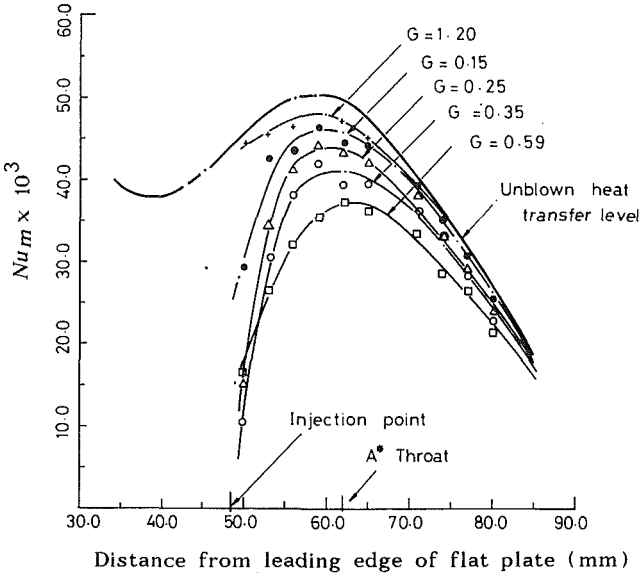

Fig. 12 30 deg single row data: effect of injection on the Nusselt number at $\theta = 1.3$, $T_{ti}/T_{t\infty} = 0.82$ for a strong favorable pressure gradient

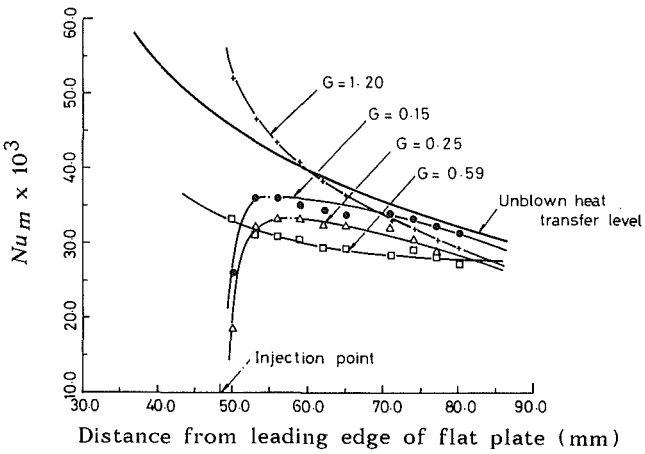

Fig. 13 30 deg single row data: effect of injection on the Nusselt number at $\theta = 1.3$, $T_{ti}/T_{t\infty} = 0.82$ for a mild adverse pressure gradient

Film-Cooling Results and Discussion

Verification of the Superposition Theory of Film-Cooling With Dissipation. Figure 9 shows a sample of the experimental data at $T_{ti}/T_{t\infty} = 0.82$ for $G = 0.23$ at given positions for a S.F.P.G. and a 30 deg inclined slot. The results show that for a given mainstream and injection flow the linear variation of the Nusselt number with θ is excellent. This applies for all positions, injection rates, coolant-to-mainstream temperature ratios and for both geometries investigated.

For the data shown, the slope (β) of the lines is greatest in the vicinity of injection ($X/D = 2$) where maximum cooling effect is normally observed. Downstream β decreases with X/D as the film-cooling performance deteriorates.

Effect of Injection on the Nusselt Number at $\theta = 1.3$ (Engine Conditions)

30 deg Slot Results. Figures 10 and 11 show the effect of injection on the Nusselt number at a typical engine value of $\theta = 1.3$ for a S.F.P.G. and M.A.P.G. at $T_{ti}/T_{t\infty} = 0.82$ for given mass flux ratios. The reason for presenting the data at this condition is in order that the general effect on the heat transfer may be appreciated. The unblown heat transfer levels are shown for comparison. For both cases, at $G = 0.15$ the decrease in

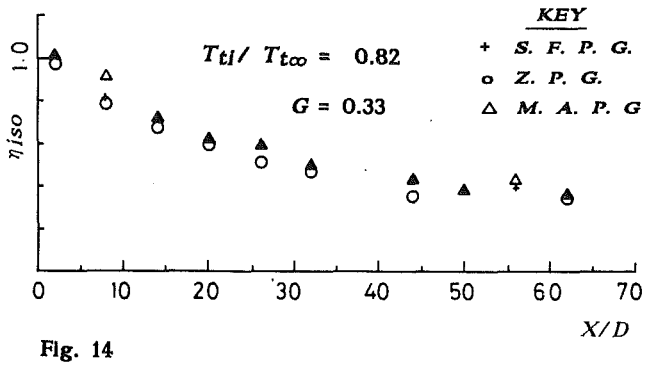

Fig. 14

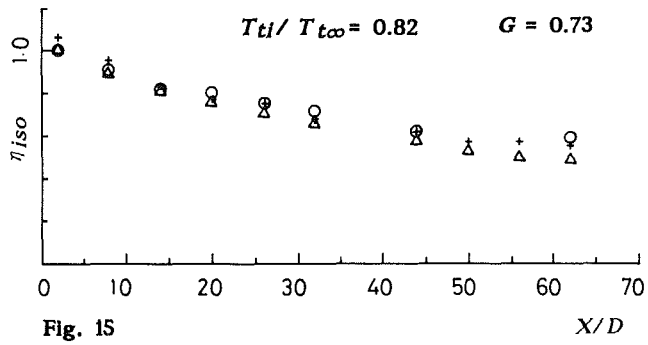

Fig. 15

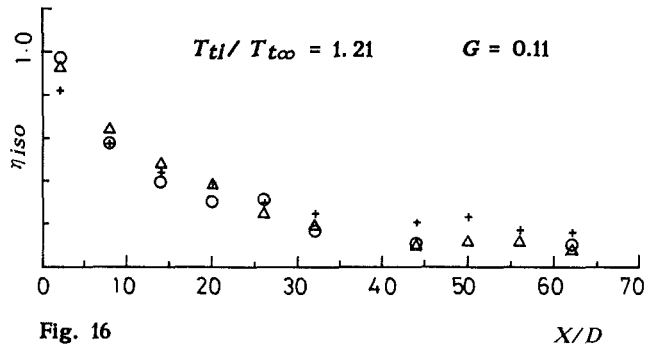

Fig. 16

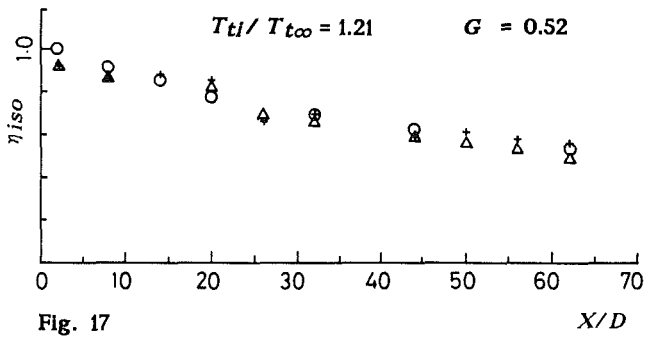

Fig. 17

Figs. 14–17 30 deg slot data: comparison of the film-cooling effectiveness with pressure gradient

Nusselt number is greatest in the vicinity of injection. Far downstream, the Nusselt number approaches the unblown heat transfer level as expected. Increased blowing increases the cooling effect at all positions. Similar trends were obtained at $T_{ti}/T_{t\infty}=1.21$.

30 deg Single Row Results. The effect of injection with pressure gradient on the Nusselt number again at engine representative conditions is illustrated in Figs. 12 and 13 for this geometry at $T_{ti}/T_{t\infty}=0.82$ and a range of injection rates. For a S.F.P.G. at $X/D=2$ maximum cooling is obtained at $G=0.35$, where the Nusselt number is decreased to approximately 22 percent of the unblown value. With a M.A.P.G. at $X/D=2$, maximum cooling occurs at $G=0.25$ with a corresponding decrease in the Nusselt number to approximately 39 percent. For both pressure gradients, the Nusselt number increases markedly in the vicinity of injection of mass flux ratios greater than 0.35 for the S.F.P.G and greater than 0.25 for the M.A.P.G. With a M.A.P.G., this effect is more pronounced. This result is not surprising since adverse pressure gradients in general are known to promote early "jet separation," which may well be the cause of the effect. At $G=1.20$, gross separation may have occurred. Reattachment of the cooling jets at this mass flux ratio, however, is evident far downstream where some cooling effect is observed. In contrast, with a S.F.P.G., this effect is less pronounced. It is also evident from Fig. 12 that in the presence of a favorable pressure gradient the cooling film performs far better in the vicinity of injection than in an adverse pressure gradient (Fig. 13) at high injection rates.

Dependence of the Film-Cooling Effectiveness on Pressure Gradient

30 deg Slot Results. Figures 14–17 show a comparison for different pressure gradients of the experimental results of film-cooling effectiveness plotted versus X/D. The effectiveness is defined as in equation (5). It is quite evident that for all positions at given injection rates and temperature ratios, the values of the effectiveness are remarkably similar for all three pressure gradients. This general result may imply that the mixing and dilution of the coolant with the free stream as a function of position are the same in all three cases.

Figure 18 shows the variation of A and B separately with distance. Again it can be seen for given injection conditions the variations of A and B are similar except in the region close to the slot. Here there is an influence of the pressure gradient. A is generally highest for the strong favorable pressure gradient close to the injection point and approaches zero pressure gradient values far downstream. The value of A for the mild adverse pressure gradient may be higher or lower than that for zero pressure gradient depending on the mass flux ratio. The change in B from that for zero pressure gradient is rather similar to the change in A as may be seen in Fig. 18. Thus when the effectiveness $-B/A$ is derived, the value of the effectiveness does not change significantly, as seen in Fig. 17.

It must be remembered that the differences in pressure gradients were quite large; for example, for the M.A.P.G. the flow decelerated from a Mach number of 0.5 to 0.4, whereas for the S.F.P.G. the flow accelerated from a Mach number of 0.5 to 1.7. Hence the similarity in effectiveness variation with distance for these cases is all the more remarkable.

30 deg Single Row Results. The influence of pressure gradient on the film-cooling effectiveness for this geometry is shown in Fig. 19 for given distances at $T_{ti}/T_{t\infty}=0.82$. The results are plotted against the mass flux ratio, since this clearly demonstrates the maximum in effectiveness that occurs as G increases. The decrease beyond the maximum may possibly be attributed to jet separation and increased mixing effects. At $X/D=2$, for low injection rates the effects of the pressure gradient are small. At injection rates approximately greater than 0.35, beyond the maximum in effectiveness, the influence of the pressure gradient is sufficient to alter the trajectory of the jet and hence the distribution of the coolant. With a S.F.P.G., the "separation" of the jets is reduced by the free-stream acceleration, causing the film-cooling effectiveness to increase relative to zero pressure gradient values. The opposite tendency occurs with an adverse pressure gradient. Similar trends are obtained at $X/D=8$. Farther downstream, at $X/D=62$, this effect diminishes and no consistent variation with pressure gradient is observed.

At $T_{ti}/T_{t\infty}=1.21$, $X/D=2$, as shown in Fig. 20, the trends

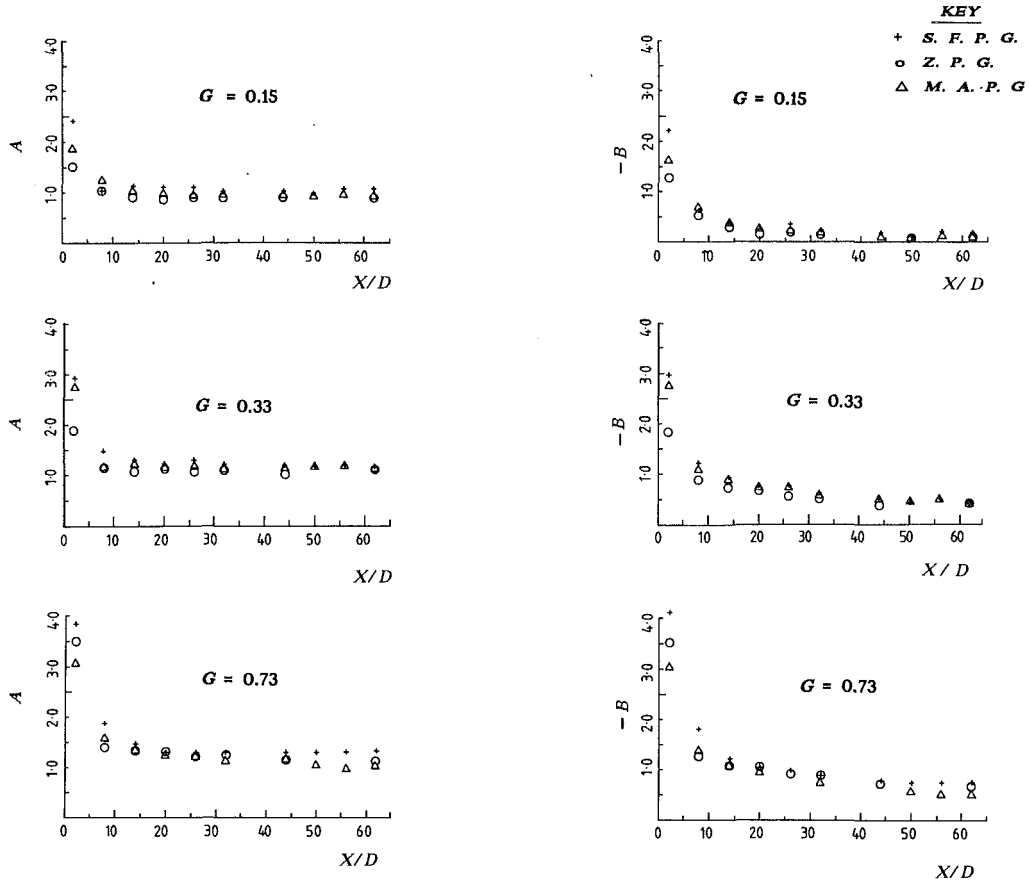

Fig. 18 30 deg slot data: A and B versus X/D with pressure gradient for given mass flux ratios at $T_{tj}/T_{t\infty} = 0.82$

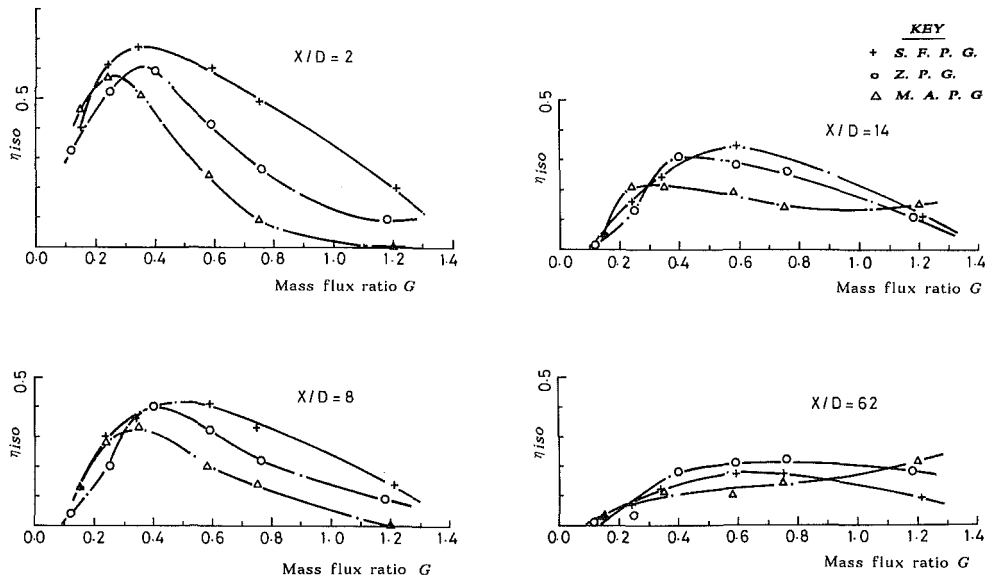

Fig. 19 30 deg single row data: comparison of the film-cooling effectiveness with pressure gradient at $T_{tj}/T_{t\infty} = 0.82$

obtained with pressure gradient differ from those in Fig. 19 at $X/D = 2$ beyond the maximum in effectiveness. This effect may be due to the added influence of changes in the coolant-to-free-stream density ratio caused by changes in the temperature ratio. This effect has been shown to be significant for zero pressure gradient (Forth, 1985). For this temperature ratio, far downstream the difference in effectiveness due to pressure gradient is small compared to the large differences at small distances.

Dependence of the Heat Transfer Coefficient, A, on Pressure Gradient. Figures 21 and 22 show the variation of A at given distances, plotted for all mass flux ratios. For both cooling geometries, it is evident the behavior of A is markedly affected by the pressure gradient in the vicinity of injection.

For two-dimensional slot injection (Fig. 21), the data plotted in this form quite clearly illustrate the effect of the free-stream acceleration on the cooling film as it exits from the slot, causing A to increase relative to zero pressure gradient values

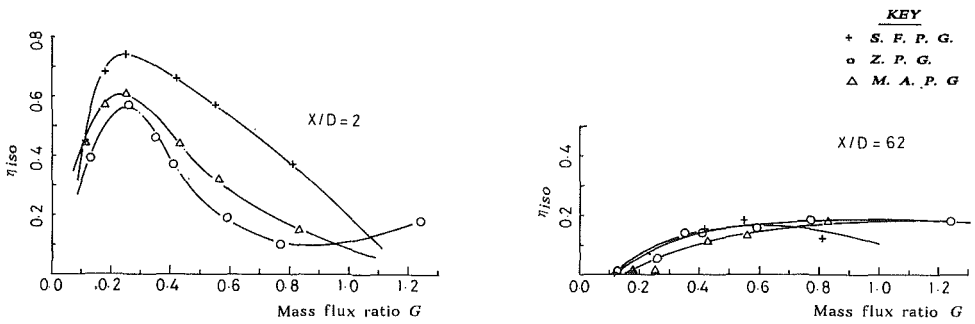

Fig. 20 30 deg single row data: comparison of the film-cooling effectiveness with pressure gradient at $T_{tl}/T_{t\infty} = 1.21$

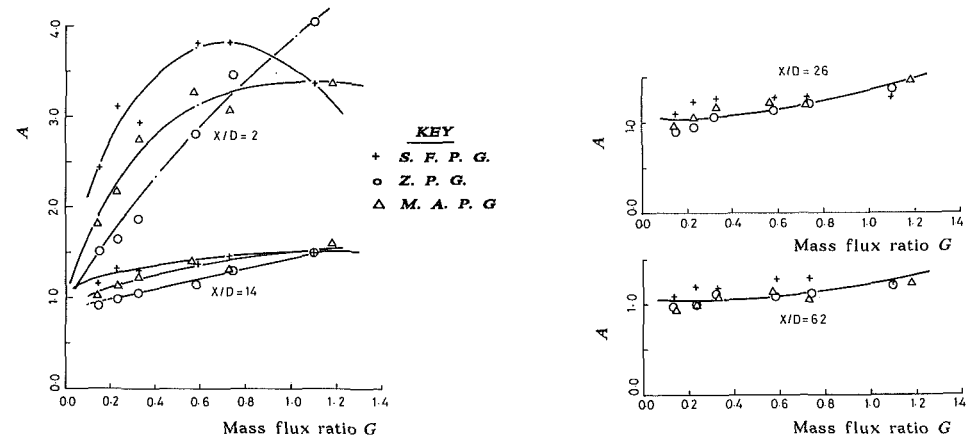

Fig. 21 30 deg slot data: comparison of the heat transfer coefficient with pressure gradient at $T_{tl}/T_{t\infty} = 0.82$

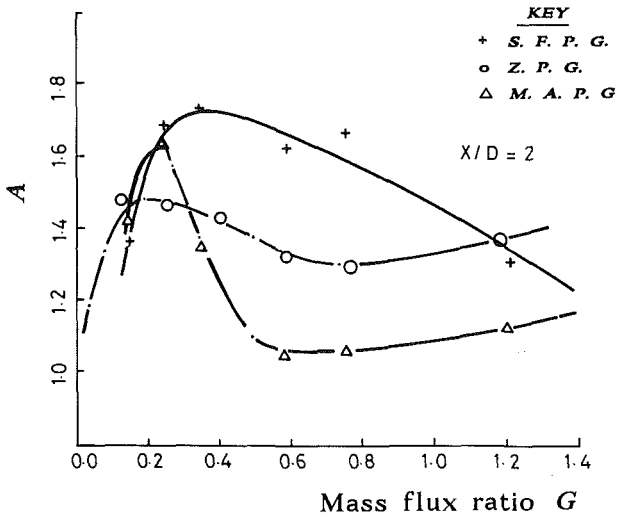

Fig. 22 30 deg single row data: comparison of the heat transfer coefficient with pressure gradient at $T_{tl}/T_{t\infty} = 0.82$

for $G \leq 0.7$. Above this value, the decrease in A with pressure gradient could be attributed to a separated region, which may exist at the rear vertex of the slot. The results of Forth for zero pressure gradient do not exhibit this trend, however. Downstream of injection at $X/D \geq 26$, there is no discernible effect of the pressure gradient on the heat transfer coefficient.

For a single row of 30 deg holes (Fig. 22), the effect of pressure gradient on A is greatest at $X/D = 2$ and above injection rates corresponding to the maximum effectiveness. The effect is, however, more pronounced with this geometry as a result of gross separation of the cooling jets that can occur. The different levels of enhancement of A at these conditions appear to vary consistently with pressure gradient. At $X/D \geq 26$, this effect was not observed.

Conclusions

1 The method of the superposition of temperature fields with film cooling has been extended to include the influence of viscous energy dissipation. A 30 deg inclined slot and a single row of 30 deg inclined holes were examined. For both cooling geometries, at all pressure gradients, positions, injection rates, and temperature ratios, the linearity of the Nusselt number with θ is confirmed, thus validating the superposition model with dissipation. The definition of the film-cooling effectiveness is applicable to flows where injection takes place at low Mach number and is subsequently accelerated to supersonic conditions.

2 For two-dimensional slot injection, there is little influence of mainstream pressure gradients on the film-cooling effectiveness. The results imply that the free-stream entrainment and hence dilution of the coolant are similar and are unaffected by the pressure gradient.

3 For three-dimensional hole injection, the effect of mainstream pressure gradients is minimal at low injection rates where the cooling jets are still attached to the surface. At these conditions, the physical processes are similar to those for two-dimensional slot injection. After the maximum effectiveness, which may be associated with "jet separation," the film-cooling effectiveness is markedly affected in the vicinity of injection. With a S.F.P.G., the effectiveness is increased relative to zero and adverse pressure gradients. Far downstream, there is no consistent variation of the film-cooling effectiveness with pressure gradient. The effects are, however, small. There is also an added influence on the film-cooling performance due to changes in the coolant-to-mainstream density ratio.

4 The heat transfer coefficient in the presence of mainstream

pressure gradients is markedly affected in the vicinity of injection. The behavior is complex but in general the favorable gradient increases the value for both types of cooling geometry.

Acknowledgments

The authors wish to acknowledge T. Godfrey for his assistance in running the test facility. They also wish gratefully to acknowledge the support of SERC for all the work and the kind permission of Rolls-Royce plc to publish the paper.

References

Forth, C. J. P., 1985, "An Investigation of Scaling Parameters Governing Film-Cooling," D. Phil. Thesis, Oxford, United Kingdom.

Hartnett, J. P., Birkebak, R. C., and Eckert, E. R. G., 1961, "Velocity Distributions, Temperature Distributions, Effectiveness and Heat Transfer in Cooling a Surface With a Pressure Gradient," *Int. Developments in Heat Transfer*, ASME, New York, Part 4, p. 682.

Hay, N., Lampard, D., and Saluja, C. L., 1985, "Effects of the Condition of the Approach Boundary Layer and of Mainstream Pressure Gradient on the Heat Transfer Coefficient on Film-Cooled Surfaces," ASME *Journal of Engineering for Gas Turbines and Power*, Vol. 107, p. 99.

Johnson, A. B., 1988, "The Aerodynamic Effects of Nozzle Guide Vane Shock Wave and Wake Passing on a Transonic Turbine Rotor," D. Phil. Thesis, Oxford, United Kingdom.

Jones, T. V., Schultz, D. L., and Hendley, A. D., 1973, "On the Flow in an Isentropic Light Piston Tunnel," ARC 34217.

Jones, T. V., 1989, "The Scaling of Film-Cooling," Oxford University Engineering Lab. Report.

Kays, W. M., and Crawford, M. E., 1980, *Convective Heat and Mass Transfer*, McGraw-Hill, New York.

Kruse, H., 1985, "Effects of Hole Geometry, Wall Curvature and Pressure Gradient on Film-Cooling Downstream of a Single Row," AGARD-CPP-390.

Launder, B. E., and York, J., 1974, "Discrete Hole Cooling in Presence of Freestream Turbulence and Strong Favorable Pressure Gradient," *Int. J. Heat Mass Transfer*, Vol. 17.

Liess, C., 1975, "Experimental Investigation of Film-Cooling With Ejection From a Row of Holes for the Application to Gas Turbine Blades," ASME *Journal of Engineering for Power*, Vol. 97, p. 21.

Loftus, P. J., 1982, "Determination of Heat Transfer Coefficients in the Presence of Film-Cooling," D. Phil Thesis, Oxford, United Kingdom.

Pai, B. R., and Whitelaw, J. H., 1969, "The Influence of Strong Favourable Pressure Gradients on Film-Cooling Effectiveness," Imperial College Report EHT/TN/A/15.

Schultz, D. L., and Jones, T. V., 1973, "Heat Transfer Measurements in Short Duration Hypersonic Facilities," AGARD Conference Proceedings 165.

Seban, R. A., and Back, L. H., 1962, "Effectiveness and Heat Transfer for a Turbulent Boundary Layer With Tangential Injection and Variable Freestream Velocity," ASME *Journal of Heat Transfer*, Vol. 84.

Smith, M. R., 1974, "A Study of Film-Cooling Effectiveness With Discrete Holes and Slots," D. Phil. Thesis, Oxford, United Kingdom.

Teekaram, A. J. H., 1989, "Film-Cooling in the Presence of Mainstream Pressure Gradients and Foreign Gas Injection," D. Phil. Thesis, Oxford, United Kingdom.

Teekaram, A. J. H., Forth, C. P., and Jones, T. V., 1989, "The Use of Foreign Gas to Simulate the Effects of Density Ratios in Film-Cooling," ASME JOURNAL OF TURBOMACHINERY, Vol. 111, p. 57.

Effect of Incidence on Wall Heating Rates and Aerodynamics on a Film-Cooled Transonic Turbine Blade

C. Camci
The Pennsylvania State University,
Aerospace Engineering Department,
University Park, PA 16802

T. Arts
The von Karman Institute for
Fluid Dynamics,
Turbomachinery Department,
Rhode Saint Genese, Belgium

This study investigates the influence of incidence on convective heat transfer to highly curved surfaces of a film-cooled turbine rotor blade. A computational study of free-stream inviscid aerodynamics without cooling at various incidences is followed by well-documented measured heat transfer data sets. The heat transfer experiments are discussed for cases with and without film cooling, performed under realistic gas turbine flow conditions in the short-duration heat transfer facility of the von Karman Institute for Fluid Dynamics. The precise location of the stagnation point and the iso-Mach number contours in the passage for each incidence (−10, 0, 10, +15 deg) are presented for a nominal exit Mach number of 0.94. The free-stream mass flow rate was kept constant for each experiment at different incidence levels. Three rows of compound angled discrete cooling holes are located near the leading edge in a showerhead configuration. Two rows of staggered discrete cooling holes are located on the suction side and a single row of cooling holes is located on the pressure side. The short-duration measurements of quantitative wall heat fluxes on nearly isothermal blade surfaces both in the presence and absence of coolant ejection are presented. The study indicated that the change of the position of the stagnation point strongly altered the aerodynamic behavior and convective heat transfer to the blade in approximately the first 30 percent of both the pressure side and the suction side in the presence and absence of film cooling. The immediate vicinity of the stagnation point was not significantly affected by changing incidence without cooling. Transitional behavior both on the suction surface and on the pressure surface was significantly influenced by the changes in approaching flow direction. Flow separation associated with incidence variations was also observed. Extremely low levels of the convective heat transfer coefficients were experienced near the regions where small separation bubbles are located.

Introduction

The gas flow around turbine airfoils is highly three dimensional and unsteady. The importance of incorporating three-dimensional effects into the turbine aerodynamic and thermal design system has already been recognized and many theoretical and experimental studies are presently available. However, there are only a very limited number of past investigations that examine the influence of unsteadiness on turbine convective heat transfer under realistically simulated gas turbine conditions. These include Marziale and Mayle (1984) and Dunn and Hause (1981). Although the turbine airfoil passage flow is highly unsteady, most of the present design systems, assume that the flow leaves a blade row in a steady manner with velocity and exit flow angles independent of the circumferential direction. These assumptions result in a design approach in which the inlet velocity and angle of attack relative to the following blade row are constant. Under actual conditions, the turbine passage unsteadiness is created by a number of different flow field features such as passage vortices, tip clearance flow, leakage flow, combustion chamber unsteadiness, random unsteadiness, and wake passing. The most significant contribution to incidence changes for a turbine airfoil is from the unsteadiness created by the wakes from the upstream row. The velocity and temperature deficits in these wakes create a periodically oscillating inlet flow relative to the following row. When the wakes pass through the blades in the following row or the blades in the following row chop through the wakes, the relative velocity with respect to the rotating following row changes its direction periodically as shown by Marziale and Mayle (1984). They investigated the effect of oscillating flow direction on stagnation point heat transfer using a large-scale oscillating cylinder in a wind tunnel. They found that the

Contributed by the International Gas Turbine Institute and presented at the 35th International Gas Turbine and Aeroengine Congress and Exposition, Brussels, Belgium, June 11–14, 1990. Manuscript received by the International Gas Turbine Institute January 11, 1990. Paper No. 90-GT-46.

stagnation point heat transfer was augmented due to incidence oscillations. The present study is focused on the effects of incidence variations on both sides of an actual high-pressure turbine blade in a linear cascade. The streamwise velocity gradients in the near stagnation zone of a turbine blade and on a cylinder in crossflow are considerably different. Although the heat transfer investigation with a cylinder in crossflow configuration is invaluable on the stagnation point, the investigations performed in a turbine cascade are more realistic in terms of resolving the heat transfer variations both on the stagnation point and near the stagnation point. A turbine airfoil in a cascade is also a better experimental simulation for the effects of incidence on film-cooling heat transfer at near downstream of the stagnation point. Blade surface boundary layers near the stagnation point are strongly affected by the large pressure gradient of both favorable and adverse, free-stream turbulence, surface curvature, surface roughness, Reynolds number variations and incidence variations. The near stagnation point of the turbine blade surface is extremely important with regard to the blade boundary layer development. The initial development of blade boundary layers in this zone ($s/c < 0.30$) with and without film cooling strongly influences the remainder of the surface. Unfortunately, detailed boundary layer experiments near the leading edge are extremely difficult to perform. The conventional probes suffer from the spatial resolution. However, surface-mounted probes may provide simple and cost effective solutions in terms of detecting transition, separation, reattachment, and local convective wall heat flux. Hodson (1984) studied the hydrodynamic behavior of the near leading edge boundary layers on a turbine airfoil by using surface-mounted thin films. The present paper describes a detailed investigation of quantitative wall heating rates in the near leading edge region of a turbine blade both with and without film cooling on the blade surfaces. The main emphasis is given to the influence of incidence variations. The film-cooling field and free-stream aerodynamics are well simulated in comparison to an aircraft engine in the isentropic compression tube facility of the von Karman Institute for Fluid Dynamics.

Experimental Apparatus

Test Facility. Quantitative wall heat flux measurements were taken on a film-cooled high-pressure turbine blade in the VKI isentropic compression tube facility. A full simulation of the Mach number distributions, Reynolds numbers, and wall-to-free-stream temperature ratio was provided. Special emphasis was made in obtaining a correct coolant-to-free-stream temperature ratio. A cryogenic heat exchanger system was developed to supply the coolant temperature at the correct simulation temperature. The operating principles of isentropic compression tube facilities were developed by Jones and Daniels (1978). A detailed description of the VKI CT-2 compression tube facility and of its capabilities is given by Richards (1980) and Ligrani et al. (1982).

Heat Transfer Model Description. All measurements reported in this study were carried out on a rotor blade section previously defined in detail by Consigny and Richards (1982) and Camci and Arts (1985a). The details of the cascade geometry were described in these references. The cascade and the cooling configuration are summarized in Fig. 1. The blade instrumented for wall heat flux measurements was milled from "Macor" glass ceramic and 45 platinum films were applied on its surface. The chord length was 80 mm. Three rows of cylindrical cooling holes (d = 0.8 mm; s/c = −0.026, 0.0, +0.026) were located around the leading edge (rows, *LP*, *LM*, *LS*). The row and hole spacing were both 2.5 mm. These holes were angled spanwise at 30 deg from the tangential direction. Two staggered rows of conical holes (d = 0.8 mm; s/c = 0.206, 0.237) were located on the suction side (row *S*). The row and hole spacing were respectively 2.5 and 2.6 mm. One row of conical holes (d = 0.8 mm; s/c = − 0.315) was located on the pressure side (row *P*). The hole spacing for this row was 2.6 mm. Three independent cavities were drilled along the blade height to act as plenum chambers. The coolant flow was supplied by a regenerative-type cryogenic heat exchanger. Pressure tappings and thermocouples provided continuous coolant characteristics at the entrance and exit of each plenum.

Measurement Technique. The convective heat flux at the wall was deduced from the corresponding time-dependent surface temperature evolution provided by the platinum thin film gages. The wall temperature/wall heat flux conversion was obtained from an electrical analogy, simulating a one-dimensional semi-infinite body configuration. A detailed description of this transient technique was given by Schultz and Jones (1973) and Ligrani et al. (1982). The convective heat transfer coefficient was defined as the ratio of the measured wall heat flux and the difference between the free-stream recovery and local wall temperature at the heat flux sensor location. A re-

Nomenclature

c = blade chord length
C_d = discharge coefficient
d = film-cooling hole diameter
h = convective heat transfer coefficient $= q/(T_{o\infty} - T_w)$
h/h_o = nondimensional cooling heat transfer coefficient
h_o = heat transfer coefficient without cooling
i = incidence angle, positive in counterclockwise direction
LP = pressure side cooling row near the leading edge
LM = midrow of cooling holes near the leading edge
LS = suction side cooling row near the leading edge
M = Mach number at a given location (any incidence)
M_o = Mach number at zero incidence at a given location
m = blowing rate $= \rho_c U_c / \rho_\infty U_\infty$ (mass flux rate ratio)
$\dot{m}$ = mass flow rate
P = pressure side row of film cooling holes
p = static pressure
$\dot{q}$ = wall heat flux rate
Re = Reynolds number
S = suction side row of film cooling holes
s = curvilinear coordinate measured from row *LM* (axis) along the blade surface (+ along the suction side, − along the pressure side)
T = temperature
T_{ref} = reference temperature for coolant mass flow rate measurements = 290 K
Tu = free-stream turbulence intensity
u' = fluctuating velocity
U = time-averaged velocity
β_1 = blade inlet angle measured from axial direction
γ = stagger angle
ρ = density

Subscripts

c = related to cooling flow
ex = exit
i = specific plenum chamber (*L*, *P*, or *S*)
in = inlet
is = isentropic
o = related to a stagnation condition
1 = free-stream upstream conditions
∞ = related to the free-stream flow

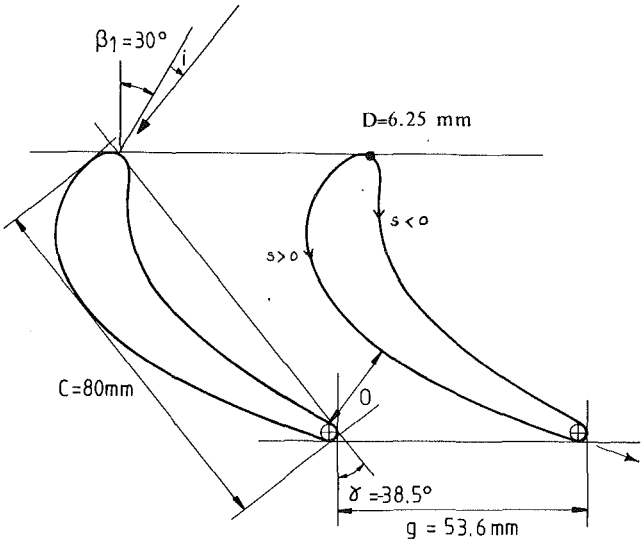

Fig. 1(*a*) High-pressure turbine blade and the cascade geometry

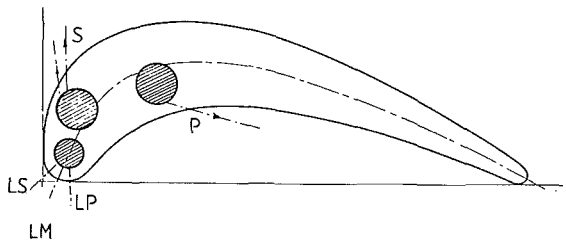

Fig. 1(*b*) Coolant plenum chamber locations

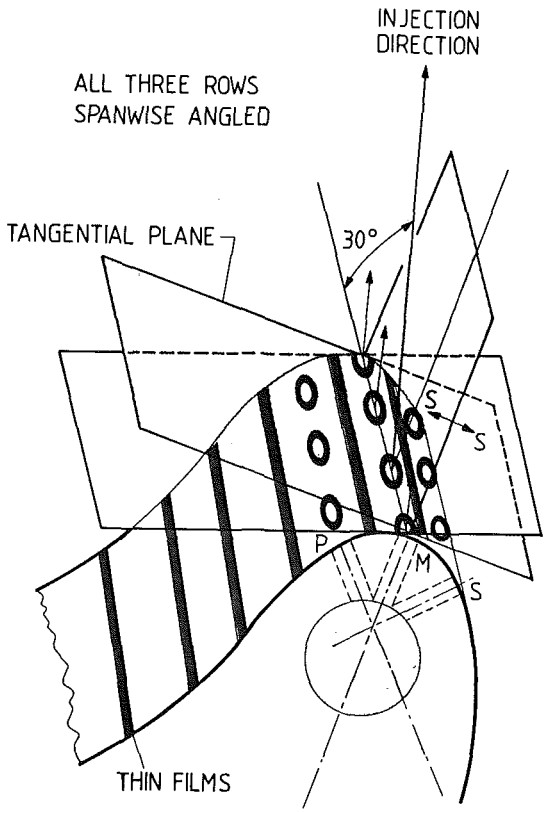

Fig. 1(*c*) Leading edge showerhead cooling geometry

covery factor of 0.896 was used, as if the boundary layer on the blade surface was turbulent everywhere. The uncertainty on the heat transfer coefficient was about 5 percent except for the two gages located between rows *LP*, *LM*, and *LS*. The details of the uncertainties were presented by Camci and Arts (1989). All pressure, temperature, and heat flux measurements were directly acquired by means of a PDP 11/34 computer through one of the VKI data acquisition systems. For the present investigation, the sampling rate was selected to be 1 kHz for each one of the 48 channels. The total flow duration was about 500 ms.

Free-Stream Turbulence Generation. The free-stream turbulence was generated by a grid of parallel, spanwise-oriented bars. The turbulence intensity was varied by displacing the grid upstream of the cascade; a maximum value of 5.2 percent was obtained. The natural turbulence of the facility was about 0.8 percent. The turbulence level was measured by means of a VKI constant-temperature hot-wire anemometer, designed and built by the von Karman Institute for Fluid Dynamics.

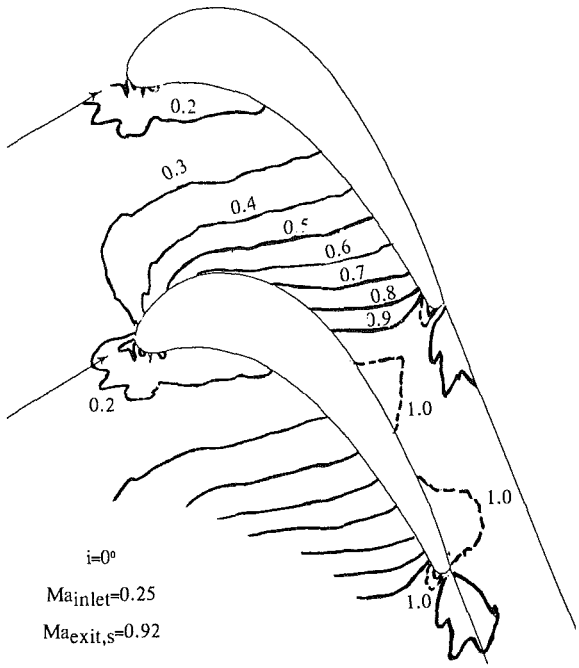

Fig. 2 Blade Mach number prediction at zero incidence

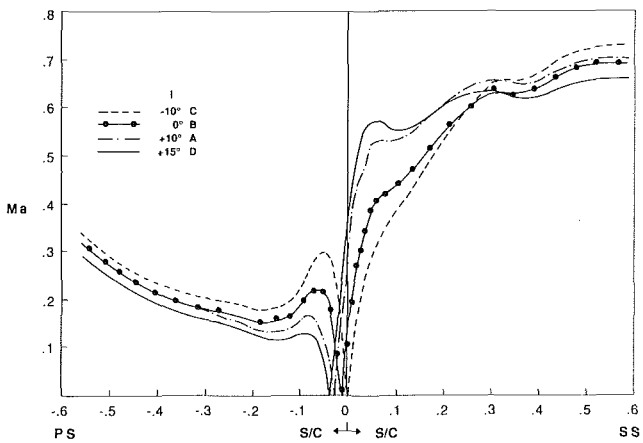

Fig. 3 Blade Mach number prediction near the leading edge

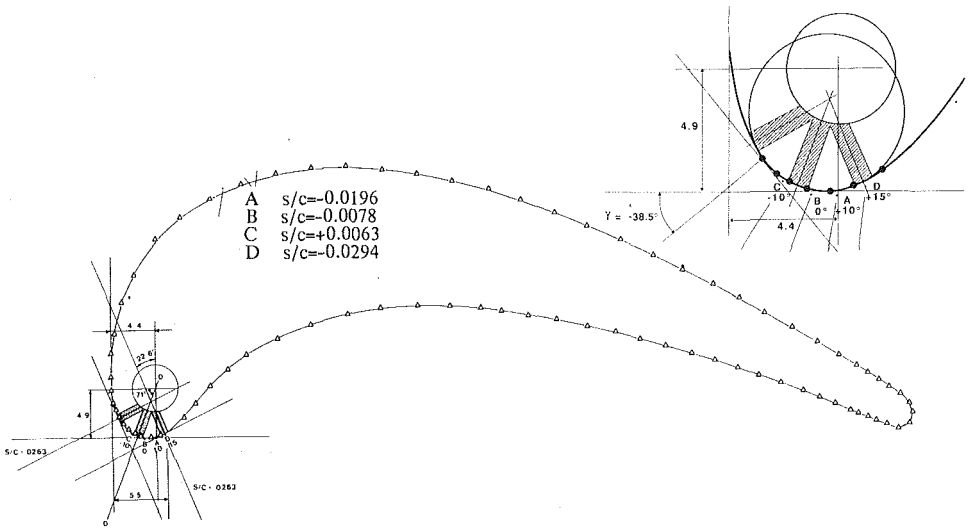

Fig. 4(*a*) Predicted stagnation point locations at various incidences

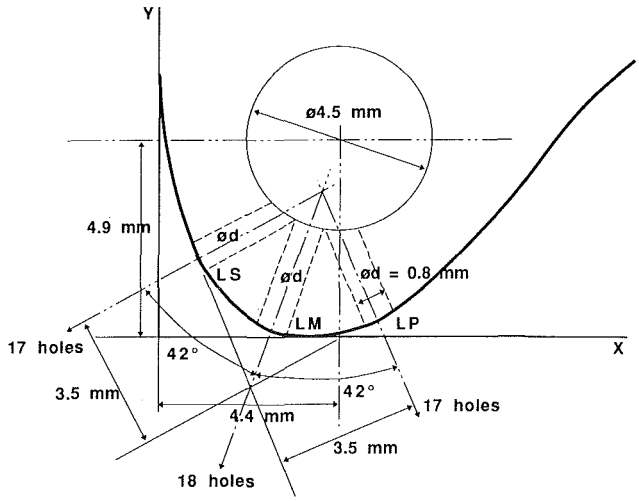

Fig. 4(*b*) Geometric details of the near leading edge region

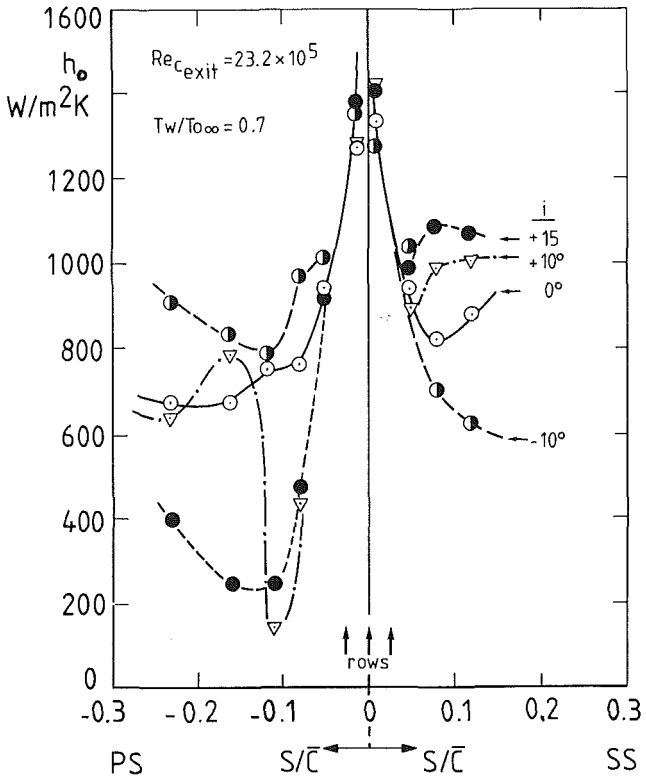

Fig. 5 Near leading edge heat transfer characteristics at various incidences without film cooling

Incidence Effects on Free-Stream Aerodynamics and Heat Transfer Without Film Cooling

Aerodynamic predictions for the inviscid free-stream flow were performed by using a two-dimensional time-marching method based on a finite area approach as described by Arts (1982). Figure 2 shows the prediction at $i = 0$ deg with an inlet Mach number of 0.25. The corresponding isentropic Mach number at the exit was about 0.92. A surface Mach number distribution and a comparison with experimental data for both the pressure side and the suction side were presented by Camci and Arts (1985b). On the suction side, between the stagnation point and $s/c = 0.05$, the free-stream accelerated to M = 0.35 in a favorable pressure gradient region. This region continued up to $s/c = 0.30$ and between $s/c = 0.30$ and 0.45 a flat zone was observed. Farther downstream, the free stream continued to accelerate and sonic velocities occurred near the trailing edge. On the pressure side, there was a strong acceleration around the leading edge, with a maximum observed at $s/c = 0.05$. A diffusion region was observed along a very short distance between $s/c = -0.08$ and -0.12. The position where the curvature changed from convex to concave and the onset of the free-stream deceleration appeared to be nearly at the same location on the blade surface. Starting from the $s/c = -0.30$, a favorable pressure gradient accelerated the mainstream up to nearly sonic velocities near the trailing edge. The described inviscid free-stream flow behavior was consistently observed from wall static pressure measurements, singularity method calculations near the leading edge, and finite area calculations in the transonic flow region. Figure 2 shows a two-dimensional Mach number distribution in the entire blade passage from finite area calculations. The dashed lines indicated the sonic velocity locus. The sonic regions occurred locally near the trailing edge along the suction side. However, a sonic throat did not appear under nominal operating conditions at zero incidence. On the pressure side, most of the acceleration took place along the rear part of the blade. A very small area covered by a sonic locus was also observed close to the trailing edge as shown in Fig. 2.

A prediction method based on a singularity solution was

found to be very useful for the calculation of the flow around the leading edge and for an accurate determination of the stagnation point location. It is a known fact that finite area (time-marching) methods originally developed for transonic flow calculations are less accurate than singularity methods in modeling the leading edge flows. The Mach number distributions and stagnation point predictions from a singularity method are shown in Fig. 3 for $i = -10$, 0, $+10$, and $+15$ deg. The stagnation point at zero incidence was found to be located very close to the midrow of cooling holes (point B). The $s/c = 0.0$ point was defined as the centerline of the midrow of cooling holes, which was also the cross-section point of the camberline and the blade profile. This result was also confirmed using an oil flow visualization technique. The pressure side boundary layer started to grow along a smooth surface between the cooling rows LM and LP. At $s/c = -0.026$, the pressure side boundary layer was only disturbed by cooling row LP. When incidence was changed to $i = -10$ deg the stagnation point moved to a location between LM and LS ($s/c = +0.0063$), point (C). Points (A) and (D) in Fig. 3 show the stagnation point location at $i = +10$ and 15 deg, respectively. At positive incidences less than 10 deg, the predicted stagnation point was always between rows LM and LP. The increasing positive incidence moved the stagnation point farther downstream on the pressure side. The increasing negative incidence moved the stagnation point farther downstream on the suction side. It was concluded that a typical showerhead cooling scheme having three rows of holes near the stagnation point could easily modify the boundary layer development on both sides of the blade near the leading edge. Figure 4 shows the details of the leading edge geometry including film-cooling holes and blade discretization for inviscid predictions. The locations of the stagnation point relative to the cooling holes are also shown in the figure.

The effect of incidence angle on convective heat transfer near the leading edge is shown in Fig. 5. When $i = 0$ deg, as a result of the tripping effect of rows LM and LS, the onset of the suction side boundary layer transition was observed at $s/c = 0.08$. In this study, the onset of transition was defined as the first measurement point where the heat transfer coefficient h_0 started to increase in a pronounced way with increasing s/c. Increasing incidence to $+10$ deg and further to $+15$ deg moved the stagnation point respectively to points (A) ($s/c = -0.0196$) and (D) ($s/c = -0.0294$), whereas the transition onset was displaced to $s/c = 0.065$ and 0.050 as shown in Figs. 4 and 5. At $i = -10$ deg, the stagnation point was located at point (C) ($s/c = +0.0063$) and only row LS disturbed the suction side boundary layer. Along the pressure side the transition was observed to occur at $s/c = 0.08$ for both $i = 0$ deg and $i = -10$ deg. This location was very close to the curvature change point or the velocity maximum on the pressure side. At $i = +15$ deg, the stagnation point D nearly coincided with row LP and the unfavorable pressure gradient almost disappeared on the pressure side. The diminishing nature of the unfavorable pressure gradient on the pressure side was expected to create larger laminar and transitional regimes. This was confirmed by the measurements shown in Fig. 5.

Predicted Mach number distributions and measured convective heat transfer coefficients were normalized with zero incidence values, (M_o, h_o). This approach visualized the relative variations in free-stream mach numbers and convective heat transfer coefficients due to incidence changes. Figures 6, 7, and 8 show normalized Mach number distributions at $i = +10$, $+15$, and -10 deg, respectively. At $+10$ deg the stagnation point moved slightly on the pressure side in the downstream direction relative to its position at zero incidence. The first 40 percent of the suction side was characterized with a Mach number excess when compared to zero incidence values. The excess Mach numbers decayed quickly to their zero incidence values after $s/c = 0.40$. On the pressure side the Mach numbers showed a reduction in comparison to their zero incidence values within the first 60 percent of the pressure side. For $i = +10$ deg, the movement of the stagnation point on the pressure side in the downstream direction to point (A) created a flow with a better chance to accelerate smoothly on the suction side and less chance to accelerate on the pressure side as shown in Fig. 6. For $i = +15$ deg this feature appeared in a more pronounced manner. Relative excess Mach numbers appeared to be higher in magnitude than the case for $i = +10$ deg on the suction side. The free-stream Mach number reduction in the first 80 percent of the pressure side was greater than the case for $i = 0$ deg. When the incidence changed to -10 deg, a reversed

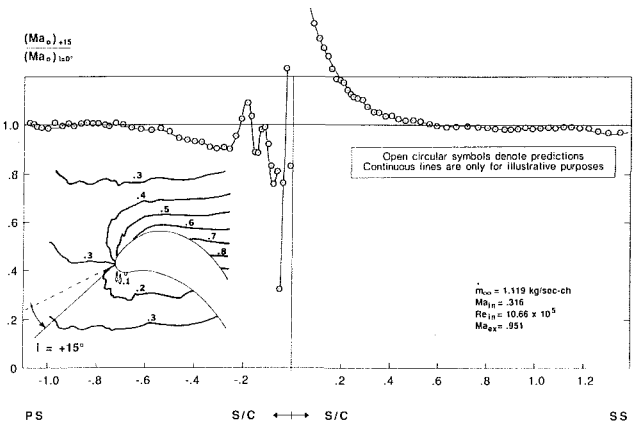

Fig. 7 Relative Mach number distribution at $i = +15$ deg

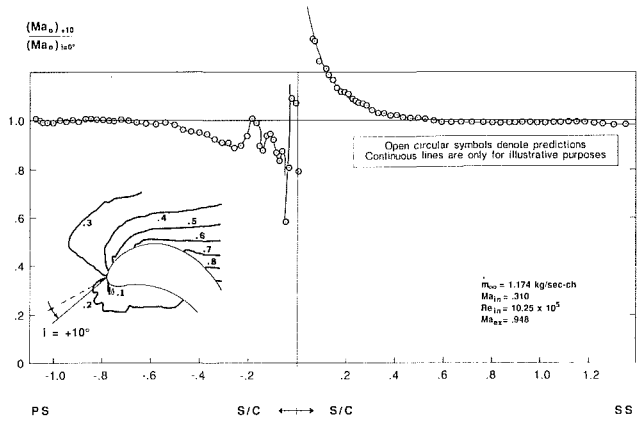

Fig. 6 Relative Mach number distribution at $i = +10$ deg

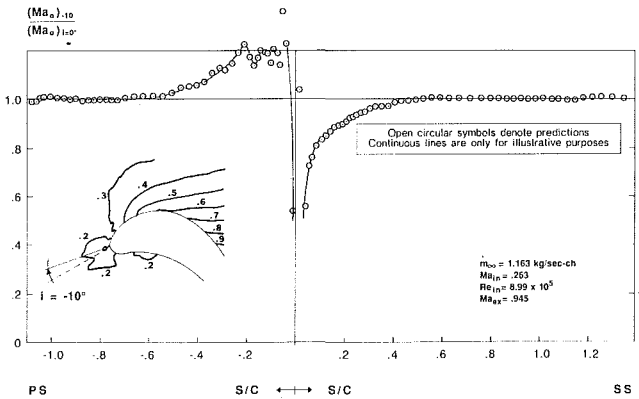

Fig. 8 Relative Mach number distribution at $i = -10$ deg

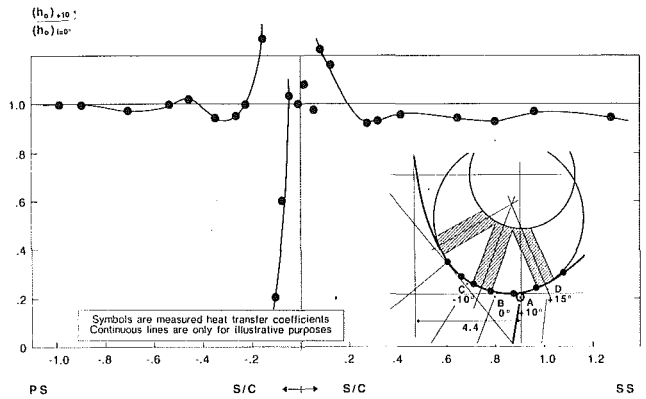

Fig. 9 Relative convective heat transfer coefficient distribution, i = +10 deg, without film cooling

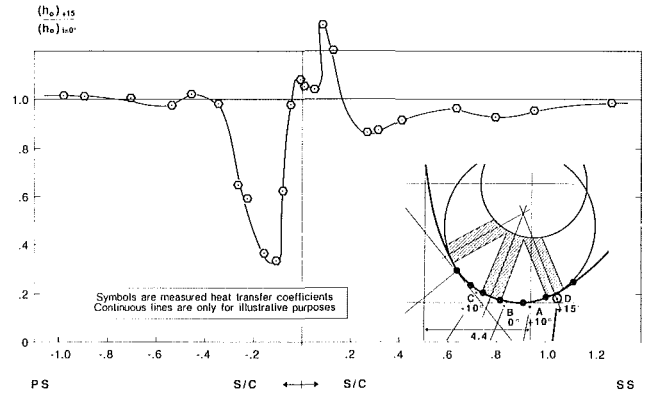

Fig. 10 Relative convective heat transfer coefficient distribution, i = +15 deg, without film cooling

trend was observed. Figure 8 shows the relative velocity deficits on the suction side and an excess velocity on the pressure side. Figures 6, 7, and 8 also show near leading edge Mach number contours in the passage where they have a strong variation. As negative incidence increased, the free-stream fluid near the stagnation point had a better chance to accelerate around the round leading edge on the pressure surface in the downstream direction due to the movement of the stagnation point on the suction side in the downstream direction.

The heat transfer coefficient distributions obtained at various incidences were also normalized with a zero incidence distribution. Figures 9, 10, and 11 show the normalized distributions of h/h_o at +10, +15, and −10 deg, respectively. Since the local free-stream Reynolds numbers are strong determining quantities in convective heat transfer, the Mach number trends discussed in the previous paragraph were expected to affect the convective heat transfer coefficients. Strong variations in convective heat transfer coefficients were localized near the leading edge. Heat transfer coefficients were augmented in the location where Mach number excess values were observed in relative to zero incidence. The suction side variation of M/M_o shown in Fig. 6 and h/h_o shown in Fig. 9 were very similar at $i = +10$ deg along the first 60 percent of the blade. The measured heat transfer coefficients very near the stagnation point did not vary significantly ($-0.03 < s/c < 0.03$). However, on the pressure side between $s/c = -0.05$ and $s/c = -0.15$ a very low heat transfer coefficient and a subsequent high heating rate just downstream of the low value indicated that, at $i = 10$ deg near $s/c = -0.05$ there was a small separation bubble. At $s/c = -0.20$ where the maximum h/h_o value occurred, a boundary layer reattachment was expected. The blade boundary layer recovers to its zero incidence state after $s/c = -0.30$ on the pressure side. For $i = +15$ deg, a large zone with low h values was observed near the leading edge on the pressure side. For this case, the heat transfer coefficients recovered to their zero incidence values at about $s/c = -0.40$. For $i = +15$ deg, the stagnation point was predicted to be very close to row LP. The monotonic increase in h/h_o between $s/c = -0.10$ and $s/c = -0.40$ was attributed to the fact that the boundary layer was smoothly transiting to its zero incidence status. As shown in Fig. 10, the stagnation point (D) was at $s/c = -0.0294$. For this case the boundary layer started near row LP along a smooth path and all of a sudden it was disturbed by row LP. This disturbance might have caused a small separation bubble and reattachment just downstream of the bubble.

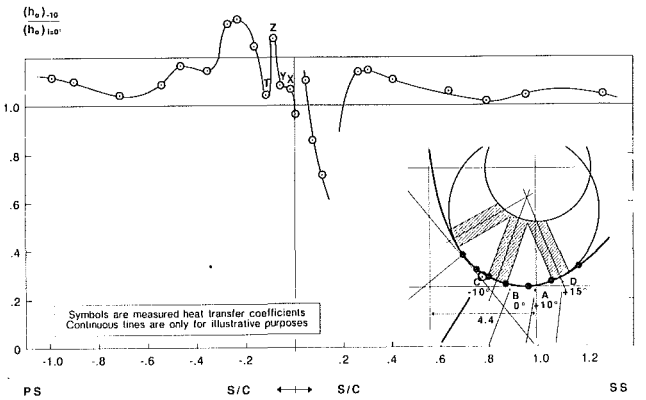

Fig. 11 Relative convective heat transfer coefficient distribution, i = −10 deg, without film cooling

Figure 11 shows the relative heat transfer coefficient distribution at $i = -10$ deg. For this incidence, the stagnation point was located just downstream of the midrow of holes (LM). Between LM and LS it developed smoothly over a short distance. When it encountered row LS it was very likely that it separated and reattached. The measurement points X, Y, Z, and T in Fig. 11 are in this region of disturbances originating from the cooling row LS. The pressure side h/h_o values for $i = -10$ deg were all greater than unity. The values were significantly higher in the first 50 percent of the pressure side. This is consistent with the Mach number predictions given in Fig. 11. Along the first 50 percent of the pressure side, the augmentations in local Reynolds numbers imposed by the specific incidence (− 10 deg) resulted in augmented h/h_o values.

Incidence Effects on Aerodynamics and Heat Transfer With Film Cooling

The effect of incidence on film-cooling heat transfer was studied by keeping the test section total mass flow rate constant and varying the incidence angle. The resulting inlet and exit Mach numbers at $i = +10$, 0, and −10 deg are as follows:

i, deg	M_{inlet}	M_{exit}	$\dot{m}_c/\dot{m}_\infty$
+10	0.31	0.95	0.0230
0	0.24	0.93	0.0231
−10	0.26	0.94	0.0233

i, deg	(T_c/T_∞)	$(P_{oc}/P_\infty)_L$	$(P_{oc}/P_\infty)_S$	$(P_{oc}/P_\infty)_P$
+10	0.39	1.270	1.404	1.454
0	0.39	1.298	1.388	1.495
−10	0.38	1.285	1.388	1.496

The coolant-to-free-stream mass weight ratio was kept constant at (2.31 ± 0.02) percent at a nominal coolant-to-free-stream temperature ratio of $T_c/T_\infty = 0.39 \mp 0.01$. The coolant air ejected throughout rows P, S, LP, LM, and LS was deliv-

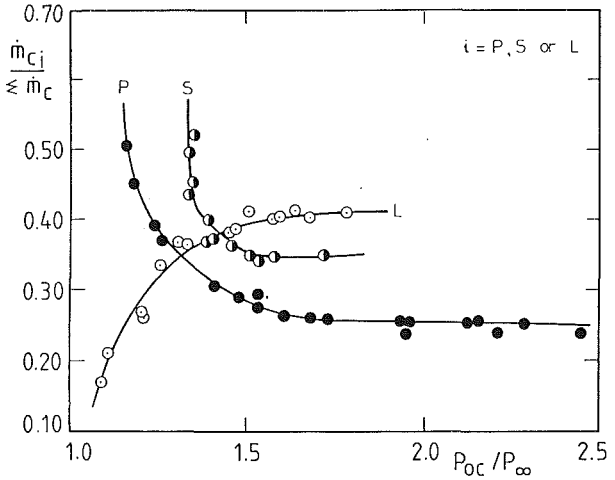

Fig. 12 Distribution of coolant mass flow rate between plenum chambers

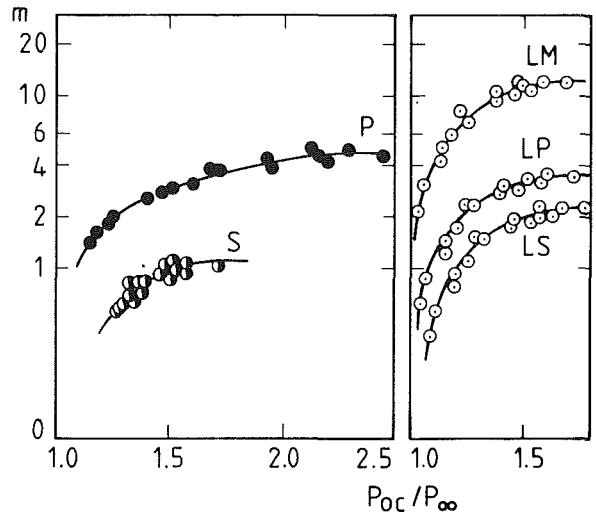

Fig. 13 Local blowing rates of the ejection sites

ered by a single, common reservoir, connected to a cryogenic heat exchanger providing the required coolant-to-free-stream temperature ratio. The total coolant mass flow rate $\Sigma \dot{m}_c/\dot{m}_\infty$ accurately measured by means of a calibrated sonic orifice was then shared between the suction side (S), the leading edge (LP, LM, LS) and the pressure side (P) plenum chambers. The amount of coolant passing through each of these ejection sites must nevertheless imperatively be determined in order to evaluate the local coolant-to-free-stream mass weight ratios and blowing rates. Since the total coolant mass flow rate is inversely proportional to $T_{oc}^{0.5}$, a normalized overall mass weight ratio $(\Sigma \dot{m}_c/T_{oc}^{0.5})/(\dot{m}_\infty/T_{\text{ref}}^{0.5})$ was defined in order to establish a single functional dependency between the total coolant flow and the coolant-to-free-stream pressure ratio (P_{oc}/P_∞). The normalized overall coolant mass weight ratio versus the coolant-to-free-stream pressure ratio variation was obtained for each one of the plenum chambers at various coolant temperature levels ($T_{oc}/T_{o\infty}$ = 0.7, 0.6, 0.5).

Mean values of the local discharge coefficients were evaluated at the location of the pressure side, leading edge, and suction side ejection rows from the independent film-cooling investigations performed previously by the same group (Camci and Arts, 1991). The relatively low C_d values (0.20–0.35) recorded in the leading edge region were expected to occur because of the highly complicated nature of the specific plenum chamber flow with compound angle ejection through the three rows. Across the pressure side and suction side rows, the C_d values varied between 0.40 and 0.50.

The quantitative determination of the coolant mass flow rate through each ejection site was obtained by combining the discharge coefficient data and local plenum chamber pressure and temperature measurements. Using the information about the normalized total coolant mass flow rate versus specific plenum chamber pressure for a given coolant temperature allowed the evaluation of the coolant-to-free-stream pressure ratio for each plenum and, hence, of the isentropic mass flux rate through the three ejection sites. Taking into account the corresponding discharge coefficients given by Camci and Arts (1990), the three actual mass flow rates including the viscous losses can be provided. Each of these was characterized by the quantity $\dot{m}_{ci}/\Sigma \dot{m}_c$ ($i = L, P, S$) as shown in Fig. 12. At very low pressure ratios, the flow conditions were not well defined in the leading edge plenum chamber and very low C_d values were responsible for substantially reduced local mass flow rates. The cooling rows S and P then performed the largest percentage of the ejection. However, for a typical value of the overall mass weight ratio $\Sigma \dot{m}_c/\dot{m}_\infty$ = 0.03, the coolant split was found to be 40, 35, and 25 percent, respectively through the leading edge, suction side, and pressure side ejection rows.

The local blowing rates across different ejection rows have been determined from independent ejection mass flow rates as shown in Fig. 12; the corresponding ejection area has been determined from the local free-stream conditions. Because of very small free-stream mass flux rates in the leading edge region and relatively small free-stream mass flux rates along the first half of the pressure side, rows LM and LP ejected the coolant at higher blowing rates, as shown in Fig. 13. Although an accurate procedure was incorporated in determining the local blowing rates and the local coolant mass flow rates, a further check of the hydrodynamic data was performed. Well-documented leading edge film cooling heat transfer tests on the same model had been performed by the author. The details of this study were discussed by Camci and Arts (1985a). In order to asses the validity of the estimated local coolant mass flow rates for the multi-location study reported here, the simultaneous ejection heat transfer data near the leading edge were compared with the only leading edge injection data presented in Camci and Arts (1985b). The leading edge coolant mass flow rates and local blowing rates of the present study were evaluated by using the information presented in Figs. 12 and 13 as discussed in the previous paragraph. The coolant mass flow rates and the local blowing rates of "only leading edge ejection" study were accurately measured in the past. The convective heat transfer coefficients measured for both of the cases were compared. Very good agreement of the heat transfer coefficients from both sets of experiments provided a quantitative check on the local hydrodynamic data presented in this study.

The effects of incidence on film-cooling heat transfer are shown in Figs. 14, 15, and 16, respectively for i = 0, +10, and − 10 deg. The solid symbols in each figure represented the case with no coolant ejection from the three plenum chambers (LP, LM, LS), S, and P. The plenum chambers were carefully blocked from inside by using flexible inserts in order to eliminate air circulation inside the chambers. The heat transfer coefficients without cooling were slightly different at each incidence angle. At +10 deg, h values on the suction side were slightly lower than the zero incidence case ($s/c > 0.2$). At i = − 10 deg the heat transfer coefficients were slightly lower than the zero incidence values ($s/c > 0.2$). The important difference between different incidence angles was mainly due to changing transition characteristics on the suction side. The transition-dominated zone on the suction side appeared along the first 20 percent of the blade. At i = +10 deg the suction side boundary layer transisted much earlier than at i = 0 deg. At i = − 10 deg a large laminar zone before s/c = 0.20 was

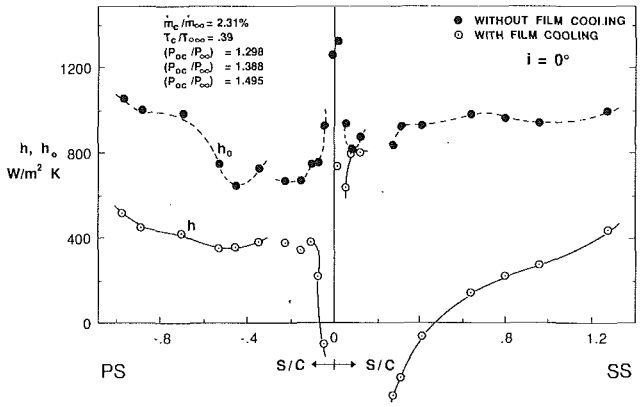

Fig. 14 Relative convective heat transfer coefficient distribution, i = 0 deg, with coolant ejection from *L*, *P*, and *S*

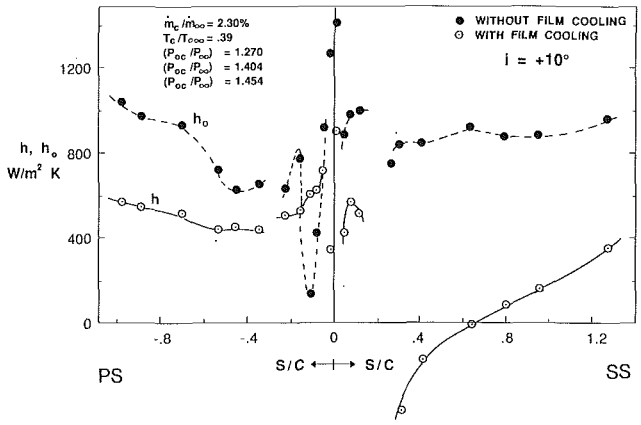

Fig. 15 Relative convective heat transfer coefficient distribution, i = +10 deg, with coolant ejection from *L*, *P*, and *S*

observed. The late transition at this specific incidence was attributed to the specific stagnation point location. The heat transfer coefficient distributions at three different incidences showed that the boundary layers are fully turbulent after s/c = 0.20 regardless of the specific incidence angle. The approaching boundary layers were disturbed in the same manner by the double rows of cooling holes at all incidence angles. However, downstream of the cooling rows, the local Reynolds numbers imposed by the specific incidence were determining factors on the magnitude of the convective heat transfer coefficient. The significant difference in heat transfer coefficient on the pressure side occurred within the first 30 percent of the blade when the incidence angle was varied. At i = 10 deg, a relatively earlier transition was observed near the leading edge when compared to the case at i = 0 deg. At i = + 10 deg the heat transfer coefficient within the first 30 percent of the blade dropped to a very low value with an immediate increase after the low values. This variation suggested the existence of a small separation bubble at i = + 10 deg where s/c = ~ 0.12 on the pressure side. The heat transfer coefficients observed at downstream locations of the pressure side after cooling row *P* were not strongly affected from the specific incidences. Variations from incidence to incidence occurred either due to changing local Reynolds numbers of different transition/separation/reattachment patterns occurring near the leading edge within the first 20 percent of the blade.

At i = 0 deg the stagnation point (*B*) was very close to the midrow of holes *LM* as shown in Fig. 4. The free-stream mass flux rate $\rho_\infty U_\infty$ was close to zero near the stagnation point. Therefore, it was expected that the local blowing rate for the midrow of holes at i = 0 deg was very high. At this incidence, the row *LP* should originate a coolant layer just downstream

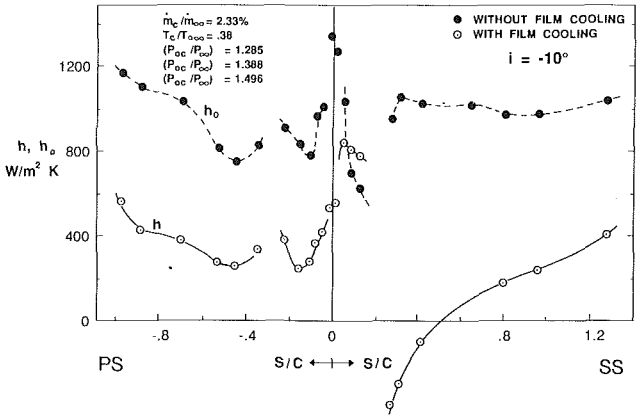

Fig. 16 Relative convective heat transfer coefficient distribution, i = −10 deg, with coolant ejection from *L*, *P*, and *S*

of *LP*. The row *LS* also provided another film layer on the suction side. Figure 14 shows the reduction in h_o near the leading edge. The cooling effect from the row *LP* was very successful on the pressure side. The introduction of the leading edge cooling (*LP*, *LM*) and pressure side cooling (*P*) provided significantly reduced pressure side heat transfer coefficient distribution.

The downstream effect of row *LS* on the suction side was not as successful as the effect of *LP* on the pressure side. This was attributed to the fact that the row *LS* was ejecting at a high blowing rate without creating a protective layer. The heat transfer coefficient level just downstream of the row *LS* was as high as the noncooled h_o values. However, the cooling effect from a double row of holes configuration on the suction side, (*S*), was extremely effective in protecting the suction surface after s/c = 0.25.

At i = + 10 deg, the stagnation point was expected between *LM* and *LP*. Rows *LM* and *LS* were ejecting on the suction side. The superposition of the two rows on the suction side provided an effective cooling on the suction side as shown in Fig. 15 (s/c<0.20). The trends were reversed on the pressure side part of the near leading edge region. The introduction of a turbulent cold film layer just downstream of row *LP* helped to eliminate the small separated flow zone that appeared near the leading edge without cooling. Downstream of row *P*, the superposition of the jets originating from *LP* and *P* provided an effectively cooled pressure side.

At −10 deg, the stagnation point *C* was located between rows *LP* and *LM*. This configuration provided the superposition of the cooling rows *LM* and *LP* on the pressure side. The pressure side cooling of the near leading edge zone was very successful as shown in Fig. 16. After s/c = ~ 0.30, with the introduction of row *P*, a full protection of the pressure side was achieved. However, on the suction side, only row *LS* was protecting the near leading edge area. The heat transfer coefficients near the leading edge were as high as the noncooled values. Downstream row *S* on the suction side was very effective in protecting the blade surface.

Figure 17 shows a comparison of heat transfer coefficients at i = 0, +10, and −10 deg. The most significant variations of h due to incidence were observed in the first 30 percent of the blade on both sides of the leading edge. The position of the stagnation point determined the distribution of the coolant fluid around the leading edge. Variation of heat transfer coefficient due to different incidences was not very pronounced far downstream on both surfaces where s/c>0.30. The slight variations in h distributions were attributed to slightly changing local blowing rates at locations *P* and *S*. The specific configuration near the leading edge was also another influencing parameter in heat transfer coefficient distribution with film cooling.

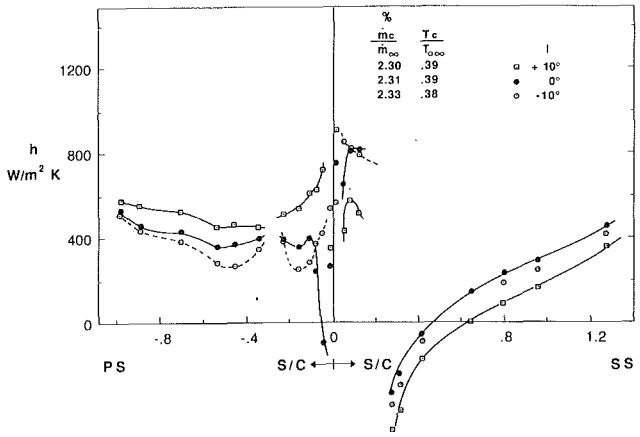

Fig. 17 Comparison of film cooling heat transfer at different incidences

Conclusions

The heat transfer nature of the development of blade surface boundary layers on a high-pressure gas turbine blade was investigated under varying incidence conditions. The heat transfer investigation was performed for cases with and without film cooling in a test facility providing well-simulated gas turbine conditions. The quantitative wall heat flux data were obtained from 45 surface-mounted thin-film platinum heat flux sensors. The data were interpreted with the help of inviscid free-stream predictions. The absolute magnitude of the convective heat transfer coefficient at the stagnation point at various incidences did not vary significantly. A strong variation of the position of the stagnation point near the leading edge was observed when the incidence was changed in a range from -10 to $+15$ deg. Variations in incidence significantly altered the acceleration and deceleration characteristics on both sides of the stagnation point. The existence of the three film-cooling rows near the leading edge strongly influenced the blade boundary layer transition even without coolant ejection. When there was film cooling, the shower head cooling system coolant split between the pressure side and suction side was strictly controlled by the position of the stagnation point at a given incidence. Due to the periodic nature of the incidence changes in an actual engine, it was concluded that a showerhead cooling system may distribute coolant mass flow on the pressure side and suction side in a periodical manner. However, during this periodic incidence change when the stagnation point coincides with a cooling row, the specific row of holes should have an extremely high blowing rate. For this case, it was concluded that most of the coolant fluid from this row was lost in the free stream. The discrete hole cooling areas (P and S in Fig. 1*b*) located far downstream of the leading edge did not strongly change their heat transfer behavior with varying incidence. The most significant variations of the convective heat transfer coefficient due to incidence were observed in the first 30 percent of the blade on both sides of the stagnation point.

Acknowledgments

The authors wish to thank F. A. E. Breugelmans of the Turbomachinery Department of the von Karman Institute for Fluid Dynamics for his continuous support and encouragment.

References

Arts, T., 1982, "Cascade Flow Calculations Using a Finite Volume Method," in: *Numerical Methods for Flow in Turbomachinery*, von Karman Institute Lecture Series 1982-05, Apr.

Camci, C., and Arts, T., 1985a, "Short Duration Measurements and Numerical Simulation of Heat Transfer Along the Suction Side of a Gas Turbine Blade," ASME *Journal of Engineering for Gas Turbines and Power*, Vol. 107, No. 4, pp. 991–997.

Camci, C., and Arts, T., 1985b, "Experimental Heat Transfer Investigation Around the Film Cooled Leading Edge of a High Pressure Gas Turbine Rotor Blade," ASME *Journal of Engineering for Gas Turbines and Power*, Vol. 107, No. 4, pp. 1016–1021.

Camci, C., and Arts, T., 1990, "An Experimental Convective Heat Transfer, Investigation Around a Film-Cooled Gas Turbine Blade," ASME JOURNAL OF TURBOMACHINERY, Vol. 112, pp. 497–503.

Consigny, H., and Richards, B. E., 1982, "Short Duration Measurements of Heat Transfer Rate to a Gas Turbine Rotor Blade," ASME *Journal of Engineering for Power*, Vol. 104, No. 3, pp. 542–551.

Daniels, L. C., 1978, "Film Cooling of Gas Turbine Blades," Ph.D. Thesis, Dept. of Engineering Science, University of Oxford, United Kingdom.

Dunn, M. G., and Hause, A., 1981, "Measurements of Heat Flux and Pressure in a Turbine Stage," ASME Paper No. 81-GT-88.

Hodson, H. P., 1985, "Boundary-Layer Transition and Separation Near the Leading Edge of a High-Speed Turbine Blade," ASME *Journal of Engineering for Gas Turbines and Power*, Vol. 107, pp. 127–134.

Jones, T. V., Schultz, D. L., and Hendley, A. D., 1973, "On the Flow in an Isentropic Free Piston Tunnel," A.R.C. R&M 3731.

Ligrani, P. M., Camci, C., and Grady, M. S., 1982, "Thin Film Heat Transfer Gauge Construction and Measurement Details," von Karman Institute Technical Memorandum No. 33.

Marziale, M. L., and Mayle, R. E., 1984, "Effect of an Oscillating Flow Direction on Leading Edge Heat Transfer," ASME *Journal of Engineering for Gas Turbines and Power*, Vol. 106, pp. 222–228.

Richards, B. E., 1980, "Heat Transfer Measurements Related to Hot Turbine Components in the von Karman Institute Hot Cascade Tunnel," AGARD Conference Proceedings, No. 281, Testing and Measurement Techniques in Heat Transfer and Combustion, Brussels.

Schultz, D. L., and Jones, T. V., 1973, "Heat Transfer Measurements in Short Duration Hypersonic Facilities," AGARDograph No. 165.

Turbine Tip and Shroud Heat Transfer

D. E. Metzger
Arizona State University,
Tempe, AZ 85287

M. G. Dunn
Calspan-UB Research Center,
Buffalo, NY 14255

C. Hah
General Electric Company,
Schenectady, NY 12301

Unshrouded blades of axial turbine stages move in close proximity to the stationary outer seal, or shroud, of the turbine housing. The pressure difference between the concave and convex sides of the blade drives a leakage flow through the gap between the moving blade tip and adjacent wall. This clearance leakage flow and accompanying heat transfer are of interest because of long obvious effects on aerodynamic performance and structural durability, but understanding of its nature and influences has been elusive. Previous studies indicate that the leakage through the gap is mainly a pressure-driven flow whose magnitude is related strongly to the airfoil pressure loading distribution and only weakly, if at all, to the relative motion between blade tip and shroud. A simple flow and heat transfer model incorporating these features can be used to estimate both tip and shroud heat transfer provided that reasonable estimates of the clearance gap size and clearance leakage flow can be made. The present work uses a numerical computation of the leakage flow to link the model to a specific turbine geometry and operating point for which a unique set of measured local tip and shroud heat fluxes is available. The resulting comparisons between the model estimates and measured heat transfer are good. The model should thus prove useful in the understanding and interpretation of future measurements, and should additionally prove useful for providing early design estimates of the levels of tip and shroud heat transfer that need to be compensated for by active turbine cooling.

Background and Objectives

In gas turbine engines, the tips of axial turbine blades rotate in close proximity to a stationary peripheral outer seal or shroud. Differential thermal expansion between the rotating turbine wheel and blades and the stationary outer ring causes variations in the size of the clearance gap at the blade tip. For an aircraft engine, significant variations in clearance occur at different operating conditions such as takeoff and cruise; even with so-called active clearance control, the gap is never eliminated entirely at all operating conditions (Henneke, 1984).

The pressure difference between the convex and concave sides of the blades drives flow through the clearance gap. Near the pressure side of the gap, the mainstream flow is turned into the gap. Strong secondary flows can be expected to be present in the gas path as a whole, and this can have the effect of bringing very hot portions of the mainstream to the vicinity of the clearance gap, especially at the downstream portions of the blade. As the flow emerges from the suction side of the gap, it is usually visualized as rolling into a vortex as it meets the oncoming wall flow (Allen and Kofskey, 1955; Bindon, 1986).

Clearance gaps in modern axial turbines are typically less than one percent of the blade height for large engines, ranging up to 1.5 percent or more for smaller engines with low aspect ratio blading. Even with the tightest possible tolerances, the leakage flow can have significant effects both on stage aerodynamic performance and on the structural durability of the blade. The surface area at the blade tip in contact with the hot working gas is an area for convection heat transfer and thermal loading on the blade, which must be removed by the blade internal cooling flows, along with heat transfer to the blade suction and pressure side surface areas. The cooling flows are supplied by the engine compressor and impose a thermodynamic penalty on engine performance, and in this general sense the blade tip heat transfer acts to degrade engine performance further.

On modern high-performance engines, cooling may also be required for the stationary tip shroud, and any increase in shroud heat transfer associated with the clearance leakage flow will also result in a performance penalty. To minimize cooling flow and their penalties, designers need accurate knowledge of the tip and shroud heat transfer characteristics. However, the apparent flow complexities near the tip region, together with the region's small size and obvious measurement difficulties in isolating it, have all served to hinder development of a thorough understanding of convection within the leakage gap. Until quite recently, only a very incomplete and largely qualitative picture existed of the clearance gap flowfield, and virtually no information was available on the heat transfer effects. However, during the last few years, a number of studies have been published that help to provide a better overall picture of the leakage-related flowfield and convection heat transfer.

Heat transfer measurements have been made by Dunn et al. (1984a, 1984b) on actual plane blade tips and shrouds and by

Contributed by the International Gas Turbine Institute and presented at the 35th International Gas Turbine and Aeroengine Congress and Exposition, Brussels, Belgium, June 11–14, 1990. Manuscript received by the International Gas Turbine Institute January 17, 1990. Paper No. 90-GT-333.

Epstein et al. (1985) on the stationary shroud. Both of these measurement programs were performed using short duration testing, and both indicated that large heat transfer rates exist in the clearance gap. In general, high heat transfer rates can be explained either by the presence of large-magnitude convection coefficients or by high leakage flow temperatures, or by a combination of both, but the measurements do not allow these factors to be separately evaluated. A model study by Mayle and Metzger (1982) suggests that the high tip and shroud heat transfer rates can best be explained by the presence of high driving temperatures acting with only ordinary levels of convection coefficients. In this analysis, later extended by Metzger and Rued (1989), the sinklike character of the flow entering the clearance gap results in a very thin entering boundary layer with boundary-layer fluid from the pressure side of the blade contributing only a small percentage of the total tip leakage flow. Thus, the clearance gap and blade tip are exposed to the full mainstream gas temperature, indicating that the source of the measured high tip heat transfer rates is likely to be high leakage flow temperatures, rather than highly enhanced convection coefficients generated by a complex flow through the gap. Experimental results from the same study, shown repeated here as Fig. 1, were conducted with a disk edge, simulating the relative motion between tip and shroud, rotated past a tip model and show no measurable effects of the moving wall on the average tip heat transfer. The study was extended numerically to much larger relative velocities by Chyu et al. (1987), with the same conclusions. These results, and related fluid studies by Booth et al. (1982), Wadia and Booth (1982), Graham (1986), and Moore and Tilton (1988), indicate that leakage through the gap is essentially a pressure-driven flow whose magnitude is related primarily to the airfoil pressure loading distribution. Normal clearance gap heights are in effect, small enough to dictate that the flow through the gap is largely uncoupled from the details of the flowfields on either side, and are also small enough to produce a gap flow that has predominantly one-dimensional features.

Such a simple model has significant potential utility as a vehicle for understanding and correlating experimental data, and as a design system tool for making estimates of the expected magnitudes of tip and shroud heat transfer that must be compensated for by active component cooling. The work reported in the present paper was undertaken to assess the model against the Calspan local heat transfer measurements obtained on the high-pressure turbine rotor blade tips and adjacent ring shroud of a Garrett 731-2 engine. The experiment utilized the full-stage HP turbine and the rotor was operating at 100 percent corrected speed (20,000 rpm in this case).

Results and Discussion

Description of Model. Figure 2 depicts the leakage flow qualitatively, in terms of velocity components in the plane of the rotor, as viewed relative to a moving solid blade tip. This is an idealized view, looking downstream through the blade passage in the absence of any secondary flows except those associated with the clearance flow. These secondary velocity components are shown as radial profiles at various circumferential locations between the blades and in the clearance gap. The shroud appears as a locus of points with constant clockwise velocity equal in magnitude to the blade tip velocity, and the blade is depicted in its average thickness with distance L across the tip from pressure to suction side. From this perspective, the no-slip condition at the shroud dictates a velocity V_t to the right at this boundary, and the leakage flow through the clearance gap dictates a mean velocity V_g to the left in the gap.

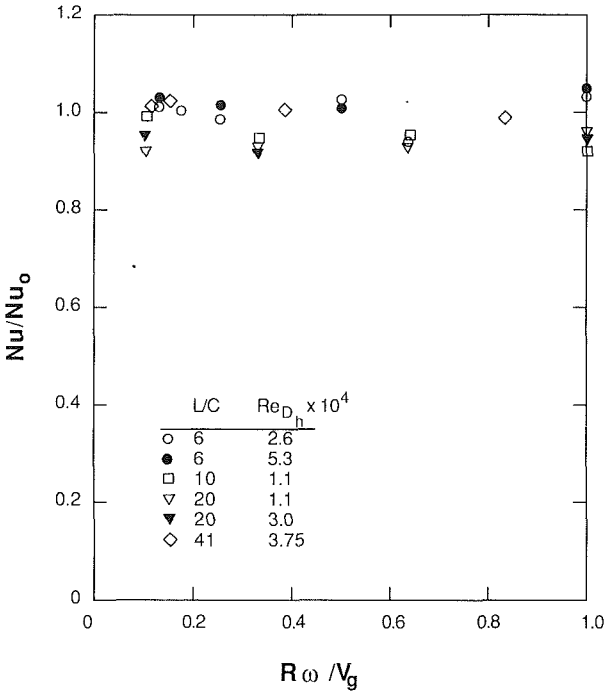

Fig. 1 Effect of shroud-to-tip relative velocity on tip heat transfer

The leakage flow, viewed from the blade tip, appears similar to a conventional stationary duct entrance flow with sharp-edged entry, as shown here in Fig. 3 replotted from Mayle and Metzger (1982) in terms of channel Reynolds number based on the clearance hydraulic diameter. The dashed line represents the results of Boelter et al. (1945), as given by Kays and Crawford (1980), for sharp-edged entry flow in a circular tube. The Boelter results are located at twice their original L/D_h values to compensate approximately for the sharp-edge entry on only one wall of the gap flow model, taking note of the qualitative similarity of a single sharp-edged entry flowfield with that of one-half of a double sharp-edged entry flowfield. Thus the results of the model study indicate that blade tip heat transfer should be predictable as a stationary channel entrance flow, provided the magnitude of the leakage flow is known.

Nomenclature

A = heat transfer area
c_p = specific heat
C = clearance height
D_h = clearance hydraulic diameter
h = heat transfer coefficient
L = flow length across blade tip
Nu = Nusselt number = hD_h/k
Nu$_{fd}$ = fully developed channel flow Nusselt number
Nu$_o$ = stationary Nusselt number
Pr = Prandtl number
q = local heat transfer rate
R = disk edge radius
Re$_{D_h}$ = channel Reynolds number = V_gD_h/ν
Re$_x$ = plate Reynolds number = $V_{rel}x/\nu$
St = Stanton number = $h/\rho V_{rel}c_p$
T_w = wall temperature
T_∞ = free-stream temperature
V_g = mean gap velocity, relative to tip
$V_{rel,g}$ = flow velocity relative to shroud, above tip
$V_{rel,p}$ = flow velocity relative to shroud, away from tip
V_t = tip velocity relative to shroud
ν = viscosity
ρ = density
ω = angular speed

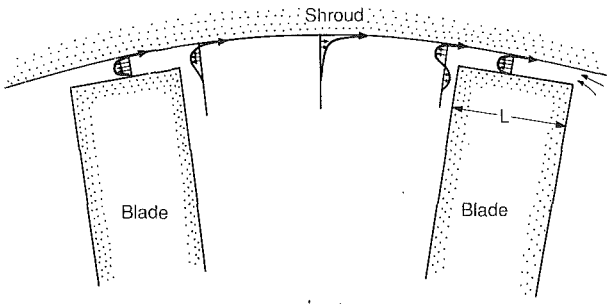

Fig. 2 Schematic of flow relative to blade tip

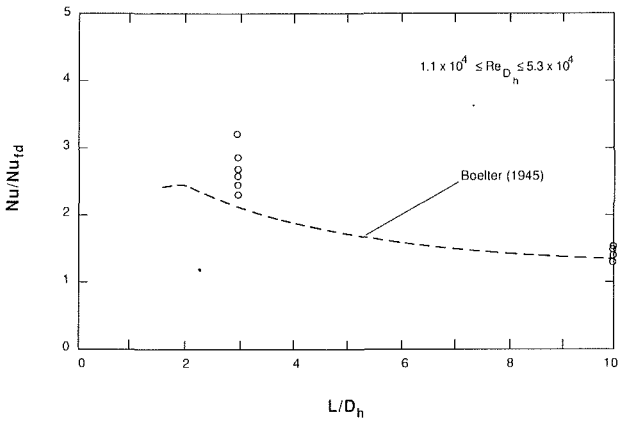

Fig. 3 Measured heat transfer on simulated blade tip

The same simple flow model can also be used, at least qualitatively, to assess the effect of the leakage flow on heat transfer rates at the stationary shroud. As a blade tip approaches and passes a particular measuring location on the shroud, the heat transfer at that point should respond to an increased resultant velocity as a result of the superposition of the blade passage velocity and the clearance gap velocity. In effect, the leakage flow must overtake and pass the blade tip, exposing the stationary shroud to a higher velocity and convection rate as it does so. Again, quantitative prediction of this effect requires knowledge of the magnitude of the leakage flow.

Leakage Flow Prediction. Early efforts in the present study to obtain a value for the magnitude of leakage flow corresponding to the Calspan test conditions attempted to utilize the T-SONIC and MERIDL computer codes that have previously been used successfully to predict surface pressure distributions for the Garrett TFE 731-2 blades. These efforts proved to be unsuccessful because of the basic nature of the code, which is incompatible with leakage flow across the tip, even though empirical compensations for tip losses are built into the program.

The present numerical leakage flow determination for the Garrett TFE 731-2 was carried out at General Electric. The entire blade passage flow, including the clearance gap flow, is calculated utilizing a full Navier–Stokes code developed by Hah (1984). A $30 \times 27 \times 102$ grid was used with six nodes in the 0.015-in. clearance gap. Figures 4 and 5 show the computed velocity vectors in the clearance gap and the computed blade surface pressure distribution at 90 percent span, respectively. The oscillation apparent in the pressure distribution near the trailing edge is thought to be the result of imperfect resolution of the blade surface profile, and should not adversely affect the overall computed results. The total flow leaking across the blade tip from pressure to suction side is computed to be 1.1 percent of the 20.5 lgm/sec total machine flow rate.

Comparisons With Measured Values. The measured values of heat flux and pressure were obtained at Calspan on the high-pressure turbine rotor blades and stationary shroud of a Garrett 731-2 full-stage rotating turbine. A shock tube was used to generate a short-duration source of heated and pressurized air. Miniature platinum thin-film gages were used for the localized heat-flux measurements and small Kulite and PCB pressure transducers were used to obtain the pressures. For these measurements, the turbine was operated at the design flow function, the design stage pressure ratio, the design stage temperature ratio, and at 100 percent corrected speed. Further details of the experimental apparatus and methods are available in the literature (Dunn et al., 1984a, 1984b; Dunn 1990).

Blade Tip Heat Transfer. Figure 6 shows the measured values of local heat flux at the blade tip along the chord from the leading edge to about 30 percent chord for tip/shroud clearance values of 0.015 in. and 0.025 in. The dashed line shown is the estimated tip heat flux level for the 0.015 in. clearance based on the simple one-dimensional model described above, calculated as an entrance flow into a short stationary duct. The numerically predicted leakage flow yields a channel Reynolds number of 4800, and this is used in the Dittus–Boelter fully developed duct correlation ($Nu_o = 0.023\ Re^{0.8}\ Pr^{0.4}$) together with an augmentation factor of 2.3 from Fig. 3 to account for the entry augmentation associated with the short duct. The estimation, especially considering the simplicity of the model, does a remarkably good job of representing the measured tip heat flux. We have a second set of tip data (Dunn et al., 1986) available for comparison with the estimation technique described here. However, that effort has not been completed at this time.

As noted above, Fig. 6 also includes measured tip heat flux values for the Garrett turbine but at a clearance gap of 0.025 in. No value of the leakage flow rate has been estimated for this case, but it is plausible that the mean leakage velocity relative to the tip remains about the same as the clearance is increased. The gap channel becomes shorter in terms of hydraulic diameters, and the increased entry augmentation might be expected to result in an approximately 20 percent greater heat transfer rate. This is consistent with the measured flux values at 12 and 20 percent chord, but the two other measurements in the vicinity of 25 to 30 percent chord suggest an increase on the order of 30 percent. In the absence of a flowfield solution for this tip gap case, we cannot explain this observation. However, at the time that these experiments were performed, it was observed that the 0.025 in. gap data were falling below the other data. The data analysis routine was reviewed in depth and the experiment was repeated 14 times to convince ourselves that there was not a basic problem with the data.

Time-Averaged Shroud Heat Transfer. The results of the simple one-dimensional model can also be used to estimate the levels of heat transfer expected on the stationary shroud. Figures 7 (*a*) and 7 (*b*) depict velocity triangles at two typical axial locations through the blade row, in the vicinity of the leading edge and trailing edge, respectively. $V_{rel,p}$ is the mean passage flow velocity relative to the stationary shroud, composed of the vector sum of the blade tip velocity V_t and mean passage velocity, V_p. These velocities relative to the stationary shroud can be used in a conventional turbulent boundary layer heat transfer correlation ($St = 0.0296\ Re_x^{-0.2}\ Pr^{-0.67}$) to estimate the expected shroud heat flux variation in the axial direction. The results of this estimation are shown as a dashed line in Fig. 8, along with the measured time-averaged values. Again, the simple one-dimensional model appears to predict both the observed axial distribution trends and the general magnitude of the measured values quite well.

Actually, the measured time-averaged heat flux values on the shroud should be expected to be larger than the above

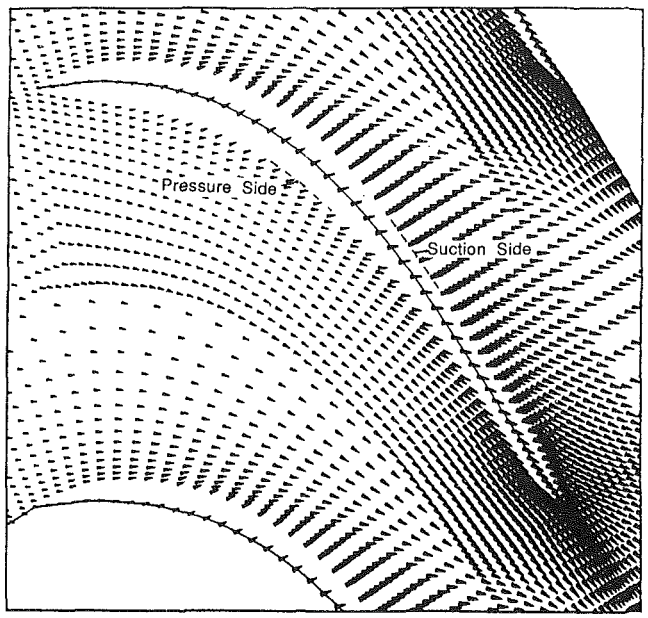

Fig. 4 Computed velocity vectors in clearance gap

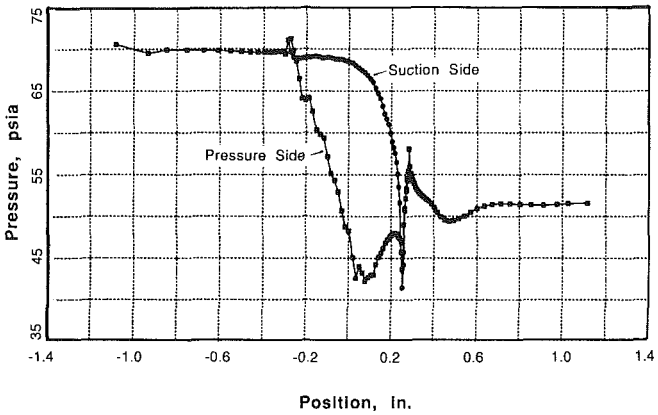

Fig. 5 Computed blade surface pressure distribution at 90 percent span

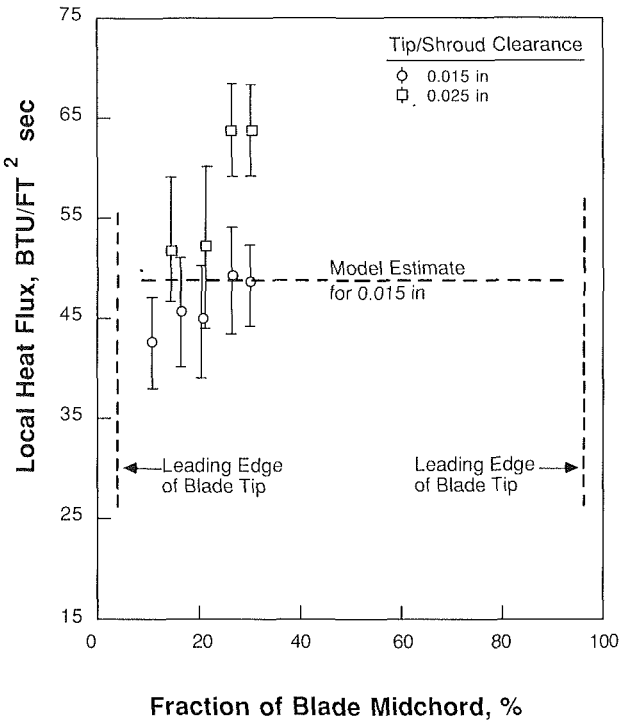

Fig. 6 Measured and estimated local heat flux on blade tip

estimates, which are based on the values of relative gas-to-shroud velocity within the blade passage between blades, $V_{rel,p}$. The relative velocity is periodically increased each time a blade tip passes the shroud measuring stations, as shown by the dashed lines in Figs. 7(*a*) and 7(*b*). The resulting periodic increase in shroud heat flux should raise the time-averaged values by approximately 10 percent, as will be apparent from the discussion in the following section.

The measured results shown on Fig. 8 include data obtained at two additional clearance values, 0.025 in. and 0.035 in. If the mean leakage velocity relative to the tip remains about the same as the clearance is increased, as speculated above, then the shroud heat transfer should be relatively unaffected by changes in the clearance size. This conclusion is in reasonable agreement with the measured results for the 0.015 and 0.035 in. spacing, but the lower shroud heat transfer measured with the intermediate 0.025 in. clearance is a feature of the data that does not appear at this time to be explainable with the simple one-dimensional model.

Time-Resolved Shroud Pressure and Heat Transfer. Figure 9 shows the layout for the stationary shroud heat flux and pressure gage locations relative to the blade location on the Garrett 731-2 installation, from which time-resolved measurements from all three gages were obtained simultaneously (Dunn, 1990). These measurements are shown in Figs. 10 and 11. The measured pressures oscillate with a period equal to the blade passage time, so it appears that the pressure transducer is responding to its alternating exposure to the blade pressure and suction sides. Indeed, the indicated peak pressures average about 50 psia, and the low point pressures average about 47 psia. These values are in reasonable agreement with the magnitude of the numerically predicted pressure side and suction side pressures (Fig. 5), considering the extreme trailing edge location of the pressure transducer and the computational oscillations in that region.

The measured heat fluxes also oscillate with a period equal to the blade passage time; and, consistent with the velocity triangles and discussion of the previous section, we expect that the peak heat transfer occurs as the blade tip and its overtaking leakage flow passes the measuring station. The measurements confirm this expectation. Heat flux gage number 115 and the pressure gage are located so that they are always both approximately the same relative distance away from a blade, and the measurements show that their responses to the blade approach and passing are in phase. Heat flux gage number 106, on the other hand, is located such that it experiences the approach of the blade sooner than does the pressure gage, and the measured responses are indeed appropriately out of phase with one another.

In the simple estimation of the shroud heat transfer levels used in the previous section, the heat flux is proportional to the 0.8 power of velocity. Thus, based on the oscillation of the magnitude of the gas velocity relative to the shroud shown in Fig. 7, we expect the variation in shroud heat transfer rate between the high values (blade passing) and low values (mid-passage) to be approximately 25 percent, at both axial locations. This estimated variation is in very good agreement with the measured variations for gage number 106, which range between 25 and 30 percent. The measured peak-to-valley variations are however much smaller than estimated for gage number 115, located axially downstream on the shroud near the trailing edge. A plausible reason for the reduced variation may be seen in the computed velocity vector plot of Fig. 4.

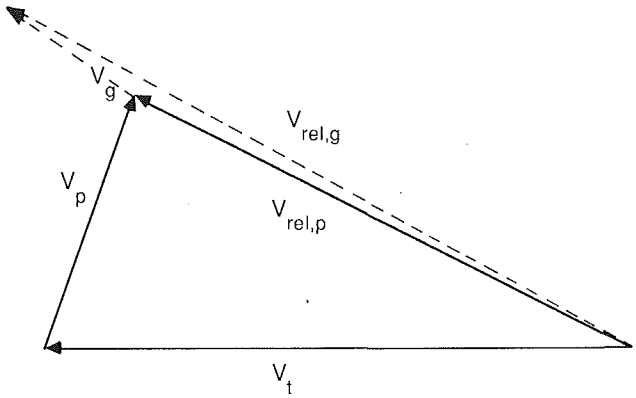

(a) Velocity Triangle near Leading Edge

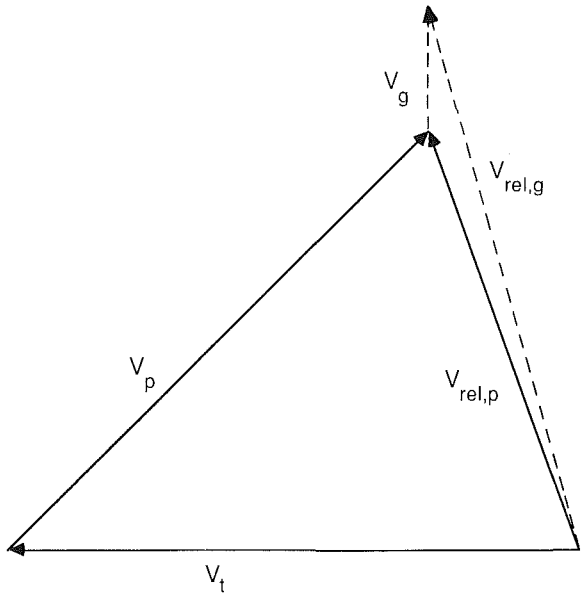

(b) Velocity Triangle near Trailing Edge

Fig. 7 Velocities relative to shroud

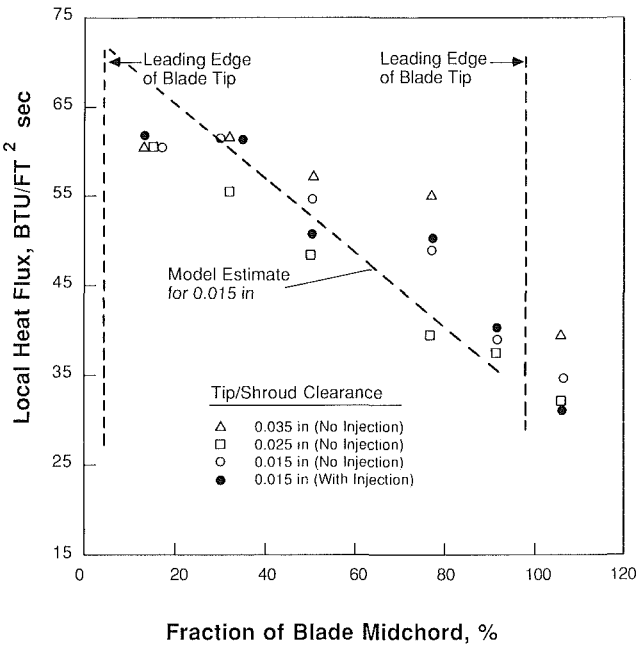

Fig. 8 Measured and estimated time-averaged shroud heat flux

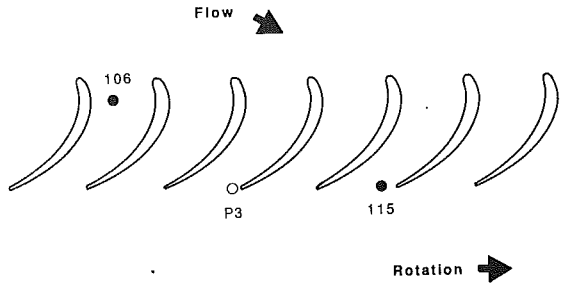

Fig. 9 Heat flux and pressure gage locations

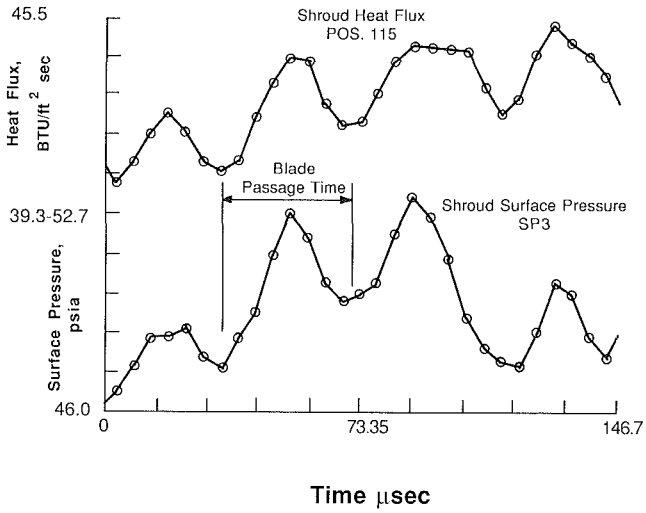

Fig. 10 Time-resolved shroud pressures and heat flux

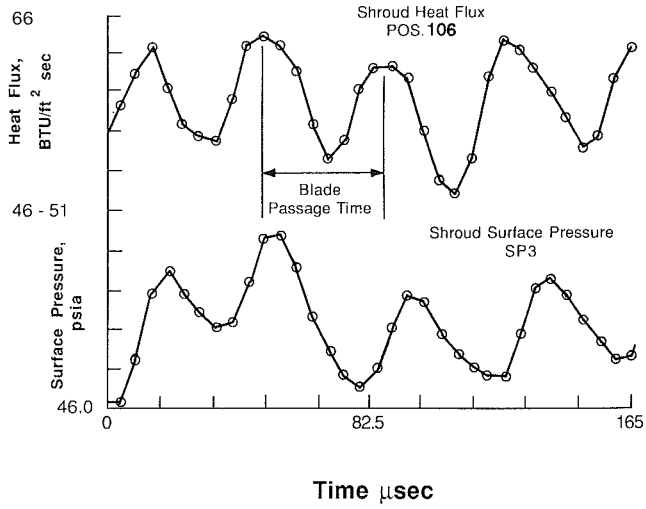

Fig. 11 Time-resolved shroud pressures and heat flux

Here it is evident that the leakage flow influence on the velocities near the shroud extends over a considerable fraction of the circumferential distance between blades.

Closure

A simple model describing flow over an axial turbine blade tip and relative to the adjacent stationary shroud can be used to estimate both tip and shroud heat transfer provided that reasonable estimates of the clearance gap size and clearance leakage flow can be made. The present work, through use of a powerful and general numerical code to compute the leakage

flow rate, links the model to a specific turbine geometry and operating point for which a unique set of measured local tip and shroud heat fluxes are available. The resulting comparisons between the model estimates and measured heat transfer, on both a time-averaged and time-resolved basis, demonstrate very good agreement in the trends and overall features of the heat transfer, and quite good agreement in numerical magnitudes as well. The model should thus prove useful in the understanding and interpretation of measured data from subsequent similar test programs, and should additionally prove useful for providing early design estimates of the levels of tip and shroud heat transfer that need to be compensated for by active turbine cooling.

Acknowledgments

This work was supported by the U.S. Air Force Aero Propulsion Laboratory, Wright-Patterson Air Force Base under Exploratory Development Funds. The technical monitor for this effort is Dr. William Troha.

References

Allen, H. W., and Kofskey, M. G., 1955, "Visualization Study of Secondary Flows in Turbine Rotor Tip Regions," NACA TN 3519.

Bindon, J. P., 1986, "Visualisation of Axial Turbine Tip Clearance Using a Linear Cascade," Report No. CUDEA/A-Turbo TR122, Whittle Laboratory, Cambridge University, United Kingdom.

Boelter, L. M. K., Young, G., and Iverson, H. W., 1945, "An Investigation of Aircraft Heaters. XXVII—Distribution of Heat Transfer Rate in the Entrance Region of a Tube," NACA TN 1451.

Booth, T. C., Dodge, P. R., and Hepworth, H. K., 1982, "Rotor-Tip Leakage: Part I—Basic Methodology," ASME *Journal of Engineering for Power*, Vol. 104, pp. 154–161.

Chyu, M. K., Metzger, D. E., and Hwan, C. L., 1987, "Heat Transfer in Shrouded Rectangular Cavities," *AIAA J. Thermophysics and Heat Transfer*, Vol. 1, pp. 247–252.

Dunn, M. G., Rae, W. J., and Holt, J. L., 1984a, "Measurement and Analysis of Heat Flux Data in a Turbine Stage: Part I—Description of Experimental Apparatus and Data Analysis," ASME *Journal of Engineering for Gas Turbines and Power*, Vol. 106, pp. 229–240.

Dunn, M. G., Rate, W. J., and Holt, J. L., 1984b, "Measurement and Analysis of Heat Flux Data in a Turbine Stage: Part II—Discussion of Results and Comparison With Predictions," ASME *Journal of Engineering for Gas Turbines and Power*, Vol. 106, pp. 229–240.

Dunn, M. G., Martin, H. L., and Stanek, M. J., 1986, "Heat-Flux and Pressure Measurements and Comparison with Prediction for a Low-Aspect-Ratio Turbine Stage," ASME JOURNAL OF TURBOMACHINERY, Vol. 108, pp. 108–115.

Dunn, M. G., 1990, "Phase and Time-Resolved Measurements of Unsteady Heat Transfer and Pressure in a Full-Stage Rotating Turbine," ASME JOURNAL OF TURBOMACHINERY, Vol. 112, pp. 531–538.

Epstein, A. H., Guenette, G. R., Norton, R. J. G., and Yuzhang, C., 1985, "Time Resolved Measurements of a Turbine Rotor Stationary Tip Casing Pressure and Heat Transfer Field," AIAA Paper No. 85-1220.

Graham, Y. A. H., 1986. "Investigation of a Tip Clearance Cascade in a Water Analogy Rig," ASME *Journal of Engineering for Gas Turbines and Power*, Vol. 108, pp. 38–46.

Hah, C., 1984, "A Navier-Stokes Analysis of Three-Dimensional Turbulent Flows Inside Turbine Blade Rows at Design and Off-Design Conditions," ASME *Journal of Engineering for Gas Turbines and Power*, Vol. 106, pp. 421–429.

Henneke, D. K., 1984, "Heat Transfer Problems in Aero-Engines," *Heat and Mass Transfer in Rotating Machinery*, Hemisphere Publishing Company, Washington, DC, pp. 353–379.

Kays, W. M., and Crawford, M. E., 1980, *Convective Heat and Mass Transfer*, McGraw-Hill, New York.

Mayle, R. E., and Metzger, D. E., 1982, "Heat Transfer at the Tip of Unshrouded Turbine Blade," *Proceedings, Seventh International Heat Transfer Conference*, Vol. 3, pp. 87–92.

Metzger, D. E., and Rued, K., 1989, "The Influence of Turbine Clearance Gap Leakage on Flowpath Velocities and Heat Transfer, Part I: Sink Flow Effects on Blade Pressure Sides," ASME JOURNAL OF TURBOMACHINERY, Vol. 111, pp. 284–292.

Moore, J., and Tilton, J. S., 1988, "Tip Leakage Flow in a Linear Turbine Cascade," ASME JOURNAL OF TURBOMACHINERY, Vol. 110, pp. 18–26.

Wadia, A. R., and Booth, T. C., 1982, "Rotor-Tip Leakage: Part II—Design Optimization Through Viscous Analysis and Experiment," ASME *Journal of Engineering for Power*, Vol. 104, pp. 162–169.